



**HAL**  
open science

# Optimization of innovative AlN-based stacks and texturing on 2D-MoS<sub>2</sub> - Applications to acoustic wave resonators and power electronics

Julien Patouillard

► **To cite this version:**

Julien Patouillard. Optimization of innovative AlN-based stacks and texturing on 2D-MoS<sub>2</sub> - Applications to acoustic wave resonators and power electronics. Materials Science [cond-mat.mtrl-sci]. Université Grenoble Alpes [2020-..], 2023. English. NNT: 2023GRALI041 . tel-04207122

**HAL Id: tel-04207122**

**<https://theses.hal.science/tel-04207122>**

Submitted on 14 Sep 2023

**HAL** is a multi-disciplinary open access archive for the deposit and dissemination of scientific research documents, whether they are published or not. The documents may come from teaching and research institutions in France or abroad, or from public or private research centers.

L'archive ouverte pluridisciplinaire **HAL**, est destinée au dépôt et à la diffusion de documents scientifiques de niveau recherche, publiés ou non, émanant des établissements d'enseignement et de recherche français ou étrangers, des laboratoires publics ou privés.

# THÈSE

Pour obtenir le grade de

## DOCTEUR DE L'UNIVERSITÉ GRENOBLE ALPES

École doctorale : I-MEP2 - Ingénierie - Matériaux, Mécanique, Environnement, Energétique, Procédés, Production

Spécialité : 2MGE - Matériaux, Mécanique, Génie civil, Electrochimie

Unité de recherche : Science et Ingénierie des Matériaux et Procédés

### Optimisation d'empilements innovants à base d'AlN et texturation sur 2D-MoS<sub>2</sub> - Applications aux résonateurs à ondes acoustiques et à l'électronique de puissance

### Optimization of innovative AlN-based stacks and texturing on 2D-MoS<sub>2</sub> - Applications to acoustic wave resonators and power electronics

Présentée par :

**Julien PATOUILLARD**

#### Direction de thèse :

**Elisabeth BLANQUET**

DIRECTRICE DE RECHERCHE, Université Grenoble Alpes

Directrice de thèse

**Arnaud MANTOUX**

Grenoble 1

Co-encadrant de thèse

**Rémy GASSILLOUD**

CEA

Co-encadrant de thèse

#### Rapporteurs :

**Yvon CORDIER**

DIRECTEUR DE RECHERCHE, CNRS délégation Côte d'Azur

**Bertrand DUBUS**

DIRECTEUR DE RECHERCHE, CNRS délégation Hauts-de-France

#### Thèse soutenue publiquement le **20 juin 2023**, devant le jury composé de :

**Elisabeth BLANQUET**

DIRECTRICE DE RECHERCHE, CNRS délégation Alpes

Directrice de thèse

**Yvon CORDIER**

DIRECTEUR DE RECHERCHE, CNRS délégation Côte d'Azur

Rapporteur

**Bertrand DUBUS**

DIRECTEUR DE RECHERCHE, CNRS délégation Hauts-de-France

Rapporteur

**Edwige BANO**

PROFESSEUR DES UNIVERSITÉS, Grenoble INP

Présidente

**Ionut RADU**

INGENIEUR DOCTEUR, SOITEC

Examineur

**Gabriel FERRO**

DIRECTEUR DE RECHERCHE, CNRS délégation Rhône Auvergne

Examineur

#### Invités :

**Mathieu BERNARD**

INGENIEUR DE RECHERCHE, CEA-LETI

**Rémy GASSILLOUD**

INGENIEUR DE RECHERCHE, CEA-LETI





## Acknowledgments

*Les travaux de recherche présentés dans ce manuscrit sont issus de la collaboration entre STMicroelectronics, le CEA-LETI et le laboratoire SIMaP.*

*J'adresse mes premiers remerciements aux membres du jury, Mme Edwige BANO, M. Yvon CORDIER, M. Bertrand DUBUS, M. Gabriel FERRO et M. Ionut RADU, d'avoir accepté d'évaluer ce travail.*

*Je tiens également à remercier chaleureusement mes (nombreux) encadrants, Mathieu BERNARD, Elisabeth BLANQUET, Frédéric GIANESELO, Rémy GASSILLOU, Arnaud MANTOUX et Christine RAYNAUD, pour leurs conseils, leur soutien et leur confiance. Merci Mathieu pour ta bonne humeur, ton investissement sur la partie PVD, les (nombreuses) discussions scientifiques (avec Rémy) et, bien entendu, d'être ardéchois ! Merci Elisabeth d'avoir accepté de diriger cette thèse, pour ton aide sur les aspects thermodynamiques et la correction du manuscrit. Merci Fred pour ta disponibilité malgré le contexte sanitaire difficile que nous avons traversé, ton recul scientifique et la vision industrielle que tu as su m'inculquer. Merci Rémy pour ta volonté de tirer le meilleur de moi-même, ta curiosité scientifique et tes qualités humaines. Merci Arnaud de m'avoir proposé ce sujet de thèse, pour ton implication sur la partie ALD et ton humour (particulier ?). Nous aurons le temps courir ensemble après cette fabuleuse aventure. Enfin, merci Christine pour ta capacité à fédérer une équipe, ton écoute attentive et l'ensemble des valeurs que tu t'es efforcée de me transmettre en tant que cheffe de projet.*

*La richesse et pluridisciplinarité de cette thèse se retrouve également dans la collaboration des équipes avec qui j'ai eu l'opportunité d'échanger.*

*Ainsi, au SIMaP, je remercie Muriel BRACCINI pour son aide sur la problématique de délamination et les essais de nanoindentation, Alexandre CRISCI pour le Raman et l'ALD, Frédéric MERCIER, Roman REBOUD et Vincent TABOURET pour leur aide sur le four « Stuart », Gilles RENOU pour les analyses ACOM, Thierry ENCINAS et Stéphane COINDEAU pour la DRX, Yves WOUTERS pour les problématiques de diffusion, et bien évidemment, l'ensemble de l'équipe TOP. Une pensée particulière et remplie de courage aux thésards d'Arnaud : Yanis et Pauline !*

*Au CEA-LETI, un merci tout particulier à Frédéric BARBIER, Amélie DUSSAIGNE, Bérangère HYOT et Guillaume VEUX pour votre contribution sur la partie MOCVD, Stéphane CADOT pour ton aide sur le matériau MoS<sub>2</sub> ainsi que Ludovic DUPRÉ et Romain THIBON pour la réalisation des dispositifs acoustiques. Un grand merci également à Nicolas BERNIER pour les analyses TEM/EDX, Nicolas GAUTHIER pour les caractérisations et discussions XPS, Roselyne TEMPLIER pour l'AFM, Nicolas VAXELAIRE, Yann MAZEL, Jérôme RICHY et Patrice GERGAUD pour les caractérisations DRX ainsi que Fabrice PERRIN et Leïla FELLOUH pour leur aide respective sur la SIGMA PVD et la CLN200. Et merci à mes collègues de bureau que j'ai vu passer (mais que j'ai aussi dû abandonner), particulièrement Bbob, Clément, Louis-David et Nicolas.*

*Je remercie l'ensemble de l'équipe IDNA RFSS de Crolles, particulièrement à Joao AZEVEDO GONCALVES, Françoise BAILLE, Cybelle BELEM GONCALVES, Simon BOUVOT, Michel BUCKZO, Romain DEBROUCKE, Cédric DURAND, Ophélie FOISSEY, Daniel GLORIA, Gérard HAURY, Metig*

## **Acknowledgments**

*HELLO, Sébastien JAN, David OUATTARA et Florence SONNERAT. Même si nos activités de recherches diffèrent, merci de m'avoir accueilli si chaleureusement lors de mes (trop) rares passages. J'adresse une pensée toute particulière aux thésards de Fred : David Alexander et Baptiste. Courage pour la dernière ligne droite !*

*Je tiens à remercier mes ami(e)s pour leur soutien au quotidien, les fous rires et bons moments que nous avons partagé et ceux qui nous attendent.*

*Enfin, merci à ma famille, et particulièrement mon frère et mes parents. Eddy, tu as toujours été un modèle à mes yeux dans les études comme dans la vie. Mon parcours est indéniablement lié à ton attitude exemplaire et cette volonté de réussir. Maman, papa, merci pour votre soutien, votre confiance et votre bienveillance. Les valeurs que vous m'avez inculquées sont à l'origine de ce travail.*

## Table of contents

<b>ACKNOWLEDGMENTS</b>	<b>2</b>
<b>TABLE OF CONTENTS</b>	<b>4</b>
<b>GLOSSARY</b>	<b>8</b>
<b>LIST OF FIGURES</b>	<b>9</b>
<b>LIST OF TABLES</b>	<b>13</b>
<b>GENERAL INTRODUCTION</b>	<b>14</b>
<b>CONTEXT</b>	<b>14</b>
<b>CHALLENGES</b>	<b>14</b>
<b>AIM OF THE THESIS AND ORGANIZATION OF THE MANUSCRIPT</b>	<b>15</b>
<b>I. CHAPTER 1: CONTEXT AND PHD APPLICATIONS</b>	<b>18</b>
<b>I.1. AN INTRODUCTION TO RF FRONT-END MODULE MARKET</b>	<b>19</b>
I.1.1. OVERVIEW	19
I.1.2. FOCUS ON FILTERS MARKET	20
<b>I.2. ACOUSTIC DEVICES</b>	<b>23</b>
I.2.1. PIEZOELECTRIC FORMALISM	23
I.2.2. OPERATING FREQUENCIES AND APPLICATIONS OF ACOUSTIC DEVICES	30
I.2.3. SURFACE ACOUSTIC WAVE (SAW) TECHNOLOGY	32
I.2.4. BULK ACOUSTIC WAVE (BAW) TECHNOLOGY	38
I.2.5. CONCLUSIONS ON ACOUSTIC DEVICES	43
<b>I.3. CHALLENGES, LINES OF RESEARCH</b>	<b>45</b>
<b>I.4. THESIS OBJECTIVES</b>	<b>46</b>
<b>II. CHAPTER 2: STATE OF THE ART ON THE GROWTH OF ALN AND DOPED ALN</b>	<b>48</b>
<b>II.1. ALUMINUM NITRIDE (ALN): BASIC PROPERTIES</b>	<b>49</b>
II.1.1. STRUCTURAL PROPERTIES	49
II.1.2. PIEZOELECTRIC PROPERTIES	50
II.1.3. MECHANICAL PROPERTIES	52
II.1.4. THERMAL PROPERTIES	52
II.1.5. OPTICAL AND ELECTRICAL PROPERTIES	53
<b>II.2. ALN ELABORATION PROCESS</b>	<b>54</b>
II.2.2. BULK GROWTH	54
II.2.3. THIN FILMS ELABORATION	56
<b>II.3. ENHANCEMENT OF ALN PIEZOELECTRIC PROPERTIES WITH DOPING</b>	<b>86</b>
II.3.1. DOPING ELEMENTS	86

II.3.2.	FOCUS ON SCANDIUM (Sc) DOPING	89
II.3.3.	CONCLUSIONS ALN PIEZOELECTRIC PROPERTIES ENHANCEMENT WITH A DOPING ELEMENT	95
<b>II.4.</b>	<b>CONCLUSIONS OF CHAPTER 2</b>	<b>96</b>
<b>III. CHAPTER 3: DEPOSITION OF ALN FILMS BY PHYSICAL VAPOR DEPOSITION (PVD) ON A 2D-MOS<sub>2</sub> LAYER</b>		<b>98</b>
<b>III.1.</b>	<b>2D-MOS<sub>2</sub> MATERIAL</b>	<b>99</b>
III.1.1.	MOS <sub>2</sub> STRUCTURE AND PROPERTIES	99
III.1.2.	DEPOSITION OF MOS <sub>2</sub> LAYERS	100
III.1.3.	CHARACTERIZATIONS OF MOS <sub>2</sub> MONOLAYERS	103
<b>III.2.</b>	<b>ALN PVD DEPOSITION ON 2D-MOS<sub>2</sub> SEED LAYER</b>	<b>110</b>
III.2.1.	EXISTING SOLUTIONS TO ALN DEPOSITION AND COMPATIBILITY WITH 2D-MOS <sub>2</sub> SEED LAYER	110
III.2.2.	INTEREST OF TMDs (MOs <sub>2</sub> AND WS <sub>2</sub> ) IN ALN TEXTURING	112
III.2.3.	DESCRIPTION OF ALN PVD DEPOSITION PROCESS	114
III.2.4.	CHARACTERIZATIONS OF ALN FILMS DEPOSITED BY PVD ON 2D-MOS <sub>2</sub> SEED LAYER	115
<b>III.3.</b>	<b>DELAMINATION ISSUE AND POTENTIAL SOLUTIONS</b>	<b>123</b>
III.3.1.	ORIGINS OF THE DELAMINATION	124
III.3.2.	PROPOSED SOLUTIONS TO THE DELAMINATION ISSUE	129
<b>III.4.</b>	<b>CONCLUSIONS OF CHAPTER 3</b>	<b>132</b>
<b>IV. CHAPTER 4: THERMOCHEMICAL MODIFICATION OF 2D-MOS<sub>2</sub></b>		<b>134</b>
<b>IV.1.</b>	<b>PLASMA TREATMENTS</b>	<b>135</b>
IV.1.1.	DESCRIPTION OF ALTACVD EQUIPMENT AND PLASMA CONDITIONS	135
IV.1.2.	PLASMA TREATMENTS (NH <sub>3</sub> , H <sub>2</sub> AND N <sub>2</sub> ) ON MOS <sub>2</sub> REFERENCE SAMPLE	136
IV.1.3.	PLASMA TREATMENTS (N <sub>2</sub> ) WITH ALN PVD SEED LAYER	140
IV.1.4.	SECOND THICK ALN GROWTH AFTER PLASMA TREATMENT	150
IV.1.5.	CONCLUSIONS AND PERSPECTIVES ON PLASMA TREATMENTS	151
<b>IV.2.</b>	<b>THERMAL HEAT TREATMENTS</b>	<b>153</b>
IV.2.1.	DESCRIPTION OF HOME-MADE FURNACE EQUIPMENT AND EXPERIMENTAL CONDITIONS	153
IV.2.2.	THERMAL BUDGET IMPACT ON MOS <sub>2</sub> REFERENCE SAMPLE	154
IV.2.3.	THERMAL HEAT TREATMENTS UNDER H <sub>2</sub> , N <sub>2</sub> AND NH <sub>3</sub> ON MOS <sub>2</sub> REFERENCE SAMPLE	158
IV.2.4.	THERMAL HEAT TREATMENTS UNDER NH <sub>3</sub> WITH ALN PVD SEED LAYER	167
<b>IV.3.</b>	<b>CONCLUSIONS OF CHAPTER 4</b>	<b>183</b>
<b>V. CHAPTER 5: ALN AND SC DOPED ALN GROWTH POST 2D-MOS<sub>2</sub> CHEMICAL MODIFICATION</b>		<b>186</b>
<b>V.1.</b>	<b>ELABORATION OF ALN FILMS BY PHYSICAL VAPOR DEPOSITION (PVD) POST-MOS<sub>2</sub> MODIFICATION</b>	<b>187</b>
V.1.1.	CHARACTERIZATIONS	187
V.1.2.	CONCLUSIONS OF ALN PVD DEPOSITION POST-MOS <sub>2</sub> MODIFICATION	194
<b>V.2.</b>	<b>ELABORATION OF SCANDIUM (Sc) DOPED ALN FILMS BY PHYSICAL VAPOR DEPOSITION (PVD) POST-MODIFICATION</b>	<b>195</b>
V.2.1.	DESCRIPTION OF SC DOPED ALN PVD DEPOSITION EQUIPMENT	195
V.2.2.	CHARACTERIZATIONS	196
V.2.3.	CONCLUSIONS OF SC DOPED ALN PVD DEPOSITION POST-MOS <sub>2</sub> MODIFICATION	202

<b>V.3. ELABORATION OF ALN FILMS BY CHEMICAL VAPOR DEPOSITION (CVD) POST-MOS<sub>2</sub> MODIFICATION</b>	<b>204</b>
V.3.1. DESCRIPTION OF THE CVD DEPOSITION PROCESS	204
V.3.2. CHARACTERIZATIONS	204
V.3.3. CONCLUSIONS OF ALN MOCVD DEPOSITION POST-MODIFICATION	211
<b>V.4. CONCLUSIONS OF CHAPTER 5</b>	<b>213</b>
<b><u>VI. CHAPTER 6: OPENING TO GAN AND SiC REGROWTH BY CVD</u></b>	<b><u>216</u></b>
<b>VI.1. INTEREST OF GAN AND SiC MATERIALS</b>	<b>217</b>
<b>VI.2. GROWTH OF GAN BY MOCVD</b>	<b>219</b>
VI.2.1. DESCRIPTION OF GAN MOCVD DEPOSITION PROCESS	219
VI.2.2. RESULTS	219
VI.2.3. CONCLUSIONS AND PERSPECTIVES ON GAN MOCVD GROWTH	225
<b>VI.3. GROWTH OF SiC BY CVD</b>	<b>226</b>
VI.3.1. DESCRIPTION OF SiC CVD DEPOSITION PROCESS	226
VI.3.2. RESULTS	228
VI.3.3. CONCLUSIONS AND PERSPECTIVES ON SiC CVD GROWTH	231
<b>VI.4. CONCLUSIONS OF CHAPTER 6</b>	<b>232</b>
<b><u>GENERAL CONCLUSIONS AND PERSPECTIVES</u></b>	<b><u>234</u></b>
REMINDER OF THE CONTEXT AND THESIS OBJECTIVE	234
RESULTS SUMMARY	234
PERSPECTIVES	235
<b><u>REFERENCES</u></b>	<b><u>238</u></b>
<b><u>ANNEX PART 1: LITERATURE REVIEW OF ALN AND DOPED ALN THIN FILMS DEPOSITION</u></b>	<b><u>268</u></b>
<b><u>ANNEX PART 2: EXPERIMENTAL CONDITIONS AND THEORETICAL MODELS</u></b>	<b><u>282</u></b>
<b>II.1. CHARACTERIZATIONS METHODS</b>	<b>282</b>
II.1.1. RAMAN SPECTROSCOPY	282
II.1.2. X-RAY PHOTOELECTRON SPECTROSCOPY (XPS)	282
II.1.3. ATOMIC FORCE MICROSCOPY (AFM)	282
II.1.4. X-RAY DIFFRACTION (XRD) AND X-RAY REFLECTOMETRY (XRR)	282
II.1.5. TRANSMISSION ELECTRON MICROSCOPY AND ENERGY DISPERSIVE X-RAY (TEM/EDX)	287
II.1.6. SCANNING ELECTRON MICROSCOPY (SEM)	287
II.1.7. AUTOMATIC CRYSTAL AND ORIENTATION MAPPING (ACOM)	288
<b>II.2. THEORY OF BEUTH MODEL</b>	<b>288</b>
<b>II.3. WAGNER'S THEORY</b>	<b>291</b>
<b>II.4. FICK'S LAWS</b>	<b>291</b>
<b><u>ANNEX PART 3: COMPLEMENTARY RESULTS</u></b>	<b><u>294</u></b>



<b>III.1. X-RAY REFLECTOMETRY (XRR)</b>	<b>294</b>
III.1.1. COMPARISON OF $\text{MoS}_2$ XRR PATTERN FITTING WITH TWO SOFTWARE	294
III.1.2. CORRESPONDENCE BETWEEN ALN DEPOSITION TIME AND THICKNESS	294
<b>III.2. X-RAY PHOTOELECTRON SPECTROSCOPY (XPS)</b>	<b>295</b>
III.2.1. $\text{SiO}_2/\text{MoS}_2$ STACK AND DELAMINATED AREA	295
III.2.2. $\text{MoS}_2$ REFERENCE AND $\text{MoS}_2 + \text{ALN}$ XS <i>BP</i> (BEFORE PLASMA) AND <i>AP</i> (AFTER PLASMA)	296
III.2.3. $\text{MoS}_2$ REFERENCE AND AFTER 700 °C AND 1000 °C VACUUM HEAT TREATMENT	301
III.2.4. $\text{MoS}_2 + \text{ALN}$ XS BEFORE AND AFTER 1000 °C $\text{NH}_3$ HEAT TREATMENT	302
<b>III.3. ATOMIC FORCE MICROSCOPY (AFM)</b>	<b>304</b>
<b>III.4. ALN/<math>\text{MoS}_2</math> LOCAL ETCHING AND EPITAXIAL LATERAL OVER GROWTH (ELOG)</b>	<b>306</b>
III.4.1. EXPERIMENTAL CONDITIONS	306
III.4.2. DIMENSIONAL OPTIMIZATION (PATTERN AND ALN THICKNESS)	307
III.4.3. CHEMICAL OPTIMIZATION (STRIPPING STEP)	308
III.4.4. CONCLUSIONS ON ALN/ $\text{MoS}_2$ LOCAL ETCHING	310
<b>RESUME DE LA THESE EN FRANÇAIS</b>	<b>312</b>
<hr/>	
<b>I. CONTEXTE ET INTRODUCTION</b>	<b>312</b>
I.1. FILTRES ACOUSTIQUES	312
I.2. CHALLENGES ET OBJECTIFS DE LA THESE	313
<b>II. LES MATERIAUX ALN ET <math>\text{MoS}_2</math></b>	<b>314</b>
<b>III. TEXTURATION DE L'ALN SUR <math>\text{MoS}_2</math></b>	<b>315</b>
<b>IV. PROBLEMATIQUE DE DELAMINATION ET SOLUTION</b>	<b>316</b>
<b>V. RESULTATS</b>	<b>318</b>
V.1. DEPOTS D'ALN PAR PVD	318
V.2. DEPOTS D'ALN DOPES AU SCANDIUM (Sc) PAR PVD	319
V.3. OUVERTURE VERS DES DEPOTS CVD HAUTE TEMPERATURE	321
<b>VI. CONCLUSIONS ET PERSPECTIVES</b>	<b>321</b>

## Glossary

**2D:** 2-Dimensional

**ACOM:** Automatic Crystal and Orientation Mapping

**ALD:** Atomic Layer Deposition

**AlN:** Aluminum Nitride

**AFM:** Atomic Force Microscopy

**BAW:** Bulk Acoustic Wave

**CVD:** Chemical Vapor Deposition

**EDX:** Energy Dispersive X-Ray

**FEM:** Front End Module

**GaN:** Gallium Nitride

**MOCVD:** Metal Organic Chemical Vapor Deposition

**MoS<sub>2</sub>:** Molybdenum disulphide

**PVD:** Physical Vapor Deposition

**RC:** Rocking Curve

**RF:** Radio Frequency

**SAW:** Surface Acoustic Wave

**Sc<sub>x</sub>Al<sub>1-x</sub>N:** Scandium doped Aluminum Nitride

**SEM:** Scanning Electron Microscopy

**SiC:** Silicon Carbide

**TEM:** Transmission Electron Microscopy

**VdW:** Van der Waals

**XPS:** X-Ray Photoelectron Spectroscopy

**XRD:** X-Ray Diffraction

**XRR:** X-Ray Reflectometry

## List of Figures

Figure I.1: RF Front-End Market Value Forecast by component.....	19
Figure I.2: Filter Market volume forecast.....	20
Figure I.3: Filter Market value Forecast.....	22
Figure I.4: a) Direct piezoelectric effect ; b) Inverse piezoelectric effect.....	23
Figure I.5: Grouping of 32 crystal classes as a function of their piezoelectric, pyroelectric and ferroelectric properties.....	24
Figure I.6: Piezoelectric thin film deposited onto a substrate ( $t_{\text{substrate}} \gg t_{\text{film}}$ ).....	26
Figure I.7: Market application and frequency band allocation of RF filtering technology.....	31
Figure I.8: Basic structure of a Surface Acoustic Wave (SAW) resonator.....	32
Figure I.9: a) Typical frequency response of an acoustic resonator ; b) two-stages ladder type SAW filter and its typical frequency response.....	33
Figure I.10: Structure of a bulk Surface Acoustic Wave (bulk SAW) resonator.....	34
Figure I.11: Structure of a Temperature-Compensated Surface Acoustic Wave (TC-SAW) resonator.....	35
Figure I.12: Structure of a Multi-Layer Surface Acoustic Wave (ML-SAW) resonator.....	36
Figure I.13: Basic structure of Bulk Acoustic Wave (BAW) resonator.....	39
Figure I.14: Structure of a Film Bulk Acoustic Resonator (FBAR).....	40
Figure I.15: Structure of a Solid Mounted Resonator (SMR).....	41
Figure I.16: New BAW alternatives: XBAW, XBAR and cREO.....	42
Figure II.1: AlN hexagonal wurtzite structure with its Al and N tetrahedrons.....	49
Figure II.2: a) Tetrahedron environments of AlN ; b) Al and N polar faces (side view).....	50
Figure II.3: a) Schematic and b) image of a typical PVT growth setup.....	55
Figure II.4: Mosaicity of a perfect and real crystal.....	57
Figure II.5: Measurement of the mosaicity of an aluminum oxide single crystal.....	57
Figure II.6: Schematic illustration of random, textured and epitaxial film.....	58
Figure II.7: Typical ALD cycle.....	61
Figure II.8: Typical Chemical Vapor Deposition (CVD) process.....	64
Figure II.9: Cross-sectional TEM image and schematic illustration of an ELOG-AlN template on a sapphire substrate.....	69
Figure II.10: Graphic representation of AlN (002) RC obtained by MOCVD on silicon, sapphire and SiC (cubic and hexagonal) substrates.....	73
Figure II.11: Typical reactive sputtering process for AlN thin films deposition.....	75
Figure II.12: Lattice (002) oriented AlN film and silicon (100), (110) and (111) substrate surface.....	78
Figure II.13: Graphic representation of AlN (002) RC obtained by reactive sputtering on silicon, sapphire and SiC (cubic and hexagonal) substrates.....	83
Figure II.14: Comparison of AlN (002) RC elaborated by MOCVD or reactive sputtering.....	84
Figure II.15: Comparison of AlN (002) RC on silicon, sapphire, hexagonal SiC (4H- or 6H-SiC) and 3C-SiC.....	85
Figure II.16: Evolution of $d_{33}$ piezoelectric for the different used elements to dope AlN.....	89
Figure II.17: Evolution of $d_{33}$ piezoelectric coefficient and $c/a$ lattice constants ration with the Sc content.....	91
Figure II.18: Dark-field TEM images showing the cross-section of a cone-shape abnormal oriented grain (AOG) grown in the ScAlN film deposited on Si/Mo.....	92
Figure II.19: Sketch of the growth mechanism of AOG in ScAlN thin films.....	93
Figure II.20: Evolution of $k_{\text{eff}}^2$ and Q as a function of Sc content.....	94
Figure III.1: MoS <sub>2</sub> crystalline structure a) Side view ; b) Top view.....	99
Figure III.2: MoS <sub>2</sub> ALD deposition process (without rapid thermal annealing).....	101
Figure III.3: Rapid Thermal Annealing (RTA) to crystallize the amorphous deposit into MoS <sub>2</sub> .....	101
Figure III.4: a) Cross-sectional TEM of three MoS <sub>2</sub> monolayers prepared by ALD and after RTA ; b) Observation of MoS <sub>2</sub> monolayer oscillations.....	102
Figure III.5: Side view and top view of MoS <sub>2</sub> crystalline domains displaying a pronounced out-of-plane orientation (along c-axis) and a random in-plane orientation.....	103

Figure III.6: Typical Raman spectrum of a three MoS <sub>2</sub> monolayers synthesized in this work ; b) E <sup>1</sup> <sub>2g</sub> and A <sub>1g</sub> active Raman modes of MoS <sub>2</sub> .....	104
Figure III.7: Out-of-plane ; b) In-plane XRD of MoS <sub>2</sub> grown on Si (100)/SiO <sub>2</sub> (500 nm).....	105
Figure III.8: XRR pattern of three MoS <sub>2</sub> monolayers prepared on Si (100)/SiO <sub>2</sub> (500 nm) .....	107
Figure III.9: AFM measurement of a three MoS <sub>2</sub> monolayers prepared on Si (100)/SiO <sub>2</sub> (500 nm) .....	108
Figure III.10: Mo 3d XPS spectrum of a three MoS <sub>2</sub> monolayers prepared on Si (100)/SiO <sub>2</sub> (500 nm).....	109
Figure III.11: Top view of the MoS <sub>2</sub> and AlN crystalline structure .....	113
Figure III.12: SIGMA PVD equipment used for AlN PVD deposition.....	114
Figure III.13: Comparison of the typical MoS <sub>2</sub> Raman spectrum before and after 100 nm AlN PVD deposition .	115
Figure III.14: Cross-sectional TEM of the 100 nm AlN PVD deposited on a) MoS <sub>2</sub> (3 monolayers) ; SiO <sub>2</sub> (500 nm) .....	116
Figure III.15: Cross-sectional TEM at atomic resolution of the 100 nm AlN PVD deposited on a) MoS <sub>2</sub> (3 monolayers) ; b) SiO <sub>2</sub> (500 nm) ; c) Defects in MoS <sub>2</sub> monolayers.....	118
Figure III.16: AlN (002) RC measurements of a typical 100 nm AlN PVD deposited on different substrates (Si, SiO <sub>2</sub> or MoS <sub>2</sub> ) .....	119
Figure III.17: Out-of-plane (red) and in-plane (green) XRD of 100 nm AlN PVD deposited on MoS <sub>2</sub> (3 monolayers) .....	119
Figure III.18: a) a-lattice parameter ; b) strain as a function of sin <sup>2</sup> ψ for a 100 nm AlN PVD deposition grown on Si (100)/SiO <sub>2</sub> (500 nm)/ MoS <sub>2</sub> (3 monolayers).....	121
Figure III.19: Delamination on a 200 mm Si (100)/SiO <sub>2</sub> (500 nm)/MoS <sub>2</sub> (3 monolayers) wafer due to an AlN PVD deposition > 200 nm.....	123
Figure III.20: Tape test on 100 nm AlN PVD deposited on Si (100)/SiO <sub>2</sub> (500 nm)/MoS <sub>2</sub> (3 monolayers) .....	124
Figure III.21: Raman spectrum on a delaminated area.....	125
Figure III.22: Evolution of the chemical surface state before MoS <sub>2</sub> ALD deposition, after one ALD cycle, after annealing and after delamination. ....	126
Figure III.23: Illustration of the Epitaxial Lateral Over Growth (ELOG) process on AlN/MoS <sub>2</sub> .....	130
Figure III.24: Illustration of the schematic thermochemical modification of MoS <sub>2</sub> .....	131
Figure III.25: Illustration of the thermochemical modification of MoS <sub>2</sub> through a thin AlN seed layer .....	131
Figure IV.1: Illustration of the thermochemical modification of MoS <sub>2</sub> through a thin AlN layer .....	134
Figure IV.2: AltaCVD 300 mm equipment used for plasma treatments .....	136
Figure IV.3: Raman spectra of MoS <sub>2</sub> Reference sample after NH <sub>3</sub> , N <sub>2</sub> and H <sub>2</sub> plasma treatment.....	137
Figure IV.4: AFM images of MoS <sub>2</sub> Reference BP (Before Plasma) and AP (After Plasma) .....	138
Figure IV.5: Mo 3d XPS spectra of MoS <sub>2</sub> Reference BP (Before Plasma) and AP (After plasma) .....	139
Figure IV.6: XRR pattern of MoS <sub>2</sub> + AlN 4s BP.....	141
Figure IV.7: a) AlN thickness before and after N <sub>2</sub> plasma ; b) AlN roughness before and after N <sub>2</sub> plasma.....	143
Figure IV.8: AFM images of MoS <sub>2</sub> + AlN 4s BP (Before Plasma) and AP (After Plasma).....	144
Figure IV.9: Comparison of the AlN roughness determined by XRR and AFM before and after N <sub>2</sub> plasma. The inset presents the AFM images of MoS <sub>2</sub> + AlN 1s AP and MoS <sub>2</sub> + AlN 2s AP.....	145
Figure IV.10: Raman spectra of MoS <sub>2</sub> + AlN xs BP (Before Plasma) and AP (After Plasma).....	146
Figure IV.11: Variation in Δω as a function of AlN seed deposition time BP (Before Plasma) and AP (After Plasma) .....	147
Figure IV.12: Mo 3d XPS spectra of MoS <sub>2</sub> Reference, MoS <sub>2</sub> + AlN 4s BP (Before Plasma) and AP (After Plasma).....	148
Figure IV.13: AlN (002) RC measurements of the 100 nm AlN PVD regrowth after N <sub>2</sub> plasma treatment. The inset shows a thicker AlN PVD growth (300 nm) on a MoS <sub>2</sub> + AlN 3s AP sample. ....	151
Figure IV.14: Home-made furnace equipped with an in situ reflectance measurements system .....	154
Figure IV.15: Vacuum only experiments, temperature profiles ramping-up to a) 1000 °C ; b) 700 °C.....	155
Figure IV.16: Raman spectra of the MoS <sub>2</sub> reference samples before and after 700 °C and 1000 °C vacuum heat treatment.....	156
Figure IV.17: XPS spectra of Mo 3d of MoS <sub>2</sub> Reference sample before (bottom) and after (top) 700 °C vacuum heat treatment.....	157
Figure IV.18: a) H <sub>2</sub> ; b) N <sub>2</sub> and c) NH <sub>3</sub> heat treatment, temperature profiles ramping-up to 700 °C .....	159
Figure IV.19: Raman spectra of MoS <sub>2</sub> Reference sample after H <sub>2</sub> , N <sub>2</sub> and NH <sub>3</sub> 700 °C heat treatment .....	160

Figure IV.20: XPS spectra of a) Mo 3d ; b) Mo 3p/ N 1s of MoS <sub>2</sub> after 700 °C vacuum experiment (bottom) and 700 °C NH <sub>3</sub> experimented with a regulated pressure of 0.5 mbar (top).....	162
Figure IV.21: Evolution of the R405 component during the 700 °C NH <sub>3</sub> temperature plateau for different NH <sub>3</sub> pressures .....	163
Figure IV.22: a) dR405/dt ≈ 0 for the different NH <sub>3</sub> pressures investigated ; b) application of the rate law .....	164
Figure IV.23: XRR patterns of MoS <sub>2</sub> Reference before (red curve) and after 700 °C NH <sub>3</sub> heat treatment (black curve).....	165
Figure IV.24: Out-of-plane XRD measurement of MoS <sub>2</sub> Reference after 700 °C NH <sub>3</sub> heat treatment.....	166
Figure IV.25: RC measurements of MoS <sub>2</sub> Reference before and after 700 °C NH <sub>3</sub> heat treatment (0.5 and 50 mbar).....	167
Figure IV.26: Evolution of the R405 component during the 1000 °C NH <sub>3</sub> temperature plateau .....	169
Figure IV.27: a) AlN thickness and b) square of AlN thickness as a function of dR405/dt = max (inflection point) .....	171
Figure IV.28: Raman spectra of MoS <sub>2</sub> Reference before heat treatment and MoS <sub>2</sub> + AlN 8s after 1000 °C NH <sub>3</sub> heat treatment.....	172
Figure IV.29: XPS spectra of MoS <sub>2</sub> + AlN 4s, Mo 3d regions before and after 1000 °C NH <sub>3</sub> heat treatment.....	173
Figure IV.30: In-plane XRD diffractograms of MoS <sub>2</sub> + AlN xs a) before and b) after 1000 °C NH <sub>3</sub> heat treatment .....	175
Figure IV.31: Cross-sectionnal TEM images at different magnifications of MoS <sub>2</sub> + AlN 10.4s sample after 1000 °C NH <sub>3</sub> heat treatment.....	176
Figure IV.32: Energy dispersion mappings of the AlN/MoS <sub>2</sub> /SiO <sub>2</sub> interfaces after 1000 °C NH <sub>3</sub> heat treatment	177
Figure IV.33: Phase and orientations mappings obtained with ASTAR technique on MoS <sub>2</sub> + AlN 10.4s after 1000 °C NH <sub>3</sub> heat treatment .....	178
Figure IV.34: Mechanism proposal of the 2D-MoS <sub>2</sub> chemical modification through the AlN seed layer during 1000 °C NH <sub>3</sub> heat treatment .....	179
Figure IV.35: AlN (002) RC measurements of the 100 nm AlN PVD growth on MoS <sub>2</sub> + AlN xs samples after 1000 °C NH <sub>3</sub> heat treatment .....	180
Figure IV.36: RC AlN (002) of a 1 μm thick AlN PVD growth on MoS <sub>2</sub> + AlN 10.4s sample after 1000 °C NH <sub>3</sub> heat treatment ; b) pictures of tape test after the 1 μm AlN PVD deposition .....	181
Figure V.1: MoS <sub>2</sub> nitridation through the AlN PVD seed layer followed by AlN or Sc doped AlN growth.....	186
Figure V.2: Comparison of AlN (002) RC deposited by PVD on various silicon-based substrates from literature (black square), CEA-LETI capabilities (grey circle) and this work (blue triangle).....	187
Figure V.3: AlN equi-biaxial stress determined by XRD (CGM method) and Raman spectroscopy .....	189
Figure V.4 : AlN in-plane and out-of-plane strain determined via CGM method .....	190
Figure V.5: Cross sectional TEM of AlN PVD regrowth/AlN seed layer/MoN <sub>x</sub> /SiO <sub>2</sub> interfaces .....	191
Figure V.6: Energy dispersion mapping of the AlN PVDregrowth/AlN seed layer/MoN <sub>x</sub> /SiO <sub>2</sub> interfaces .....	192
Figure V.7: Virtual bright field, phase and orientation mapping of the AlN PVDregrowth/AlN seed layer/MoN <sub>x</sub> /SiO <sub>2</sub> interfaces .....	193
Figure V.8: Schematic representation of the CLUSTERLINE (CLN) 200 mm magnetron reactor.....	195
Figure V.9: Sc <sub>x</sub> Al <sub>1-x</sub> N (002) RC measurements for the different Sc investigated content.....	197
Figure V.10: Comparison of Sc <sub>x</sub> Al <sub>1-x</sub> N (002) RC deposited by PVD on various silicon-based substrates from literature (blacksquare), CEA-LETI capabilities (grey dash line) and this work (blue triangle).....	199
Figure V.11: Sc <sub>x</sub> Al <sub>1-x</sub> N equi-biaxial stress determined by XRD (CGM method).....	201
Figure V.12: a) In-plane ; b) out-of plane strain of Sc <sub>x</sub> Al <sub>1-x</sub> Ns and comparison with AlN strain.....	202
Figure V.13: AlN MOCVD (002) RC measurements and comparison with AlN PVD.....	205
Figure V.14: AlN (102) pole figure of the 600 nm thick AlN MOCVD sample .....	206
Figure V.15: SEM images of the AlN MOCVD samples top surface .....	207
Figure V.16: Cross-sectionnal TEM of AlN MOCVD/SiO <sub>2</sub> + particles interfaces after thick AlN 200 nm thick MOCVD growth.....	208
Figure V.17: Energy dispersion mapping of the AlN MOCVD/SiO <sub>2</sub> + particles interfaces.....	209
Figure V.18: Virtual bright field, phase and orientation mapping of the AlN MOCVD/SiO <sub>2</sub> + particles interfaces .....	210

*Figure VI.1: Potential applications of GaN and SiC from the aspects of outpower and operating frequency and comparison with Si* ..... 218

*Figure VI.2: Elaboration process of the 300 nm GaN MOCVD layer*..... 219

*Figure VI.3: SEM images of the surface morphology and stack representation of the 300 nm thick GaN grown at different temperatures*..... 220

*Figure VI.4: SEM images of the surface morphology of 600 nm thick GaN grown at 840 °C on an AlN PVD seed layer of 8s and 10.4s* ..... 221

*Figure VI.5: GaN (002) RC measurements of the 600 nm thick MOCVD layers deposited on 8s and 10.4s AlN seed layers*..... 222

*Figure VI.6: Elaboration process of the 300 nm GaN MOCVD layer with an in situ AlN MOCVD buffer layer* .... 223

*Figure VI.7: SEM images of the surface morphology of 300 nm thick GaN grown at 840 °C using the 200 nm AlN MOCVD buffer on an AlN PVD seed layer of 8s and 10.4s*..... 224

*Figure VI.8: GaN (002) RC measurements of the 300 thick MOCVD layers deposited on a 200 nm AlN MOCVD buffer layer with an AlN seed of 8s and 10.4s*..... 224

*Figure VI.9: Home-made reactor used for SiC CVD growth in LMI facilities* ..... 226

*Figure VI.10:  $2\theta/\omega$  scan with a  $\omega$  offset of  $3^\circ$  of the SiC-1 sample*..... 228

## List of Tables

Table I.1: Symbol, unit and matrix size of the electrical and mechanical components	25
Table I.2: Symbol, unit and matrix size of the four piezoelectric coefficients	25
Table I.3: Electromechanical coupling coefficient $k^2_{eff}$ , quality factor Q, FOM and availability of the main piezoelectric materials	29
Table I.4: Comparison of SAW resonator technologies	37
Table I.5: Comparison of BAW resonator technologies	43
Table I.6: Summary of SAW and BAW technologies	44
Table II.1: Comparison of the AlN piezoelectric coefficients (thin film and bulk)	51
Table II.2: AlN mechanical elastic constants issue from the literature	52
Table II.3: Bandgap, electric breakdown field and electron mobility of AlN	53
Table II.4: Lattice constants, CTE and corresponding mismatches between AlN and the main AlN growth substrates	60
Table III.1: Extracted values from the fitting of a XRR pattern of a three MoS <sub>2</sub> monolayers prepared on Si (100)/SiO <sub>2</sub> (500 nm)	107
Table III.2: Crystal structure and lattice parameters of WS <sub>2</sub> , MoS <sub>2</sub> and AlN	112
Table III.3: Comparison of the substrate, AlN deposition technique and AlN (002) RC obtained in this work with AlN deposition on 2D-TMDs from the literature.	120
Table III.4: In-plane and out-of-plane strains of AlN PVD 100 nm deposited on Si (100), SiO <sub>2</sub> (500 nm) and MoS <sub>2</sub> (3 monolayers)	122
Table III.5: AlN stiffness constants and equations for Transverse Young's and shear moduli calculations	128
Table III.6: Elastic energy release form the AlN film failure with the different $g(\alpha, \theta)$ and critical AlN thickness combinations	128
Table IV.1: Plasma treatment conditions investigated	136
Table IV.2: Extracted values from the MoS <sub>2</sub> + AlN 4s fitting and comparison with MoS <sub>2</sub> Reference sample	141
Table IV.3: Positions and FWHM of MoS <sub>2</sub> + AlN xs BP (before Plasma) and AP (After Plasma)	146
Table IV.4: Experimental conditions of the heat treatments performed on MoS <sub>2</sub> Reference samples	154
Table IV.5: Extracted positions and FWHM of $E^1_{2g}$ and $A_{1g}$ modes	156
Table IV.6: Experimental conditions of the NH <sub>3</sub> heat treatments performed in the home-made furnace on MoS <sub>2</sub> + AlN xs Characterizations	168
Table IV.7: Experimental conditions of the NH <sub>3</sub> heat treatments performed in AIXTRON on MoS <sub>2</sub> + AlN xs	172
Table V.1: List of Sc doped AlN samples elaborated by co-sputtering in this work	196
Table VI.1: Comparison of some properties, availability and cost of Si, AlN, 4H-SiC and GaN	217
Table VI.2: Experimental conditions for each SiC CVD growth	227
Table VI.3: AlN (002) and SiC (111) RC for each SiC samples	229

## General introduction

### Context

Tablets, watches, bracelets, headphones... Connected objects are everywhere. The most stark and prime example is surely smartphones with nearly 7 billion of users. These objects ensure the transmission and reception of data through various wireless communication technologies daily used: Bluetooth, Wi-Fi, cellular connections (2G to 5G)... This development of connected objects and wireless communication technologies thanks to the progress in microelectronics. Over the past 20 years, this industry has intensively grown, both from a technological (Moore's law) and economic (manufacturing cost reduction) point of view. Hence, the resulting connected objects are increasingly efficient, functional and compact. However, the current increase in complexity and functionality of these objects, and especially smartphones, do not longer translate by constraints relating to a reduction in size, cost or energy consumption, but by the wide distribution and use of these products and wireless communication technologies among the general public. This rapid development leads to a continuous exponential growth of associated data traffic. Hence, the frequency spectrum dedicated to mobile communication becomes overcrowded which results in more requirements for Radio-Frequency (RF) applications, especially concerning filtering technologies.

### Challenges

To address this challenge, the telecommunication industry has been relying on the introduction of additional frequency bands generally wider and positioned in higher frequency through new wireless technologies (6G or Wi-Fi 7). The current filtering technologies used in smartphones are Surface Acoustic Wave (SAW) and Bulk Acoustic Wave (BAW) filters. Their operating principle is respectively based on the propagation of surface and volume acoustic waves within a piezoelectric material. These devices are characterized by two parameters. First, the electromechanical coupling coefficient  $k^2_{\text{eff}}$  determines the bandwidth of the filter. The higher this value, the greater the bandwidth of the filter. Second, the quality factor  $Q$  characterizes the insertion loss (signal attenuation) and the selectivity of the filter. However, the current SAW and BAW technologies are not adapted to address wider and higher frequency band envisioned by the next standards.



On one hand, the low-cost SAW technology presents limitations in operating frequencies above 2 GHz. On the other hand, BAW technologies enable to operate at higher operating frequencies typically up to 3.5 GHz. However, the current crystalline quality of the Aluminum Nitride (AlN) piezoelectric material of AlN-based BAW devices is insufficient to address wider frequency bandwidth (limited  $k_{\text{eff}}^2$  around 7 %). Different lines of research have been investigated such as doped AlN with scandium (Sc) leading to an enhancement of the electromechanical coupling coefficient  $k_{\text{eff}}^2$  but to the detriment of quality factor Q. Another alternative is to improve AlN crystal quality, classically deposited by low-temperature sputtering reactive process using high-temperature deposition method such as Metal Organic Chemical Vapor Deposition (MOCVD) to tend towards a single crystal. However, the enhancement of  $k_{\text{eff}}^2$  remains to be proven and an AlN MOCVD deposition is significantly more expensive than a reactive sputtering growth which may limit a large-scale adoption.

### [Aim of the thesis and organization of the manuscript](#)

This work thesis takes place in this context. Its main objective is to develop an innovative and cost-effective solution to address the new challenges faced by RF filters technologies thanks to the collaboration between STMicroelectronics, CEA-LETI and SIMaP laboratory.

The **first chapter** aims at providing a quick overview of RF filters challenges. It enables to determine that BAW approach seems the most promising. Consequently, the main challenge is to propose an innovative solution to improve the AlN material quality using a low-temperature deposition technique on silicon-based substrate.

The **second chapter** presents the basic AlN properties and gives an overview of the challenges faced by the AlN growth as a bulk material or a thin film. The state of the art of AlN thin films elaboration enables to give tendencies about the obtained AlN crystal quality depending on the deposition method (Atomic Layer Deposition, Metal Organic Vapor Deposition or reactive sputtering) and growth substrate. The different AlN doping or co-doping element, especially scandium (Sc), and their impact on crystalline quality and piezoelectric properties are discussed.

The **third chapter** describes the innovative approach implemented in this work to improve AlN crystalline quality. It relies on the use of a two-dimensional molybdenum disulphide (2D-MoS<sub>2</sub>) material displaying a reasonable in-plane mismatching with AlN. Sputtered AlN thin

films with an enhanced crystal quality are synthesized. However, an inherent delamination issue related to the AlN/MoS<sub>2</sub> stack is identified and described.

The **fourth chapter** presents the investigated solutions based on the MoS<sub>2</sub> thermochemical modification to solve this inherent delamination issue, either by plasma or reactive heat treatments. The reactive heat treatment under ammonia demonstrates the proof of concept of the resolution of the delamination issue while preserving an enhanced AlN crystal quality. It opens a new low-cost and easier way to process high quality AlN thin films on silicon substrates.

The **fifth chapter** enables to confirm and deeply study the process developed in the previous chapter and the resulting quality of the AlN films. Hence, pure and Sc doped AlN sputtered films are elaborated. They both show an enhanced crystalline quality compared to what is achieved in the literature on silicon-based substrate. Finally, this approach has also been extended to AlN MOCVD deposition and lays the first stone to potential AlN MOCVD films on low-cost silicon substrate addressing power applications.

The **final and sixth chapter** opens up the growth perspectives which may result from the process developed in this work thesis to Gallium Nitride (GaN) and Silicon Carbide (SiC) CVD growth. Both materials are dominating the power market and display a reasonable in-plane lattice mismatch with AlN and MoS<sub>2</sub>.

Finally, the **Annex** of this work thesis are divided in three parts. The first part presents a non-exhaustive literature review of AlN and doped AlN crystal quality thin films. The second part briefly describes the characterization methods and the theoretical models used in this thesis. The third part shows complementary results, including a study based on AlN/MoS<sub>2</sub> local etching followed by an Epitaxial Lateral Over Growth (ELOG) which has been identified as a potential solution to the delamination issue.



## I. Chapter 1: Context and PhD applications

In recent years, the rapid development of wireless communication leads to a continuous exponential growth of associated data traffic. To address this challenge, the telecommunication industry has been relying on the introduction of additional frequency bands generally wider and positioned in higher frequency. The fifth generation of wireless communication (5G) is a good example with the introduction of new frequencies in C band (around 3.5 GHz) and in the millimeter wave spectrum (around 28 GHz). As it will be discussed in the next sections, the support of additional frequency bands poses a severe technical challenge since more filters need to be added in the architecture of the Radio Frequency (RF) system. Moreover, new wider frequency bands operating higher in frequency induce new requirements which may be difficult to address with incumbent acoustic filter technologies currently used in smartphone.

This chapter aims at providing a quick overview of RF filters challenges, in a first step by introducing Radio Frequency Front End Module (RF FEM) market to illustrate the importance of RF filters. In a second step, the filter market dominated by acoustic filters is detailed to provide a preliminary positioning of the various existing technologies. Subsequently, the different acoustic filters technologies are described in terms of structure and constitutive materials. Their operating frequencies, process complexity, advantages and limitations are presented and compared. Current materials challenges faced in acoustic filter technologies and new investigated alternatives are then discussed. Finally, the objectives of this thesis and proposed axis of research will be presented making the link with previously detailed acoustic filter market challenges.

I.1. An introduction to RF Front-End Module market

I.1.1. Overview

A Radio Frequency (RF) chain includes all the elements involved in the transmission and reception of RF waves. Basic functions can be identified such as amplification, switching or filtering. All these technologies are commonly called “RF Front-End” technologies. In recent years, the development of wireless communication experienced an exponential increase which has a direct impact on the RF FEM market size and associated technical requirements.

The creation of new technology and especially 5G boosts the RF Front-End module market. In fact, its development requires the addition of new frequency bands to complement existing ones and achieve higher data rate. Therefore, the frequency spectrum dedicated to mobile communication becomes overcrowded which results in more requirements for RF Front-End devices (especially concerning filtering technologies). This market value forecast by type of functions is presented in Figure I.1 and is based on the data of Yole Group <sup>1</sup>.

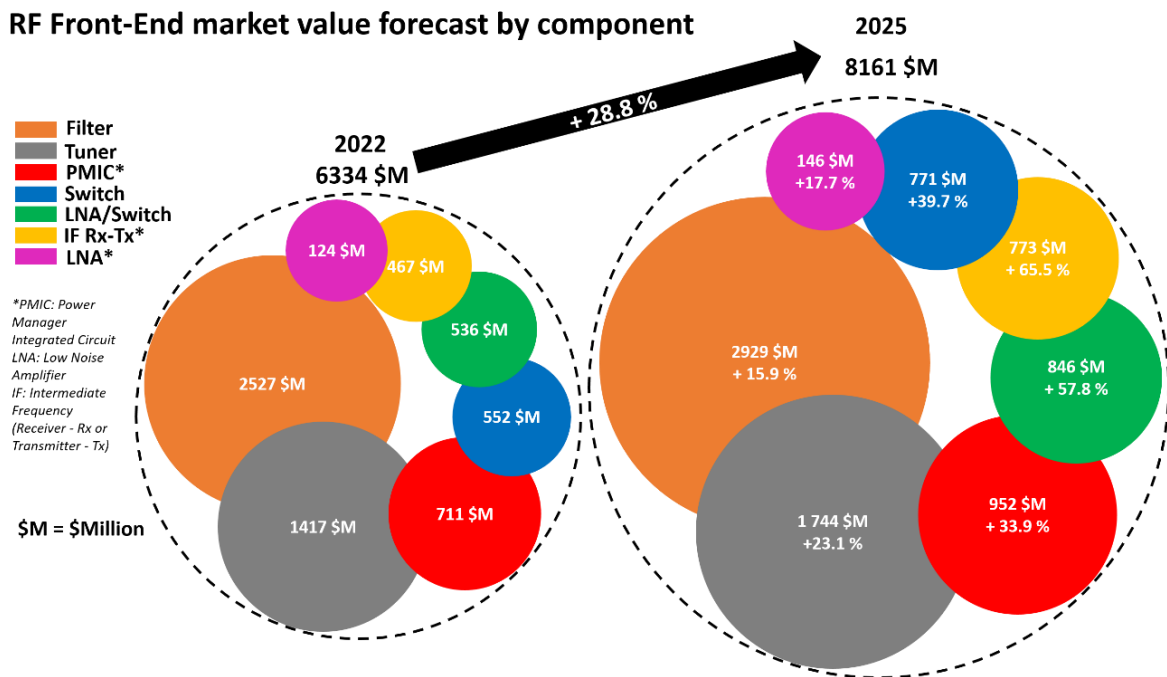


Figure I.1: RF Front-End Market Value Forecast by component. For each year, the area circle is proportional to the market value, excepted for LNA

This forecast clearly highlights the strong growth of RF Front End market (with a Compound Annual Growth Rate of 6 %). Moreover, filter components represent the largest value of RF Front End market (> 33 %) and will continue to represent the lion share. We can also note that RF switch technologies will also play a key role (antenna tuner, switch and LNA/switch experiencing a growth rate exceeding the RF FEM market one) even if associated value remains below the RF filters one.

1.1.2. Focus on Filters Market

Different kind of filtering technologies can be used and have their own characteristics (operating frequencies, bandwidth, power handling, insertion loss...). We can distinguish Multi-Layered Ceramic (MLC), Integrated Passive Devices (IPD), Surface Acoustic Wave (composed of standard SAW, Temperature-Compensated SAW and Multi-Layer SAW) and Bulk Acoustic Wave (divided in Film Bulk Acoustic Resonator and Solid Mounted Resonator). The RF filter market volume forecast is presented in Figure I.2 and is also based on the data of Yole group <sup>1</sup>.

Filter market volume forecast

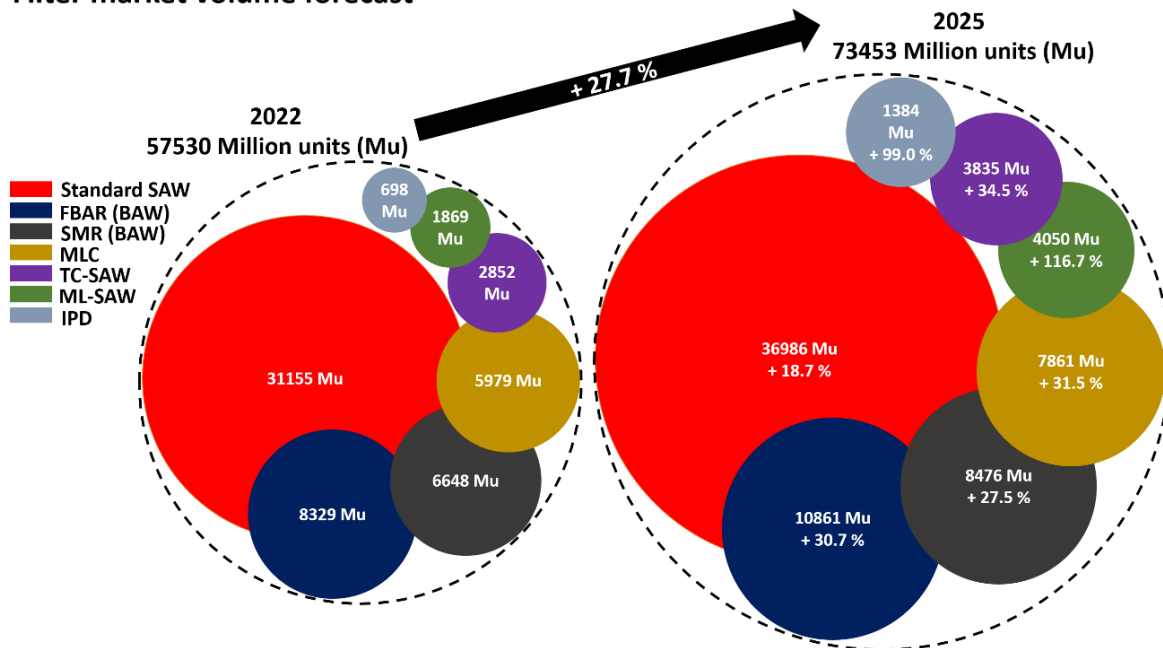


Figure I.2: Filter Market volume forecast. For each year, the area circle is proportional to the market volume expected for IPD.

In 2022, standard SAW devices are representing the main volume among filter technologies with more than the half of the manufactured units (31.1 billion units). BAW filters are in second position with FBAR and SMR technologies representing less than a quarter of the market volume (15 billion units). MLC filters are in third position with almost 6 billion units. Next, we find TC-SAW and ML-SAW, those derivatives of SAW technology correspond to a niche market with less than 5 billion units. Finally, IPD technology represents only a few hundred million units. This tendency seems to be confirmed by 2025 forecast with a total volume filters increase of around 28 %. The filter market volume will likely remain dominated by standard SAW filters (half on the units). BAW technologies (FBAR and SMR) should experience a significant increase due to their domination at higher frequencies (between 1.7 GHz and 2.7 GHz). We can observe an important increase of MLC and IPD (with almost 10 billion units) since they should take advantage of the adoption of 5G (today the only technologies being able to address the wide bandwidth required by 5G filters operating in C band). Finally, the demand of SAW derivatives technologies (TC-SAW and ML-SAW) should increase but seems to stay a niche market with less than 8 billion units.

To complement previous market volume forecast, filter market value forecast is depicted in Figure I.3. It is worth to notice that standard SAW devices represent in 2022 capture 45 % of the value while representing 54 % of the volume. On the contrary, BAW technologies (FBAR and SMR) capture 36 % of the value while representing 26 % of the manufactured parts. SAW derivatives (TC-SAW and ML-SAW) are in third position with around 1 \$ billion (13 % of the market value) followed by MLC and IPD filters. In 2025, the market value is expected to grow around 19 %. Standard SAW filters will likely still dominate this market but BAW technology will grow at a faster pace. This result highlights the dynamism of these technologies and justifies interest shown by many companies in BAW devices. SAW derivatives are also expected to increase but will still represent less than 1.4 \$ billion. Finally, 5G adoption should be profitable to MLC and IPD technologies, with a growth of around 35 % and 82 %, respectively, but still representing a small fraction of the value generated by standard SAW and BAW technologies ( $\approx 5$  % of the overall RF filters market value).

Filter market value forecast

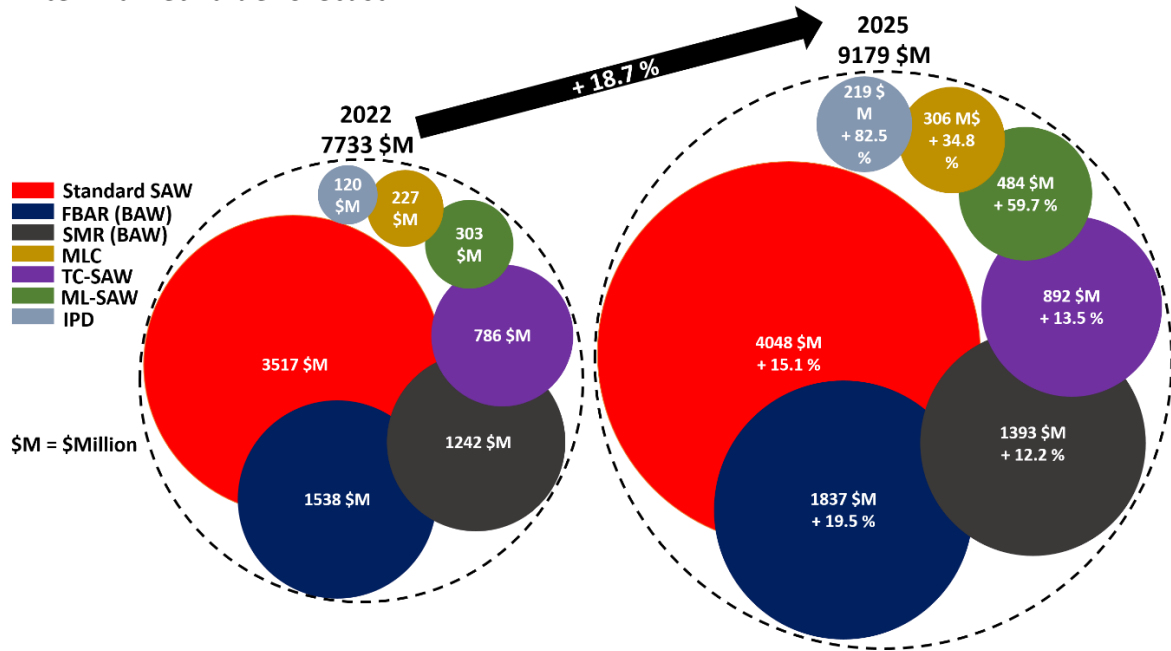


Figure 1.3: Filter Market value Forecast. For each year, the area circle is proportional to the market value, excepted for IPD.

To conclude, these different forecasts issued from Yole group shows the importance of filter technologies in RF Front-End market since they represent more than a third of the market value. The details of filters market show that the main volume comes from bulk SAW devices. However, even if bulk SAW devices largely dominate the volume market, it is expected that BAW technologies should have a higher market value than bulk SAW while they represent only a quarter of the market in terms of volume. The others MLC, IPD and SAW derivatives technologies seem to be limited to play a second role on niche markets.

These forecasts clearly show the importance of acoustic devices (SAW and BAW) on the RF filters market. The new requirements induced by the development of new wireless communication standard should lead to a higher growth of BAW technologies since it is the only viable acoustic approach able to operate at high frequency (today up to 5 GHz). Therefore, many companies have expressed their interest to develop innovative BAW technologies and enter this dynamic and high value market. Hence, the remainder of this section will focus on providing an overview of SAW and BAW acoustic devices with the description of their applications areas, operating frequency and the details of operating principles.



## 1.2. Acoustic devices

Acoustic devices are relatively similar since they are based on the use of a piezoelectric material to generate an acoustic wave which propagates laterally for SAW technologies and vertically for BAW technologies. Hence, in a first step, this section is dedicated to the piezoelectric formalism and the description of the materials properties used in acoustic device. In a second step, the operating frequencies and applications of SAW and BAW devices are described. Finally, each SAW and BAW technologies are presented and compared to identify their advantages and limitations.

### 1.2.1. Piezoelectric formalism

#### 1.2.1.1. Definition and equations

The piezoelectricity linearly relates a mechanical variable with an electrical one. Direct piezoelectric effect has been discovered by Curie's brothers in 1880 and is defined by the apparition of a spontaneous electrical polarization (or the variation of an existing polarization) of a material <sup>2</sup>. The inverse effect (deformation of a material when an electric field is applied) was suggested by Lippman and proved by Curie's brothers <sup>3</sup>. The direct and inverse piezoelectric effects are schematically sketched in Figure 1.4 a) and b), respectively.

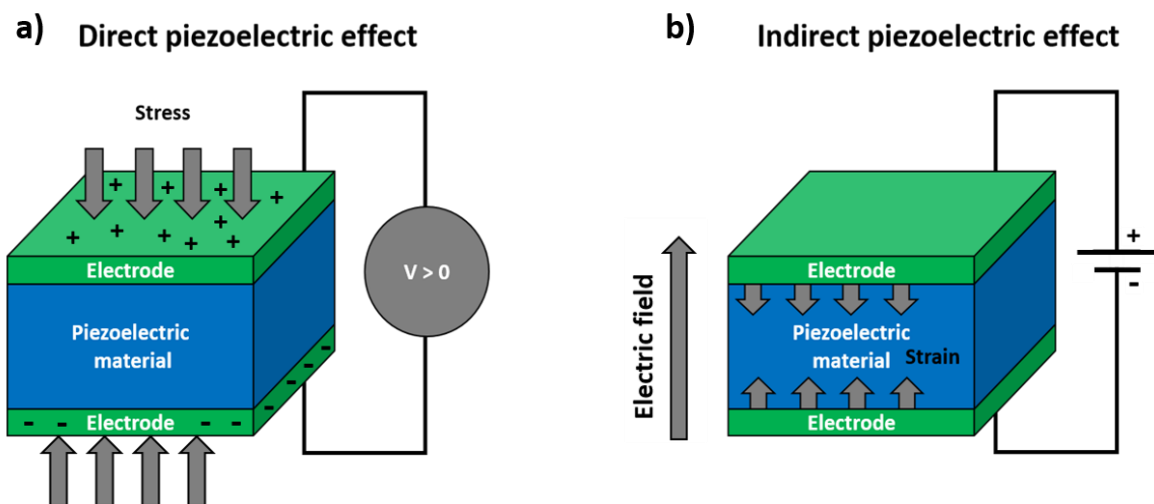


Figure 1.4: a) Direct piezoelectric effect ; b) Inverse piezoelectric effect

This property is directly related to the crystalline structure of the solids. The symmetry elements present in the crystalline lattice allow to class the materials in 32 crystalline classes. Hence, the knowledge of these symmetries within the crystalline lattice lead to the atoms arrangement that could result in a piezoelectric effect and other properties such as pyroelectricity and ferroelectricity.

To do this, the crystal must show noncentrosymmetry which is the case of 21 crystalline classes. Among these 21 classes, only one is non piezoelectric (class 432) since the charges displacement under a mechanical sollicitation does not induce the apparition of a dipole. The piezoelectric charges produced along the [111] polar axis cancel each other <sup>4</sup>. Therefore, 20 crystalline classes are piezoelectric. Figure I.5 regroupes these classes as a function of their piezoelectric, pyroelectric (variation of spontaneous polarization with temperature) or ferroelectric (reorientation or reverse of the spontaneous polarization direction under the action of an external electric field) properties.

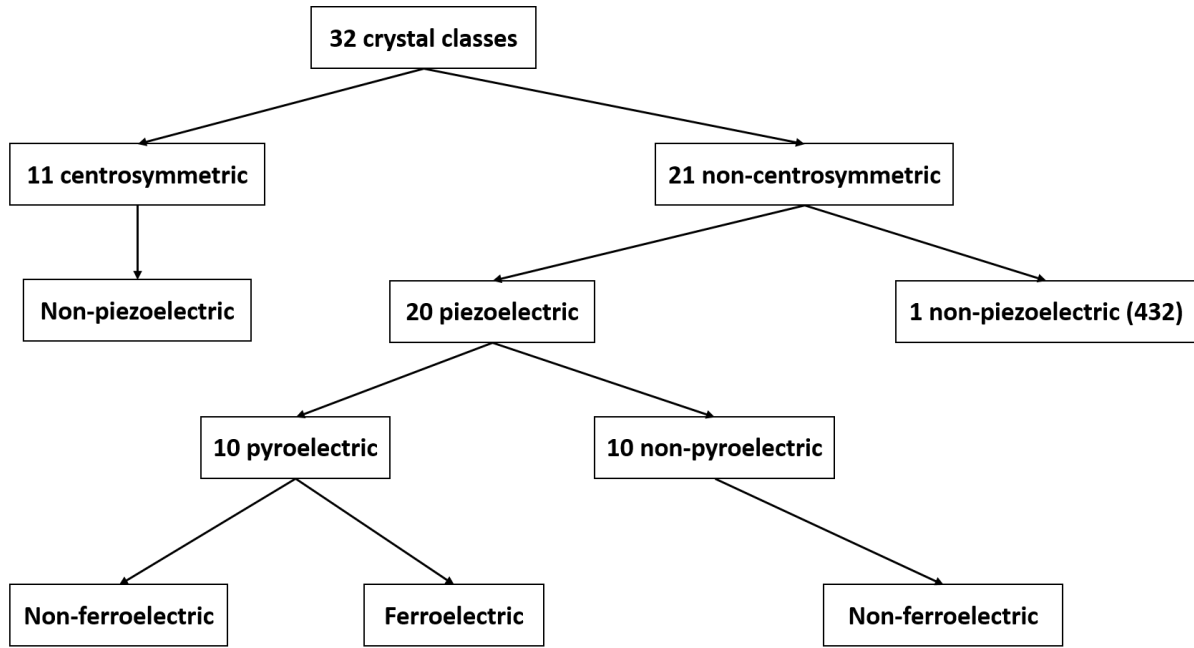


Figure I.5: Grouping of 32 crystal classes as a function of their piezoelectric, pyroelectric and ferroelectric properties

According to the norm “ANSI/IEEE Standard on Piezoelectricity” <sup>5</sup> edited in 1987 and updated in 1996, the constitutive equations of the piezoelectricity are grouped in 8 state equations usually divided into pairs and expressed as follows:

$$\begin{aligned}
 T_{ij} &= c_{ijkl}^E S_{kl} - e_{kij} E_k & S_{ij} &= s_{ijkl}^E T_{kl} + d_{kij} E_k \\
 D_i &= e_{ijkl} S_{kl} + \varepsilon_{ij}^S E_k & D_i &= d_{ikl} T_{kl} + \varepsilon_{il}^T E_k \\
 S_{ij} &= s_{ijkl}^D T_{kl} + g_{kij} D_k & T_{ij} &= c_{ijkl}^D S_{kl} - h_{kij} D_k \\
 E_i &= -g_{ikl} T_{kl} + \beta_{ik}^T D_k & E_i &= -h_{ikl} S_{kl} + \beta_{ik}^S D_k
 \end{aligned}$$

Equations I.1

These equations include the electrical components D and E being the electric displacement and the electric field, and tie these components with the mechanical part through T and S, being the stress and strain, respectively. We distinguish four piezoelectric coefficients d, g, e and h reflecting the coupling between the electrical and mechanical components. The relationships between these coefficients are determined from Equations I.1 and can be expressed as:

$$\begin{aligned}
 d_{mi} &= \epsilon_{mn}^T g_{ni} = e_{mj} S_{ji}^E & g_{mi} &= \beta_{mn}^T d_{ni} = h_{mj} S_{ji}^D \\
 e_{mi} &= \epsilon_{nm}^S h_{ni} = d_{mj} c_{ji}^E & h_{mi} &= \beta_{nm}^T e_{ni} = g_{mj} S_{ji}^D
 \end{aligned}$$

*Equations I.2*

*With m, n = 1 to 3 and i, j = 1 to 6*

These quantities, their unit, relationships and matrix size are summarized in Table I.1 and Table I.2.

Physical parameter	Symbol	Unit	Matrix size
Electric displacement	D	C.m <sup>-2</sup>	3 x 1
Electric field	E	V.m <sup>-1</sup>	3 x 1
Stress	T	N.m <sup>-2</sup> (Pa)	6 x 1
Mechanical strain	S	/	6 x 1
Dielectric permittivity	ε	F.m <sup>-1</sup>	3 x 3
Dielectric permeability	β	m.F <sup>-1</sup>	3 x 3
Elastic stiffness	c	N.m <sup>-2</sup> (Pa)	6 x 6
Elastic compliance	s	m <sup>2</sup> .N <sup>-1</sup> (Pa <sup>-1</sup> )	6 x 6

*Table I.1: Symbol, unit and matrix size of the electrical and mechanical components*

Coefficients reflecting the proportionality between:	Symbol	Unit	Matrix size
Electric displacement and stress	d	m.V <sup>-1</sup>	3 x 6
Electric displacement and strain	e	C.m <sup>-2</sup>	3 x 6
Strain and electric field	h	V.m <sup>-1</sup>	3 x 6
Stress and electric field	g	m <sup>2</sup> .C <sup>-1</sup>	3 X 6

*Table I.2: Symbol, unit and matrix size of the four piezoelectric coefficients*

However, these equations are valid for a bulk material. In the case of a thin film clamped onto a substrate and as illustrated in Figure 1.6, the film thickness is considered negligible compared to the substrate ( $t_{\text{substrate}} \gg t_{\text{film}}$ )<sup>6,7</sup>. Hence, in-plane strain  $S_1$  and  $S_2$  (considered as equi-biaxial) resulting from an out-of-plane stress  $T_3$  are assumed to be null.

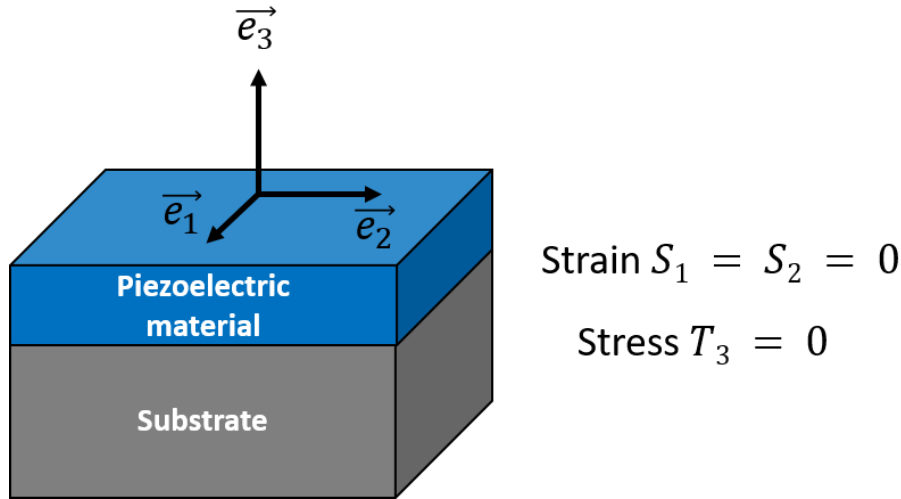


Figure 1.6: Piezoelectric thin film deposited onto a substrate ( $t_{\text{substrate}} \gg t_{\text{film}}$ )

In these conditions, the used piezoelectric coefficients are not valid since they do not consider the influence of the substrate. Therefore, it is necessary to introduce effective piezoelectric coefficients which are determined from these assumptions ( $S_1 = S_2 = 0$  and  $T_3 = 0$ ) and constitutive equations of the piezoelectricity. In the rest of the manuscript, the piezoelectric coefficients mentioned are considered to be effective.

#### 1.2.1.2. Electromechanical coupling coefficient ( $k^2$ )

The notion of electromechanical coupling coefficient is usually used for a piezoelectric material and is a key parameter to characterize an acoustic device. This parameter enables to quantify the capacity of a piezoelectric material to convert the electrical energy into mechanical energy and reciprocally, i.e. the conversion yield. Stated differently, it is a ratio usually expressed in %, between the energy supplied and the energy transformed ( $k^2 < 1$ ). This parameter depends on the frequency and is useful to evaluate the bandwidth that can be reached in a filter. It can be expressed differently depending on the technology since its expression depends on resonance modes (longitudinal or shears modes) and limits conditions such as the device geometry (for the case of a piezoelectric thin film, the thickness is low compared to the lateral dimension enabling to simplify its expression)<sup>8</sup>.

For example, in a BAW acoustic resonator where the acoustic wave propagates in the thickness of the piezoelectric layer (longitudinal mode), the electromechanical coupling coefficient denoted as  $k_t^2$  (t referring as “thickness”) can be expressed in terms of material properties<sup>9</sup>. Hence, it is often noted  $k_{mat}^2$  and expressed as follows:

$$k_t^2 = k_{mat}^2 = \frac{e_{33}^2}{c_{33}^D \epsilon_{33}^S} = \frac{e_{33}^2}{c_{33}^E \epsilon_{33}^T} \quad \text{Equation 1.3}$$

Where  $e_{33}$ ,  $c_{33}^D$  and  $\epsilon_{33}^S$  are piezoelectric coefficient, stiffness at constant displacement field  $D$  (or constant electric field  $E$ ) and relative permittivity of the piezoelectric material at constant strain  $S$  (or stress  $T$ ), respectively.

Although this notation from piezoelectric formalism exists, it is not widely used. The electromechanical coupling coefficient  $k_t^2$  is generally expressed from the resonance and anti-resonance frequencies of the device (acoustic formalism) by the following equation<sup>8,10</sup>:

$$k_t^2 = \frac{\pi f_r}{2 f_a} \tan\left(\frac{\pi f_a - f_r}{2 f_a}\right) \quad \text{Equation 1.4}$$

Where  $f_a$  and  $f_r$  are the resonance and anti-resonance frequencies (Hz), respectively.

It is common to assume that the difference between  $f_a$  and  $f_r$  is low enabling to approximate this expression to:

$$k_t^2 \approx \frac{\pi^2 f_r f_a - f_r}{4 f_a f_a} \approx \frac{\pi^2 f_a - f_r}{4 f_a} \quad \text{Equation 1.5}$$

However, this expression is only valid for a lossless resonator. When the loss of the piezoelectric thin film and the effect of electrodes cannot be ignored, the resonance and anti-resonance frequencies differ and influence the electromechanical coupling coefficient. Hence, it is suitable to introduce an effective electromechanical coupling  $k_{eff}^2$  coefficient which is determined by the same Equation 1.5 described above:  $k_{eff}^2 \approx \frac{\pi^2 f_r f_a - f_r}{4 f_a f_a} \approx \frac{\pi^2 f_a - f_r}{4 f_a}$ .

### 1.2.1.3. Quality factor (Q)

Together with the electromechanical coupling coefficient, the quality factor  $Q$  is another key parameter used to characterize an acoustic device. It determines the heat losses of a filter which are assimilated to the insertion loss (loss of signal power) and the selectivity (ratio between bandwidth and transition bands). We distinguish two quality factors:  $Q_r$  determined

from the resonance frequency and  $Q_a$  determined from the anti-resonance frequency. Its extraction is critical since it is particularly sensitive to measurements and acoustic noise.

The quality factor can be determined by different methods (- 3dB method, Modified Butterworth-Van Dyke model, Bode method or from the derivative of the impedance phase) which are not described in this manuscript <sup>11</sup>.

#### 1.2.1.4. Figure Of Merit (FOM) of acoustic devices

The previous descriptions of the electromechanical coupling coefficient  $k_{eff}^2$  and quality factor  $Q$  are determinant since they are the most important parameters to define an acoustic wave resonator. Therefore, the Figure Of Merit (FOM) is naturally defined as the product of these two parameters:

$$FOM = k_{eff}^2 \cdot Q \quad \text{Equation 1.6}$$

In fact, a large  $k_{eff}^2$  enables wider bandwidth and higher  $Q$  reduces the insertion losses and improve the selectivity of the filter (two significant objectives in resonator design optimization).

#### 1.2.1.5. Piezoelectric materials used in acoustic devices

The main piezoelectric materials investigated for their use in acoustic devices are aluminium nitride (AlN), Scandium doped AlN ( $Sc_xAl_{1-x}N$ ) zinc oxide (ZnO), lead zirconate titanate ( $PbZr_xTi_{1-x}O_3$ ) commonly called PZT, lithium tantalate ( $LiTaO_3$  - LTO) and lithium niobate ( $LiNbO_3$  - LNO). Their electromechanical coupling coefficient  $k_{eff}^2$  and quality factor  $Q$  are listed in Table I.3. This comparison is based on the study of Benech *et al.* <sup>12</sup> in which they report the  $k_{eff}^2$  and  $Q$  values of different piezoelectric materials tested at around 2 GHz.

We have to consider that this list is non-exhaustive since limited data are available in the literature about the piezoelectric materials properties used in RF applications. Moreover, the electromechanical coupling coefficient of a material can be highly dependent of its elaboration process and crystal quality. The quality factor is also highly impacted by the frequency of test. Finally, the variety of design of the device and extraction method of the quality factor  $Q$  make difficult a consistent and exhaustive study.

	Electromechanical coupling coefficient ( $k^2_{\text{eff}}$ )	Quality factor (Q)	FOM ( $k^2_{\text{eff}} \cdot Q$ )	Availability
<b>AlN</b>	7.0 %	2000	140	Thin film
<b>Sc<sub>0.12</sub>Al<sub>0.88</sub>N</b>	7.5 %	650	48.75	Thin film
<b>LiNbO<sub>3</sub> (LNO)</b>	20.0 %	1000	200	Bulk
<b>LiTaO<sub>3</sub> (LTO)</b>	20.0 %	1000	200	Bulk
<b>ZnO</b>	9.0 %	1770	159.3	Thin film
<b>PZT</b>	9.6 %	237	22.75	Thin film

Table 1.3: Electromechanical coupling coefficient  $k^2_{\text{eff}}$ , quality factor Q, FOM and availability of the main piezoelectric materials

In acoustic devices, AlN is typically deposited by Physical Vapor Deposition (PVD) and displays a  $k^2_{\text{eff}}$  up to around 7.0 %. Slightly higher values up to 7.63 % have been reported in the literature based on the AlN elaboration by Metal Organic Chemical Vapor Deposition (MOCVD) <sup>13–15</sup>. In addition, the quality factor of AlN is relatively higher than the other piezoelectric materials (ScAlN, LNO, LTO, ZnO and PZT). Hence it displays a suitable FOM for acoustic devices. Another approach to increase this  $k^2_{\text{eff}}$  is to dope AlN with an element such as scandium (Sc). It enables to reach  $k^2_{\text{eff}}$  exceeding 10 % <sup>16–18</sup> but to the detriment of the quality factor Q <sup>19</sup>.

LiNbO<sub>3</sub> and LiTaO<sub>3</sub> are similar piezoelectric materials with a larger  $k^2_{\text{eff}}$  around 20 %. A great advantage of these materials is their availability as a bulk substrate which is perceived as a commodity in Surface Acoustic Wave (SAW) devices integration. Recently,  $k^2_{\text{eff}}$  up to 25 % <sup>20,21</sup> have been achieved but the main limitation is the achievable quality factor Q which seems limited to a few hundreds.

ZnO is also an interesting material displaying a higher  $k^2_{\text{eff}}$  a reasonable quality factor Q compared to AlN. Hence, ZnO and AlN were competing in 70s and 80s as piezoelectric material for telecommunication in the GHz frequency range <sup>22</sup>. However, ZnO is not compatible with Complementary Metal-Oxide-Semiconductor (CMOS) technology and the better reproducibility of AlN process put ZnO material in the background <sup>22,23</sup>.

Finally, PZT has also been widely used and  $k_{\text{eff}}^2$  values as high as 35 % were demonstrated in acoustic devices <sup>22</sup>. However, the poor-quality factor of this material is a major hindrance which result in inferior filter performances than with other piezoelectric materials. Moreover, due to its preparation process, an uniform composition is generally difficult to achieve <sup>23</sup> and the regulations tend to progressively band lead-based material in device integrations <sup>12</sup>.

To conclude, the choice of the piezoelectric material is mainly a tradeoff between  $k_{\text{eff}}^2$  and Q but also other parameters related to its integration compatibility in acoustic devices. In the last decades, several materials have been widely studied to address the demand in acoustic devices. Currently, AlN is the material of choice for BAW technology while LiNbO<sub>3</sub> and LiTaO<sub>3</sub> are used for SAW based devices.

### 1.2.2. Operating frequencies and applications of acoustic devices

The development of SAW and BAW devices has been done in an incremental way enabling to enhance the performance of these technologies. SAW devices are divided in three types: standard SAW, Temperature-Compensated SAW (TC-SAW) and Multi-Layer SAW (ML-SAW). Each technology is discussed in detail in the next section 1.2.3. BAW technologies follow two main integration solutions, either Film Bulk Acoustic Resonator (FBAR) or Solid Mounted Resonator (SMR). They are also discussed in detail in section 1.2.4.

As depicted in Figure 1.7, the use of these technologies in electronics are directly related to their operating frequencies. SAW technologies are a significant component in all smartphones since they have been supporting filtering functions in mobile phones since the early 90s <sup>24,25</sup>. Hence, a standard SAW device operates easily up to 2 GHz. As they are easier to integrate, they are widely used in this frequency range and are even dominating the low band region (up to 1 GHz) <sup>26</sup>. These frequencies below 2 GHz are dedicated to 2G, 3G and some 4G bands used for mobile communications. TC-SAW technology, which include a thermal compensation to adjust frequency band drifts, is mainly dedicated to 4G mobile communication, where thermal management may become an issue. Finally, the most advanced SAW device named “ML-SAW” enable to reach higher operating frequencies (up to 3.5 GHz) and is expected to address 4G, 5G and Wi-Fi communication.



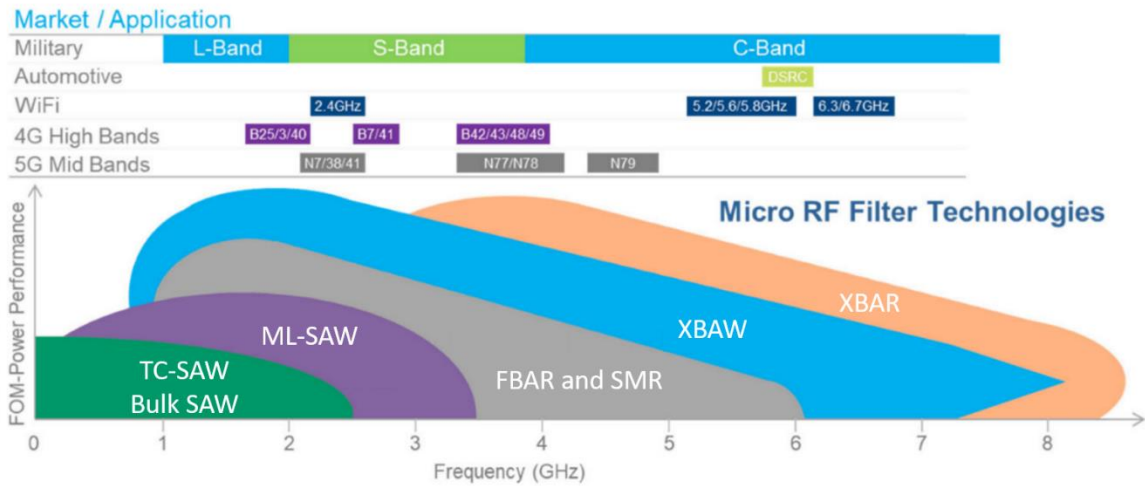


Figure I.7: Market application and frequency band allocation of RF filtering technology <sup>27</sup>

The main BAW technologies are Film Bulk Acoustic Resonator (FBAR) and Solid Mounted Resonator (SMR). Currently, other recent alternatives are being developed such as XBAW or XBAR. As shown in Figure I.7, FBAR and SMR technologies which are based on a polycrystal piezoelectric material are dominating the filtering operation beyond 2 GHz since these filters typically operate from 1.5 GHz to 6 GHz <sup>28</sup>. They can also be used at lower frequencies (1.5 – 2 GHz) where they are competing with SAW devices and no technology seems to displace the others <sup>26,28</sup> (but BAW process is more expensive). Therefore, FBAR and SMR technologies are currently used for 4G communication.

At a first sight, their operating frequencies seem also suitable for the higher radio frequencies required by 5G (> 3 GHz). However, in BAW technology, the increase in operating frequency causes a dramatic increase in acoustic and ohmic losses. Moreover, the 5G frequencies bands (N77, N78 and N79) require a larger bandwidth (500 MHz to 900 MHz) which are currently not achievable with the current FBAR or SMR technologies <sup>23</sup> (this explains why MLC and IPD technology are used, taking advantage of relaxed rejection specification in comparison with what is necessary < 3 GHz).

However, to meet the needs required by future 6G deployment < 7 GHz (inducing key coexistence challenges with Wi-Fi), important efforts are ongoing to develop innovative BAW technology able to offer suitable performances up to 7 GHz. Therefore, new BAW alternatives are under research development such as the disruptive XBAW or XBAR technologies and are expecting to enter on this market in the next years.

### 1.2.3. Surface Acoustic Wave (SAW) technology

In the early 90s, the miniaturization needs imposed by the mobile communication contribute to the development of SAW filters<sup>28–30</sup>. Currently, after three decades of material, design and process developments, different SAW filters are commercialized on the market: Bulk SAW, Temperature-Compensate SAW (TC-SAW) and Multi-Layer SAW (ML-SAW) which can be implemented either using Incredible High-Performance SAW (I.H.P SAW) or Piezoelectric On Insulator (POI) approaches. In this section, the main SAW technologies are detailed as well as the operating principle of a SAW device and its constitutive materials. Finally, the advantages and limitations of these technologies are compared.

#### 1.2.3.1. Basic structure, operating principle and frequency response

The key element of a SAW filter is a surface acoustic wave resonator. Its basic structure is visible in Figure I.8. It is composed of interdigital transducer (IDT) deposited on a piezoelectric material which can be a bulk substrate or a thin film depending on the SAW technology.

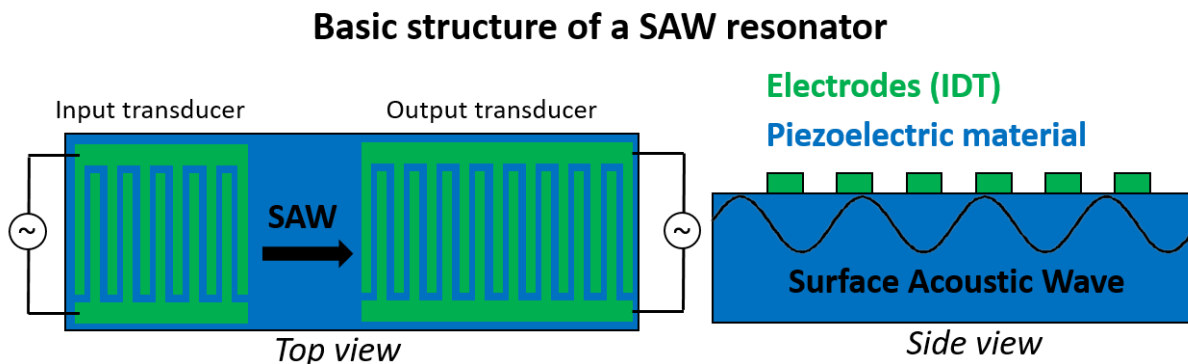


Figure I.8: Basic structure of a Surface Acoustic Wave (SAW) resonator

This IDT consists in periodic metallic electrodes deposited on the piezoelectric material. These interdigitated electrodes are polarised by the input signal and generate surface acoustic waves (SAW)<sup>31</sup>. The acoustic distance between the electrodes on the input IDT enables to sample the input signal at a given frequency. The acoustic wave propagates along the surface and the signal is collected at the output transducer<sup>30</sup>.

Such resonator geometry shows a characteristic frequency response presented in Figure I.9 a). It is composed of a resonance frequency  $f_r$  with a high admittance ( $Y$ ) and an anti-resonance frequency  $f_a$  with a low admittance. These frequencies are used to determine the electromechanical coupling coefficient  $k^2_{\text{eff}}$  following the previously presented Equation I-5.

Subsequently, these SAW resonators are assembled to elaborate a bandwidth SAW filter. Different assembly architectures can be implemented to fabricate the filter such as ladder-type filter or coupled resonator filter. A two-stage ladder type SAW filter and its characteristic frequency response are presented in Figure I.9 b) and described hereafter.

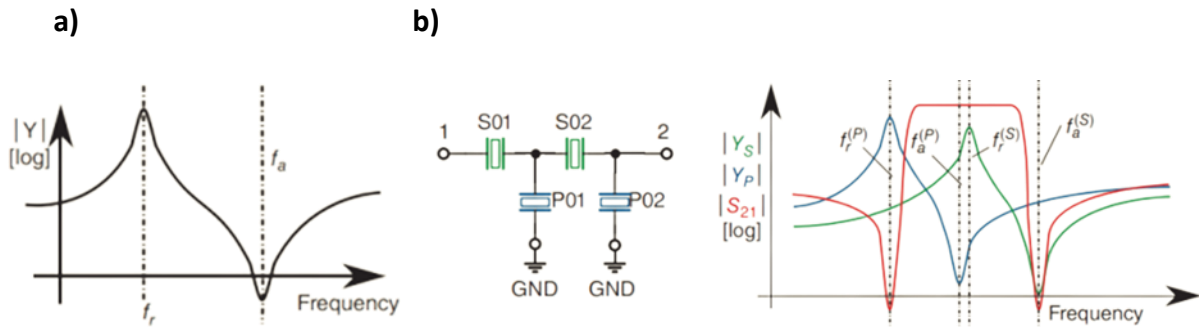


Figure I.9: a) Typical frequency response of an acoustic resonator ; b) two-stages ladder type SAW filter and its typical frequency response.

SAW resonators in series ( $S01$  et  $S02$ ) have the same resonance ( $f_r^{(S)}$ ) and anti-resonance frequencies ( $f_a^{(S)}$ ) and a typical frequency response (green curve). SAW resonators in parallels ( $P01$  et  $P02$ ) also have the same resonance ( $f_r^{(P)}$ ) and anti-resonance frequencies ( $f_a^{(P)}$ ) and a typical frequency response (blue curve). Their assembly enables to fabricate a SAW filter with a characteristic bandwidth (red curve) which depends on these resonance and anti-resonance frequencies<sup>32</sup>. It is worth to notice that the  $S_{21}$  parameter represents a transmission parameter between the input and output. It is often expressed in decibel (dB).

### 1.2.3.2. Standard SAW

First, standard SAW devices were developed to address the needs imposed by mobile communication in the early 90s. Its structure is depicted in Figure I.10. It is the most basic structure since it is composed of IDT electrodes deposited on a piezoelectric substrate. As previously discussed, this market is the most important in terms of volume in filters market and different companies are competing such as Murata, Wisol or Qualcomm<sup>1</sup>.

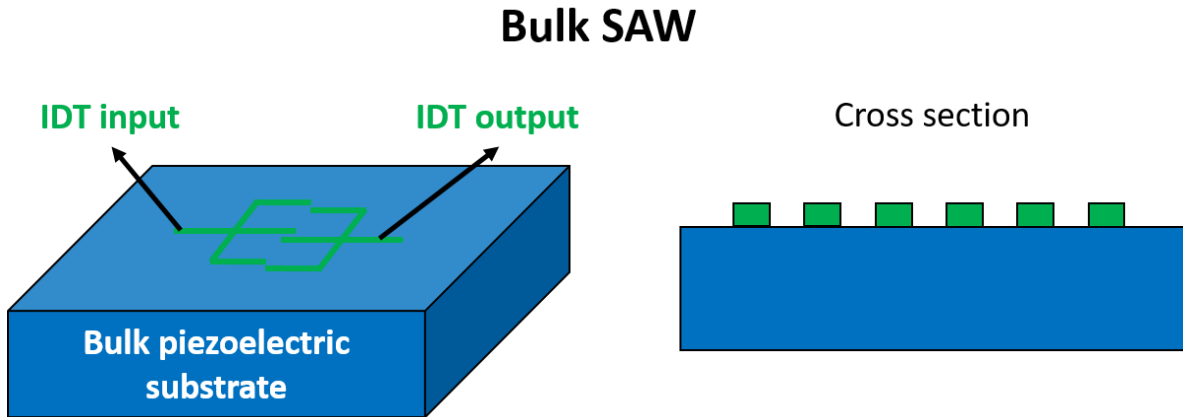


Figure 1.10: Structure of a bulk Surface Acoustic Wave (bulk SAW) resonator

This technology is low cost and easy to manufacture but displays a limited power handling and a poor quality factor  $Q$  when operating at high frequencies ( $> 2$  GHz)<sup>27</sup>. Moreover, standard SAW devices are sensitive to temperature changes. In fact, when the device is subject to temperature changes, the operating frequencies shift linearly with the temperature. This phenomenon is characterized by the Temperature Coefficient of Frequency (TCF).

The piezoelectric material choice obviously depends on its properties (electromechanical coupling coefficient  $k^2_{\text{eff}}$ , quality factor  $Q$ , acoustic velocity...) and its compatibility with SAW technology fabrication process. The structure of a bulk SAW devices requires bulk piezoelectric materials. Two substrates are dominating this technology:  $\text{LiNbO}_3$  (LNO) and  $\text{LiTaO}_3$  (LTO)<sup>24,27</sup>. LTO and LNO are elaborated using the well-known Czochralski growth (as used in silicon substrates elaboration). Due to the anisotropy of piezoelectric materials, their properties are affected by the crystal orientation. Therefore, these materials are usually cut along a preferential orientation such as  $42^\circ\text{Y-X}$   $\text{LiTaO}_3$ <sup>33,34</sup> or  $128^\circ\text{Y-X}$   $\text{LiNbO}_3$ <sup>35,36</sup> to achieve a highest piezoelectric response. The specification “ $42^\circ\text{Y}$ ” indicates the outwardly directed normal to the surface and “ $\text{X}$ ” specifies the propagation direction of the wave<sup>37</sup>.

The choice of the electrode material and its geometry are also an important factor for the acoustic wave propagation in SAW devices<sup>31,36</sup>. For example, frequency bandwidth and electrical impedance are dependent on electrode width, number of fingers IDT, spacing or aperture. Moreover, the use of high density electrodes enables to obtain large electromechanical coupling coefficient but affects the SAW phase velocity<sup>38</sup>. Typical metal used to prepare the electrodes are aluminum (Al), silver, (Ag), copper (Cu), gold (Au), Titanium (Ti) or platinum (Pt).

### 1.2.3.3. Temperature-Compensated SAW (TC-SAW)

TC-SAW technology has been developed to compensate the frequency shift related to the temperature (in particular, difficult to manage in mobile application due to confinement). The structure of a TC-SAW resonator is shown in Figure I.11. A TC-SAW device presents an additional thin layer deposited between the bulk piezoelectric substrate and IDT electrodes. Even if it is a niche market, different companies are competing to develop TC-SAW such as Murata, Qualcomm, Qorvo, Skyworks or Taiyo Yuden <sup>1</sup>.

## Temperature Compensated SAW (TC-SAW)

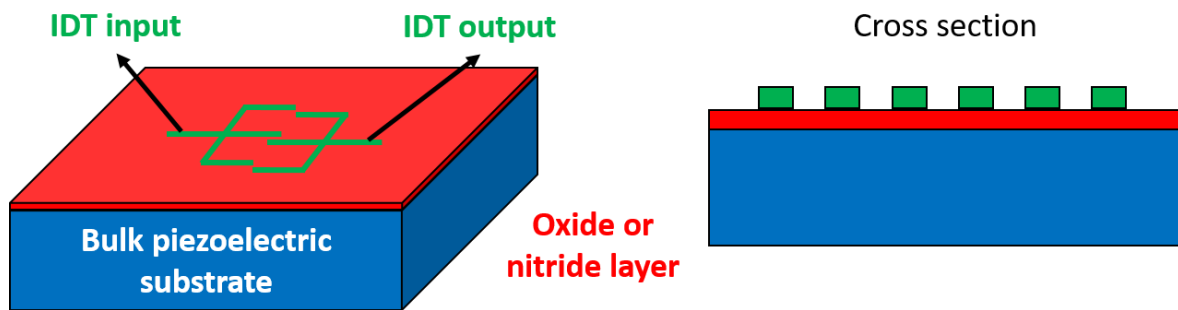


Figure I.11: Structure of a Temperature-Compensated Surface Acoustic Wave (TC-SAW) resonator

Since the piezoelectric substrate ( $\text{LiTaO}_3$  or  $\text{LiNbO}_3$ ) has a negative Temperature Coefficient of Frequency (TCF), the deposition of a material with a positive TCF on this substrate enables to reduce the absolute value of TCF and compensate this frequency shift <sup>39,40</sup>. However, this insertion of a layer in-between the IDT and active substrate also affects the electromechanical coupling coefficient  $k_{\text{eff}}^2$  and the reflections characteristics of the TC-SAW device. For example, this technique is used by Murata or Panasonic <sup>27</sup>.

A TC-SAW resonator is generally based on LTO and LNO. However, as previously mentioned, these piezoelectric materials have a negative TCF. The interlayer thin film deposited between the piezoelectric substrate and the IDT must display a positive TCF and generally silicon oxide ( $\text{SiO}_2$ ) <sup>41,42</sup> or silicon nitride or oxynitride ( $\text{Si}_3\text{N}_4$  or  $\text{SiO}_x\text{N}_y$ ) <sup>43</sup> are preferred.

Concerning the electrode, a wide range of metallic electrodes can be used in TC-SAW but Cu is widely employed as an IDT since it has a larger reflection than Al <sup>27</sup>. Other solutions based on layered electrode structure with different metals are also developed to enhance the power

durability in TC-SAW devices. For example, Su et al. <sup>44</sup> propose a 5-layer electrode Ti/Cu/Ti/Cu/Ti to address high power and low loss TC-SAW.

1.2.3.4. Multi-Layer SAW (ML-SAW)

Finally, the last ML-SAW technology also called hybrid substrate SAW is based on the deposition of a piezoelectric thin films on a handling substrate. This structure sketched in Figure I.12 is composed of different thin materials deposited/transferred onto a substrate. In this case, the substrate does not act anymore as the active part of the layer and served as handling for the deposited layers. This approach is also a suitable temperature compensation method. Using a thin piezoelectric layer and a handling substrate with a low Coefficient of Thermal Expansion (CTE) significantly reduces the TCF <sup>24,45</sup>. It is most the recent SAW technology in which the main players are Murata, Qualcomm and recently Avago-Broadcom. Similarly to TC-SAW devices, this technology should increase with the development of wireless communication but seems to stay a niche market.

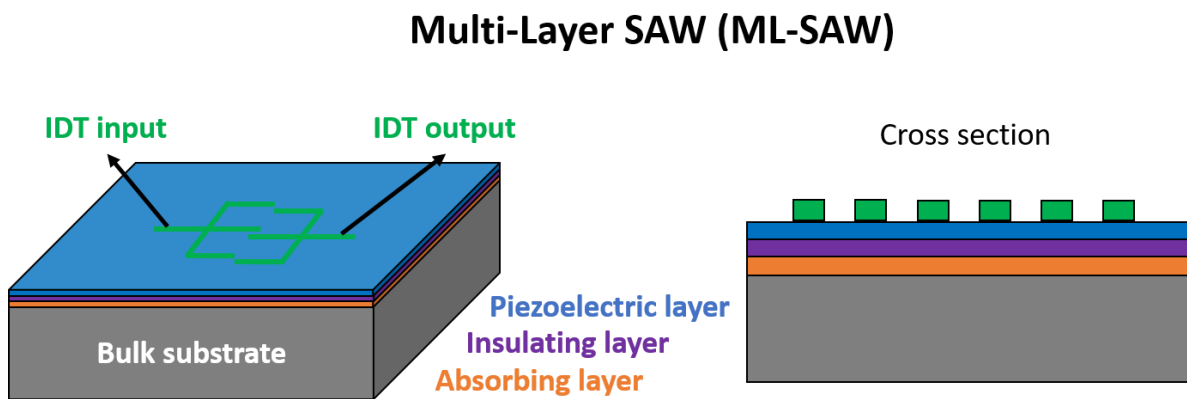


Figure I.12: Structure of a Multi-Layer Surface Acoustic Wave (ML-SAW) resonator

The main objective is to confine the acoustic wave in the vicinity of the surface to reduce the substrate losses and increase the quality factor  $Q$  <sup>46,47</sup>. Two well-known ML-SAW technologies are currently under development: Incredible High-performance SAW (I.H.P.SAW) <sup>46</sup> and Piezoelectric On Insulator (POI) <sup>47,48</sup> proposed by Murata and Soitec, respectively. This technology is the last generation of SAW devices and enables to achieve high  $Q$  and operating frequencies but faces some issues such as substrate linearity, resistivity and thermal conductivity <sup>27</sup>.

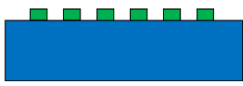

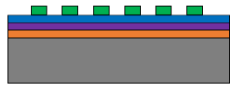
The structure of a ML-SAW resonator does not require a bulk piezoelectric substrate. Hence, it allows to use thin film processing such as AlN (which can be eventually doped) <sup>49,50</sup> or zinc oxide (ZnO) deposition <sup>51,52</sup>. LTO and LTO bulk piezoelectric materials are also possible. In this case, the substrates must be transferred and mechanically polished to use it on a as a thin film as proposed by Murata and Soitec with their I.H.P.SAW <sup>46</sup> and POI technology <sup>47,48</sup>, respectively.

In terms of electrodes, we can report Al <sup>53,54</sup> and Cu <sup>55</sup> IDT electrodes but the metal choice should be optimized with the development of this engineered structure, in particular in term of metal diffusion within the thin layers.

Finally, the multi-layered stack of ML-SAW resonator includes an insulating and absorbing layer also called functional and high velocity layer, respectively. Different materials are envisaged for each such as sapphire, alumina, SiN or AlN for the insulating layer and SiO<sub>2</sub>, silicon oxynitride (SiO<sub>x</sub>N<sub>y</sub>) or tantalum oxide (Ta<sub>2</sub>O<sub>5</sub>) for the absorbing layer <sup>46</sup>.

*1.2.3.5. Conclusions on SAW technology*

Since few decades, SAW filter aroused a particular interest to meet the needs required by wireless communication. The SAW devices development has been done in an incremental way with bulk SAW, TC-SAW and currently continues with ML-SAW. A comparison of each SAW technology issued from Yole group <sup>56</sup> is presented in Table I.4.

	<b>Standard SAW</b> 	<b>TC-SAW</b> 	<b>ML-SAW</b> 
<b>Operating frequencies</b>	1.5 – 2.5 GHz	1.5 – 2.5 GHz	2.5 – 3.5 GHz
<b>Application</b>	2G/3G/4G	4G	4G/5G/Wifi
<b>Cost (- High Cost / + Low cost)</b>	+++	++	+
<b>Process (- simple / + complex)</b>	-	+	++
<b>Piezoelectric material</b>	LNO or LTO	LNO or LTO	AlN, ZnO, LNO, LTO...

*Table I.4: Comparison of SAW resonator technologies*

Currently, standard SAW technology largely dominates the SAW industry in terms of volume and market value due to their low-cost and easy-manufacture process. The development of TC-SAW enables to compensate the frequency shift due to temperature. The development of ML-SAW allows to reach higher operating frequencies. However, both technologies are still a niche market due to their more complex architecture. These TC-SAW and ML-SAW technologies are also competing with BAW technology which limits their application.

#### 1.2.4. Bulk Acoustic Wave (BAW) technology

BAW technology was officially developed by Agilent<sup>57</sup> and pushed on the market in 2001<sup>32</sup>. Subsequently, several well-known semiconductor companies such as Qorvo, Taiyo Yuden etc... have dedicated a lot of effort to develop this technology<sup>23</sup>. Two types of BAW technologies are dominating the market: Film Bulk Acoustic Resonator (FBAR) and Solid Mounted Resonator (SMR). Currently, other alternatives based on the improvement of the piezoelectric layer are developed by Akoustis<sup>58</sup> and Resonant<sup>20</sup> such as the denoted XBAW or eXcited Bulk Acoustic Resonator (XBAR), respectively. Moreover, IQE company proposes an epitaxy-based approach using a crystal Rare Earth Oxide (cREO) layer<sup>59</sup>.

In this section, these BAW technologies are detailed as well as the operating principle of a BAW device and its constitutive materials. Finally, the advantages and limitations of these technologies are compared.

##### 1.2.4.1. Basic structure, operating principle and frequency response

As for SAW device, the key element of a BAW filter is a BAW resonator. It consists in a piezoelectric thin film sandwiched between two metallic electrodes and deposited on a substrate as illustrated in Figure I.13. The application of an electric field between the electrodes generates an acoustic wave which propagates in the volume of the structure via a vertical propagation<sup>30</sup>. The most common FBAR and SMR BAW technologies are discussed in the next sections.



## Basic structure of a BAW resonator

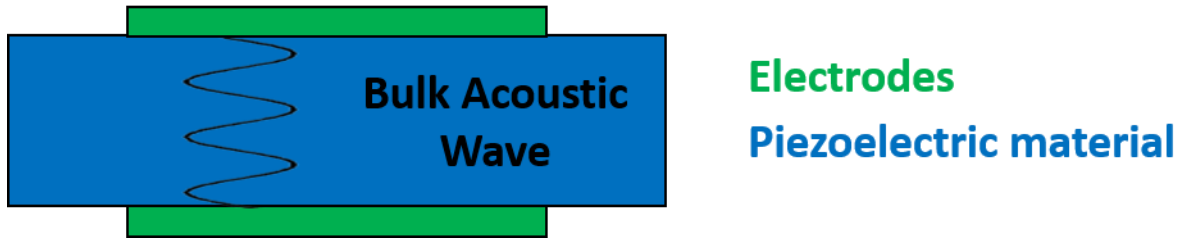


Figure 1.13: Basic structure of Bulk Acoustic Wave (BAW) resonator

The characteristic response of a BAW resonator is identical as a SAW resonator and composed of a resonance frequency  $f_r$  with a high admittance and an anti-resonance frequency  $f_a$  with a low admittance. However, contrary to a SAW filter where the operating frequency is limited by the IDT, the operating frequency depends directly on the piezoelectric film thickness:

$$f_r = \frac{v}{2d} \quad \text{Equation 1.7}$$

where  $f_r$  is the resonant frequency,  $v$  the acoustic velocity and  $d$  is the thickness of the piezoelectric layer.

Hence, using thin piezoelectric films, it enables to achieve higher operating frequency than their SAW counterparts. These resonators can be mainly implemented in three basic topologies to obtain a bandwidth BAW filter: lattice, ladder or modified lattice. The chosen topology directly impacts the targeted bandwidth and the steep of the skirts (selectivity) <sup>23</sup>.

### 1.2.4.2. Film Bulk Acoustic Resonator (FBAR)

The FBAR structure is based on an air cavity located under the resonant structure. A typical FBAR structure is visible in Figure 1.14. This air gap has a low acoustic impedance enabling a better confinement of the acoustic waves <sup>60</sup>. This technology can be divided in three types having each its own manufacturing process: cavity type, via-hole type and bridge type which are not detailed in this manuscript. Their structure is relatively fragile and its process is more complex than a SAW resonator <sup>30</sup>.

## Film Bulk Acoustic Resonator (FBAR)

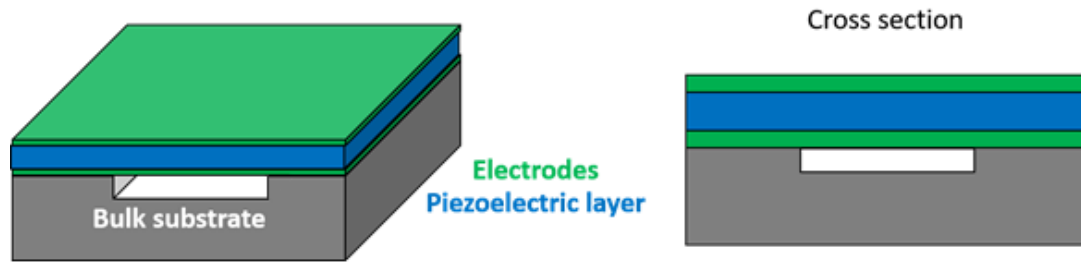


Figure I.14: Structure of a Film Bulk Acoustic Resonator (FBAR)

The BAW technology uses thin films piezoelectric materials. Aluminum nitride (AlN)<sup>61,62</sup> and zinc oxide (ZnO)<sup>63,64</sup> have been widely studied. However, and as previously mentioned, AlN is the material of choice for RF devices based on piezoelectric thin films. To increase its piezoelectric properties, AlN can also be doped with various elements. The most widely studied is Scandium (Sc) since Akiyama et al.<sup>65</sup> demonstrate a significant increase in piezoelectric response of Sc doped AlN. This discovery leads to important research efforts devoted to the incorporation of new doping elements such as yttrium (Y)<sup>66</sup>, chromium (Cr)<sup>67-69</sup>, tantalum (Ta)<sup>70,71</sup> or vanadium (V)<sup>71</sup> as well as co-doping with magnesium-zirconium (Mg-Zr)<sup>72,73</sup>, magnesium-hafnium (Mg-Hf)<sup>73,74</sup> or magnesium-niobium (Mg-Nb)<sup>75</sup> to name a few. Finally, more recently, important efforts are achieved to use LiTaO<sub>3</sub> (LTO)<sup>76</sup> and LiNbO<sub>3</sub> (LNO)<sup>77,78</sup> as a piezoelectric thin film.

As a FBAR is based on the use of a piezoelectric film sandwiched between two electrodes, the choice of the metal is very important since its structure has a direct impact on the crystal quality and piezoelectric response of the thin films. Therefore, a wide range of metals have been studied to find the most suitable bottom electrode to texture the AlN piezoelectric layer. We can mention tungsten (W)<sup>79</sup>, platinum (Pt)<sup>80</sup>, molybdenum (Mo)<sup>61</sup>, iridium (Ir)<sup>81</sup>... We can refer to the detailed study of Akiyama et al.<sup>82</sup> who investigated 15 different metallic bottom electrodes and their subsequent influence on the AlN crystal. Beyond the structural compatibility with AlN, the metallic electrode must include a low density, a low resistivity and a high acoustic impedance to confine the acoustic wave in the piezoelectric layer, this to optimize the electromechanical coupling coefficient  $k_{\text{eff}}^2$  and quality factor  $Q$ <sup>23</sup>. Currently, Mo seems to be the most adapted metal since it displays the best tradeoff between all these required characteristics<sup>30,83</sup>. It is worth to notice that in the case of LiNbO<sub>3</sub> which has a different structure than AlN, AlSi electrodes are employed<sup>77,78</sup>.

#### 1.2.4.3. Solid Mounted Resonator (SMR)

The SMR consists of a stacked structure with repeated layers composed of low and high acoustic impedances films. It enables to elaborate a reflective structure called “Bragg reflector” which acts like an acoustic mirror. This concept was introduced by Lakin et al.<sup>84</sup> and is depicted in Figure I.15.

It is another method to confine the acoustic waves and isolate the piezoelectric resonator from the substrate. The optimal reflection is obtained when the thickness of Bragg reflector layers corresponds to a quarter of the wavelength of the longitudinal acoustic wave  $\lambda_{\text{long}}$  at the resonant frequency  $f_r$ <sup>85</sup>. This resonator is more adapted to a large-scale production due to its robustness and its low-cost. Moreover, the Bragg reflector provides a good heat dissipation enabling a low temperature drift compared to FBAR technology.

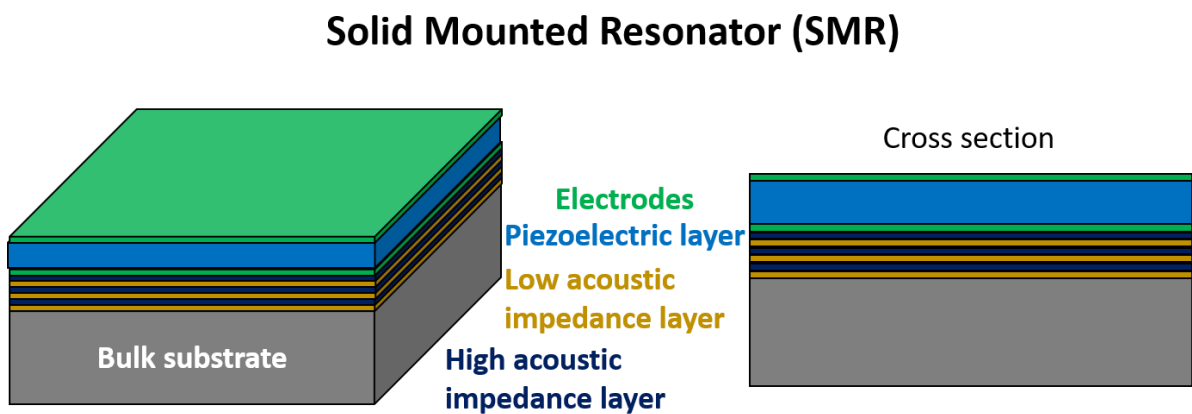


Figure I.15: Structure of a Solid Mounted Resonator (SMR)

As the active part of the SMR structure is still a piezoelectric thin film sandwiched between two electrodes, the piezoelectric materials and metallic electrodes used are similar to those employed in FBAR structure. Hence, we mainly find AlN-based SMR technology eventually with a doping element deposited on Mo electrodes<sup>23</sup>. We can also report a recent study which proposed a SMR structure with a transferred LiNbO<sub>3</sub> piezoelectric layer<sup>86</sup>.

About the Bragg mirror, different materials combinations have been investigated. Typically, the high acoustic impedance layers are made of tungsten (W)<sup>87</sup>, molybdenum (Mo)<sup>88</sup> or tantalum oxide (Ta<sub>2</sub>O<sub>5</sub>)<sup>86</sup> while the most common material for the low acoustic impedance layers is silicon oxide (SiO<sub>2</sub>)<sup>86-88</sup>.

#### 1.2.4.4. Other alternatives

Although FBAR and SMR technologies are dominated the BAW market, other alternatives to improve the device performances are available. Currently, three alternative technologies have been identified: XBAW<sup>58</sup>, XBAR<sup>20</sup> and crystal Rare Earth Oxide (cREO)<sup>59</sup> developed by Akoustis, Resonant and IQE, respectively. These three different approaches are depicted in Figure I.16.

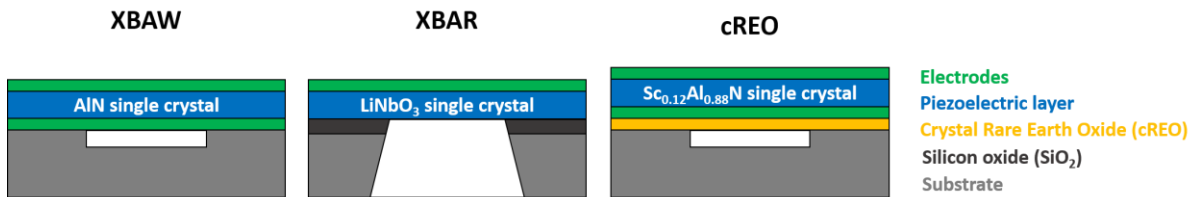


Figure I.16: New BAW alternatives: XBAW, XBAR and cREO

XBAW technology is a FBAR structure based on the elaboration of a single crystal piezoelectric layer to enhance the piezoelectric effect. Akoustis<sup>58</sup> proposed to grow an AlN layer by Metal Organic Chemical Vapor Deposition (MOCVD) to obtain this single crystal while the typical process of AlN-based BAW devices is Physical Vapor Deposition (PVD) and leads to polycrystalline films.

XBAR technology developed by Resonant is based on the use of a monocrystalline LiNbO<sub>3</sub> (LNO) piezoelectric thin film on silicon<sup>20</sup>. The particularity of a XBAR device is that there is no bottom electrode to generate an acoustic wave which propagates in the thickness of the piezoelectric layer. In fact, due to the strong  $e_{24}$  piezoelectric coefficient, the ZY orientation of the LNO layer is suitable to obtain an acoustic wave which propagates in the volume of the structure.

Finally, IQE<sup>59</sup> proposed to use a crystal Rare Earth Oxide (cREO) layer to epitaxially grow a molybdenum (Mo) bottom electrode. This layer enables to grow a Sc<sub>0.12</sub>Al<sub>0.88</sub>N single crystalline deposited by Molecular Beam Epitaxy (MBE).

#### 1.2.4.5. Conclusions on BAW technology

To meet the needs in high frequencies required by the wireless communication technologies, BAW devices have been developed and are currently dominated by two main solutions: FBAR and SMR. A comparison of these two technologies reported by Yole group is proposed in Table I.5.



	BAW-FBAR	BAW-SMR
		
<b>Operating frequencies</b>	3.5 – 6.0 GHz	3.5 – 6.0 GHz
<b>Application</b>	4G/5G/Wifi	4G/5G/Wifi
<b>Cost (- High Cost / + Low cost)</b>	-	+
<b>Process (- simple / + complex)</b>	++	+++
<b>Piezoelectric material</b>	AlN	AlN

Table 1.5: Comparison of BAW resonator technologies

Currently, FBAR and SMR technologies aroused a particular interest since their market value is expected to significantly increase in the future and may even exceed bulk SAW devices value. However, these technologies seem to reach their limits in terms of performance due to limitations in the AlN crystal quality. This inconvenient leads to the development of new approaches such as XBAR, XBAW and cREO alternatives. Besides, XBAR and XBAW devices are expected to enter on this market in the next years.

#### 1.2.5. Conclusions on acoustic devices

Two acoustic technologies are dominating the wireless mobile communication: SAW and BAW. Currently, the limitation in SAW operating frequencies restricts their use up to 2 GHz even if the more advanced ML-SAW technology is competing with BAW technologies above these frequencies. FBAR and SMR acoustic devices typically operate from 1.5 GHz to 3.5 GHz but present limitation to address higher operating frequencies (loss issue) or wide bandwidth ( $k^2_{\text{eff}}$  issue). In BAW technology, the increase in operating frequency causes a dramatic increase in acoustic and ohmic losses and 5G frequencies bands require a wider bandwidth (500 MHz to 900 MHz) which are currently not achievable with the current FBAR or SMR technologies<sup>23</sup>. Hence new alternatives are investigated to meet these needs, especially XBAR and XBAW technologies are expected to enter on this market in the next few years. A summary of all these technologies is presented in Table 1.6.



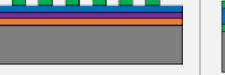
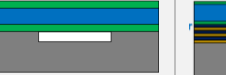




	SAW technologies			BAW technologies		New BAW alternatives		
	Bulk SAW	TC-SAW	ML-SAW	FBAR	SMR	XBAW	XBAR	cREO
								
<b>Operating frequencies</b>	1.5 – 2.5 GHz	1.5 – 2.5 GHz	2.5 – 3.5 GHz	3.5 – 6.0 GHz	3.5 – 6.0 GHz	> 5 GHz (target)	≈ 5 GHz (target)	> 5 GHz (target)
<b>Application</b>	2G/3G/4G	4G	4G/5G/Wifi	4G/5G/Wifi	4G/5G/Wifi	5G/Wifi	4G/5G/Wifi	5G/Wifi
<b>Cost (- High Cost / + Low cost)</b>	+++	++	+	-	+	++	--	/
<b>Process (- simple / + complex)</b>	-	+	++	++	+++	++	++	/
<b>Piezoelectric material</b>	LNO or LTO	LNO or LTO	AlN, ZnO, LNO, LTO...	AlN polycrystal	AlN polycrystal	AlN single crystal	LNO	AlN, ScAlN

Table 1.6: Summary of SAW and BAW technologies

### 1.3. Challenges, lines of research

The current challenges in wireless mobile communication are relatively simple: SAW and BAW devices are not adapted to address wider and higher frequency band envisioned by next standard (for example Wi-Fi 7 and 6G). On one hand, the low-cost SAW technology presents limitations in operating frequencies above 2 GHz which explains why it is perceived as a commodity technology. On the other hand, BAW technologies enable to operate at higher operating frequencies typically up to 3.5 GHz and are perceived as higher end. However, the current AlN crystal quality of AlN-based BAW resonators (FBAR and SMR) is not optimized leading to insufficient electromechanical coupling coefficient  $k_{\text{eff}}^2$  and quality factor Q to address future RF filters requirements. Typically, the current AlN  $k_{\text{eff}}^2$  is limited to around 7 % while wider bandwidth may require  $k_{\text{eff}}^2$  around 10 %<sup>23</sup> with a limited impact on achievable Q factor.

Different lines of research have been investigated. One of them is to dope AlN with an element increasing its piezoelectric properties leading to an enhancement of its electromechanical coupling coefficient  $k_{\text{eff}}^2$ <sup>65</sup>. Typically, scandium (Sc) is the most studied element. The increase in  $k_{\text{eff}}^2$  above 10 % has been widely demonstrated in  $\text{Sc}_x\text{Al}_{1-x}\text{N}$  thin films deposited by Physical Vapor Deposition (PVD)<sup>16,18</sup>. However, Sc doping leads to a dramatic decrease in quality factor Q which is not suitable to address higher operating frequencies<sup>19</sup>. Other deposition techniques at higher temperature such as Molecular Beam Epitaxy are also investigated but are still in their infancy<sup>49,89</sup>.

Another alternative is to improve AlN crystal quality to tend towards a single crystal. This approach is investigated by Akoustis<sup>14,58,90</sup> who proposes to elaborate AlN by Metal Organic Chemical Vapor Deposition (MOCVD) to obtain a higher crystal quality compared to polycrystalline AlN films typically synthesized by Physical Vapor Deposition (PVD) for FBAR and SMR devices. It seems that this alternative could be implemented on high-cost silicon carbide (SiC) substrates<sup>14,15</sup> to take advantage of the close lattice matching between AlN and SiC but also on low-cost silicon (Si) substrates<sup>58,90</sup>. However, even if the MOCVD growth of AlN single crystal has been demonstrated, the increase in  $k_{\text{eff}}^2$  remains below 10 %. Moreover, an AlN MOCVD deposition is significantly more expensive than a PVD growth which may limit its large-scale adoption. Finally, other approaches such as XBAR or cREO proposed by Resonant and IQE, respectively, are currently investigated but are still pioneering works.

#### I.4. Thesis objectives

The main objective of this thesis is to develop an innovative and cost-effective solution to address the new challenges faced by RF filters technologies. According to previous analysis, it has been determined that BAW approach seems the most promising. Consequently, **the main challenge is the material one**, the objective being to propose an innovative solution to improve the material quality.

In a first step, the work focuses on the enhancement of aluminium nitride (AlN) crystal quality film targeting acoustic devices applications. AlN is elaborated via a low-cost and low-temperature Physical Vapor Deposition (PVD) technique on low-cost silicon-based substrate. The innovation comes from the use of a two-dimensional (2D) material as a seed layer and displaying a reasonable lattice mismatching with AlN. Its use is expected to significantly increase AlN crystal quality enabling to enhance its piezoelectric properties as  $k_{\text{eff}}^2$ .

In a second step, scandium doped AlN ( $\text{Sc}_x\text{Al}_{1-x}\text{N}$ ) PVD deposition is investigated. If the use of the innovative 2D material as a texturing seed layer for AlN PVD is proven, Sc doped AlN could be an appealing solution to meet the needs required on acoustic devices and especially the  $k_{\text{eff}}^2$  - Q tradeoff. In fact, it could be possible to reach relatively high  $k_{\text{eff}}^2$  (close to 10 %) with low Sc doping enabling to preserve a reasonable quality factor Q. Hence, the acoustic resonator FOM ( $k_{\text{eff}}^2 \cdot Q$ ) could be increased.





## II. Chapter 2: State of the art on the growth of AlN and doped AlN

Aluminum nitride (AlN) is a wide bandgap material (6.2 eV) which is at the operating heart of Bulk Acoustic Wave (BAW) Devices. Its properties such as its high resistivity or high breakdown field also make AlN an interesting material for power applications. However, the growth of AlN faces some severe issues which drastically limit the integration of this material in several applications. In fact, AlN bulk growth is expensive, hardly reproducible and the AlN wafer size is limited to 50 mm. In addition, thin films AlN elaboration suffers from the lack of growth substrate displaying a suitable lattice and Coefficient of Thermal Expansion (CTE) matching while remaining low-cost. Hence, the high-quality AlN growth is an important challenge which needs to be addressed.

This chapter aims at providing an overview of the challenges faces by the AlN growth. In a first step, we introduce the basic AlN properties. We detail its structure which conditions its piezoelectric property is detailed and briefly describe other properties such as thermal, mechanical, electrical or optical properties. In a second step, we address the AlN growth process dependence. A reminder of the AlN crystal quality and c-axis orientation is given. We detail the bulk growth and its limitations and describe the AlN elaboration as a thin film through three different techniques: Atomic Layer Deposition (ALD), Metal Organic Chemical Vapor Deposition (MOCVD) and Physical Vapor Deposition (PVD) by reactive sputtering. For each technique, we discuss the deposition parameters influencing the AlN crystal quality as well as the influence of the growth substrate. Finally, we address the influence of the use of a doping element on AlN piezoelectric properties. We present the different doping or co-doping element reported in the literature and their impact on the AlN piezoelectric properties and crystal quality. A focus on scandium (Sc) doped AlN which is the most widely studied element to enhance AlN piezoelectric properties is performed.

## II.1. Aluminum nitride (AlN): basic properties

In this section, the AlN general properties are described. A strong focus is done on its structural properties, which directly conditioned to its piezoelectric properties. Mechanical, thermal, optical and electrical properties are also briefly addressed as well as its applications.

### II.1.1. Structural properties

Aluminum nitride (AlN) is an allotropic material, which means that it can crystallise under different structures: zinc-blende (ZB) cubic structure, Na-Cl like rocksalt (RS) cubic structure and hexagonal wurtzite (W) structure <sup>91</sup>. In ambient condition, only the hexagonal wurtzite structure is stable ( $P6_3mc$  space group, N° 186). This phase, visible in Figure II.1, is also easy to elaborate in bulk or thin films in an oxygen-free environment <sup>92</sup>.

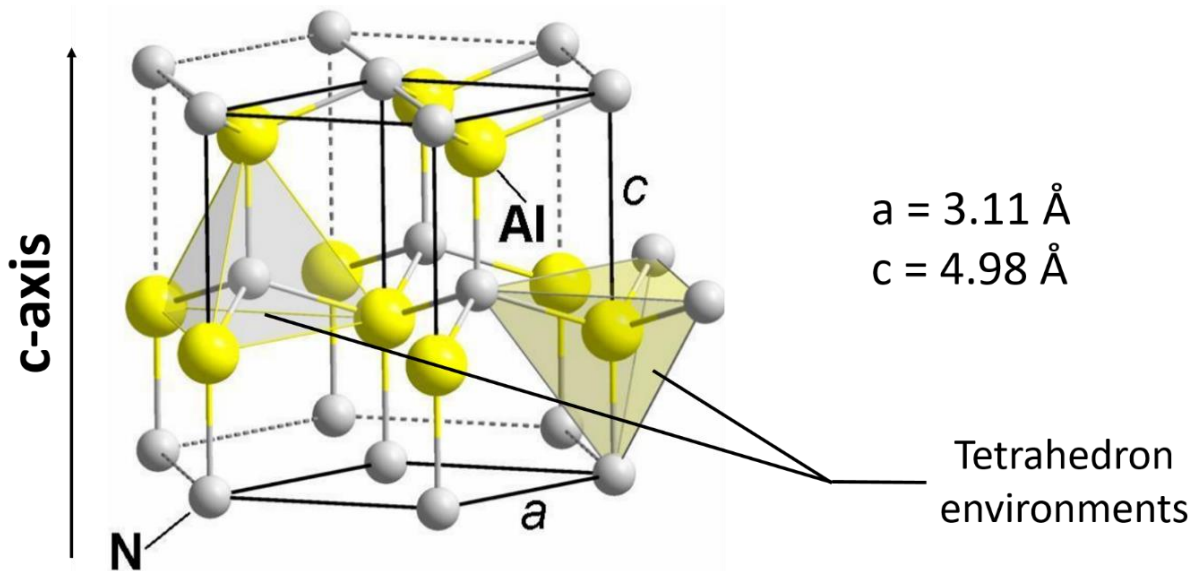


Figure II.1: AlN hexagonal wurtzite structure with its Al and N tetrahedrons.

If we refer to the nomenclature used for silicon carbide (SiC) polytype, AlN wurtzite structure is 2H type (stacking sequence is AB type). According to the literature, AlN lattice constants roughly vary around  $a \approx 3.1 \text{ \AA}$  and  $c \approx 5.0 \text{ \AA}$  depending on calculations method <sup>93-96</sup>. We can use the values mentioned in Joint Committee Powder Diffraction Standards (JCPDS) database which are  $a = 3.11 \text{ \AA}$  and  $c = 4.98 \text{ \AA}$ .

Another interesting approach is to describe AlN wurtzite structure as a hexagonal close packed (hcp) layers composed Al and N tetrahedrons. As presented in Figure II.2 a), all the N atoms are occupying the interstitial site of the Al tetrahedron and reciprocally. These two tetrahedrons environments are deduced from each other by a  $180^\circ$  rotation along c-axis.

As each tetrahedrons environment is chemically different (Al and N) it means that c-axis is a polar axis. A consequence of this polarity by inversion between the layers of Al and N tetrahedrons is that two surfaces (001) oriented of an AlN crystal can be structurally different. This specificity introduces the notion of Al-polar and N-polar faces as mentioned in Figure II.2 b).

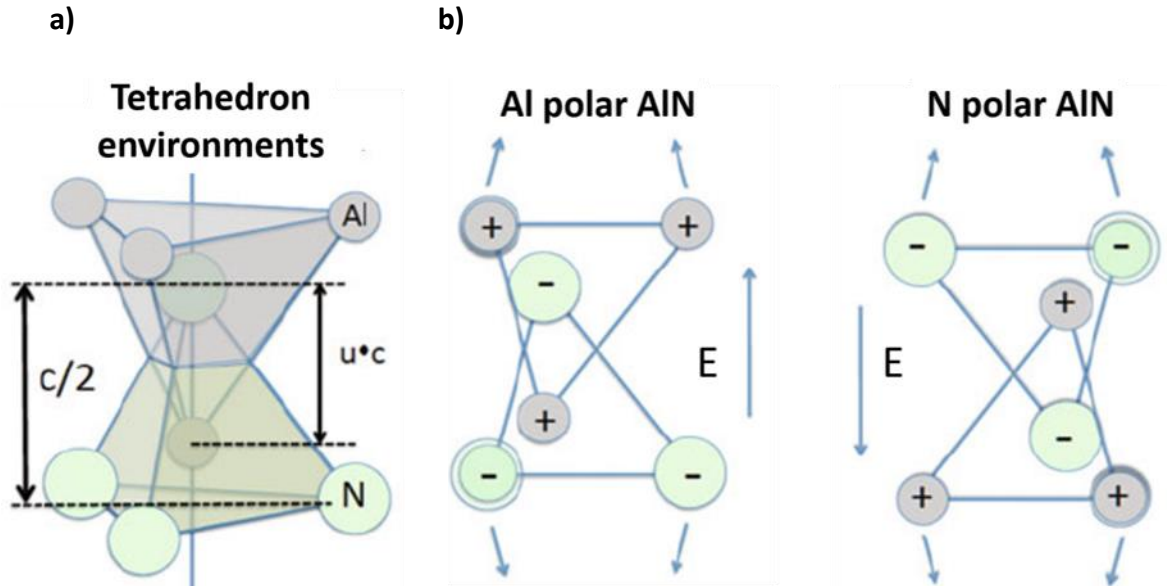


Figure II.2: a) Tetrahedron environments of AlN ; b) Al and N polar faces (side view)

Moreover, this inversion does not imply a symmetry center, which means that this polar structure allows piezoelectricity and pyroelectricity. However, AlN is not a ferroelectric material since it has been shown that this polarization cannot be reverse by the application of an electric field <sup>22</sup>.

### II.1.2. Piezoelectric properties

We consider polarizations along c-axis because standard AlN bulk and thin films are typically grown along this direction. As previously mentioned, the non-centrosymmetry of the hexagonal AlN structure justifies its piezoelectric character. AlN presents a spontaneous polarization along c-axis. Different groups of workers <sup>97-101</sup> estimated this spontaneous polarization  $P$  by various methods and is roughly around  $-0.9 \text{ C.m}^{-2}$ . When AlN material is under stress (tensile or compressive and assumed equi-biaxial), a piezoelectric polarization appears. It can be determined as follows <sup>97</sup>:

$$P_{\text{piezo}} = e_{33}\varepsilon_z + e_{31}(\varepsilon_x + \varepsilon_y) \quad \text{Equation II.1}$$

Where  $\varepsilon_z = \frac{c-c_0}{c_0}$  is the strain along c-axis,  $\varepsilon_x = \varepsilon_y = \frac{a-a_0}{a_0}$  is the in-plane strain,  $e_{31}$  and  $e_{33}$  (C.m<sup>-2</sup>) are the AlN piezoelectric coefficients. Considering the symmetry conditions, the tensor  $[e]$  is expressed as:

$$[e] = \begin{bmatrix} 0 & 0 & 0 & 0 & e_{15} & 0 \\ 0 & 0 & 0 & e_{15} & 0 & 0 \\ e_{31} & e_{31} & e_{33} & 0 & 0 & 0 \end{bmatrix}$$

This presents the AlN  $e_{mi}$  piezoelectric coefficients used in the literature. The  $e_{15}$  coefficient is related to a polarization by a shear strain. We can also express the  $d_{15}$ ,  $d_{31}$  and  $d_{33}$  according to:

$$d_{mj} = \frac{e_{mi}}{c_{ji}^E} \quad \text{Equation II.2}$$

Where  $d_{mj}$  reflects the proportionality between the electric displacement and stress,  $e_{mi}$  reflects the proportionality between the electric displacement and strain and  $c_{ji}^E$  is the elastic constant as defined in the next section II.1.3. With  $m = 1$  to 3 and  $i, j = 1$  to 6.

The values usually mentioned in the literature are those reported by Tsubouchi et al.<sup>102</sup>. They are compared with another study based on a bulk AlN single crystal<sup>103</sup> in Table II.1.

piezoelectric coefficients	$e_{15}$ (C.m <sup>-2</sup> )	$e_{31}$ (C.m <sup>-2</sup> )	$e_{33}$ (C.m <sup>-2</sup> )	$d_{15}$ (pm.V <sup>-1</sup> )	$d_{31}$ (pm.V <sup>-1</sup> )	$d_{33}$ (pm.V <sup>-1</sup> )
Thin film <sup>102</sup>	- 0.48	- 0.58	1.55	- 4.07	- 2.65	5.53
Bulk <sup>103</sup>	- 0.32	- 0.60	1.34	/	/	/

Table II.1: Comparison of the AlN piezoelectric coefficients (thin film and bulk)

These results show that the highest AlN piezoelectric response is along c-axis (max reach for  $e_{33}$  and  $d_{33}$ ). Therefore, optimize this c-axis orientation during the AlN elaboration process is essential to address acoustic devices applications.

Finally, as mentioned in the previous chapter, these piezoelectric coefficients can be used to determine the electromechanical coupling coefficient. Hence, the electromechanical coupling coefficient  $k_{mat}^2$  of a wave propagation in the thickness of the AlN piezoelectric layer (longitudinal mode) can be expressed as:

$$k_{mat}^2 = \frac{e_{33}^2}{c_{33}^D \varepsilon_{33}^S} = \frac{e_{33}^2}{c_{33}^E \varepsilon_{33}^T} \quad \text{Equation II.3}$$

Hence, according to the values of Tsubouchi et al.<sup>102</sup>, we obtain a  $k_{mat}^2$  of 5.7 %.

### II.1.3. Mechanical properties

AlN elastic properties has been widely investigated. The Hooke's law enables to bind the stress  $\sigma_{ij}$  and the strain  $\epsilon_{kl}$  via the elastic constants  $c_{ijkl}$  with the following linear expression:

$$\sigma_{ij} = c_{ijkl}\epsilon_{kl} \quad \text{Equation II.4}$$

Considering the AlN crystal symmetry, Equation II.4 can be expressed as a simplified tensor:

$$\begin{bmatrix} \sigma_1 \\ \sigma_2 \\ \sigma_3 \\ \sigma_4 \\ \sigma_5 \\ \sigma_6 \end{bmatrix} = \begin{bmatrix} c_{11} & c_{12} & c_{13} & 0 & 0 & 0 \\ c_{12} & c_{11} & c_{13} & 0 & 0 & 0 \\ c_{13} & c_{13} & c_{33} & 0 & 0 & 0 \\ 0 & 0 & 0 & c_{44} & 0 & 0 \\ 0 & 0 & 0 & 0 & c_{44} & 0 \\ 0 & 0 & 0 & 0 & 0 & \frac{c_{11} - c_{12}}{2} \end{bmatrix} \cdot \begin{bmatrix} \epsilon_1 \\ \epsilon_2 \\ \epsilon_3 \\ \epsilon_4 \\ \epsilon_5 \\ \epsilon_6 \end{bmatrix}$$

In the literature, the elastic constants can vary of a dozen of GPa depending the calculation method and obviously the AlN elaboration method <sup>102-106</sup>. Table II.2 indicates the elastic constants issued from different studies and extracted from different methods.

Method	C <sub>11</sub> (GPa)	C <sub>12</sub> (GPa)	C <sub>13</sub> (GPa)	C <sub>33</sub> (GPa)	C <sub>44</sub> (GPa)	Reference
Experimental (thin film)	345	125	120	395	118	102
Experimental (bulk)	402	135	101	387	123	103
Experimental (bulk)	411	389	125	149	99	104
Theory (density-functional-theory calculations)	396	137	108	373	116	105
Theory (quantum mechanical calculations)	426	146	113	395	132	106

Table II.2: AlN mechanical elastic constants issue from the literature

Hence, these elastic constants highlight that AlN presents a high mechanical strength. It is also an extremely hard material which presents a Vickers hardness of 17.7 GPa at room temperature (bulk single crystal) with a high mechanical stability at high temperatures <sup>107</sup>. These properties combined with a high chemical stability, in particular an important resistance to oxidation <sup>108</sup> and chemical etching <sup>109</sup> make AlN an interesting candidate for protective coatings applications <sup>110-112</sup>. We can also note that N- or Al-polarity affects the chemical resistance: a (002) nitrogen basal plane is faster etched than a (002) aluminium basal plane <sup>113</sup>.

### II.1.4. Thermal properties

AlN shows a high thermal conductivity. According to Slack <sup>114</sup>, high purity AlN single crystal displays a thermal conductivity  $\lambda = 319 \text{ W}\cdot\text{m}^{-1}\cdot\text{K}^{-1}$  in ambient conditions. It makes AlN an interesting heat spreader material <sup>115,116</sup>. However, this value can significantly vary for

polycrystalline AlN <sup>117</sup>: 17 W.m<sup>-1</sup>.K<sup>-1</sup> to 285 W.m<sup>-1</sup>.K<sup>-1</sup>. Also, the Coefficient of Thermal Expansion (CTE) of AlN was studied by Yim et al. <sup>118</sup> in a range of temperature between 20 °C and 800 °C. The temperature dependence along a-axis and c-axis have been expressed as:

$$a_T = 3.1113 + 1.3130.10^{-5}T + 4.147.10^{-9}T^2 \quad \text{Equation II.5}$$

$$c_T = 4.9793 + 1.4789.10^{-5}T + 7.255.10^{-9}T^2 \quad \text{Equation II.6}$$

Where  $T$  is the temperature (K)

Hence, the mean CTE between 20 °C and 800 °C are  $\alpha_a = 4.2 \times 10^{-6} \text{ K}^{-1}$  and  $\alpha_c = 5.3 \times 10^{-6} \text{ K}^{-1}$ .

#### II.1.5. Optical and electrical properties

AlN shows a high transmittance (70 % to 90 %) in the visible spectrum <sup>119,120</sup> and a refractive index ranging from  $n = 1.99 - 3.25$  <sup>109</sup>. It is also a well-known material for its wide band gap energy close to 6.2 eV <sup>121,122</sup> naturally associated with a very high electrical resistivity  $\rho = 10^{11} - 10^{13} \text{ } \Omega.\text{cm}$  <sup>109</sup>. It displays a breakdown field  $E_c = 12 \text{ MV.cm}^{-1}$ . and an electron mobility  $\mu_n = 1100 \text{ V}^{-1}.\text{s}^{-1}$  <sup>123</sup>. A comparison of some of these properties with silicon and other wide bandgap semiconductors materials is given in Table II.3 (values issued from refs <sup>123-126</sup>).

	Si	4H-SiC	6H-SiC	GaN	Diamond	AlN	References
<b>Bandgap (eV)</b>	1.12	3.26	/	3.49	5.00	6.20	<sup>123</sup>
	1.10	3.26	3.03	3.45	5.45	/	<sup>124</sup>
	1.12	3.26	/	3.39	5.47	6.28	<sup>125</sup>
	1.12	3.28	2.96	3.40	5.50	/	<sup>126</sup>
<b>Electric breakdown field (MV.cm<sup>-1</sup>)</b>	0.3	3.2	/	3.0	5.7	12.0	<sup>123</sup>
	0.3	2.2	2.5	2.0	10.0	/	<sup>124</sup>
	0.3	2.0	/	3.3	5.6	11.7	<sup>125</sup>
	0.3	2.2	3.2	2.0	20.0	/	<sup>126</sup>
<b>Electron mobility (V<sup>-1</sup>.s<sup>-1</sup>)</b>	1480	1000	/	1200	2800	300	<sup>123</sup>
	1500	1000	500	1250	2200	/	<sup>124</sup>
	1350	720	/	900	1900	1100	<sup>125</sup>
	1350	800	370	1700	2200	/	<sup>126</sup>

Table II.3: Bandgap, electric breakdown field and electron mobility of AlN

Although slight differences in absolute values are observed, the literature agrees and shows that AlN displays the higher bandgap and electric breakdown field than the others materials. These properties, coupled with the high electrical resistivity, make AlN an interesting material for power applications. However, GaN and SiC materials due to their lower cost and availability dominate the power market <sup>127</sup>.

## II.2. AlN elaboration process

Since a few decades, the elaboration of AlN is a research subject which arises a particular interest in bulk and in thin films. However, its growth faces some severe issues which limit the integration of this material in a wide range of devices.

First, this section focuses on the growth of AlN as a bulk material. Its elaboration process by Physical Vapor Transport (PVT) is described and its limitations are presented. Second, we address three thin films AlN elaboration techniques: Atomic Layer Deposition (ALD), Metal Organic Chemical Vapor Deposition (MOCVD) and Physical Vapor Deposition (PVD) via reactive sputtering. For each, we briefly describe the typical AlN deposition technique and address the deposition parameters affecting the AlN crystal quality. A strong focus is performed on the influence of the growth substrate on AlN MOCVD and sputtered thin films.

### II.2.2. Bulk growth

#### II.2.2.1. Typical Physical Vapor Transport (PVT) process

The first serious attempts to grow bulk AlN single crystals started in the 60s<sup>128</sup>. However, in the 90s, the need of wide bandgap semiconductor drives the development of new techniques able to grow AlN bulk single crystals on large-area.<sup>129</sup> One main solution consists to use an AlN powder as a source material which sublimates at temperature exceeding 1700 °C. Note that Al powder (or liquid) as source material put in a nitrogen atmosphere can also be used. This method called Physical Vapor Transport (PVT) is performed in a crucible with a temperature gradient. The species transport is facilitated from the hotter source to a colder area by sublimation. This colder area is the growth area where the species recondense to form the crystal. A typical PVT growth setup is given in Figure II.3 and is briefly described hereafter.



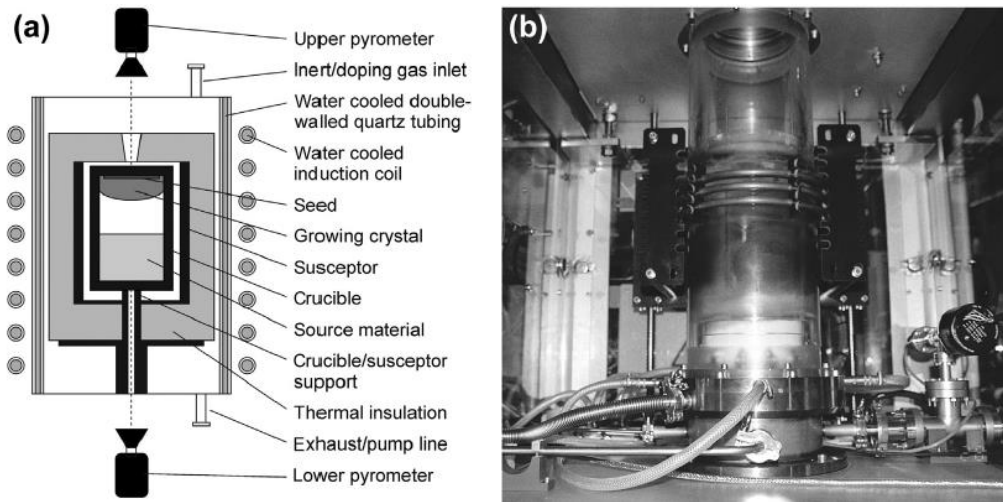


Figure II.3: a) Schematic and b) image of a typical PVT growth setup <sup>129</sup>

A porous crucible is heated with a gradient temperature by induction or resistive heating in a quartz tube. This temperature gradient makes a hotter area appear at the bottom of the crucible (source material area) and a colder area at the top (growth area). The temperatures are controlled by two pyrometers positioned at the bottom and the top of the crucible. It is filled with an AlN powder as source material. The AlN powder is sublimated to facilitate its transport to the growth where AlN recondenses to form a crystal. The recrystallization region can be the crucible walls or a selected seed crystal such as silicon carbide (SiC) corresponding to a self-seeded growth or seeded growth, respectively <sup>130</sup>.

#### II.2.2.2. Limitations in bulk AlN growth

Compared to other materials, bulk AlN single crystal growth looks to be in its infancy. On one hand, even if self-seeded growth leads to AlN single crystal almost free of defects (dislocation densities  $< 100$  per  $\text{cm}^{-2}$  without any volume defects), the yield and AlN crystals size is limited <sup>131</sup>. On the other hand, the AlN growth on a SiC seed enables to elaborate bulk AlN with industrial relevant sizes. However, this approach presents limitations such as the gradual degradation of AlN crystal with the thickness (limited to 5 mm) or the partial SiC decomposition under Al vapor starting below 2000 °C. Moreover, although the lattice and CTE mismatches between both materials are reasonable, the high temperature of PVT process leads to partial stress relaxation at the AlN/SiC interface which risks to induce cracks during the growth <sup>129</sup>.

Therefore, bulk single crystal AlN growth remains a current research topic. Different growth alternatives are investigated such as High-Temperature Chemical Vapor Deposition (HT-CVD)<sup>132</sup>, high temperature solution/flux growth<sup>133</sup> or PVT variations<sup>134</sup> but are still at a research level. Currently, the AlN wafer dimension is limited since only few companies and research groups have demonstrated the growth of AlN single crystals with a diameter up to 50 mm while SiC wafer is 200 mm with a similar dislocation density (100 per cm<sup>-2</sup>)<sup>127</sup>. Therefore, the worldwide AlN wafer production is poor compared to SiC production.

### II.2.3. Thin films elaboration

The previous section highlighted the challenges in AlN single crystal as a bulk. Hence, a lot of effort were employed to synthesize AlN single crystal as a thin film. A wide range of high-temperature epitaxial elaboration methods have been investigated such as Hydride Vapor Phase Epitaxy (HVPE)<sup>135–137</sup>, Chemical Vapor Deposition (CVD) and its derivatives<sup>132,138,139</sup>, Molecular Beam Epitaxy (MBE)<sup>140,141</sup>, Liquid-Phase Epitaxy (LPE)<sup>142,143</sup>... Lower-temperature deposition techniques also aroused an important interest. We can mention Physical Vapor Deposition (PVD) and its derivatives<sup>144–146</sup> usually leading to polycrystalline thin films or Atomic Layer Deposition (ALD)<sup>147–149</sup> in which AlN displays a poor crystalline quality.

In this section, we give a reminder on the notions of epitaxy, mosaicity and texture. Then, we discuss the influence of the growth substrate on the quality of the deposited AlN thin film. Finally, we focus on the state of the art of AlN deposition by ALD, CVD and PVD, especially by reactive sputtering. The deposition technique is briefly described at the beginning of each subsection. It is followed by a review of the parameters influencing the AlN crystal quality.

#### II.2.3.1. Crystalline quality of AlN thin films

##### II.2.3.1.1. Mosaicity: definition and characterization method

As AlN shows the highest piezoelectric response along c-axis, the optimization of this preferential orientation is primordial in AlN-based piezoelectric applications. A perfect c-axis oriented AlN crystal presents perfect AlN planes normal to the c-axis. However, the crystals are not comprised of perfect crystal planes and show slightly misoriented domains with respect to one another as illustrated in Figure II.4. This misorientation of the domains are characteristics of a crystal and referred as the crystal's mosaicity.

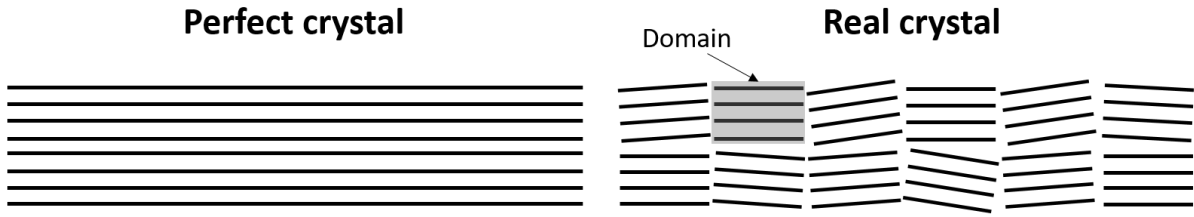


Figure II.4: Mosaicity of a perfect and real crystal

This mosaicity is determined by a X-Ray Diffraction (XRD) measurement called Rocking Curve. This measurement and mosaicity notion were well-described by Guinebretière<sup>150</sup> and illustrated with the (110) planes of an aluminum oxide single crystal as plotted in Figure II.5.

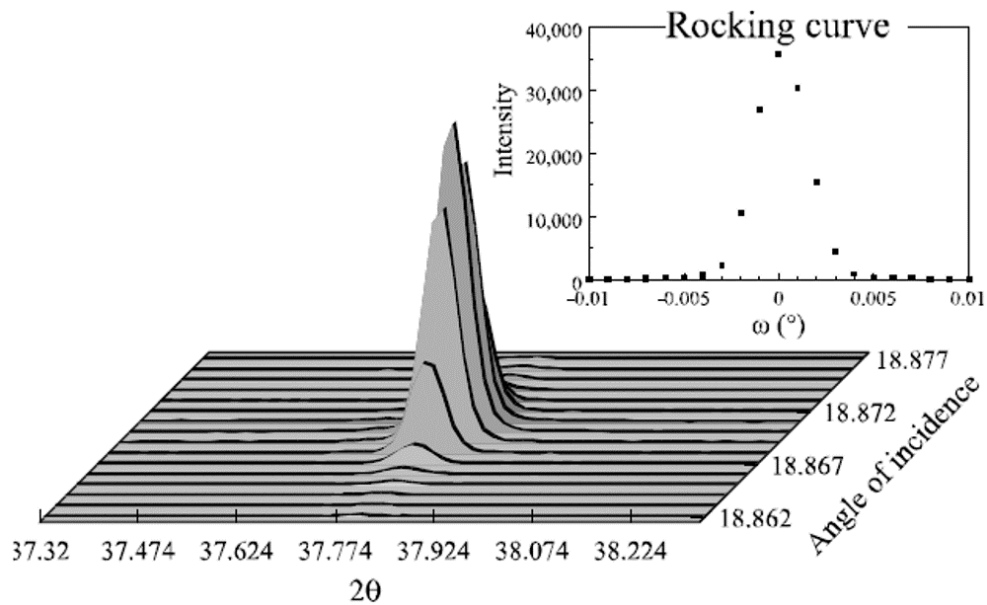


Figure II.5; Measurement of the mosaicity of an aluminum oxide single crystal

When the incidence angle of the X-Ray beam ( $\omega$ ) is close to the Bragg angle of a chosen family of planes, the diffracted intensity measured slightly varies. In fact, for each angle of incidence, a certain diffracted intensity is measured and corresponds to the integral of the measured peak. If the evolution of this integrated intensity is plotted according the difference between the Bragg angle and the incidence angle of the X-Ray beam of the chosen crystal planes, the width of the resulting graph (inset of Figure II.5) is the direct measurement of the crystal's mosaicity. This type of graph is called a "Rocking Curve" or " $\omega$ -scan". By extension the Full Width at Half Maximum (FWHM) of the peak is also denominated "Rocking Curve" (RC). In the rest of this manuscript, the FWHM of this Rocking Curve measurement is denoted as "RC" and is used to assess the crystal quality.

Typically, the RC is close to a few thousandths of a degree for single crystals. In the case of a c-axis oriented AlN crystal, the misorientation along this axis is evaluated by considering the (002) planes.

II.2.3.1.2. Epitaxy, texture and influence of the growth substrate

Thin films “deposition” is a generic term which simply implies the coverage of a substrate by a material. It means that the substrate can be crystalline (single crystal or polycrystal) or amorphous and does not transfer any crystallographic information to the deposited layer. When a particular structure is sought in the deposited thin film such as a preferential orientation, the choice of the substrate is primordial. For this purpose, the term “epitaxy” is usually employed and means that the crystallographic structure of the deposited material is determined by the crystalline substrate <sup>151</sup>. If the substrate has the same nature than the epitaxial film, we refer to “homoepitaxy”, in the other case, we use the term “heteroepitaxy”.

An epitaxial film can be described as a film with an orientation to registry with the substrate in both in-plane and out-of-plane orientation. When the deposited film presents a preferential out-of-plane orientation but is randomly in-plane oriented, the term “texture” is employed. Typically, a textured film displays a mosaic structure (mosaicity) of crystals domains which are slightly misoriented from each other out of the surface plane <sup>152</sup>. Figure II.6 schematically represents a random, textured and epitaxial film deposited onto a substrate.

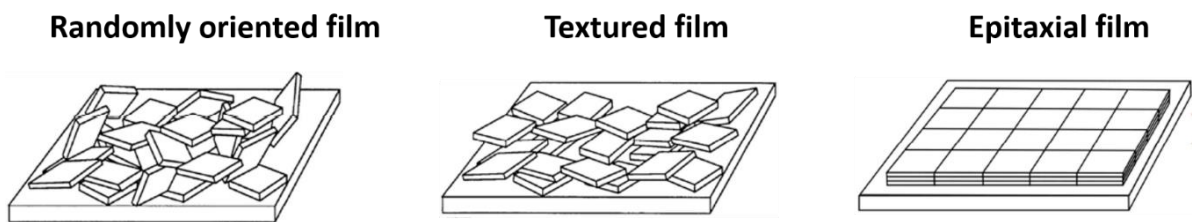


Figure II.6: Schematic illustration of random, textured and epitaxial film

As briefly provided, the choice of suitable substrate is primordial to perform an epitaxial or a textured growth. Hence, in the case of heteroepitaxy, the lattice mismatch between the substrate and the deposited material must be minimized. At the growth temperature, this lattice mismatch can lead to the formation of strain/stress during the growth and induce the nucleation of stress-relieving defects. Based on Shen et al. <sup>153</sup> study, in the case of both film and substrate are hexagonal and the basal plane of each is used to perform the deposition, the strain (assumed equi-biaxial) can be expressed as:

$$\varepsilon_x = \varepsilon_y = \frac{a_{film} - a_{substrate}}{a_{substrate}} \quad \text{Equation II.7}$$

Where  $\varepsilon_x = \varepsilon_y$  is the equi-biaxial strain and  $a_{film}$  and  $a_{substrate}$  are the lattice parameters of the film and the substrate, respectively.

The normal stress to the film substrate interface issued from the lattice mismatch can be written as:

$$\sigma_x = \sigma_y = \frac{1}{s_{11} + s_{12}} \frac{a_{film} - a_{substrate}}{a_{substrate}} \quad \text{Equation II.8}$$

Where  $\sigma_x = \sigma_y$  is the equi-biaxial stress and  $s_{11}$  and  $s_{12}$  are the elastic compliances constants of the film, respectively.

It is clear that the stress increases with lattice mismatch between the film and substrate, and will induce to the formation of defects which can lead to film cracks. Typically, a lattice mismatch above 14 % lead do the formation of dislocations without activation energy <sup>154</sup>.

Beyond the structural aspect, the thermal contribution and especially the Coefficient of Thermal Expansion (CTE) between the substrate and the deposited material must be considered. In fact, a large temperature change from the growth temperature to the room temperature can induce important thermal stress expressed as <sup>155</sup>:

$$\sigma_{th} = E_{film}^0 \Delta\alpha \Delta T \quad \text{Equation II.9}$$

Where  $\sigma_{th}$  is the thermal stress,  $E_{film}^0 = \frac{E_{film}}{1 - \nu_{film}}$  is the effective Young modulus of the film calculated from its Young modulus  $E_{film}$  and Poisson ratio  $\nu_{film}$ ,  $\Delta\alpha = \alpha_{film} - \alpha_{substrate}$  is the CTE difference between the film and the substrate and  $\Delta T$  is the temperature difference.

Similarly to the stress induced by the lattice mismatch, the thermal stress increases with the CTE difference between the substrate and the deposited film. This stress is also amplified with the temperature which must be considered, especially for high-temperature deposition. These two combined factors can induce the formation of defects and lead to films cracks.

#### II.2.3.1.3. Main substrates for AlN thin film deposition

In the literature, the substrates investigated to grow AlN as a thin film are usually recurring. We find silicon (Si) which is mainly (100)-or (111)-oriented as well as other substrate displaying a reasonable lattice mismatch with AlN to perform an epitaxial (or highly textured) growth such as different silicon carbide (SiC) polytype or sapphire. We can note that due to

instability at high temperature, 3C-SiC polytype is grown on silicon substrates but monocrystal can be achieved<sup>156</sup>. The lattice parameters, CTE as well as the lattice and CTE mismatches of these substrates with AlN issued from Dobrovinskaya et al.<sup>157</sup> and Cimalla et al.<sup>158</sup> studies are listed in Table II.4. Gallium nitride (GaN) has been added to the list since AlN is widely used as buffer layer for GaN growth<sup>159,160</sup>.

	Lattice constants	CTE	In-plane lattice mismatch	In-plane CTE mismatch
<b>AlN</b>	a = 3.11 Å c = 4.98 Å	$\alpha_a = 4.2 \times 10^{-6} \text{ K}^{-1}$ $\alpha_c = 5.3 \times 10^{-6} \text{ K}^{-1}$	/	/
<b>Si (100)</b>	a = 5.43 Å	$\alpha = 2.6 \times 10^{-6} \text{ K}^{-1}$	42.7 %	61.5 %
<b>Si (111)</b>	a' = 3.84 Å for (111)	$\alpha = 2.6 \times 10^{-6} \text{ K}^{-1}$	19.0 %	61.5 %
<b>3C-SiC (100)</b>	a = 4.36 Å	$\alpha = 3.3 \times 10^{-6} \text{ K}^{-1}$	28.7 %	27.3 %
<b>3C-SiC (111)</b>	a' = 3.08 Å for (111)	$\alpha = 3.3 \times 10^{-6} \text{ K}^{-1}$	0.9 %	27.3 %
<b>4H-SiC</b>	a = 3.07 Å c = 10.08 Å	$\alpha_a = 3.2 \times 10^{-6} \text{ K}^{-1}$ $\alpha_c = 3.3 \times 10^{-6} \text{ K}^{-1}$	1.3 %	31.3 %
<b>6H-SiC</b>	a = 3.07 Å c = 15.12 Å	$\alpha_a = 3.3 \times 10^{-6} \text{ K}^{-1}$ $\alpha_c = 3.3 \times 10^{-6} \text{ K}^{-1}$	1.3 %	27.3 %
<b>Sapphire</b>	a = 4.76 Å c = 12.99 Å	$\alpha_a = 5.3 \times 10^{-6} \text{ K}^{-1}$ $\alpha_c = 5.9 \times 10^{-6} \text{ K}^{-1}$	34.7 % (13.2 % after 30° rotation)	- 20.8 %
<b>GaN</b>	a = 3.19 Å c = 5.19 Å	$\alpha_a = 3.2 \times 10^{-6} \text{ K}^{-1}$ $\alpha_c = 5.6 \times 10^{-6} \text{ K}^{-1}$	2.5 %	31.3 %

Table II.4: Lattice constants, CTE and corresponding mismatches between AlN and the main AlN growth substrates

This table clearly highlights the lack of suitable substrate displaying both a reasonable lattice and CTE mismatches for high-quality AlN growth. First, although a Si (111) substrate display a lattice mismatch of 19.0 % with AlN, the CTE mismatch between Si and silicon remains important (61.5 %). Second, several substrates such as GaN, SiC hexagonal polytypes (4H and 6h) and (111)-oriented 3C-SiC show a close lattice matching with AlN. However, the CTE mismatch of these substrates with AlN is still significant. Finally, it is worth to notice that during an AlN deposition on sapphire, a 30° in-plane orientation of the AlN lattice with respect to sapphire substrate is observed reducing the lattice mismatch from 34.7 % to 13.2 %. However, despite this rotation, the lattice and CTE mismatches with AlN remain important. Therefore, the CTE and lattice mismatches between AlN and these substrates is a significant issue in AlN growth, which induce the formation of defects and can lead to cracks in the films.

II.2.3.2. Influence of the deposition technique

II.2.3.2.1. Atomic Layer Deposition (ALD)

Atomic Layer Deposition (ALD) is a low-temperature and “soft” deposition technique enabling a growth control at the atomic scale which has grown substantially in the 70s. First, this section briefly describes a typical ALD process and the main aluminum (Al) and nitrogen (N) used precursors used for AlN growth by ALD. Finally, the influence of several ALD parameters on AlN crystal quality are addressed.

II.2.3.2.1.1. Brief description of the technique

Atomic Layer Deposition (ALD) is a CVD derivative elaboration technique based on the sequential introduction of precursors leading to saturated, self-limiting and separated gas-solid reactions. Alternating pulses serving as introduction of precursors and purges repeat these reactions cyclically. A typical ALD cycle is represented in Figure II.7. As an ALD deposition is self-limiting, it is performed in a temperature range in which the Growth Per Cycle (GPC) is constant. This temperature is called “ALD window”<sup>161</sup>.

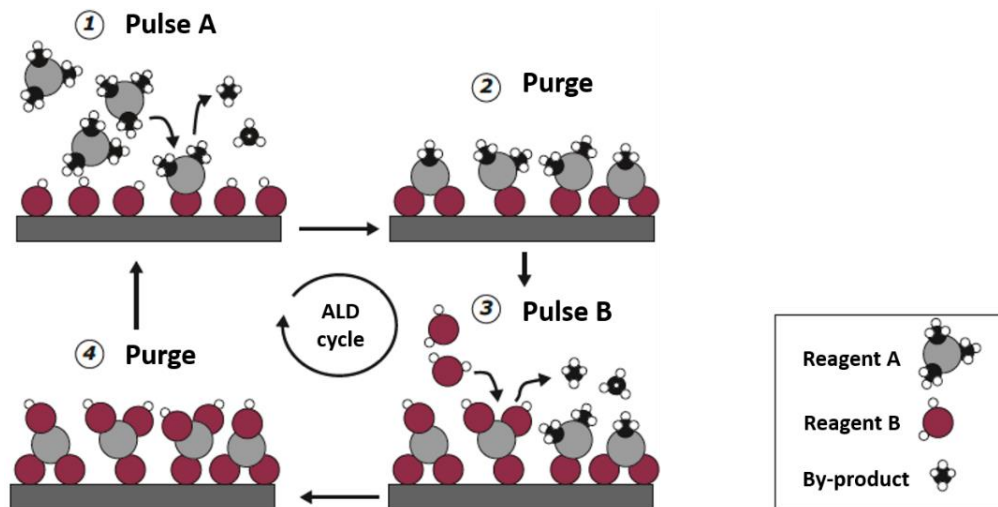


Figure II.7: Typical ALD cycle<sup>161</sup>

In the literature, we can mainly distinguish two types of ALD deposition applied to AlN: pure Thermal ALD (T-ALD) and Plasma-Enhanced ALD (PE-ALD). The main Al and N precursors employed are TriMethylAluminum (TMA) and ammonia (NH<sub>3</sub>), respectively. Some studies report more exotic precursors such as N<sub>2</sub>/H<sub>2</sub> or based on hydrazine (N<sub>2</sub>H<sub>4</sub>)<sup>162,163</sup> and derivatives like hydrazinium chloride (NH<sub>2</sub>H<sub>4</sub>HCl)<sup>164</sup> or monomethylhydrazine (MeHNNH<sub>2</sub>)<sup>165</sup> for N precursors. Triisobutylaluminum (Al(C<sub>4</sub>H<sub>9</sub>)<sub>3</sub>)<sup>164</sup>, Tris(DiEthylAmido)Aluminum (TDEAA)<sup>162</sup> or aluminum hydride<sup>166,167</sup> are also mentioned for Al precursor.

II.2.3.2.1.2. ALD parameters influencing the AlN crystal quality

Depending on the ALD equipment and experimental conditions, the ALD window of AlN slightly varies. For example, for a PE-ALD process, an ALD window between 100 °C and 225 °C was identified by Alevli et al.<sup>168</sup> while Banerjee et al.<sup>147</sup> find it between 300 °C and 350 °C. This latest is in good agreement with Tian et al.<sup>148</sup> which display a narrower ALD window between 325 °C and 350 °C. Whatever the study, the ALD window of AlN not exceed 400 °C which made ALD a low-temperature deposition technique. This characteristic combined with an atomic scale control of the deposition resulting in a low growth rate does not make ALD the preferred technique to grow high crystalline quality AlN films.

However, certain changes in ALD experimental conditions can influence the crystallinity of AlN film. The promotion of AlN (002) peak measured in XRD or Grazing Incidence XRD (GIXRD) with the increase in deposition temperature has been demonstrated in several studies<sup>147,168,169</sup>. These results are sometimes obtained beyond the ALD window. Therefore, we are in a CVD regime in which the Growth Per Cycle (GPC) is dependent of the temperature. Banerjee et al.<sup>147</sup> show that an increase in plasma power and temperature deposition promote the formation of AlN (002) planes. They also indicate that an *in situ* plasma pre-treatment can slightly affect the preferential orientation and demonstrate that the choice of the substrate is important since AlN deposited onto SiO<sub>2</sub> displays a decrease in (002) peak intensity compared to Si (100) or Si (111) substrates. The application of a substrate biasing also promotes AlN (002) peak<sup>170</sup>.

Finally, the general observed tendency with typical XRD or GIXRD structural characterizations is that ALD deposited AlN is not a highly ordered crystal. According to our knowledge, no study has investigated the mosaicity of an AlN thin film deposited by the classical T-ALD and PE-ALD techniques due to its poor crystallinity. These results are inherent of the deposition technique of this material and are not surprising since ALD is a deposition technique known to have a low growth rate (typically around 0.005 nm.s<sup>-1</sup> for AlN) compared to PVD or CVD technique, which enable to have an atomic scale control of the deposition giving access to conformal and homogeneous thin films.

Recently, an ALD derivative called “Atomic Layer Annealing” (ALA) aroused a particular interest. It consists in a classic ALD cycle in which the last step is an Ar or H<sub>2</sub>/Ar plasma step enabling to crystallize the AlN film cycle per cycle. This derivative ALD technique enables to



achieve high crystalline quality AlN thin films. Several studies report an AlN thin film elaborated by ALA with a (002) RC below  $0.05^\circ$  <sup>171–173</sup>.

#### II.2.3.2.1.3. Conclusions on AlN ALD deposition

Beyond its low growth rate which is not compatible to elaborate thick films in the industry, this low-temperature and “soft” deposition technique is not suitable to obtain high quality AlN films. In fact, although some parameters can affect the AlN crystal quality, the overall studies in the literature agree to say that the crystallinity is still poor. As it will be mentioned in chapter 3, section III.2.1.2, these results have been experimentally confirmed since T-ALD and PE-ALD AlN deposition were investigated and led in the better conditions to a weak c-axis preferential orientation.

#### II.2.3.2.2. Chemical Vapor Deposition (CVD)

The term “Chemical Vapor Deposition” (CVD) is a generic term referring to a wide range of deposition techniques such as Hydride Vapor Phase Epitaxy (HVPE), High-Temperature CVD (HT-CVD), Low-Pressure CVD (LP-CVD), Plasma-Enhanced CVD (PE-CVD) or Metal Organic CVD (MOCVD). It is a high-temperature deposition technique enabling to achieve AlN single crystal thin film when the growth is performed on a suitable substrate.

As the AlN elaboration has been investigated by different variants of CVD techniques and to be consistent with the content of this work, this section is dedicated to AlN elaboration by MOCVD technique. First, we describe a typical CVD process and mention the main Al and N precursors used to grow AlN by MOCVD. Second, we address the main MOCVD parameters influencing the AlN crystal quality. Finally, we discuss the choice of the substrate and the AlN crystal quality obtained in the literature.

##### II.2.3.2.2.1. Brief description of the MOCVD technique

Chemical Vapor Deposition (CVD) is based on chemical reactions of gas-phase precursors to enable the elaboration of thin films. A typical CVD deposition process is schematically sketched in Figure II.8.

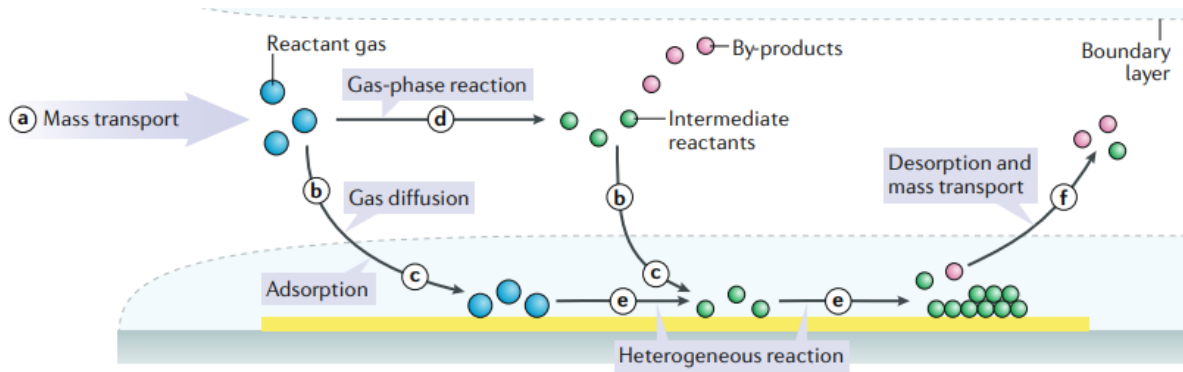


Figure II.8: Typical Chemical Vapor Deposition (CVD) process <sup>174</sup>

Independently of the CVD type, the fundamental process is similar and can be described as follows <sup>174,175</sup>. First, gaseous precursors are transported into the reactor. They form intermediate reactants and by-products via homogeneous reactions or diffuse at the substrate surface where they are adsorbed. Second, these species diffuse at the substrate surface and a thermally activated gas-solid reaction occurs on preferential sites. It leads to the formation of a continuous thin films. Finally, the unreacted species and gaseous products desorb from the surface and are transported away from the reaction zone.

Currently, almost only TMA and  $\text{NH}_3$  are reported as Al and N precursors, respectively, in AlN MOCVD deposition. We can note that during the 80s and 90s, several groups of research explored the use of others precursors such as hydrazine <sup>176</sup> for N precursor and dimethylaluminum amide  $((\text{CH}_3)_2\text{AlNH}_2)_3$  <sup>177</sup>, dimethylaluminum azide  $((\text{Et}_2\text{AlN}_3)_3$  <sup>178,179</sup> or dimethylethylamine alane (DMEAA) <sup>166</sup> for Al precursor. Some studies also investigated the use of a single precursor to deposit AlN by MOCVD <sup>180,181</sup>.

#### II.2.3.2.2.2. MOCVD parameters influencing the AlN crystal quality

According to Table II.4 previously discussed, the lattice and CTE mismatches between AlN and its main substrates remain not negligible. This effect combined with the high deposition temperature of AlN MOCVD (typically  $> 1000\text{ }^\circ\text{C}$ ) leads to high dislocation density in the AlN film and induces cracks fort thick epilayers <sup>182,183</sup>. To manage this issue and reduce the dislocation density, two tendencies are mainly employed in AlN MOCVD deposition: multi-steps deposition or Epitaxial Lateral Over Growth (ELOG). The multi-steps deposition mainly results in a “low” and “high” temperature AlN deposition while ELOG is based on a local etching of the substrate or AlN template.

In this sub-section, we first discuss the influence of classical parameters such as deposition temperature or V/III ratio on AlN MOCVD crystal quality. Second, we focus on the influence of the growth substrates (silicon, sapphire and silicon carbide). The multi-steps AlN deposition and ELOG approaches are detailed in the sapphire substrate sub-section since they are only exclusively implemented on this substrate.

*II.2.3.2.2.2.1. Influence of deposition temperature*

In AlN MOCVD growth, the deposition temperature is a primordial parameter affecting the growth mode of the layer: 2-dimensional (2D) or 3-dimensional (3D) growth mode. The temperature is also directly related to the multi-steps deposition approach. In fact, to avoid the formation of high dislocation density leading to cracks in the films, the AlN MOCVD growth is generally divided in two steps: a “low” temperature deposition enabling a 3D growth mode and a “high” temperature deposition allowing a 2D mode growth. Chen et al.<sup>184</sup> investigated the influence on this temperature on these modes on sapphire substrate. They demonstrate that the 3D growth mode is predominant at low temperature (880 °C) due to a poor Al adatoms mobility. However, the formed 3D islands lead to an increase in surface roughness. Increasing the deposition temperature increases the Al adatoms mobility and leads continuously to a mix of 3D-2D growth towards a full 2D growth. It is on these different growth modes that the multi-steps AlN MOCVD approach is based and detailed in section II.2.3.2.2.3.2.1.

The improvement of AlN MOCVD crystal quality with a reduce dislocation density by adjusting these temperatures, and by extension these growth modes, has been widely investigated. Therefore, many studies<sup>184–187</sup> proposed a simple two-steps deposition method. Other more complex approaches based on multi-step deposition at various temperatures are proposed and discussed later<sup>188–191</sup>.

*II.2.3.2.2.2.2. Influence of V/III ratio*

A second primordial parameter during AlN MOCVD deposition is the V/III ratio (N/Al ratio). Its effect is similar to the deposition temperature since it affects the Al adatoms mobility enabling to promote either a 3D growth mode or a 2D growth mode. In fact, high V/III ratio decreases the Al adatoms diffusion length promoting a 3D growth mode and consequently contributes to surface roughness<sup>189</sup>. Streicher et al.<sup>192</sup> demonstrate that high V/III (2540) enables to decrease significantly the AlN (002) and (102) RC down to 0.12° and 0.33°,

respectively, attesting a decrease in dislocation density. However, a V/III of 3840 leads to an increase in these RC.

Moreover, an increase in V/III ratio affects the growth rate and contributes to longer and therefore more expensive processes. It is typically an issue in AlN ELOG approach in which too high V/III ratio can lead to not coalesced AlN stripes<sup>193</sup>. Hence, and as for the deposition temperature, a tradeoff must be found to perform a suitable and high-quality AlN MOCVD growth.

#### *II.2.3.2.2.2.3. Other parameters*

Although the AlN MOCVD deposition temperature and V/III ratio are the most widely studied parameters in the literature since they directly pilot the AlN growth mode, other parameters are also mentioned. For example, Streicher et al.<sup>192</sup> investigate the effect of pressure and demonstrate a decrease in AlN (002) and (102) RC by increasing the pressure. However, the AlN surface becomes rougher. Chen et al.<sup>187</sup> show that an optimum exists in the AlN thickness of the low temperature buffer layer to promote low dislocation density and crack-free AlN epilayers. We can also mention that some studies investigated substrate orientations and off-cut to optimize the AlN MOCVD growth<sup>185,194</sup>.

#### *II.2.3.2.2.3. Influence of the growth substrate*

##### *II.2.3.2.2.3.1. Silicon-based substrate*

The high temperature of MOCVD process, typically > 1000 °C, makes the substrate a primordial choice for AlN growth to avoid film cracks induced by lattice or CTE mismatches. Hence, the direct growth of AlN by MOCVD Si (100)- or (111)-oriented is not widely studied. An AlN (002) RC of 0.68° is reported by Feng et al.<sup>195</sup> with a direct AlN growth on Si (111). The same issue persists with the growth of GaN that is why an AlN layer is typically used for the MOCVD growth of GaN on Si (111) serving as nucleation, buffer and barrier layer between GaN and Si<sup>196-198</sup>.

In the case of AlN MOCVD for Bulk Acoustic Wave (BAW) devices on silicon-based substrates, the deposition is not performed directly on silicon but partially on the bottom metallic electrode. Moreover, the AlN MOCVD thickness rarely exceeds 1 μm enabling to obtain crack-free AlN films. For example, Aota's group obtains lower results in terms of AlN

crystal quality and acoustic device performance with the use of Mo electrodes <sup>199</sup> than Ru/Ta electrodes <sup>200</sup>.

Finally, the control of MOCVD deposition process seems primordial since disparate AlN (002) RC are achieved. For example, Feng *et al.* <sup>195</sup> and Yi *et al.* <sup>201</sup> show an AlN (002) RC of 0.68° and 0.33° for a 0.38 μm and 0.17 μm thick AlN layer, respectively. In this latest study, the enhancement of AlN PVD regrowth using an AlN MOCVD buffer layer has been demonstrated by decreasing the (002) RC from 1.48° to 0.68°. However, these values are far away of what have been achieved by Akoustis <sup>58,90</sup>. In fact, they indicate the deposition of an AlN single crystal by MOCVD displaying a (002) RC around 0.03° with exceptional acoustic performances. However, the deposition and acoustic device elaboration processes are not fully described in their studies.

A non-exhaustive review of AlN MOCVD deposition on silicon-based substrates is presented in Annex part 1, Table I. When available, the Si substrate orientation, bottom electrode material and characteristics parameters  $k_{\text{eff}}^2$  and Q for acoustic wave devices are mentioned.

#### *II.2.3.2.2.3.2. Sapphire-based substrate*

The literature on MOCVD growth of AlN on sapphire substrates is rich compared to silicon counterpart. In fact, sapphire is the most popular substrate for AlN growth due to its stability at high temperatures and transparency in ultraviolet band region <sup>202</sup>. However, the lattice and CTE mismatches between AlN and sapphire remain not negligible leading to high dislocation density in the AlN film and inducing cracks for thick epilayers <sup>182,183</sup>. Hence, two tendencies are mainly employed to overcome this issue: multi-steps AlN deposition or Epitaxial Lateral Over Growth (ELOG).

##### *II.2.3.2.2.3.2.1. Multi-steps deposition*

The multi-steps deposition consists in the growth of a “low-temperature” (LT) layer serving as a buffer and nucleation layer for a second-thick growth at “high temperature” (HT) <sup>203</sup>. This approach was first investigated for the growth high-quality GaN epilayer and leads to 2014 Nobel Prize of Physics award due to the development on p-type GaN and GaN-based blue leds <sup>204</sup>. During the LT growth of GaN nucleation layer, the formation of high-density 3D islands promotes vertical growth over lateral growth. During the *in situ* annealing process,

GaN is decomposed and redeposited on other areas to form large 3D islands of GaN. These large and faceted 3D islands are used to promote dislocation bending and annihilation during the HT growth which enhance the crystal quality of GaN. Finally, the coalescence of these 3D islands leads to a smooth GaN surface.

However, the application of this approach for AlN growth is not so effective. The higher stability of AlN and the lower chamber pressure during the growth make its decomposition more difficult. Moreover, Al adatoms issued from AlN decomposition hardly migrate to preferential sites leading to a 2D growth without 3D islands due to a higher diffusion barrier. Hence, dislocations are not effectively annihilated during the HT AlN growth<sup>205</sup>. Important efforts are devoted to optimize this technique and especially the LT AlN layer.

As previously mentioned, research groups investigated the influence of a wide range of parameters and processes on AlN templates such as deposition temperature<sup>184</sup> or thickness<sup>187</sup> of LT AlN layer, V/III ratio<sup>192,193</sup> or sapphire substrate orientation<sup>185,194</sup>. This gives rise to multi-steps AlN deposition more or less complex<sup>182,188–191,206</sup>. A relatively classic approach is to perform an AlN MOCVD deposition by alternating low and high temperature deposition (2D and 3D growth mode)<sup>188,189</sup>. Some studies proposed more complex structures with different deposition temperatures<sup>182</sup> or via a sandwich method to grow high quality AlN layers<sup>206</sup>. It is also possible to adjust both deposition temperature and V/III ratio<sup>190</sup> which shows a wide range of future possible investigations.

A non-exhaustive review of AlN MOCVD deposition processes on sapphire substrates by multi-steps method is presented in Annex part 1, Table II. The AlN (002) and (102) RC are usually measured since they are proportional to screw and edge dislocations, respectively<sup>207</sup>. According to our knowledge, only one publication deals with AlN deposited on a sapphire substrate targeting an acoustic wave device<sup>102</sup>. An electromechanical coupling coefficient  $k^2_{\text{eff}}$  of 0.8 % at 1 GHz has been obtained.

#### II.2.3.2.2.3.2.2. Epitaxial Lateral Over Growth (ELOG)

These 3D faceted islands enabling to reduce the dislocation density during a second thicker growth can also be produced by patterning the sapphire substrate or template. This technique called Epitaxial Lateral Over Growth (ELOG) can be implemented directly on sapphire substrates or on AlN/sapphire templates. Imura *et al.*<sup>208,209</sup> were pioneers in ELOG of AlN on

patterned AlN/sapphire templates with trenches (2  $\mu\text{m}$ -deep and 3  $\mu\text{m}$ -wide) and demonstrate a significant decrease in dislocation density from  $10^9 \text{ cm}^{-2}$  to less than  $10^7 \text{ cm}^{-2}$ . The direction of the trenches in the sapphire affects the AlN thickness at which coalescence occurs. It should be along [11-20] to promote the entire surface coalescence <sup>203</sup>.

However, the microscale ELOG localized the threading dislocations in the coalescence boundaries above. Moreover, the low migration of Al adatoms combined to these large voids require a thick AlN layer ( $> 5 \mu\text{m}$ ) to obtain a smooth and coalescent surface as observed in Figure II.9.

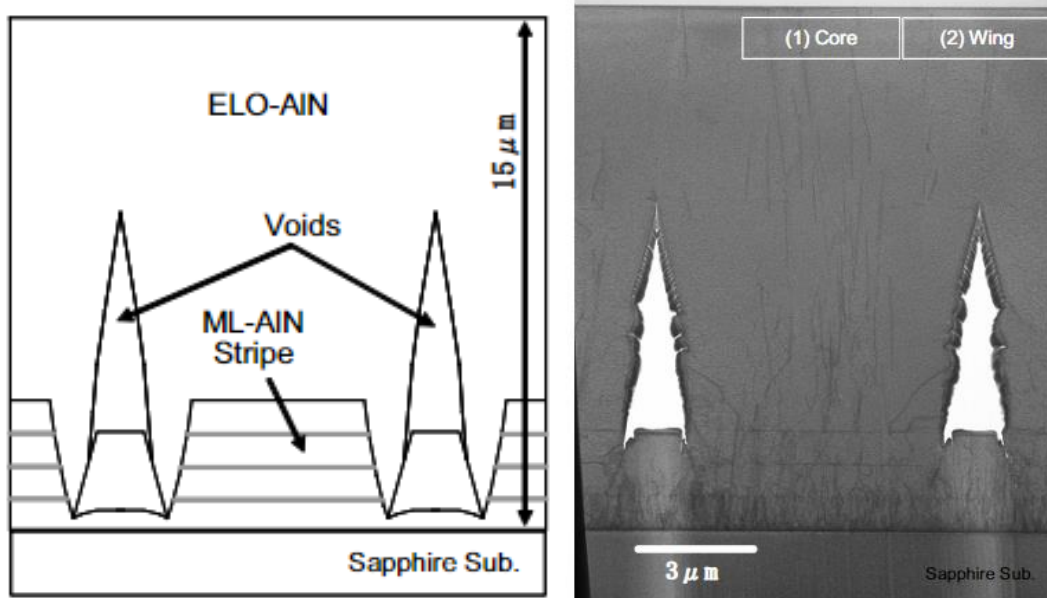


Figure II.9: Cross-sectional TEM image and schematic illustration of an ELOG-AlN template on a sapphire substrate <sup>193</sup>

To overcome this issue and benefit of the development of nano-development technology, nano-patterned sapphire substrates was introduced via various approaches such as nanospheres (polystyrene or  $\text{SiO}_2$ ) <sup>122,123</sup> or nano-imprint resist <sup>212,213</sup>. The coalescence thickness was significantly decreased below 3  $\mu\text{m}$ . A non-exhaustive review of AlN MOCVD elaborated with ELOG technique on sapphire substrates is presented in Annex part 1, Table III. To the best of our knowledge, no study focuses on the elaboration of AlN by MOCVD on a sapphire substrate targeting an acoustic device is mentioned in the literature.

II.2.3.2.2.3.2.3. Conclusions on multi-steps deposition and ELOG

To conclude on this section, the direct growth of high-quality AlN MOCVD on sapphire substrate requires specific precautions due to lattice and CTE mismatches between both materials. The multi-step growth approach faces to limitations due to AlN properties (high AlN stability, hard Al adatoms migration...). A wide range of parameters such as deposition temperature, V/III ratio, optimization of AlN template and others have been investigated but remain at a research level. The ELOG technique has demonstrated to significantly reduce dislocation density. However, this approach usually requires important AlN thickness which make it a high fabrication cost technique with multi and complex processes such as lithography, etching, growth and regrowth.

We should also mention another alternative approach to grow high AlN quality layer with a reduced dislocation density on sapphire substrate. In fact, several groups of research investigated *ex situ* High Temperature Annealing (HTA) <sup>214-218</sup>. This technique enables to elaborate high quality AlN layers with lower thicknesses. The HTA is usually performed on an AlN nucleation layer which can deposited by PVD or MOCVD at a temperature exceeding 1500 °C. However, this technique also faces some issues such as strong residual stress, carbon contamination and high-concentration point defects <sup>203</sup>.

II.2.3.2.2.3.3. Silicon Carbide-based substrates

II.2.3.2.2.3.3.1. Cubic Silicon Carbide (3C-SiC)

As a reminder, 3C-SiC is a metastable polytype but monocrystalline 3C-SiC thin layers can be achieved on silicon substrates <sup>156</sup>. Although a reasonable lattice and CTE mismatches between 3C-SiC (especially (111)-oriented) and AlN, its deposition, as well as other III-nitrides deposition by MOCVD on 3C-SiC substrates has not been widely investigated in the literature. In fact, AlN growth on 3C-SiC seems particularly tricky compared to other substrates.

For example, Tanaka *et al.* <sup>219</sup> compare the growth of 140 nm AlN MOCVD thin film deposited on c-plane sapphire and 3C-SiC (100) deposited on Si (100). The AlN growth on sapphire shows a c-axis normal to substrate surface while c-axis lies on the (100) planes of 3C-SiC. The results are different for AlN MOCVD on (111)-oriented 3C-SiC buffer layer since Hong *et al.* <sup>220</sup> indicate the successful growth of monocrystalline AlN films by MOCVD on 3C-SiC (111) while a direct deposition on Si (111) lead to polycrystalline AlN. However, the c-axis orientation was not assessed in this study. With a similar approach, Liaw *et al.* <sup>221</sup> demonstrate



a drastic improvement of AlN c-axis improvement by decreasing AlN (002) RC from 12° to 1.8° with the use of 3C-SiC (111) buffer layer deposited on Si (111). Gallium nitride (GaN) growth are also reported on 3C-SiC (111)<sup>222,223</sup>. Abe et al.<sup>223</sup> show a slight decrease in GaN (002) RC from 0.27° to 0.21° with a 3C-SiC (111) buffer layer. To the best of our knowledge, only one study report proposed an AlN-based acoustic device on a 3C-SiC buffer. This result is not experimental but based on simulation by Finite Element Method (FEM) and displays a  $k_{\text{eff}}^2$  of 1.45 %<sup>224</sup>.

Although these results on the use of 3C-SiC (111) buffer layer highlight an improvement of AlN (or GaN) crystalline quality, they do not compete what can be achieved using sapphire substrate as previously discussed or with other 4H or 6H-SiC polytypes as it will be addressed. The few studies dealing with AlN MOCVD growth on cubic silicon carbide substrates are presented in Annex part 1, Table IV.

#### II.2.3.2.2.3.3.2. Hexagonal Silicon Carbide (4H- and 6H-SiC)

Although the growth of AlN by MOCVD on hexagonal silicon carbide is not studied as much as on sapphire, AlN and hexagonal silicon carbide (4H- or 6H-SiC) display a reasonable lattice mismatch of 1.3 % which makes this material a substrate of choice for AlN growth. However, the CTE mismatch remains important with 31.3 % and 27.3 % for 4H- and 6H-SiC, respectively. Hence, the needed requirements to perform a crack-free and high crystalline AlN growth with a reduced dislocation density on sapphire substrate are applied on hexagonal silicon carbide. It means that high V/III ratio and moderate deposition temperature enable a 3D islands AlN growth while promoting a high crystalline quality. For example, Zuo et al.<sup>225</sup> have successfully grown a bulk AlN single crystal with a (002) RC of 0.12° using AlN MOCVD buffer layer deposited at 1100 °C and high V/III ratio enabling a 3D growth mode. Similarly, Yoshida et al.<sup>226</sup> show a crack-free and low dislocation density AlN layer grown in 3D mode while cracks are observed on the layer grown on 2D mode.

Moreover, several studies show the importance to perform an AlN growth at relatively high temperature to achieve a sufficient crystal quality. For example, Kakanakova et al.<sup>227</sup> demonstrate that a 1100 °C AlN MOCVD growth on 4H-SiC can lead to nanopipes defects and significant C- or O-contamination compared to 1200 °C. Similar results have been obtained by Zhang et al.<sup>228</sup> where the increase in AlN deposition temperature up to 1220 °C annihilates the formation of pits defects while enabling a smoother surface and better crystal quality.

However, this increase in deposition temperature leads to an important AlN tensile stress. Finally, Imura et al.<sup>229</sup> show a decrease in dislocation density by increasing the deposition temperature of AlN up to 1600 °C on 6H-SiC resulting from the formation of loop structure which annihilated the dislocations. The remaining dislocations are mainly edge-type due to the lattice mismatch at the AlN/SiC interface.

Another interesting study proposed by Yin et al.<sup>202</sup> is to compare the growth of AlN by MOCVD on sapphire and 6H-SiC substrate. They demonstrate a better growth rate on 6H-SiC than sapphire due to differences in the mobility of Al atoms on both substrates leading to a thickness of 0.25 µm on sapphire and 0.68 µm on 6H-SiC. Despite this thickness difference, they compare the AlN crystal quality on both substrates. The AlN layer on 6H-SiC shows a better crystal quality in terms of c-axis orientation, grain size and a lower AlN strain/stress grown on 6H-SiC. However, the dislocation density of the samples is similar. These results are attributed to a lower lattice mismatch between AlN and 6H-SiC than AlN and sapphire. A comparison on the AlN layers with an identical thickness on both substrates would be interesting.

The multi-steps approach is also investigated to achieve high quality AlN MOCVD layers on hexagonal silicon carbide substrates. For example, Chen et al.<sup>230</sup> propose a multi-layered structure alternating between a 2D and 3D AlN growth obtained at high temperature (1170 °C), low V/III ratio and low temperature (1070 °C), high V/III ratio, respectively. They achieved a 1.5 µm AlN layer with a reduce dislocation density while a 1.0 µm thick grown in 3D standard conditions is cracked. It is also worth to notice that more exotic can be reported. Lu et al.<sup>231</sup> use an interface atomic layer between an AlN nucleation layer and SiC substrate. This interface layer composed of a gradient of AlSiN enables to reduce the lattice mismatch between AlN and SiC by sharing the in-plane symmetry and providing a compositional gradient across these layers.

However, the growth of AlN MOCVD on hexagonal silicon carbide targeting acoustic devices is not widely spread. To the best of our knowledge, Uehara et al.<sup>232</sup> demonstrate the growth of AlN single crystal with smooth surface (RMS = 1.35 nm) by MOCVD on 6H-SiC targeting a Surface Acoustic Wave (SAW) device. As for AlN MOCVD deposition on sapphire, high V/III ratio promote AlN crystal quality. They demonstrate an AlN phase velocity of 6600 m.s<sup>-1</sup> but no electromechanical coupling coefficient  $k_{\text{eff}}^2$  or quality factor Q were determined.

It is also worth to mention two studies of Akoustis<sup>233,234</sup> on 4H-SiC indicating the elaboration of a Bulk Acoustic Wave (BAW) device. In both studies, the deposition conditions of the AlN single crystal piezoelectric layer are not described but they achieve decent  $k^2_{\text{eff}}$  between 6.32 % and 7.63 % with a relatively good FOM around 90.

A review of studies dealing with AlN MOCVD growth on hexagonal silicon carbide substrates is presented in Annex part 1, Table V.

#### II.2.3.2.2.4. Conclusions on AlN MOCVD deposition

Beyond the deposition parameters such as temperature or V/III ratio, the AlN crystal quality deposited by MOCVD is significantly affected by its growth substrate. Figure II.10 presents an overview of the AlN MOCVD (002) RC as a function of the AlN thickness according to the studies reviewed from Table I to Table V presented in Annex part 1.

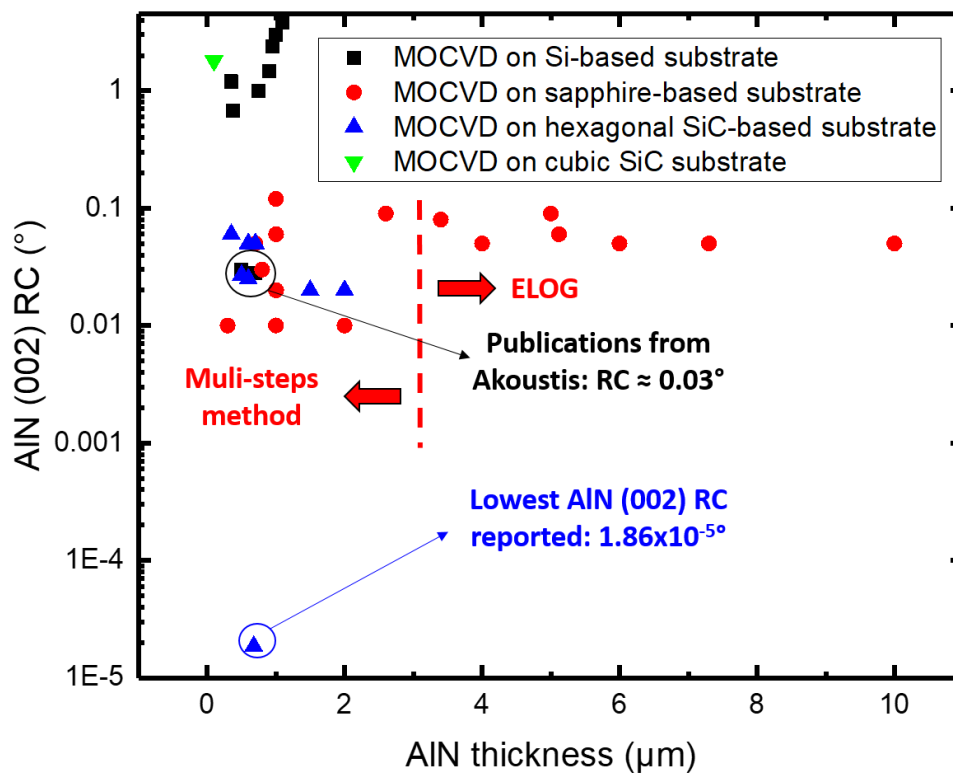


Figure II.10: Graphic representation of AlN (002) RC obtained by MOCVD on silicon, sapphire and SiC (cubic and hexagonal) substrates

First, the AlN growth on 3C-SiC buffer layer has not been widely studied and seems difficult (RC value of 1.8°). Second, we clearly distinguish that silicon-based substrate leads to a poor c-axis orientation compared to sapphire or hexagonal SiC substrate. We observe an exception for the three results published by Akoustis displaying a (002) RC around 0.03°.

However, and as previously mentioned, AlN MOCVD process and template is not fully described in their studies. Subsequently, the MOCVD AlN crystal quality obtained on sapphire and hexagonal SiC is relatively similar although an extremely low (002) RC has been reported on a hexagonal SiC substrate. Finally, focusing on sapphire substrates, we clearly observed a significant difference in the target thickness depending on the elaboration method: ELOG or multi-steps approach. Therefore, this figure shows that the most suitable substrates for the growth of high quality AlN films by MOCVD are sapphire and hexagonal SiC. As provided in Table II.4, this tendency is in line with what we could expect since these substrates are those who display the most reasonable lattice and CTE mismatches with AlN.

#### II.2.3.2.3. Physical Vapor Deposition (PVD)

Similarly to Chemical Vapor Deposition (CVD), Physical Vapor Deposition (PVD) is a generic technique which groups different variants. We can mention vacuum evaporation, sputter deposition (eventually reactive), arc vapor deposition, ion plating deposition or Ion Beam Assisted Deposition (IBAD) <sup>235</sup>.

This sub-section focuses on AlN PVD deposition by reactive sputtering. High quality AlN thin films with a pronounced c-axis textured can be deposited by this technique. Moreover, the deposition temperature can be kept low (< 400 °C) which is extremely suitable for Micro Electro Mechanical Systems (MEMS) applications. In contrast to CVD techniques, the stress can also be tuned by adjusting bias or Ar/N<sub>2</sub> ratio. Finally, although sputtered AlN thin films are polycrystalline, the properties are similar to MOCVD AlN single crystal epitaxially grown on sapphire. In fact, as long as the structure is dense, the in-plane properties are not affected by the arbitrary in-plane orientation of AlN hexagonal grains growing along c-axis and grain boundaries do not degrade AlN properties <sup>22</sup>.

In first, we briefly describe a typical reactive sputtering process as well as the reaction mechanism. In second, we address the influence of various process parameters on the AlN crystal quality. Finally, and similarly to what has been done for CVD deposition, we discuss the influence of the growth substrate.

II.2.3.2.3.1. Brief description of the reactive sputtering technique

A typical reactive sputtering process for AlN thin film deposition is given in Figure II.11. It consists in a vacuum chamber in which a pure aluminum (Al) target (cathode) is mounted on a magnetron sputter source and a heating substrate chuck serving as an electrode on which a self-bias (lower than cathode voltage) can be applied. The inlet feeds the chamber in argon (Ar) and nitrogen (N<sub>2</sub>) gases. The Ar and N<sub>2</sub> gases are ionized to create an Ar + N<sub>2</sub> plasma whose the discharge volume is enclosed between the target and the substrate using anodes and shields. When a positive and negative potential is applied to the anode and the cathode, respectively, the positive ions are accelerated toward the Al target (cathode), collide with it and sputter off Al atoms, which react with N and create an AlN thin film onto a substrate <sup>236</sup>.

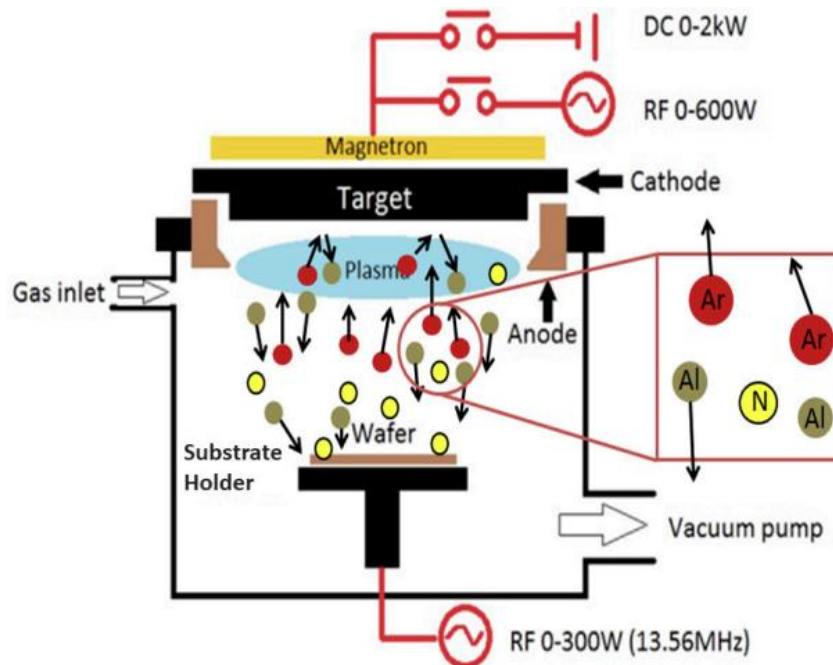


Figure II.11: Typical reactive sputtering process for AlN thin films deposition <sup>236</sup>

The target (cathode) sputtering also causes secondary electron emission enabling to the Ar + N<sub>2</sub> plasma to sustain itself. During the reactive sputtering deposition, an AlN layer is formed on the Al target (poisonous regime). To annihilate this layer, either pulsed Direct Current (DC) or Radio Frequency (RF) enable to reverse the biasing powers on the source. In a modern industrial equipment, the Al target is larger than the substrate to obtain a good uniformity and the magnets used in the magnetron are rotating to erode homogeneously the complete target <sup>22</sup>.

II.2.3.2.3.2. PVD parameters influencing the AlN crystal quality

II.2.3.2.3.2.1. Influence of sputtering pressure

The influence of sputtering pressure on AlN deposition has been widely investigated in the literature. For example, Ababneh *et al.*<sup>144</sup> show a decrease in intensity of AlN (002) peak by with the increase in sputtering pressure. These results have been confirmed by several studies<sup>161–163</sup> and (100) oriented AlN layers have been reported by Cheng *et al.*<sup>240</sup> with the increase in AlN sputtering pressure. It can be explained by the kinetic theory of molecular gases. At low sputtering pressures, the sputtered Al atoms arrive on the substrate with a higher kinetic energy than at higher sputter. Their energy is transferred to the growing film which leads to an increase in adatoms mobility and form a closest-packed (002) plane enabling films<sup>238</sup>. Hence, a low sputtering pressure is primordial to achieve highly c-axis oriented AlN thin film.

II.2.3.2.3.2.2. Influence of deposition temperature

The influence of deposition temperature is also an important parameter affecting AlN c-axis orientation. An interesting study proposed by Medjani *et al.*<sup>241</sup> demonstrate an increase in intensity of AlN (002) peak up to 400 °C suggesting an enhancement in c-axis orientation. It could be expected that a higher temperature promotes grain size and c-axis orientation by increasing adatom surface mobility. However, beyond 400 °C, AlN films display a (100) preferred orientation. It is explained by a decrease in AlN (002) planes vertical growth resulting from a higher adatoms mobility with less nucleation centers on (001) than (100) planes. Several studies obtained very similar results<sup>242,243</sup>.

However, this optimum temperature can be affected by the substrate characteristics. In fact, Iqbal *et al.*<sup>244</sup> investigate AlN deposition between 250 °C and 450 °C on on-axis and off-axis (4°) 3C-SiC (111) deposited on Si (111). They obtain an optimum AlN c-axis orientation ((002) RC of 2.58°) at 400 °C on on-axis 3C-SiC (111) while the c-axis orientation is continuously promoted up to 450 °C (decrease in (002) RC from 2.78 ° to 1.91°) on off-axis 3C-SiC (111).

In keeping with the influence of deposition temperature, the effect of *ex situ* annealing on sputtered AlN layer is sometimes investigated. For example, Kar *et al.*<sup>245</sup> demonstrate a decrease in the FWHM of AlN (002) peak after a thermal annealing at 600 °C and 800 °C while a 1000 °C annealed AlN layer presents some cracks. Similar results have been obtained by Phan *et al.*<sup>246</sup> where an AlN layer displays some cracks after a 900 °C annealing. In addition

and contrary to Kar et al. <sup>245</sup>, they indicate no decrease in FWHM of AlN (002) peak after a thermal annealing at 600 °C accompanied with a slight increase in Surface Acoustic Wave (SAW) velocity in their device. Moreover, Vergara et al. <sup>247</sup> show that tensile AlN grains appear after a 1300 °C thermal annealing while the as-deposited AlN layer is compressive and other orientations than (002) can be observed on some samples. These results suggest that combined AlN reactive sputtering process with an *ex situ* annealing seem difficult since it leads to various microstructure depending on the annealing conditions. We can also mention that laser annealing is investigated <sup>248</sup>.

#### *II.2.3.2.3.2.3. Influence of sputtering power*

The sputtering power is an easy parameter to tune and investigated by many research groups. Increase of the sputtering power is combined with an increase of ions kinetic energy. Similarly, to as what been explained on sputtering pressure, an increase in sputtering power promote the elaboration of highly c-axis textured AlN films. Hence, this tendency has been demonstrated by several studies <sup>249–251</sup>. Especially, Kumada et al. <sup>252</sup> demonstrate an important decrease in AlN (002) RC down to 0.41° on sapphire substrate. In the same study, the AlN (002) RC is drastically decreased down to 0.01° - 0.02° when the sapphire substrate is nitrided. We can note that the increase in sputtering power also enable to increase the growth rate which can also modify the surface morphology and AlN grain size.

Finally, Lin et al. <sup>253</sup> propose a two-steps AlN deposition on 3C-SiC (100). First, 50 nm thick AlN is deposited at 3 kW and followed by a thick AlN regrowth at 5.5 kW. They obtained an AlN (002) RC of 1.31° for a 3 µm thick AlN layer and elaborated a SAW device displaying an acoustic velocity of 5200 m.s<sup>-1</sup>.

#### *II.2.3.2.3.2.4. Ar/N<sub>2</sub> ratio*

The Ar/N<sub>2</sub> ratio is another parameter affecting the AlN crystal quality. However, no precise tendency seems to be observed since some groups obtained highly c-axis textured AlN thin films at low or high N<sub>2</sub> concentration. On one hand, several studies <sup>240,254</sup> demonstrate that at high/pure N<sub>2</sub>, the AlN films are fully (002)-oriented while this preferential orientation decreases by decreasing the N<sub>2</sub> concentration up to becoming (100)-oriented. Similarly, Zhong et al. <sup>255</sup> indicate a decrease in AlN (002) peak by increasing N<sub>2</sub> concentration. On the other hand, other studies display opposite results. Liu et al. <sup>256</sup> show a significant increase in AlN (002) RC from 3.1° to 7.4° by increasing N<sub>2</sub> concentration.

Currently, two opposite theories are discussed to explain these results. The groups promoting the low N<sub>2</sub> concentration suggest that AlN atomic bonds can only be formed when Ar particles with high kinetic energy dominate. The other groups indicate AlN close-pack (002) plane could only be formed where N<sub>2</sub> particles dominate. We can refer to Iqbal et al.<sup>257</sup> study to discuss about these assumptions.

*II.2.3.2.3.2.5. Other parameters*

A wide range of other parameters can affect the AlN crystal quality. We can mention substrate bias voltage, the target to substrate distance, base pressure which is related to oxygen contamination or simply the AlN thickness. For example, substrate bias voltage is well-known to tune the AlN stress<sup>258</sup>. We can also note that a too high substrate bias voltage degrades the AlN (002) c-axis orientation<sup>259</sup>. Naturally, an important oxygen content in the chamber will affect the AlN stoichiometry and lead to the deposition of an oxidized AlN film with a degraded crystal quality<sup>260</sup>. Finally, an enhancement of AlN c-axis orientation occurs with the thickness<sup>261</sup>.

*II.2.3.2.3.3. Influence of the growth substrate*

*II.2.3.2.3.3.1. Silicon-based substrates*

The elaboration of AlN thin films on silicon-based substrates by reactive sputtering has been intensively investigated in the literature. According to Table II.4, the lattice mismatch between AlN and (111)-oriented Si substrate is better than AlN and (100)-oriented Si substrate. Hence, the crystal quality of AlN should be better on Si (111) substrates. This assumption is confirmed in several studies<sup>262–264</sup> comparing sputtered AlN thin films on Si (100) and Si (111) (and eventually Si (110)) substrates and can easily be illustrated as depicted in Figure II.12.

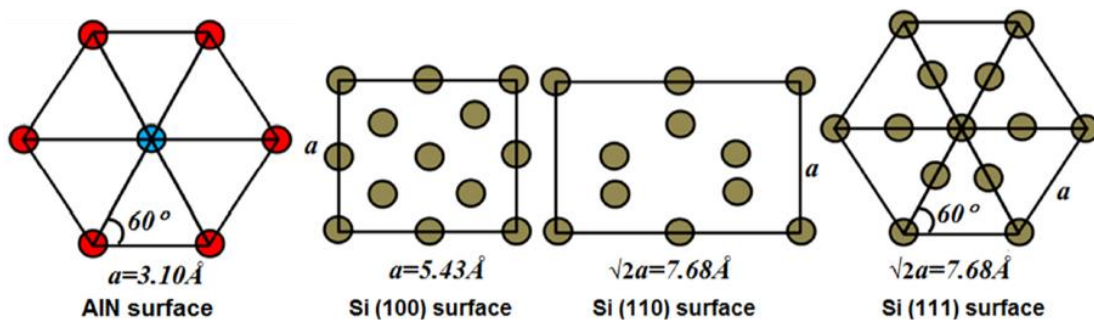


Figure II.12: Lattice (002) oriented AlN film and silicon (100), (110) and (111) substrate surface<sup>264</sup>



In fact, we clearly observed that the (111)-oriented silicon substrate displays a hexagonal lattice arrangement whereas Si (110) and Si (100) have a square and rectangular lattice arrangements, respectively. Hence Pandey et al.<sup>264</sup> demonstrate a better AlN c-axis orientation on Si (111) than Si (100) with a (002) RC of 4.2° and 13.5° (and 16.0° on Si (110)), respectively. A decrease in AlN residual stress have also been observed on Si (111). In addition, Zhang et al.<sup>263</sup> show a more pronounced AlN (002) peak, a larger grain size and a lower strain on AlN deposited on Si (111) than Si (100). They also demonstrate that the power discharge can affect AlN crystal quality. An increase in power discharge leads to a better pronounced AlN (002) peak but an increased strain on both substrates. Moreover, an AlN (110) orientation is also observed on Si (111) at the higher power discharge investigated (500 W). Similar results have been obtained by Riah et al.<sup>265</sup> showing an AlN (002) RC of 2.3° and 3.2° deposited on Si (111) and Si (100), respectively. They also demonstrate that a very thin (1 nm) AlN buffer deposited by Molecular Beam Epitaxy (MBE) enables to achieve higher crystal quality of the sputtered AlN regrowth by decreasing the (002) RC to 1.2°.

Beyond the silicon substrate orientation and deposition parameters, an elegant approach proposed by Shin et al.<sup>266</sup> is to enhance AlN crystal quality deposited by reactive sputtering using a two-steps deposition method. A 5 nm thick Al layer is pre-deposited before the AlN growth by switching off the N<sub>2</sub> gas. With this approach, they achieve a 0.1 μm thick AlN single crystal while a polycrystalline is obtained without this Al pre-deposition. The use of Al pre-deposition was also investigated by Dadgar et al.<sup>267</sup> before a high temperature (900 °C) AlN reactive sputtering deposition. They deposit a 0.1 μm thick AlN layer displaying a (002) RC of 0.63° on Si (111) substrate. In this study, we can note that the AlN deposition is performed in two-steps. First, the AlN layer is grown under N<sub>2</sub> to prevent the formation of SiN on the Si top surface. Second, the N<sub>2</sub> is switched by NH<sub>3</sub> to pursue the growth and enables to achieve smoother layers.

Finally, the choice of the bottom electrode material to texture the sputtered AlN layer is also primordial. Although Mo is the most widespread electrode material, the use of an Ir bottom electrode seems particularly interesting. In fact, Iborra et al.<sup>268</sup> demonstrate an AlN (002) RC of 0.89° for a 1 μm thick AlN layer integrated in an acoustic device. The device displays a  $k_{\text{eff}}^2$  of 6.5 % with a FOM of 37. Another study shows a AlN (002) RC of 1.0° deposited on a Ru bottom electrode with a  $k_{\text{eff}}^2$  of 6.5 %<sup>269</sup>. The influence of the substrate roughness has also

been investigated. In fact, Iborra et al. <sup>270</sup> elaborate a SMR acoustic device on Si(100) with a polished as-deposited Bragg reflector. They demonstrate a drastic improvement of AlN (002) RC on polished substrate and its enhanced c-axis textured growth is directly related to better  $k_{\text{eff}}^2$  values.

A non-exhaustive review of the crystal quality of sputtered AlN thin films on silicon-based substrate is presented in Annex part 1, Table VI. When available, the  $k_{\text{eff}}^2$  and quality factor Q parameters have been extracted.

#### *II.2.3.2.3.3.2. Sapphire-based substrates*

The AlN growth by reactive sputtering on sapphire substrate is often performed at higher deposition temperature (> 500 °C) compared the typical AlN growth on silicon-based substrates. This higher temperature combined with a lower lattice mismatch between AlN and sapphire than AlN and silicon enable to enhance the crystal quality. For example, Uchimaya et al. <sup>271</sup> demonstrate AlN (002) RC < 0.1° and confirm that increase the deposition temperature is suitable to enhance AlN crystal quality.

Although a well-controlled AlN sputtering process on sapphire substrate enables to achieve highly c-axis oriented layer, the thermal annealing is also studied. Hence, to compete with the “low-temperature” AlN layer deposited in the multi-steps approach implemented on AlN MOCVD growth on sapphire, the sputtered AlN layer is usually annealed afterwards <sup>214,218,272–274</sup>. These thermal treatments are often performed in a temperature range around 1700 °C and lead to an improvement of the sputtered AlN layer. In fact, Mogami et al. <sup>274</sup> show a decrease in AlN (002) RC from 0.27° to 0.01° after annealing. Others studies also mentioned an enhancement in crystal quality after annealing <sup>214,272,275</sup>.

Finally, another approach is to work on the sapphire substrate preparation. In fact, several groups of research agree to say that nitridation of the sapphire surface before the AlN reactive sputtering deposition increases the AlN crystal quality leading to AlN (002) RC below 0.1° <sup>252,276,277</sup>.

A review of the publications focusing on AlN sputtered layers deposited on sapphire substrate is presented in Annex part 1, Table VII. To the best of our knowledge, only one publication is targeting an acoustic device with a sputtered AlN layer deposited on sapphire-based substrate using Pt electrode and displays a  $k_{\text{eff}}^2$  of 0.6 % <sup>278</sup>.

II.2.3.2.3.3.3. Silicon Carbide-based substrates

II.2.3.2.3.3.3.1. Cubic Silicon Carbide (3C-SiC)

The work on sputtered AlN growth on 3C-SiC buffer layer is mainly led by two groups of research: Chung's group from University of Ulsan and Lin's group from University of California. Within each group, the research was done incrementally and the resulting studies are very similar.

In 2007, Chung *et al.*<sup>279</sup> obtain a AlN (002) RC of 1.3° for a 1.0 μm thick AlN layer deposited on Si (100) using a 3C-SiC (111) buffer layer. They pursue their research and published results in two other publications<sup>280,281</sup> up to realize a SAW-type acoustic device in 2009<sup>282,283</sup>. In their first SAW device<sup>282</sup>, they obtain poor performances with a device displaying an acoustic velocity of 153.6 m.s<sup>-1</sup>. This result is explained by some non-(002) peak contributions observed in XRD. In their second publication<sup>283</sup>, they indicate SAW velocity of 5020 m.s<sup>-1</sup> and  $k^2_{\text{eff}}$  of 0.79 % for 2.0 μm thick AlN layer with a (002) RC of 1.3°. They also indicate that the same layer deposited directly on Si (100) has a (002) RC of 0.2° without displaying the XRD scan. This latest seems absurd to us because of their sputtering conditions and the nature of the substrate.

Similarly, Lin's group published complementary articles in 2010<sup>284,285</sup>. They obtain an AlN (002) RC of 1.31° for a 3 μm thick layer deposited on Si (100) with a 3C-SiC (100) buffer layer. Their SAW device exhibits an acoustic velocity of 5200 m.s<sup>-1</sup> for a 2 μm<sup>284</sup> and 1 μm<sup>285</sup> thick AlN layer. In 2013 and from these results, they obtain a  $k^2_{\text{eff}}$  of 0.42 % with a 2.5 μm thick AlN layer<sup>286</sup>.

We can also mention the study of Iqbal *et al.*<sup>244</sup> in which the influence of AlN temperature deposition on on-axis and off-axis 3C-SiC (111) is investigated previously discussed in section II.2.3.2.3.2.2. A theoretical study of SAW propagation in 3C-SiC/AlN is also proposed<sup>287</sup>.

A review of the publications focusing on AlN sputtered layers deposited on 3C-SiC substrate is presented in Annex part 1, Table VIII.

II.2.3.2.3.3.3.2. Hexagonal Silicon Carbide (4H- and 6H-SiC)

The AlN deposition by reactive sputtering has not been widely investigated in the literature. In fact, the use of a high-cost hexagonal SiC substrate is usually associated to a high-quality epitaxial growth AlN which is performed by a high temperature deposition technique such as CVD. However, some studies mentioned sputtered AlN layers on 4H- or 6H-SiC to

elaborate acoustic devices<sup>288,289</sup> or AlN template<sup>290</sup>, eventually annealed, serving as a buffer layer for a thicker AlN CVD growth.

For example, Esteves et al.<sup>288</sup> elaborate a microresonator displaying a  $k^2_{\text{eff}}$  around 0.3 % with a quality factor Q roughly varying between 900 and 1500 depending on the test temperature. However, and despite the reasonable lattice matching between AlN and hexagonal SiC, the AlN c-axis orientation is relatively weak since the (002) is only of 1.8° (increased up to 1.7° with a thermal annealing). In fact, other studies<sup>289–291</sup> reported lower AlN (002) RC down to 0.13°.

Especially, Uesugi et al.<sup>290</sup> investigate the influence of AlN thickness serving as a buffer layer for a thick AlN MOCVD regrowth. In their sputtering conditions, they demonstrate an increase in the (002) RC of the sputtered AlN layers from around 0.05° to 0.42° by increasing the thickness from 0.1 μm to 0.6 μm. They also show that a 1700 °C thermal annealing can drastically improve the AlN crystal quality and decrease the (002) RC below 0.005° (around 20 arcsec).

A review of the publications focusing on AlN sputtered layers deposited on hexagonal silicon carbide is presented in Annex part 1, Table IX.

#### II.2.3.2.3.4. Conclusions on reactive sputtering AlN deposition

Beyond the sputtering deposition parameters such as temperature, pressure, Ar/N<sub>2</sub> ratio and others, the crystal quality of sputtered AlN thin films is once again affected by its growth substrate. Figure II.13 presents an overview of the sputtered AlN (002) RC as a function of the AlN thickness according to the studies reviewed from Table VI to Table IX in Annex part 1. These results are also compared with CEA-LETI capabilities in which AlN films are sputtered on Si (100) substrate.

First, if we compare these values to those obtained for AlN MOCVD deposition, we observe that they are very disparate whatever the growth substrate. For example, RC values ranging from more than 10° to 0.63° for silicon-based substrates and from 4.15° to 0.01° for sapphire substrate. It indicates that a non-optimized AlN sputtering process drastically degrades the AlN crystal quality.

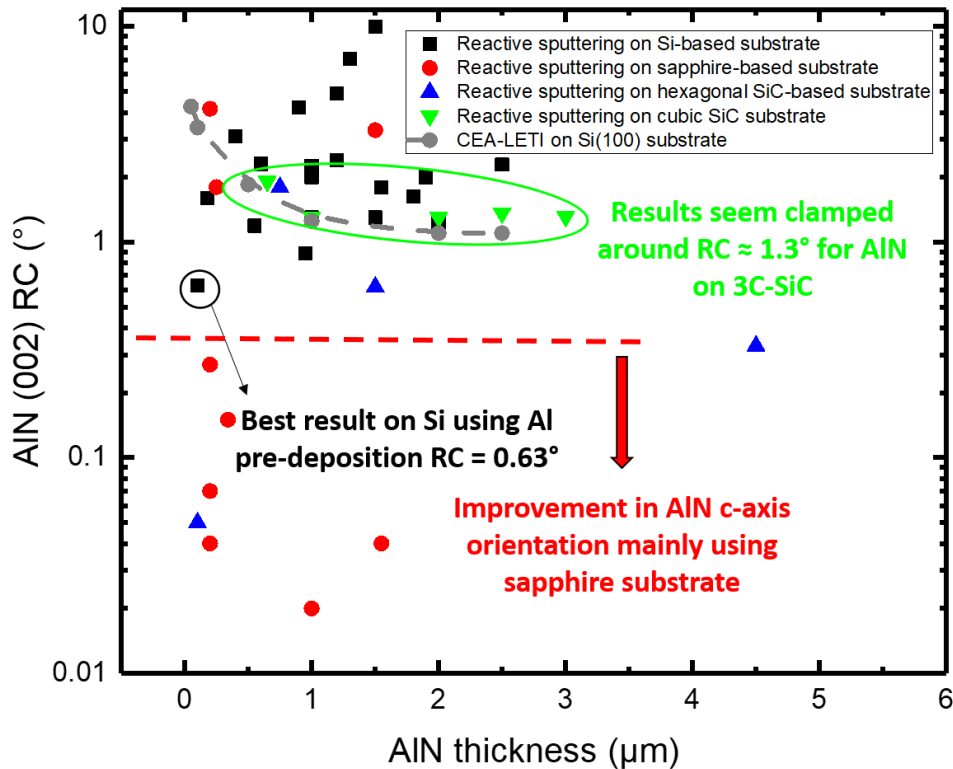


Figure II.13: Graphic representation of AlN (002) RC obtained by reactive sputtering on silicon, sapphire and SiC (cubic and hexagonal) substrates

Second, we can also note that the value of  $0.63^\circ$  is obtained with an elegant approach using a 5 nm thick Al seed layer before the AlN growth. Subsequently, the AlN growth by reactive sputtering on the other substrates have not been widely investigated. However, several studies reported (002) RC values below  $0.1^\circ$  on sapphire substrate (and one on hexagonal SiC substrate). These results show the proof of concept the elaboration of highly c-axis textured AlN layer on both substrates. Moreover, the c-axis orientation on 3C-SiC seems to be clamped with a RC around  $1.3^\circ$ . Finally, although a decrease in AlN (002) RC with the thickness is observed on CEA-LETI results obtained on Si (100) substrates, they are also clamped around  $1.1^\circ$ .

### II.2.3.3. Conclusions on AlN thin films elaboration

To conclude this section on AlN thin films elaboration, we are going to compare the influence of the deposition method (MOCVD or reactive sputtering) and of the growth substrate. Figure II.14 compares the AlN (002) RC obtained by MOCVD and reactive sputtering, without distinguishing the growth substrate. The values are issued from Table I to Table IX presented in Annex part 1.

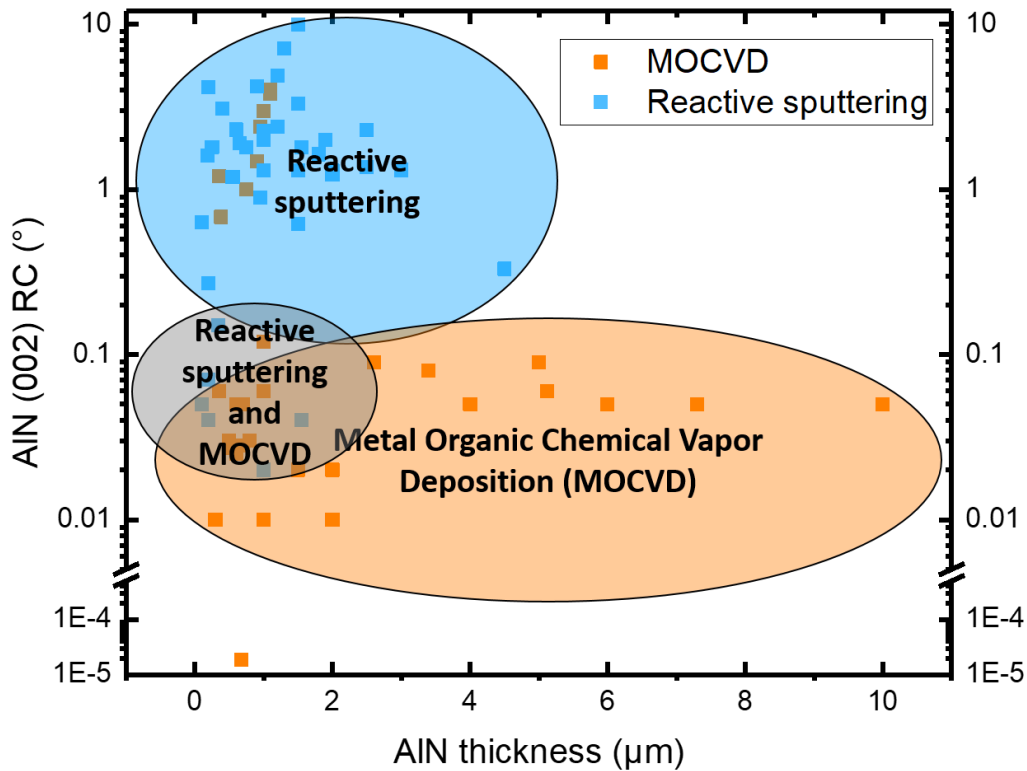


Figure II.14: Comparison of AlN (002) RC elaborated by MOCVD or reactive sputtering

On one hand and in most studies, we clearly observe that reactive sputtering lead to a limited AlN crystal quality (blue area). Moreover, the low-temperature sputtered AlN films rarely exceed a thickness of 2 μm since they are targeting piezoelectric devices which does not require important thickness. On the other hand, high-temperature AlN MOCVD deposition (orange area) enable to achieve a higher crystalline quality than reactive sputtering. Higher thicknesses are investigated, especially through ELOG approach. Hence, MOCVD is the technique of choice to obtain high quality AlN layers. However, and especially at low thickness (< 2 μm), we begin to observe an area in which AlN crystal quality obtained by reactive sputtering is competing with that achieved by MOCVD (grey area). Due to their reasonable lattice mismatching with AlN, the growth substrates of the sputtered AlN layers located in this area are mainly sapphire or hexagonal SiC substrates.

Similarly to what has been previously discussed, Figure II.15 compares the AlN (002) RC obtained on silicon, sapphire, hexagonal SiC (4H- or 6H-SiC) and 3C-SiC, without distinguishing the deposition technique (MOCVD or reactive sputtering).

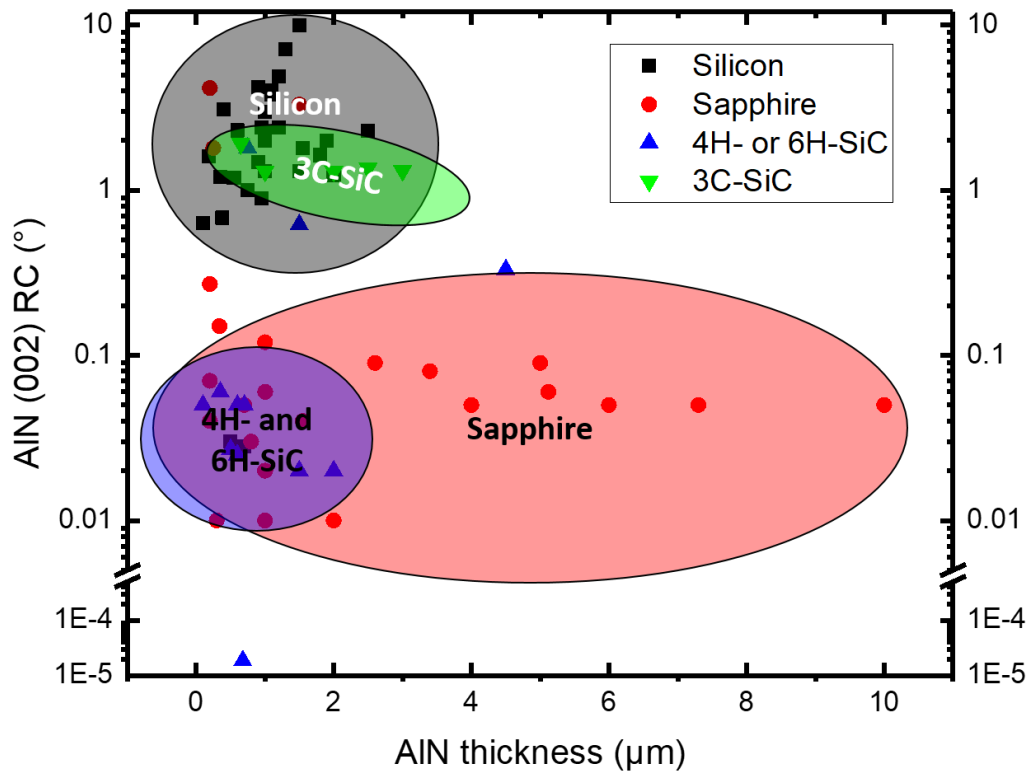


Figure II.15: Comparison of AlN (002) RC on silicon, sapphire, hexagonal SiC (4H- or 6H-SiC) and 3C-SiC

First, we clearly observe that (002) RC obtained on silicon or 3C-SiC substrates are mainly above  $1.0^\circ$ . It clearly suggests that both substrates are not suitable to perform a high quality AlN growth, either by reactive sputtering or by MOCVD although (111)-oriented 3C-SiC displays a lattice mismatch of 0.9% with AlN. However, an exception is observed with Akoustis study (ref) in which they obtain a RC of  $0.03^\circ$  on a silicon-based substrate. Second, different results are obtained using hexagonal SiC (4H- or 6H-SiC) or sapphire substrates. In fact, these substrates enable to achieve highly c-axis textured AlN layers by MOCVD or reactive sputtering.

Hence, and in view of these results, it is clear that combining MOCVD technique with a suitable growth substrate (sapphire or hexagonal SiC) will lead to high AlN crystal quality films, provided that the deposition process is well controlled. However, the high-cost of these substrates and deposition technique compared to silicon substrates and reactive sputtering deposition do not appear as a suitable cost-effective solution to address the new challenges faced by RF filters technologies.

### II.3. Enhancement of AlN piezoelectric properties with doping

In microelectronics, the term “doping” is the intentional introduction of element(s) called impurities into an intrinsic semi-conductor in small amount (typically particles per million – ppm). When it refers to AlN “doping” targeting an enhancement in piezoelectric response, this term is misused in the literature since the “doping” atomic concentration is typically of several percent and more. Hence, the term “alloying” should be employed but “doping” is abusively used.

In 2008, Akiyama *et al.*<sup>292</sup> discovered an increase about 400 % of  $d_{33}$  AlN piezoelectric coefficient after scandium (Sc) doping. This result paves the way to another effective approach to improve AlN piezoelectric properties and lot of effort has been devoted to explore the effects of various doping elements on AlN piezoelectric thin films. On one hand, this section presents the different doping elements currently investigated to increase AlN piezoelectric properties. Their effects and efficiency are compared when available. On the other hand, it focuses on Scandium (Sc) doped AlN since it is the element studied in this work.

#### II.3.1. Doping elements

Since the Akiyama’s discovery, a wide range of doping element has been investigated to potentially enhance AlN piezoelectric properties. Except Scandium (Sc), which is naturally the most studied element discussed in the next section, we find titanium (Ti)<sup>293,294</sup>, chromium (Cr)<sup>67,68,295,296</sup>, yttrium (Y)<sup>297</sup>, tantalum (Ta)<sup>298,299</sup>, vanadium (V)<sup>299</sup>, ytterbium (Yb)<sup>300</sup>, erbium (Er)<sup>301</sup>, niobium (Nb)<sup>302</sup> or magnesium (Mg)<sup>303</sup>. Co-doping was also investigated with magnesium-zirconium (Mg-Zr)<sup>304,305</sup>, magnesium-hafnium (Mg-Hf)<sup>305,306</sup>, magnesium-titanium (Mg-Ti)<sup>307</sup> or magnesium-niobium (Mg-Nb)<sup>308</sup>. We can also mention some studies based on theoretical calculations investigated Cr<sup>69</sup>, Y<sup>309</sup>, boron (B)<sup>309</sup>, Yb<sup>310</sup> doping or magnesium-niobium (Mg-Nb) co-doping<sup>302</sup>.

Chromium doping studies report that the optimal Cr content seems around 4 – 6 %. Beyond this content, a significant degradation of  $\text{Cr}_x\text{Al}_{1-x}\text{N}$  c-axis orientation,  $k^2_{\text{eff}}$  and/or  $d_{33}$  piezoelectric coefficient is observed. Especially, Luo *et al.*<sup>296</sup> show that an increase in  $d_{33}$  is closely related to the decrease in (002) RC. The  $\text{Cr}_x\text{Al}_{1-x}\text{N}$  degradation at higher Cr content (typically above 6 %) is not well understood but it could be attributed to CrN or  $\text{Cr}_2\text{N}$  grains<sup>68</sup>. Very similar results have been obtained with other doping elements. Especially, Uehara *et*



*al.*<sup>300</sup> investigate Yb doped AlN and demonstrate that an increase in  $d_{33}$  is also closely related to the decrease in (002) RC. The  $d_{33}$  piezoelectric coefficient increases up to Yb = 33 % and dramatically decreases above. This result is explained by a deterioration of  $\text{Yb}_x\text{Al}_{1-x}\text{N}$  crystallinity above  $x = 33\%$  which is followed by a change in crystal phase difficult to assign for  $x \geq 39\%$ . Mayrhofer *et al.*<sup>297</sup> observe the same tendency up to a yttrium (Y) content about 6 – 8 % with a crystalline degradation for Y = 11.6 %. Hu *et al.*<sup>301</sup> investigate the influence of substrate temperature on an  $\text{Er}_x\text{Al}_{1-x}\text{N}$  thin film with  $x = 6.43\%$  and demonstrate an increase in intensity of (002) planes with the increase in substrate temperature up to 200 °C. This result is consistent with the observed increase in  $d_{33}$  piezoelectric coefficient at this temperature. Above it,  $d_{33}$  decreases due to a degradation in (002) orientation attributed to bonds breaking between Er and Al.

However, other doping elements shows different results. For example, the studies about Ta doped AlN are in contradiction. On one hand, Liu *et al.*<sup>298</sup> show an increase in  $d_{33}$  with the decrease in (002) RC (optimum for Ta = 5.1 %). This observation should lead to an increase in  $k_{\text{eff}}^2$  but this study is only focused on deposition and no device is elaborated. On the other hand, Iborra *et al.*<sup>299</sup> indicate a decrease in  $k_{\text{eff}}^2$  with the increase of Ta content. Vanadium (V) doping seems also difficult to implement since the best  $k_{\text{eff}}^2$  is 2.5 % which is lower than pure AlN. Moreover, VN inclusions occur from V = 6.4 % and the crystallinity/piezoelectricity is totally destroyed for  $V > 7\%$ <sup>299</sup>. Finally, Anggraini *et al.*<sup>311</sup> demonstrate a slight increase in  $d_{33}$  for a Mg content between 2.5 % - 7.0 % followed by a drastic degradation for higher content.

An overview of all these results as well as for co-doping issue from the results presented in Annex part 1, Table X, is given in Figure II.16. This figure displays the evolution  $d_{33}$  piezoelectric coefficient as a function of the (co-)doping content for the different elements. Since all the studies do not elaborate an acoustic device and measure the  $k_{\text{eff}}^2$ , the  $d_{33}$  coefficient has been chosen as comparison parameter. Hence, the data about Er and V doping are not presented since the evolution of  $d_{33}$  with content of this element was not investigated.

In addition, this figure clearly enables to distinguish the suitable doping elements, and for some, the doping range, to enhance AlN piezoelectric character. Referring to the best  $d_{33}$ , value of pure AlN obtained in these studies and represented by a horizontal black dash line, only Cr, Ta, Mg and Yb seem to lead to an enhancement of piezoelectric properties. However, the use of Cr, Mg and Ta results in a poor enhancement of  $d_{33}$  coefficient and their doping

range is drastically limited and does not exceed 6 %. Hence, only Yb seem to be a suitable doping element. We can also observe that Y could be an interesting doping element since it leads to an increase in  $d_{33}$  coefficient but the related study mentioned  $d_{33}$  values below the highest value reported for pure AlN thin film.

Research about co-doping is also interesting. Yokoyama et al.<sup>304–306</sup> investigate in several studies the influence of Mg-Zr and Mg-Hf as co-doping elements. They demonstrate an increase in  $d_{33}$  piezoelectric coefficient with the increase in these co-doping elements. This result is explained by an elastic softening and local instability of the structure resulting from an increase in the bond length between Al and N atom along the c-axis in the tetrahedral structure (decrease in c/a ratio). In both cases, an enhancement of  $k^2_{\text{eff}}$  is observed compared to pure AlN (7.1 %) but better results have been obtained with Mg-Hf than Mg-Zr with an increase in  $k^2_{\text{eff}}$  up to 10.0 % and 8.5 %, respectively. In particular, they show a remarkable and an almost constant (002) RC around  $1.35^\circ$  up to a 1.1  $\mu\text{m}$  thick Mg-Hf<sub>x</sub>Al<sub>1-x</sub>N film with a Mg-Hf content up to 34.8 %. Hence, these co-doping are also suitable to enhance AlN piezoelectric properties.

Finally, the research about Mg-Ti<sup>307</sup> and Mg-Nb<sup>308</sup> are relatively similar. In each study, Mg, Ti and Nb were first introduced as a single dopant. The increase in Mg content leads to a decrease in  $d_{33}$  except at low content (around 2.5 %) due to crystalline degradation of AlN wurtzite based-structure resulting from the formation of unknown additional compounds. This observation is echoing Anggraini et al.<sup>311</sup> in which this degradation is also observed. Similar results have been obtained with Ti and Nb as single dopant. Especially, the increase in Nb content leads to an increase c/a ratio resulting in a degradation of piezoelectric properties.

However, used as co-doping, these elements show different results. An increase in  $d_{33}$  is observed by increasing Mg-Ti content up to 18 % with an optimized Mg/Ti ratio of 1.3. Beyond this content, additional compounds degrade the crystallinity quality and contribute to a lower  $d_{33}$ . Similar results have been observed for Mg-Nb with a content up to 60 % and a Mg/Nb ratio of 1.6. Therefore, Mg-Ti and Mg-Nb co-doping elements are also interesting to enhance AlN piezoelectric properties.

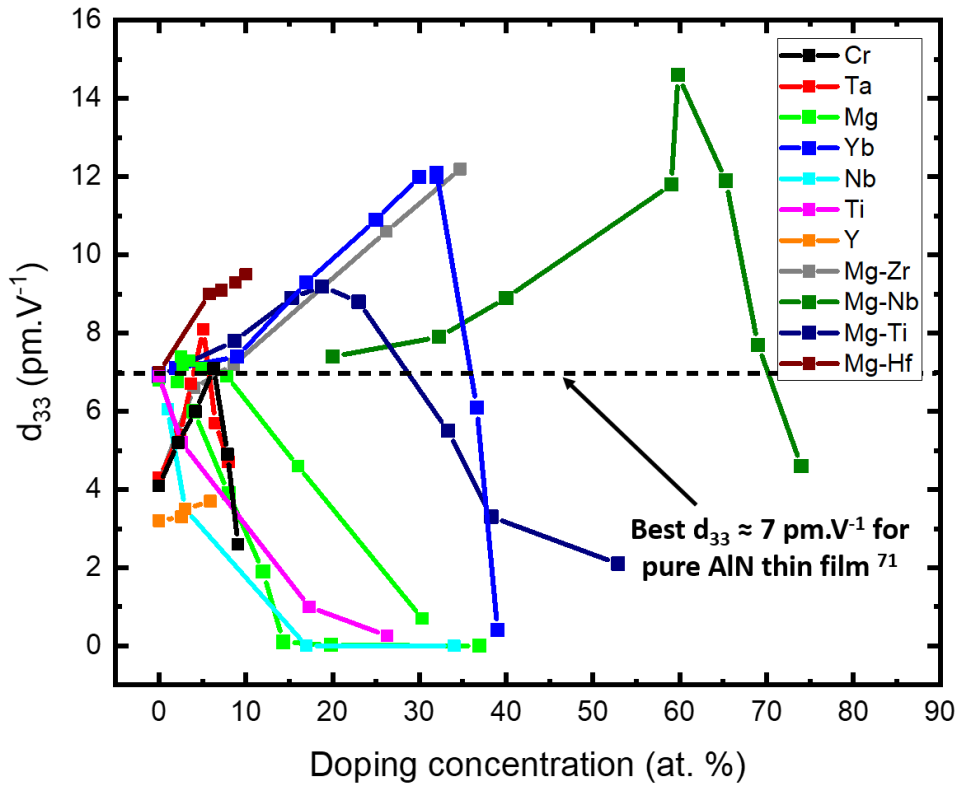


Figure II.16: Evolution of  $d_{33}$  piezoelectric for the different used elements to dope AlN. The horizontal black dashed line represents the highest  $d_{33}$  value mentioned in the literature <sup>71</sup>

A summary of these studies is given in Annex part 1, Table X. When available, the (002) RC of the (co-)doped AlN layer and the characteristics parameters of an acoustic device  $k^2_{eff}$  and Q are mentioned.

### II.3.2. Focus on scandium (Sc) doping

As previously mentioned, Sc is the most used AlN doping element to enhance its piezoelectric properties. The elaboration of  $Sc_xAl_{1-x}N$  thin films has been reported by various deposition technique such as Hydride Vapor Phase Epitaxy (HVPE) <sup>312</sup>, Molecular Beam Epitaxy (MBE) <sup>313,314</sup>, Metal Organic Chemical Vapor Deposition (MOCVD) <sup>315</sup> but the most common deposition technique is reactive sputtering.

The sputtered  $Sc_xAl_{1-x}N$  layers can be elaborated either with a single ScAl target via a classic reactive sputtering deposition or with Sc and Al multi-targets. The first method constraints the study to a single Sc content while the second method enables to tune the Sc content of the as-deposited  $Sc_xAl_{1-x}N$  thin films by adjusting the target powers.

*II.3.2.1. Origin of the enhancement of piezoelectric response*

As previously mentioned, Akiyama et al.<sup>316</sup> discover in 2008 a drastic enhancement of the piezoelectric response in  $\text{Sc}_x\text{Al}_{1-x}\text{N}$  alloy thin films with the increase in Sc content. Figure II.17 presents the measured  $d_{33}$  coefficient as a function of Sc atomic concentration as well as the evolution of  $c/a$  lattice ratio. We clearly observed a  $d_{33}$  value almost 4 times higher for 43 % Sc content compare to pure AlN.

This result is directly related to structural and electronegativity changes. In fact, like Al, Sc is a strictly 3- valent cation. However, its ionic radius is larger: 88.5 pm whereas Al displays an ionic radius of 32 pm. Hence, Al substitution by a Sc atom lead to a change in lattice structure. Especially,  $a$ -lattice constant increase monotonically with the Sc content while  $c$ -lattice constant is almost untouched reaches a maximum values at  $\text{Sc} \approx 15\%$ <sup>22</sup>. It leads in a decrease of  $c/a$  axial ratio (blue curve in Figure II.17) accompanied with a softening of the ScAlN structure, especially with a decrease in  $c_{33}$  elastic constant with the increase in Sc content<sup>317</sup>.

These evolutions of structural parameters with the increase in Sc content are directly in line with the notion of compressibility (inverse of bulk modulus)<sup>318,319</sup>. Basically, an increase in bond length (or in lattice constant) is coupled with an increase in compressibility. On one hand, in the basal plane, the compressibility is less affected but tends to increase slightly up to a Sc content of 14 % and then decreases. This behaviour is related to the non-linear evolution of the lattice constants with Sc content:  $c$ -parameter reaches a maximum value for a Sc content close to 15 % while  $a$ -parameter increases monotonically. Hence, as the concentration of Sc content increases, the  $\text{Sc}_x\text{Al}_{1-x}\text{N}$  material softens along  $c$ -axis and hardens in the basal plane (for Sc content higher than 15 %)<sup>320</sup>.

Moreover, this softening along  $c$ -axis is also enhanced by the lower electronegativity of Sc (1.36) than Al (1.61) (and 3.04 for N). In fact, Yu et al.<sup>321</sup> show that the larger the difference of electronegativity with N atom, the lower is  $c_{33}$ . These two combined phenomena increase the intrinsic sensitivity to axial strain resulting in a significant increase in piezoelectric response.

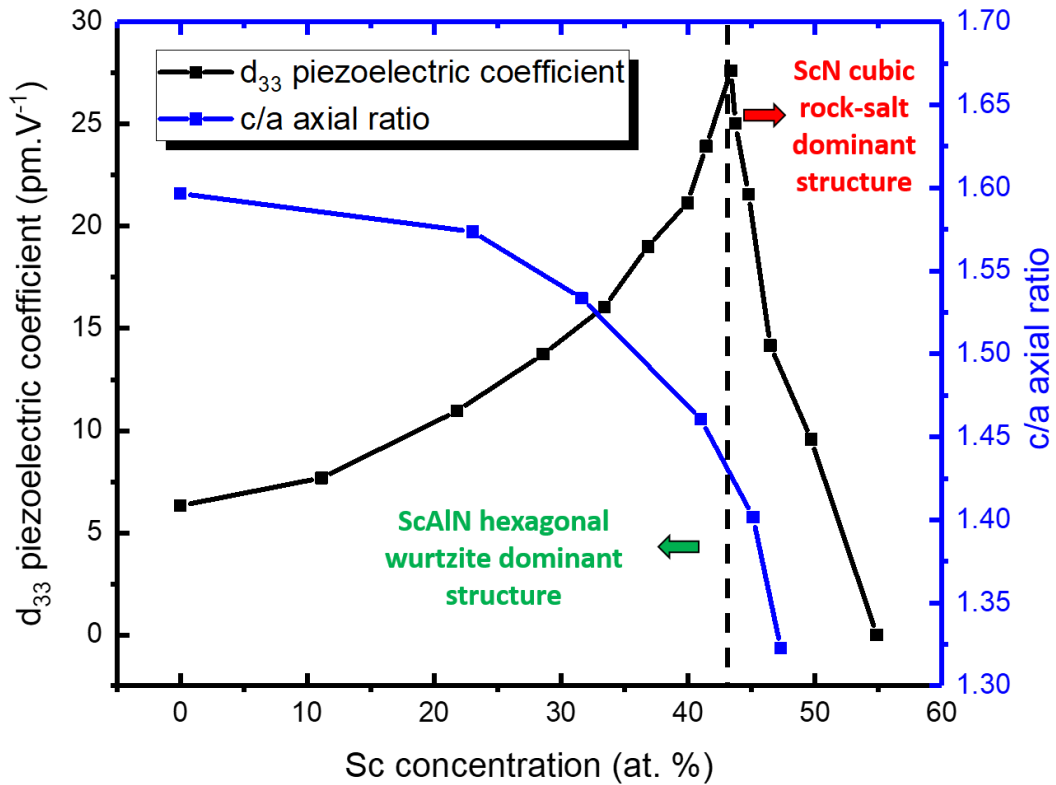


Figure II.17: Evolution of  $d_{33}$  piezoelectric coefficient and  $c/a$  lattice constants ratio with the Sc content <sup>316</sup>

Finally, this increase in ScAlN piezoelectric response with Sc content is observed only up to Sc  $\approx$  43 %. Beyond this content, the ScN rock-salt structure which is non-piezoelectric dominates leading to a drastic decrease in piezoelectric response.

### II.3.2.2. Problematic of Abnormal Oriented Grains (AOG)

Another challenge in ScAlN thin films elaboration is the formation of Abnormally Oriented Grains (AOG). These grains are ScAlN wurtzite exhibiting a specific range of crystallographic orientations deviating of 50° - 90° from the c-axis growth direction and is promoted at high Sc content. An example of AOG is depicted in Figure II.18.

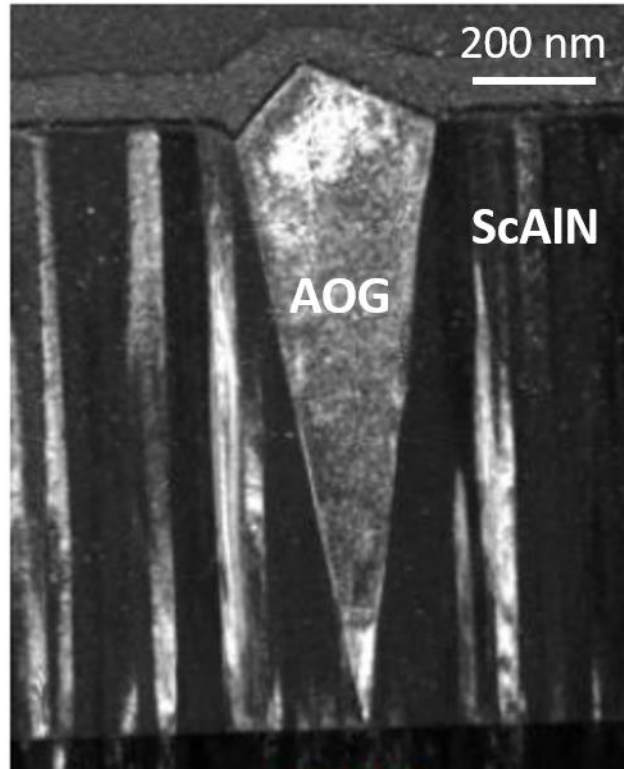


Figure II.18: Dark-field TEM images showing the cross-section of a cone-shape abnormal oriented grain (AOG) grown in the ScAlN film deposited on Si/Mo<sup>322</sup>

An AOG formation mechanism is proposed by Sandu *et al.*<sup>323</sup> and described as follows.

First, a Sc accumulation at grains boundaries exhibiting a bad match of in-plane orientation occurs. This accumulation is directly related to differences of Sc with Al such as ionic radius or electronegativity leading to a lower chemisorption of Sc than Al. Second, a rocksalt complexion layer is formed due to its Sc accumulation. In fact, and as shown in Figure II.19, the tetrahedrons of wurtzite structure would change into an octahedral coordination characteristic of the rocksalt structure. Third, a secondary nucleation on the rocksalt complexion interface lead to the growth of wurtzite AOG. Large rocksalt grains cannot grown due to too much Al atoms in the average composition. Finally, a nucleation of wurtzite phase occurs on the rocksalt complexion putting the c-axis along the threefold axis [111] of the rocksalt phase.

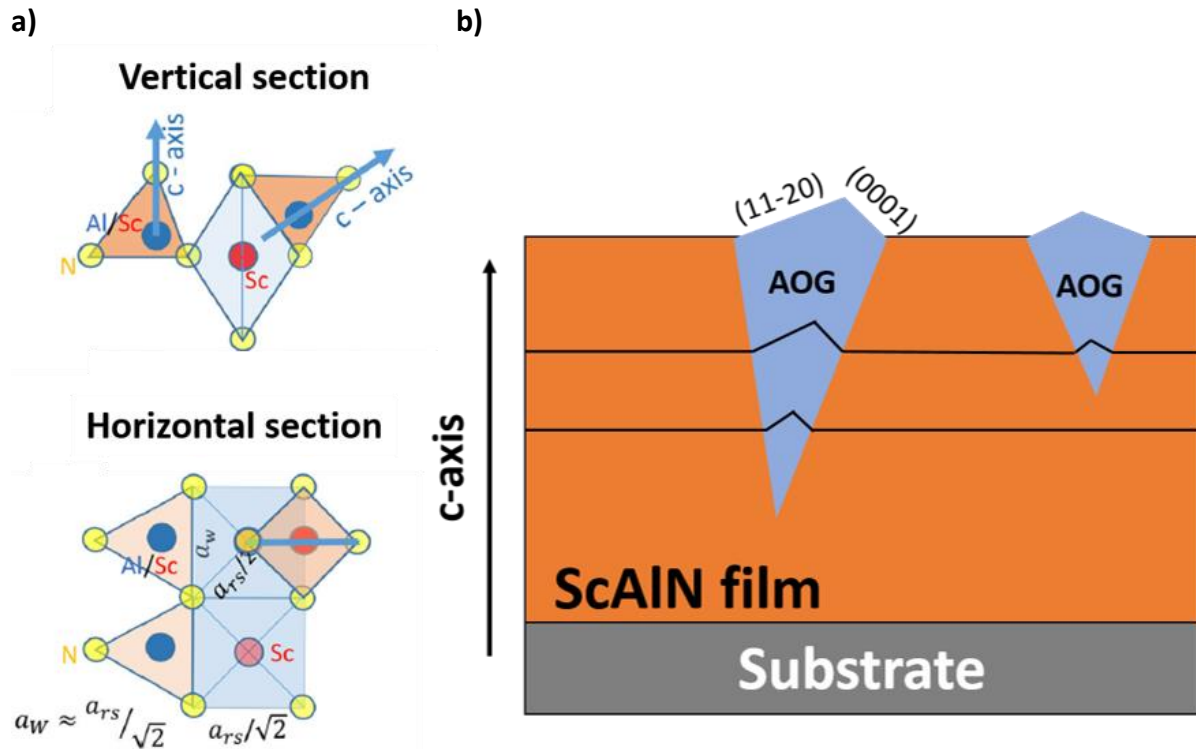


Figure 11.19: Sketch of the growth mechanism of AOG in ScAlN thin films. a) Local epitaxy at the rocksalt complex interfaces between normal grain (on the left) and AOG nucleus (on the right). The drawing shows a vertical section and a horizontal section ; b) Growth of AOG from the nucleus. Inspired from Sandu et al. <sup>323</sup>

This proposed mechanism explained the formation of AOG displaying a pyramidal shape with (0001) and  $(11\bar{2}0)$  facets. Hence, these AOG lead to a rougher surface and disturbs the piezoelectric response.

### 11.3.2.3. Influence of Sc content on crystal quality, $k_{eff}^2$ and $Q$

A clear tendency can be distinguished between  $Sc_xAl_{1-x}N$  and pure AlN deposition: a decrease in c-axis orientation. In fact, to the best of our knowledge, the lowest ScAlN (002) RC obtained by reactive sputtering is around  $1.3^\circ$  <sup>324</sup> compare to  $0.63^\circ$  for pure AlN. It is important to note that this value is achieved using a pure AlN pre-deposition layer to promote  $Sc_xAl_{1-x}N$  nucleation. As previously mentioned, this result can partially be explained with the formation of AOG. As shown by Moreira et al. <sup>16</sup>, these AOG also suggest a degradation of  $Sc_xAl_{1-x}N$  c-axis orientation with Sc content. However, other studies demonstrate almost constant (002) RC up to Sc > 30 % <sup>17,292</sup>. These results suggest that a well-control deposition process enable to maintain a suitable c-axis orientation even at high Sc doping.

However, we have to keep in mind that the use of Sc has come the rescue of AlN-based acoustic devices to achieve higher  $k_{\text{eff}}^2$ . This result has been demonstrated several times in the literature with  $k_{\text{eff}}^2$  exceeding 10 %<sup>17,325,326</sup> which is extremely appreciable to enhance the bandwidth of the acoustic filters. However, and as shown in Figure II.20, the increase in Sc content is coupled with a significant decrease of the quality factor Q. In fact, the softer  $\text{Sc}_x\text{Al}_{1-x}\text{N}$  structure along c-axis increase the heat losses and results in a decrease in quality factor Q<sup>327</sup>.

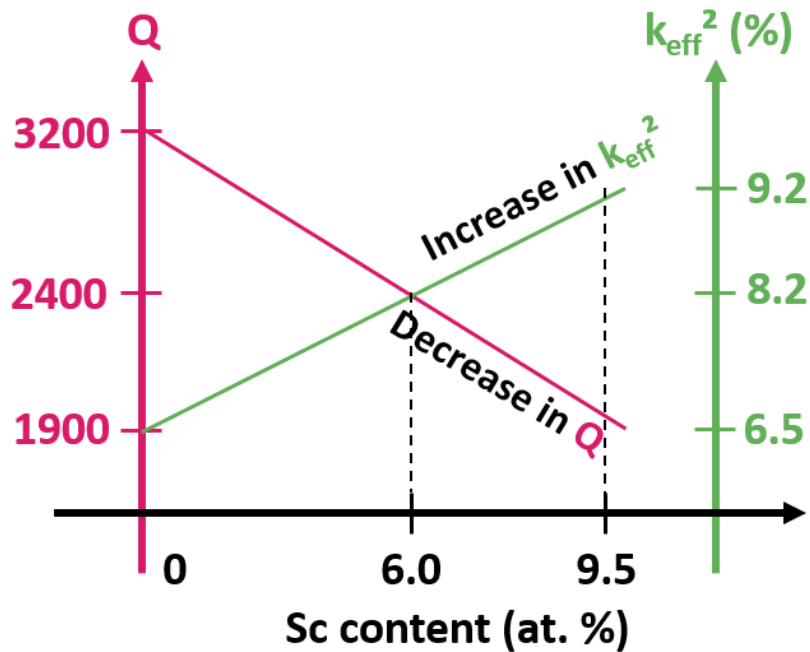


Figure II.20: Evolution of  $k_{\text{eff}}^2$  and Q as a function of Sc content. Inspired from Aigner et al.<sup>328</sup>

Therefore, a tradeoff must be found between increase in  $k_{\text{eff}}^2$  and decrease in Q to maintain a suitable FOM ( $k_{\text{eff}}^2 \cdot Q$ ) and an efficient acoustic device. To the best of our knowledge and similarly to what has been achieved on pure AlN-based acoustic device via a MOCVD deposition, the best results have been obtained by Akoustis which indicate a  $k_{\text{eff}}^2$  of 13.2 % with a FOM of 149. However, Sc content,  $\text{Sc}_x\text{Al}_{1-x}\text{N}$  thickness and electrode materials are not mentioned in their study<sup>326</sup>. Although few investigations, we can also report  $\text{Sc}_x\text{Al}_{1-x}\text{N}$  thin films elaborations on sapphire<sup>278</sup> or SiC<sup>329</sup> substrate but the  $k_{\text{eff}}^2$  obtained not exceed 5 %.

A non-exhaustive summary of the studies dealing with Sc doped AlN thin films is presented in Annex part 1, Table XI. When available, the (002) RC of the Sc doped AlN layer and the characteristics parameters of an acoustic device  $k_{\text{eff}}^2$  and Q are mentioned.



II.3.3. Conclusions AlN piezoelectric properties enhancement with a doping element

A wide range of elements has been investigated to dope AlN and enhance its piezoelectric properties, but only a few seems suitable. Among them, Sc is the most studied and the elaboration of  $\text{Sc}_x\text{Al}_{1-x}\text{N}$  thin films has been extended up to the industrial scale. Control the Sc doping and deposition process is key since it can lead to the formation of AOG and deteriorate the crystal quality resulting in a degradation of the piezoelectric. However, in optimized conditions, its use leads to a significant increase in  $k^2_{\text{eff}}$ . This observation is extremely suitable for acoustic device but it is combined with a decrease in quality factor Q. Hence, to meet the needs required by the new wireless communication, low Sc content (typically < 10 %) are required to maintain a suitable Q factor but the resulting  $k^2_{\text{eff}}$  is not high enough to sufficiently extend the bandwidth.

#### II.4. Conclusions of chapter 2

In a first step, the AlN basic properties have been presented. Its piezoelectric properties are at the heart of the operating of the acoustic device. This ultra-wide bandgap (6.2 eV), high electric breakdown field combined with its high electrical resistivity and thermal conductivity also make AlN a promising material for power applications.

In a second step, the AlN elaboration has been discussed. Its bulk growth is challenging, expensive and hardly reproducible. Hence, only few companies and research groups have demonstrated the growth of AlN single crystals with a limited wafer size of 50 mm. The AlN thin films elaboration also suffers from the lack of suitable growth substrate displaying a reasonable lattice and CTE mismatching with AlN. On one hand, high AlN crystal quality is obtained by MOCVD on sapphire or hexagonal SiC substrates which are expensive. The growth on silicon-based substrates usually lead to cracked films using this high-temperature deposition method. On the other hand, the sputtered AlN growth also displays limitation in crystal quality. In fact, although the growth of high quality AlN has been proven on sapphire or hexagonal SiC substrate, the cost of these growth substrates largely exceeds the growth cost. However, the use of low-cost silicon substrates limits the crystal quality. Therefore, it seems that there is no current cost-effective solution enabling to achieve high quality AlN piezoelectric layers on silicon-based substrates targeting AlN-based acoustic devices or other applications.

Finally, and instead to improve AlN crystal quality, another alternative to enhance its piezoelectric response is to investigate AlN doping. A wide range of doping has been studied but only a few seems suitable to increase AlN piezoelectric properties. Among them, Sc is the most studied and its use leads to a significant increase in  $k_{\text{eff}}^2$  which is extremely appreciable for acoustic devices. However, a degradation of the quality factor Q occurs with the Sc content leading to a tradeoff between degraded Q and high  $k_{\text{eff}}^2$ .

Hence, the elaboration of high quality AlN or doped AlN layers with a cost-effective method appears extremely challenging. In the next chapter, we propose to use a two-dimensional (2D) material displaying a reasonable lattice mismatch with AlN on a low-cost silicon based-substrate to enhance the crystal quality of sputtered AlN and  $\text{Sc}_x\text{Al}_{1-x}\text{N}$  layers.



### III. Chapter 3: Deposition of AlN films by Physical Vapor Deposition (PVD) on a 2D-MoS<sub>2</sub> layer

As mentioned in the previous chapter, the lack of bulk aluminium nitride substrates and the large lattice mismatch between AlN and silicon make AlN a material usually epitaxially grown on sapphire or silicon carbide (SiC) at high growth temperature ( $> 1000$  °C) to achieve higher crystalline quality and hence better device performance <sup>22,330,331</sup>. However, high cost, limited wafer size or differences in CTE between AlN and these substrates drastically limit the integration and applications of AlN.

In recent years, the emergence of 2-Dimensional (2D) materials and particularly 2D-Transition Metal Dichalcogenides (2D-TMDs) such as tungsten or molybdenum disulphide (WS<sub>2</sub> and MoS<sub>2</sub>) seems to be a promising approach for the growth of III-nitride materials. In fact, these materials present a hexagonal structure with a close lattice matching with III-nitride (1 % to 3 %) and a chemical compatibility enabling the direct growth of these materials <sup>332,333</sup>.

First, this chapter presents the 2D-MoS<sub>2</sub> material, its structure, properties, deposition method and characterizations. Second, we discuss its interest in AlN texturing growth by Physical Vapor Deposition (PVD) and illustrate it with different characterizations. Subsequently, we describe a delamination issue inherent to the use of 2D-MoS<sub>2</sub> as a seed layer for the AlN growth by PVD. Finally, we propose different potential solutions to solve this delamination.

### III.1. 2D-MoS<sub>2</sub> material

Molybdenum disulphide (MoS<sub>2</sub>) is an inorganic compound member of a material class called Transition-Metal Dichalcogenides (TMDs). A dichalcogenide is a chemical compound consisting of a transition metal (such as molybdenum) and a chalcogen element (such as sulphur)<sup>334</sup>. This material class has aroused a considerable interest since there are emerging new materials with tunable properties and many potential applications<sup>335,336</sup>. In this section, we focus on the structure of MoS<sub>2</sub> in the form of 2D-nanosheets and especially 2H-MoS<sub>2</sub> polytype.

#### III.1.1. MoS<sub>2</sub> structure and properties

MoS<sub>2</sub> has a natural two-dimensional structure with the sandwich-like S-Mo-S layers serving as building blocks, in which the atoms in the layer are bonded with strong covalent bonds while the layers are packed together with weak interlayer forces (Van der Waals - VdW interactions)<sup>335,337</sup>. Thus, each MoS<sub>2</sub> layer is composed of three-atom-thick often referred as “monolayer”.

MoS<sub>2</sub> is known in the form of three polytypes called 1T, 2H and 3R-MoS<sub>2</sub>, depending on the stacking order of the monolayers and the coordination of Mo atom in the monolayer<sup>338</sup>. However, natural MoS<sub>2</sub> is almost exclusively present with a hexagonal structure (2H-MoS<sub>2</sub>). The side view and top view of 2H-MoS<sub>2</sub> are presented in Figure III.1 a) and b), respectively. According to the literature, the distances between atoms (and therefore the inter- and intra-sheet distance) may slightly vary. The distances indicated in Figure III.1 are taken from crystallographic data published by Wyckoff<sup>339</sup>.

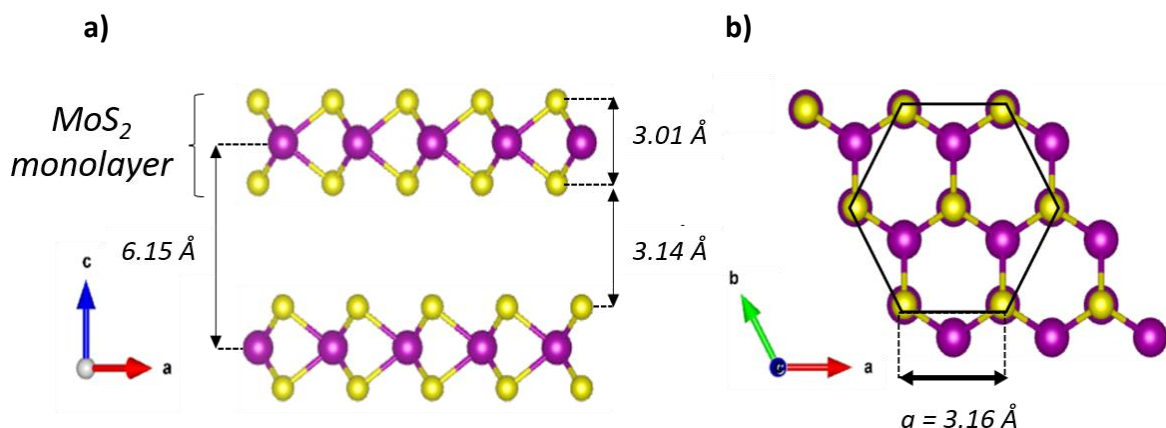


Figure III.1: MoS<sub>2</sub> crystalline structure a) Side view ; b) Top view

In terms of electrical properties, one of the first studies that popularized the interest of 2D-MoS<sub>2</sub> is the discovery of its semiconductor behaviour with a direct bandgap (1.9 eV) while its bulk form presents an indirect bandgap (1.2 eV)<sup>335,338</sup>. In addition, depending on the doping element and its level, it is possible to change a MoS<sub>2</sub> monolayer from a p-type semiconductor to a n-type semiconductor<sup>334</sup>. Moreover, if we take a look at the optical properties, MoS<sub>2</sub> monolayers present a strong photoluminescence in visible light<sup>340</sup>. This photoluminescence<sup>341</sup> and its associated refractive index<sup>342,343</sup> can be tuned by modifying the number of monolayer(s) within 2D-MoS<sub>2</sub>. These properties make MoS<sub>2</sub> in 2D form an interesting material for photovoltaic devices<sup>344</sup>, photodetectors<sup>345</sup>, transistors<sup>346</sup> or memory devices<sup>347</sup>.

### III.1.2. Deposition of MoS<sub>2</sub> layers

The two most common methods to obtain MoS<sub>2</sub> controllable layers are mechanical exfoliation and Chemical Vapor Deposition (CVD). On one hand, mechanical exfoliation is a powerful method to elaborate and transfer 2D-MoS<sub>2</sub> film with various monolayers and excellent electronic or optical properties on different substrates<sup>348,349</sup>. However, this method is not ideal for large-scale fabrication and can suffer from solvent contamination which can lead to discrete flakes rather than continuous films. On the other hand, the synthesis of MoS<sub>2</sub> by CVD technique leads to large crystallites size up to few μm, especially on substrates with a reasonable lattice matching MoS<sub>2</sub> such as sapphire<sup>350</sup>, graphene<sup>351</sup> or gallium nitride (GaN)<sup>352</sup>. However, this technique requires high temperature deposition (> 600 °C) which limits substrate scope and patterning techniques such as photolithography<sup>353,354</sup>.

In this work, MoS<sub>2</sub> thin films are deposited by Atomic Layer Deposition (ALD) using an Applied Materials equipment on 200 mm Si (100)/SiO<sub>2</sub> (500 nm) wafers obtained by wet thermal oxidation of Si standard wafers. ALD enables a growth of MoS<sub>2</sub> at low-temperature (substrate < 100 °C) with a low deposition rate enabling an excellent control of its thickness. The ALD process is performed at 90 °C and is described in Figure III.2. It is based on the sequential introduction of two precursors: Tetrakis(dimethylamino)-molybdenum (TDMA-Mo) as molybdenum precursor and 1,2-ethanedithiol (EDT) as sulphur precursor. EDT is an interesting precursor since it is an organosulfur compound which can be used as an alternative to toxic H<sub>2</sub>S gas, enhancing the compatibility of the process with semiconductor fabs. For more information about the deposition process, we can refer to Cadot et *al.* study<sup>336</sup>.

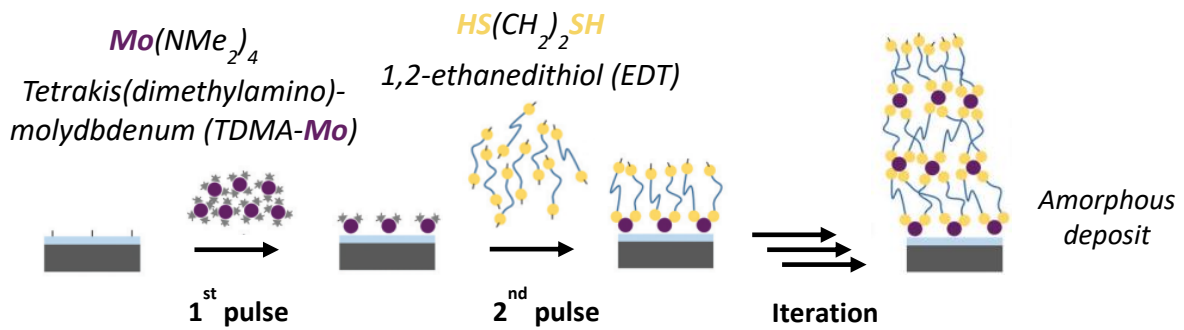


Figure III.2: MoS<sub>2</sub> ALD deposition process (without rapid thermal annealing)

The first pulse introduces Tetrakis(dimethylamino)-molybdenum (TDMA-Mo) used as molybdenum precursor. During this pulse, the molybdenum precursor reacts with the silanol groups present at the substrate surface. The second pulse introduces ethanedithiol (EDT) used as sulphur precursor. During this pulse, dimethylamino ligands are substituted by EDT. Then, the next introduction of TDMA-Mo (not presented here) corresponds to a grafting of the molybdenum ligands onto the thiol functions. By iteration, we obtain an amorphous coordination polymer. Thus, the as-deposited material is amorphous and has to be annealed with a Rapid Thermal Annealing (RTA) at 900 °C under nitrogen during 30 seconds to form a well-crystallized and uniform MoS<sub>2</sub> thin film as depicted in Figure III.3. Three MoS<sub>2</sub> monolayers typically correspond to 15 ALD cycles.

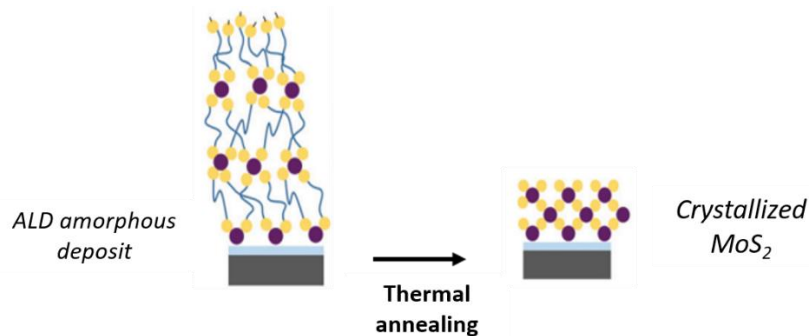
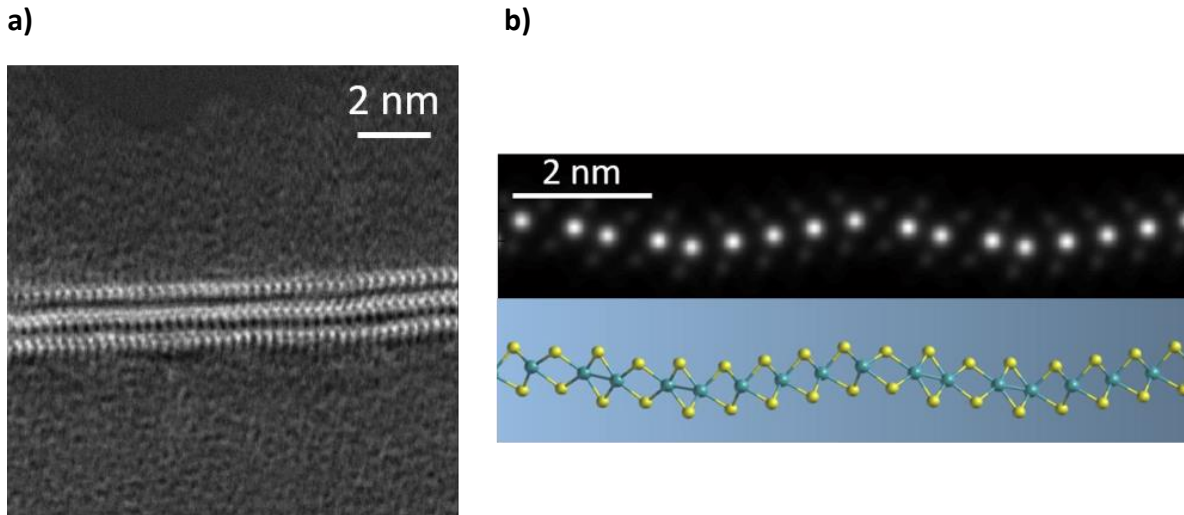


Figure III.3: Rapid Thermal Annealing (RTA) to crystallize the amorphous deposit into MoS<sub>2</sub>

A TEM cross-section of a three MoS<sub>2</sub> monolayers obtained after RTA is presented in Figure III.4 a). At first sight, omitting the scale effect, MoS<sub>2</sub> monolayers appears relatively flat but some oscillations are visible, especially on the first MoS<sub>2</sub> monolayer. In fact, and as illustrated on a TEM image processed given in Figure III.4 b), MoS<sub>2</sub> monolayer can locally oscillate spatially in its length. This observation could be due to a possible relaxation by local phase change.

Moreover, other TEM acquisitions measured after AlN PVD deposition and presented in section III.2.4.1 display distortions in MoS<sub>2</sub> monolayers such as bucking or twisting. Therefore, even with a deposition enabling a thickness control and an optimized crystallization process, some local defects are still visible in the three MoS<sub>2</sub> monolayers.



*Figure III.4: a) Cross-sectional TEM of three MoS<sub>2</sub> monolayers prepared by ALD and after RTA ; b) Observation of MoS<sub>2</sub> monolayer oscillations*

It is well-known that annealing of MoS<sub>2</sub> under inert conditions at high temperature conducts to the formation of local defects (sulphur vacancies) and Mo-rich edges leading to a MoS<sub>x</sub> compound ( $x < 2$ )<sup>355,356</sup>. In order to correct this stoichiometry and ensure that first AlN growth is performed on an optimal MoS<sub>2</sub> thin film, MoS<sub>2</sub> samples are sulfurized before the RTA. The sulfurization agent is EDT, which is the same molecule used as sulphur precursor for deposition. It enables to chain deposition and sulfurization processes in the same equipment. This step is performed at 450°C for 10 min. Finally, MoS<sub>2</sub> samples are annealed up to 900 °C under argon.

Note that MoS<sub>2</sub> ALD deposition on SiO<sub>2</sub> amorphous substrates and its annealing have been widely studied in Cadot thesis<sup>357</sup>. After annealing, MoS<sub>2</sub> monolayers displaying crystalline domains around 10 – 20 nm are formed. These nano-domains are parallel to the substrate highlighting a preferential out-of-plane orientation along c-axis. However, they are randomly oriented in the plane of the substrate which is characteristic of a heterogeneous nucleation process on amorphous substrate. Therefore, the crystallized 2D-MoS<sub>2</sub> seed layer has a so-called “fiber texture”. This structure is schematically represented in Figure III.5.



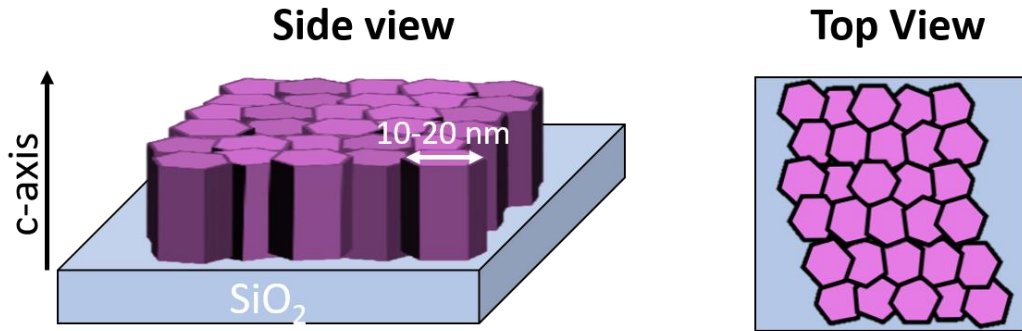


Figure III.5: Side view and top view of MoS<sub>2</sub> crystalline domains displaying a pronounced out-of-plane orientation (along c-axis) and a random in-plane orientation.

### III.1.3. Characterizations of MoS<sub>2</sub> monolayers

The MoS<sub>2</sub> thin films have been characterized by various techniques to assess its structure, crystallinity, surface morphology and chemical composition. The experimental of each characterization are briefly described in Annex part 2, section II.1.

#### III.1.3.1. Structural characterizations

##### III.1.3.1.1. MoS<sub>2</sub> crystalline quality (Raman)

Raman spectroscopy is a well-adapted characterization solution to check MoS<sub>2</sub> crystalline quality. A typical MoS<sub>2</sub> Raman spectrum is presented in Figure III.6 a). The peak at  $\approx 520 \text{ cm}^{-1}$  is due to the Si substrate, and is used as reference to adjust the position of the spectra. Two well-known pronounced  $E_{2g}^1$  and  $A_{1g}$  modes at  $\approx 382.6 \pm 0.2 \text{ cm}^{-1}$  and  $\approx 407.9 \pm 0,1 \text{ cm}^{-1}$  are attributed to MoS<sub>2</sub><sup>358,359</sup> and depicted in Figure III.6 b) The  $E_{2g}^1$  mode corresponds to an in-plane vibration (perpendicular to c-axis) while  $A_{1g}$  is an out-of-plane vibration (along c-axis)<sup>360</sup>.

Moreover, the Full Width at Half Maximum (FWHM) of Raman peaks gives a direct information of the crystal quality<sup>361</sup>. In this work, these peaks show a FWHM of  $E_{2g}^1 = 4.7 \pm 0.2 \text{ cm}^{-1}$  and  $A_{1g} = 5.6 \pm 0.1 \text{ cm}^{-1}$ . Pollard<sup>362</sup> demonstrates on a stabilization of  $E_{2g}^1$  and  $A_{1g}$  FWHM around  $4 \text{ cm}^{-1}$  and  $6 \text{ cm}^{-1}$ , respectively, with an identical laser wavelength (532 nm) to that used in this work. These values are relatively close to those obtained in this work confirming the synthesis of a low defects and well-crystallized MoS<sub>2</sub> thin film at the grain scale.

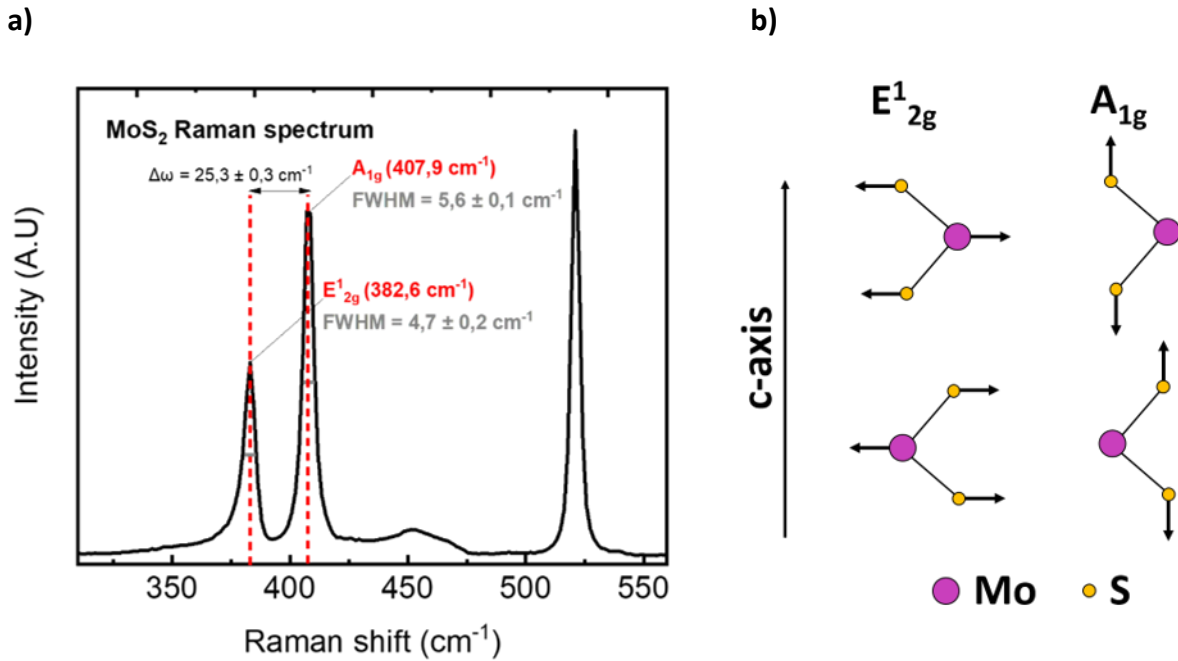


Figure III.6: Typical Raman spectrum of a three MoS<sub>2</sub> monolayers synthesized in this work ; b) E<sup>1</sup><sub>2g</sub> and A<sub>1g</sub> active Raman modes of MoS<sub>2</sub>

The E<sup>1</sup><sub>2g</sub> and A<sub>1g</sub> Raman positions of MoS<sub>2</sub>, and more precisely, the separation distance between both modes ( $\Delta\omega$ ) are expected to depend on the number of layers<sup>363,364</sup>. Here, the distance between both modes is  $\Delta\omega = 25.3 \pm 0.3 \text{ cm}^{-1}$  which is not totally in agreement with the one expected for a three layers MoS<sub>2</sub> thin film<sup>363</sup>. However, the main publications dealing with the influence of MoS<sub>2</sub> layers number on the Raman spectrum use MoS<sub>2</sub> layers exfoliated from bulk material as reference material<sup>363–367</sup>. It has been demonstrated that the growth methods and deposition conditions of MoS<sub>2</sub> can lead to significant variations in the Raman peaks positions<sup>368,369</sup>. In fact, MoS<sub>2</sub> Raman peaks positions are influenced by several parameters such as the strain<sup>370,371</sup>, the monolayers number<sup>363,364</sup> or the sulphur vacancies<sup>372</sup>. Moreover, even if the TEM cross-section presented in Figure III.4 a) clearly displays three monolayers, a TEM measurement is extremely localized contrary to a Raman measurement (laser spot diameter around 0.7  $\mu\text{m}$  in our analysis condition). Hence, the monolayers number can locally slightly vary between two and four. This scale effect probably contributes to the observed variation between a characteristic  $\Delta\omega$  value for a three MoS<sub>2</sub> monolayers and that reported in this work. However, Tuschel<sup>373</sup> has recently reported a  $\Delta\omega$  value of 25  $\text{cm}^{-1}$  for a three layers MoS<sub>2</sub> thin film prepared by chemical Vapor Deposition (CVD) on silicon substrates, which is in excellent agreement with the values reported in this study.

III.1.3.1.2. MoS<sub>2</sub> structural properties (XRD and XRR)

MoS<sub>2</sub> out-of-plane and in-plane XRD scans are presented in Figure III.7 a) and b), respectively. Out-of-plane measurement presents only a broad peak at  $2\theta = 44.1^\circ$  attributed to MoS<sub>2</sub> (006) reflection suggesting a fiber texture of the MoS<sub>2</sub> thin film. In-plane measurement also shows also a single peak at  $2\theta = 58.2^\circ$  attributed to MoS<sub>2</sub> (110) reflection (more visible in the inset). Finally, a  $\varphi$ -scan on MoS<sub>2</sub> (110) reflection, not presented here, does not highlight any peak suggesting no preferential in-plane orientation which confirms the MoS<sub>2</sub> fiber texture.

Furthermore (006) and (110) have been fitted for out-of-plane and in-plane strain analysis. Compared to MoS<sub>2</sub> bulk lattice parameter, the out-of-plane and in-plane strain gives tensile values of 0.15 % and 0.14%, respectively. Mechanically, this result is unexpected since a tensile out-of-plane strain produces a compressive in-plane strain via Poisson coefficient as illustrated in the inset of Figure III.7 a). It seems that, for such thin layer, we cannot neglect the surface relaxation (pending bonds effect) that can induce variations in interreticular distances (d-spacing) for the first MoS<sub>2</sub> monolayers and Van der Waals planes.

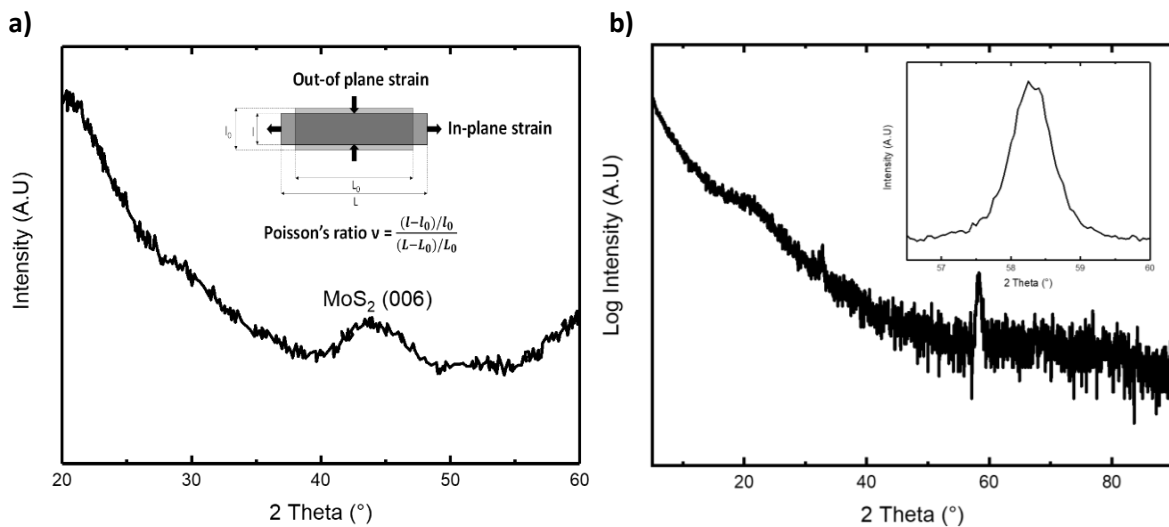


Figure III.7: Out-of-plane ; b) In-plane XRD of MoS<sub>2</sub> grown on Si (100)/SiO<sub>2</sub> (500 nm)

MoS<sub>2</sub> XRR pattern is presented in Figure III.8. To remind, a XRR scan is an absolute measurement from which a fitting is performed to estimate the thicknesses, densities and roughness of a stack. Hence, determine the uncertainty resulting from the measurement and the fitting is difficult. In the rest of this manuscript, the XRR values are considered as absolute and given without uncertainty.

### ***Chapter 3: Deposition of AlN films by Physical Vapor Deposition (PVD) on a 2D-MoS<sub>2</sub> layer***

An interesting result is the MoS<sub>2</sub> XRR response displaying a clear response up to  $\omega = 8^\circ$  highlighting a very flat MoS<sub>2</sub> surface. In order to correctly fit the MoS<sub>2</sub> XRR pattern, and especially the Kiessig fringe presents between  $\omega = 5^\circ$  to  $\omega = 8^\circ$ , a signification optimization leading to model detailing each VdW and MoS<sub>2</sub> planes is necessary to apprehend the variations within the MoS<sub>2</sub> film of the monolayers and the Van der Waals in-planes distances. It is worth to notice that the same model has been used and fitted with another software and leads to similar results as presented in Annex part 3, section III.1.1.

The densities, thicknesses and roughness determined with this model are listed Table III.1. According to Wyckoff crystallographic data, a three monolayers MoS<sub>2</sub> film (three atomic planes and three VdW planes) is 1.845 nm thick. In this work, the determined total thickness of the MoS<sub>2</sub> film is 2.06 nm. This measured value is relatively close to the theoretical one which confirms the use of XRR technique and the proposed model to determine the thickness. This higher value can be easily explained by a local variation in the MoS<sub>2</sub> monolayers number as well as the oscillations presented in Figure III.4 a) leading to an increase in MoS<sub>2</sub> total thickness.

The parameters determined for each layer detailed in the model are difficult to interpret. First, the density of MoS<sub>2</sub> planes oscillates roughly between 6 and 7 which is close to the MoS<sub>2</sub> theoretical value of 5<sup>357</sup>. The VdW planes density is close to 0 which makes sense as it is void without any matter. Second, according to Wyckoff crystallographic data, the MoS<sub>2</sub> monolayer thickness (distance between bottom and top sulphur atoms within a monolayer) and VdW plane (distance of two sulphur atoms between two distinct monolayers) is 0.301 nm and 0.314 nm, respectively. The MoS<sub>2</sub> monolayer tends to be thicker than the theoretical value while the opposite is observed for VdW planes. It could be explained by the oscillations observed in the MoS<sub>2</sub> monolayer leading to an electronic cloud displacement and changes in X-ray photons and electrons interactions. Localized defects such as bucking or twisting as well as the assumption of variations in d-spacing related to surface relaxation could also contribute to these results. Finally, the roughness values are in range of the extracted thicknesses.

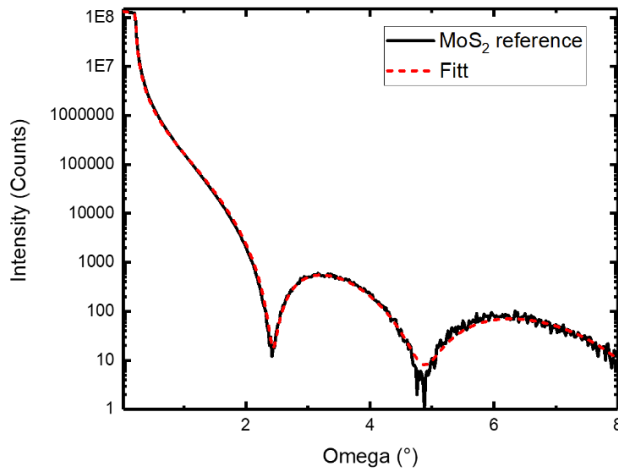


Figure III.8: XRR pattern of three MoS<sub>2</sub> monolayers prepared on Si (100)/SiO<sub>2</sub> (500 nm)

Formula	Density (g.cm <sup>-3</sup> )	Thickness (nm)	Roughness (nm)
MoS <sub>2</sub> monolayer	7.21	0.61	0.38
VdW plan	0.09	0.19	0.19
MoS <sub>2</sub> monolayer	6.00	0.31	0.17
VdW plan	0.09	0.12	0.14
MoS <sub>2</sub> monolayer	6.99	0.56	0.35
VdW plan	0.09	0.27	0.24
SiO <sub>2</sub>	2.29	/	0.08

Table III.1: Extracted values from the fitting of a XRR pattern of a three MoS<sub>2</sub> monolayers prepared on Si (100)/SiO<sub>2</sub> (500 nm)

An interesting approach that could be implemented would be to carry out the same types of measurements with MoS<sub>2</sub> samples of different thicknesses (from 1 to 10 monolayers for example). The idea would be to observe and confirm the assumption of MoS<sub>2</sub> d-spacing variations occurring close to the SiO<sub>2</sub>/MoS<sub>2</sub> interface (on the first MoS<sub>2</sub> monolayers).

To conclude on these XRD characterizations, the combined out-of-plane and in-plane scans highlight the fiber texture of the MoS<sub>2</sub> deposited by ALD. Subsequently, the MoS<sub>2</sub> XRR pattern displays a clear response up to  $\omega = 8^\circ$  highlighting a very flat MoS<sub>2</sub> surface. This XRR pattern has been fitted with a model detailing each monolayer and VdW plane to correctly fit the MoS<sub>2</sub> XRR pattern. The extracted values seem consistent with what we could expect for a three MoS<sub>2</sub> monolayers thin film.

#### II.1.3.1.1. MoS<sub>2</sub> surface morphology (AFM)

The roughness and surface morphology of MoS<sub>2</sub> has been assessed by Atomic Force Microscopy (AFM). The AFM image is presented in Figure III.9. We observe the presence of a few small particles at the top surface. To consistently interpret the RMS and P.V. valued which exacerbated by the small particles at the MoS<sub>2</sub> top surface, a post processing treatment was performed to annihilate their contributions. Hence, the RMS value is  $0.244 \pm 0.012$  nm and the Peak to Valley (P.V) is  $1.43 \pm 0.072$  nm. This RMS value is very low, which highlights the smoother texture of the MoS<sub>2</sub> surface. This value is also slightly lower than the MoS<sub>2</sub> surface roughness determined by XRR.

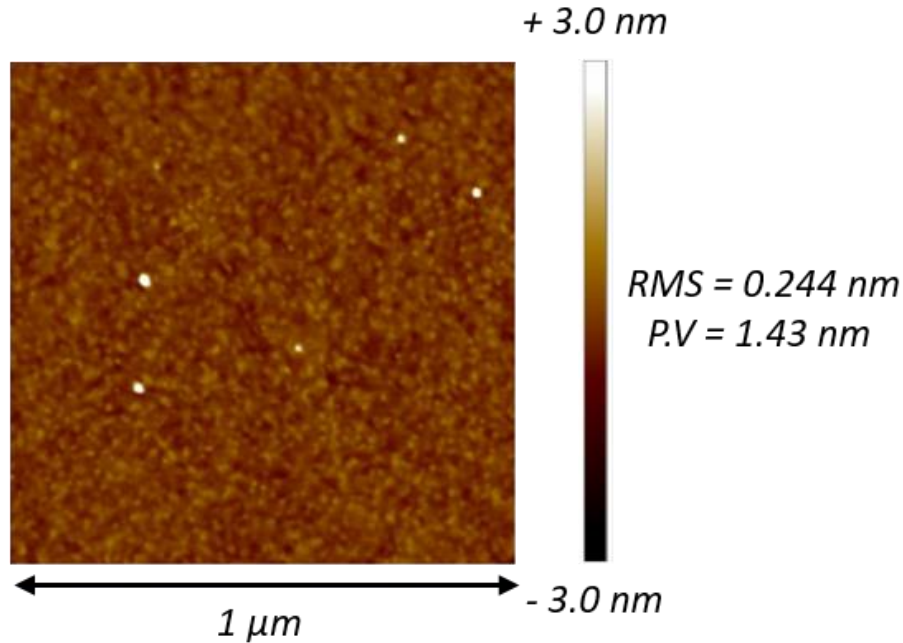


Figure III.9: AFM measurement of a three MoS<sub>2</sub> monolayers prepared on Si (100)/SiO<sub>2</sub> (500 nm)

This difference can be explained by a scale effect. The presented AFM image is a local measurement (1 μm<sup>2</sup> scan) while an X-Ray beam of the XRR measurement analyses a significant larger surface (around 0.2 mm<sup>2</sup> for  $\omega = 8^\circ$  in our analysis conditions). Hence, the surface roughness determined by XRR is averaged. Moreover, AFM and XRR measurements are based on totally different principles. XRR is based on a photon X/electron interaction while AFM is a physical surface analysis point by point thanks to a scan by a probe.

Therefore, these AFM results highlight a very smooth MoS<sub>2</sub> surface which is consistent with the XRR characterizations.

#### III.1.3.2. Surface chemical analysis (XPS)

X-ray Photoelectron Spectroscopy (XPS) is used to determine MoS<sub>2</sub> surface chemical composition. The experimental conditions of these XPS measurements performed in this work are briefly detailed in Annex part 2, section II.1.2. A typical high-resolution XPS Mo 3d of MoS<sub>2</sub> is depicted in Figure III.10. The main part of the spectra is composed of two peaks centered at 229.8 eV and 232.8 eV and attributed to core levels Mo<sup>4+</sup> 3d<sub>5/2</sub> and Mo<sup>4+</sup> 3d<sub>3/2</sub>, respectively. These binding energies are in excellent agreement with MoS<sub>2</sub> literature values<sup>374–376</sup>. The Mo 3d<sub>5/2</sub> and Mo 3d<sub>3/2</sub> peaks at 233.4 eV and 236.5 eV are attributed to Mo<sup>6+</sup> state corresponding to a small amount of MoO<sub>3</sub> at the top surface<sup>377,378</sup>. We can also observe a slight peak at 227.0 eV due to the overlapping of Mo 3d and S 2s contribution.

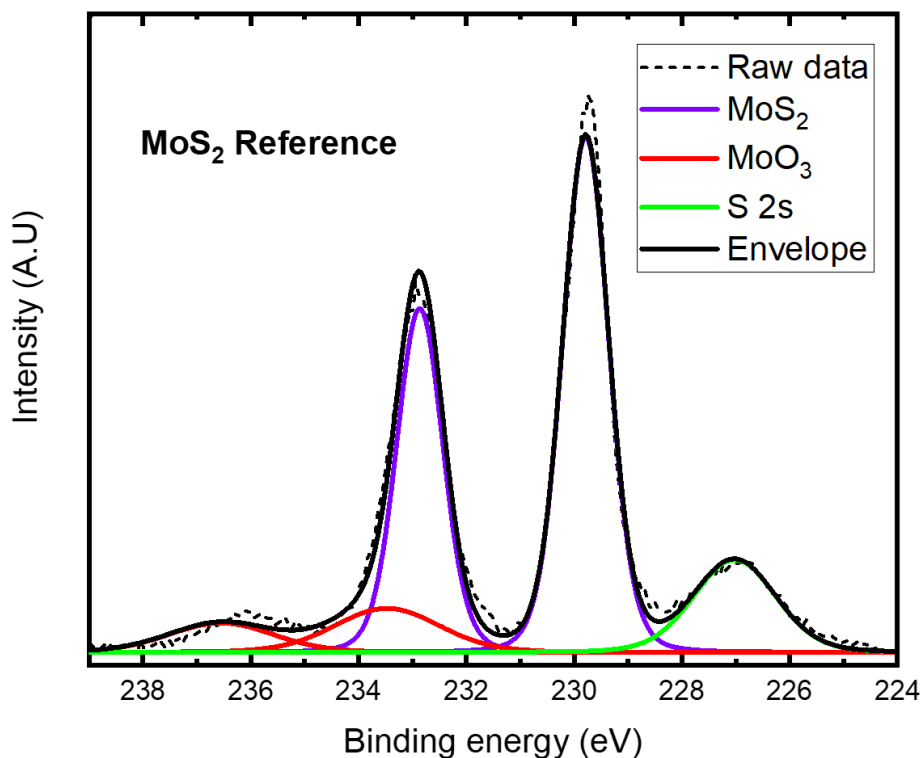


Figure III.10: Mo 3d XPS spectrum of a three MoS<sub>2</sub> monolayers prepared on Si (100)/SiO<sub>2</sub> (500 nm)

Overall atomic concentrations of SiO<sub>2</sub>/MoS<sub>2</sub> stack determined by XPS are detailed Annex part 3, Table. The [S]/[Mo] ratio attributed to MoS<sub>2</sub> contribution is 1.7. These XPS results also suggest that MoS<sub>2</sub> is substoichiometric. However, as indicated by Baker et al.<sup>379</sup> MoS<sub>2</sub> stoichiometry can be more precisely determined using the energy difference between Mo 3d<sub>5/2</sub> peak and S 2p<sub>3/2</sub> peaks. According to this publication, a stoichiometric MoS<sub>2</sub> has a characteristic energy difference between those peaks of 67.2 eV, which is exactly the value obtained in this study.

### III.2. AlN PVD deposition on 2D-MoS<sub>2</sub> seed layer

As mentioned in the second chapter, the growth of high-quality AlN films is challenging and presents an intrinsic difficulty: there is no monocrystalline substrate whose price is negligible compared to the growth cost and having close lattice matching and Coefficient of Thermal Expansion (CTE) with AlN<sup>92</sup>. Therefore, to achieve high crystalline quality, AlN is usually epitaxially grown on high-cost substrates such as sapphire and SiC which does not appear to be a cost-effective solution and limits the integration and applications of highly textured AlN.

This section focuses on the use of a 2D-TMDs material (MoS<sub>2</sub>) as a seed layer deposited on a low-cost silicon-based substrate (Si (100)/SiO<sub>2</sub> (500 nm)) to obtain high quality and c-axis textured AlN film. Firstly, we give an overview of the main AlN deposition techniques and their compatibility with the use of 2D-MoS<sub>2</sub> is discussed. Secondly, the interest of 2D-TMDs for AlN texturing is described. Subsequently, we present the AlN PVD deposition. Finally, we discuss the different characterizations performed on AlN films deposited by PVD on 2D-MoS<sub>2</sub> and compare them to other AlN deposited films on silicon-based substrates.

#### III.2.1. Existing solutions to AlN deposition and compatibility with 2D-MoS<sub>2</sub> seed layer

##### III.2.1.1. Chemical Vapor Deposition (CVD)

Chemical Vapor Deposition of AlN is a high temperature process in which the substrate temperature reaches above 1000 °C. When AlN is deposited by CVD on low-cost silicon substrates, the high deposition temperature, the difference of CTE combined with the large lattice mismatch between AlN and silicon generate high-tensile AlN films which can lead to cracks<sup>141,380,381</sup>. Therefore, AlN is usually epitaxially grown on sapphire or silicon carbide (SiC) substrates enabling to achieve single crystal AlN films highly c-axis oriented. However, the high-cost of these substrates added to the growth cost is not a cost-effective solution to improve AlN performances.

According to the literature, only one AlN deposition by CVD on 2D-TMDs (WS<sub>2</sub>) is mentioned<sup>382</sup>. The authors elaborate an AlN MOCVD layer in two steps. First, an AlN nucleation layer is deposited at low-temperature (890 °C). Then the temperature is increased up to 1200 °C to deposit a 500 nm thick AlN layer reaching an AlN (002) RC of 0.15°. Growth trials at 1100 °C on 2D-MoS<sub>2</sub> have been performed at CEA-LETI facilities but were unsuccessful



to achieve highly c-axis AlN films. As we will see in the next chapter, this result can be explained by the use of ammonia (NH<sub>3</sub>) as nitrogen precursor leading to a direct MoS<sub>2</sub> conversion into MoN<sub>x</sub> at high temperature. Therefore, a solution would be to take inspiration from Yin et al.<sup>382</sup> study and perform a two-steps AlN MOCVD deposition: a low-temperature AlN nucleation layer deposition (< 1000 °C) followed by a thick AlN deposition at high temperature (1100 °C).

#### *III.2.1.2. Atomic Layer Deposition (ALD)*

Another deposition technique to elaborate AlN films is Atomic Layer Deposition (ALD). In the literature, it is well-known that the AlN crystal quality and c-axis orientation deposited by thermal ALD (T-ALD) or Plasma-Enhanced ALD (PE-ALD) is poor<sup>147-149</sup>. To our knowledge, only one publication deals with AlN deposition by PE-ALD on various 2D-TMDs: WS<sub>2</sub>, MoS<sub>2</sub> and WSe<sub>2</sub>, which demonstrates the compatibility on this method with 2D-MoS<sub>2</sub> seed layer<sup>383</sup>.

Thus, an optimized AlN deposition by ALD on MoS<sub>2</sub> allowing a control at the atomic scale combined with the reasonable lattice mismatching between both materials could potentially lead to a highly c-axis textured AlN ALD layer. However, as discussed in chapter 2, section II.2.3.2.1, and despite multiple AlN depositions by T-ALD or PE-ALD with variations in process conditions (deposition temperature, AlN thickness, chemical precursors...) performed at SIMaP laboratory, the AlN films grown by ALD are only poorly c-axis oriented. Moreover, with the targeted AlN thicknesses for acoustic resonators (several hundreds of nm up to 1 μm), ALD technique presents a major drawback which is its slow deposition rate compared to CVD or PVD techniques.

#### *III.2.1.3. Physical Vapor Deposition (PVD)*

Among various AlN deposition techniques, PVD and especially reactive sputtering has been widely investigated to fabricate piezoelectric AlN films. This low-temperature deposition method rarely exceeding 500 °C enables to achieve AlN polycrystalline films with a sufficient c-axis orientation and small surface roughness to utilize its properties in various electrodevices such as acoustic resonators, lamb wave devices or harvesting devices<sup>238,384,385</sup>. Adjusting the PVD deposition parameters also allows the properties of AlN to be tailored efficiently and economically for many applications<sup>238</sup>. Therefore, reactive sputtering is the most common route to fabricate AlN films in mass at an economic cost. However, the low-temperature

coupled with low-cost silicon-based substrates exhibiting a large lattice matching with AlN limit the crystal quality and the AlN-based devices performances.

Despite the lamellar structure on the 2D-MoS<sub>2</sub> seed layer displaying weak interplanar bonding, the compability of AlN reactive sputtering deposition on 2D-MoS<sub>2</sub> or other 2D-TMDs has ever been proven in few studies <sup>332,333,382,386</sup> described in section III.2.4.3.1. Moreover, preliminary experiments performed in CEA facilities enable to find suitable deposition conditions to preserve the MoS<sub>2</sub> crystal integrity. In addition, as the targeted AlN-based acoustic resonators are deposited by reactive sputtering for a cost/efficiency tradeoff, the choice of this deposition technique is in good agreement with the targeted cost-effective solution to enhance AlN performances.

### III.2.2. Interest of TMDs (MoS<sub>2</sub> and WS<sub>2</sub>) in AlN texturing

Interest of TMDs, and especially MoS<sub>2</sub> and WS<sub>2</sub> (a very similar material to MoS<sub>2</sub>) in AlN texturing is based on their crystal structure compatibility. As mentioned in Table III.2: Crystal structure and lattice parameters of WS<sub>2</sub>, MoS<sub>2</sub> and AlN and illustrated in Figure III.11, both TMDs show a hexagonal structure close to AlN and present a slight in-plane lattice mismatch (1.6 % considering the respective a parameter of hexagonal AlN, MoS<sub>2</sub> and WS<sub>2</sub>). The first proof of concept to use TMDs as growth surface of crystalline AlN was proposed in 1996 by Chung and Ohuchi <sup>387</sup>. In this study, the use of WS<sub>2</sub> deposited by MOCVD as a substrate for the growth of AlN is demonstrated. In this pioneer work, the results published by Ohuchi in 1998 prove the successful epitaxy of c-axis oriented AlN on WS<sub>2</sub>, as well as a new concept of AlN transfer using a lift-off technique based on the weak Van der Waals interaction between WS<sub>2</sub> monolayers <sup>388</sup>.

	Crystal structure	Lattice parameter (Å)	
		<i>a</i>	<i>c</i>
<b>MoS<sub>2</sub></b>	Hexagonal	3.16	12.30
<b>WS<sub>2</sub></b>	Hexagonal	3.16	12.30
<b>AlN</b>	Hexagonal	3.11	4.98

Table III.2: Crystal structure and lattice parameters of WS<sub>2</sub>, MoS<sub>2</sub> and AlN

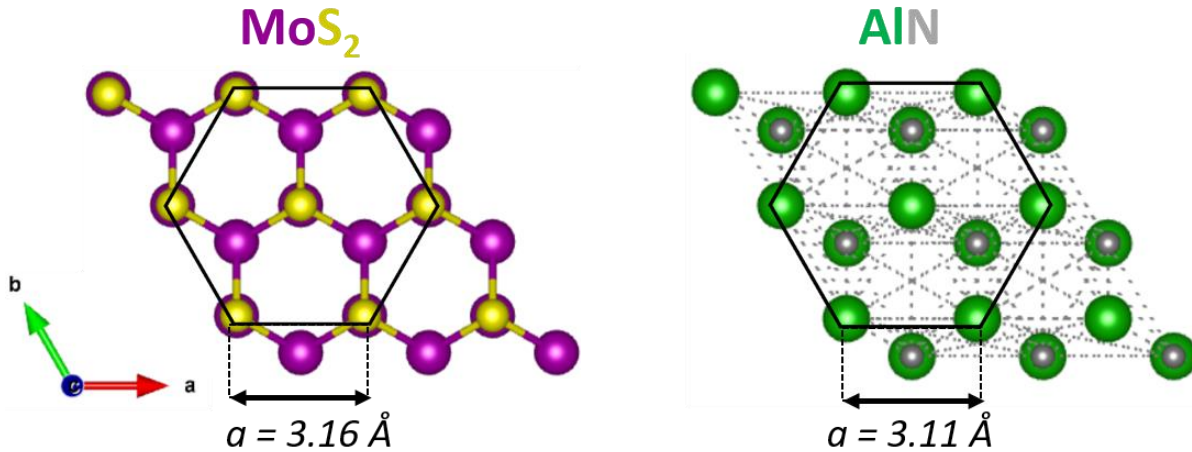


Figure III.11: Top view of the MoS<sub>2</sub> and AlN crystalline structure

The use of these 2D-TMDs materials as seed layer for III-V growth/epitaxy has not been investigated during the first decade of the millennium, until new high area 2D growth solutions based on CVD and ALD were developed. The approach of 2D induced heteroepitaxy has been revisited using WS<sub>2</sub><sup>382</sup> and MoS<sub>2</sub><sup>386,332,333</sup> as seed layers, with a strong focus on the improvement on the AlN texture compared to standard silicon or sapphire substrates as reference. This concept is yet commonly called “Van der Waals Epitaxy” (VdW epitaxy).

Hence, Hsu et al.<sup>332</sup> demonstrate a direct growth of AlN deposited by helicon sputtering on CVD-grown MoS<sub>2</sub> monolayers transferred on Si (100) substrate. The AlN mosaicity, assessed by  $\omega$ -scan XRD measurement, reveals to be not degraded and even slightly superior to that obtained on c-oriented sapphire substrate, avoiding the use of such non-standard substrates. Similar results have been obtained by Chien et al.<sup>333</sup> on sputtered AlN deposited on CVD-grown MoS<sub>2</sub> on sapphire substrate. The  $\omega$ -scan XRD measurement highlights that the use of MoS<sub>2</sub> as seed layer decreases AlN (002) RC down to an order of magnitude compared to as-deposited AlN on sapphire substrate.

Also, the improvement of the 2D deposition techniques, in particular on large surfaces such as on 300 mm Si wafers, paved the way towards AlN 300 mm CVD growth, since 300 mm sapphire substrates are not yet available for production. In addition, the direct AlN CVD growth on Si may lead to wafer deformations and AlN cracks due to internal stress accommodation on Si.

### **Chapter 3: Deposition of AlN films by Physical Vapor Deposition (PVD) on a 2D-MoS<sub>2</sub> layer**

Therefore, due to their reasonable lattice mismatch with AlN (and other III-V materials such as GaN) these 2D-TMDs materials appear very promising to enhance III-V materials crystal quality grown by PVD or CVD. Moreover, the proof of concept of their use has been demonstrated by several groups of workers and displays appealing results.

#### III.2.3. Description of AlN PVD deposition process

AlN thin films with a thickness of 100 nm were deposited by reactive sputtering in a SPTS (Trikon) Sigma fxP 200 mm magnetron PVD reactor located in CEA-LETI. It is an industrial process platform equipped with three deposition chambers (one for Al and AlN deposition, one for Mo deposition and one for W deposition) and one pre-clean chamber also used for wafer thermalization as described in Figure III.12.



Figure III.12: SIGMA PVD equipment used for AlN PVD deposition <sup>389</sup>

The deposition parameters were initially tuned to achieve the best texture of the AlN films on Si (100)/SiO<sub>2</sub> (500 nm)/MoS<sub>2</sub> (3 monolayers) wafers. The temperature was set to 350°C with a standard target power of 2 kW. The argon and nitrogen flow rates for the plasma are set to 10 sccm and 50 sccm, respectively. As substrate bias is suspected to degrade MoS<sub>2</sub>, no bias was applied on the 200 mm Si (100)/SiO<sub>2</sub> (500 nm)/ MoS<sub>2</sub> (3 monolayers) wafers to ensure soft conditions and preserve the MoS<sub>2</sub> surface.

III.2.4. Characterizations of AlN films deposited by PVD on 2D-MoS<sub>2</sub> seed layer

III.2.4.1. MoS<sub>2</sub> crystalline quality after AlN PVD deposition (Raman and TEM)

An easy and quick way to check the 2D-MoS<sub>2</sub> crystal integrity after AlN PVD deposition is to perform a Raman spectroscopy inspection before and after deposition. It is worth to notice that at the working wavelength (532 nm), AlN is highly transparent (transmittance close to 80 – 90 %) <sup>119,120</sup>. As presented in Figure III.13, no significant degradation of the MoS<sub>2</sub> Raman signal is observed after AlN deposition. We still observe the presence of E<sub>2g</sub><sup>1</sup> and A<sub>1g</sub> modes, at reduced intensities since the MoS<sub>2</sub> is capped with 100 nm thick AlN. Also, after AlN deposition, a slight redshift is visible on both modes. In fact, E<sub>2g</sub><sup>1</sup> and A<sub>1g</sub> modes are located at 379.2 ± 0.4 cm<sup>-1</sup> and 405.5 ± 0.1 cm<sup>-1</sup> after deposition, respectively, and at 382.6 ± 0.2 cm<sup>-1</sup> and 407.9 ± 0.1 cm<sup>-1</sup> before deposition. This redshift could be related to the deployment of an in-plane tensile stress in the MoS<sub>2</sub> induced by the deposition of the AlN PVD layer. Finally, the decrease in intensity is difficult to interpret since it is an absolute data and still difficult to relate with an expected phenomenon. In fact, a wafer orientation dependence of intensity is observed on silicon peak around 520 cm<sup>-1</sup> <sup>390</sup>. Moreover, this decrease could be related to a local modification of the MoS<sub>2</sub> band structure at the MoS<sub>2</sub>/AlN interface and potentially to AlN capping, despite AlN is highly transparent at the working wavelength.

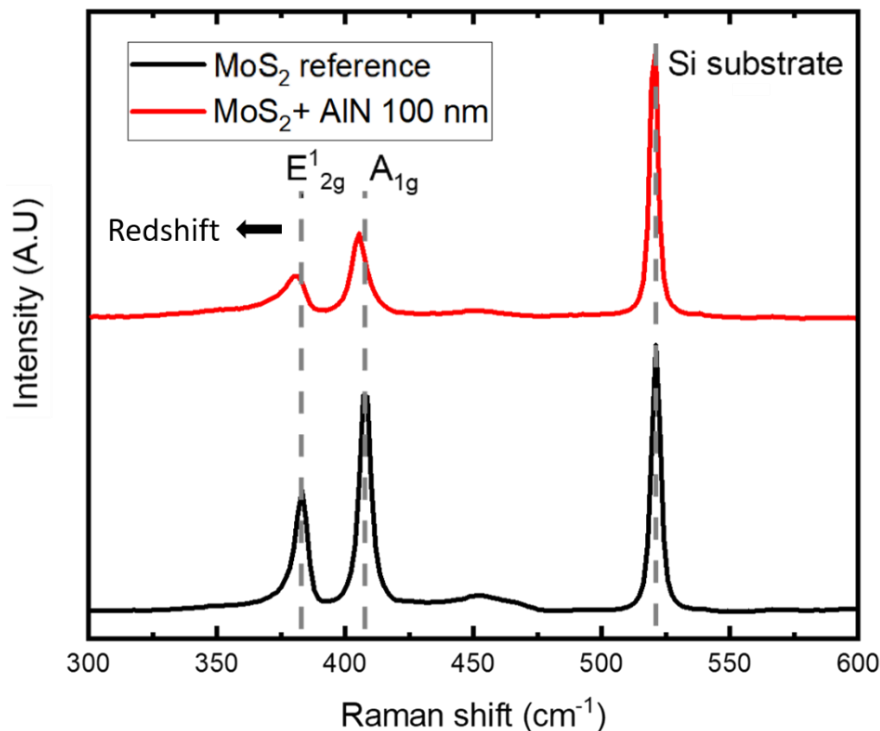


Figure III.13: Comparison of the typical MoS<sub>2</sub> Raman spectrum before and after 100 nm AlN PVD deposition

The MoS<sub>2</sub> crystalline state post-AlN deposition has also been investigated by TEM high-resolution cross section. TEM cross micrographs of AlN/MoS<sub>2</sub> stack are visible in Figure III.14 a) and Figure III.15 a). These TEM cross micrographs are compared with an identical AlN PVD deposition without the 2D-MoS<sub>2</sub> seed layer (directly deposited on Si (100)/ SiO<sub>2</sub> (500 nm)) in Figure III.14 b) and Figure III.15 b). In Figure III.14 a), on the right side, the polycrystalline AlN film displays a typical columnar structure with 15-20 nm wide grains. According to Cadot<sup>357</sup>, this size corresponds to the lateral MoS<sub>2</sub> domain size. This preferential c-axis orientation may appear during the very first stages of the growth if the lateral growth rate of some seeds at the surface is greater. Another way to obtain a preferential orientation is the evolutionary selection based on competitive growth proposed by Van der Drift in 1967<sup>391</sup>. According to the Van der Drift model, the crystallographic directions with the fastest vertical growth rate prevail over the slow-growing crystallographic directions.

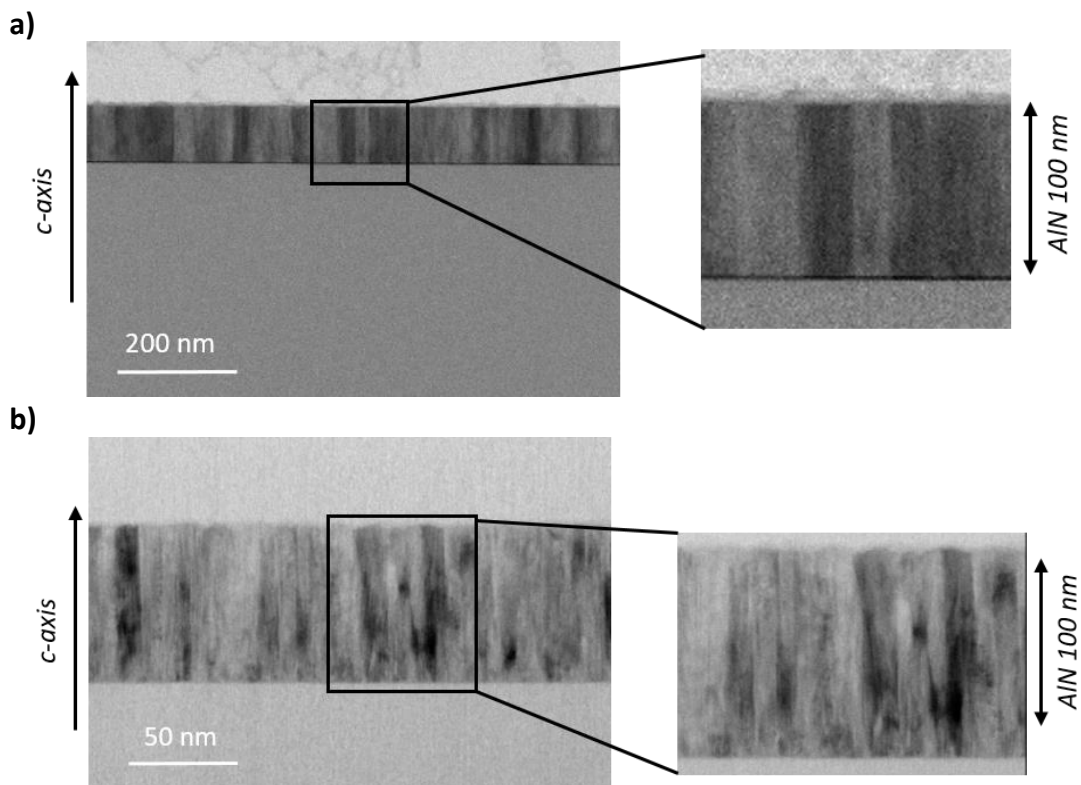


Figure III.14: Cross-sectional TEM of the 100 nm AlN PVD deposited on a) MoS<sub>2</sub> (3 monolayers) ; SiO<sub>2</sub> (500 nm)

In Figure III.14 b), the AlN wide grains seems slightly lower to the growth on 2D-MoS<sub>2</sub>, the typical columnar growth remains visible but less obvious suggesting a lower c-axis orientation. In addition, the AlN top surface also seems rougher on SiO<sub>2</sub> than MoS<sub>2</sub> which could be explained by more tilted AlN grains. Figure III.15 a) shows an atomic resolution image of the MoS<sub>2</sub>/AlN interface. We clearly observe a clean and sharp interface without any visible

damage in the 2D-MoS<sub>2</sub> bulk, and within the limit of the scale of the image, highlighting a perfect VdW epitaxy process between MoS<sub>2</sub> and AlN crystals. This AlN VdW epitaxy is not visible in Figure III.15 b). The stacking Al and N atoms seems disordered compared to the growth on 2D-MoS<sub>2</sub>.

First, we must insist that the AlN PVD deposition recipe is performed here without biasing the chunk to limit any damages on the MoS<sub>2</sub>. Even under this caution, such observation was un-expected. By principle, the PVD deposition technique relies on the atomic sputtering of a target, where sputtered elements can gain sufficient kinetic energy to induce an implantation effect on the substrate. As the MoS<sub>2</sub> lamellar structure and subsequent crystalline state are expected to be quite sensitive to such implantation effect, we would expect a degradation of the 2D-MoS<sub>2</sub>, in particular at extreme surface. However, TEM images coupled with Raman spectroscopy clearly show that the MoS<sub>2</sub> keeps its integrity, structure and crystallinity.

Second, the stacking of Al and N atoms on the MoS<sub>2</sub> surface is also un-expected. In a CVD process, the high deposition temperature provides energy which acts on the surface mobility of the species and helps crystal stacking. In this low-temperature PVD deposition process, the atoms arrive at the surface and stack with a remarkable lattice matching with the 2D-MoS<sub>2</sub> seed layer. This result opens up an area of development. Should an increase in AlN PVD temperature deposition lead to improvement in c-axis orientation? Should we switch to Pulsed Laser Deposition (PLD) which generates a high temperature on the target material and what would be the benefits? A wide axis of development remains to be studied.

Finally, TEM high-resolution performed post-AlN PVD deposition also highlights localized defects as presented in Figure III.15 c). This observation suggests that MoS<sub>2</sub> can relax the strain with buckling oscillations and twists due to the flexibility of the Mo backbone possibly associated with local phase changes. This kind of defects could be observed before the AlN deposition but would be exacerbated after deposition. In fact, despite a reasonable lattice mismatching between AlN and MoS<sub>2</sub>, the MoS<sub>2</sub>/AlN interface is strained and stressed, especially because AlN is a stiff material. Therefore, MoS<sub>2</sub> may accommodate this strain/stress by twisting and bucking.

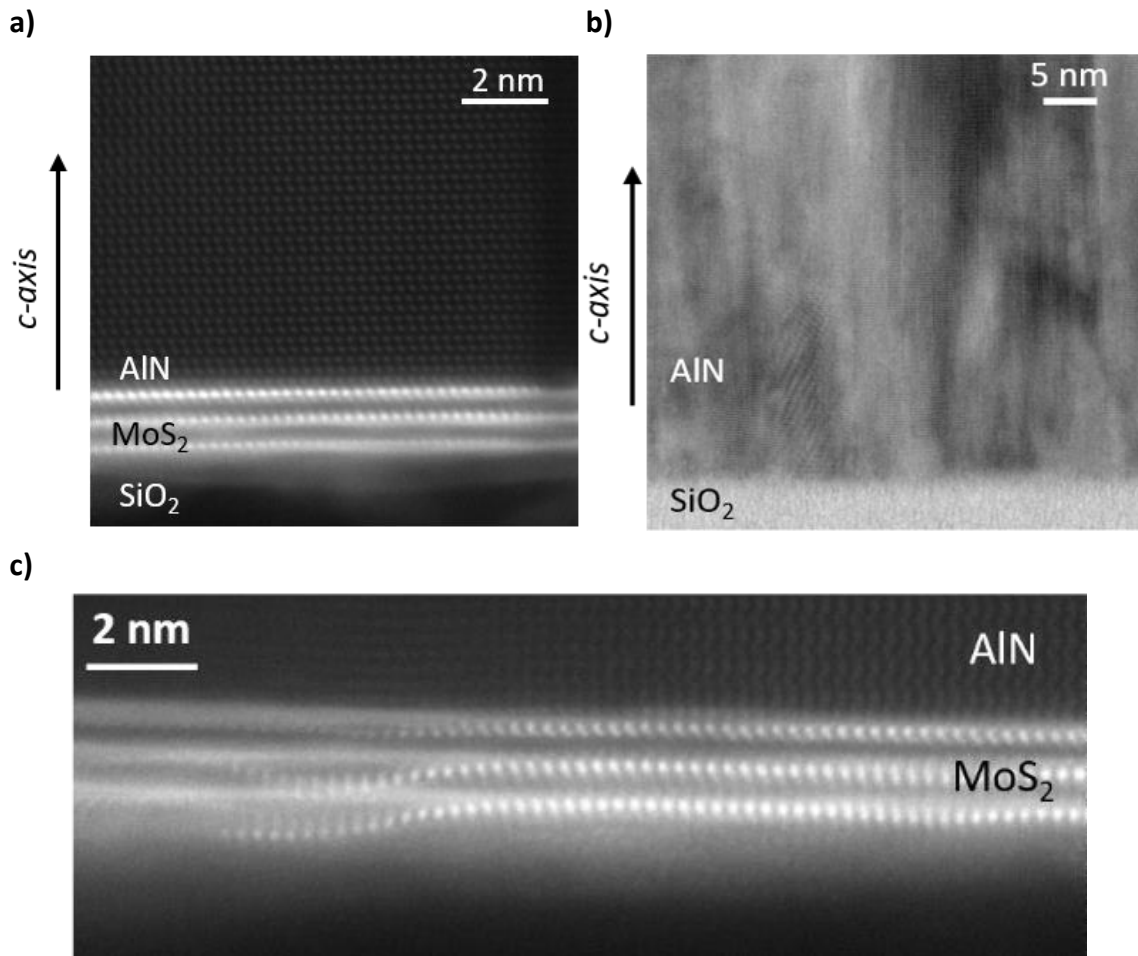


Figure III.15: Cross-sectional TEM at atomic resolution of the 100 nm AlN PVD deposited on a) MoS<sub>2</sub> (3 monolayers); b) SiO<sub>2</sub> (500 nm); c) Defects in MoS<sub>2</sub> monolayers

#### III.2.4.2. Mosaicity and stress calculations (XRD)

##### III.2.4.3.1. Mosaicity

To assess the mosaicity of the 100 nm AlN PVD deposition on Si (100)/SiO<sub>2</sub> (500 nm)/MoS<sub>2</sub> (3 monolayers), a  $\omega$ -scan XRD measurement on AlN (002) planes has been performed and compared with an identical deposition on Si (100)/ SiO<sub>2</sub> (500 nm) and on Si (100) with native oxide. Omega measurements are presented in Figure III.16. The AlN (002) RC ( $\approx 0.5^\circ$ ) is strongly enhanced due to the MoS<sub>2</sub> substrate compared to the two other substrates ( $\approx 4.0^\circ$  for SiO<sub>2</sub> and  $\approx 3.8^\circ$  for Si (100)). This experiment, showing a clearly improvement of the c-axis textured growth of AlN PVD on MoS<sub>2</sub>, paves the way toward the development of this thesis work. We can note that a good approach to assess the measurement uncertainty is to measure the Si (004) RC of the silicon substrate. The value is  $\approx 0.03^\circ$  which corresponds to the  $\omega$  instrumental resolution in the measurement configuration.



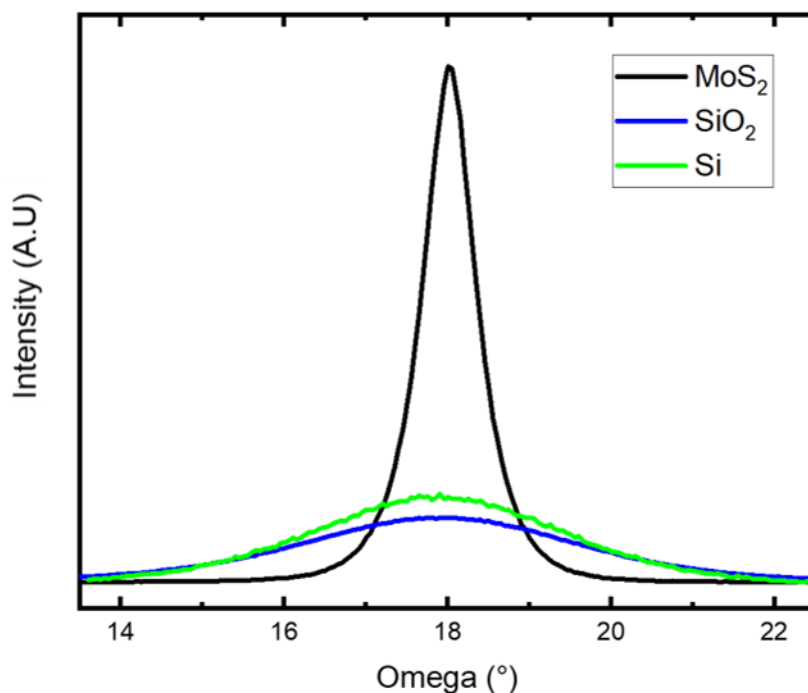


Figure III.16: AlN (002) RC measurements of a typical 100 nm AlN PVD deposited on different substrates (Si, SiO<sub>2</sub> or MoS<sub>2</sub>)

The c-axis preferential orientation was also confirmed using out-of-plane measurements as presented in Figure III.17 (red curve). A pronounced peak located at  $2\theta = 36.1^\circ$  and attributed to AlN (002) planes is clearly visible as well as a broader one at  $2\theta = 13.5^\circ$  corresponding to MoS<sub>2</sub> (002) contributions. In-plane measurements (in Figure III.17, green curve) display four peaks attributed to AlN (100), (110), (200) and (210) contributions.

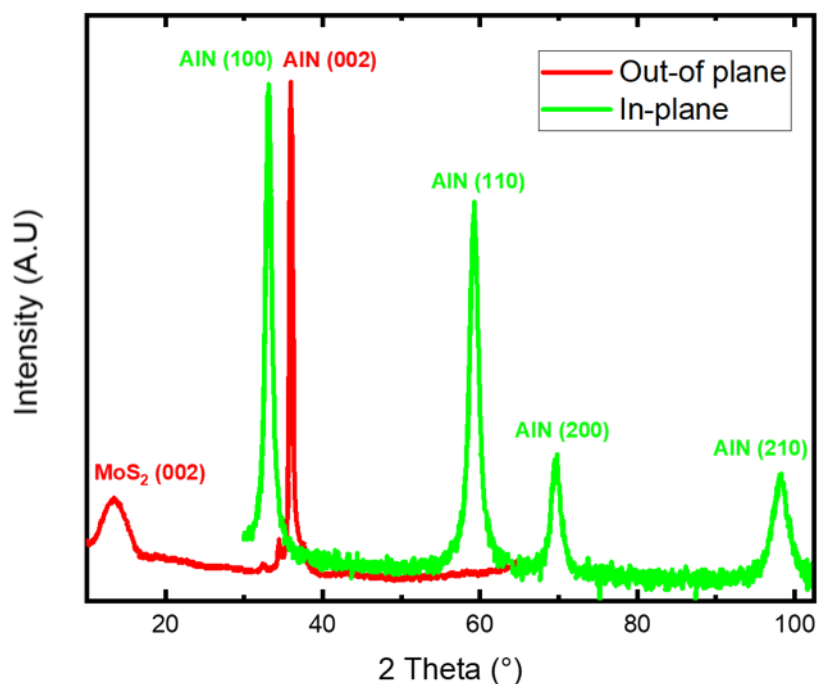


Figure III.17: Out-of-plane (red) and in-plane (green) XRD of 100 nm AlN PVD deposited on MoS<sub>2</sub> (3 monolayers)

### Chapter 3: Deposition of AlN films by Physical Vapor Deposition (PVD) on a 2D-MoS<sub>2</sub> layer

To conclude this section and situate this work with the literature, the AlN (002) RC obtained in this study is compared with AlN deposition on 2D-TMDs from the literature. The results are synthesized in Table III.3. We can note that the reported values are not absolute and depend on the instrumental resolution of the different XRD devices.

Substrate	AlN deposition technique	Thickness (nm)	AlN (002) RC	Authors
Si (100)/MoS <sub>2</sub>	Helicon sputtering (400 °C)	320	0.336°	Hsu et al. (2019) <sup>332</sup>
Sapphire/MoS <sub>2</sub>	Helicon sputtering (400 °C)	≈ 320	0.05°	Chien et al. (2020) <sup>333</sup>
Sapphire/WS <sub>2</sub>	MOCVD (1200 °C)	500	0.15°	Yin et al. (2018) <sup>382</sup>
Si (100)/SiO <sub>2</sub> (500 nm)/MoS <sub>2</sub>	Reactive sputtering (350 °C)	100	0.5°	This work

Table III.3: Comparison of the substrate, AlN deposition technique and AlN (002) RC obtained in this work with AlN deposition on 2D-TMDs from the literature.

First, this work presents an AlN (002) RC close to that reported by Hsu et al.<sup>332</sup> working on a silicon substrate. Moreover, the deposition method, deposition temperature and MoS<sub>2</sub> growth method (CVD-grown in Hsu et al. vs. ALD in this work) are different which could explain this variation and give us some axis of improvement.

Second, Chien et al.<sup>333</sup> seem to highlight the influence of the based-substrate on the AlN crystal quality. In fact, these authors have relatively similar conditions than Hsu et al. (deposition method, deposition temperature and CVD-grown MoS<sub>2</sub>) except that the based-substrate is different. The use of a sapphire substrate displaying a reasonable in-plane lattice mismatch with MoS<sub>2</sub> compared to Si (100) should improve the MoS<sub>2</sub> quality and c-axis orientation which results in an enhancement of the AlN (002) textured growth.

Finally, Yin et al.<sup>382</sup> also seem to demonstrate the influence of the growth method on the obtained AlN film. The higher temperature deposition of MOCVD promotes the AlN grain coalescence leading to an AlN (002) planes realignment and a decrease in AlN (002) RC<sup>141,380,381</sup>. Therefore, even if the AlN crystal quality is drastically increased by the use of 2D-TMDs as seed layers, the based substrate and deposition method also have a non-negligible impact.

III.2.4.3.2. Stress calculation

In this work, AlN equi-biaxial stress has been determined by “Crystallit Group Method” (CGM) by XRD. As the AlN PVD layer exhibits a c-axis preferential orientation, the classical  $\sin^2 \psi$  method employed is not adapted. We can refer to Annex part 2, section II.1.4.2 for more explanation of stress analysis by XRD and CGM method.

Figure III.18 a) and b) present the AlN a-lattice constant and AlN strain as a function of  $\sin^2 \psi$ , respectively. The process to obtain these curves is detailed in Annex part 2, section II.1.4.2.

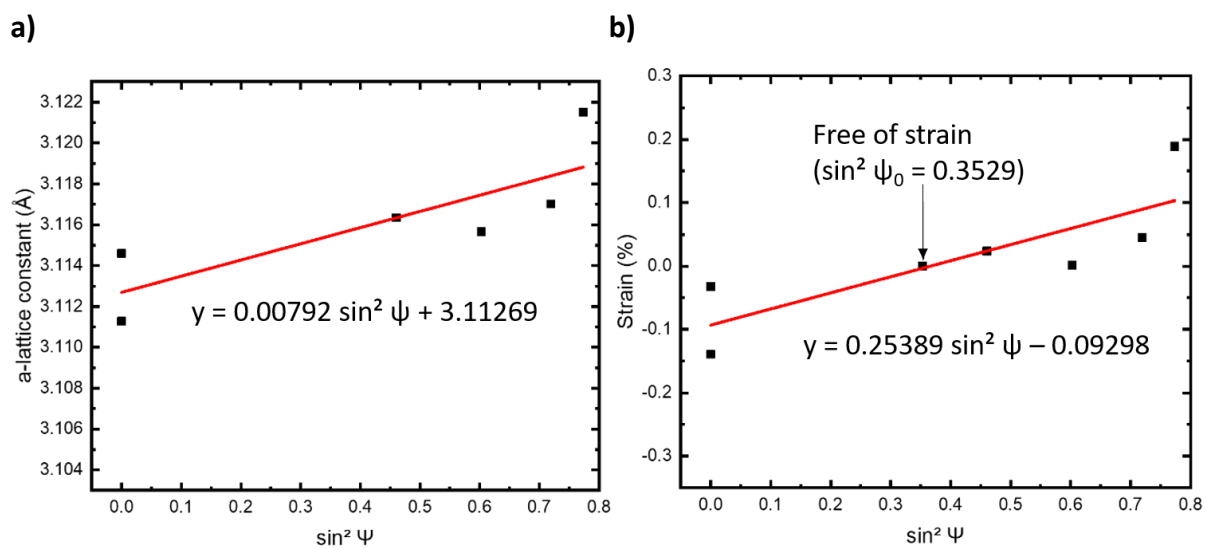


Figure III.18: a) a-lattice parameter ; b) strain as a function of  $\sin^2 \psi$  for a 100 nm AlN PVD deposition grown on Si (100)/SiO<sub>2</sub> (500 nm)/ MoS<sub>2</sub> (3 monolayers).

According to Equation 1 presented in Annex part 2, section II.1.4.2, the equi-biaxial stress  $\sigma$  is the slope of the linear regression in Figure III.18 b), weighted by the elastic compliances. The AlN stress value extracted on MoS<sub>2</sub> is estimated at  $\sigma = 0.75 \pm 0.08$  GPa. The same CGM method has been applied to determine AlN stress deposited in the same conditions on Si (100) and Si (100)/SiO<sub>2</sub> (500 nm) substrates and lead to an AlN equi-biaxial stress of  $0.77 \pm 0.09$  GPa and  $0.64 \pm 0.11$  GPa, respectively. These values are extremely close to that estimated for AlN 100 nm deposited on MoS<sub>2</sub>. Hence, it seems to indicate that at this thickness, the equi-biaxial stress of the AlN PVD layer is independent of the substrate. Moreover, the pronounced AlN c-axis textured growth on MoS<sub>2</sub> compared to Si (100) or Si (100)/SiO<sub>2</sub> (500 nm) does not affect the stress.

### Chapter 3: Deposition of AlN films by Physical Vapor Deposition (PVD) on a 2D-MoS<sub>2</sub> layer

Second, these values are difficult to compare with literature. In fact, no AlN stress investigations deposited on 2D-TMDs have been mentioned. Moreover, AlN PVD films elaborated on silicon-based substrates are generally deposited using a bias applied to the substrate<sup>261,392,393</sup>. This bias is used to tune the stress within the bulk enabling the PVD growth of highly compressive AlN films ( $\sigma < 0$  approximately up to 500 nm – 1  $\mu\text{m}$  thick depending on the bias power) to the transition from compressive to tensile films near 1  $\mu\text{m}$ . Therefore, the comparison with the obtained AlN stress on values Si (100) and Si (100)/SiO<sub>2</sub> (500 nm) substrates are also difficult to compare. However, Knisely et al.<sup>392</sup> mention a stress around 0.8 GPa for a 750 nm thick AlN PVD film deposited without bias. Beyond the different thicknesses, this value is in good agreement with our values on Si (100) and Si (100)/SiO<sub>2</sub> (500 nm) and could suggest an almost constant AlN stress with the increase in thickness in these deposition conditions.

Finally, and as mentioned in Annex part 2, section II.1.4.2, the CGM method also enable to determine the AlN in-plane and out-of-plane strains. These AlN strains deposited on Si (100), SiO<sub>2</sub> (500 nm) and MoS<sub>2</sub> (3 monolayers) are listed in Table III.4.

AlN Strain $\epsilon$ (%)	Si (100)	SiO <sub>2</sub> (500 nm)	MoS <sub>2</sub> (3 monolayers)
Out-of-plane ( $\epsilon_{\text{out}}$ )	- 0.09 $\pm$ 0.02	- 0.08 $\pm$ 0.03	- 0.09 $\pm$ 0.02
In-plane ( $\epsilon_{\text{in}}$ )	0.17 $\pm$ 0.04	0.14 $\pm$ 0.03	0.16 $\pm$ 0.03

Table III.4: In-plane and out-of-plane strains of AlN PVD 100 nm deposited on Si (100), SiO<sub>2</sub> (500 nm) and MoS<sub>2</sub> (3 monolayers)

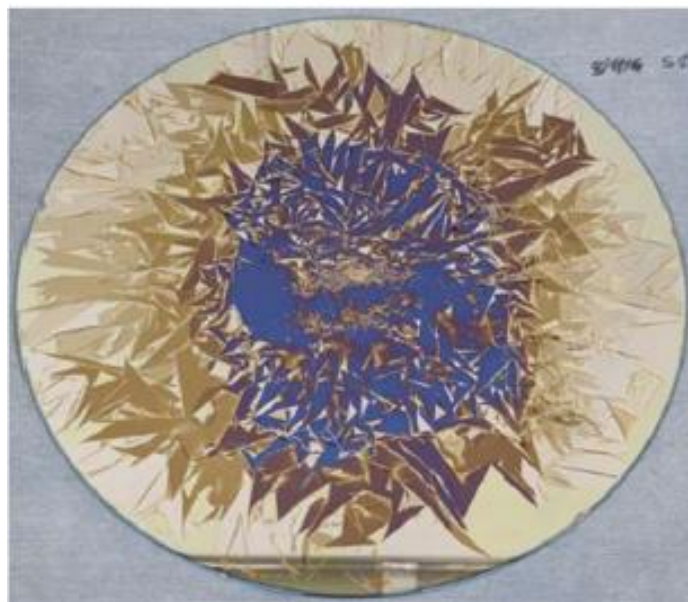
For each sample, as the AlN equi-biaxial stress is positive (tensile stress), these results logically lead to a negative and positive out-of-plane and in-plane strain, respectively. In addition, as the AlN stress is similar on each sample ( $\sigma \approx 0.7$  GPa), the strains are also similar.

To conclude on these AlN PVD stress investigations and their comparison with the literature enable to draw some conclusions. Firstly, our results strongly show that the 100 nm AlN PVD stress is independent of the growth substrate and c-axis orientation of the film. The obtained stress values are consistent with that measured by Knisely et al.<sup>392</sup> for a 750 nm thick AlN PVD layer suggesting an almost constant AlN stress with the increase in thickness, assuming that the PVD equipment and growth conditions are similar. Secondly, and as mentioned in the previous chapter, the PVD growth conditions and especially the use of a bias significantly affects the resulting AlN stress.

### III.3. Delamination issue and potential solutions

As shown in the previous section, the insertion of a 2D-MoS<sub>2</sub> seed layer in a SiO<sub>2</sub>/AlN stack results in the improvement of the c-axis AlN texture. It is well-known in the literature<sup>261</sup> that the c-axis orientation increases with the AlN thickness deposited on Si. Stated differently, generally the AlN texturing is improved with the AlN film thickness. Hence, we wonder if such effect is also effective to further improve the AlN texturing on MoS<sub>2</sub>, i.e. how far we can increase the AlN film thickness knowing that the stress deployment is high within bulk AlN, and that the adhesion of the AlN on its substrate is affected by the VdW inter-plane bonds within 2D-MoS<sub>2</sub>.

To address this adhesion question, we deposited a thicker 200 nm AlN by PVD using the same parameters as described in section III.2.3, and as expected in Figure III.19, a delamination of the stack occurs. In this picture, we see the dark blue colour of the bottom SiO<sub>2</sub> and the AlN in yellowish color. The blue color suggests that the delamination interface is between the SiO<sub>2</sub> and AlN, more precisely within MoS<sub>2</sub>.



*Figure III.19: Delamination on a 200 mm Si (100)/SiO<sub>2</sub> (500 nm)/MoS<sub>2</sub> (3 monolayers) wafer due to an AlN PVD deposition > 200 nm*

Several additional attempts have confirmed that using AlN PVD growth deposited on 2D-MoS<sub>2</sub> seed layer, the maximum achievable AlN film thickness is around 200 nm. This issue is a major limitation limiting our capability to fully exploit the potential of highly crystalline AlN growth on 2D-MoS<sub>2</sub> seed layer. The root cause of this delamination issue and potential solutions are discussed in the following sections.

III.3.1. Origins of the delamination

III.3.1.1. Tape test

We assumed that delamination issue is induced by two competing phenomena: the first one is the Van der Waals interaction between each 2D-MoS<sub>2</sub> monolayer. This weak interaction contributes to the low adhesion of the AlN deposited on MoS<sub>2</sub><sup>394,395</sup>. The second phenomenon is the stress/strain of the AlN layer which cannot be handled by the 2D-MoS<sub>2</sub>. In fact, spontaneous delamination may occur at any time because of residual stress-induced crack growth, wrinkle formation, and other separations between the thin film and substrate<sup>394</sup>. An easy experimental way to evaluate the poor adhesion is to perform a simple tape test on top of Si (100)/SiO<sub>2</sub> (500 nm)/MoS<sub>2</sub> (3 monolayers)/AlN (100 nm) stack. A picture post tape experiment is visible in Figure III.20. The tape has been stucked on five different zones on AlN. We clearly observe that the entire surfaces covered by the tape are removed. Here again, the dark blue colour is attributed to the bottom SiO<sub>2</sub> surface.

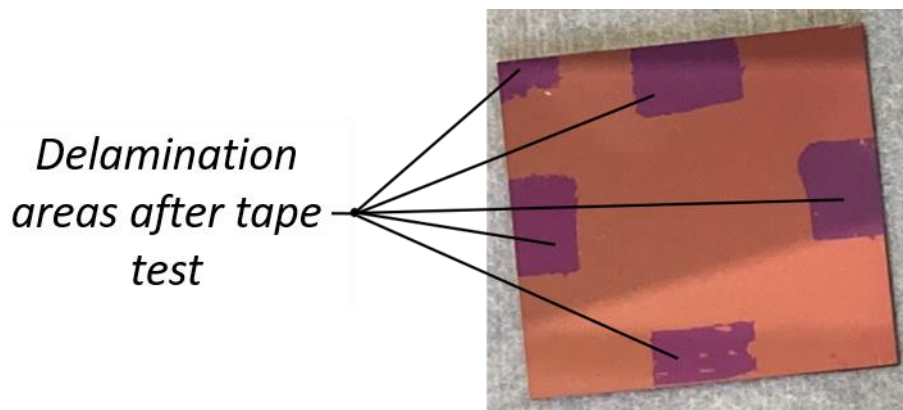
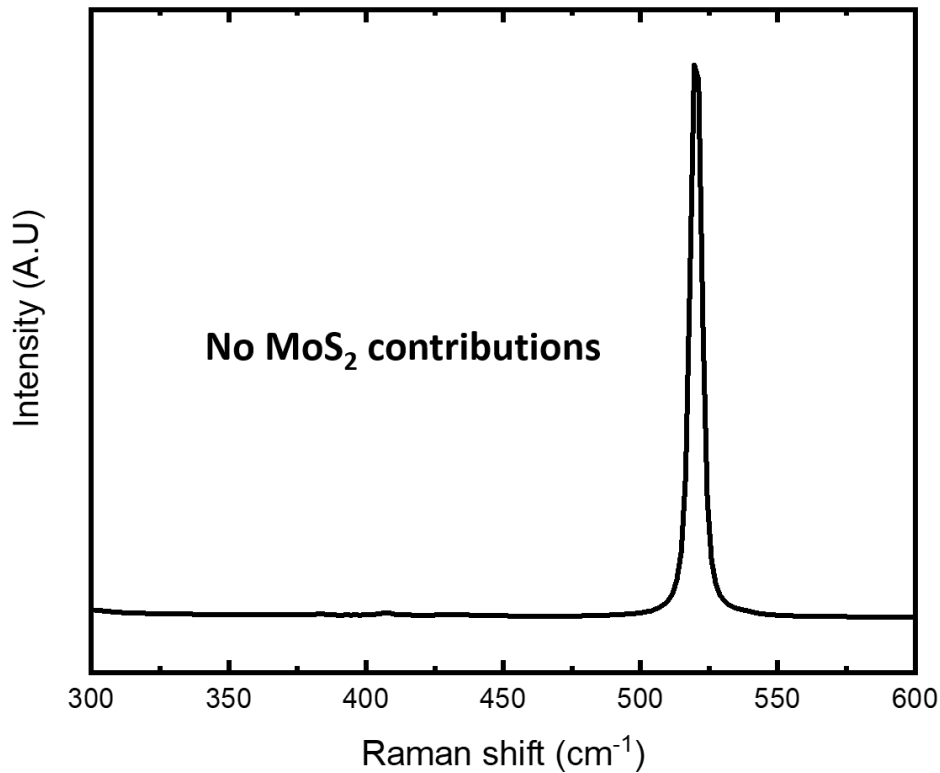


Figure III.20: Tape test on 100 nm AlN PVD deposited on Si (100)/SiO<sub>2</sub> (500 nm)/MoS<sub>2</sub> (3 monolayers)

III.3.1.2. Determination of the delamination interface

To push further the investigations about the delamination issue, XPS analysis have been performed on the delaminated area (i.e. blue colour) after tape test. Overall atomic concentrations, binding energies and attributions determined by XPS of the delaminated area are detailed in Annex part 3, section III.2.1. These results clearly show the absence of sulphur contributions. Rather, a small amount of molybdenum attributed to MoO<sub>x</sub> bonds is detected. Also, we observe that the predominant contributions come from the Si 2*p* and O 1*s* and are attributed to the SiO<sub>2</sub> thermal oxide on which MoS<sub>2</sub> was deposited. It confirms that the delamination occurs at the MoS<sub>2</sub>/SiO<sub>2</sub> interface.

To confirm the absence of residual MoS<sub>2</sub> grains on the substrate, we performed Raman spectroscopy on the dark blue region. As expected in Figure III.21, Raman spectrum performed on a delaminated area only displays the 520 cm<sup>-1</sup> single peak from the silicon substrate. This result is in line with the XPS characterizations and definitely confirms that the delamination occurs at the MoS<sub>2</sub>/SiO<sub>2</sub> interface.



*Figure III.21: Raman spectrum on a delaminated area*

As a first assumption, the molybdenum oxide could be induced by the air exposure of the sample, but we know that crystallised MoS<sub>2</sub> is quite stable under air, and the direct conversion of MoS<sub>2</sub> into MoO<sub>x</sub> under air is not expected. The MoO<sub>x</sub> environment is rather attributed to the residual chemical bonds present between the first MoS<sub>2</sub> monolayer and the SiO<sub>2</sub> substrate. They are formed at the very first instants of the ALD growth. These nucleation bonds were required to initiate the growth by ALD at first cycle, and they were consolidated by the high temperature annealing. Under annealing, as the amorphous ALD sulphur layer crystallizes, we think that these bonds are pushed away at grain boundaries. There, they lay between the border of the grain and link the grain to the SiO<sub>2</sub> substrate insuring a relative adhesion of the 2D layers. Based on Cadot's thesis work <sup>357</sup>, a proposition of the evolution of the chemical surface state is illustrated in Figure III.22.

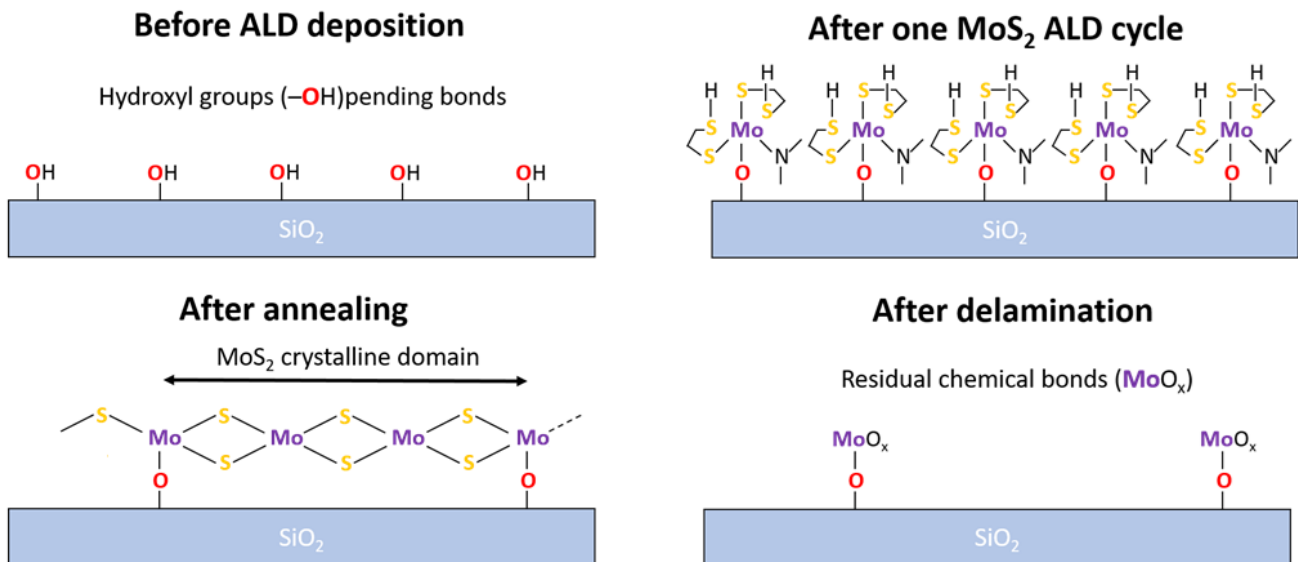


Figure III.22: Evolution of the chemical surface state before MoS<sub>2</sub> ALD deposition, after one ALD cycle, after annealing and after delamination.

This observation seems not surprising since several studies<sup>394–396</sup> determine by different methods that the MoS<sub>2</sub> adhesion energy mechanically exfoliated and transferred onto SiO<sub>2</sub> is slightly lower than the MoS<sub>2</sub> adhesion energy between two MoS<sub>2</sub> monolayers. To illustrate this, Deng et al.<sup>394</sup> and Torres et al.<sup>396</sup> determine an adhesion energy at the MoS<sub>2</sub>/SiO<sub>2</sub> interface of 0.252 J.m<sup>-2</sup> (determined via wrinkle formation) and 0.482 J.m<sup>-2</sup> (determined via nanoparticles intercalation), respectively. As the interfacial adhesion energy is not determined by the same method, it could be difficult to compare these values.

However, more recently, Rokni et al.<sup>395</sup> evaluate by AFM the adhesion energy of the MoS<sub>2</sub>/SiO<sub>2</sub> interface and also between two MoS<sub>2</sub> monolayers at room temperature (22 °C) being 0.189 J.m<sup>-2</sup> and 0.384 J.m<sup>-2</sup>, respectively. This last study tends to confirm that the delamination occurs at the MoS<sub>2</sub>/SiO<sub>2</sub> interface due to a strong predominance of Van der Waals interactions. In fact, MoS<sub>2</sub> basal plane is considered as inert unless sulphur vacancies are introduced into its plane<sup>395</sup>. Thus, no chemical covalent bonds are formed at the MoS<sub>2</sub>/SiO<sub>2</sub> interface. However, a transfer process does not lead to the formation of covalent bonds as previously assumed for an annealed MoS<sub>2</sub> sample deposited by ALD where bonds would be formed at the grain boundaries. Therefore, we could expect that the MoS<sub>2</sub>/SiO<sub>2</sub> adhesion energy of MoS<sub>2</sub> monolayers transferred onto SiO<sub>2</sub> is lower than the MoS<sub>2</sub>/SiO<sub>2</sub> adhesion energy of our sample.



To conclude, two competing phenomena are expected based on the 2D-MoS<sub>2</sub> seed layer crystalline quality, in particular the grain size. Firstly, the MoS<sub>2</sub> crystalline state affects c-axis AlN crystalline state, i.e. the higher the crystalline state, the better c-axis orientation. This MoS<sub>2</sub> crystalline state is also directly related with its lamellar structure, i.e. the higher the crystalline state, the more the VdW structure is present, and it is strongly assumed that this VdW structure cannot handle the AlN stress. Secondly, the grain size indirectly impacts the adhesion since larger grains result on lower amount of MoO<sub>x</sub> bonds. Hence, to fully take advantage of proposed AlN PVD growth on ALD deposited 2D-MoS<sub>2</sub> seed layer, it is mandatory to either reduce AlN film strain/stress or transform the MoS<sub>2</sub>/SiO<sub>2</sub> Van der Waals interface (and by extension of the MoS<sub>2</sub> lamellar structure) into an interface with strong and covalent bonds while preserving the well c-axis textured growth of the AlN.

### *III.3.1.3. Estimation of elastic energy from AlN film failure*

#### *III.3.1.3.1. Introduction to Beuth model*

A well-known characterization used to determine the elastic energy from a film failure is mechanical nanoindentation. Briefly, this technique is based on the indentation of a material by a nano-indenter (spherical, Berkovitch...). The analysis of the indented depth, the length of the cracks and the applied force provides access to the mechanical properties of the film such as hardness, Young's modulus or elastic energy. To solicit the material of interest without undergoing the influence of the substrate, the latter must have a sufficient thickness (several hundred nanometers minimum). Therefore, as the delamination occurs for an AlN PVD thickness around 200 nm, this method cannot be properly employed.

However, the fracture energy of the AlN PVD film failure can be determined applying Beuth model. This model enables the determination of this fracture energy using the AlN PVD equi-biaxial stress for a 100 nm AlN PVD thick film ( $\sigma = 0.70$  GPa) determined in section III.2.4.3.2, the critical delamination thickness of the AlN film ( $t_f \approx 200$  nm) estimated in section III.3 and mechanical parameters (Young and shear moduli, Dundurs coefficients...). As every model, Beuth model is imperfect and presents assumptions that can be strong given the studied stack and the nature of the interfaces (especially Van der Waals). However, it is the only tool we had available to estimate this energy and compare it to the adhesion energy of the MoS<sub>2</sub>/SiO<sub>2</sub> interface. The theory of Beuth model and the mechanical parameters used are detailed in Annex part 2, section II.2.

### Chapter 3: Deposition of AlN films by Physical Vapor Deposition (PVD) on a 2D-MoS<sub>2</sub> layer

#### III.3.1.3.2. Beuth model - application to delamination issue

We applied the Beuth model described in Annex III.3 on the AlN/MoS<sub>2</sub>/SiO<sub>2</sub> stack. Due to its very low thickness, the 2D-MoS<sub>2</sub> seed layer is assumed negligible and is not considered in the treatment.

The mechanical constants and equations used for the calculation are listed in Table III.5.

AlN stiffness constants (GPa)		Transverse Young's Modulus (GPa)	Transverse shear modulus (GPa)
<b>c<sub>11</sub></b>	394.0	$E_{AlN} = \frac{(c_{11} - c_{12})(c_{11}c_{33} + c_{12}c_{33} - 2c_{13}^2)}{(c_{11}c_{33} - c_{13}^2)}$ $= 338.4 \text{ GPa}$	$\mu_{AlN} = \frac{(c_{11} - c_{12})}{2} = 130.3 \text{ GPa}$
<b>c<sub>12</sub></b>	133.4		
<b>c<sub>13</sub></b>	95.2		
<b>c<sub>33</sub></b>	402.0		

Table III.5: AlN stiffness constants and equations for Transverse Young's and shear moduli calculations

We achieved many AlN PVD depositions on 2D-MoS<sub>2</sub> to estimate the critical delamination thickness  $t_f$ . We evaluated that the delamination occurs for  $t_f \approx 200$  nm (set between 175 nm and 225 nm for calculation). Equi-biaxial stress  $\sigma_f$  of a 100 nm AlN PVD layer was determined previously by XRD measurements (0.70 GPa). We used this value for the calculation of the energy release rate  $G$  assuming that the equi-biaxial stress between a 100 nm AlN PVD film and 175-225 nm thick is close. Transverse Young's and shear moduli of AlN ( $E_{AlN}$  and  $\mu_{AlN}$ ) are calculated from mechanical constants and equations presented in Table III.5. We use this value to calculate  $E^*_{AlN}$  and  $\nu_{AlN}$  using the equations presents in Annex part 2, section II.2. Finally, Dundurs coefficient  $\alpha$  is calculated with  $E_{AlN}$  and  $E_{SiO_2} = 74$  GPa and as  $\beta$  is insignificant compared to  $\alpha$ , it is fixed at these extreme values 0 and  $\alpha/4$  giving a  $g(\alpha, \beta)$  set between 2.47 and 2.63.

Thus, according to Annex part 2, section II.2, the elastic energy released  $G$  and toughness  $K_I$  from the AlN film failure are evaluated between 0.98 J.m<sup>-2</sup> and 1.35 J.m<sup>-2</sup>, and 0.58 MPa.m<sup>-1/2</sup> and 0.67 MPa.m<sup>-1/2</sup>, respectively (details in Table III.6).

	Energy release rate $G$ (J.m <sup>-2</sup> )		Toughness $K_I$ (MPa.m <sup>-1/2</sup> )	
<b>Critical AlN thickness <math>t_f</math> (nm)</b>	$g(\alpha, \beta) = 2.47$	$g(\alpha, \beta) = 2.63$	$g(\alpha, \beta) = 2.47$	$g(\alpha, \beta) = 2.63$
<b>175</b>	0.98	1.05	0.58	0.60
<b>225</b>	1.26	1.35	0.65	0.67

Table III.6: Elastic energy release form the AlN film failure with the different  $g(\alpha, \beta)$  and critical AlN thickness combinations

### **Chapter 3: Deposition of AlN films by Physical Vapor Deposition (PVD) on a 2D-MoS<sub>2</sub> layer**

These results about AlN energy release rate  $G$  or toughness  $K_I$  are lower to what we can find in the literature. In fact, Chiu et al.<sup>397</sup> estimate the toughness of a 1  $\mu\text{m}$  AlN film deposited by helicon sputtering on sapphire substrate around 1.5 – 1.8  $\text{MPa}\cdot\text{m}^{-1/2}$ . Other studies<sup>398,399</sup> mentioned a higher AlN toughness of 3.98  $\text{MPa}\cdot\text{m}^{-1/2}$  and 6.70  $\text{MPa}\cdot\text{m}^{-1/2}$  determined from sintered AlN powder. However, as these results are lower than those reported in other studies, they clearly highlight the poor adhesion on AlN on the SiO<sub>2</sub>/MoS<sub>2</sub> template resulting in its cracking. In addition, we have to keep in mind the different assumptions (MoS<sub>2</sub> seed layer neglected) and a questionable adherent interface between AlN/MoS<sub>2</sub> and SiO<sub>2</sub> which should overestimate the energy release rate and toughness which contribute to strengthen these results.

#### *III.3.1.4. Conclusions of the delamination issue*

The different characterizations investigated enable to understand the interface subject to the delamination (MoS<sub>2</sub>/SiO<sub>2</sub> interface) and identified the phenomena leading to this issue. The VdW interaction within MoS<sub>2</sub> contributing to the weak adhesion of the AlN deposited on MoS<sub>2</sub> combined with the high AlN PVD residual stress lead to a spontaneous delamination of the AlN/MoS<sub>2</sub> stack. The energy release rate  $G$  and toughness  $K_I$  have been estimated with the Beuth model. Despite the assumptions, the use of this model clearly highlights the poor adhesion on AlN on the SiO<sub>2</sub>/MoS<sub>2</sub> template resulting in its delamination. This delamination occurs for  $t_f \approx 200$  nm thick AlN PVD deposition which is insufficient for the targeted RF and power applications since AlN film thickness up to 1  $\mu\text{m}$  is required. Even though a 200 nm thick AlN layer would be sufficient, we have to consider the integration process (etching, photolithography...) which could be critical for the integrity and the adhesion of the layer. Therefore, this delamination issue is a major hindrance for the integration of these materials in AlN-based devices and needs to be solved.

#### *III.3.2. Proposed solutions to the delamination issue*

The previous section enables to identify the phenomena behind the delamination issue. The first one is the Van der Waals interaction between each 2D-MoS<sub>2</sub> monolayer which contributes to the fragile adhesion of the AlN deposited on MoS<sub>2</sub>. The second phenomenon is the strain of the AlN layer leading to high residual stress which cannot be handle by the MoS<sub>2</sub> lamellar structure. Hence, it is necessary to solve one or both phenomena to improve the adhesion on the AlN layer. Therefore, two main potential solutions have been identified to

solve this issue and are discussed hereafter. The first one is based on the local etching of MoS<sub>2</sub>/AlN stack (Epitaxial Lateral Over Growth) to reduce AlN stress/strain and ensures its anchorage on the substrate. The second one is the thermochemical modification of the MoS<sub>2</sub>/SiO<sub>2</sub> interface to transform the Van der Waals interaction into strong covalent bonds.

*III.3.2.1. AlN/MoS<sub>2</sub> local etching*

AlN strain being identified as a phenomenon contributing to the delamination, a local etching of the AlN/MoS<sub>2</sub> is one potential solution to anchor AlN on the substrate. In fact, as illustrated in Figure III.23, the goal is to reduce AlN strain by etching locally the AlN and MoS<sub>2</sub> layers. Then, a thick AlN deposition is achieved on etched layers, which improves adhesion through direct growth on bottom SiO<sub>2</sub> before a thicker second AlN deposition. This approach is called “Epitaxial Lateral Over Growth ” (ELOG) in the literature <sup>209,211</sup>.

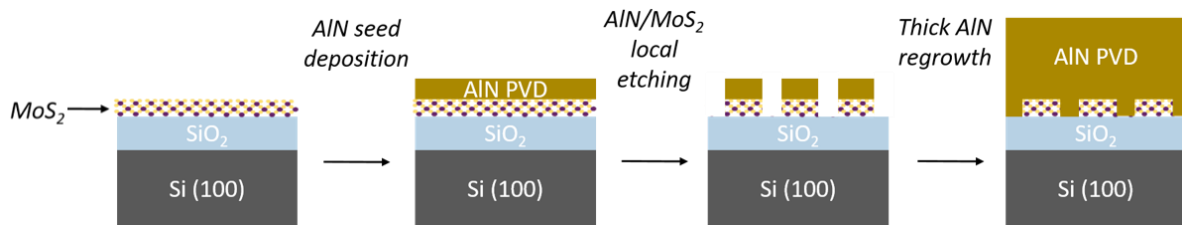


Figure III.23: Illustration of the Epitaxial Lateral Over Growth (ELOG) process on AlN/MoS<sub>2</sub>

We applied this approach on several wafers, but some challenges remain. We give here the conclusions of what we observed: first, we saw that any exposure of the layers to water results in the direct delamination of the stack. It is related to the nature of the hydrophobic MoS<sub>2</sub>/hydrophilic SiO<sub>2</sub> interface which leads to a water-induced lateral delamination (lateral diffusion along 2D-MoS<sub>2</sub>) also known as water-splitting <sup>400–402</sup>. Water exposure of this interface must be avoided. We faced many delamination issues during the wet stripping removal of the polymers formed on structures by plasma etching. We developed a specific stripping process which was efficient to remove polymers but tends to cause stochastic delamination.

The second challenge is related to the texture of the second thick AlN deposition. We must take care of the surface of the first AlN layer (low roughness, prevent oxidation and carbonaceous residues...) to ensure the transfer of the texture to the second thick AlN layer. Once again, the stripping step must be optimized and should ensure the full removal of the resist on the top of the first AlN layer while guaranteeing the transfer of the c-axis textured

growth. Note that the texture transfer also depends on the size and geometry of the openings in the first stack. Thought, we tried and optimized this process route during a year, we never succeeded in depositing a second-thick high quality AlN layer. The results obtained with this ELOG approach are detailed in Annex part 3, section III.4. So, we decided to work on the MoS<sub>2</sub> materials properties, trying to alter VdW bonding between 2D layers.

*III.3.2.2. Thermochemical treatments of the MoS<sub>2</sub>/SiO<sub>2</sub> interface*

A second potential solution to solve the delamination issue consists in transforming the Van der Waals mechanically fragile MoS<sub>2</sub>/SiO<sub>2</sub> interface into a stronger interface with covalent bonds. The conversion of the MoS<sub>2</sub> lamellar structure should anchor the AlN film on the substrate. This approach is schematically sketched in Figure III.24. It is based on a thermochemical modification followed by a thick AlN deposition.

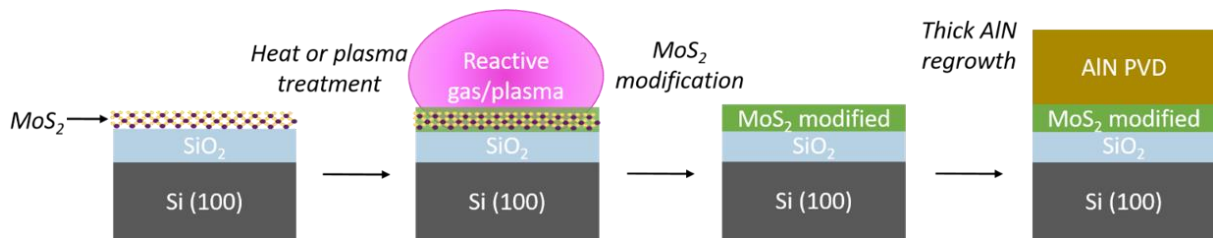


Figure III.24: Illustration of the schematic thermochemical modification of MoS<sub>2</sub>

Obviously, the transformation of the MoS<sub>2</sub> must also ensure that the resulting seed layer still improves the c-axis orientation of the AlN during PVD deposition. Thus, either the transformation induces a modified MoS<sub>2</sub> that shows a close lattice matching with AlN or the transformation should be performed through a thin AlN layer previously deposited. The first case is almost impossible to fill because there are only a few materials with an acceptable lattice matching with AlN. The second case is challenging since the AlN layer must be thick enough to be well textured along the c-axis and thin enough to enable the transformation of the MoS<sub>2</sub> structure and MoS<sub>2</sub>/SiO<sub>2</sub> interface through with AlN as illustrated in Figure III.25.

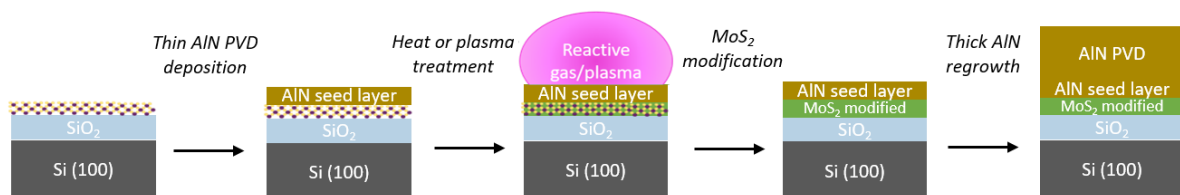


Figure III.25: Illustration of the thermochemical modification of MoS<sub>2</sub> through a thin AlN seed layer

#### III.4. Conclusions of chapter 3

The proof of concept of 2D seed layer based on MoS<sub>2</sub> to texture AlN PVD has been demonstrated on 200 mm silicon wafer (proposed process already being compatible with 300 mm wafer). Highly c-axis textured 100 nm AlN PVD films with an AlN (002) RC value of around 0.5° has been obtained. The AlN (002) RC is drastically lower than the same AlN PVD deposited on other substrates such as Si (100) or SiO<sub>2</sub> (0.5 ° on MoS<sub>2</sub> vs. 3.8°- 4° on Si (100) and SiO<sub>2</sub>). Moreover, the comparison of the AlN crystal quality obtained in this work with the few studies dealing with this subject and presented in Table III.3 seems to indicate that the deposition method and the growth substrate contribute to the AlN crystal quality. In fact, high temperature deposition (CVD method) and growth substrate with a reasonable lattice mismatching with 2D-TMDs (and therefore AlN) promote a high quality AlN growth.

However, beyond an AlN PVD deposition of 200 nm, the lamellar VdW structure of MoS<sub>2</sub> combined with the mechanical bi-axial stress deployment in the AlN bulk leads to a delamination at the MoS<sub>2</sub>/SiO<sub>2</sub> interface. This delamination issue is a major hindrance to the integration of these materials in AlN-based Radio Frequency or power devices (since AlN film thickness up to 1 μm are required). Two mains potential solutions have been identified. The first, based on the local etching of MoS<sub>2</sub>/AlN stack to ensure anchorage of the AlN was unsuccessful. The second rel on the thermochemical modification of the MoS<sub>2</sub>/SiO<sub>2</sub> interface to transform the Van der Waals interaction into strong covalent bonds will be developed in the next chapter.



## IV. Chapter 4: Thermochemical modification of 2D-MoS<sub>2</sub>

As a reminder, the delamination issue is due to two competing phenomena: the MoS<sub>2</sub> lamellar structure (Van der Waals interactions between each monolayer and at the MoS<sub>2</sub>/SiO<sub>2</sub> interface) and the AlN stress/strain. A potential solution identified to solve this delamination is based on the thermochemical modification of the 2D-MoS<sub>2</sub> layer. The idea is to find a way to convert the MoS<sub>2</sub> VdW interactions into strong covalent bonds, potentially through a thin AlN seed serving as a pre-texturing layer. We envisaged oxygen or nitrogen to convert the MoS<sub>2</sub> into another alloy free of VdW interactions. On one hand, the exposure of MoS<sub>2</sub> to oxygen induces the direct oxidation of the Mo metallic element into MoO<sub>x</sub> that volatilizes at approximately 700°C. On the other hand, the exposure to nitrogen forms MoN<sub>x</sub> ceramic alloys. Indeed, the nitridation of 2D-MoS<sub>2</sub> was already studied in the pioneer works of Marchand *et al.*<sup>403–406</sup> and followed by others researchers<sup>407–409</sup> to synthesize molybdenum nitride from MoS<sub>2</sub>. Ammonia-based reactive heat treatments are used to achieve the complete conversion of sulphides bonds. Nitrogen plasma treatments was also proposed in the literature, in particular to tune the MoS<sub>2</sub> bulk electrical properties<sup>410–414</sup>, i.e. by adding localized Mo-N electrically active doping bonds into the MoS<sub>2</sub> hexagonal structure.

This chapter is divided in two sections. In a first step, we address plasma treatments in which different chemistries (H<sub>2</sub>, N<sub>2</sub> and NH<sub>3</sub>) are investigated directly on the 2D-MoS<sub>2</sub> layer. Then, we focus on N<sub>2</sub> plasma treatments in the aim to modify 2D-MoS<sub>2</sub> through a thin AlN PVD seed layer. The physical and chemical impacts of this plasma are detailed. In a second step, we describe thermal heat treatments. A focus on the thermal budget and the corresponding impact on 2D-MoS<sub>2</sub> seed layer is addressed. Then, the feasibility of the MoS<sub>2</sub> chemical modifications under different atmospheres (H<sub>2</sub>, N<sub>2</sub> and NH<sub>3</sub>) is investigated. Finally, NH<sub>3</sub> heat treatments in the aim to modify 2D-MoS<sub>2</sub> through a thin AlN PVD seed layer are detailed. This proposed approaches which appears challenging due to stack complexity is reminded in Figure IV.1.

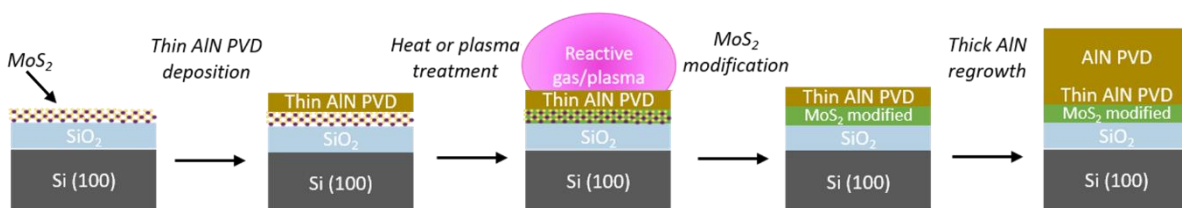


Figure IV.1: Illustration of the thermochemical modification of MoS<sub>2</sub> through a thin AlN layer



#### IV.1. Plasma treatments

The aim of studying a plasma solution is twice. On one hand, a plasma brings a physical component to species due to collisions that could penetrate deeply into matter. This implantation effect could promote a potential MoS<sub>2</sub> chemical modification. However, this component must be finely controlled, especially on MoS<sub>2</sub> since its lamellar structure and subsequent crystalline state are expected to be quite sensitive to such implantation effect which could lead to cracks and/or increase in roughness. On the other hand, plasma forms radicals that are very reactive and can modify the bonding environments into the layers. We could expect that these species transform the MoS<sub>2</sub> VdW interactions into strong covalent bonds or diffuse through a thin AlN seed layer.

First, this section describes the equipment and the investigated plasma conditions. Second, we address the physical and chemical impact of the different plasma chemistries (H<sub>2</sub>, N<sub>2</sub> and NH<sub>3</sub>) on 2D-MoS<sub>2</sub>. Subsequently, we focus on N<sub>2</sub> plasma treatments through a thin AlN seed layer. We also describe the physical and chemical of these treatments on AlN/MoS<sub>2</sub> stack. Finally, in order to conclude on the efficiency of this plasma approach to solve the delamination issue, we discuss the quality of a thick AlN growth deposited on the N<sub>2</sub> plasma treated samples.

##### IV.1.1. Description of ALTACVD equipment and plasma conditions

Plasma treatments were made in an AltaCVD 300 mm tool from Altatech Semiconductor. A picture of this equipment is given in Figure IV.2. It is an industrial equipment enabling (PE)CVD and (PE)ALD deposition. The deposition reactor includes a capacitive plasma technology, based on a RF polarized shower-head. The plasma is generated in an aluminum chamber under vacuum from the capacitive discharge on a 300 mm Si substrate. In order to limit plasma induced-defects, the substrate holder is grounded which limits the energy of the ions.

As this equipment is a 300 mm tool, 2 cm x 2 cm samples were clived and placed on a 300 mm silicon holder for the plasma heat treatment. Preliminary experiments have been implemented to optimize different plasma conditions and check its stability. From these experiments, the plasma conditions have been fixed and are listed in Table IV.1. We can note that the temperature cannot exceed 450 °C due to the aluminum chamber.

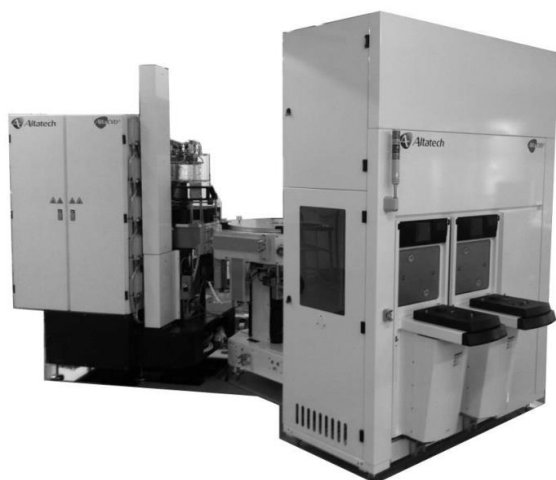


Figure IV.2: AltaCVD 300 mm equipment used for plasma treatments

Gas	NH <sub>3</sub>	H <sub>2</sub>	N <sub>2</sub>
Temperature (°C)	450	450	450
Power (W)	500	500	500
Pressure (mbar)	1.33	1.33	1.33
Gas flow (sccm)	300	300	300
Argon flow (sccm)	1100	1100	1100
Time (min)	20	20	20

Table IV.1: Plasma treatment conditions investigated

For plasma treatments through the thin AlN PVD seed layer, the thickness of the seed is expressed in seconds corresponding to the deposition time and not in nm for practical reasons. The correspondences between the deposition time and the thickness have been measured by XRR and are given in Annex, section 0. The idea was to fix the plasma conditions and vary the AlN seed thickness to determine a screening thickness. Thus, AlN PVD with a thickness set between 1s and 8s were deposited on 2D-MoS<sub>2</sub> and compared with a 2D-MoS<sub>2</sub> Reference sample (without the thin AlN PVD seed layer). The sample without AlN PVD layer is named *MoS<sub>2</sub> Reference* and the samples with AlN PVD layer are named *MoS<sub>2</sub> + AlN xs* (*x* being the AlN PVD deposition time). When it is necessary, the term *BP* or *AP* is added to refer to *Before Plasma* or *After Plasma*, respectively.

#### IV.1.2. Plasma treatments (NH<sub>3</sub>, H<sub>2</sub> and N<sub>2</sub>) on *MoS<sub>2</sub> Reference* sample

The first plasma treatments were made directly on the *MoS<sub>2</sub> Reference* samples in order to choose the most suitable plasma chemistry to perform the chemical modification and transform Van der Waals interaction into strong covalent bonds. After each plasma treatment, *MoS<sub>2</sub> Reference* samples were analysed by Raman spectroscopy to check the presence/absence of the MoS<sub>2</sub>. The Raman spectra are shown in Figure IV.3. In the investigated conditions, E<sub>12g</sub><sup>1</sup> and A<sub>1g</sub> MoS<sub>2</sub> Raman are detected after the NH<sub>3</sub> plasma treatment. Their FWHM is 8.2 ± 0.4 cm<sup>-1</sup> and 7.6 ± 0.3 cm<sup>-1</sup>, respectively which are higher than *MoS<sub>2</sub> Reference* sample before any treatment (4.7 ± 0.2 cm<sup>-1</sup> and 5.6 ± 0.1 cm<sup>-1</sup> as described in the previous chapter) suggesting a slight degradation of the 2D-MoS<sub>2</sub>. For both N<sub>2</sub> and H<sub>2</sub> plasma treatments, MoS<sub>2</sub> Raman modes completely vanished, only a single peak localized at 520 cm<sup>-1</sup> and attributed to Si substrate is visible.

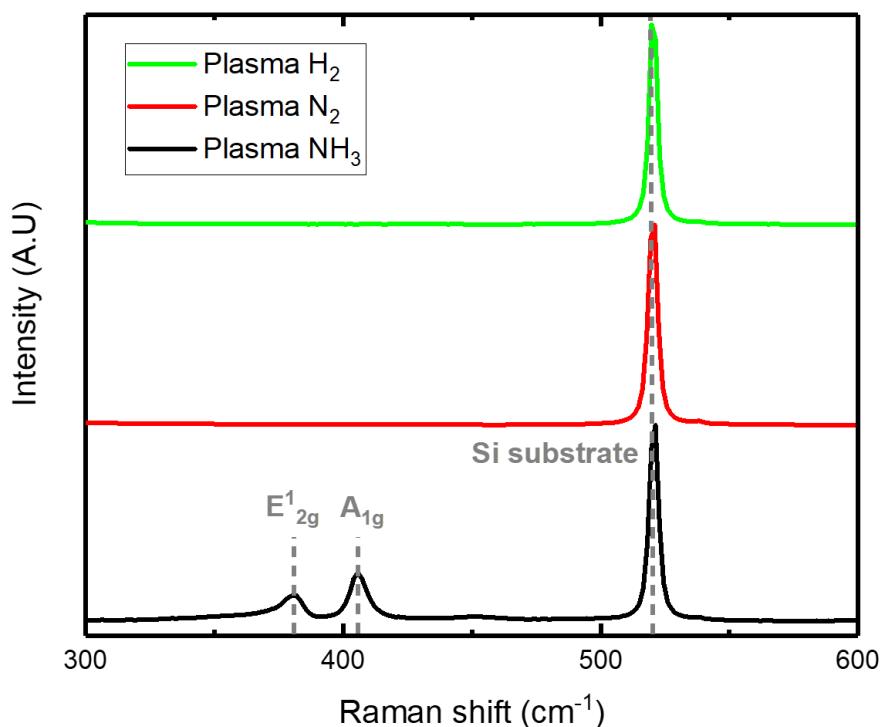


Figure IV.3: Raman spectra of MoS<sub>2</sub> Reference sample after NH<sub>3</sub>, N<sub>2</sub> and H<sub>2</sub> plasma treatment

Hence, these Raman characterizations enable to highlight the suitable plasma chemistry leading to a potential MoS<sub>2</sub> modification. On one hand, NH<sub>3</sub> plasma treatment applied directly on MoS<sub>2</sub> does not modify its lamellar structure. It could be explained by an under-dosing of NH<sub>3</sub> during the plasma treatment. On the other hand, H<sub>2</sub> and N<sub>2</sub> plasma treatments lead to a disappearance of the E<sub>2g</sub><sup>1</sup> and A<sub>1g</sub> MoS<sub>2</sub> Raman modes suggesting a potential chemical modification. From these results, we decided to mainly pursue N<sub>2</sub> treatments. Some H<sub>2</sub> plasma trials have also been investigated but are not detailed in this manuscript. The N<sub>2</sub> plasma allows to consider the formation of Mo-N bonds while H<sub>2</sub> plasma could lead to a potential formation of H<sub>2</sub>S (g). In both case, Mo-S bonds are broken and could result in a non-lamellar structure. These suggested phenomena are complementary and could be found in a NH<sub>3</sub> plasma treatment. However, in the investigated conditions, the use of a NH<sub>3</sub> plasma treatment does not affect the MoS<sub>2</sub> structure.

Another point to address is the presence of argon (Ar) in the plasma. The terms “N<sub>2</sub> plasma” and “H<sub>2</sub> plasma” are misused and should be replaced by “Ar + N<sub>2</sub> plasma” and “Ar + H<sub>2</sub> plasma”. The use of argon has an abrasive effect which could degrade the MoS<sub>2</sub> lamellar. This remark suggests two competing phenomena: a chemical impact coming from the use of N<sub>2</sub> or H<sub>2</sub> and a physical impact coming from the Ar. These aspects are discussed hereafter.

IV.1.2.1. Physical impact of N<sub>2</sub> plasma on MoS<sub>2</sub> Reference sample

The physical impact of N<sub>2</sub> plasma applied directly on 2D-MoS<sub>2</sub> has been assessed by Atomic Force Microscopy (AFM). The AFM images of *MoS<sub>2</sub> Reference BP (Before Plasma)* and *AP (After Plasma)* are presented in Figure IV.4 a) and b), respectively. A post processing treatment was performed to annihilate the contributions of the particles on the RMS and peak to valley (P.V) values.

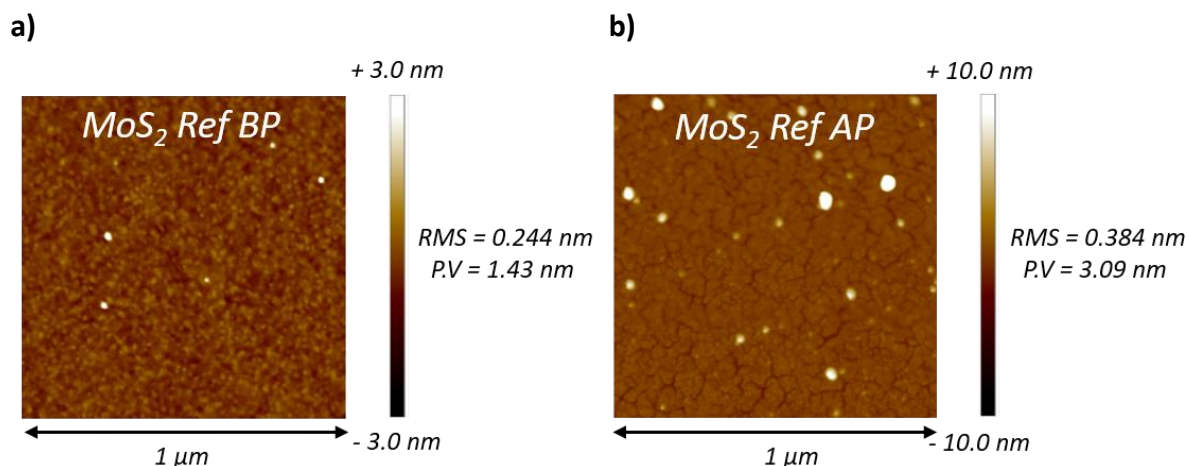


Figure IV.4: AFM images of *MoS<sub>2</sub> Reference BP (Before Plasma)* and *AP (After Plasma)*

As mentioned in the previous chapter and illustrated in Figure IV.4 a), the *MoS<sub>2</sub> Reference BP* sample displays RMS and P.V values of 0.244 nm and 1.43 nm, respectively, which highlights the smoother texture of the MoS<sub>2</sub> surface. The 2D-MoS<sub>2</sub> film seems also dense and homogeneous. The AFM image of the *MoS<sub>2</sub> Ref AP* presented in Figure IV.4 b) shows totally different results. The most prominent observation is the highly degradation of the *MoS<sub>2</sub> Reference AP* surface. We clearly observe cracks at the surface after the N<sub>2</sub> plasma highlighting a significant physical impact of the treatment. Despite a larger amount of particles, the RMS and P.V values increase up to 0.384 nm and 3.09 nm, respectively. These values also demonstrate the surface roughness of the N<sub>2</sub> plasma treatment.

To conclude, the N<sub>2</sub> plasma treatment applied directly on 2D-MoS<sub>2</sub> highly degrades its surface. The formation of cracks probably resulting to an abrasive effect coming from Ar is observed. Therefore, the physical impact of the N<sub>2</sub> plasma is not negligible and should result in a poor crystal quality of AlN growth as it will be demonstrated in section IV.1.4. The few trials of H<sub>2</sub> plasma treatment have not been characterized by AFM. However, as mentioned in Table IV.1, both H<sub>2</sub> and N<sub>2</sub> plasma treatments have been carried out with the same experimental

conditions. Hence, it seems reasonable to think that similar results are obtained since the abrasive effect coming from Ar should remain present.

#### IV.1.2.2. Chemical impact of N<sub>2</sub> plasma on MoS<sub>2</sub> Reference sample

The chemical impact of N<sub>2</sub> plasma treatment applied directly on 2D-MoS<sub>2</sub> has been assessed by X-Ray Photoelectron Spectroscopy (XPS). Figure IV.5 shows Mo 3d core-level (CL) spectra for MoS<sub>2</sub> Reference BP (Before Plasma) and AP (After Plasma).

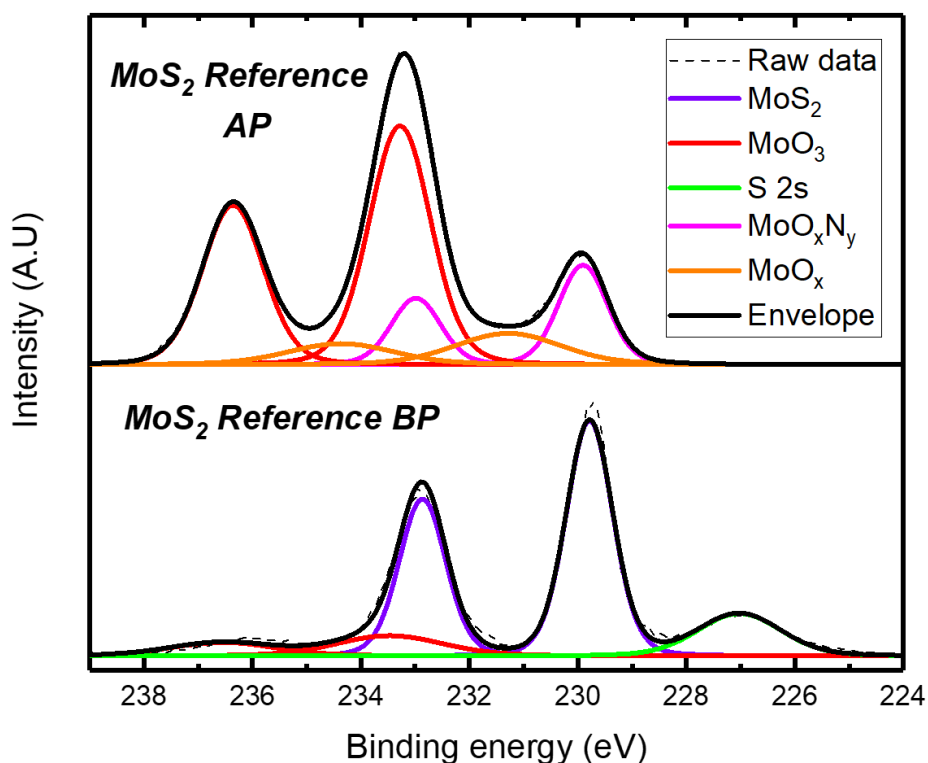


Figure IV.5: Mo 3d XPS spectra of MoS<sub>2</sub> Reference BP (Before Plasma) and AP (After plasma)

The typical high-resolution XPS Mo 3d of MoS<sub>2</sub> Reference BP sample has previously been described in the previous chapter, section III.1.3.2. It displays a main MoS<sub>2</sub> environment (purple), a S 2s contribution (green) and a slight amount MoO<sub>3</sub> (red) attributed to a MoS<sub>2</sub> surface oxidation. The high-resolution XPS Mo 3d of MoS<sub>2</sub> Ref AP sample shows different results. First, and despite the significant degradation of the MoS<sub>2</sub> top surface observed in AFM and presented in the previous section, we observe an important signal on Mo 3d spectra. It indicates the initial MoS<sub>2</sub> layer has not been fully abraded. Second, the main part of the spectra is composed of two peaks at 233.3 eV and 236.4 eV attributed to Mo<sup>6+</sup> state corresponding to MoO<sub>3</sub>. This important amount of oxide is resulting from an air intake during the air break. Third, we can note that S 2s contribution vanished after N<sub>2</sub> plasma. These results confirmed the chemical impact of the plasma since Mo-S bonds are broken.

Hence, the two peaks centered at 229.9 eV and 233.0 eV which could correspond to MoS<sub>2</sub> have been attributed to MoO<sub>x</sub>N<sub>y</sub>. Finally, a last environment located at intermediate binding energies (231.3 eV and 234.4 eV) is attributed to MoO<sub>x</sub>. We can note also that the amount of Mo decrease after the N<sub>2</sub> plasma treatment: 11.2 % *AP* vs. 16.2 % *BP* confirming the abrasive effect of Ar. The overall atomic concentrations, binding energies and attributions are presented in Annex part 3, section III.2.2.

These XPS characterizations confirm the chemical impact of N<sub>2</sub> plasma by breaking Mo-S bonds. New Mo-N bonds seem to be formed during the treatment. However, the sample air break lead to a significant surface oxidation resulting in the formation of MoO<sub>x</sub>/MoO<sub>3</sub>. This oxidation is surely promoted by the surface degradation clearly visible on the AFM images displaying cracks presented in section IV.1.2.1. The H<sub>2</sub> plasma treated samples, which have not been characterized, should lead to similar results with a different reaction mechanism: H<sub>2</sub>S (g) formation. Hence, even if N<sub>2</sub> and H<sub>2</sub> plasma treatments are complementary, their direct application on 2D-MoS<sub>2</sub> seem efficient to break Mo-S bonds but to the detriment of the resulting surface quality.

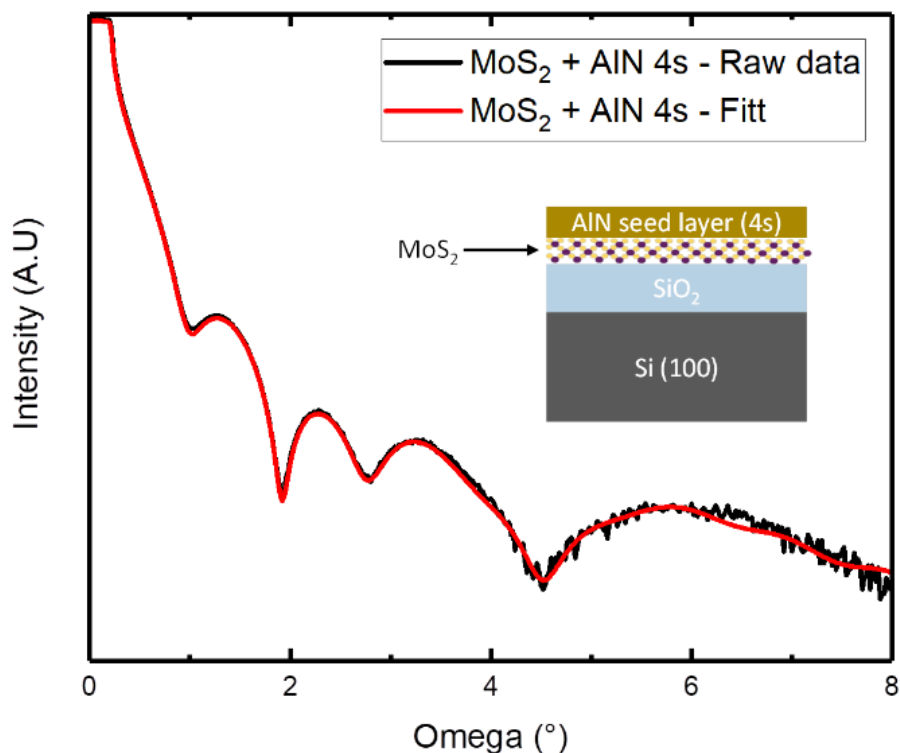
### IV.1.3. Plasma treatments (N<sub>2</sub>) with AlN PVD seed layer

As the direct application of a N<sub>2</sub> plasma treatment on 2D-MoS<sub>2</sub> results in a significant surface degradation prohibiting an AlN growth of quality, the next step is to add a thin AlN PVD seed layer on the MoS<sub>2</sub> *Reference BP* samples. Here, the idea is to modify the MoS<sub>2</sub> layer through a nanometre thin AlN PVD seed, used to ensure AlN crystalline regrowth. As mentioned previously, the thickness of the thin AlN PVD seed is expressed in seconds corresponding to the deposition time and not in nm. Each MoS<sub>2</sub> + AlN *xs BP* and *AP* are compared to a MoS<sub>2</sub> *Reference BP* and *AP*. The characterizations of the MoS<sub>2</sub> + AlN *4s BP* and *AP* samples are described to illustrate the tendencies observed for each sample.

#### IV.1.3.1. Physical impact (XRR and AFM)

##### IV.1.3.1.1. Determination of the AlN seed thickness and illustration of plasma abrasive effect

MoS<sub>2</sub> + AlN *4s BP* XRR pattern is illustrated in Figure IV.6. Two new layers were added on the basis of the MoS<sub>2</sub> model to include AlN seed contribution on the signal: bulk AlN and oxidized AlN. The extracted densities, roughness and thicknesses values after adjustments are given in Table IV.2 and compared with those extracted from the MoS<sub>2</sub> *Reference BP* sample.

Figure IV.6: XRR pattern of MoS<sub>2</sub> + AlN 4s BP

Formula	MoS <sub>2</sub> Reference BP			MoS <sub>2</sub> + AlN 4s BP		
	Density (g.cm <sup>-3</sup> )	Thickness (nm)	Roughness (nm)	Density (g.cm <sup>-3</sup> )	Thickness (nm)	Roughness (nm)
<b>Oxidized AlN</b>	/	/	/	2.71	0.18	0.27
<b>AlN</b>	/	/	/	3.23	1.81	0.19
<b>MoS<sub>2</sub> monolayer</b>	7.21	0.61	0.38	8.27	0.39	0.52
<b>VdW plan</b>	0.09	0.19	0.19	0.09	0.30	0.29
<b>MoS<sub>2</sub> monolayer</b>	6.00	0.31	0.17	6.82	0.30	0.22
<b>VdW plan</b>	0.09	0.12	0.14	0.08	0.12	0.13
<b>MoS<sub>2</sub> monolayer</b>	6.99	0.56	0.35	8.70	0.56	0.29
<b>VdW plan</b>	0.09	0.27	0.24	0.08	0.32	0.84
<b>SiO<sub>2</sub></b>	2.29	/	0.08	2.36	/	0.07

Table IV.2: Extracted values from the MoS<sub>2</sub> + AlN 4s fitting and comparison with MoS<sub>2</sub> Reference sample

Once again, given the atomic thickness of MoS<sub>2</sub> film, densities values are difficult to interpret and roughness can be assimilated to MoS<sub>2</sub> monolayer or Van der Waals plane thickness. However, interesting results can be observed. First, after the 4s AlN PVD seed layer deposition, the MoS<sub>2</sub> total thickness is almost identical to that determined before deposition: 1.99 nm after deposition vs. 2.06 nm before. To remind, these values are close to the theoretical one expected for three MoS<sub>2</sub> monolayers (1.85 nm).

Second, the MoS<sub>2</sub> XRR pattern display significative variations MoS<sub>2</sub> monolayer (distance between bottom and top sulphur atoms within a monolayer) and VdW plane thicknesses (distance of two sulphur atoms between two distinct monolayers). These variations have been discussed in chapter 3, section III.1.3.1.2 and could be attributed to oscillations within the MoS<sub>2</sub> monolayer. After the AlN seed deposition, these oscillations seem attenuated from the second MoS<sub>2</sub> monolayer. It could suggest that the tensile stress coming from the AlN seed deposition is also applied on the 2D-MoS<sub>2</sub> and results in a MoS<sub>2</sub> monolayers tensioning.

Finally, the roughness values are in range of the extracted thicknesses. Concerning the AlN contribution, the extracted thickness is adjusted at 1.99 nm (1.81 + 0.18) which is the expected value for a 4s deposition time on standard Si in the conditions described in section III.2.3. Moreover, the density is 3.23 g.cm<sup>-3</sup> in line with the theoretical value (3.26 g.cm<sup>-3</sup>). Finally, the XRR roughness is around 0.3 nm which is in the range of the roughness (although, it cannot be directly compared) determined via Atomic Force Microscopy (AFM) in the following part.

Each *MoS<sub>2</sub> + AlN* sample was characterized by XRR before and after N<sub>2</sub> plasma treatment and fitted with model presented in Table III.1. AlN thicknesses and roughness of the top layers (AlN and oxidized AlN) are extracted and plotted in Figure IV.7 a) and b), respectively. In Figure IV.7 a) the AlN deposition rate is determined at 0.60 nm.s<sup>-1</sup> by linear regression (black square points before N<sub>2</sub> plasma). It is worth to notice that this deposition rate has been refined at 0.57 nm.s<sup>-1</sup> by adding other points as demonstrated in Annex part 3, section III.1.2. Interestingly, the AlN thicknesses after N<sub>2</sub> plasma treatment is lower than before N<sub>2</sub> plasma treatment and virtually lower the expected deposition rate at 0.51 nm.s<sup>-1</sup>. It suggests that N<sub>2</sub> plasma is either abrasive or it induces a densification of the AlN seed. An abrasion phenomenon is rather expected as exhibited in Figure IV.7 b) (and as demonstrated in the previous section IV.1.2), where we clearly observe an increase in the AlN roughness after N<sub>2</sub> plasma treatment, suggesting clustering and removal of Al atoms.



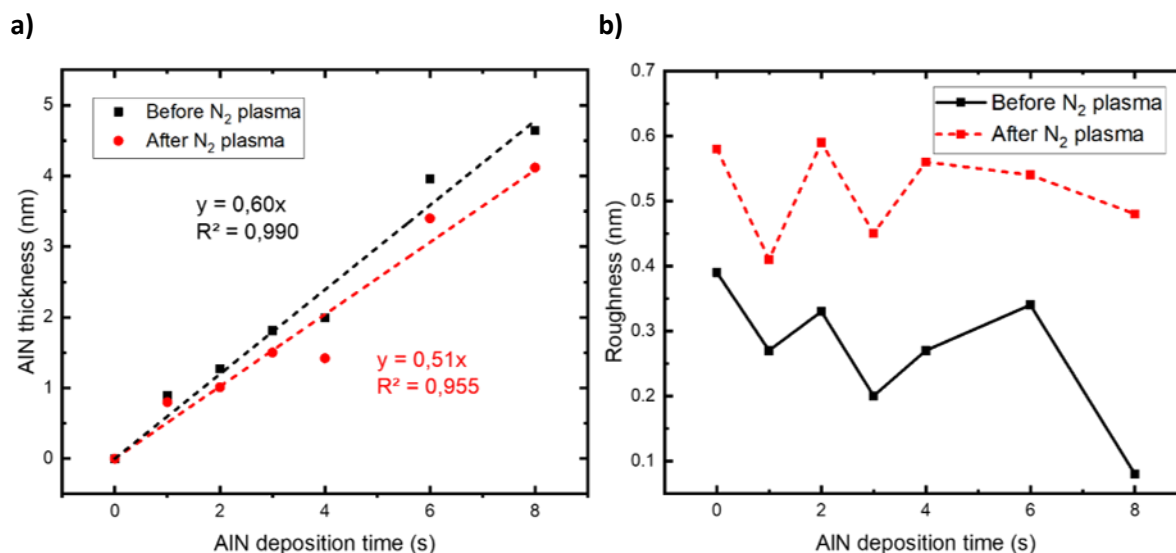


Figure IV.7: a) AIN thickness before and after N<sub>2</sub> plasma ; b) AIN roughness before and after N<sub>2</sub> plasma

Therefore, beyond the expected chemical impact of N-radicals on the bottom MoS<sub>2</sub> by plasma treatment (see section IV.1.3.2.2 below), the N<sub>2</sub> plasma has a direct physical impact on the AIN seed layer. Hence, the plasma may affect the crystalline quality of the AIN PVD regrowth, either in term of surface re-oxidation during air exposure (a defective surface is prompt to re-oxidized during process air break), or seed layer crystal quality since the seed may be locally amorphized.

#### IV.1.3.1.2. Surface morphology (AFM)

To complete the conclusions brought by the X-Ray Reflectometry study, Atomic Force Microscopy (AFM) were performed before and after N<sub>2</sub> plasma treatment. AFM images of *MoS<sub>2</sub> + AIN 4s BP* and *MoS<sub>2</sub> + AIN 4s AP* are visible in Figure IV.8 a) and b), respectively.

Comparing the MoS<sub>2</sub> AFM image presented in Figure IV.4 and as illustrated in Figure IV.8 a), the smooth surface of *MoS<sub>2</sub> Reference BP* promotes the deposition of a smooth AIN PVD seed layer observed on *MoS<sub>2</sub> + AIN 4s BP* sample. The as-deposited AIN film appears homogenous and dense with a RMS = 0.204 nm and P.V = 1.77 nm which are close to those of as-deposited MoS<sub>2</sub> (RMS = 0.244 nm and P.V = 1.43 nm).

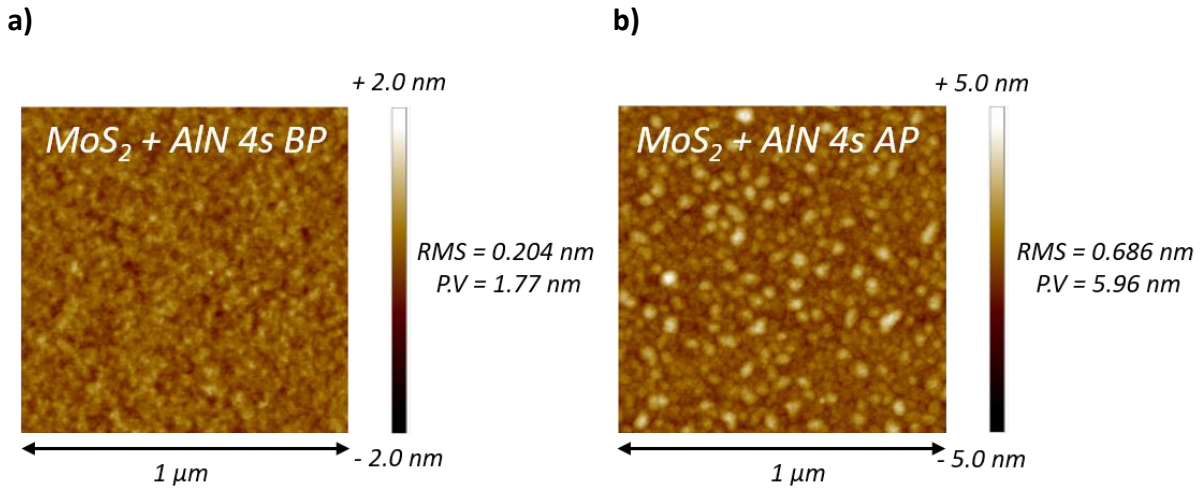


Figure IV.8: AFM images of MoS<sub>2</sub> + AlN 4s BP (Before Plasma) and AP (After Plasma)

After N<sub>2</sub> plasma treatment (Figure IV.8 b)), significant changes in AlN surface morphology and roughness are observed. In fact, MoS<sub>2</sub> + AlN 4s AP top surface is degraded and displays grains of different sizes. It leads to an increase in RMS and P.V values which is consistent with the X-Ray Reflectometry (XRR) measurements. This increase is in line with the AFM results obtained on the MoS<sub>2</sub> Reference AP sample and presented in section IV.1.2.1.

#### IV.1.3.1.3. Comparison of XRR and AFM measurements

To conclude this section on the physical impact of the N<sub>2</sub> plasma on MoS<sub>2</sub> + AlN *xs* samples, we compared the XRR and AFM measurements previously discussed.

Figure IV.9 compares the roughness before (solid lines) and after (short dash lines) N<sub>2</sub> plasma treatment measured by AFM (red circles) with roughness determined by XRR (black squares). Before N<sub>2</sub> plasma treatment, the top surface is extremely smooth with a RMS < 0.3 nm independently to the AlN seed thickness. The values are in good agreement with the roughness determined by XRR (< 0.4 nm on each sample). Similarly to XRR measurements, the roughness measured by AFM is significantly increased after N<sub>2</sub> plasma treatment, confirming the strong impact of the plasma on the AlN top surface.

Moreover, and similarly to the AFM image of the MoS<sub>2</sub> Reference AP sample presented in Figure IV.4, cracks due to the physical impact of N<sub>2</sub> plasma are observed on MoS<sub>2</sub> + AlN 1s AP and MoS<sub>2</sub> + AlN 2s AP samples (presented is the inset of Figure IV.9).

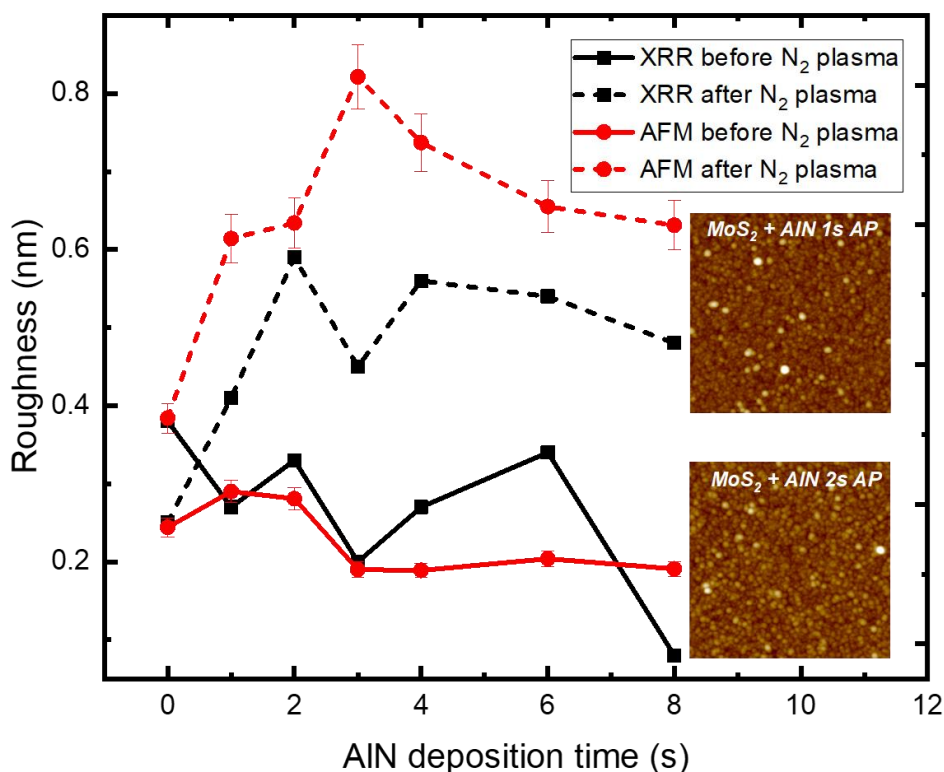


Figure IV.9: Comparison of the AlN roughness determined by XRR and AFM before and after N<sub>2</sub> plasma. The inset presents the AFM images of MoS<sub>2</sub> + AlN 1s AP and MoS<sub>2</sub> + AlN 2s AP

Therefore, AFM measurements confirmed the tendencies observed in XRR: N<sub>2</sub> plasma treatment leads to surface roughening. Beyond the increase in roughness, cracks are also observed on MoS<sub>2</sub> Reference AP, MoS<sub>2</sub> + AlN 1s AP and MoS<sub>2</sub> + AlN 2s AP which will affect the quality of the thick AlN PVD regrowth. Hence, the plasma physical impact cannot be negligible on the surface quality.

#### IV.1.3.2. Chemical impact

##### IV.1.3.2.1. MoS<sub>2</sub> bond vibrations and crystalline quality (Raman)

Raman spectroscopy was performed to check the modifications in bonds vibration of the MoS<sub>2</sub> below AlN seed. Raman spectra of each sample before and after N<sub>2</sub> plasma treatment are presented in Figure IV.10. Positions and FWHM are listed in Table IV.3.

As expected, E<sub>2g</sub><sup>1</sup> and A<sub>1g</sub> MoS<sub>2</sub> Raman modes are clearly visible before N<sub>2</sub> plasma treatment. In the left graph in Figure IV.10, the increase in AlN thickness leads to a redshift of Raman modes which seems to stabilize from MoS<sub>2</sub> + AlN 4s. It can be attributed to strain in 2D-MoS<sub>2</sub> induced by the AlN layer<sup>415</sup> but we can also consider that this shift could be due to the introduction of a doping element into the 2D-MoS<sub>2</sub> seed layer<sup>416–419</sup>. In fact, an Al-doped MoS<sub>2</sub> induces a slight redshift which can be attributed to a p-type doping.

We also observe a slight increase in FWHM values for MoS<sub>2</sub> Raman modes on MoS<sub>2</sub> + AlN samples compared to MoS<sub>2</sub> Reference suggesting a slight degradation of the 2D-MoS<sub>2</sub> layer during the very beginning (first monolayers) of the AlN deposition. This increase in FWHM is quickly stabilized with the increase in AlN thickness since the deposition is performed on AlN and not on MoS<sub>2</sub> anymore.

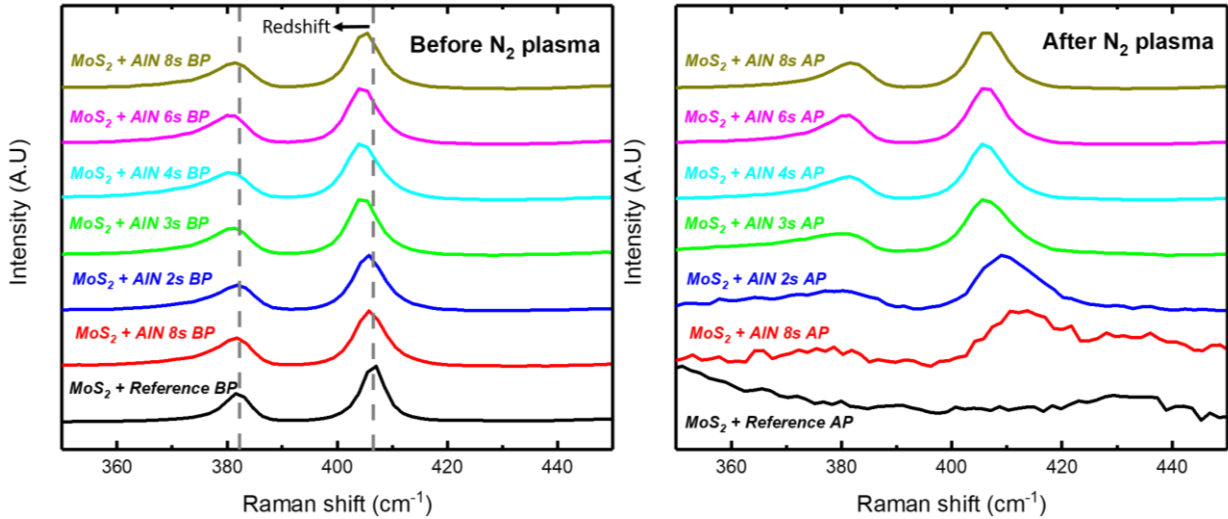


Figure IV.10: Raman spectra of MoS<sub>2</sub> + AlN vs BP (Before Plasma) and AP (After Plasma)

		Before N <sub>2</sub> plasma (BP)							After N <sub>2</sub> plasma (AP)						
		0s	1s	2s	3s	4s	6s	8s	0s	1s	2s	3s	4s	6s	8s
E <sub>2g</sub> <sup>1</sup>	Position (cm <sup>-1</sup> )	381.8 ± 0.1	381.2 ± 0.1	381.2 ± 0.1	380.7 ± 0.3	380.1 ± 0.3	380.3 ± 0.1	380.8 ± 0.1	/	/	/	379.3 ± 0.2	380.5 ± 0.1	380.4 ± 0.1	381.3 ± 0.1
	FWHM (cm <sup>-1</sup> )	5.5 ± 0.1	7.6 ± 0.2	8.6 ± 0.3	8.1 ± 0.4	8.5 ± 0.5	7.8 ± 0.4	8.1 ± 0.4	/	/	/	10.6 ± 0.5	9.7 ± 0.4	8.2 ± 0.3	8.4 ± 0.2
A <sub>1g</sub>	Position (cm <sup>-1</sup> )	406.5 ± 0.1	406.0 ± 0.1	405.7 ± 0.1	404.9 ± 0.2	404.9 ± 0.3	404.7 ± 0.1	405.1 ± 0.1	/	/	409.8 ± 0.2	406.6 ± 0.5	406.2 ± 0.1	406.3 ± 0.1	406.4 ± 0.1
	FWHM (cm <sup>-1</sup> )	5.1 ± 0.1	7.2 ± 0.1	7.1 ± 0.1	6.8 ± 0.1	7.5 ± 0.2	7.1 ± 0.3	6.8 ± 0.2	/	/	12.6 ± 0.2	10.0 ± 0.3	8.2 ± 0.2	7.8 ± 0.2	7.6 ± 0.1

Table IV.3: Positions and FWHM of MoS<sub>2</sub> + AlN vs BP (before Plasma) and AP (After Plasma)

After N<sub>2</sub> plasma treatment, the MoS<sub>2</sub> Raman signal has completely vanished for MoS<sub>2</sub> Reference and is highly degraded for MoS<sub>2</sub> + AlN 1s and MoS<sub>2</sub> + AlN 2s. These observations are consistent with the AFM images since the surface of these samples shows cracks due to the plasma physical impact. These cracks induce preferential paths enabling the modification of the 2D-MoS<sub>2</sub>. From MoS<sub>2</sub> + AlN 3s, the MoS<sub>2</sub> signal is clearly visible. Slight differences are observed compared with the signals before N<sub>2</sub> plasma treatment, some small increases in FWHM Raman modes are noticeable in Table IV.3 suggesting a slight degradation of the MoS<sub>2</sub> crystal quality as well as a blueshift especially on A<sub>1g</sub> mode. This blueshift is hard to explain

but could be due to the formation of sulphur vacancies<sup>372</sup>. A stress relaxation of the AlN and MoS<sub>2</sub> induced by potential micro-cracks can also be an explanation.

This blueshift on the A<sub>1g</sub> mode lead to an increase in the separation distance between E<sup>1</sup><sub>2g</sub> and A<sub>1g</sub> MoS<sub>2</sub> Raman modes ( $\Delta\omega$ ). This distance related to the number of MoS<sub>2</sub> monolayers is plotted in Figure IV.11 for the samples before and after N<sub>2</sub> plasma. On one hand, before N<sub>2</sub> plasma, we observe an almost constant  $\Delta\omega$  value with the increase in AlN thickness seed layer. As demonstrated with the XRR pattern of the *MoS<sub>2</sub> + AlN 4s BP* sample and the fitting presented in section IV.1.3.1.1, it confirms that the three monolayers are preserved after the AlN seed deposition. It suggests that AlN an excellent diffusion barrier against N\* radicals, since no significant changes in bond vibrations is observed.

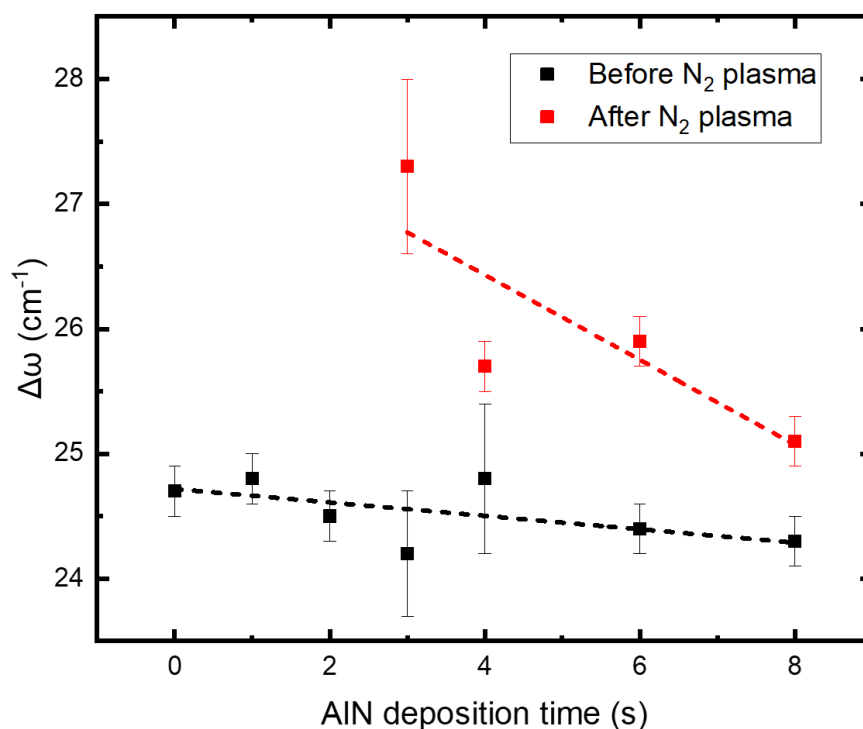


Figure IV.11: Variation in  $\Delta\omega$  as a function of AlN seed deposition time BP (Before Plasma) and AP (After Plasma)

On the other hand, after N<sub>2</sub> plasma, we observe a significant increase in  $\Delta\omega$  compared to the values reported before the treatment. Theoretically, this increase is related to an increase in MoS<sub>2</sub> monolayers. However, this explanation does not make any sense with the aim of the N<sub>2</sub> plasma treatment. Hence, this observation is only due to significant modifications in bond vibrations of the MoS<sub>2</sub> probably resulting from AlN seed degradation due to the physical impact of the plasma. Moreover, we observe that the thicker the AlN seed layer, the more the  $\Delta\omega$  distance tends to those reported before N<sub>2</sub> plasma. It shows that from an AlN seed layer of 8s, the AlN acts like an efficient capping layer which preserved the MoS<sub>2</sub> crystal integrity.

To conclude, in the N<sub>2</sub> plasma conditions investigated, these Raman results show that an AlN layer of 3s is sufficient to screen the MoS<sub>2</sub> against modifications. Thus, the delamination should persist above 3s of AlN seed deposition since MoS<sub>2</sub> lamellar structure is preserved. In the meantime, as illustrated by the AFM study, top surface of AlN below 3s deposition time shows defects, and even cracks after N<sub>2</sub> plasma. So, even if the delamination could be solved below 3s, we do not expect to obtain an improvement in the crystalline quality of the regrown AlN on the seed.

#### IV.1.3.2.2. Surface chemical analysis (XPS)

In order to understand the chemical changes which occurs in MoS<sub>2</sub> after N<sub>2</sub> plasma treatment, X-Ray Photoelectron Spectroscopy (XPS) analysis was performed. Figure IV.12 shows Mo 3d core-level (CL) spectra for MoS<sub>2</sub> + AlN 4s BP (Before Plasma) and AP (After Plasma) and is compared to MoS<sub>2</sub> Ref sample. The overall atomic concentration, binding energy position and their attribution are presented in Annex part 3, section III.2.2.

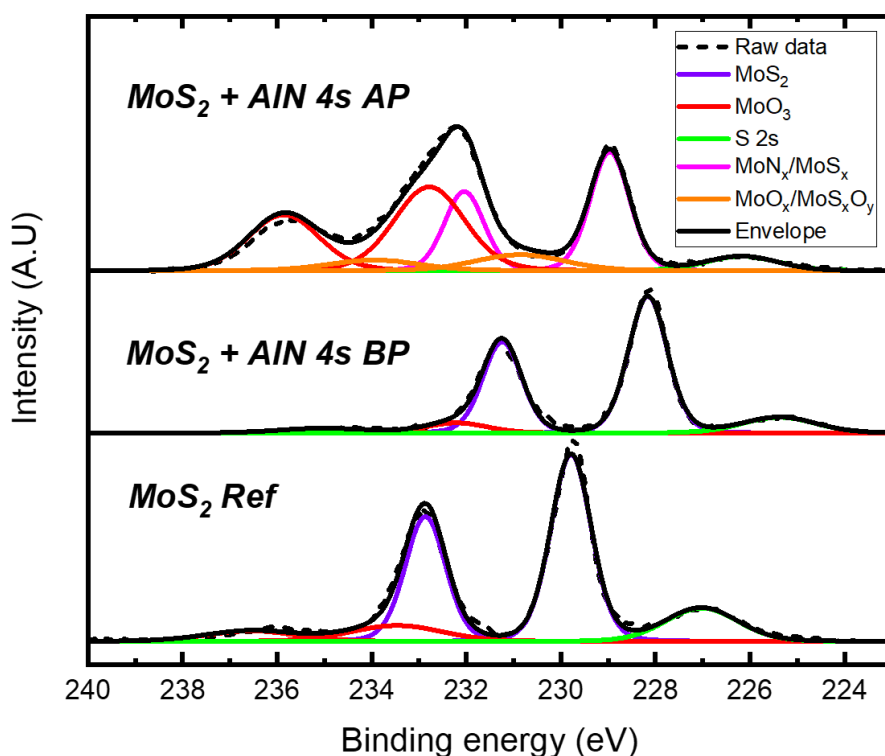


Figure IV.12: Mo 3d XPS spectra of MoS<sub>2</sub> Reference, MoS<sub>2</sub> + AlN 4s BP (Before Plasma) and AP (After Plasma)

First, identical chemical environments are observed for MoS<sub>2</sub> Ref and MoS<sub>2</sub> + AlN 4s BP samples. A main MoS<sub>2</sub> environment fitted by a spin-orbit doublet, a second MoO<sub>3</sub> environment attributed to a small amount of molybdenum oxides and S 2s due to its overlapping with Mo 3d spectra. However, after the AlN seed layer deposition, a down-shifting

in binding energies is clearly visible. It is commonly observed on all MoS<sub>2</sub> with the AlN seed layer, whatever the AlN seed thickness, and is visible on Mo 3*d*, S 2*p*, Si 2*p* and O 2*s* spectra (see Annex part 3, section III.2.2) It seems to indicate an interaction between the 2D-MoS<sub>2</sub> and AlN PVD seed layers. Several phenomena can explain this observation such as MoS<sub>2</sub> doping, AlN screening effect or calibration. We can refer to Annex part 3, section III.2.2 for more details about this down-shifting.

After plasma treatment, the Mo 3*d* spectra deconvolution is more complex. We observe an important increase in molybdenum oxide with peaks located at 230.9 eV and 233.9 eV attributed to MoS<sub>x</sub>O<sub>y</sub> and 232.8 eV and 235.9 eV corresponding to Mo<sup>6+</sup>, MoO<sub>x</sub>/MoO<sub>3</sub>. The S 2*s* contribution still present at 226.2 eV. The other part of the spectrum is composed of doublet peaks at 229.0 eV and 232.0 eV. Their attribution is difficult since it is lower than MoS<sub>2</sub> contributions for *MoS<sub>2</sub> Reference* sample but higher to the main part of the Mo 3*d* spectra before N<sub>2</sub> plasma treatment. It could potentially be attributed to a partial nitridation of the 2D-MoS<sub>2</sub> seed layer. However, this assumption seems not really coherent with Raman results where MoS<sub>2</sub> signal is well preserved. Moreover, the increase in N concentration is difficult to highlight due to different effects: plasma abrasive effect, N signal mainly comes from AlN layer, sample re-venting which promotes its oxidation. Thus, it seems more accurate to attribute these peaks to MoS<sub>x</sub> than MoN<sub>x</sub>.

Even if the MoS<sub>2</sub> nitridation is not clearly highlighted after N<sub>2</sub> plasma treatment, the degradation and the oxidation of the stack is clearly visible. In fact, we can observe a drastic increase in MoO<sub>x</sub>/MoO<sub>3</sub> after N<sub>2</sub> plasma. In addition, if we extend this analysis with the results presented in Annex part 3, section III.2.2, interesting observations can be highlighted. For example, the significant stack oxidation after plasma is confirmed by an increase in AlO<sub>x</sub> atomic concentration and the addition of a supplementary environment at high energies (168.8 eV and 169.9 eV) on S 2*p* which can be attributed to MoSO<sub>x</sub>. Moreover, the abrasive effect of the plasma is also highlighted since an important decrease in Al atomic concentration is observed after plasma treatment. Finally, the energy difference between Mo 3*d*<sub>5/2</sub> and S 2*p*<sub>3/2</sub> is not coherent with a stoichiometric MoS<sub>2</sub> (67.2 eV) for *MoS<sub>2</sub> + AlN 0s AP*, *MoS<sub>2</sub> + AlN 1s AP* and *MoS<sub>2</sub> + AlN 2s AP* samples. It indirectly highlights the important degradation of the 2D-MoS<sub>2</sub> seed layer after plasma treatment.

To conclude, these XPS characterizations demonstrate that the N<sub>2</sub> plasma treatment lead to an important oxidation of the stack. It highly suggests that the degradation of the AlN seed layer by plasma treatment observed in AFM (section IV.1.3.1.2) induces microcracks which promotes the stack oxidation during the reventing. Moreover, the physical impact of the plasma is also observed with a decrease in Al concentration after treatment. However, despite the oxidation and Al abrasion, the 2D-MoS<sub>2</sub> layer seems relatively preserved for samples with an AlN seed of 4s and above (Mo 3d<sub>5/2</sub> and S 2p<sub>3/2</sub> = 67.2 eV). These observations are in line with the Raman analysis presented in section IV.1.3.2.1 in which an important degradation of the MoS<sub>2</sub> Raman signal is observed for the sample with an AlN seed below 4s. Hence, and similarly to Raman and AFM characterizations, this analysis seems to confirm that we do not expect to obtain an improvement in the crystalline quality of the regrown AlN on the seed.

Finally, we can assume that the few trials of H<sub>2</sub> plasma treatments could lead to similar results. The stack should be degraded by the plasma treatment resulting in a pronounced oxidation. The 2D-MoS<sub>2</sub> should also be preserved for the samples with the thicker AlN seed. However, it is possible that the amount of S could be at least lower than those reported for N<sub>2</sub> plasma by promoting H<sub>2</sub>S (g) formation.

#### IV.1.4. Second thick AlN growth after plasma treatment

In order to conclude this plasma treatment approach, a 100 nm thick AlN PVD growth was performed on each plasma treated samples by taking care to reduce the time between the plasma treatment and the 100 nm AlN PVD deposition, and this to prevent any surface oxidation. Then, the c-axis orientation was assessed by RC measurements. The obtained (002) RC values of the 100 nm thick AlN regrowth as a function of the AlN deposition time (1s to 8s) of the seed layer (on which the regrowth is performed) are plotted in Figure IV.13. We clearly observe that for *MoS<sub>2</sub> Reference AP*, *MoS<sub>2</sub> + AlN 1s AP* and *MoS<sub>2</sub> + AlN 2s AP*, the RC AlN (002) is highly degraded (RC > 2°). This result is expected since these samples present surface defects and cracks as evidenced in AFM measurements.

Above 3s of AlN seed deposition time, the RC is moderately affected (below 1°) compared to the reference RC = 0.5° obtained on 100 nm AlN PVD growth directly on MoS<sub>2</sub>. This observation indicates that the increase in roughness observed on these samples in XRR and AFM measurements and the stack oxidation demonstrate in XPS contribute only to a moderate degradation of c-axis orientation.



Hence, the most suitable sample to check if the N<sub>2</sub> plasma treatment is effective to solve the delamination issue is MoS<sub>2</sub> + AlN 3s AP. In fact, this sample is supposed to be the one where 2D-MoS<sub>2</sub> is the most modified while displaying a quite good RC value (0.91°) after a second 100 nm AlN PVD regrowth. Thus, a 300 nm thick AlN PVD was performed on MoS<sub>2</sub> + AlN 3s AP. A picture of this sample is presented in the inset of Figure IV.13. As observed, despite the N<sub>2</sub> plasma treatment, this thicker second AlN PVD growth leads inexorably to the delamination of the AlN/MoS<sub>2</sub> stack. We suppose that the 2D-MoS<sub>2</sub> and MoS<sub>2</sub>/SiO<sub>2</sub> interface are not enough modified to handle the stress that built up during the growth of 300 nm AlN PVD film.

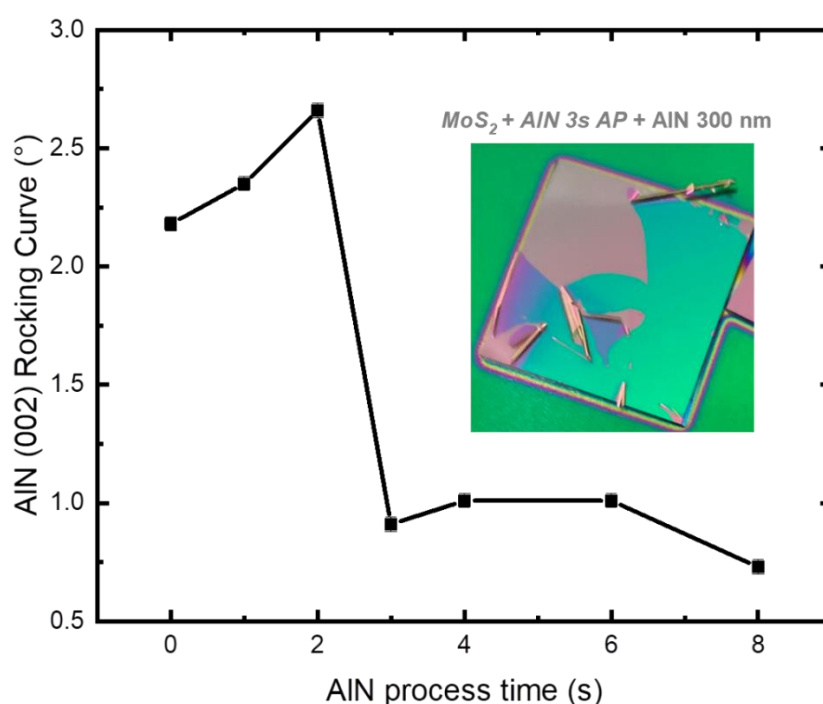


Figure IV.13: AlN (002) RC measurements of the 100 nm AlN PVD regrowth after N<sub>2</sub> plasma treatment. The inset shows a thicker AlN PVD growth (300 nm) on a MoS<sub>2</sub> + AlN 3s AP sample.

#### IV.1.5. Conclusions and perspectives on plasma treatments

Plasma treatments using NH<sub>3</sub>, H<sub>2</sub>, and N<sub>2</sub> were tested on MoS<sub>2</sub> and MoS<sub>2</sub> + AlN stack. The aim of studying a plasma solution was twice. First, a plasma brings a physical component to species due to collisions that could penetrate deeply into matter. Second, plasma forms radicals that are very reactive and can modify the bonding environments into the layers. On one hand, in the investigated conditions, the direct application of NH<sub>3</sub> plasma on 2D-MoS<sub>2</sub> is ineffective to modify the bonding environments. This result directed our choices towards N<sub>2</sub> and H<sub>2</sub> plasma which seem more suitable to modify MoS<sub>2</sub> but to the detriment of surface quality related to plasma physical impact.

On the other hand, N<sub>2</sub> plasma on MoS<sub>2</sub> + AlN xs samples clearly highlights that the physical impact coming from Ar is predominant and cannot be negligible. It has an abrasive effect which can induce cracks and increase the AlN surface roughness. This surface degradation results in a drastic increase in stack oxidation (MoO<sub>x</sub>/MoO<sub>3</sub> and AlO<sub>x</sub>) after the N<sub>2</sub> plasma. Also, we assume that the AlN is an excellent diffusion barrier against N\* radicals, since no significant chemical modification is observed, with monoatomic N\* species at 450°C during 20 min through 4s thick AlN. Finally, the second AlN PVD deposition performed leads either to highly degraded c-axis textured growth (AlN seed layer below 3s) or to the delamination of the AlN/MoS<sub>2</sub> stack (AlN seed above 3s). Therefore, we didn't find any suitable conditions to solve the delamination issue using a plasma treatment. Even if the few samples treated with a H<sub>2</sub> plasma have not been deeply characterized, we can assume that the results could be similar with those presented for N<sub>2</sub> plasma. The plasma abrasive effect coming from Ar should remain and result in a surface degradation promoting the stack oxidation, the increase in surface roughness and potentially cracks formation.

A potential alternative would be to investigate new plasma conditions in order to have a more efficient chemical impact while minimizing the physical impact of the plasma. For example, the use of a remote plasma could be a way to reduce the physical impact. Another alternative could be to investigate a mixture of N<sub>2</sub>/H<sub>2</sub>. Another proposition could be to investigate a higher temperature range (typically 450 °C – 700 °C) in a thermal tool equipped with a plasma source.

## IV.2. Thermal heat treatments

Plasma treatments being ineffective to enough modify the 2D-MoS<sub>2</sub> layer while preserving a c-axis AlN textured growth without delamination, we decided to focus on pure thermal heat treatments. These thermal heat treatments are complementary with the plasma treatments discussed in the previous section since they enable to investigate higher temperature than plasma treatment. They also allow to deeply study the thermal contribution.

First, this section describes the home-made furnace equipment and experimental conditions. Second, we address the thermal budget impact on *MoS<sub>2</sub> Reference* sample is assessed in order to find suitable temperature conditions. Subsequently, and similarly to plasma treatments, we investigate N<sub>2</sub>, H<sub>2</sub> and NH<sub>3</sub> reactive heat treatments directly on *MoS<sub>2</sub> Reference* to identify the most suitable chemistry. Finally, we discuss NH<sub>3</sub> thermal heat treatments on *MoS<sub>2</sub> + AlN xs* samples to potentially perform a “remote” modification of the 2D-MoS<sub>2</sub> sub-layer.

### IV.2.1. Description of home-made furnace equipment and experimental conditions

Thermal heat treatments were carried out in a home-made furnace in SIMaP facilities. Figure IV.14 shows a schematic illustration of the furnace. Sample temperature is controlled by an optical pyrometer facing the sample surface. The furnace is equipped with a LayTec EpiTT system to monitor *in situ* reflectances with three different wavelengths at 405 nm, 633 nm and 949 nm called R405, R633 and R949, respectively. The reflectance is calculated from the ratio (value between 0 and 1) of the reflected luminous flux to the incident luminous flux. The sample is positioned on a graphite susceptor crossed by a resistance used for heating. The overall is located on a sample holder platform and described in Figure IV.14.

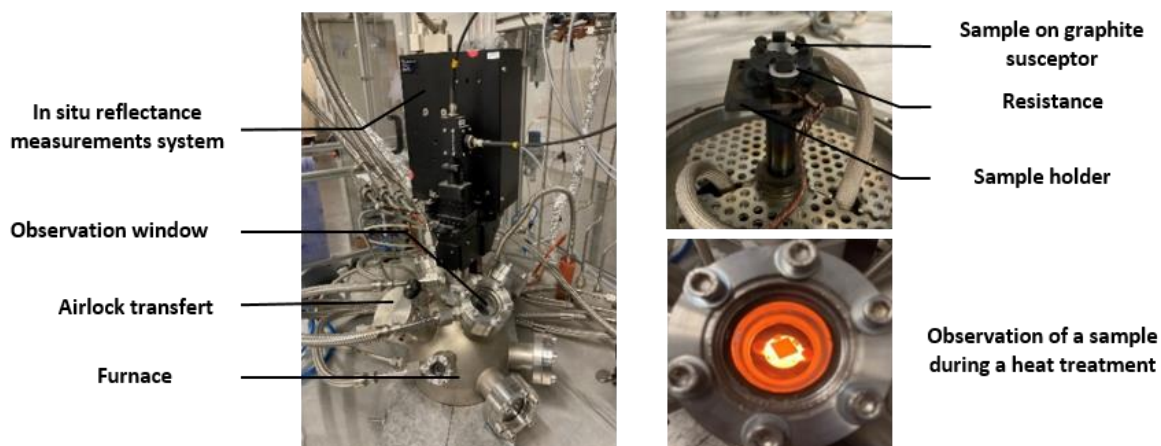


Figure IV.14: Home-made furnace equipped with an in situ reflectance measurements system

The sample holder horizontal position is adjusted through three springs whose compression ensures a horizontal surface. The aging of the springs due to the heating cycles can affect the horizontality and therefore the reflectance measurements, in particular during the increase and decrease of the temperature.

First, vacuum only experiments were achieved at base pressure to evaluate how the thermal budget and the vacuum ambient within the furnace affects the 2D-MoS<sub>2</sub>. Second, heat treatments under N<sub>2</sub>, H<sub>2</sub> and NH<sub>3</sub> were performed. The experimental conditions of these treatments are detailed in Table IV.4.

	<b>Vacuum</b>	<b>N<sub>2</sub></b>	<b>H<sub>2</sub></b>	<b>NH<sub>3</sub></b>
<b>Temperature (°C)</b>	700 and 1000	700	700	700
<b>Pressure (mbar)</b>	0.05 (base pressure)	50	50	0.5 ; 1 ; 2 ; 10 ; 30 ; 50
<b>Gas flow (sccm)</b>	/	50	50	50
<b>Time (min)</b>	60	60	60	60

Table IV.4: Experimental conditions of the heat treatments performed on MoS<sub>2</sub> Reference samples

#### IV.2.2. Thermal budget impact on MoS<sub>2</sub> Reference sample

##### IV.2.2.1. In situ reflectance measurements

A first *in situ* reflectance experiment in temperature until 1000 °C has been performed to determine the behaviour of MoS<sub>2</sub> Reference sample under vacuum in the furnace. The results are visible in Figure IV.15 a) at 1000°C and Figure IV.15 b) at 700 °C. The black curve shows the temperature profile starting at 400 °C (low limit of temperature sensor). In this first experiment, under vacuum only, we achieved many temperature plateaus at 500 °C, 700 °C and 1000 °C. In the meantime, we recorded the change in color of the sample surface by following the purple wavelength at 405 nm, the orange at 633 nm, and the far red at 949 nm.

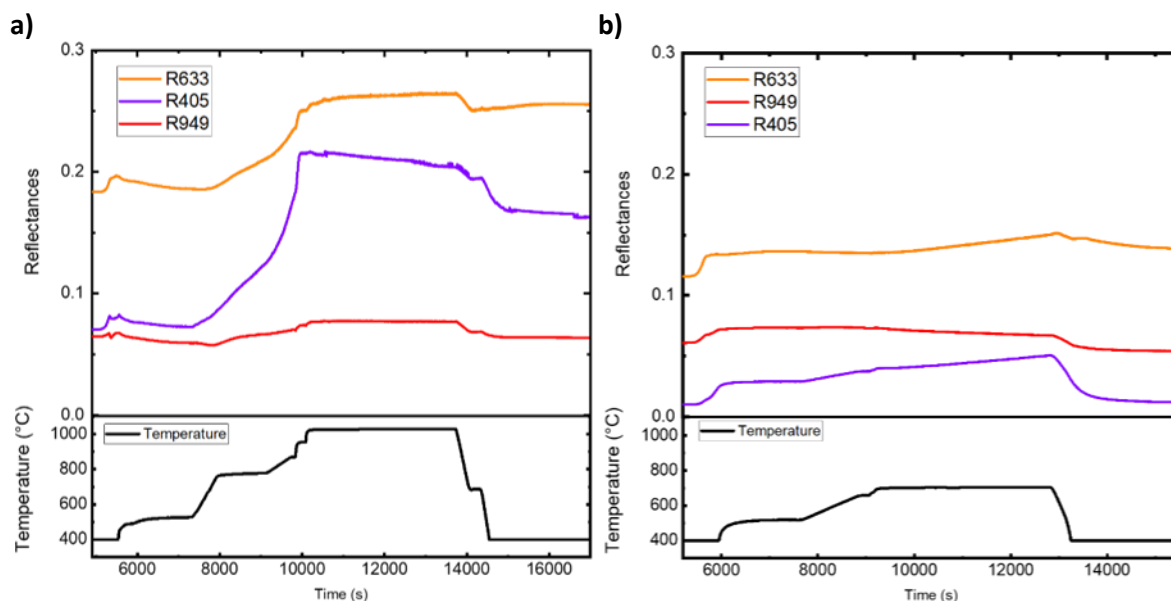


Figure IV.15: Vacuum only experiments, temperature profiles ramping-up to a) 1000 °C ; b) 700 °C. The purple component is very sensible to any surface color changes. Nearly no changes are visible at 700 °C, which indicates that the temperature is not high enough to induce surface modifications

On one hand, in the 1000 °C experiment (Figure IV.15 a), we observe a drastic increase in R405 and R633 from around 600 °C – 700 °C up to 1000 °C while there is nearly no change in R949. During the 1000 °C temperature plateau, R405, R633 and R949 remain nearly constant, and then they slightly decrease at the end of the experiment. This result shows that the surface color has clearly changed during the experiment, and that at the end of the annealing procedure the final surface state has changed, at least in color, but probably also in composition. On the other hand, we also performed the same test on another sample, but at lower temperature as visible in Figure IV.15 b). Compared to the 1000 °C case, the 700 °C experiment shows nearly no change in the color components all along the anneal profile, indicating that 700 °C is probably not high enough to induce a color change, and subsequent structural modification. Also, we see that the purple based sensor is more sensible to any change of the sample surface.

#### IV.2.2.2. MoS<sub>2</sub> crystalline quality (Raman)

To confirm the modifications of the MoS<sub>2</sub> surface states at 1000 °C under vacuum, we achieved Raman analysis on the samples after the heat treatment. The Raman spectra are visible in Figure IV.16 and the peaks positions and FWHM extracted from the fitting are displayed in Table IV.5. Before any heat treatment, the Raman spectrum shows the two well-known pronounced E<sup>1</sup><sub>2g</sub> and A<sub>1g</sub> modes at  $\approx 382$  cm<sup>-1</sup> and  $\approx 407$  cm<sup>-1</sup> (the peak at  $\approx 520$  cm<sup>-1</sup> is attributed to the Si substrate)<sup>358,359</sup>. In comparison, the sample annealed at 700 °C shows the

two  $E_{2g}^1$  and  $A_{1g}$  vibrations, while at 1000 °C both Raman mode vanished completely, which indicates a clear disappearance of the MoS<sub>2</sub> layer.

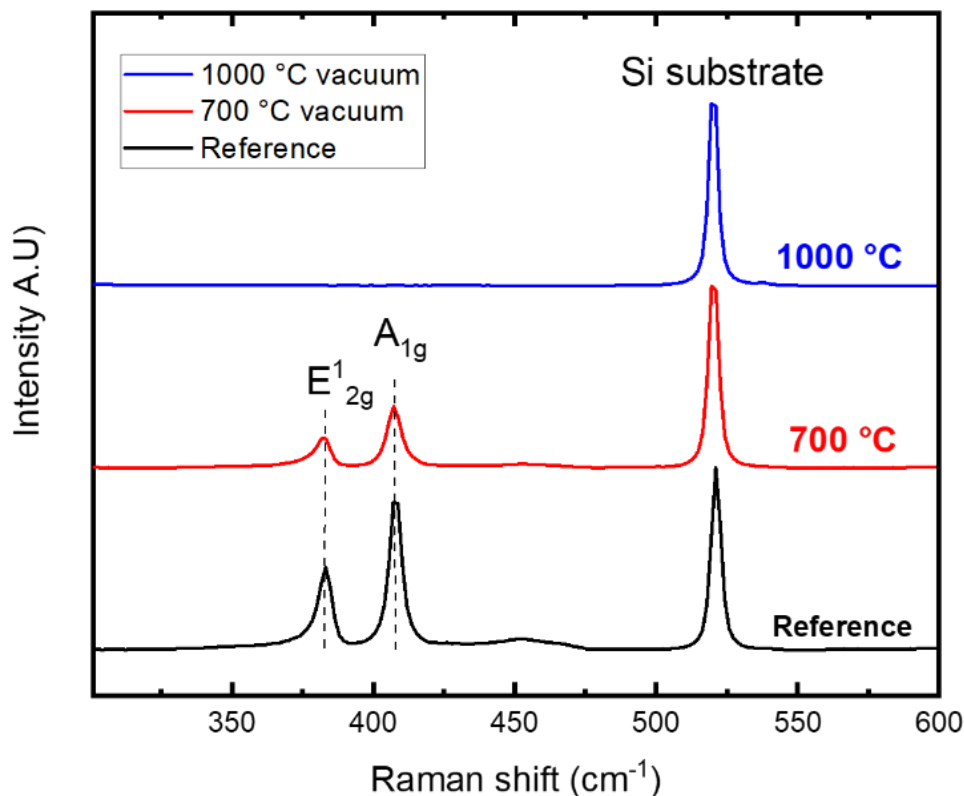


Figure IV.16: Raman spectra of the MoS<sub>2</sub> reference samples before and after 700 °C and 1000 °C vacuum heat treatment

		Reference	700 °C vacuum
$E_{2g}^1$	Position (cm <sup>-1</sup> )	382.6 ± 0.2	382.3 ± 0.1
	FWHM (cm <sup>-1</sup> )	5.1 ± 0.3	4.7 ± 0.2
$A_{1g}$	Position (cm <sup>-1</sup> )	407.9 ± 0.1	407.3 ± 0.1
	FWHM (cm <sup>-1</sup> )	5.1 ± 0.2	5.6 ± 0.1
$\Delta\omega$ (cm <sup>-1</sup> )		25.3 ± 0.3	25.0 ± 0.2

Table IV.5: Extracted positions and FWHM of  $E_{2g}^1$  and  $A_{1g}$  modes

The Raman Full Width at Half Maximum (FWHM) of these modes after the 700 °C heat treatment suggest that the MoS<sub>2</sub> layer is still well-crystallized after annealing. However, although the  $\Delta\omega$  value is similar before and after the 700 °C heat treatment, a redshift of  $E_{2g}^1$  and  $A_{1g}$  modes is observed suggesting a potential degradation of the MoS<sub>2</sub> layers.

## IV.2.2.3. Surface chemical analysis (XPS)

These results are confirmed by the XPS characterizations. The binding energies position and atomic concentrations of the *MoS<sub>2</sub> reference*, after 700 °C and 1000 °C vacuum heat treatments are detailed in Annex part 3, section III.2.3. High-resolution XPS spectra for Mo 3*d* region are shown in Figure IV.17.

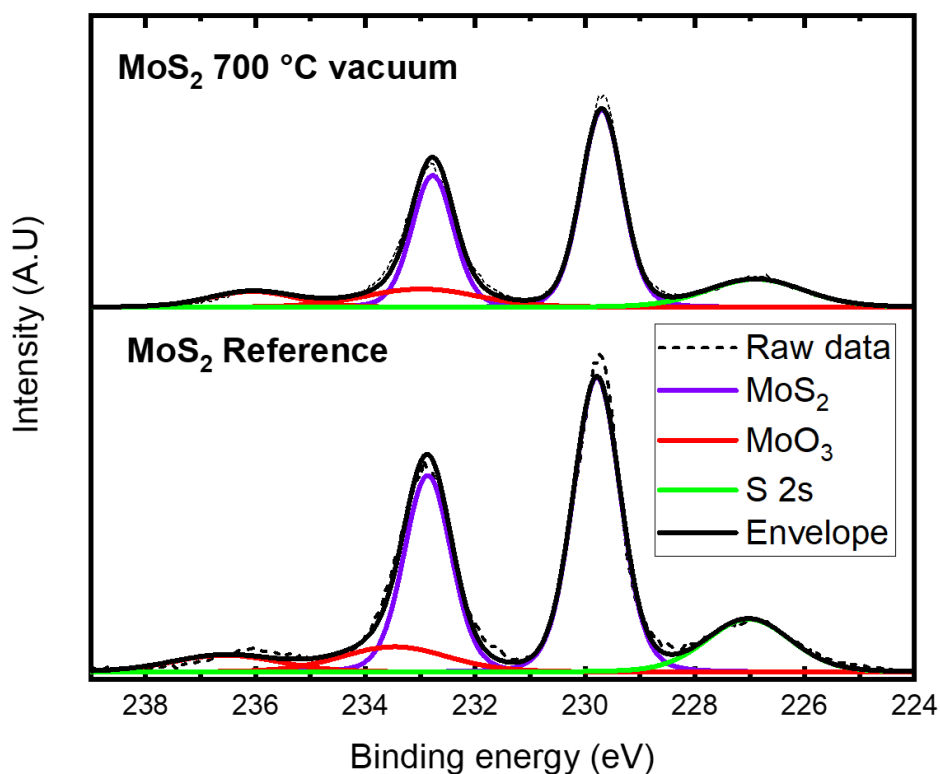


Figure IV.17: XPS spectra of Mo 3*d* of MoS<sub>2</sub> Reference sample before (bottom) and after (top) 700 °C vacuum heat treatment

For the *MoS<sub>2</sub> reference* and after 700 °C heat treatment, the main part of the spectra is composed of two peaks at 229.8 eV and 232.8 eV attributed to Mo<sup>4+</sup> 3*d*<sub>5/2</sub> and Mo<sup>4+</sup> 3*d*<sub>3/2</sub>, respectively. These binding energies are in excellent agreement with MoS<sub>2</sub> literature values<sup>374–376</sup>. The Mo 3*d*<sub>5/2</sub> and Mo 3*d*<sub>3/2</sub> peaks at 233.4 eV and 236.5 eV are attributed to Mo<sup>6+</sup> state corresponding to a small amount of MoO<sub>3</sub> at the top surface<sup>377,378</sup>. We can also observe a slight peak at 227.0 eV attributed to S 2s. Finally, and as expected, no contributions were observed in the Mo 3*d* region for the 1000 °C annealed sample as shown Annex part 3, section III.2.3). This suggests that the Mo element has been desorbed from the surface, possibly in the form of a MoO<sub>x</sub> volatile group, since we cannot exclude some remaining ppm of O<sub>2</sub> molecules under vacuum in our experiment. It is well known in the binary Mo-O diagram

that Mo under pure O<sub>2</sub> is volatilized in the form of MoO<sub>3</sub> gas at above 700°C. This fact coupled with the relative long annealing time used during the experiment (i.e. a plateau of around 1h at 1000°C) can explain the absence of Mo at 1000°C and the reduction in the number of 2D plans at 700°C.

#### IV.2.3. Thermal heat treatments under H<sub>2</sub>, N<sub>2</sub> and NH<sub>3</sub> on MoS<sub>2</sub> Reference sample

The previous section enabled to assess the thermal budget impact on the 2D-MoS<sub>2</sub> layer. A suitable temperature range was identified allowing to preserve the 2D-MoS<sub>2</sub> layer. From these results, we pursue this study through reactive heat treatments under N<sub>2</sub>, H<sub>2</sub> and NH<sub>3</sub> at 700 °C, directly on MoS<sub>2</sub> Reference samples.

##### IV.2.3.1. In situ reflectance measurements

Following the results on vacuum only experiments, the temperature during H<sub>2</sub>, N<sub>2</sub>, and NH<sub>3</sub> heat treatment has been fixed to 700 °C. The gas was introduced only during the 700 °C temperature plateau indicated by vertical dash lines in Figure IV.18 and the pressure was set at 50 mbar with a flow of 50 sccm. The increase and decrease in temperature were performed under vacuum. The temperature profile, especially the increase in temperature, and the evolution of the reflectance during this step can be slightly different from one treatment to another due to experimental artefacts in the furnace (slight leak increasing the base pressure, aging of the heating resistance or the springs, change in the horizontal position of the sample holder or environmental disturbances). The H<sub>2</sub>, N<sub>2</sub> and NH<sub>3</sub> 700 °C heat treatment with the *in situ* reflectance measurements at 405 nm, 633 nm and 949 nm are presented in Figure IV.18 a), b) and c), respectively.

In Figure IV.18 a) (H<sub>2</sub> heat treatment), we clearly observe that the reflectances are almost constant all along the temperature profile. Slight changes are observed during the increase and decrease in temperature and also during the beginning of the H<sub>2</sub> plateau at 700 °C mainly due to the stabilization in gas flow/pressure and temperature. Hence, this 700°C experiment under H<sub>2</sub> shows nearly no change in the color components all along the anneal profile, indicating that H<sub>2</sub> is probably not a suitable reactive gas to induce a chemical modification of MoS<sub>2</sub> as the surface states seem identical at the beginning and the end of the treatment.



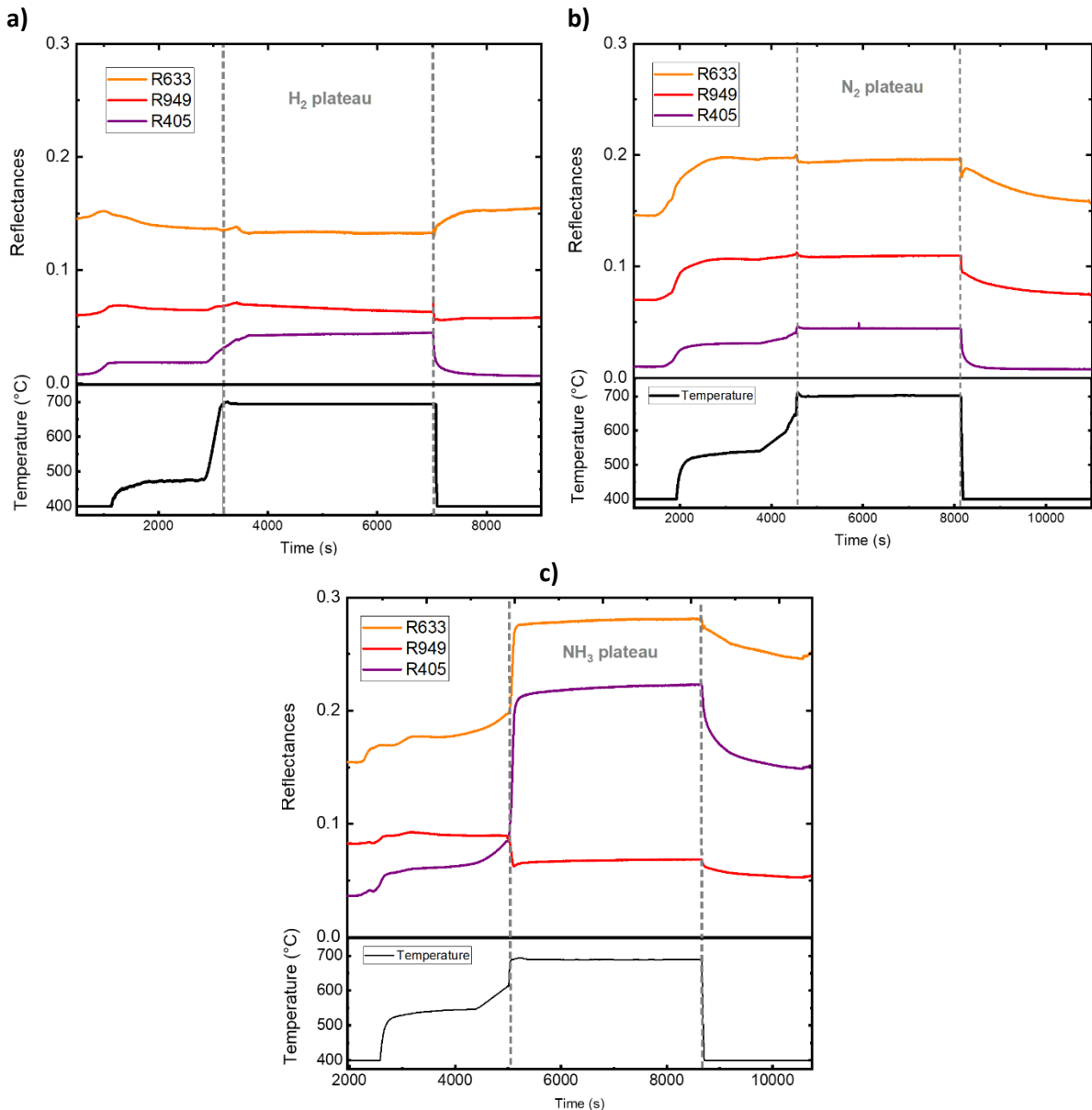


Figure IV.18: a) H<sub>2</sub>; b) N<sub>2</sub> and c) NH<sub>3</sub> heat treatment, temperature profiles ramping-up to 700 °C

Similar results have been obtained in Figure IV.18 b) (N<sub>2</sub> heat treatment) since we observe constant reflectance on the N<sub>2</sub> temperature plateau. An increase in reflectance is visible during the increase in temperature which could be due to experimental artefacts in the furnace such as slight changes in sample holder horizontal position during the heating. An inverse phenomenon (decrease in reflectance) is observed for the decrease in temperature. But once again, nearly no change in the color components is shown since the surface states seem identical at the beginning and the end of the treatment suggesting that N<sub>2</sub> is also not a suitable gas for the investigated conditions.

The reactive heat treatment under NH<sub>3</sub> presented in Figure IV.18 c) clearly displays a drastic difference with the previous heat treatments at 700 °C under vacuum, H<sub>2</sub> or N<sub>2</sub>. In fact, as soon as NH<sub>3</sub> is sent, a quasi-instantly increase in R405 and R633 and decrease in R949 followed by their stabilizations is observed. Moreover, each reflectance value at the beginning and at the end of this treatment is totally different. This behaviour indicates that the optical properties of the initial 2D-MoS<sub>2</sub> seed layer have changed probably due to a change in composition.

#### IV.2.3.2. MoS<sub>2</sub> chemical modification (Raman)

To deeply understand the changes in surface states due to a potential chemical modification of the 2D-MoS<sub>2</sub> layer, Raman spectroscopy has been achieved after each heat treatment. Raman spectra after H<sub>2</sub>, N<sub>2</sub> and NH<sub>3</sub> heat treatment are presented in Figure IV.19.

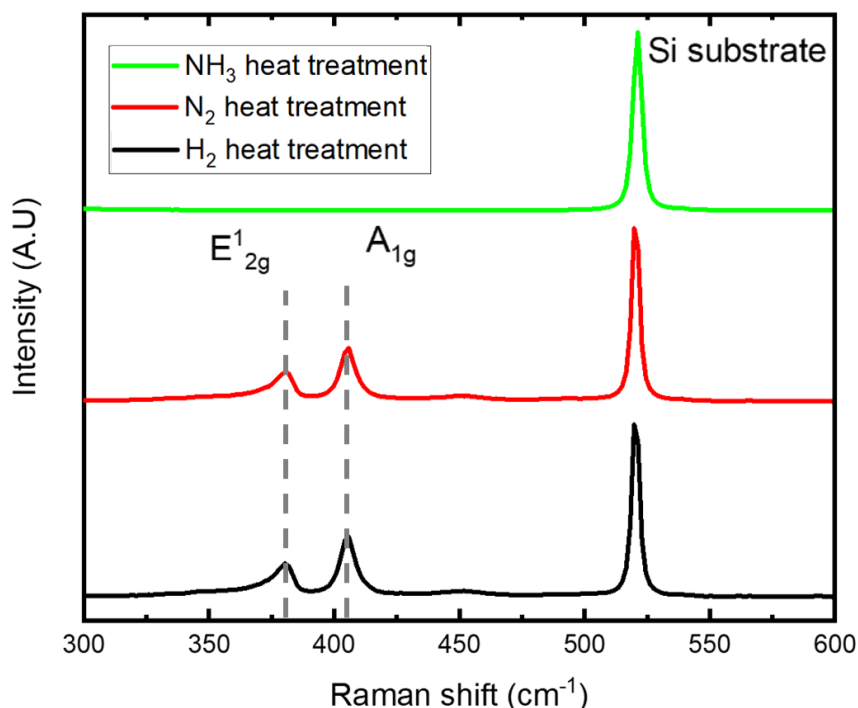


Figure IV.19: Raman spectra of MoS<sub>2</sub> Reference sample after H<sub>2</sub>, N<sub>2</sub> and NH<sub>3</sub> 700 °C heat treatment

On one hand, Raman spectra after H<sub>2</sub> and N<sub>2</sub> heat treatment clearly display E<sup>1</sup><sub>2g</sub> and A<sub>1g</sub> MoS<sub>2</sub> Raman modes at  $\approx 382$  cm<sup>-1</sup> and  $\approx 407$  cm<sup>-1</sup>, respectively. These results seem consistent with *in situ* reflectance measurements where nearly no change in the color components all along the anneal profile is observed for both heat treatments suggesting no chemical modification. Hence, the MoS<sub>2</sub> lamellar structure is preserved after both treatment indicating that the use of H<sub>2</sub> or N<sub>2</sub> is not a suitable choice to convert the Van der Waals interactions into covalent bonds and solve the delamination issue.

On the other hand, Raman spectrum after NH<sub>3</sub> heat treatment shows that both MoS<sub>2</sub> Raman modes vanished completely, only a single peak located at  $\approx 520 \text{ cm}^{-1}$  attributed to the Si substrate is visible. It suggests either a disappearance of the MoS<sub>2</sub> layer (as during the 1000 °C heat treatment under vacuum presented in section IV.2.2.1) or a chemical modification of this layer into a no or poor Raman active material. Chemical characterizations of the top surface must be implemented to find out more.

##### IV.2.3.3. Surface chemical analysis (XPS)

To confirm the potential change in composition of MoS<sub>2</sub> at 700 °C under NH<sub>3</sub>, we achieved X-ray photoelectron spectroscopy on the sample after the heat treatment. The Mo 3*d* and Mo 3*p*/N 1*s* regions for the samples after 700 °C treatment under vacuum and under the lowest NH<sub>3</sub> regulated pressure (0.5 mbar) are depicted in Figure IV.20 a) and b), respectively.

In Mo 3*d* region, we clearly observe a change in the XPS signal. First of all, after the NH<sub>3</sub> heat treatment, we clearly see the absence of S 2*s* signal while Mo 3*d* is still present with multiple environments. It means that MoS<sub>2</sub> sample has been chemically converted during the NH<sub>3</sub> heat treatment. By deconvoluting Mo 3*d* spectra, we can attribute the Mo 3*d*<sub>5/2</sub> and Mo 3*d*<sub>3/2</sub> peaks at 228.8 eV and 231.9 eV, respectively, to Mo-N bond<sup>420 421</sup>.

However, the main part of the spectra is composed of the Mo3*d*<sub>5/2</sub> and Mo3*d*<sub>3/2</sub> peaks at 229.5 eV and 232.6 eV. This Mo 3*d*<sub>5/2</sub> binding energy is between those assigned to Mo<sup>4+</sup> (230.0 eV) and Mo<sup>0</sup> (227.8 eV)<sup>422</sup> and several studies<sup>421,423–425</sup> attribute these peaks to the formation of Mo<sub>2</sub>N. However, a significant increase in the atomic oxygen concentration can be observed after the NH<sub>3</sub> heat treatment. Thus, it is probably more accurate to attribute these peaks to a mixture of MoO<sub>2</sub>, MoO<sub>3</sub> and Mo<sub>2</sub>N<sup>426</sup>. The formation of this molybdenum oxynitride probably results from air exposure of the sample. Finally, the Mo 3*d*<sub>5/2</sub> and Mo 3*d*<sub>3/2</sub> peaks at 232.7 eV and 235.7 eV are assigned to a significant amount of MoO<sub>x</sub> also linked to the re-venting after the heat treatment.

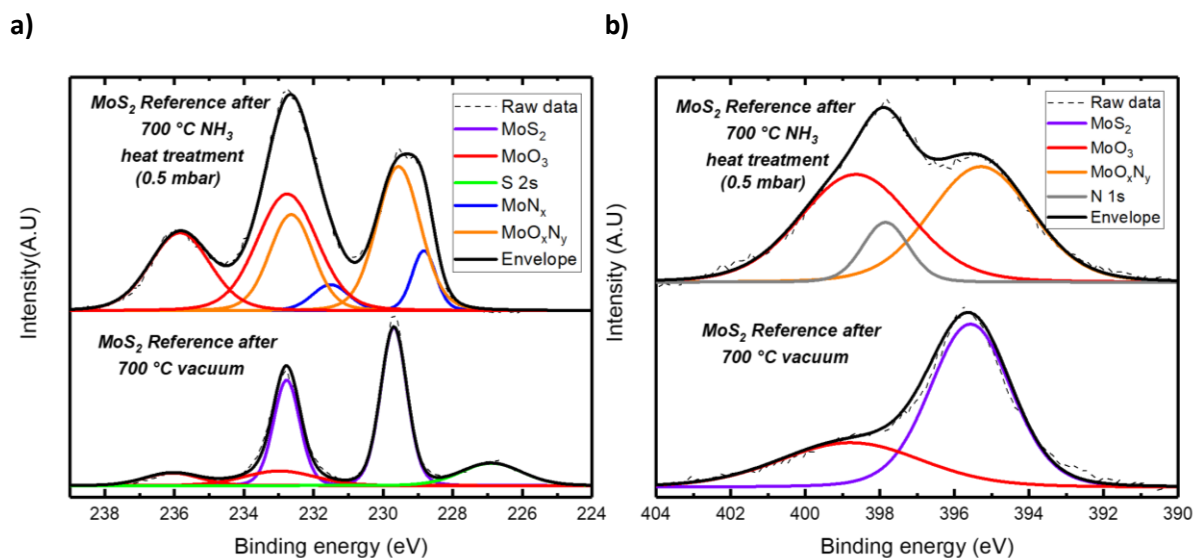


Figure IV.20: XPS spectra of a) Mo 3d ; b) Mo 3p/ N 1s of MoS<sub>2</sub> after 700 °C vacuum experiment (bottom) and 700 °C NH<sub>3</sub> experimented with a regulated pressure of 0.5 mbar (top)

In the Mo 3p/N 1s regions, we also observe a clear difference between the sample treated at 700°C under vacuum and with NH<sub>3</sub> at 0.5 mbar. In fact, the main difference is a significant shoulder around 398 eV on the spectrum of the sample after NH<sub>3</sub> treatment. Spectrum deconvolution indicates a peak at 397.9 eV assigned to N 1s. This N 1s peak at 397.9 eV and Mo 3p<sub>3/2</sub> peak at 395.4 eV are close to the values reported by Cao et al.<sup>409</sup> (397.9 eV and 395.3 eV) suggesting that chemical bonds are formed between Mo and N.

From a thermodynamical point of view, this conversion is unexpected because Molybdenum-Nitrogen system is characterized by an almost complete inertness of Mo metal towards N<sub>2</sub> gas. In fact, according to Jehn<sup>427</sup>, the solubility of N in Mo is only up to about 0.1 at % at 2000 °C and atmospheric pressure of N<sub>2</sub>. In agreement with thermodynamic data, nitrides are formed only at high N<sub>2</sub> or NH<sub>3</sub> pressures. However, the synthesis of molybdenum nitrides from MoS<sub>2</sub> has already been reported in the literature. In fact, Marchand et al.<sup>406,428,429</sup> group were pioneers in the synthesis of molybdenum nitride from MoS<sub>2</sub> by reduction of sulphides by ammonia reactive heat treatments. Later, Ganin et al.<sup>407</sup> used the same method to prepare molybdenum nitrides and finally, Sun et al.<sup>430</sup> and Cao et al.<sup>409</sup> have demonstrated the transformation of MoS<sub>2</sub> nanosheets exfoliated from bulk material into molybdenum nitride nanosheets with ammonia and urea reactive heat treatments, respectively. As demonstrated in this work, the conversion of MoS<sub>2</sub> into MoN<sub>x</sub> is experimentally possible but seems lead to unstable phases which could explained the differences observed with thermodynamic investigations.

## IV.2.3.4. Kinetic investigations

According to *in situ* reflectance measurements presented in Figure IV.18 c) (NH<sub>3</sub> heat treatment), the MoS<sub>2</sub> chemical transformation is almost quasi-instantaneous with a NH<sub>3</sub> regulated pressure of 50 mbar since each reflectance reach a plateau as soon as NH<sub>3</sub> is introduced in the furnace. Hence, by adjusting the NH<sub>3</sub> pressure, it could be possible to control the kinetic conversion of MoS<sub>2</sub>. Also, we see that the purple based sensor is more sensible to any change of the sample surface. Therefore, in the rest of this work, we will mainly present results at 405 nm. Thus, to evaluate this approach, NH<sub>3</sub> pressure was regulated between 0.5 and 50 mbar. Figure IV.21 presents the evolution of R405 reflectance for each NH<sub>3</sub> pressure investigated and focuses only on the NH<sub>3</sub> plateau. The values of R405 on the Y-axis and of time on the X-axis have been normalized for more visibility. An inset of the Raman spectrum of 2D-MoS<sub>2</sub> after the NH<sub>3</sub> heat treatment with the lowest pressure (0.5 mbar) is present to justify the chemical conversion.

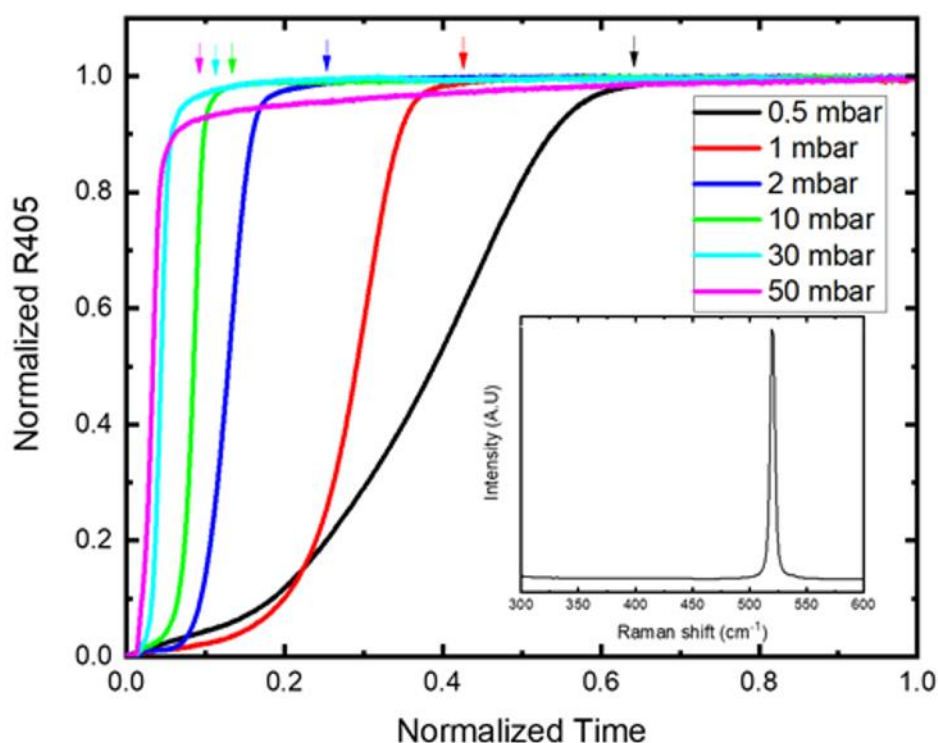


Figure IV.21: Evolution of the R405 component during the 700 °C NH<sub>3</sub> temperature plateau for different NH<sub>3</sub> pressures.

For each curve,  $dR_{405}/dt \approx 0$  is represented by an arrow

We observe that the higher the NH<sub>3</sub> pressure, the faster the increase in R405 and its stabilization. This result indicates that the color change of the material can be adjusted with the NH<sub>3</sub> pressure. Thus, the kinetic change in the composition of MoS<sub>2</sub> is dependent of the

NH<sub>3</sub> pressure. For each NH<sub>3</sub> pressure, R405 has been derivated in order to determine the points where  $\frac{dR405}{dt} \approx 0$  corresponding to the point where the MoS<sub>2</sub> conversion into MoN<sub>x</sub> is completed. In fact, as in Tsakonas et al.<sup>431</sup> study, the reflectance reaches a plateau when no more chemical or morphological changes beyond the steady-state thermal dynamics are occurring. These points are represented by arrows in Figure IV.21.

From these values, the points where  $\frac{dR405}{dt} \approx 0$  as a function of the different NH<sub>3</sub> pressures investigated is plotted and Figure IV.22 a) and a rate law of a chemical reaction law has been applied in Figure IV.22 b).

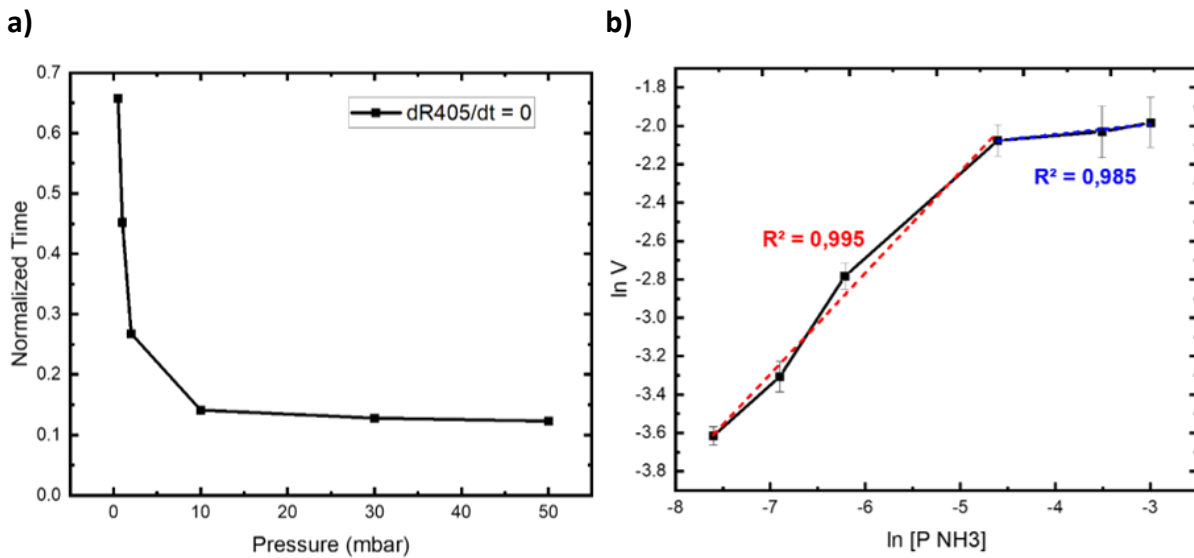


Figure IV.22: a)  $dR405/dt \approx 0$  for the different NH<sub>3</sub> pressures investigated ; b) application of the rate law

By applying the rate law, we can write:

$$V = k \cdot [MoS_2]^\alpha \cdot [NH_3]^\beta \quad \text{Equation IV.1}$$

Where  $V$  is the overall rate of the reaction,  $k$  is a kinetic constant,  $[MoS_2]$  and  $[NH_3]$  are molar concentrations and  $\alpha$  and  $\beta$  are the stoichiometric coefficients relative to the MoS<sub>2</sub> and NH<sub>3</sub>, respectively.

As shown in Figure IV.22 a), the conversion rate of MoS<sub>2</sub> into MoN<sub>x</sub> is dependent on the NH<sub>3</sub> pressure. Thus, we can postulate that the NH<sub>3</sub> pressure ( $P_{NH_3}$ ), which can be assimilated to the NH<sub>3</sub> concentration noted  $[NH_3]$ , is the limiting species and will impose its rate on the reaction. So, we can write:

$$V = k \cdot [P_{NH_3}]^\beta \Leftrightarrow \ln(V) = \ln(k) + \beta \ln[P_{NH_3}] \quad \text{Equation IV.2}$$

The curve  $\ln(V) = f(\ln[P_{\text{NH}_3}])$  is depicted in Figure IV.22 b). Two different regimes seem to be distinguished. In fact, a first linear part indicates that the MoS<sub>2</sub> conversion into MoN<sub>x</sub> depends linearly on the NH<sub>3</sub> pressure. This part corresponds to the heat treatment with a NH<sub>3</sub> pressure between 0.5 mbar and 10 mbar. It means that the kinetic limiting factor is the amount of NH<sub>3</sub> species at the MoS<sub>2</sub> surface leading to its conversion. The second part is a constant part suggesting that the MoS<sub>2</sub> conversion into MoN<sub>x</sub> is independent of NH<sub>3</sub> pressure. It means that we have a quasi-instant MoS<sub>2</sub> conversion and thus that the limiting factor is the amount of MoS<sub>2</sub>. If we focused on the linear part, we can extract  $\ln(k) = 0.29 \pm 0.32$  and  $\beta = 0.51 \pm 0.05$  being the y-intercept and the slope, respectively.

IV.2.3.5. Structural characterizations and AlN PVD growth (XRR and XRD)

In order to potentially identify the molybdenum nitride thus formed with the nitridation of the MoS<sub>2</sub> layer, we pursue the analysis with XRR and XRD structural characterizations. First, the nitrated MoS<sub>2</sub> sample (NH<sub>3</sub> pressure of 50 mbar) has been characterized by XRR. Its pattern is compared with the MoS<sub>2</sub> Reference XRR pattern in Figure IV.23. After NH<sub>3</sub> heat treatment, the MoS<sub>2</sub> XRR pattern does not display a clear response up to  $\omega = 8^\circ$  as for MoS<sub>2</sub> Reference highlighting a rougher surface. Moreover, air exposure could also lead to the formation of an oxygen gradient within the layer thickness. Hence, the corresponding XRR pattern is difficult to fit. Several fitting attempts have been performed but were unsuccessful.

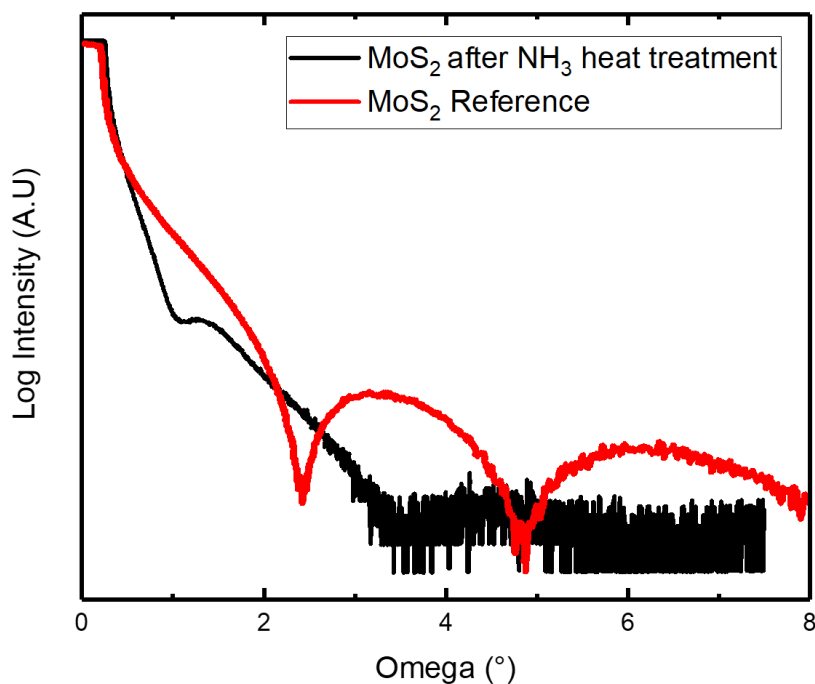


Figure IV.23: XRR patterns of MoS<sub>2</sub> Reference before (red curve) and after 700 °C NH<sub>3</sub> heat treatment (black curve)

Although, the layer is very thin, XRD analysis was implemented to potentially determine the molybdenum (oxy)nitride structure. Out-of-plane XRD scan is presented in Figure IV.24. The narrow and intense peaks are attributed to Si substrate. Only a large peak at  $2\theta \approx 21^\circ$  is visible and difficult to identify. It could be attributed to (111) planes of a MoO<sub>2</sub>(NO<sub>3</sub>)<sub>2</sub> monoclinic compound, without certainty. This peak could suggest a Mo(O<sub>x</sub>)N<sub>y</sub> metastable layered structure which could be texturizing.

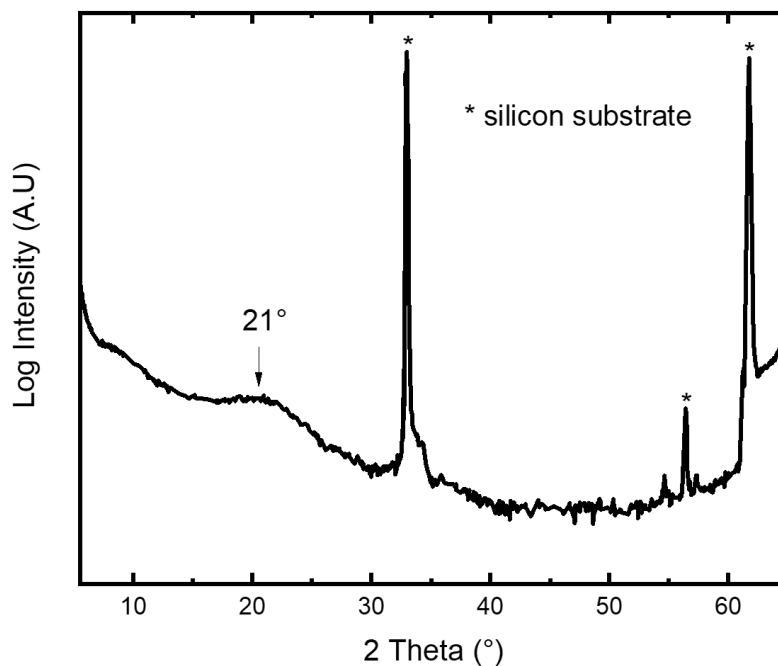


Figure IV.24: Out-of-plane XRD measurement of MoS<sub>2</sub> Reference after 700 °C NH<sub>3</sub> heat treatment

Sun et al.<sup>408</sup> published the possible MoN<sub>x</sub> structures due to the reduction process of MoS<sub>2</sub> by NH<sub>3</sub>. A cubic structure, a tetragonal structure and two different hexagonal structures are reported resulting on the formation of a  $\gamma$ -Mo<sub>2</sub>N phase (space group Fm $\bar{3}$ m), a  $\beta$ -Mo<sub>2</sub>N (space group I4<sub>1</sub>/amd), a  $\delta$ -MoN (space group P6<sub>3</sub>mc) and a Mo<sub>5</sub>N<sub>6</sub> (space group (P6<sub>3</sub>/m). Ultimately, we wonder if the hexagonal phases could induce the texturation of AlN. To address this point, we performed a 100 nm AlN PVD growth on the modified MoS<sub>2</sub> after NH<sub>3</sub> heat treatment (0.5 mbar and 50 mbar) and the c-axis texture was determined by a RC measurement. The  $\omega$ -scan XRD measurement is presented in Figure IV.25. We clearly observe that the RC is 4-5 times higher (RC  $\approx$  2.0°-2.5°) than an identical AlN PVD deposition directly on the 2D-MoS<sub>2</sub> (RC = 0.5°) indicating a poor c-axis orientation.



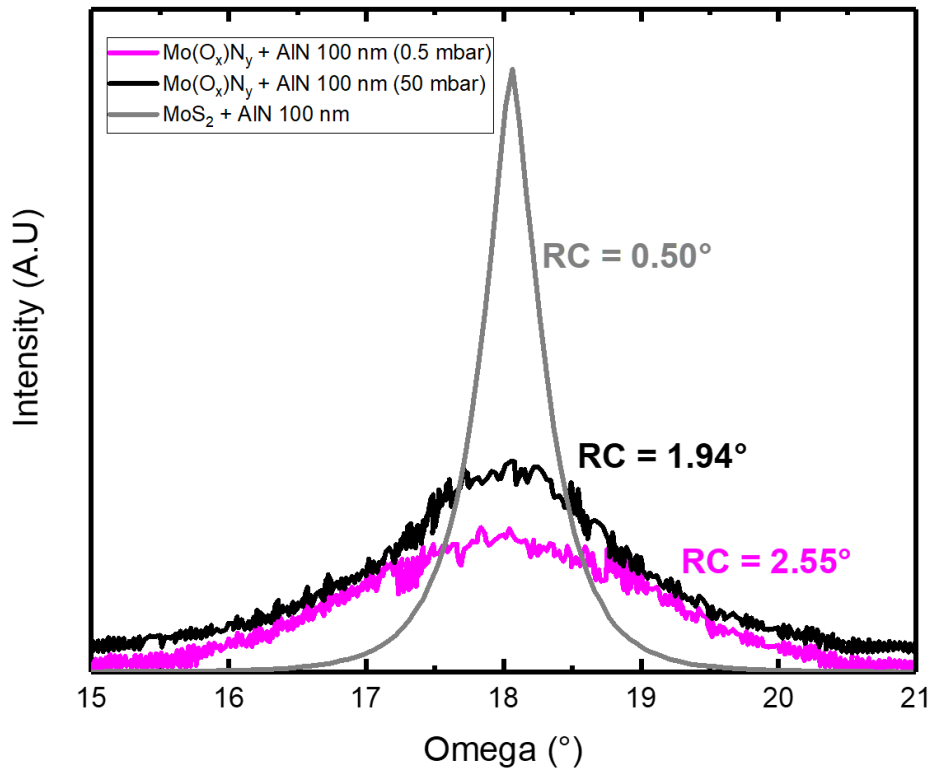


Figure IV.25: RC measurements of MoS<sub>2</sub> Reference before and after 700 °C NH<sub>3</sub> heat treatment (0.5 and 50 mbar)

Hence, although molybdenum nitride alloys are suitable to solve the delamination issue since most metal nitrides show non-layered structures<sup>432</sup>, the resulting Mo(O<sub>x</sub>)N<sub>y</sub> layer is not texturizing. It could be explained by an important lattice mismatch between this layer and AlN. Moreover, the roughness shown in XRR and the significant oxidation demonstrated in XPS probably contribute to this poor AlN c-axis orientation. Finally, even if in the assumption of a δ-MoN or Mo<sub>5</sub>N<sub>6</sub> hexagonal phase is formed, both structures display a large lattice mismatch with AlN ( $\approx 85\%$  for δ-MoN and  $\approx 57\%$  Mo<sub>5</sub>N<sub>6</sub>).

Therefore, since the MoS<sub>2</sub> transformation into molybdenum (oxy)nitride does not lead to an alloy able to directly texture AlN, we decided to perform the indirect transformation of the 2D-MoS<sub>2</sub> layer through a thin AlN seed layer previously deposited and textured by this 2D layer. This approach is presented in the following part.

#### IV.2.4. Thermal heat treatments under NH<sub>3</sub> with AlN PVD seed layer

To remind the scope, an AlN seed must be thick enough to ensure the regrowth (and the subsequent crystalline quality) of a second AlN film and thin enough to enable the diffusion of a reactive element inducing the transformation of the 2D-MoS<sub>2</sub> sub-layer. From this and the results presented in the previous section, we decided to focalize these heat treatments

through an AlN PVD seed layer with NH<sub>3</sub>. On one hand, contrary to N<sub>2</sub> which is a very stable molecule, NH<sub>3</sub> can be decomposed into reactive NH<sub>x</sub> species with the temperature. These NH<sub>x</sub> species have a dimension close to N (hydrogen atoms are small) and could diffuse in the AlN seed layer. On the other hand, NH<sub>x</sub> species have already been implemented in the NH<sub>3</sub> plasma study at 450 °C. However, despite the mechanical contribution by implantation of the plasma, we do not observe any 2D-MoS<sub>2</sub> modification. Hence, the thermal contribution remains to be assessed in order to verify if the N species could diffuse in the AlN seed layer and at at which temperature.

*IV.2.4.1. Experimental conditions*

The AlN seed deposition was performed in the same SPTS (Trikon) Sigma fxP 200 mm equipment under identical conditions to those described in section III.2.3. To remind, and for practical reasons, the thickness of the AlN PVD layer is expressed in seconds corresponding to the deposition time and not the real thickness nm.

NH<sub>3</sub> heat treatments were carried out in the home-made furnace located in SIMaP facilities and described in section IV.2.1. As for the NH<sub>3</sub> heat treatment directly performed on 2D-MoS<sub>2</sub>, NH<sub>3</sub> was introduced only during the temperature plateau. Different annealing temperatures, duration and NH<sub>3</sub> pressures have been investigated in order to find a suitable process window enabling the MoS<sub>2</sub> modification. Then, the thermal heat treatment conditions were optimized and are reported in Table IV.6.

<b>Sample name</b>	<b>AlN deposition time (s)</b>	<b>Temperature (°C)</b>	<b>NH<sub>3</sub> Flow (sccm)</b>	<b>NH<sub>3</sub> pressure (mbar)</b>	<b>Time (min)</b>
MoS <sub>2</sub> + AlN 4s	4 s	1000	50	50	60
MoS <sub>2</sub> + AlN 5s	5 s	1000	50	50	60
MoS <sub>2</sub> + AlN 6s	6 s	1000	50	50	60
MoS <sub>2</sub> + AlN 7s	7 s	1000	50	50	60
MoS <sub>2</sub> + AlN 8s	8 s	1000	50	50	60

*Table IV.6: Experimental conditions of the NH<sub>3</sub> heat treatments performed in the home-made furnace on MoS<sub>2</sub> + AlN xs*

*IV.2.4.2.1. In situ reflectance measurements*

*In situ* reflectance acquisitions were performed during the overall NH<sub>3</sub> heat treatments but only the acquisitions during the NH<sub>3</sub> temperature plateau have been exploited. Figure IV.26 shows R405 normalized measurements for MoS<sub>2</sub> + AlN 4s up to MoS<sub>2</sub> + AlN 8s. An experimental issue occurred during the measurement of MoS<sub>2</sub> + AlN 7s at the end of its thermal treatment, but beginning of the curve can be exploited.

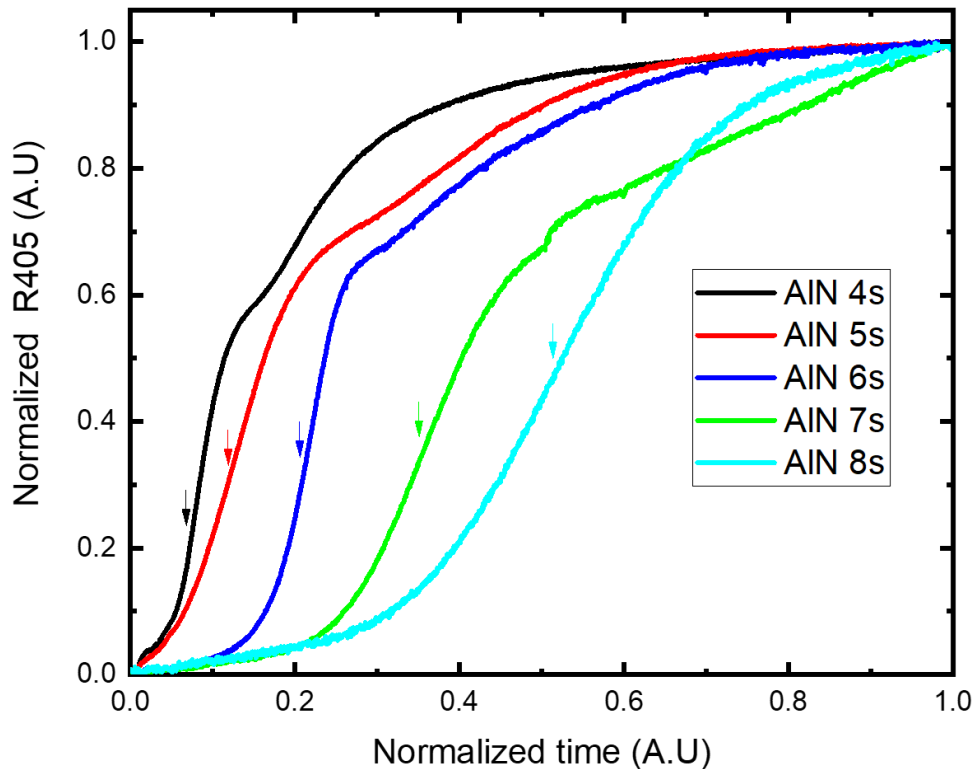


Figure IV.26: Evolution of the R405 component during the 1000 °C NH<sub>3</sub> temperature plateau

We clearly observe a progressive increase in R405 followed by a stabilization suggesting a change in color due to a chemical modification in the stack. Moreover, the increase in R405 and its stabilization is dependent on the AlN thickness. In fact, the greater the AlN thickness, the more the increase in R405 is delayed. As AlN is highly transparent at the working wavelength (405 nm), we assume that the change in color is only due to a MoS<sub>2</sub> modification.

From these results, we decided to apply a kinetic law based on Wagner's theory<sup>433</sup>. This theory is briefly described in Annex part 2, section II.3. It is worth to notice that these kinetic models have been developed to describe the kinetic oxidation of metals and that oxides are ionic solids contrary to AlN (covalent solid). Kinetic laws are mainly linear, parabolic, or logarithmic<sup>434</sup>. Other laws such as cubic or mixed laws can also be observed. Depending on the law, the oxidation process is limited by different phenomena: interface reactions (linear law), diffusion through the oxide layer (parabolic law), low oxidation process (logarithmic law)... In this work, we decide to investigate two laws: a linear kinetic law and a parabolic kinetic law.

When the oxidation rate is constant, the kinetic is linear and can be written as:

$$Y = k_1 t \quad \text{Equation IV.3}$$

Where  $Y$  is the thickness of the oxide formed,  $k_l$  a linear constant and  $t$  the time.

When the oxidation is limited by the diffusion through the oxide, the kinetic is parabolic and can be written as:

$$Y^2 = k_p t \quad \text{Equation IV.4}$$

Where  $Y$  is the thickness of the oxide formed,  $k_p$  a parabolic constant and  $t$  the time.

In the current case, we need first to determine which time parameters must be extracted from the curves in Figure IV.26 to apply the kinetic model. Two solutions are possible, either we determine the time corresponding to the points where  $\frac{dR_{405}}{dt} = 0$  (as done in the kinetic investigations discussed in section IV.2.3.4) or the points where  $\frac{dR_{405}}{dt} = \max$ , i.e. the curve inflection points. As we had some experimental issues, in particular for the case of AlN 7s, we decided to choose the last solution, and extracted the points indicated by arrows in Figure IV.26. The inflection of the curve could be assimilated to the moment where the nitriding reaction is faster. For each curve, the AlN thickness or square thickness (determined by XRR) has been plotted as a function of the value of  $\frac{dR_{405}}{dt} = \max$  (normalized time) in Figure IV.27 and b), respectively.

In each case, and according to the kinetic laws describe Equation IV.3 and Equation IV.4, a linear regression has been performed. Comparing these two curves, we observe that the linear regression is better in Figure IV.27 b) ( $R^2 = 0.904$  vs.  $R^2 = 0.987$ ). In this work, this result suggests that the MoS<sub>2</sub> nitridation reaction through the AlN seed layer is limited by the diffusion of nitrogen species (parabolic law). This linear regression also gives access to the parabolic constant:  $k_p = 4.351 \times 10^{-17}$ . This constant is directly related to the diffusion coefficient  $D$  (of N in AlN in this work). However, the expression of  $k_p$  depends on pressure law and reaction rate which require a pressure and temperature study to extract a diffusion coefficient  $D$  and elaborate a complete model. However, we consider that the MoS<sub>2</sub> nitridation through the AlN seed is performed in a pure regime. It means that we only have an elementary process having a unique constant rate and diffusion coefficient. Hence, even though a pressure and temperature study will be implemented to elaborate a complete model, the complexity of the stack (multiple interfaces) and of the reaction mechanism will lead to a very complex model (without mentioned the possibility to have a mixed regime).

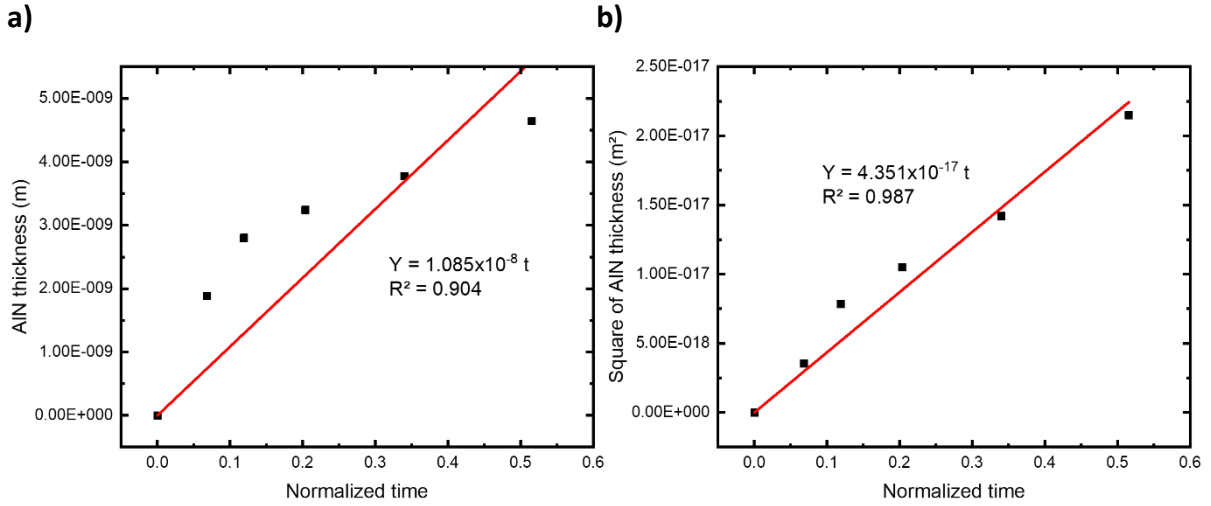


Figure IV.27: a) AIN thickness and b) square of AIN thickness as a function of  $dR405/dt = \max$  (inflection point)

However, to determine a diffusion coefficient of N in AlN, we pursue this study by applying a diffusion model based on Fick's law. This model is also briefly described in Annex part 2, section II.4. For this purpose, we assume that the N concentration at the inflection is  $C_0/2$  where  $C_0$  is the concentration leading to the total conversion of MoS<sub>2</sub>. From this assumption and the integration of the second Fick's law, we obtain:

$$c(x, t) = \frac{C_0}{2} = \frac{M}{\sqrt{\pi Dt}} e^{-\frac{x^2}{4Dt}} \Leftrightarrow x = \sqrt{-4Dt \ln\left(\frac{C_0 \sqrt{\pi Dt}}{2M}\right)} \quad \text{Equation IV.5}$$

Where  $M$  is a constant related to an amount of matter,  $D$  is the diffusion coefficient and  $C$  is the concentration leading to the total conversion of MoS<sub>2</sub>.

By defining  $M$ ,  $D$  and  $C_0$  as fitting parameters and applying this equation to the curve plotted in Figure IV.27 b), we can extract a diffusion coefficient of N in AlN:  $D \approx 2.42 \times 10^{-21} \text{ m}^2 \cdot \text{s}^{-1}$ . This value is difficult to compare since, to the best of our knowledge, no publication mention a diffusion coefficient of N in AlN. However, a similar value of  $D = 5.7 \times 10^{-20} \text{ m}^2 \cdot \text{s}^{-1}$  has been reported by Abautret et al.<sup>435</sup> for the diffusion of N in titanium nitride (TiN). Hence, the diffusion coefficient  $D$  determined is not absurd and could well described the N diffusion in AlN.

#### IV.2.4.2.2. MoS<sub>2</sub> chemical modification (Raman) and process transfer in an industrial equipment

To confirm the changes of the 2D-MoS<sub>2</sub> through the AlN seed layer, Raman spectroscopy has been achieved. Figure IV.28 presents Raman spectrum of MoS<sub>2</sub> + AlN 8s after the NH<sub>3</sub> heat treatments perform in the home-made furnace and is compared with the typical MoS<sub>2</sub> Reference Raman spectrum. It displays that both E<sub>2g</sub><sup>1</sup> and A<sub>1g</sub> MoS<sub>2</sub> Raman modes located at

$\approx 382 \text{ cm}^{-1}$  and  $\approx 407 \text{ cm}^{-1}$  completely vanished (the peak at  $\approx 520 \text{ cm}^{-1}$  is attributed to the Si substrate). It seems to confirm that R405 *in situ* changes observed previously is due to a modification of the stack and especially on MoS<sub>2</sub>.

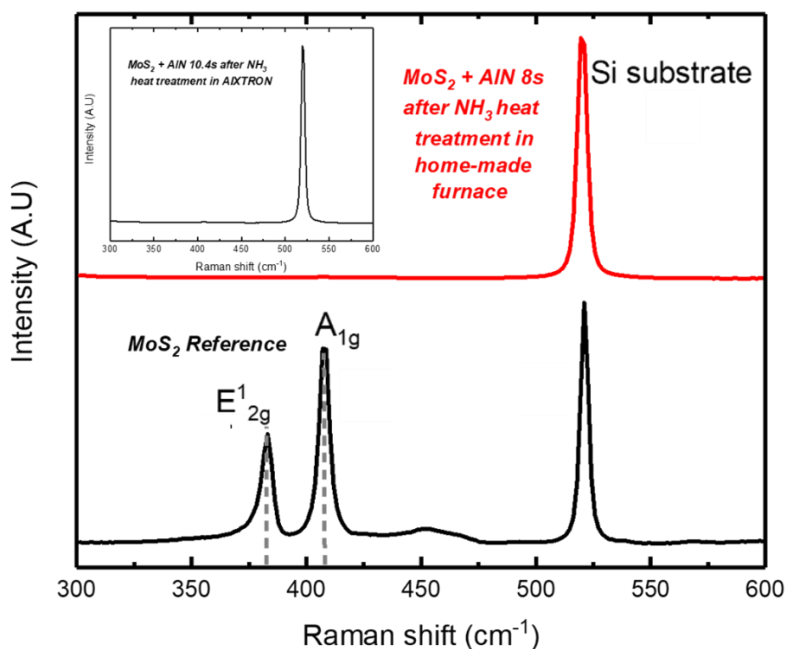


Figure IV.28: Raman spectra of MoS<sub>2</sub> Reference before heat treatment and MoS<sub>2</sub> + AIN 8s after 1000 °C NH<sub>3</sub> heat treatment. The inset presents the Raman spectrum of MoS<sub>2</sub> + AIN 10.4s after NH<sub>3</sub> heat treatment in AIXTRON equipment

These results also seem to confirm that we have identified suitable conditions (temperature, pressure and duration) in the home-made furnace enabling to modify the MoS<sub>2</sub> layer. Hence, we have transferred this process in an industrial equipment located at CEA-LETI: an AIXTRON CRIUS R200 MOCVD reactor. A similar NH<sub>3</sub> heat treatment to that performed in the SIMaP home-made furnace has been implemented on a MoS<sub>2</sub> + AIN 10.4s sample. The resulting Raman spectrum is presented in the inset of Figure IV.28. Similarly to the results obtained in the home-made furnace, we clearly observe that both E<sub>12g</sub> and A<sub>1g</sub> MoS<sub>2</sub> Raman modes located at  $\approx 382 \text{ cm}^{-1}$  and  $\approx 407 \text{ cm}^{-1}$  completely vanished and only a peak coming from the Si substrate remains. It seems to confirm that the process has been successfully transferred to the AIXTRON tool. Subsequently, the annealing conditions have been optimized and are reported in Table IV.7.

Sample name	AIN deposition time (s)	Temperature (°C)	NH <sub>3</sub> Flow (sccm)	NH <sub>3</sub> pressure (mbar)	Time (min)
MoS <sub>2</sub> + AIN 4s	4 s	1000	3000	400	10
MoS <sub>2</sub> + AIN 6s	6 s	1000	3000	400	10
MoS <sub>2</sub> + AIN 8s	8 s	1000	3000	400	10
MoS <sub>2</sub> + AIN 10.4s	10.4 s	1000	3000	400	10

Table IV.7: Experimental conditions of the NH<sub>3</sub> heat treatments performed in AIXTRON on MoS<sub>2</sub> + AIN xs

From now, we only focus only the samples treated in the AIXTRON equipment.

#### IV.2.4.2.3. Surface chemical analysis (XPS)

To confirm the potential change in composition of MoS<sub>2</sub> through the AlN seed layer after 1000 °C NH<sub>3</sub> heat treatment, we achieved X-ray photoelectron spectroscopy on *MoS<sub>2</sub> + AlN 4s*, *MoS<sub>2</sub> + AlN 6s*, *MoS<sub>2</sub> + AlN 8s* and *MoS<sub>2</sub> + AlN 10.4s* before and after heat treatments.

The Mo 3*d* regions for the *MoS<sub>2</sub> + AlN 4s* samples before and after heat treatment under are visible in Figure IV.29 (and detailed in Annex part 3, section III.2.4). Mo 3*p*/N 1*s* region are not treated since N 1*s* contribution is predominant due to the presence of Al and N bonds from top AlN seed layer. Moreover, the binding energies between Mo and N and Al and N bonding are very similar making deconvolution difficult.

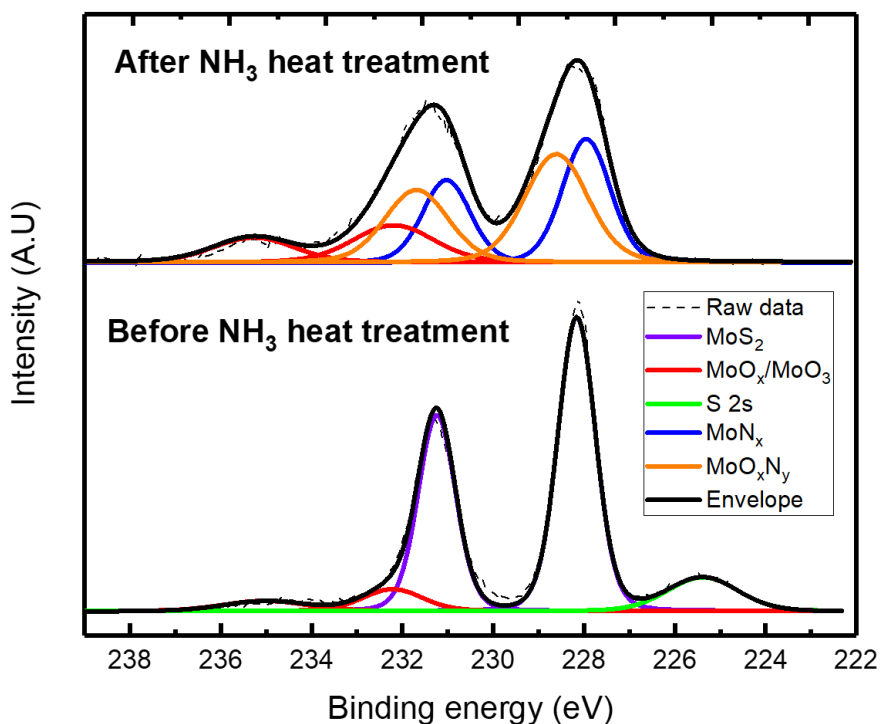


Figure IV.29: XPS spectra of *MoS<sub>2</sub> + AlN 4s*, Mo 3*d* regions before and after 1000 °C NH<sub>3</sub> heat treatment

Deconvolution of the Mo 3*d* region before heat treatment clearly displays two peaks at 228.2 eV and 231.2 eV corresponding to Mo<sup>4+</sup> 3*d*<sub>5/2</sub> and Mo<sup>4+</sup> 3*d*<sub>3/2</sub>, respectively, and attributed to Mo-S bond (down-shifting of the binding energies positions with AlN capping compared to a *MoS<sub>2</sub> Reference* sample is explained Annex part 3, section III.2.2). The Mo3 *d*<sub>5/2</sub> and Mo3 *d*<sub>3/2</sub> peaks at 232.2 eV and 235.0 eV are attributed to Mo<sup>6+</sup> state corresponding to a small amount of MoO<sub>3</sub> at the top surface. We also observe a slight peak at 225.4 eV attributed

to S 2s due to the overlapping of Mo 3d with S 2s spectrum. The corresponding, S 2p contribution is also visible in another energy region (see Annex part 3, section III.2.4).

After heat treatment, we clearly observe a change in the XPS signal. First, we notice the absence of S 2s signal while Mo 3d is still visible with multiple environments. The disappearance of the S 2s signal is also confirmed in S 2p region. Second, the Mo 3d FWHM is larger after annealing than prior, indicating a noticeable evolution in the Mo bonding environment. By deconvoluting Mo 3d spectra, we can attribute the Mo 3d<sub>5/2</sub> and Mo 3d<sub>3/2</sub> peaks at 228.0 eV and 231.0 eV, respectively, to Mo-N bond<sup>420 421</sup> which is the main part of the spectra. Peaks located at 228.6 eV and 231.7 eV are attributed to molybdenum oxynitride which is probably a mixture of MoO<sub>2</sub>, MoO<sub>3</sub> and Mo<sub>2</sub>N<sup>426</sup>. Finally, the Mo 3d<sub>5/2</sub> and Mo 3d<sub>3/2</sub> peaks at 232.2 eV and 235.3 eV are assigned to a slight amount of MoO<sub>x</sub> which is also present before AlN deposition as indicated in section III.1.3.2.

To conclude, the disappearance of S 2s (and S 2p) contributions coupled with the Mo 3d deconvolution highlighting different Mo(O<sub>x</sub>)N<sub>y</sub> environments prove the effective chemical conversion of the 2D-MoS<sub>2</sub> during the NH<sub>3</sub> heat treatment. It strongly suggests that the N species diffuse in the AlN seed layer and convert MoS<sub>2</sub> into Mo(O<sub>x</sub>)N<sub>y</sub> layer.

In addition, in Annex part 3, section III.2.4, we note an increase in the Si atomic concentration after NH<sub>3</sub> heat treatment which could be due to the formation of a discontinuous film or a densification of the stack (Si signal is incoming from the bottom SiO<sub>2</sub> substrate below the layers). A densification of the stack could be due to the effective conversion of the MoS<sub>2</sub> VdW inter-distance into a denser inter-layer. Finally, a 1000 °C heat treatment under ammonia also seems to modify the bottom SiO<sub>2</sub>. In fact, a shoulder of Si 2p signal (not presented here) is visible after heat treatment due to the appearance of a new environment around 101 eV and 102 eV and attributed to SiO<sub>x</sub>N<sub>y</sub><sup>436,437</sup>. This environment is not present after a 700 °C NH<sub>3</sub> heat treatment without the AlN seed layer, which could indicate that the temperature was not high enough to induce the nitridation under ammonia of the bottom substrate. The presence of SiO<sub>x</sub>N<sub>y</sub> confirms the real diffusion of N through the stack.

However, even though these results prove the effective conversion of MoS<sub>2</sub> into Mo(O<sub>x</sub>)N<sub>y</sub> through the AlN seed layer, they also raise an important question: where are the sulphur atoms and by which mechanism they can vanish? We hypothesized that sulphur atoms have



diffused into the substrate after thermal anneal. Time-of-Flight Secondary Ion Mass Spectrometry (ToF-SIMS) was performed and no sulphur was detected in the stack or within the substrate suggesting that sulphur atoms have rather counter-diffused through the AlN seed layer. We will discuss this point in section IV.2.4.2.

IV.2.4.2.4. Structural properties (XRD)

To further confirm the formation of a new molybdenum nitride phase, XRD measurements were carried before and after NH<sub>3</sub> heat treatment. Figure IV.30 a) and b) show the in-plane XRD spectra before and after NH<sub>3</sub> heat treatment, respectively, for each sample: MoS<sub>2</sub> + AlN 4s, MoS<sub>2</sub> + AlN 6s, MoS<sub>2</sub> + AlN 8s and MoS<sub>2</sub> + AlN 10.4s.

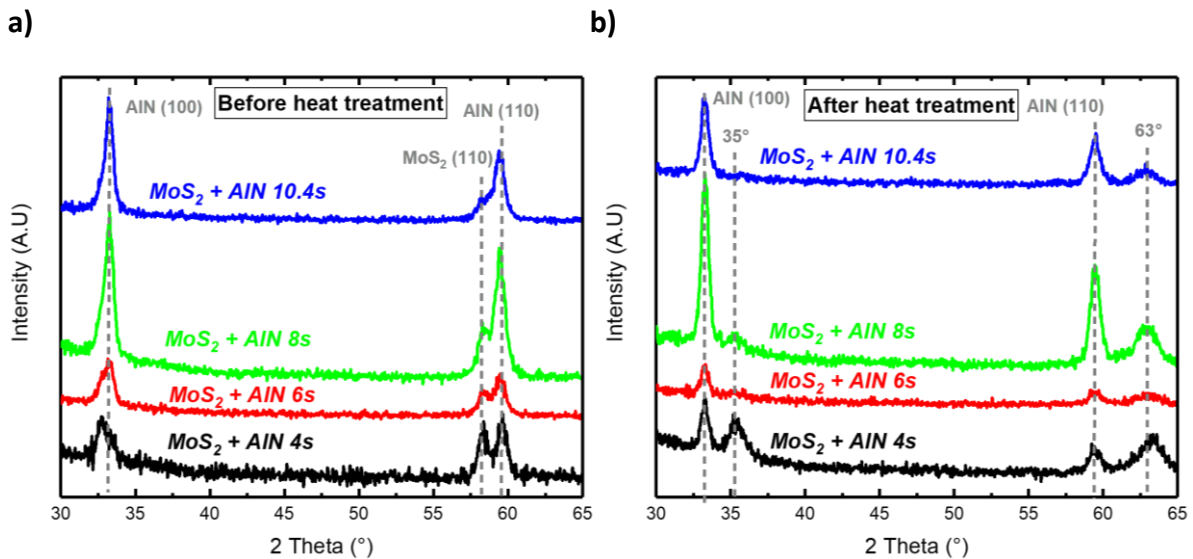


Figure IV.30: In-plane XRD diffractograms of MoS<sub>2</sub> + AlN xs a) before and b) after 1000 °C NH<sub>3</sub> heat treatment

Before heat treatment, in-plane measurements display three distinct peaks. Two of them located at  $2\theta \approx 33.2^\circ$  and  $2\theta \approx 59.5^\circ$  are attributed to AlN (100) and AlN (110) planes, respectively. The last one at  $58.3^\circ$  corresponds to the MoS<sub>2</sub> (110) plane diffraction. After heat treatment, AlN planes are still visible but the MoS<sub>2</sub> planes have vanished. This first observation agrees with the previous Raman and X-Ray Photoelectron Spectroscopy (XPS) characterizations. We also observe two new slight peaks located at  $2\theta \approx 35^\circ$  and  $2\theta \approx 63^\circ$  after heat treatment. Their attributions are uncertain but they could be attributed to a MoN<sub>0,46</sub> or a Mo<sub>2</sub>N alloy. In any case, whatever the precise structure formed after the MoS<sub>2</sub> modification, these analyses confirm that MoS<sub>2</sub> has been well modified and the quality of the thin AlN PVD seed layers seems to be preserved.

## IV.2.4.2.5. Crystal quality and chemical composition (TEM/EDX)

Previous analysis, and especially X-Ray Photoelectron Spectroscopy (XPS), clearly highlight that MoS<sub>2</sub> is chemically modified as well as MoS<sub>2</sub>/SiO<sub>2</sub> interface. In this context, Transmission Electron Microscopy (TEM) was performed to observe the MoS<sub>2</sub>/SiO<sub>2</sub> interface after NH<sub>3</sub> heat treatment. The experimental conditions of these TEM/EDX measurements performed in this work are briefly detailed in Annex part 2, section II.1.5.

Cross-sections of MoS<sub>2</sub> + AlN 10.4s at different magnifications are shown in Figure IV.31. They indicate a totally different stack compare to the one presented in section III.1.2 where we clearly observe a homogenous and continuous MoS<sub>2</sub> film with its VdW structure. After NH<sub>3</sub> heat treatment, cross-sections display a discontinuous film instead of 2D-MoS<sub>2</sub>. This structural reorganization lead to the formation of islands up to several tens of nanometers. Therefore, the AlN seed is locally directly anchor onto the SiO<sub>2</sub> substrate which is favourable to ensure its adhesion. The magnification at atomic resolution image shows that MoS<sub>2</sub> is modified into a covalent structure, no VdW interactions are visible anymore. It strongly suggests that the issues at the origin of the delamination are solved with this NH<sub>3</sub> reactive heat treatment. Moreover, even if the AlN seed is very thin, it seems well crystallized and displays distinct planes parallel to the growth direction suggesting a preferential c-axis textured growth.

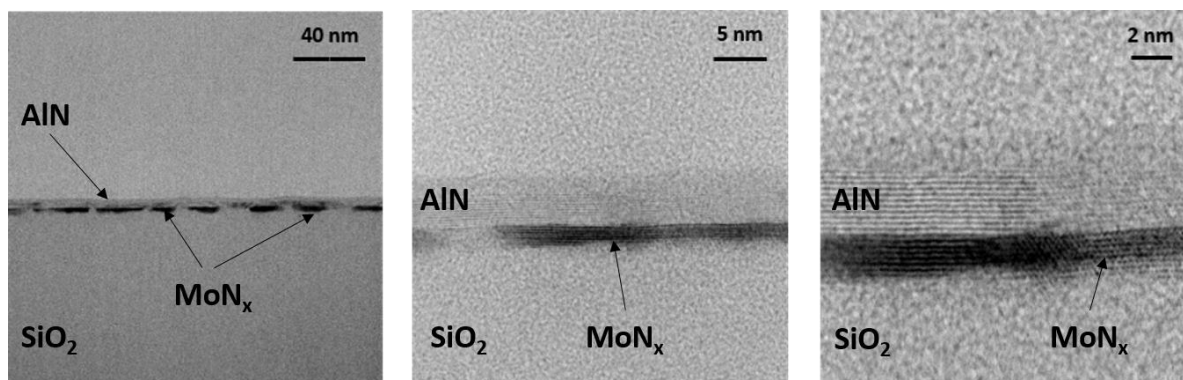


Figure IV.31: Cross-sectionnal TEM images at different magnifications of MoS<sub>2</sub> + AlN 10.4s sample after 1000 °C NH<sub>3</sub> heat treatment

TEM analysis were coupled with Energy Dispersive X-Ray (EDX). The measurements are presented in Figure IV.32. Oxygen (O) signal in green mainly comes from the SiO<sub>2</sub> substrate and the top of the aluminium (Al) signal, indicating that the AlN top seed layer is significantly oxidized possibly due to the reventing of the sample. Silicon (Si) signal in cyan is predominant at the bottom of the image and comes from SiO<sub>2</sub>. Next, we focus on Mo signal in yellow. It corresponds to the bright area in the HAADF image. Such contrast in dark field is generally

associated to a mass contrast (Z-contrast). It confirms a structural reorganization in the form of islands due to the heat treatment which induces a kind of de-wetting of the Mo-based layer. Interestingly, the Mo islands seem recessed in the SiO<sub>2</sub> oxide, as if the oxide participates to the round shape of the Mo areas. This is possible if we imagine that at 1000°C, the SiO<sub>2</sub> starts to soften and affects the surface cohesion energy of the Mo-based layer leading to round shapes. Finally, the N signal in red is associated to Al, and part of the nitrogen seems localized on the Mo islands.

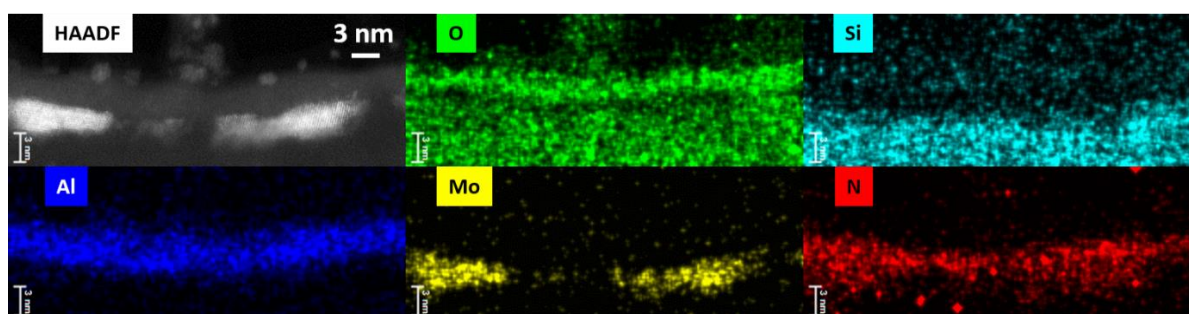


Figure IV.32: Energy dispersion mappings of the AlN/MoS<sub>2</sub>/SiO<sub>2</sub> interfaces after 1000 °C NH<sub>3</sub> heat treatment

Thus, even if EDX characterization does not allow to obtain quantitative analysis but only qualitative, the presence of Mo and N signals in the same bright areas coupled with XPS and XRD results seems to strongly confirm the formation of a molybdenum (oxy)nitride islands after the NH<sub>3</sub> heat treatment.

#### IV.2.4.2.6. Phase and orientation mapping (ACOM)

ACOM is an automatic crystallographic indexing and orientation phase mapping tool developed at SIMaP laboratory and which can be adapted to any Transmission Electronic Microscope. This technique is briefly described in Annex part 2, section II.1.7 and we can also refer to Rauch et *al.*<sup>438</sup> study to obtain a detailed explanation of the technique.

The phase and Z-orientation mapping outputs of the tool as well as indexing are shown in Figure IV.33. The orientations indexing corresponds to a crystallographic map. The X- and Y-orientation mapping are not presented due to a low reliability which could lead to misinterpretation.

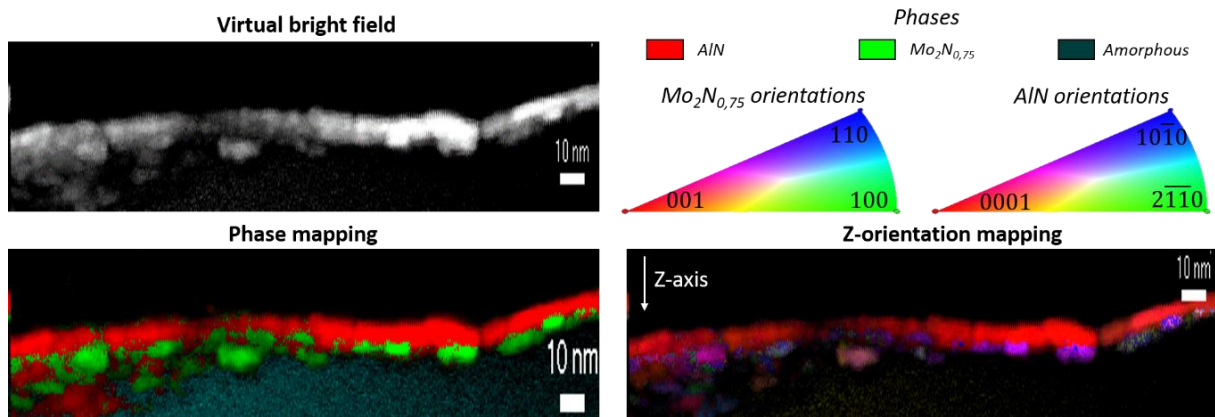


Figure IV.33: Phase and orientations mappings obtained with ASTAR technique on MoS<sub>2</sub> + AlN 10.4s after 1000 °C NH<sub>3</sub> heat treatment

The phase mapping is relatively easy to interpret. We clearly observe three different phases. The first phase in red is the AlN seed layer laying on the surface. We see that the AlN covers the entire surface of the sample. The second phase in green is the molybdenum nitride. It is located under the AlN seed layer. As observed in the TEM images, these domains are discontinuous confirming a structural reorganization during heating. Two different phases (MoN<sub>0.5</sub> and Mo<sub>2</sub>N<sub>0.75</sub>) were assumed. Indexing with Mo<sub>2</sub>N<sub>0.75</sub> is slightly better than MoN<sub>0.5</sub> but the phase reliability factor between these two molybdenum nitrides is low. The size of the molybdenum nitride diffracting volume is quite small and the ACOM reaches a limit in term of measurement precision. Therefore, the small diffraction volumes together with the acquisition spot size leads to uncertainties in the identification of a precise molybdenum nitride phase. Finally, the Z-orientation mapping indicates that the AlN is mainly (0001) oriented which confirms its preferential c-axis orientation normal to the surface. Hence, AlN seems well aligned to induce a c-axis texturation of a second AlN thick deposition.

#### IV.2.4.2. 2D-MoS<sub>2</sub> seed layer modification: mechanism proposal

The characterizations performed to proof and understand the chemical modifications of the 2D-MoS<sub>2</sub> through the AlN seed layer enable to propose a potential mechanism. This mechanism is presented in Figure IV.34 and described hereafter.

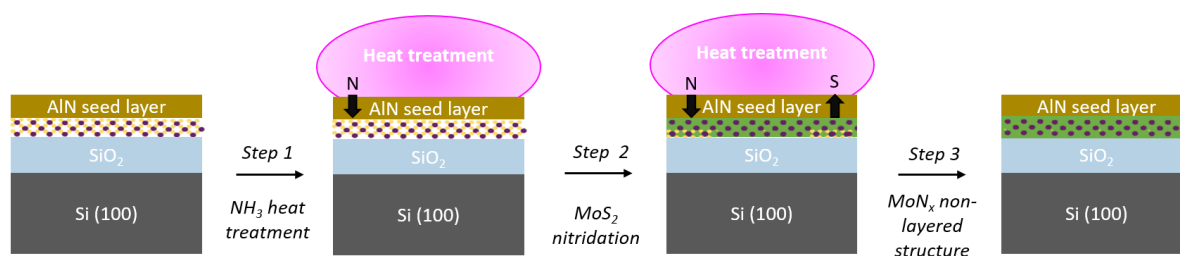


Figure IV.34: Mechanism proposal of the 2D-MoS<sub>2</sub> chemical modification through the AlN seed layer during 1000 °C NH<sub>3</sub> heat treatment

**Step 1:** during the 1000 °C heat treatment, NH<sub>3</sub> (g) arrives in the vicinity of the AlN seed surface and is adsorbed. Its adsorption leads to chemisorbed N atoms and a gas release (H<sub>2</sub> (g)). The adsorbed nitrogen diffuses in the AlN seed layer through the grain boundaries up to the 2D-MoS<sub>2</sub> sub-layer.

**Step 2:** N reacts with MoS<sub>2</sub> and leading to the formation of a molybdenum nitride MoN<sub>x</sub>:  $xN (s) + MoS_2 (s) \rightarrow MoN_x (s) + 2S (s)$ . It leads to a conversion of the Van der Waals interactions into strong covalent bonds and results in an increase of the adherence of the AlN seed layer on the substrate. The MoS<sub>2</sub>/SiO<sub>2</sub> interface is also transformed since SiO<sub>2</sub> substrate is partially nitride. Since no sulphur atoms were detected in the stack nor in the substrate, S probably counter-diffuses through the grain boundaries of the AlN seed layer and forms H<sub>x</sub>S (g) (probably H<sub>2</sub>S(g)) at the surface. Yet, we didn't prove the counter-diffusion of S and the formation of H<sub>2</sub>S (g), since it probably requires other experimental setups that could include NH<sub>3</sub>/H<sub>2</sub> mixtures with and without H<sub>2</sub>S. However, we think that it is the most probable scenario. Following this idea, a nitridation in a reducing ambient seems mandatory to insure the correct conversion of the 2D-sulphide.

**Step 3:** at the end of the heat treatment, 2D-MoS<sub>2</sub> seed layer is fully converted into MoN<sub>x</sub>. This MoN<sub>x</sub> layer can be slightly oxidized since a small amount of oxygen is present in the as-deposited MoS<sub>2</sub>. Moreover, the change in structure lead to structural reorganization resulting in a discontinuous film. Thus, the AlN seed layer is locally anchor onto the SiO<sub>2</sub> substrate enhancing its adherence.

IV.2.4.3. Second thick AlN growth after NH<sub>3</sub> heat treatment

Similarly, to plasma treatment approach, a second 100 nm thick AlN PVD growth was performed on each sample after NH<sub>3</sub> heat treatment samples in taking care to reduce the time between the heat treatment and AlN PVD deposition to prevent the surface oxidation. Then, the c-axis orientation was assessed by X-Ray Diffraction RC measurements. The obtained RC values after the 100 nm thick AlN growth as a function the AlN deposition time (4s, 6s, 8s and 10.4s) of the seed layer are plotted in Figure IV.35.

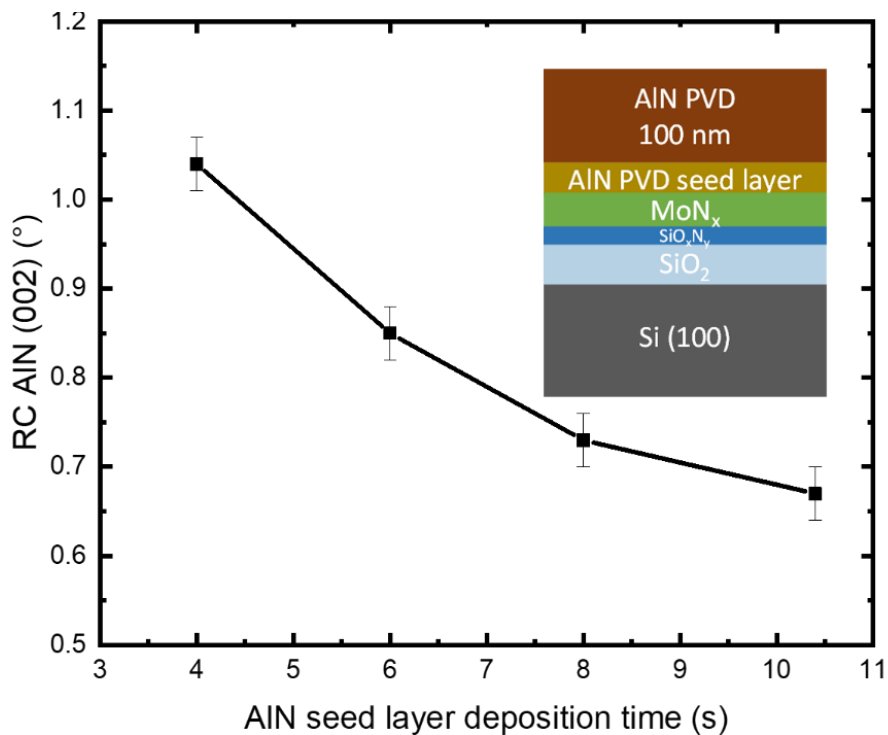


Figure IV.35: AlN (002) RC measurements of the 100 nm AlN PVD growth on MoS<sub>2</sub> + AlN xs samples after 1000 °C NH<sub>3</sub> heat treatment

The figure shows that the second AlN growth is oriented along the c-axis. Also, the AlN c-axis orientation is reduced (and subsequently improved) on a thick AlN PVD seed layer. A value of 0.67° is obtained for the 100 nm thick second AlN growth deposited on the 10.4s AlN seed. This value competes with the one reported by Dadgar et al.<sup>439</sup> (0.63°) using an Al seed layer before a 900 °C PVD deposition of a 0.1 μm thick AlN thin film. However, in this work, the AlN PVD deposition temperature is significantly lower (350 °C). These results are in line with the AFM measurements presented in Annex part 3, section III.3, in which the AlN seed surface integrity is better preserved for the thicker layer (10.4s). Hence, it results in a better c-axis orientation of the AlN regrowth.

This result opens up an axis of development. What is the optimized thickness of the AlN seed layer which result in the best c-axis orientation of the second AlN growth? To address this point, we performed the same 1000 °C NH<sub>3</sub> heat treatment to modify the 2D-MoS<sub>2</sub> through a 21 s AlN seed layer ( $\approx$  10 nm). However, the MoS<sub>2</sub> layer was preserved. This result suggests that, in the investigated conditions, the AlN seed layer is too thick to enable the NH<sub>x</sub> species diffusion up to the 2D-MoS<sub>2</sub> sub-layer. Hence, the optimized AlN seed layer thickness seems to be between  $\approx$  5 nm (10.4 s) and  $\approx$  10 nm (21 s).

Finally, to check if this NH<sub>3</sub> heat treatment approach is an adequate solution to solve the delamination issue, a 1  $\mu$ m thick AlN PVD growth was performed on MoS<sub>2</sub> + AlN 10.4s after heat treatment. Figure IV.36 a) and b) displays the XRD  $\omega$ -scan and tape test after 1  $\mu$ m thick AlN deposition, respectively.

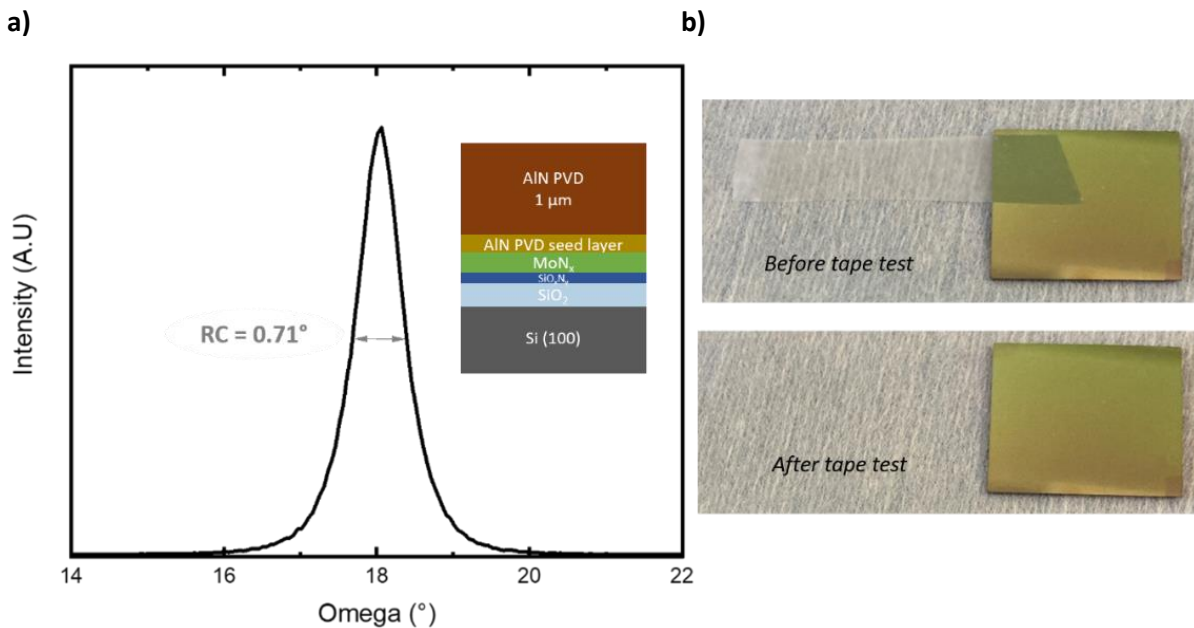


Figure IV.36: RC AlN (002) of a 1  $\mu$ m thick AlN PVD growth on MoS<sub>2</sub> + AlN 10.4s sample after 1000 °C NH<sub>3</sub> heat treatment ; b) pictures of tape test after the 1  $\mu$ m AlN PVD deposition

First, the RC measurement confirms that the thick AlN layer is aligned along the c-axis perpendicular to the growth surface with a RC = 0.71 $^{\circ}$ . Notice that such low RC value for a 1  $\mu$ m thick AlN sputtered layer has never been published in the literature on a silicon-based substrate. Then, the tape test gives a direct proof on the improvement of the AlN adhesion on the silicon substrate and demonstrates the proof of concept of this approach to solve the delamination issue.

*IV.2.4.4. Conclusions and perspectives on the heat treatments*

First, the thermal budget affects the 2D-MoS<sub>2</sub> seed layer and enables to identify suitable to potentially transform MoS<sub>2</sub> into molybdenum nitride. Then, the proof of concept of the 2D-MoS<sub>2</sub> chemical “remote” modification through a thin AlN seed into Mo(O<sub>x</sub>)N<sub>y</sub> has been demonstrated through different characterizations under NH<sub>3</sub> heat treatment at 1000 °C. Second, in order ensures the c-axis oriented regrowth of AlN on silicon-based substrate using a 2D-MoS<sub>2</sub> as template, the NH<sub>3</sub> heat was implemented through a thin AlN PVD seed layer. The thickness of this AlN requires optimisation in term of thickness to ensure the c-axis regrowth of AlN. It must also be thin enough to enable the diffusion of nitrogen-based species. Moreover, the heat treatment conditions were investigated, and an optimized point at around 1000°C under NH<sub>3</sub> was found and suitable to nitride the 2D-MoS<sub>2</sub> through the AlN PVD seed. This modification has been demonstrated through several characterizations enabling to propose a mechanism presented in section IV.2.4.2. Finally, by followed closely the second thick AlN PVD growth after the NH<sub>3</sub> heat treatment to prevent the surface oxidation, the c-axis orientation of the thin AlN PVD seed layer is transferred to the second thicker deposition. But beyond this transfer of preferential orientation, the AlN deposition is adherent to the substrate solving the delamination issue.

Optimal conditions were found in this study including a 3 monolayers MoS<sub>2</sub>, capped with 10.4s AlN seed, which corresponds to ≈ 5 nm in thickness, and followed by a 1000°C NH<sub>3</sub> annealing at 400 mbar. By improving these parameters individually or in group, it could be possible to obtain a micrometer thick AlN PVD layer on a silicon-based substrate without any delamination and enhancing the reported record value of RC = 0.71°. Hence, higher NH<sub>3</sub> pressures could be investigated to favour a quicker MoS<sub>2</sub> modification and reduce the thermal budget (time and temperature). Also, studies on native SiO<sub>2</sub> or chemical oxide on Si, or SiN substrate must be achieved to see if the formation of Mo(O<sub>x</sub>)N<sub>y</sub> islands is still effective on such substrates, and mandatory to address the delamination issue. In that sense, the role of SiO<sub>2</sub>, which is close to a molten matter at 1000°C, could play a fundamental role on the Mo(O<sub>x</sub>)N<sub>y</sub> islands formation. Following this idea, a 1000°C temperature or so must be at least required to induce the transformation. Finally, the counter-diffusion of S must be clarify in particular the formation of H<sub>2</sub>S, and its counter diffusion through the AlN seed layer. This may be useful to expand this work to other 2D layers, such as selenides or tellurides 2D films.



### IV.3. Conclusions of Chapter 4

This chapter described solutions based on the thermochemical modification of the 2D-MoS<sub>2</sub> to solve the delamination issue. This path was divided in two sections, either plasma or thermal treatments.

In the first section, we investigate plasma treatments in which a mechanical contribution (implantation) is coupled with a thermal contribution (450 °C). On one hand, plasma treatments have a noticeable physical impact on the surfaces, which leads to degradations, and limits any possible regrowth of a well-textured AlN layer. Hence, the use of a remote plasma could be a way to reduce the physical impact and preserve the surface integrity (surface and oxidation). On the other hand, the chemical effect is almost insignificant as AlN, which shows barrier properties against N\* radicals below 450°C. Therefore, we did not find a satisfactory process window to grow an adherent and textured AlN PVD layer. Hence, investigated temperatures above 450 °C (typically up to 700 °C) in a thermal tool equipped with a plasma source could be an interesting perspective to increase the thermal contribution and favour N\* diffusion through the AlN seed.

In the second section, we studied the thermal heat treatment under NH<sub>3</sub> enabling to cover higher temperatures than plasma treatment. We show that it is suitable way to nitride MoS<sub>2</sub>, remotely through a thin AlN seed layer. The MoS<sub>2</sub> modification into molybdenum (oxy)nitride was confirmed enabling to propose a mechanism based on the diffusion of N through the AlN seed, the conversion of MoS<sub>2</sub> into MoN<sub>x</sub> and the S counter-diffusion. This mechanism leads to the conversion of the Van der Waals interaction into strong covalent bonds as well as of the transformation of the MoS<sub>2</sub>/SiO<sub>2</sub> interface with the partial nitridation of the bottom substrate made of thermal oxide. These changes are also associated to structural reorganisation resulting in a discontinuous film suitable to anchor AlN onto the SiO<sub>2</sub> substrate.

Finally, we show that this modified stack allows thick AlN regrowth up to at least 1 µm without delamination. The regrown AlN follows the crystalline orientation of the bottom seed layer, and results on a c-axis oriented AlN perpendicular to the growth surface, with a maximum off-axis orientation of the grains of 0.71°. This solution opens a new low-cost and easier way to process high quality AlN on silicon-based substrates. The next step is to doped AlN with other elements such as scandium (Sc), and assess if the crystalline quality is still

appropriate for the filter application. Also, this approach makes use of a thin PVD seed layer, followed by a thick AlN PVD regrowth. We wonder if the modified AlN seed/MoS<sub>2</sub> stack could be used as a nucleation surface to AlN deposition by CVD, and see if epitaxial growth could be possible. These points are addressed in the next chapters of this manuscript.



## V. Chapter 5: AlN and Sc doped AlN growth post 2D-MoS<sub>2</sub> chemical modification

The proof of concept of the resolution of the delamination issue (chapter 4) while preserving a highly c-axis textured film enables to push further this approach for AlN PVD deposition. Firstly, we initiate a deeper study on the AlN crystal quality with various thickness (100 nm up to 1 μm) deposited by PVD. It is focused on the influence of AlN thickness on different parameters such as mosaicity or stress/strain. We also address the potential structural or chemical evolution of the initial 2D-MoS<sub>2</sub> layer converted into MoN<sub>x</sub> during the PVD growth. Secondly, we investigate the PVD growth Sc doped AlN (Sc<sub>x</sub>Al<sub>1-x</sub>N) and characterize the films by XRD to assess the mosaicity and stress/strain. Finally, as the 2D-MoS<sub>2</sub> layer is totally transformed and capped with an AlN PVD seed layer, this proof of concept is not limited to low-temperature AlN PVD deposition. Hence, this approach is extended to AlN MOCVD deposition. Thus, we compare the results obtained on the AlN growth by PVD with AlN MOCVD films with a thickness of 200 nm, 400 nm and 600 nm to highlight the influence of the growth method and the deposition temperature on the AlN crystal quality.

As a reminder, Figure V.1 presents the process implemented including the 2D-MoS<sub>2</sub> nitridation (step 1) through the AlN PVD seed layer and the AlN or Sc doped AlN growth (step 2). The step 1 is simplified but we can refer to the chapter 4, section IV.2.4.2, in which a reaction mechanism is proposed for more details.

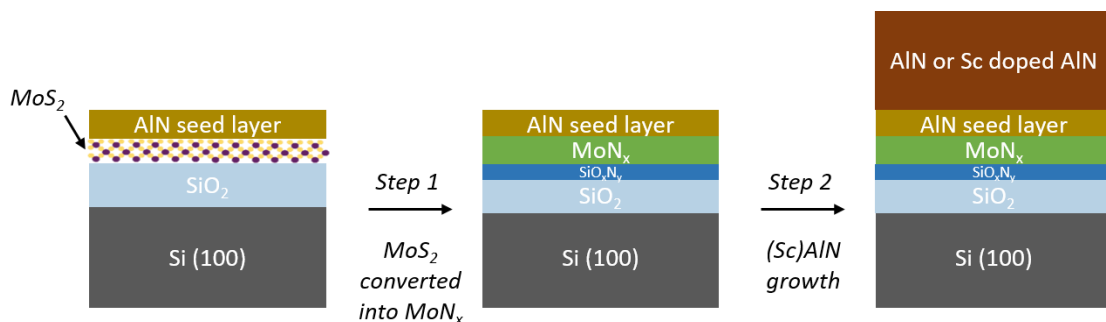


Figure V.1: MoS<sub>2</sub> nitridation through the AlN PVD seed layer followed by AlN or Sc doped AlN growth

### V.1. Elaboration of AlN films by Physical Vapor Deposition (PVD) post-MoS<sub>2</sub> modification

AlN thin films were deposited as described in section III.2.3 in a SPTS (Trikon) Sigma fxP 200 mm magnetron PVD reactor. To remind, the deposition is performed at 350 °C with a standard target power of 2 kW. The argon and nitrogen flow rates for the plasma are set to 10 sccm and 50 sccm, respectively, and no bias was applied during the deposition. The deposition time was varied in order to elaborate AlN films with a targeted thickness of 100 nm, 200 nm, 400 nm, 600 nm, 800 nm and 1 μm.

#### V.1.1. Characterizations

##### V.1.1.1. Mosaicity

To assess the mosaicity, a  $\omega$ -scan XRD measurement on AlN (002) planes was performed for each AlN deposition. The AlN (002) RC values are presented in Figure V.2 and compared with other RC values of AlN deposited by PVD from CEA-LETI capabilities on Si (100) substrate and literature issued from Annex part 1, Table VI, on various silicon-based substrates.

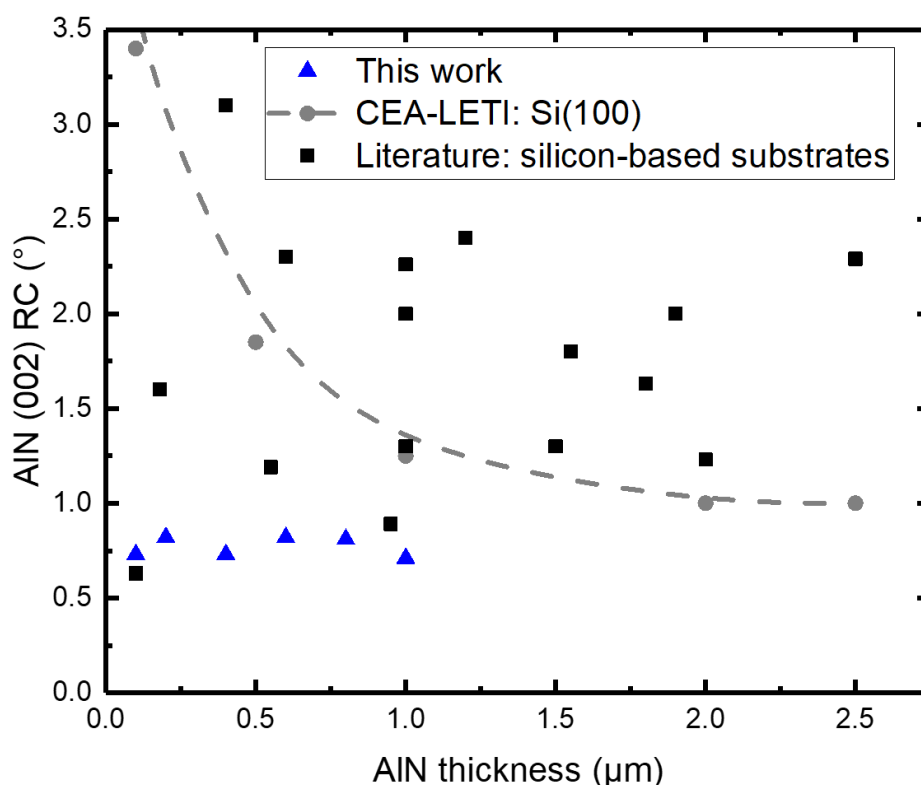


Figure V.2: Comparison of AlN (002) RC deposited by PVD on various silicon-based substrates from literature (black square), CEA-LETI capabilities (grey circle) and this work (blue triangle)

Values from the literature (black square) are relatively disparate and do not show a clear tendency as a function of AlN thickness. This result is expected since each study has its own PVD deposition conditions which can affect the crystal quality and c-axis orientation. However, as mentioned previously in this manuscript, we can refer to Murali et al.<sup>261</sup> study which investigated the thickness dependence on c-axis textured AlN films and highlighted a decrease in AlN (002) RC with the increase in thickness up to approximately 2  $\mu\text{m}$ . This tendency is clearly observed on CEA-LETI capabilities (grey dash curve) where AlN PVD is directly deposited on Si (100) 200 mm wafer with native oxide. The AlN (002) RC decreases with the thickness. The alignment of the AlN crystalline planes improves due to growth mechanisms reaching a RC close to  $1^\circ$  for a 2  $\mu\text{m}$  film<sup>261,440</sup>.

For AlN PVD films elaborated in this work, the results are notably different. Firstly, the RC values are lower than  $1^\circ$  (around  $0.7^\circ - 0.8^\circ$ ). This result has been confirmed several times with other similar samples. To our knowledge, these values are comparable with the lowest ever mentioned by Dadgar et al.<sup>267</sup> for an AlN film deposited by PVD on a Si (111) substrate. To remind, they use a two-steps deposition method which consists in a thin Al pre-deposition (around 2  $\text{\AA}$ ) before a thicker AlN growth at  $900^\circ\text{C}$ . They obtain an AlN (002) RC of  $0.63^\circ$  for a 0.1  $\mu\text{m}$  thick layer. This increase in c-axis textured growth should improve AlN piezoelectric properties. Hence, it could be interesting to integrate this stack in AlN-based RF devices. Secondly, there is no dependence of the AlN thickness on the RC values which is the opposite of what can be found in the literature. There is no improvement in AlN planes alignment during the growth. It suggests that the crystal quality and c-axis texture are limited by the quality of the thin AlN seed layer serving as a pre-texturizing film before a thicker growth. It allows to obtain very low RC values for thin AlN PVD films (few hundreds nm) but it highlights the importance of the crystal quality and c-axis orientation of the AlN seed layer. Therefore, improving the quality of this seed layer should increase the crystal quality of the thicker AlN growth.

#### *V.1.1.2. Strain/stress measurements*

The stress of the AlN films deposited by PVD has been determined with “Crystallit Group Method” (CGM) technique as described in Annex part 2, section II.1.4.2. As it is now possible to deposit an AlN films with a thickness above 100 nm, the diffracting volume increase enables to consider other planes for stress calculations. Therefore, (002), (004), (101), (102), (112) and

(203) planes are considered for all the AlN thicknesses, (103) and (213) planes have been added for 800 nm and 1  $\mu\text{m}$  thick AlN films.

Moreover, for these specific samples, it was also possible to determine the stress with Raman Spectroscopy at SIMaP facilities due the availability of a 325 nm wavelength laser. In fact, AlN  $E_2$  (high) Raman mode is usually used to determine AlN strain or stress<sup>441-445</sup>. Therefore, Raman acquisitions with a 325 nm wavelength laser diode in subtractive mode were performed on each sample. According to the literature, the position of the AlN Raman mode can slightly vary depending on the reference but is generally between  $656\text{ cm}^{-1}$  and  $658\text{ cm}^{-1}$ . In our case, a monocrystalline AlN sample was used as reference sample and assumed unstressed ( $E_2 = 656.3 \pm 0.1\text{ cm}^{-1}$ ). Stress calculations are based on Yang et al.<sup>444</sup> study indicating a linear relation between stress and  $E_2$  Raman position with a slope of  $-4.04 \pm 0.3\text{ cm}^{-1}/\text{GPa}$ . This slope value is also around  $-4\text{ cm}^{-1}/\text{GPa}$  in other publications<sup>442,443,445</sup>. The calculated stress with CGM method and Raman acquisitions are presented in Figure V.3.

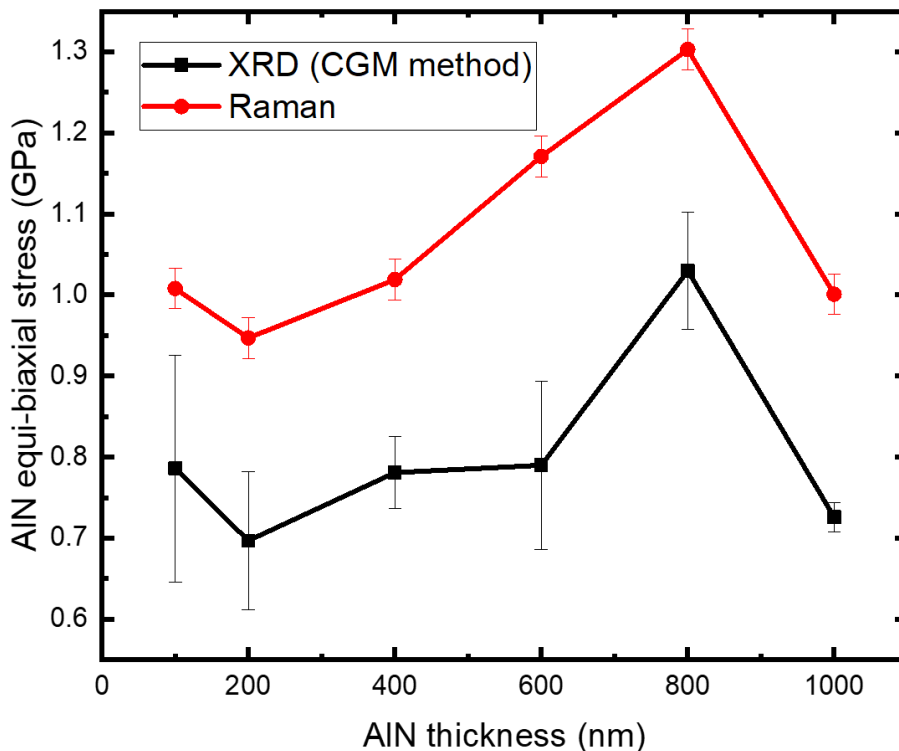


Figure V.3: AlN equi-biaxial stress determined by XRD (CGM method) and Raman spectroscopy

Firstly, AlN equi-biaxial stress determined by XRD via CGM method or Raman measurements follows the same tendency. Raman stress is just slightly higher by about 0.25 - 0.30 GPa. These results are essential since they validate the use of CGM method (or Raman)

to determine AlN stress. Secondly, as for RC measurements, AlN stress shows no thickness dependency. The stress oscillates between 0.7 – 0.8 GPa, except for the 800 nm thick AlN sample where it is 1.03 GPa. These results differ with some studies<sup>261,392</sup> that show different an increase in AlN stress with the thickness. Finally, in addition to c-axis orientation and independently to the deposition conditions, it strongly suggests that AlN stress is partially imposed by the thin AlN seed layer serving as a pre-texturizing film before a thicker growth. As previously mentioned, an interesting way to decrease the algebraic value of the AlN stress is to apply a bias during the PVD deposition.

To remind, and as explained in Annex part 2, section II.1.4.2, CGM method also enables to determine the AlN in-plane and out-of-plane strain. In fact, as presented in Figure V.4, for each sample, we observe a positive in-plane strain confirming a tensile equi-biaxial stress of the AlN PVD layer. It leads logically to a negative out-of-plane strain. Moreover, in-plane and out-of-plane strain show no AlN thickness dependency with a value around 0.18 % and -0.10 %, respectively. It seems to indicate that there is no relaxation of AlN planes with the increase in AlN thickness.

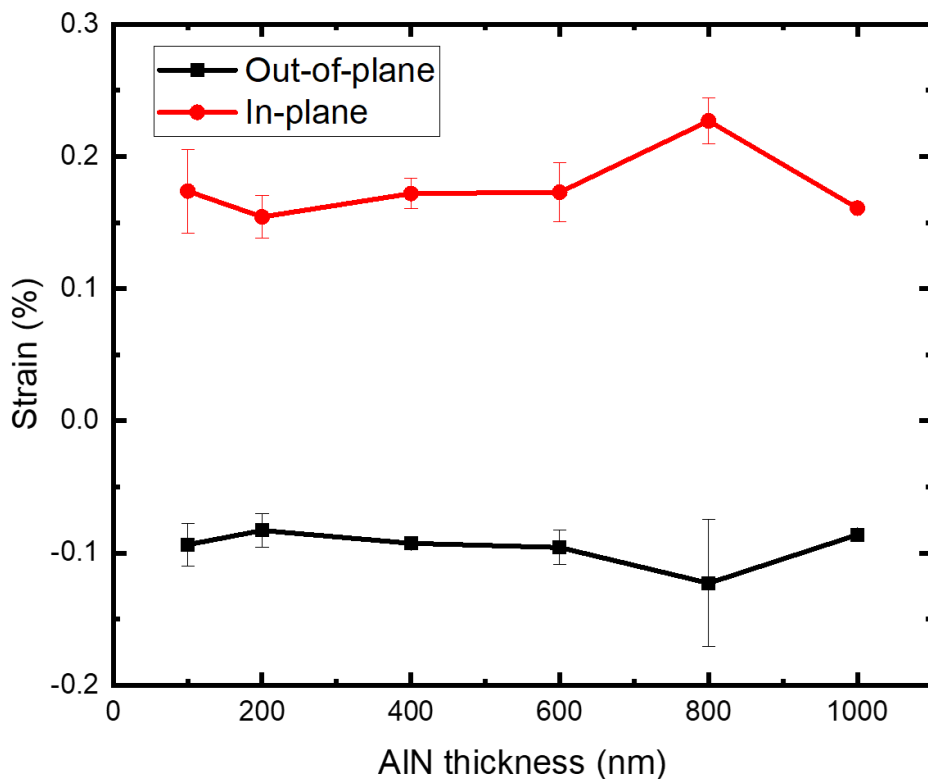


Figure V.4 : AlN in-plane and out-of-plane strain determined via CGM method



V.1.1.3. Crystal quality and chemical composition (TEM/EDX)

In order to observe the crystal quality of the thick AlN growth, the interfaces of interest, and a potential evolution of the modified seed layer during/after the AlN PVD growth, TEM observations were performed. Cross-sections of a 600 nm thick AlN growth at different magnifications are presented in Figure V.5.

On one hand, on the left TEM cross-section, we clearly observe vertical grains as well as their facets arranged in a typical columnar growth which is characteristic of a highly c-axis textured AlN film<sup>446–448</sup>. As mentioned in chapter 3, section III.2.4.1, this preferential orientation could be explained, either with a greater lateral growth of the certain seeds at the surface during the first stages of the growth, or by a Van der Drift type evolutionary selection mode where the (002) orientation would have the fastest growth rate compared to the other orientations. It is also worth to notice that the top surface on the AlN PVD seems relatively smooth.

On the other hand, this TEM cross-section displays a discontinuous MoN<sub>x</sub> film which is similar as the one presented in Figure IV.31. This observation is confirmed in the atomic scale resolution cross-section where the structural reorganization is still presents with the loss of Van der Waals interactions. We also have an abrupt and smooth interface between the AlN seed layer and the thicker AlN PVD regrowth. The AlN planes of both layers are well aligned perpendicular to the growth direction. It is even more obvious on the right TEM cross-section where these layers seem to be merged without clear interface suggesting a perfect epitaxial growth of the AlN seed layer and thicker PVD regrowth.

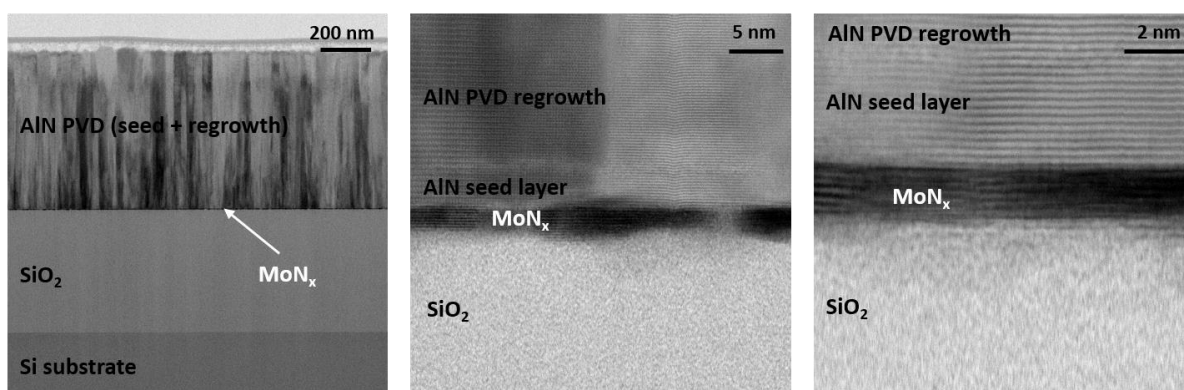
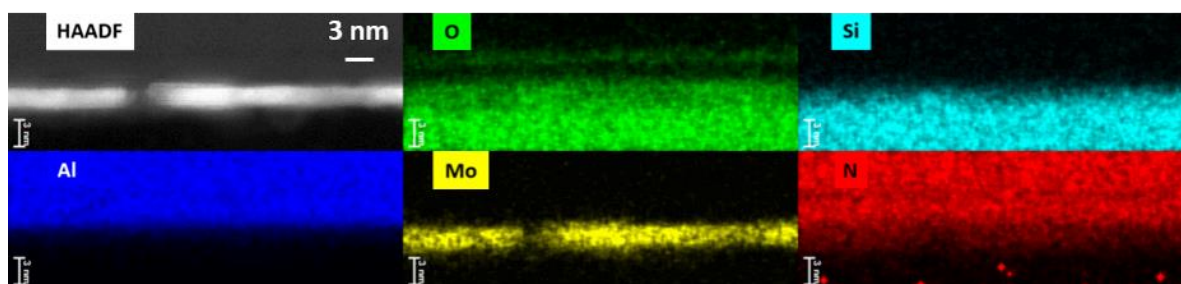


Figure V.5: Cross sectional TEM of AlN PVD regrowth/AlN seed layer/MoN<sub>x</sub>/SiO<sub>2</sub> interfaces

These TEM analysis were coupled with Energy Dispersive X-Ray (EDX). The measurements are presented in Figure V.6. As for EDX before the AlN PVD regrowth presented in Figure IV.32, oxygen (O) signal in green mainly comes from the SiO<sub>2</sub> wet thermal oxide. A thin O layer corresponding to a surface oxidation of the AlN seed layer due to air intake during the air break is also observed. Silicon (Si) signal in cyan location is predominant at the bottom of the image and comes from SiO<sub>2</sub>. Next, we focus on molybdenum (Mo) signal in yellow. As for the EDX analysis before the thick AlN PVD growth presented in section IV.2.4.2.5, it corresponds to the bright area in HAADF image. Once again, the Mo islands seem recessed in the SiO<sub>2</sub> oxide suggesting that this layer affects the surface cohesion energy of these Mo-based layer leading to Mo-islands. Finally, Aluminum (Al) signal in blue and nitrogen (N) signal in red signal are in total agreement with the AlN layers (seed and thick regrowth), and a part of N seems localized in the Mo islands.



*Figure V.6: Energy dispersion mapping of the AlN PVD regrowth/AlN seed layer/MoN<sub>x</sub>/SiO<sub>2</sub> interfaces*

To conclude, on one hand, TEM analysis enable to highlight a typical columnar growth of the AlN polycrystalline films with a smooth surface. The abrupt and merged interface between the AlN seed layer and AlN regrowth suggests a perfect PVD epitaxial growth. Due to the scale effect, it is difficult to observe potential structural changes comparing the analysis before and after the AlN PVD regrowth. However, the resulting MoN<sub>x</sub> layer is still discontinuous which suggest no significant structural rearrangement. On the other hand, the quantitative EDX analysis highlight no drastic chemical modification of the 2D-MoS<sub>2</sub> layer modified into MoN<sub>x</sub> after the AlN PVD regrowth. Therefore, the MoN<sub>x</sub>/AlN seed stack seems not structurally or chemically affected by the AlN PVD regrowth.

#### *V.1.1.4. Phase and orientation mapping (ACOM)*

Similarly to what have been achieved after the NH<sub>3</sub> heat treatment modifying 2D-MoS<sub>2</sub> into MoN<sub>x</sub>, ACOM analysis was performed after the thick AlN PVD regrowth. The phases and orientation mapping are presented in Figure V.7. The phase mapping is identical to that

presented just after the NH<sub>3</sub> heat treatment in section IV.2.4.2.5. It displays a red phase corresponding to AlN and a green phase corresponds to MoN<sub>x</sub>. As observed in the TEM images, these domains seem discontinuous and recessed in the SiO<sub>2</sub> oxide. Moreover, and as discussed in section IV.2.4.2.6, the Mo<sub>2</sub>N<sub>0.75</sub> phase indexing is better than MoN<sub>0.5</sub> but the reliability still poor between these two phases suggests a mixture of molybdenum (oxy)nitride phases. Therefore, these results are very similar to those previously presented indicating no significant chemical modification of the MoN<sub>x</sub> after the 350 °C thick AlN PVD regrowth. Finally, the dark phase is attributed to the amorphous phase coming from SiO<sub>2</sub>.

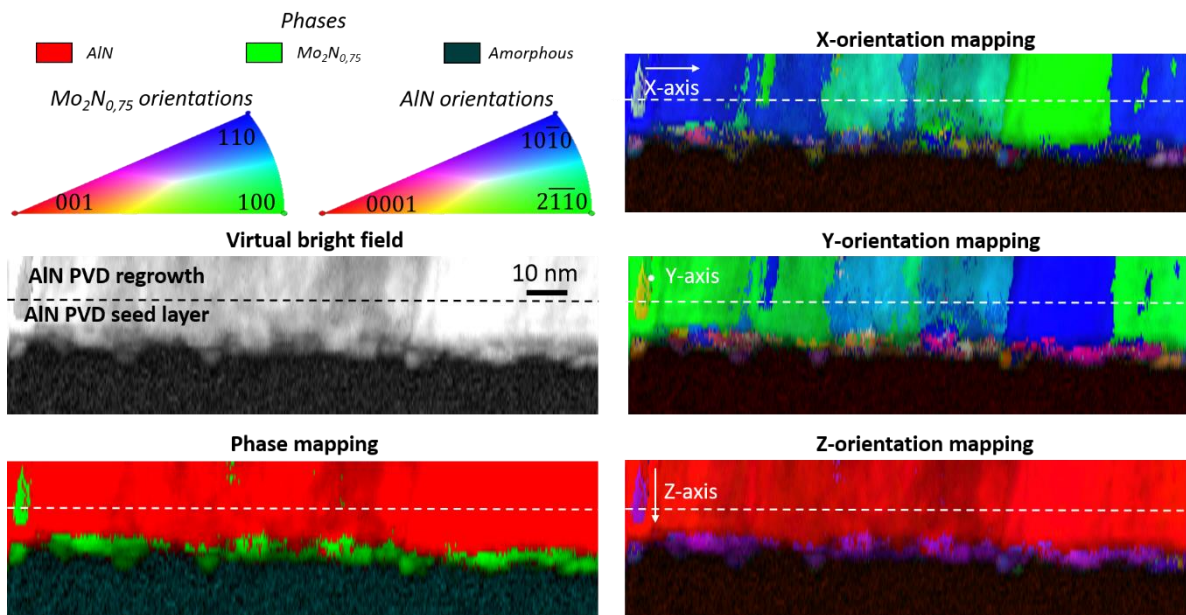


Figure V.7: Virtual bright field, phase and orientation mapping of the AlN PVD regrowth/AlN seed layer/MoN<sub>x</sub>/SiO<sub>2</sub> interfaces

X-, Y- and Z-orientations are interesting especially for AlN phase. The size of MoN<sub>x</sub> areas and their small diffraction volume lead to an orientation indexing with a poor reliability which cannot be properly interpreted. However, for AlN phase, Z-orientation mapping shows a unique (0001) orientation which confirms a pronounced c-axis textured growth of the layer. Focusing on X- and Y-orientations, two main results can be extracted. First, the X- and Y-orientations of the AlN seed and AlN PVD regrowth are identical (these layers are separated by a horizontal dash line). This result is in line with the merged interface observed in Figure V.5 observed and highly suggests an epitaxial growth between both layers. Second, we do not observe any in-plane preferential orientation: (10 $\bar{1}$ 0), (2 $\bar{1}$ 10) and a mixture of these orientations are clearly visible. These results demonstrate a non negligible in-plane twist of the AlN grains. These twisted AlN grains are known to affect the mosaicity of the AlN film<sup>175</sup>.

Stated differently, they contribute to the tilt of the AlN lattice along the growth direction (c-axis). Hence, optimize the AlN in-plane (for example along (102) direction) is an interesting perspective to enhance the AlN crystal quality. Their effect could be more deeply studied by considering XRD measurements of these planes and used to determine threading dislocations

449.

#### V.1.2. Conclusions of AlN PVD deposition post-MoS<sub>2</sub> modification

The modification of 2D-MoS<sub>2</sub> through an AlN seed layer by a NH<sub>3</sub> reactive heat treatment enables to elaborate and study AlN PVD films with a thickness up to 1 μm. First, the TEM/EDX completed with ACOM indicate that the AlN PVD regrowth does not affect the stack structure, morphology or chemistry: the MoN<sub>x</sub> film is still a discontinuous, most likely composed of molybdenum nitride phases slightly oxidized.

Second, the AlN films are polycrystalline and display a pronounced c-axis orientation with no preferential in-plane orientation. The pronounced c-axis textured growth is confirmed with the (002) RC which are lower than 1°. These RC and AlN equi-biaxial residual stress/strain are independent of the thickness. It strongly suggests that the quality of thick AlN PVD regrowth mostly depends on the crystal quality of the AlN seed layer. Hence, optimize this seed in terms of crystal quality (in-plane and out-of-plane orientation) and preventing its oxidation due to air intake during the air break seems primordial to enhance the AlN PVD films elaborated with this approach.

Finally, to push further towards the targeted applications, these results and especially the enhancement of AlN c-axis textured growth is attractive to improve its piezoelectric properties. It would lead to an enhancement in  $k^2_{\text{eff}}$  coefficient resulting in better performances of AlN-based RF devices. To confirm, a surface Acoustic Wave (SAW) device has been fabricated from a 400 nm thick AlN PVD sample. RF tests are going on in order to obtain first devices results.

V.2. Elaboration of Scandium (Sc) doped AlN films by Physical Vapor Deposition (PVD) post-modification

V.2.1. Description of Sc doped AlN PVD deposition equipment

Scandium doped AlN ( $Sc_xAl_{1-x}N$ ) films were deposited in an EVATEC CLUSTERLINE II (CLN200 II) 200 mm magnetron sputtering reactor from Evatec. It is an industrial equipment equipped with five process modules. Two modules are used for the surface preparation (Ar etching, degassing...), two modules are single target sputtering reactor used for the carbon (C), Si(N) and Al(N) deposition and one module is a co-sputtering chamber dedicated to doped AlN deposition with different elements (Sc, Cr, Ga...). The equipment is represented in Figure V.8.

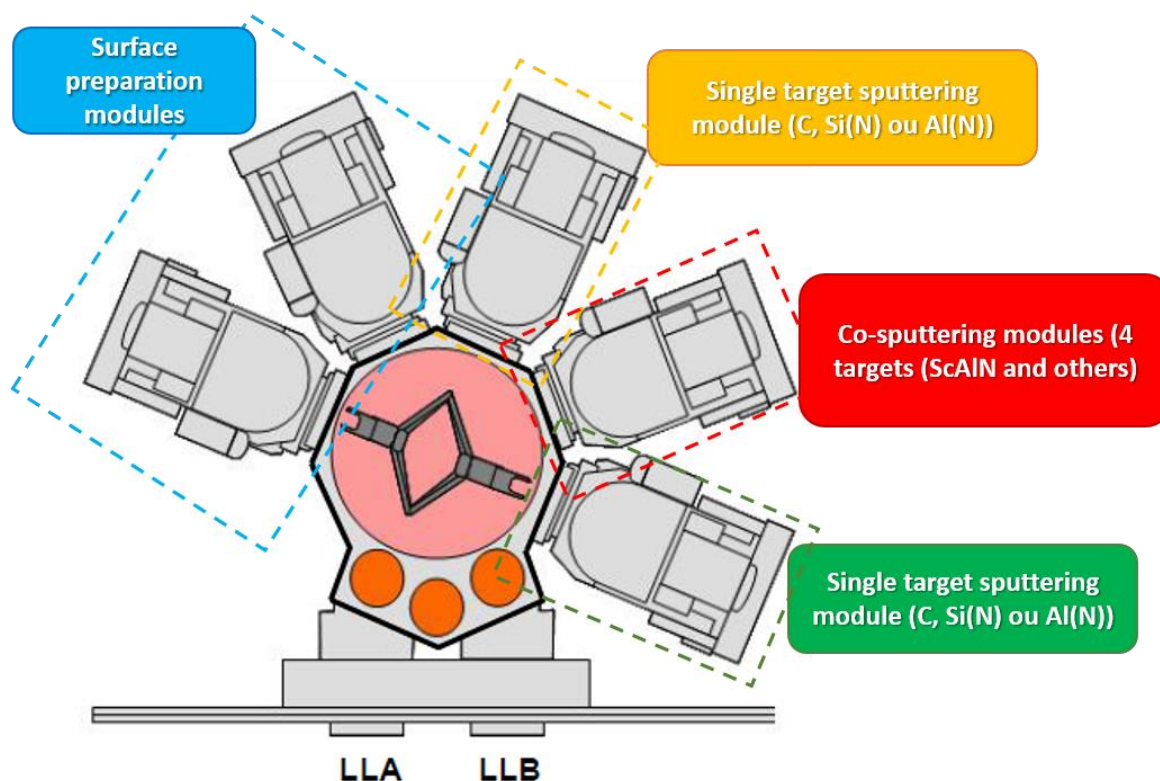


Figure V.8: Schematic representation of the CLUSTERLINE (CLN) 200 mm magnetron reactor

The co-sputtering chamber is composed of four cathodes but only three are used for Sc doped AlN deposition (two Al targets and one Sc target). The deposition temperature was set at 350 °C. The argon and nitrogen flow rates are set to 6 sccm and 12 sccm, respectively. The Sc doping level in AlN was controlled by adjusting the Sc target power between 166 W and 385 W while both Al targets power were fixed at 1000 W. The deposition time was tuned to perform  $Sc_xAl_{1-x}N$  PVD deposition with a targeted thickness between 100 nm and 1  $\mu$ m. Scandium atomic concentration and  $Sc_xAl_{1-x}N$  thickness were evaluated by Wavelength

Dispersive X-Ray Diffraction Spectroscopy (WDXRF) and ellipsometry, respectively, during the equipment qualification performed on Si (100) 200 mm wafers. Therefore,  $Sc_xAl_{1-x}N$  with various targeted Sc atomic concentrations of 4 %, 5 %, 6 %, 10 % and 13 % were investigated. The different samples are listed in Table V.1.

Thickness (nm)	100	200	400	600	800	1000
Sc at. = 4 %	✓	✓	✓	✓	✓	✓
Sc at. = 5 %	✓	✗	✓	✗	✗	✓
Sc at. = 6 %	✓	✗	✓	✗	✗	✓
Sc at. = 10 %	✓	✗	✓	✗	✗	✓
Sc at. = 13 %	✓	✓	✓	✓	✓	✓

Table V.1: List of Sc doped AlN samples elaborated by co-sputtering in this work

## V.2.2. Characterizations

### V.2.2.1. Mosaicity

As for pure AlN PVD deposition, the mosaicity of  $Sc_xAl_{1-x}N$  films with various Sc doping level has been assessed with a XRD  $\omega$ -scan measurement. The  $Sc_xAl_{1-x}N$  (002) RC are presented in Figure V.9. We observe different tendencies depending on the Sc doping level. The RC with the lower contents (4 %, 5 % and 6 %) tend to increase with the thickness. The opposite trend seems to be observed for the upper Sc level (13 %) while the (002) RC values of a 10 % Sc doping are totally independent of the thickness. It suggests that, for thick  $Sc_xAl_{1-x}N$  films (1  $\mu m$  and potentially above), the c-axis orientation is promoted for higher Sc content.

First, similar results have been published by Lu et al.<sup>450</sup> and Beaucejour et al.<sup>451</sup> which indicate a decrease in  $Sc_xAl_{1-x}N$  (002) RC deposited on silicon with the increase in Sc content. However, Mertin et al.<sup>452</sup> observe the opposite tendency in their study. On the other hand, Fichtner et al.<sup>453</sup> show no dependency of the Sc content for  $Sc_xAl_{1-x}N$  (002) RC deposited on silicon. Hence, the influence of Sc content in  $Sc_xAl_{1-x}N$  films does not seem to be well understood.

A potential explanation of these overall results could be related to the variation between a simple reactive sputtering (single ScAl target) and a co-reactive sputtering (Sc and Al targets). In fact, for a Sc content < 26 % deposited with a single ScAl target, we sputter a mix of ScAl<sub>3</sub> and Al phases. Hence, the resulting layers present a mix of ScAlN and

AlN phases. However, the mentioned studies <sup>450-453</sup> are all based on co-reactive sputtering. Therefore, these results are still difficult to interpret and cannot be compared with others.

A repeatability study would be interesting but it could not be realized due to a lack of samples and equipment availability. Moreover, as the samples are clived 2 cm x 2 cm coupons extracted from a 200 mm wafer, another potential explanation to these results could be a variation in 2D-MoS<sub>2</sub> crystal quality between the center and the edge of the 200 mm wafer. It could lead to variation in c-axis orientation of the AlN PVD seed layer which influence the Sc<sub>x</sub>Al<sub>1-x</sub>N regrowth.

Second, these results also imply that there is no clear tendency of the thickness influence on the Sc<sub>x</sub>Al<sub>1-x</sub>N (002) RC for a fixed a Sc content. Contrary to Sc content, this trend is different to what we can find in the literature. In fact, Knisely <sup>324</sup> shows a clear decrease in Sc<sub>0.2</sub>Al<sub>0.88</sub>N (002) RC deposited by PVD sputtering with the increase in thickness. As for pure AlN PVD deposition, it highly suggests that the Sc<sub>x</sub>Al<sub>1-x</sub>N crystal quality and c-axis texture is limited by the quality of the thin AlN seed layer serving as a pre-texturizing film before a thicker Sc doped regrowth.

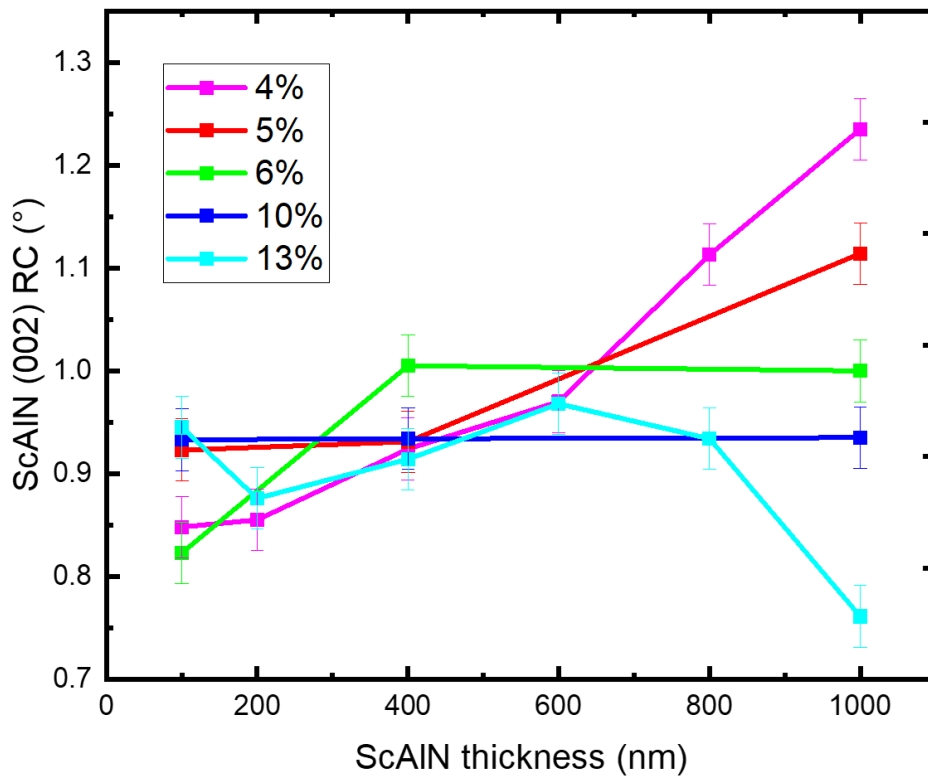


Figure V.9: Sc<sub>x</sub>Al<sub>1-x</sub>N (002) RC measurements for the different Sc investigated content

Finally,  $\text{Sc}_x\text{Al}_{1-x}\text{N}$  (002) RC are compared in Figure V.10 with others RC of  $\text{Sc}_x\text{Al}_{1-x}\text{N}$  deposited by PVD from CEA-LETI capabilities and literature, on Si (100) and various silicon-based substrates, respectively. The literature values are issued from Annex part 1, Table XI.

Similarly to pure AlN PVD regrowth, values from literature (black square) are disparate since the c-axis orientation depends highly on the  $\text{Sc}_x\text{Al}_{1-x}\text{N}$  PVD deposition conditions. And as previously mentioned, Knisely<sup>324</sup> indicates that the RC values decrease with the increase in  $\text{Sc}_x\text{Al}_{1-x}\text{N}$  thickness. This trend is clearly confirmed on CEA-LETI capabilities (grey dash curve) where  $\text{Sc}_x\text{Al}_{1-x}\text{N}$  PVD (Sc = 4 % at.) is directly deposited on Si (100) 200 mm wafer with native oxide. We observe that  $\text{Sc}_{0.04}\text{Al}_{0.96}\text{N}$  (002) RC decreases with the thickness and these results have also been confirmed with the other investigated Sc contents (5 %, 6 %, 10 % and 13 %). Hence, the alignment of the  $\text{Sc}_x\text{Al}_{1-x}\text{N}$  crystalline planes improves due to growth mechanisms reaching a RC close to 1.5°.

For  $\text{Sc}_x\text{Al}_{1-x}\text{N}$  PVD films deposited in this work (blue triangle), the results are notably different. First, the RC values are roughly around 1° (0.75° to 1.25°) for each  $\text{Sc}_x\text{Al}_{1-x}\text{N}$  PVD deposition, whatever the Sc doping content. To our knowledge, these values are the lowest ever mentioned for a  $\text{Sc}_x\text{Al}_{1-x}\text{N}$  film deposited by PVD on a silicon-based substrate. They are comparable to a 400 nm thick  $\text{Sc}_{0.118}\text{Al}_{0.982}\text{N}$  deposited by Molecular Beam Epitaxy (MBE) at 700 °C on silicon substrate displaying a (002) RC of 1.2°<sup>49</sup>. This increase in c-axis textured growth should improve  $\text{Sc}_x\text{Al}_{1-x}\text{N}$  piezoelectric properties which could be interesting to integrate this stack in  $\text{Sc}_x\text{Al}_{1-x}\text{N}$ -based RF devices.

Second, in the investigated thicknesses, no dependence of the RC with the  $\text{Sc}_x\text{Al}_{1-x}\text{N}$  thickness is observed. It strongly suggests that the crystal quality and c-axis texture are limited by the quality of the AlN seed layer serving as a pre-texturizing film before a  $\text{Sc}_x\text{Al}_{1-x}\text{N}$  regrowth. Once again, the quality of the AlN seed layer seems to be a central element enabling to obtain high crystallinity on  $\text{Sc}_x\text{Al}_{1-x}\text{N}$  PVD films.



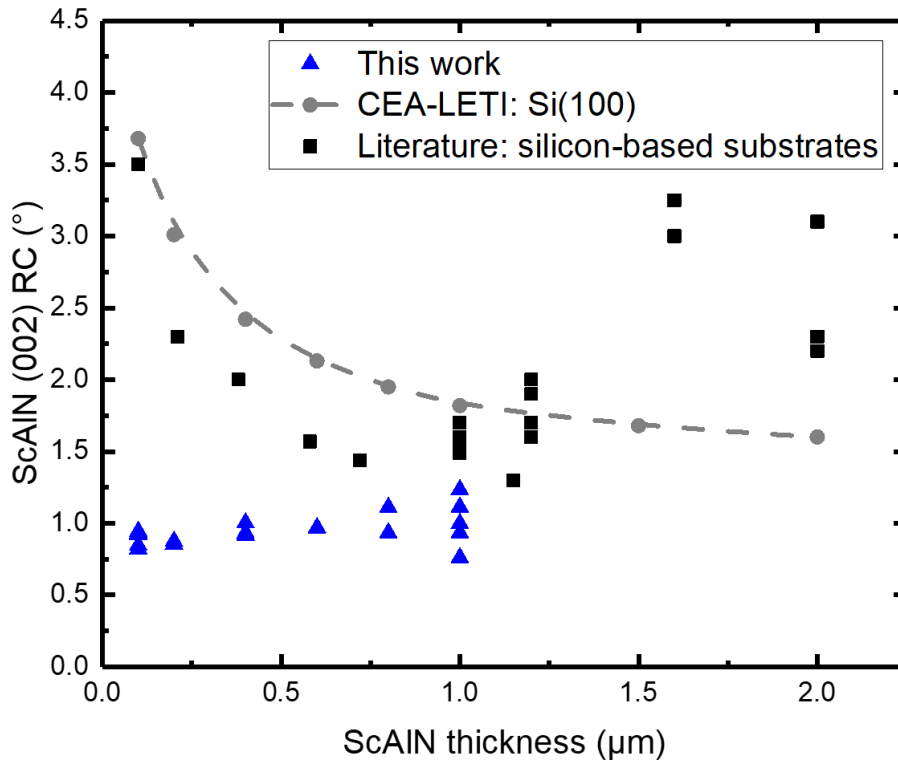


Figure V.10: Comparison of  $Sc_xAl_{1-x}N$  (002) RC deposited by PVD on various silicon-based substrates from literature (blacksquare), CEA-LETI capabilities (grey dash line) and this work (blue triangle)

#### V.2.2.2. Strain, stress measurements and domain sizes

The strain/stress of the  $Sc_xAl_{1-x}N$  films deposited by PVD have also been determined by XRD with “Crystallit Group Method” (CGM) described in Annex part 2, section II.1.4.2. However, the  $Sc_xAl_{1-x}N$  films properties (structural, mechanical, dielectrical...) change with the Sc content<sup>65,320,452</sup>. Hence, the elastic compliances  $S_{ij}$  used to determine the stress with CGM method are not those of AlN anymore and must be determined for each Sc content investigated. To address this point, we base on Ambacher et al.<sup>318</sup> study in which a detailed investigation of the Sc content influence on structural, elastic, dielectric, and piezoelectric properties of  $Sc_xAl_{1-x}N$  films is presented to use appropriate  $S_{ij}$  values.

Hence, the  $Sc_xAl_{1-x}N$  stress calculated with appropriate  $S_{ij}$  values is plotted in Figure V.11 for the different investigated Sc doping content. First, contrary to pure AlN PVD deposition presented in section V.1.1.2, all  $Sc_xAl_{1-x}N$  samples have an equi-biaxial stress higher than 1 GPa. This higher stress in  $Sc_xAl_{1-x}N$  films is difficult to compare with pure AlN deposition since AlN and  $Sc_xAl_{1-x}N$  deposition are not performed in the same equipment (SPTS (Trikon) Sigma fxP 200 mm magnetron PVD reactor for AlN and EVATEC CLUSTERLINE II (CLN200 II) 200 mm magnetron sputtering reactor  $Sc_xAl_{1-x}N$ ). These tools have each different reactor geometry,

deposition parameters and sources (multi-targets in CLN200 II and a simple target in Sigma fxP 200 mm). A pure AlN deposition in the co-sputtering chamber is necessary to perform a consistent comparison. These results are also difficult to compare with the literature since stress in  $Sc_xAl_{1-x}N$  films is not widely studied and the authors of the pertinent publications applied a bias on the substrate during the deposition<sup>324,453</sup>.

Second, according to the literature, evolutions of structural parameters due to the increase in Sc content lead to an increase in compressibility along the c-axis<sup>318,319</sup>. In fact, in the basal plane, the compressibility is less affected but tends to increase slightly up to a Sc content of 14 % and then decreases. This behaviour is due to the non-linear evolution of the lattice constants with Sc content: c-parameter reaches a maximum value for a Sc content close to 15 % while a-parameter increases monotonically. Hence, as the concentration of Sc content increases, the  $Sc_xAl_{1-x}N$  material softens along c-axis and hardens in the basal plane (for Sc content higher than 15 %)<sup>320</sup>. This softening along c-axis indirectly suggests a capability of the material to relax its internal equi-biaxial stress more easily with the increase in Sc content. This is what is observed in few studies where  $Sc_xAl_{1-x}N$  stress starts tensile (with x close to 0) and becomes highly compressive with the increase in Sc content<sup>451</sup>.

In this work, and as presented in Figure V.11, this tendency seems also visible where the  $Sc_xAl_{1-x}N$  stress tends to decrease with the increase in Sc content. This observation is relatively true for the  $Sc_xAl_{1-x}N$  films up to 800 nm. However, it is less obvious for the 1  $\mu m$  films. Based on these results, a repeatability study on a larger Sc content range would be interesting to confirm its tendency.

Finally, the deposited  $Sc_xAl_{1-x}N$  films display an equi-biaxial stress independent of the thickness. Once again, these results differ from the literature where  $Sc_xAl_{1-x}N$  stress tends to increase with the thickness<sup>451,454</sup>. It strongly suggests that, independently of the deposition conditions,  $Sc_xAl_{1-x}N$  stress is partially imposed by the AlN seed layer serving as a pre-texturizing film before the  $Sc_xAl_{1-x}N$  regrowth. Although the impact of the stress still needs to be proved, it potentially could influence the performances on the  $Sc_xAl_{1-x}N$  based devices. However, different levers are identified to tune this stress such as the gas flow (Ar and  $N_2$ )<sup>324,454,455</sup> or substrate bias<sup>324,456</sup>.

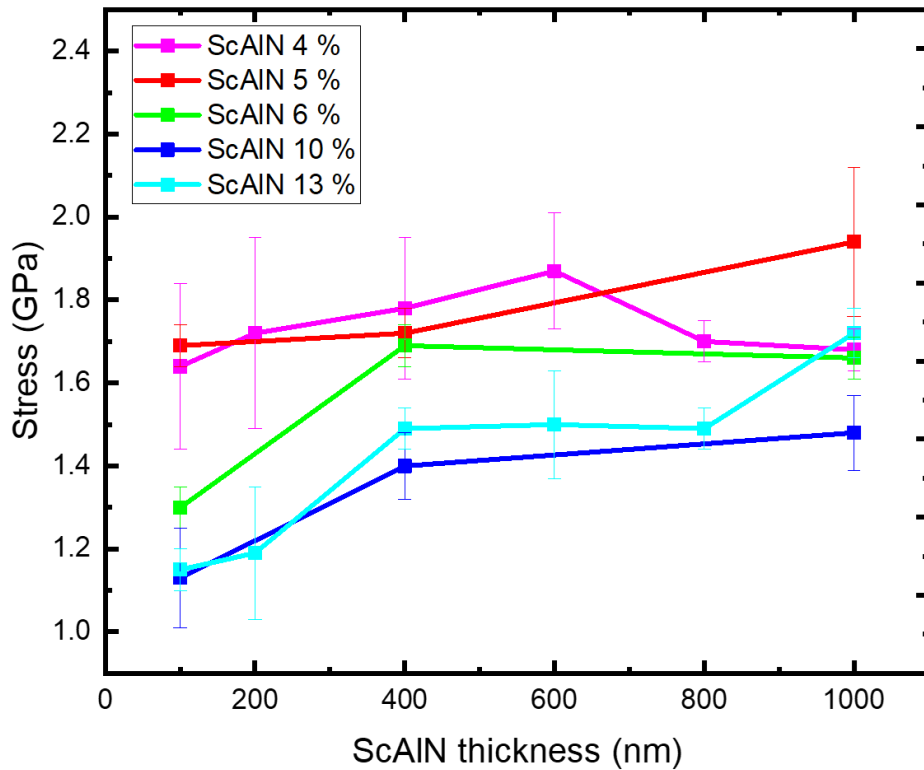


Figure V.11:  $Sc_xAl_{1-x}N$  equi-biaxial stress determined by XRD (CGM method)

Moreover, in the same way as pure AlN PVD deposition, out-of-plane and in-plane strain have also been determined with CGM method for  $Sc_xAl_{1-x}N$  films. The results of out-of-plane and in-plane strain as a function of the thickness are presented and compared with pure AlN in Figure V.12 a) and b), respectively. Only the extreme Sc contents (4 % and 13 %) are plotted since these contents have been investigated for each thickness (100 nm, 200 nm, 400 nm, 600 nm, 800 nm and 1  $\mu$ m).

First, omitting that the AlN and  $Sc_xAl_{1-x}N$  films are deposited in different equipments, the out-of-plane and in-plane strain are clearly higher for Sc doped AlN PVD deposition compared to pure AlN PVD deposition. As previously mentioned, this result is expected since in the Sc content range investigated, the compressibility along c-axis and in the basal plane increases.

Second, as for pure AlN, out-of-plane and in-plane strain of Sc doped AlN films seem to show no thickness dependency suggesting no relaxation of Sc doped AlN planes with the increase in thickness.

Finally, it seems difficult to observe tendencies about the influence of Sc content on the strain. In fact,  $Sc_{0.04}Al_{0.96}N$  and  $Sc_{0.13}Al_{0.87}N$  films have both out-of-plane and in-plane strain roughly around - 0.25 % and 0.35 %, respectively. The same observations have been made for the other Sc contents (not plotted here). Therefore, no clear dependency is observed between

strain and Sc doping level. A material study with a larger range of Sc doping level would be interesting to deepen these results and the influence of Sc content on stress/strain. However, investigate high Sc content will affect the  $k^2_{\text{eff}}$  - Q tradeoff which is primordial for the targeted RF applications.

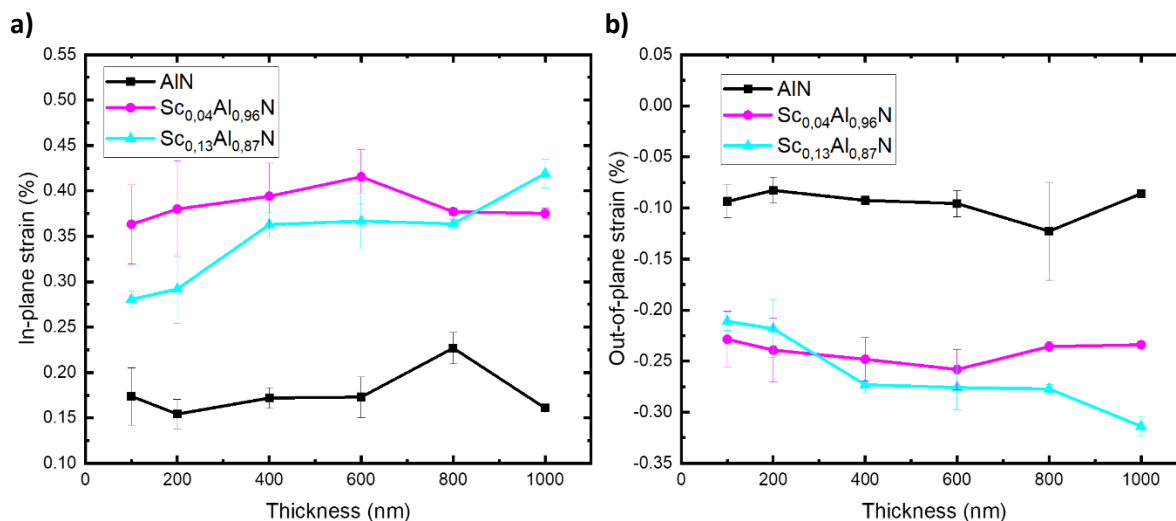


Figure V.12: a) In-plane ; b) out-of plane strain of Sc<sub>x</sub>Al<sub>1-x</sub>Ns and comparison with AlN strain

### V.2.3. Conclusions of Sc doped AlN PVD deposition post-MoS<sub>2</sub> modification

This second section of this chapter demonstrates that the modification of 2D-MoS<sub>2</sub> through an AlN seed layer by a NH<sub>3</sub> reactive heat treatment can be applied to doped AlN films. Here, as it is the most studied element in the literature to increase AlN piezoelectric properties, this section was focused on Sc as doping element but other elements could have been investigated such as Cr, Y, V, MgZr, MgHf... In this regard, it was planned to investigate Cr and V doped AlN deposition. However, this subject could not be addressed due to a lack of samples and equipment availability.

First, and similarly to pure AlN PVD deposition presented in section V.1.1.1, the approach used in this work enable to elaborate Sc<sub>x</sub>Al<sub>1-x</sub>N PVD films with a pronounced c-axis orientation. In fact, Sc<sub>x</sub>Al<sub>1-x</sub>N (002) RC values roughly around 1° have been achieved and are independent of the film thickness. To our knowledge, such RC have never been published for Sc<sub>x</sub>Al<sub>1-x</sub>N sputtered on a silicon-based substrate. Second, the equi-biaxial stress of the Sc<sub>x</sub>Al<sub>1-x</sub>N films seems to decrease with the Sc content suggesting a structure softening along c-axis. However, the strain analysis does not show this trend. Hence, Sc content influence on Sc<sub>x</sub>Al<sub>1-x</sub>N PVD stress/strain is difficult to comment and compare with the literature. A repeatability study with a larger Sc content is necessary to clarify potential trends.

Finally, these results are still extremely interesting since they potentially pave the way to an enhancement of  $\text{Sc}_x\text{Al}_{1-x}\text{N}$  piezoelectric properties used in RF devices. On one hand, this study enables to obtain highly c-axis textured  $\text{Sc}_x\text{Al}_{1-x}\text{N}$  films which could lead to increase in piezoelectric properties and especially  $k^2_{\text{eff}}$ . On the other hand, this increase in c-axis textured growth can be performed at low Sc content ( $< 10\%$ ) allowing to not drastically degrade the quality factor Q. Therefore, by combining highly c-axis texture and low Sc content ( $< 10\%$ ), this elaboration method could lead to an important enhancement of the  $\text{Sc}_x\text{Al}_{1-x}\text{N}$  piezoelectric properties while preserving a suitable  $k^2_{\text{eff}}$  - Q tradeoff which is determinant in RF devices<sup>19</sup>. As for pure AlN PVD deposition, 400 nm thick  $\text{Sc}_{0.10}\text{Al}_{0.90}\text{N}$  and  $\text{Sc}_{0.13}\text{Al}_{0.87}\text{N}$  films have been used to realize a SAW device which are also awaiting RF tests.

### V.3. Elaboration of AlN films by Chemical Vapor Deposition (CVD) post-MoS<sub>2</sub> modification

#### V.3.1. Description of the CVD deposition process

AlN MOCVD deposition was performed in the same equipment used for the NH<sub>3</sub> thermal heat treatments through the AlN PVD seed layer: AIXTRON CRIUS R200 MOCVD reactor. It enables to chain the 2D-MoS<sub>2</sub> modification through the AlN seed with a direct AlN MOCVD deposition without any air break. Hence it prevents the surface oxidation of the AlN PVD seed layer. Trimethylaluminum (TMA) and ammonia was used as Al and N precursors with a flow rates of 25 sccm (equivalent to a growth rate of 0.14  $\mu\text{m}\cdot\text{h}^{-1}$ ) and 500 sccm, respectively. The deposition temperature was fixed at 1100 °C. The targeted thicknesses of the AlN MOCVD layer are 200 nm, 400 nm and 600 nm. These growths were performed on two different AlN seed layer thicknesses (4s and 10.4s). The idea is to confirm the tendency observed on the thick AlN PVD regrowth where its crystal quality is promoted when the deposition is performed on the thicker AlN seed layer (10.4s).

#### V.3.2. Characterizations

##### V.3.2.1. Mosaicity

As for thick AlN PVD deposition, a  $\omega$ -scan XRD measurement on AlN (002) planes was performed on each AlN MOCVD samples to assess the mosaicity. The results are presented in Figure V.13 and compared with the RC obtained for thick AlN PVD deposition. First, we clearly observe a lower AlN (002) RC for MOCVD deposition than PVD deposition. In fact, AlN (002) RC is around 0.55° for MOCVD deposition on AlN seed 4s and can reach 0.3° on AlN seed 10.4s while AlN (002) RC is relatively constant around 0.7° - 0.8° for PVD deposition films. This result suggests that the higher temperature deposition enables a grain coalescence leading to an AlN (002) realignment. Moreover, these AlN (002) RC values are lower than what we can find in the literature for AlN CVD deposition on silicon-based substrates where AlN (002) RC of 2.4°<sup>199</sup>, 1.2°<sup>457</sup> or 0.68°<sup>195</sup> are mentioned. Nevertheless, they are still far from the highly AlN CVD c-axis textured growth obtained on sapphire or silicon carbide (SiC) substrates where AlN (002) RC can be less than 0.05°<sup>138,187,458,14</sup>. Therefore, a clear axis of improvement and optimization is identified to tend towards AlN (002) RC as close as possible to those obtained on sapphire or SiC substrate.

Second, similarly to AlN PVD deposited films, AlN MOCVD crystal quality is enhanced when the deposition is performed on the thick AlN seed layer (10.4s). This observation is echoing the results discussed in the section IV.2.4.3 of chapter 4. In this section, we demonstrate that the crystal quality of the 10.4s AlN seed layer is well preserved after the NH<sub>3</sub> heat treatment contrary to that of 4s. It enables a better crystallinity of the AlN regrowth.

Finally, as we only investigated three thicknesses for AlN MOCVD deposition, it is still difficult to interpret its influence on the c-axis orientation. AlN (002) RC seems relatively constant with the thickness. However, as deposition temperature in MOCVD is higher than PVD, we could expect a significant grain coalescence leading to a notable increase in c-axis AlN orientation for thicker AlN MOCVD films.

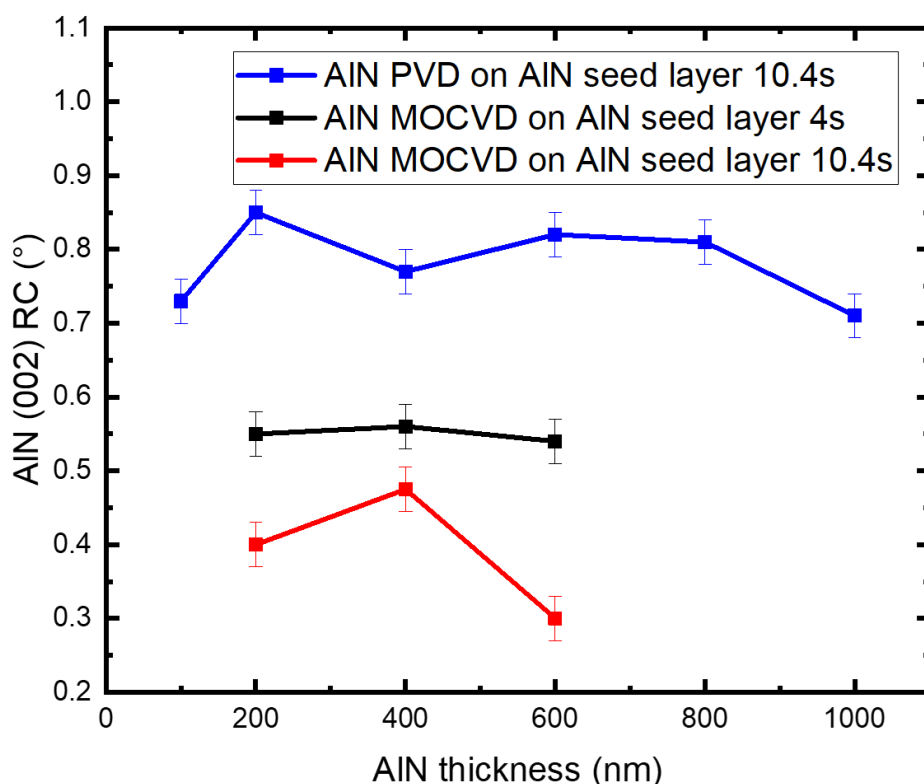


Figure V.13: AlN MOCVD (002) RC measurements and comparison with AlN PVD

For this kind of deposit, we use the XRD pole figure to determine the preferential orientation of the crystalline domains. The measurement geometry of this method is presented in Annex part 2, section II.1.4.3. The AlN (102) reflection pole figure of the 600 nm thick AlN MOCVD sample is represented in Figure V.14. The pole figure pattern displays a uniform and closed circle corresponding to (102) AlN reflection. This pattern indicates that, whatever the  $\varphi$  or  $\chi$  angles investigated, the AlN (102) reflection is uniformly presents. It means that we have a random AlN (102) orientation (in-plane) which also reveals the

pronounced (002) out-of-plane fiber texture (along c-axis) of the 600 nm thick AlN MOCVD sample. We can observe four high intensity poles overlapped with AlN (102) reflection corresponding to Si (220) reflection of the silicon substrate. Hence, another axis of improvement is to orient the in-plane grains in order to obtain a (102) RC of the same order of magnitude to the (002) RC.

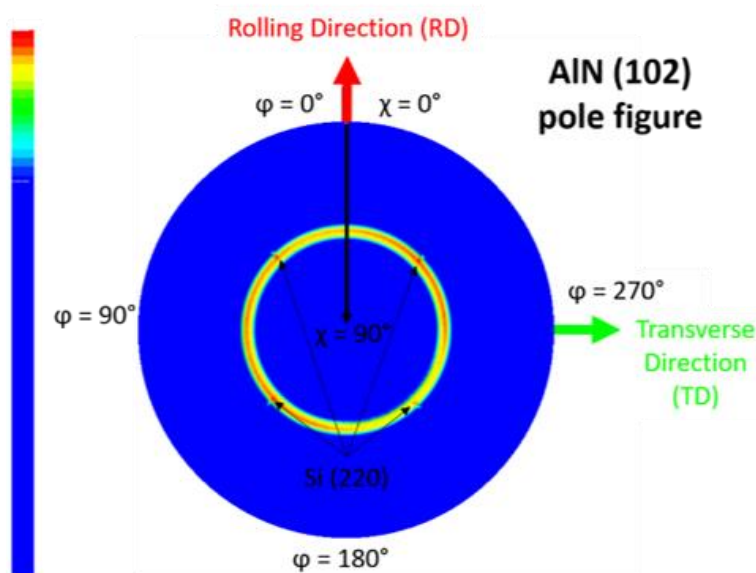


Figure V.14: AlN (102) pole figure of the 600 nm thick AlN MOCVD sample

To complete, a stress/strain analysis would be interesting to compare with AlN PVD deposited films and literature. However, it could not be implemented due to a lack of samples and equipment availability.

#### V.3.2.1. Surface morphology (SEM)

The surface morphology of the AlN MOCVD depositions was evaluated with Scanning Electronic Microscopy (SEM). The experimental conditions of these SEM measurements performed in this work are briefly detailed in Annex part 2, section II.1.6.

The images are presented in Figure V.15. On one hand, focusing on the thinnest AlN PVD seed layer (4s), the surface of the deposited AlN MOCVD films is unexpected. It displays small grains and seems disorderly with asperities whatever the thickness of the AlN MOCVD regrowth. We can note that the grain size increases with the AlN MOCVD thickness suggesting their coalescence during the growth. This curious surface morphology probably results from the degradation of the 4s AlN PVD seed layer after the NH<sub>3</sub> heat treatment compared to a well-preserved surface of the 10.4s AlN PVD seed layer after the same treatment.



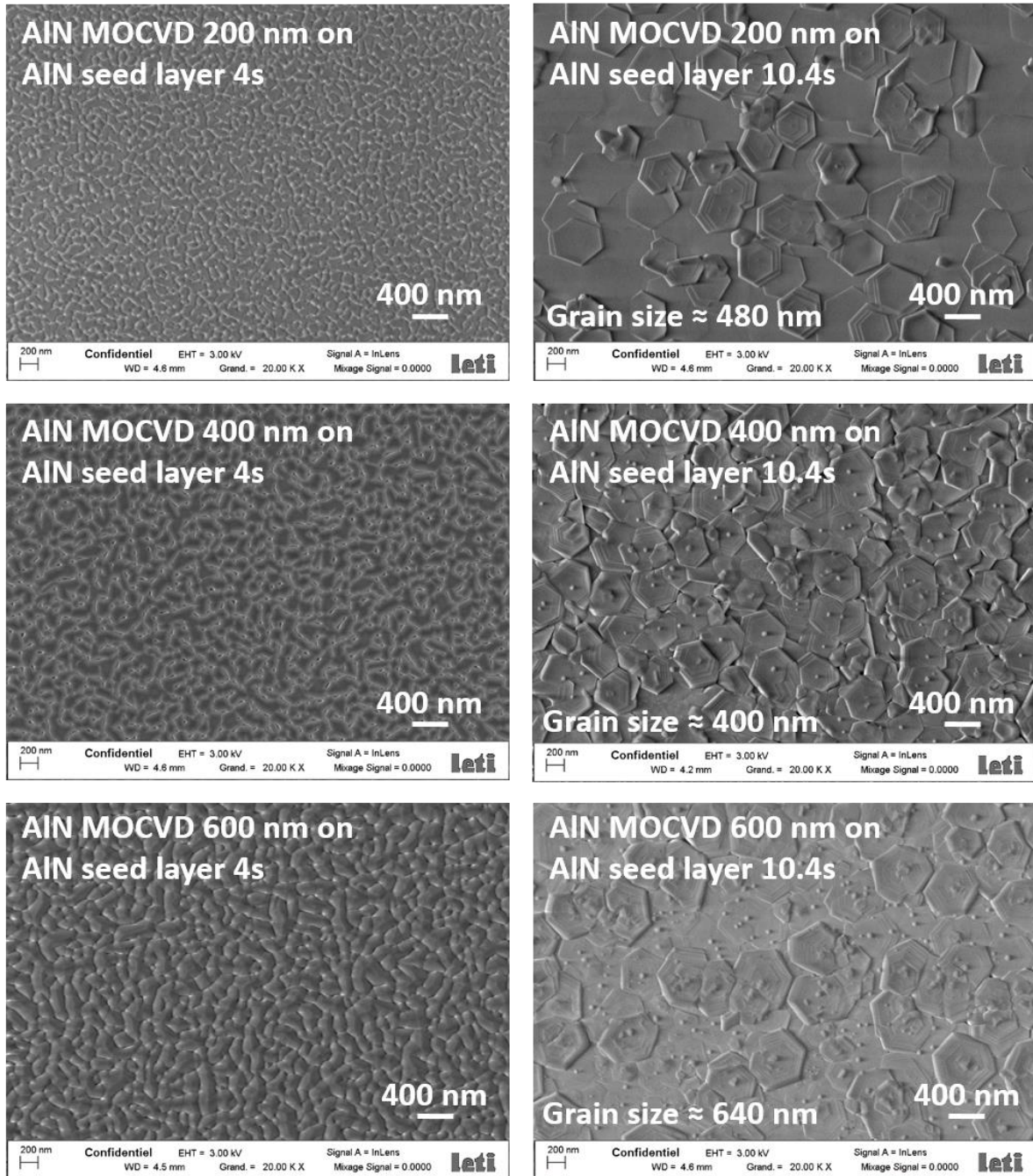


Figure V.15: SEM images of the AlN MOCVD samples top surface

On the other hand, the surface morphology of the AlN MOCVD deposited of the thicker AlN PVD seed layer (10.4s) clearly displays AlN hexagonal grains. The grain diameter is around 480 nm, 400 nm and 640 nm for the 200 nm, 400 nm and 600 nm thick AlN MOCVD, respectively. If we compare the AlN grain size with the AlN (002) RC presented in Figure V.13, the higher the grain size, the lower the RC. Therefore, a precise control of the AlN grain coalescence leading to an AlN planes realignment is interesting to promote a highly c-axis textured growth. Moreover, we can also note a defect approximately located at the center of

almost each hexagon. This defect could be a threading screw dislocation. It must be avoided since they have a metallic like character enabling the formation of preferential pathways to leakage currents in III-nitride based electronic devices<sup>459</sup>. We can also note that no cracks are visible in the AlN MOCVD film which is recurrent observed issue for the CVD deposition of this material on silicon substrate.

V.3.2.2. Crystalline quality and chemical composition (TEM/EDX)

Cross-sectional TEM of a 200 nm thick AlN MOCVD regrowth at different magnifications are presented in Figure V.16. On one hand, the left cross-section displays larger AlN CVD grains compared to AlN PVD grains. In fact, the higher temperature deposition (1100 °C for AlN MOCVD vs. 350 °C for AlN PVD) promotes a grain coalescence during the growth. This coalescence is clearly visible since we observe AlN grains of a few tens of nanometer close to the bottom of the film and AlN grains greatly exceeding 100 nm at the top. Moreover, at this scale, the AlN MOCVD top surface is not smooth compared to AlN PVD, steps are visible between each grain.

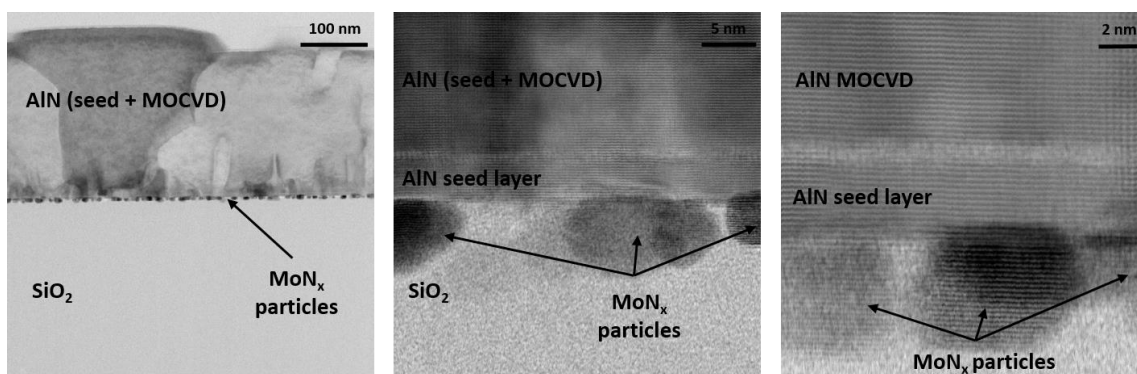
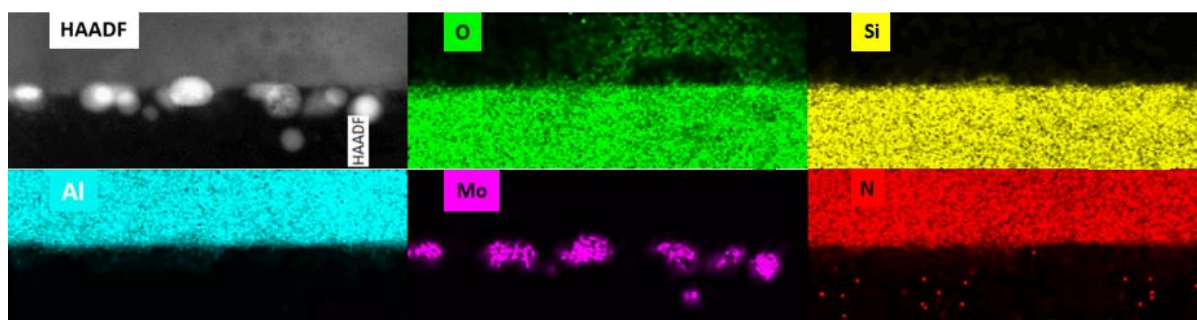


Figure V.16: Cross-sectional TEM of AlN MOCVD/SiO<sub>2</sub> + particles interfaces after thick AlN 200 nm thick MOCVD growth

On the other hand, the initial 2D-MoS<sub>2</sub> layer converted into a discontinuous MoN<sub>x</sub> film through the AlN seed is different compared to what has been observed after the thick AlN PVD regrowth. The discontinuous MoN<sub>x</sub> film seems to be reorganised into smaller particles after the AlN MOCVD regrowth. These changes are clearly visible on the TEM cross-sections with an atomic scale magnification. A structural reorganisation occurred during the AlN MOCVD growth. The higher deposition temperature may modify the mobility of the atoms leading to this structural reorganisation in particles. We can also observe that we have a clean and sharp interface between the AlN PVD seed layer and the AlN MOCVD regrowth. We clearly

distinct planes parallel to the substrate highlighting the preferential c-axis textured growth and suggesting an epitaxial growth.

These TEM characterizations were coupled with EDX analysis to highlight potential chemical composition changes. The measurements are presented in Figure V.17. Oxygen (O) signal in green mainly comes from SiO<sub>2</sub> and shows that the AlN PVD seed layer is locally oxidized. Silicon signal in yellow is also predominant at the bottom of the image and comes from SiO<sub>2</sub>. Molybdenum (Mo) signal in pink is only localized into the bright areas of the top left HAADF image corresponding to the particles formed during the 1100 °C AlN MOCVD regrowth. Finally, aluminum (Al) and nitrogen (N) signals in cyan and red, respectively, perfectly overlap and correspond to the AlN layers (seed and MOCVD regrowth).



*Figure V.17: Energy dispersion mapping of the AlN MOCVD/SiO<sub>2</sub> + particles interfaces*

This EDX analysis show similar results to those discussed in section IV.2.4.2.6 and V.1.1.4, except for the N signal. In fact, nitrogen is only localized in the AlN layers and not in the bright areas of the HAADF image which should correspond to MoN<sub>x</sub>. Hence, this observation strongly suggests that the structural reorganization due to higher deposition temperature is also accompanied by the loss of nitrogen atoms in MoN<sub>x</sub> leading to the formation of Mo particles. This thermally activated phenomenon has been mentioned in the literature on tungsten nitride (WN<sub>x</sub>) and is called “denudation”<sup>460–462</sup>. For WN<sub>x</sub>, this denudation starts roughly from 700 °C and occurs at higher temperature (1200 °C) which is consistent with the AlN MOCVD deposition temperature (1100 °C).

In this work, the NH<sub>3</sub> heat treatment performed at 1000 °C during 10 min does not lead to any MoN<sub>x</sub> denudation. Hence, this phenomenon should occur slightly higher than 1000 °C, which means during the AlN MOCVD deposition. However, we have to keep in mind that the kinetic must be consider and this denudation could occur at 1000 °C for a longer NH<sub>3</sub> heat treatment. This result opens up an elementary question: what become the nitrogen atoms? A

potential answer which seems to be confirmed with the XPS characterizations presented in Annex part 3, section III.2.4 is their chemical reaction with SiO<sub>2</sub>. In fact, this annex shows environments attributed to SiO<sub>x</sub>N<sub>y</sub> on Si 2p spectrum after the 1000 °C NH<sub>3</sub> heat treatment. Therefore, it seems more possible and appropriate that nitrogen atoms react with SiO<sub>2</sub> substrate to form SiO<sub>x</sub>N<sub>y</sub>.

V.3.2.3. Phase and orientation mapping (ACOM)

As highlighted in the previous section, a MoN<sub>x</sub> denudation combined with a structural occurs after the AlN MOCVD regrowth. The MoN<sub>x</sub> discontinuous film have been reorganized into Mo particles with a diameter of only a few nm. The particles size makes the ACOM characterization more difficult since the areas of interest are even smaller than after the AlN PVD regrowth. The phase and orientations mapping outputs of ACOM are given in Figure V.18.

On one hand, the phase mapping is extremely interesting and displays clearly three distinct phases. The red one is still the AlN phase coming from the PVD seed layer and AlN MOCVD regrowth. The black one is the amorphous SiO<sub>2</sub> substrate. Finally, the green phase located in the small particles are not Mo<sub>2</sub>N<sub>0.75</sub> or another molybdenum nitride phase anymore, but Mo metal phase. Despite their small size associated with a small diffraction volume, these Mo particles display a high crystallinity and as they mainly located into the SiO<sub>2</sub> amorphous layer, they enable to obtain a reliable orientation indexing.

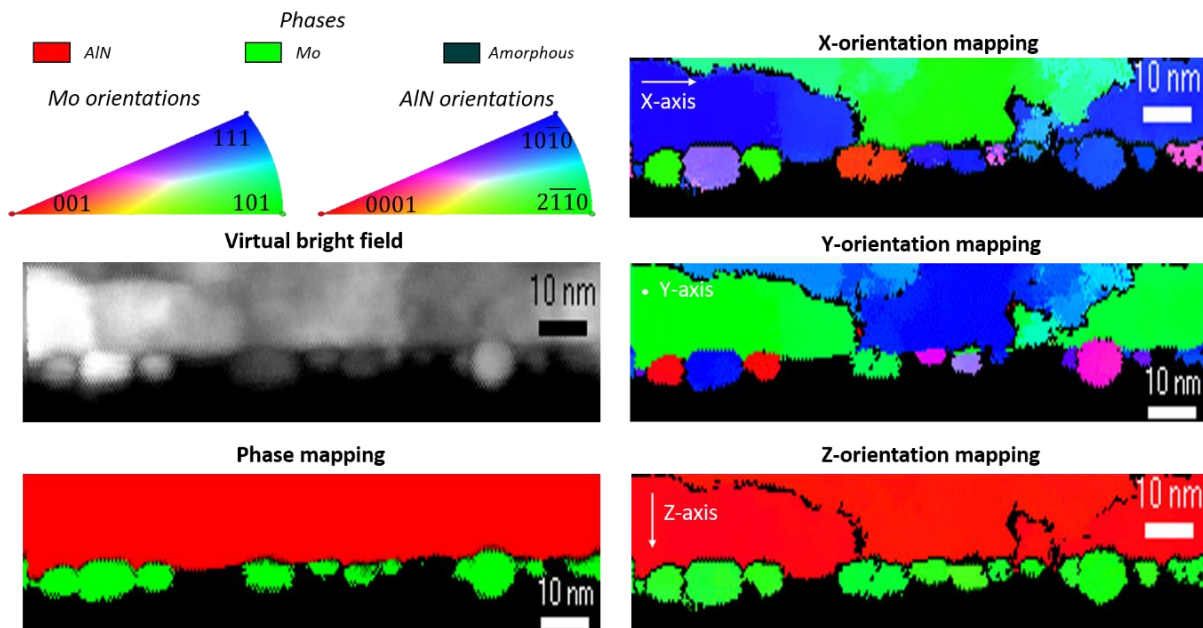


Figure V.18: Virtual bright field, phase and orientation mapping of the AlN MOCVD/SiO<sub>2</sub> + particles interfaces

Hence, these results are consistent with EDX analysis presented in the previous section. They confirm that the 1100 °C AlN MOCVD regrowth step leads to MoN<sub>x</sub> denudation and a structural reorganization into Mo particles.

On the other hand, focusing of the orientation mappings, the Z-orientation of the thick AlN (seed + MOCVD regrowth) shows a unique (0001) orientation which is consistent with the pronounced c-axis preferential orientation of the AlN. Molybdenum particles also seem to have a preferential (101) orientation. However, we have to keep in mind that this characterization is extremely local. An analysis on a larger scale or on other similar samples would be interesting to confirm this result. Then, no AlN preferential in-plane orientations (X- and Y-orientation mapping) are visible: (10 $\bar{1}$ 0), (2 $\bar{1}$  $\bar{1}$ 0) and a mixture of these orientation are observed. These results complete the XRD pole figure presented in Figure V.14. Nevertheless, at this scale, the X- and Y-orientations of the AlN seed and AlN MOCVD regrowth are identical which suggests an epitaxial growth between both layers. As for AlN PVD deposited films, these results highlight an in-plane twist of the AlN grains which contribute to the tilt of the AlN lattice along the growth direction (c-axis). Hence, optimize the AlN in-plane is an interesting perspective to enhance the AlN crystal quality and decrease the AlN (002) RC. Finally, Mo particles shows (001), (101) and (111) orientations.

### V.3.3. Conclusions of AlN MOCVD deposition post-modification

The approach based on the 2D-MoS<sub>2</sub> modification through an AlN seed layer has been extended to AlN MOCVD deposition. First, the AlN MOCVD films deposited on a silicon-based substrate are crack-free, polycrystalline and display a pronounced c-axis orientation with no preferential in-plane orientation confirmed by ACOM and XRD pole figure. An AlN (002) RC of 0.3° has been reached for a 600 nm thick film which is significantly lower than a similar PVD growth. This result is mainly explained by a higher deposition temperature which promote an AlN grains coalescence leading to a realignment along c-axis. Hence, a precise control of this phenomenon and an optimization of the AlN in-plane orientation is an interesting approach to enhance the c-axis texture of the AlN films.

Second this higher deposition temperature also leads to a denudation of the discontinuous MoN<sub>x</sub> film and its structural reorganization into Mo particles, as confirmed by TEM/EDX and ACOM. Based on previous XPS results, it is assumed that the N atoms react with the SiO<sub>2</sub> layer and form a SiO<sub>x</sub>N<sub>y</sub> layer.

Finally, this approach seems particularly interesting since it could allow to solve the issues faced on III-nitride CVD growth on silicon-based substrates. In fact, as described in the chapter 2, section II.2.3.2.2, AlN MOCVD growth on silicon-based substrate suffers of high dislocation density leading to cracked AlN films or is usually based on the use of thick buffer layer to adapt the lattice mismatch with silicon. Hence, this approach opens up a new fabrication process which could compete with AlN MOCVD crystal obtained on sapphire or SiC substrates, especially in terms of crystal quality/cost ratio.

#### V.4. Conclusions of chapter 5

The approach developed in the chapter 4 and based on the 2D-MoS<sub>2</sub> modification into MoN<sub>x</sub> through an AlN seed layer has been applied to AlN PVD, Sc doped AlN PVD and AlN MOCVD regrowth. First, the AlN PVD deposited films display a pronounced c-axis orientation (RC around 0.7° - 0.8°) which is close to the lowest RC (0.63°) reported on silicon-based substrates. It should promote an increase in AlN piezoelectric properties, especially  $k_{\text{eff}}^2$ , and lead to better AlN-based devices performances, such as SAW or BAW filters. Moreover, this pronounced c-axis textured growth as well as stress/strain are independent of the AlN thickness. It suggests that the crystal quality of the AlN PVD regrowth is limited by the quality of the AlN seed layer serving as a pre-texturizing film.

Second, the Sc<sub>x</sub>Al<sub>1-x</sub>N PVD films synthesized by co-sputtering show a (002) RC roughly around 1°, whatever the thickness (100 nm to 1 μm) and Sc content (4 % to 13 %). To the best of our knowledge, such RC values have never been reported for a Sc<sub>x</sub>Al<sub>1-x</sub>N PVD film sputtered on a silicon-based substrate. Similarly to AlN PVD regrowth, it strongly suggests that the quality of the Sc<sub>x</sub>Al<sub>1-x</sub>N films is limited by the quality of the AlN seed layer. Moreover, these results pave the way to an enhancement of Sc<sub>x</sub>Al<sub>1-x</sub>N piezoelectric properties while ensuring a suitable  $k_{\text{eff}}^2$  - Q tradeoff which is determinant in RF devices. It also opens up this approach towards the investigation of other (co-)doping elements (Cr, V, MgZr, MgHf...).

Third, this approach has been extended to AlN MOCVD depositions. The higher deposition temperature enables to enhance the c-axis texture up to 0.3° mainly due to grain coalescence during the growth. The high crystal quality combined with crack-free AlN MOCVD films lays the first stone to potential AlN MOCVD films on low-cost substrate addressing power applications.

In addition, these pure and doped AlN deposition enable to highlight some perspectives. On one hand, all the characterized films display a random in-plane orientation with twisted AlN grains which affect the film mosaicity (c-axis orientation). Hence, control and optimize this in-plane orientation should enhance the c-axis textured growth and result in a better piezoelectric response. On the other hand, for each investigated deposition the crystal quality seems to be limited by the quality of AlN seed layer. In fact, no enhancement of the (Sc)AlN (002) RC is observed with the increase in the thickness. These two results strongly suggest that

the AlN seed layer is the technological and scientific limitation. In fact, this pre-texturing seed elaborated by a PVD low-deposition temperature process (350 °C) has its own crystal quality, roughness, in-plane and out-of-plane orientation... Its properties directly impact the quality of the pure or Sc doped AlN regrowth. Hence, optimize this seed in terms of crystal quality, orientation, for example with a low-temperature MOCVD deposition, should lead to a better crystal quality of regrowth film. Therefore, the quality of the seed layer is an interesting lever to optimize and enhance pure or doped AlN crystal quality.

Finally, even if this approach was focused on pure or doped AlN deposition, we can also take advantage of the reasonable in-plane lattice mismatch between AlN and other interesting materials in microelectronics. Especially, gallium nitride (GaN) and silicon carbide (SiC) in its hexagonal structure, are materials driving power electronics market and displaying an in-plane lattice mismatch with AlN below 3 %. The following and last chapter is dedicated to the growth of these materials.





## VI. Chapter 6: Opening to GaN and SiC regrowth by CVD

In the previous chapter, the approach based on the 2D-MoS<sub>2</sub> modification into MoN<sub>x</sub> through an AlN seed layer has been applied to AlN PVD, Sc doped AlN PVD and AlN MOCVD regrowth and shows promising results. Hence, as AlN displays a reasonable in-plane lattice mismatch with GaN and SiC materials, the proposed approach can be extended to the regrowth of these materials driving the power market.

This last chapter opens up the growth perspectives which may result from the use of the 2D-MoS<sub>2</sub> modification into MoN<sub>x</sub> through the AlN seed layer in the GaN and SiC CVD regrowth. First, we present a reminder of the interest of these materials in power market. Second, we focus on the attempts of GaN MOCVD, discuss SEM and XRD characterizations and propose different perspectives to optimize the GaN crystal quality. Finally, we address the few trials of SiC CVD growth. We describe the different investigated growth conditions and the XRD characterizations of the SiC films.

VI.1. Interest of GaN and SiC materials

As mentioned in chapter 2, the exceptional AlN properties make this material an excellent candidate for high power and frequency applications. However, beyond the difficulties encountered during its growth, the cost of AlN wafers is extremely high and its availability remains limited. The maximum wafer diameter in production is 50 mm<sup>127</sup>. Hence, the power and high-frequency market is focusing on two other wideband gap materials: gallium nitride (GaN) and silicon carbide (mainly 4H-SiC)<sup>463</sup>. A comparison of properties, availability and cost of Si, AlN, 4H-SiC and GaN are given in Table VI.1.

	Si	AlN	4H-SiC	GaN
<b>Bandgap (eV)</b>	1.12	6.1	3.26	3.39
<b>Electric breakdown field (MV.cm<sup>-1</sup>)</b>	0.3	12.0 – 17.0	2.5	3.3
<b>Thermal conductivity (W.cm<sup>-1</sup>.K<sup>-1</sup>)</b>	1.3	2.85	4.2	1.3 – 2.0
<b>Maximum device operating temperature (°C)</b>	150	>750	700	750
<b>Production wafer size (mm)</b>	300	50	200	100 (150 to 200 on Si)
<b>Cost (\$.cm<sup>-2</sup>)</b>	≈ 0.1	≈ 200	≈ 10	≈ 100

Table VI.1: Comparison of some properties, availability and cost of Si, AlN, 4H-SiC and GaN<sup>127,464</sup>

These GaN and SiC materials display appealing properties such as electric breakdown field, thermal conductivity and others enabling to replace silicon material in certain applications. This tendency is well illustrated in Figure VI.1. We clearly observed that GaN material is targeting applications with high operating frequencies. However, and as the breakdown field of GaN is limited up to 1000 V due to its epitaxial growth on silicon, it is not suitable for high output power. Hence, the higher output power applications are covered by SiC taking advantage of its higher breakdown field and thermal conductivity than GaN on Si<sup>464</sup>.

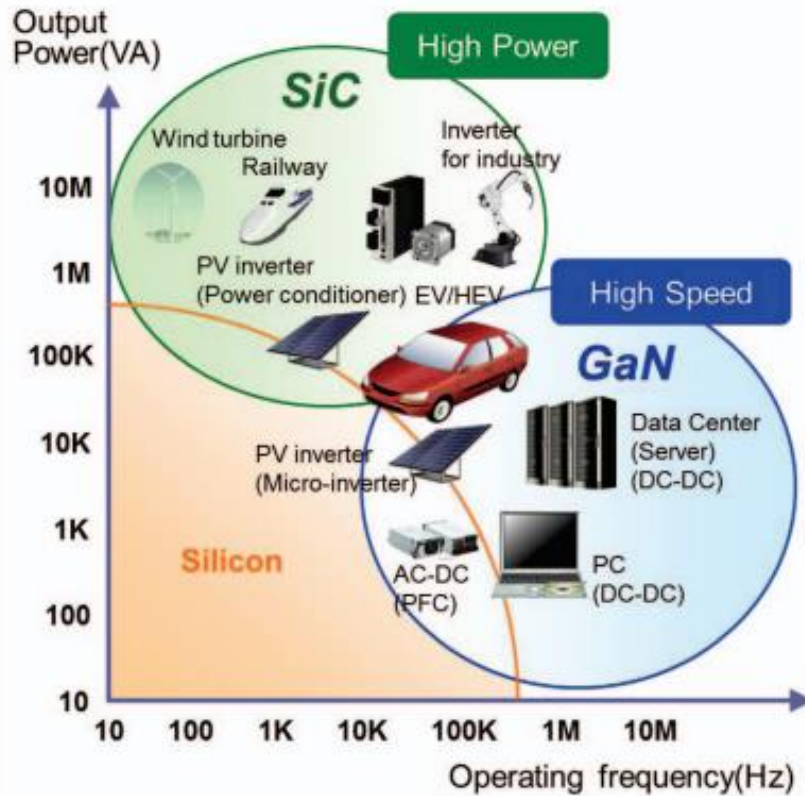


Figure VI.1: Potential applications of GaN and SiC from the aspects of outpower and operating frequency and comparison with Si

In addition, the GaN growth on silicon substrate is challenging due to the large lattice and CTE mismatches between both materials ( $\approx 17\%$  and  $\approx 54\%$ , respectively). To address this issue and achieve high quality and crack-free GaN layers on Si, the main approaches rely on the use of AlN/GaN superlattice, low-temperature AlN interlayer and AlGaIn buffer layer<sup>465</sup>. The idea is to obtain a compressive GaN layer at the growth temperature to avoid cracks during the cooling. However, these approaches are complex and time-consuming. Hence, develop a faster, easier and cost-effective GaN growth process on Si is extremely interesting to address power or high frequency applications.

Finally, and as depicted in chapter 2, Table II.4, GaN and SiC (hexagonal polytypes or (111)-oriented 3C-SiC) materials have a reasonable in-plane lattice mismatch with AlN ( $< 3\%$ ). Hence, we can take advantage of this structural property to grow GaN and SiC material using the cost-effective process developed in this thesis work. It could lead to the elaboration of high-quality GaN and SiC layers deposited on low-cost silicon-based substrate and potentially fuel high power and frequency applications.

VI.2. Growth of GaN by MOCVD

VI.2.1. Description of GaN MOCVD deposition process

GaN MOCVD deposition was performed in the same equipment used for the NH<sub>3</sub> thermal heat treatments through the thin AlN PVD seed layer and AlN MOCVD growth: 6x2 inch close coupled shower head AIXTRON MOCVD reactor. As for AlN MOCVD deposition, it enables to pursue the 2D-MoS<sub>2</sub> modification through the AlN PVD seed layer directly with a direct GaN MOCVD deposition without any air break. Trimethylgallium (TMG) and ammonia was used as Ga and N precursors with a flow rate of 58 sccm and 7300 sccm, respectively. The deposition temperature ranges from 840 °C to 1040 °C. The targeted thicknesses of the GaN MOCVD layers are 300 nm and 600 nm. These growths were performed on the two different AlN seed layer thicknesses (8s and 10.4s).

VI.2.2. Results

VI.2.2.1. Influence of growth temperature

The aim of the first attempts of GaN MOCVD growth was to investigate the influence of the growth temperature. Hence, 300 nm thick GaN MOCVD films deposited on a 8s AlN seed at 840 °C, 940 °C and 1040 °C have been investigated. The growth is schematically sketched in Figure VI.2. Subsequently, the samples have been characterized by XRD with a  $\omega$ -scan and Scanning Electronic Microscopy (SEM) to assess the c-axis orientation and surface morphology, respectively.

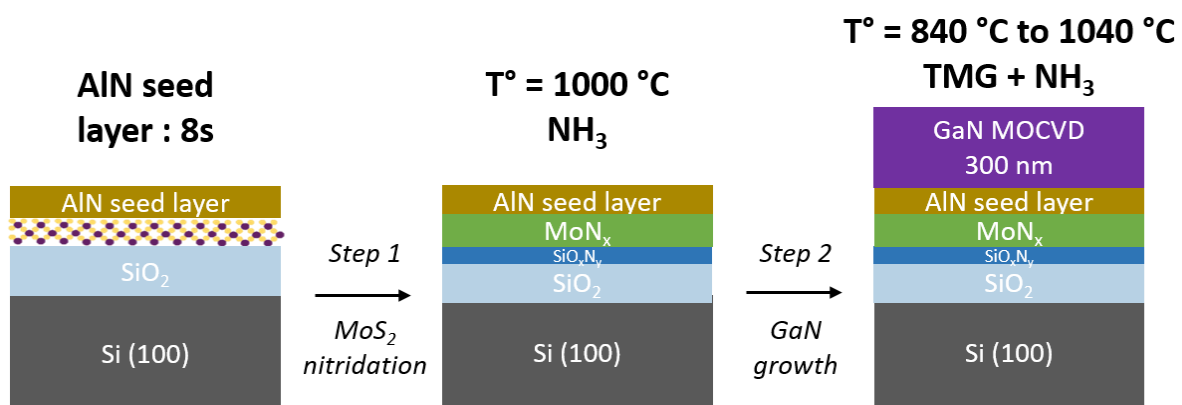


Figure VI.2: Elaboration process of the 300 nm GaN MOCVD layer

First, no clear tendency is observed about the influence of the GaN deposition temperature on the c-axis orientation. The GaN films deposited at 840 °C, 940 °C and 1040 °C display a (002) RC of  $0.52^\circ \pm 0.03^\circ$ ,  $0.47^\circ \pm 0.03^\circ$  and  $0.58^\circ \pm 0.03^\circ$ , respectively. These RC values are between those obtained for AlN PVD (around  $0.7^\circ - 0.8^\circ$ ) and MOCVD deposition (best RC

of 0.3°). It shows the need to optimize the GaN MOCVD process and perform other structural characterizations of the film such TEM or in-plane XRD.

Second, the surface morphology of the GaN layer grown at different temperatures was characterized by SEM. The SEM images are presented in Figure VI.3. Depending on the temperature deposition, drastic differences can be observed. In fact, the as-deposited 1040 °C GaN film presents a rough surface. The growth seems heterogeneous and not well controlled. We observe faceted islands of several microns. A few hexagonal grains are visible showing the presence of a (002) orientation. By reducing the temperature at 940 °C, the size of the faceted islands decreases. In addition, although the GaN film is not covering like for the 1040 °C growth, the surface seems less rough. Finally, even if the GaN film is not covering, the 840 °C regrowth leads to a better surface coverage. The grain hexagonal shape seems more obvious. However, it does not result in a better c-axis orientation as demonstrated with the GaN (002) RC measurements. Finally and as for AlN MOCVD growth, we can note that a defect approximately located at the center of almost each hexagonal grain is visible which could be a threading screw dislocation <sup>459</sup>.

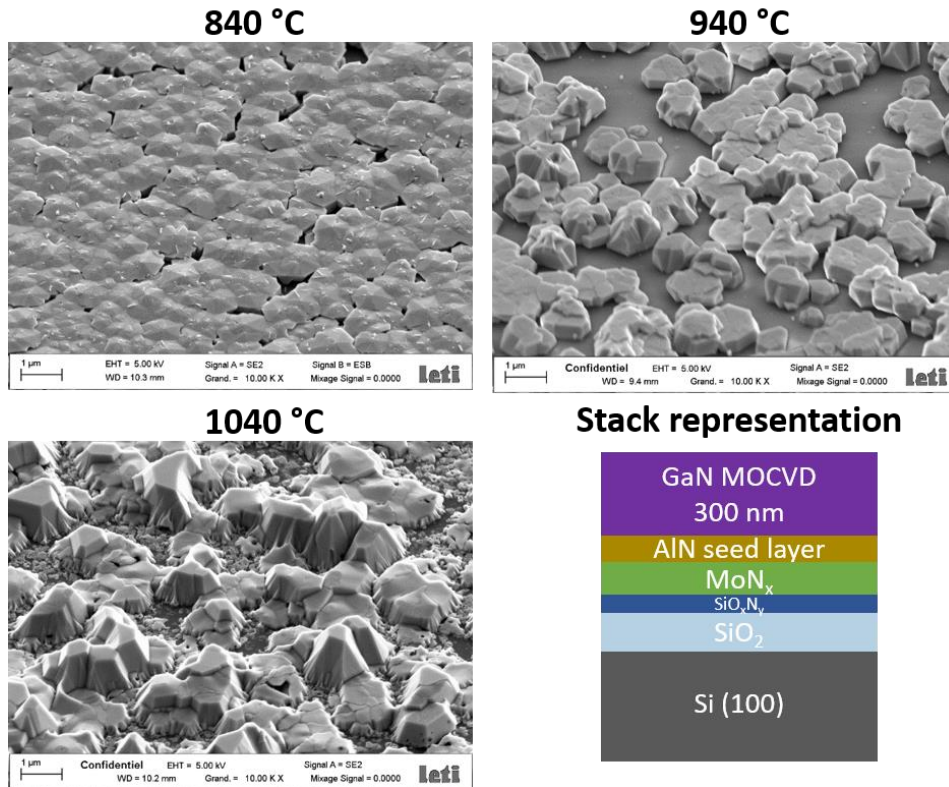


Figure VI.3: SEM images of the surface morphology and stack representation of the 300 nm thick GaN grown at different temperatures

Finally, the relationship between GaN (002) RC measurements with the top surface images are not clear. On one hand, the GaN (002) RC is roughly around  $0.5^\circ$  independently of deposition temperature. On the other hand, despite similar RC values, significant differences in surface morphology are observed. The decrease in GaN deposition temperature seems to promote smoother surface with a better surface coverage. These results show the need to optimize the GaN MOCVD process in order to enhance the GaN surface state and crystal quality to be competitive with the results obtained in the literature.

#### VI.2.2.2. Influence of GaN MOCVD thickness

As previously mentioned, the  $840^\circ\text{C}$  GaN regrowth seems to display the better results (better surface coverage and RC similar to higher deposition temperature). Hence, new GaN regrowth have been performed at this temperature with a thickness of 600 nm. The AlN PVD seed layer thickness AlN PVD is 8s and 10.4s. The SEM images of these samples are presented in Figure VI.4. With the increase in GaN thickness, the surface coverage is significantly enhanced. The surface is also smoother than that observed for the 300 nm thick GaN regrowth and appears similar on the 8s and 10.4s AlN PVD seed layers. However, the hexagonal grains are larger and seem more easily to distinguish on this latest, which suggests a better c-axis orientation.

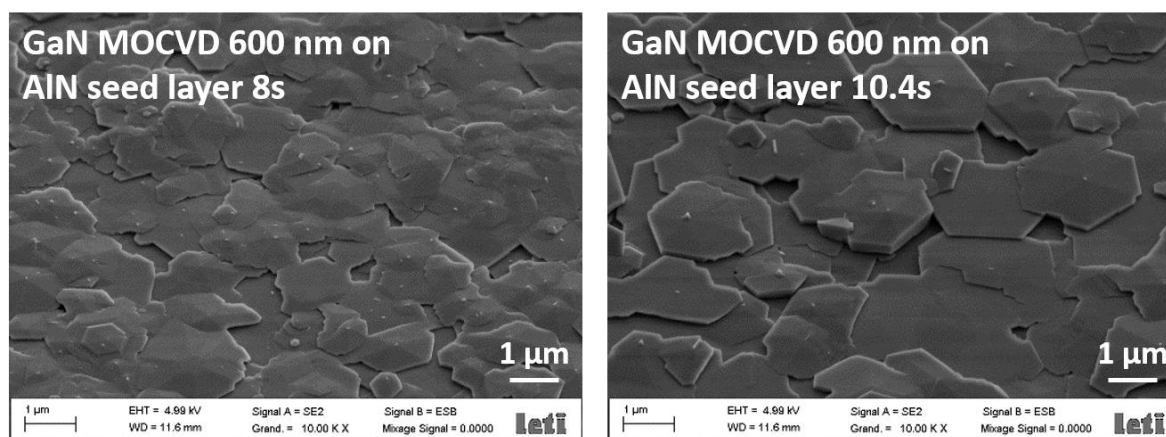


Figure VI.4: SEM images of the surface morphology of 600 nm thick GaN grown at  $840^\circ\text{C}$  on an AlN PVD seed layer of 8s and 10.4s

This assumption is confirmed by the  $\omega$ -scan measurements given in Figure VI.5. In fact, the GaN (002) RC are  $0.56^\circ \pm 0.03^\circ$  and  $0.38^\circ \pm 0.03^\circ$  on the AlN seed of 8s and 10.4s, respectively. First, we can note that the GaN (002) RC value measured on the 8s AlN seed is similar to those reported in section VI.2.2.1 for the 300 nm thick GaN regrowth ( $0.52^\circ \pm 0.03^\circ$ ). It suggests that there is no enhancement of the GaN c-axis orientation with the increase in thickness. Hence

and as discussed in chapter 5 with the pure and Sc doped AlN deposition, the GaN crystal quality is limited by the quality of the AlN seed layer. Second, the GaN (002) RC is better on the thicker AlN seed (10.4s). This result is echoing what have been obtained in chapter 5 on the AlN films deposited by PVD and MOCVD where the c-axis orientation is promoted when the regrowth is performed on the thicker AlN PVD seed layer (10.4s).

Therefore, these observations show that optimize this AlN seed layer (in-plane and out-of-plane orientations, thickness, surface roughness and oxidation...) is primordial to enhance the quality of the grown layer. Finally, although the GaN (002) RC values are promising for first attempts and show wide axis of improvement, they remain relatively away of what can be achieved in the literature since GaN (002) RC below  $0.1^\circ$  are usually mentioned<sup>466–469</sup>. For example, SweGaN shows high-quality GaN thin film grown on AlN nucleation layer displaying a (002) RC of  $0.02^\circ$ <sup>470</sup>.

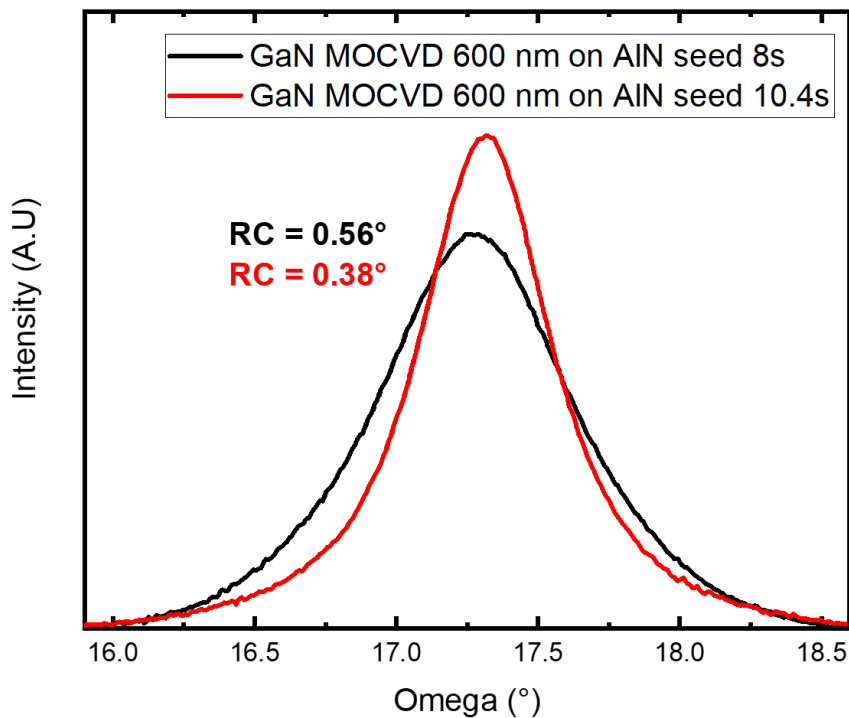


Figure VI.5: GaN (002) RC measurements of the 600 nm thick MOCVD layers deposited on 8s and 10.4s AlN seed layers

To conclude, it is clear than the GaN MOCVD growth process must be optimized. Beyond the deposition parameters (temperature, flux, pressure...) and based on the state of the art discussed in chapter 2, section II.2.3.2.2, several levers have been identified. First, a multi-step GaN deposition can be interesting and should lead to an enhancement of GaN crystal quality. Second, the *in situ* elaboration of an AlN or  $\text{Al}_x\text{Ga}_{1-x}\text{N}$  gradient layer using as a buffer before a thick GaN growth could also be appealing. This proposed solution is discussed hereafter.



## VI.2.2.3. Insertion of AlN MOCVD layer

The *in situ* elaboration of the 200 nm AlN buffer layer before a 300 nm thick GaN MOCVD process is given in Figure VI.6. The growth of the AlN MOCVD buffer layer was performed in the same conditions as those described in the chapter 5, section V.3.1 on a 8s and 10.4s AlN PVD seed layer.

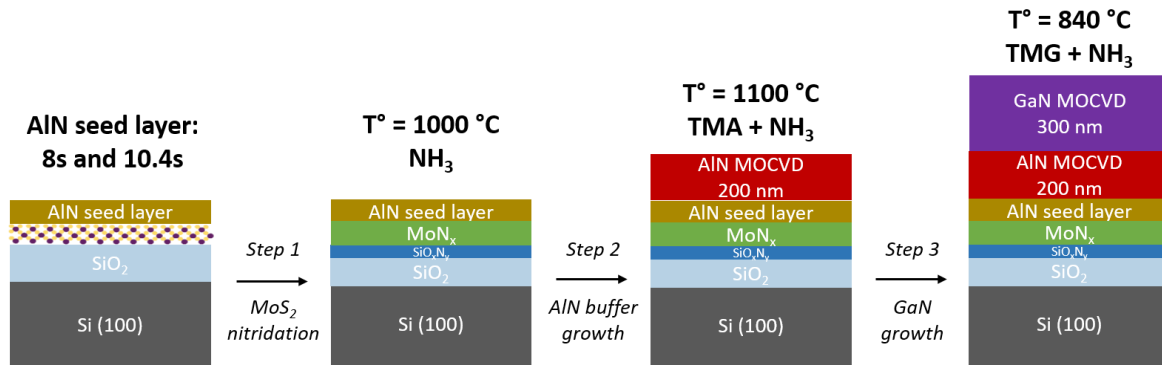


Figure VI.6: Elaboration process of the 300 nm GaN MOCVD layer with an *in situ* AlN MOCVD buffer layer

As the AlN MOCVD growth is well controlled and its reproducibility has been demonstrated on the AlN seed layer, the idea is to use this deposition to enhance the GaN quality in terms of crystalline quality, coverage and surface smoothness. As previously, the samples have been characterized by XRD with a  $\omega$ -scan and SEM images to assess the c-axis orientation and surface morphology, respectively.

Figure VI.7 shows the GaN MOCVD films surface morphology with the AlN MOCVD buffer layer obtained by SEM images. First, the results are relatively similar with the SEM images of the 600 nm GaN layer and presented in section VI.2.2.2. However, the surface seems smoother for the sample grown on the 8s AlN PVD seed layer than 10.4s.

Second, the film coverage is significantly better than the 300 nm GaN direct growth presented in Figure VI.3. It suggests that the use of an *in situ* AlN buffer layer enhance the surface coverage of the GaN film. We can also distinguish hexagonal grains at the surface on each sample.

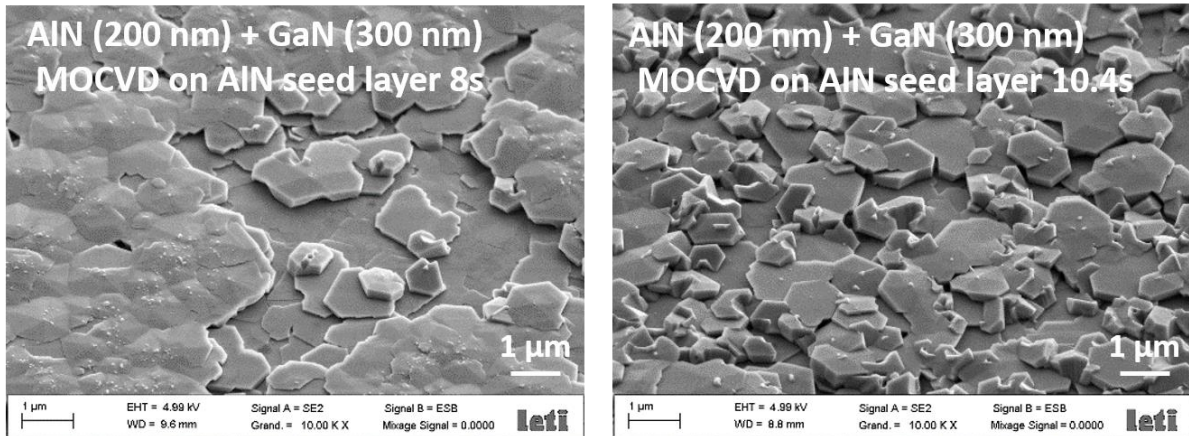


Figure VI.7: SEM images of the surface morphology of 300 nm thick GaN grown at 840 °C using the 200 nm AlN MOCVD buffer on an AlN PVD seed layer of 8s and 10.4s

In addition, and contrary to what have been demonstrated previously, the c-axis textured growth of the GaN layers deposited on the *in situ* elaborated AlN MOCVD buffer is similar, whatever the AlN seed thickness (8s or 10.4s). In fact, and as presented in Figure VI.8, the GaN MOCVD films display RC values of  $0.56^\circ \pm 0.03^\circ$  and  $0.59^\circ \pm 0.03^\circ$ . It can be assumed that the *in situ* AlN MOCVD buffer layer is slightly better on the 10.4s AlN seed. However, this slight increase in AlN buffer crystal quality is insufficient to be transferred to the GaN regrowth.

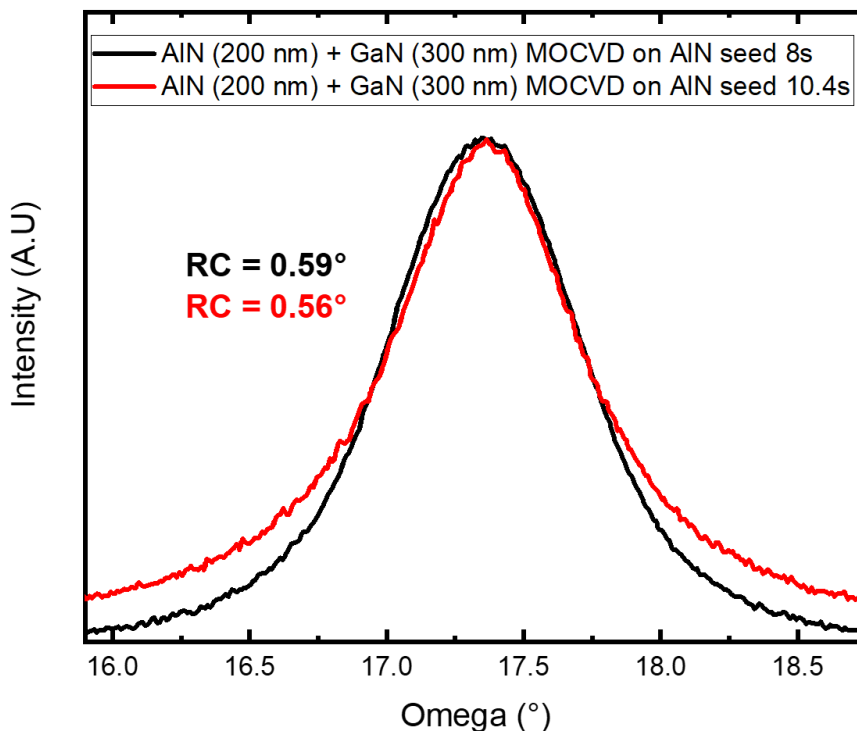


Figure VI.8: GaN (002) RC measurements of the 300 nm thick MOCVD layers deposited on a 200 nm AlN MOCVD buffer layer with an AlN seed of 8s and 10.4s

Finally, comparing these results with the direct 300 nm thick GaN growth at 840 °C presented in section VI.2.2.1, we do not observe any improvement of the GaN c-axis orientation using the *in situ* 200 nm AlN MOCVD buffer layer. In fact, the first GaN attempt without the AlN buffer presents a (002) RC of  $0.52^\circ \pm 0.03^\circ$  which is similar to the obtained values with the AlN buffer ( $0.56^\circ \pm 0.03^\circ$  and  $0.59^\circ \pm 0.03^\circ$ ). Hence, although the use of an *in situ* AlN MOCVD buffer layer seems to be an interesting approach to enhance the GaN crystal quality, a significative optimization work needs to be addressed (deposition parameters, thickness...).

### VI.2.3. Conclusions and perspectives on GaN MOCVD growth

These attempts of GaN MOCVD using the approach based on the 2D-MoS<sub>2</sub> modification into MoN<sub>x</sub> through an AlN seed layer show promising results in heteroepitaxial growth. First, the GaN films are cracks-free and display a preferential c-axis orientation. A GaN (002) RC of  $0.38^\circ \pm 0.03^\circ$  has been achieved for a 600 nm thick layer. However, the surface smoothness needs to be improved and the c-axis orientation is still far of what can be achieved on sapphire or SiC substrates. Second, these few attempts also highlight different axis of improvement. Especially, the deposition parameters such as temperature, gas flow or pressure must be optimized to enhance the surface coverage and surface smoothness. These investigations should result in a better GaN MOCVD crystal quality.

Beyond the deposition parameters, different solutions have been proposed to optimize the GaN growth such as multi-steps GaN deposition or the *in situ* elaboration of an AlN or Al<sub>x</sub>Ga<sub>1-x</sub>N gradient MOCVD using as a buffer layer. This latest has been investigated with a 200 nm thick AlN MOCVD buffer layer. However, this approach which could be promising needs to be optimized to promote a c-axis textured growth of the GaN MOCVD layer. Hence, we could investigate different AlN MOCVD deposition process (temperature, multi-steps, thickness...) since it can affect the GaN crystal quality and surface roughness as demonstrated in the literature<sup>159,468,471,472</sup>. Therefore, wide axis of improvement need to be investigated and could be addressed in another study.

### VI.3. Growth of SiC by CVD

#### VI.3.1. Description of SiC CVD deposition process

The investigation of SiC deposition was possible thanks to the collaboration with the Multimaterials and Interfaces Laboratory (LMI) at Lyon. The SiC CVD deposition was performed in their facilities in a home-made reactor. This equipment is presented in Figure VI.9.



Figure VI.9: Home-made reactor used for SiC CVD growth in LMI facilities

Silane ( $\text{SiH}_4$ ) and propane ( $\text{C}_3\text{H}_8$ ) are used as Si and C precursors, respectively, with a C/Si ratio of 2.25. The growth temperature was fixed at  $1300\text{ }^\circ\text{C}$  or  $1350\text{ }^\circ\text{C}$  and the deposition was set to 1 hour leading to a SiC film thickness around  $3.0\text{ }\mu\text{m}$ . A direct SiC CVD growth was performed on the samples SiC-1 and SiC-6. A carbonization step under  $\text{C}_3\text{H}_8$  was added before the SiC growth for the samples SiC-2 to SiC-4. Finally, a low-temperature SiC buffer was elaborated on the samples SiC-5 with a C/Si ratio of 9. The experimental conditions of each sample are given in Table VI.2.

		SiC-1	SiC-2	SiC-3	SiC-4	SiC-5	SiC-6
<b>1<sup>st</sup> ramp up</b>	Temperature (°C)	25 to 1300	25 to 1150	25 to 1150	25 to 1100	25 to 1200	25 to 1350
	Time (min)	1.5	4	1.5	1.5	1.5	1.5
	Gas	H <sub>2</sub>	H <sub>2</sub> + C <sub>3</sub> H <sub>8</sub>	H <sub>2</sub> + C <sub>3</sub> H <sub>8</sub>	H <sub>2</sub> + C <sub>3</sub> H <sub>8</sub>	H <sub>2</sub>	H <sub>2</sub>
<b>Carbonization step</b>	Temperature (°C)	/	1150	1150	1100	/	/
	Time (min)	/	10	2	2	/	/
	Gas	/	H <sub>2</sub> + C <sub>3</sub> H <sub>8</sub>	H <sub>2</sub> + C <sub>3</sub> H <sub>8</sub>	H <sub>2</sub> + C <sub>3</sub> H <sub>8</sub>	/	/
<b>Buffer elaboration</b>	Temperature (°C)	/	/	/	/	1200	/
	Time (min)	/	/	/	/	2	/
	Gas	/	/	/	/	H <sub>2</sub> + SiH <sub>4</sub> + C <sub>3</sub> H <sub>8</sub>	/
<b>2<sup>nd</sup> ramp up</b>	Temperature (°C)	/	1150 to 1350	1150 to 1350	1100 to 1350	1200 to 1350	/
	Time (min)	/	0.75	0.75	0.75	0.75	/
	Gas	/	H <sub>2</sub> + SiH <sub>4</sub> + C <sub>3</sub> H <sub>8</sub>	H <sub>2</sub> + SiH <sub>4</sub> + C <sub>3</sub> H <sub>8</sub>	H <sub>2</sub> + SiH <sub>4</sub> + C <sub>3</sub> H <sub>8</sub>	H <sub>2</sub> + SiH <sub>4</sub> + C <sub>3</sub> H <sub>8</sub>	/
<b>SiC growth</b>	Temperature (°C)	1300	1350	1350	1350	1350	1350
	Time (min)	60	60	60	60	60	60
	Gas	H <sub>2</sub> + SiH <sub>4</sub> + C <sub>3</sub> H <sub>8</sub>	H <sub>2</sub> + SiH <sub>4</sub> + C <sub>3</sub> H <sub>8</sub>	H <sub>2</sub> + SiH <sub>4</sub> + C <sub>3</sub> H <sub>8</sub>	H <sub>2</sub> + SiH <sub>4</sub> + C <sub>3</sub> H <sub>8</sub>	H <sub>2</sub> + SiH <sub>4</sub> + C <sub>3</sub> H <sub>8</sub>	H <sub>2</sub> + SiH <sub>4</sub> + C <sub>3</sub> H <sub>8</sub>

Table VI.2: Experimental conditions for each SiC CVD growth

As the ramp up and ramp down in temperature was under H<sub>2</sub>, the SiC CVD growth was not directly performed on the AlN seed layer. In fact, according to Kumagai et al.<sup>473</sup> the hydrogen etching rate of Al- or N-polar AlN face starts at 1300 °C and is around 100 – 200 nm.h<sup>-1</sup>. Hence, although the SiC growth temperature is limited up to 1350 °C due to the silicon substrate, the H<sub>2</sub> ramp up in temperature could etch AlN PVD seed through the grain boundaries and degrade its quality or even diffuse into the SiO<sub>2</sub> sub-layer. Therefore, a 500 nm thick AlN PVD film was deposited in the same conditions as those described in chapter 3, section III.2.3. The final stack is represented in the inset of Figure VI.10.

## VI.3.2. Results

## VI.3.2.1. Determination of the SiC polytype and orientation

The SiC polytype of the grown layer is determined by the growth conditions and especially the temperature. In this work, the growth temperature is restricted due to the silicon substrate displaying a melting point at 1415 °C. Hence, the growth temperature does not exceed 1350 °C. In addition, as the growth is performed on a 500 nm thick AlN (heteroepitaxial growth) with a pronounced (002) preferential orientation, the polytype of the SiC layer should be 3C-SiC with a (111) preferential orientation<sup>474</sup>. We can note that the growth of hexagonal SiC is performed at higher temperature (typically 1400 °C – 1500 °C) exclusively through a homoepitaxial growth<sup>474</sup>.

Figure IV.10 shows the asymmetric  $2\theta/\omega$  scan with a  $\omega$  offset of 3° of the SiC-1 sample. The offset enables to annihilate the contributions of the phases which have plans parallel to the surface, typically AlN (00l) and Si (400). The observed contributions are all attributed to 3C-SiC and are indexed on the diffractogram. Although the 3C-SiC phase is polycrystalline, it displays a preferential (111) orientation. Hence, and according to the SiC growth conditions, these results confirmed that the layer is a (111)-oriented 3C-SiC polytype. Similar diffractograms have been obtained for the other samples.

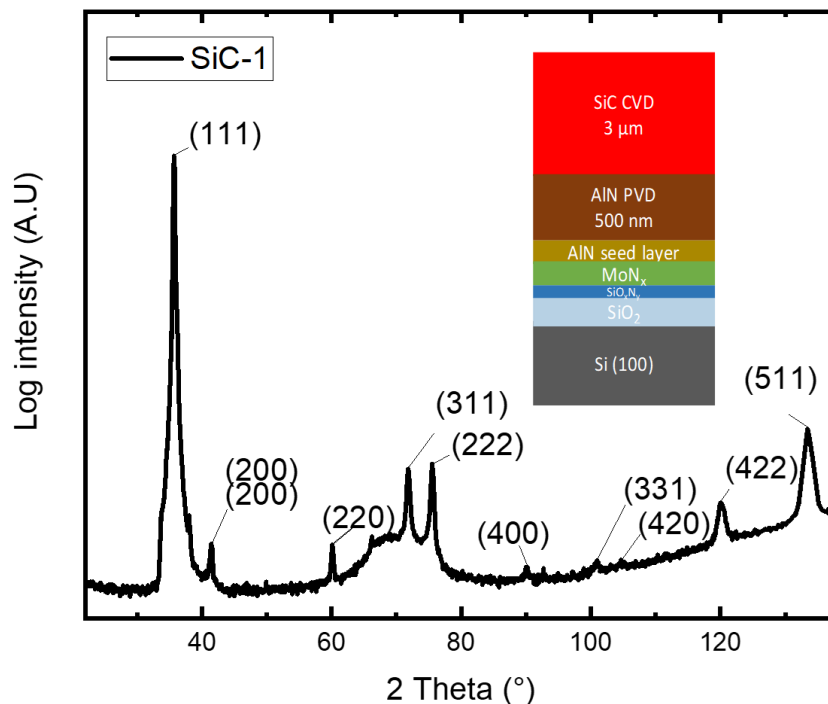


Figure VI.10:  $2\theta/\omega$  scan with a  $\omega$  offset of 3° of the SiC-1 sample.

In addition, an important amount of defects (whiskers) has also been observed by optical microscopy on sample SiC-1. These whiskers could be related to the other observed contributions than (111). Hence, different conditions in ramp up and carbonization steps were investigated on sample SiC-2 to SiC-5 to reduce these defects. A notable whiskers reduction was observed on some samples, especially SiC-3.

VI.3.2.2. Interest of carbonization step

The classical approach of a direct SiC growth on a silicon substrate is to perform a carbonization step under  $C_3H_8$  before the SiC deposition. Hence, the Si is carburized forming a SiC layer serving as a seed for the SiC growth under  $SiH_4 + C_3H_8$  <sup>474</sup>. In this work, the carbonization has another interest. In the assumption of the ramp up in temperature under  $H_2$  would etch the 500 nm thick AlN PVD layer, the quality of SiC growth will be affected. Hence, the aim of the carbonization step is to form an aluminum carbide (typically  $Al_4C_3$ ) enabling to avoid the potential  $H_2$  etching which would result in a degradation of the AlN layer and a degradation of the SiC crystal quality.

VI.3.2.3. Mosaicity of 3C-SiC

The mosaicity of each SiC samples was assessed with a  $\omega$ -scan on the (111) contribution. The mosaicity of the 500 nm thick (002)-oriented AlN layer has also been checked. The results are given in Table VI.3.

		SiC-1	SiC-2	SiC-3	SiC-4	SiC-5	SiC-6
RC (°)	AlN (002)	0.59	0.74	0.73	0.76	0.70	0.73
	SiC (111)	1.09	2.94	2.83	3.78	2.99	1.39

Table VI.3: AlN (002) and SiC (111) RC for each SiC samples

We observe the AlN (002) RC are similar for samples SiC-2 to SiC-6 and slightly lower for sample SiC-1 while the SiC (111) RC range roughly between 1° to almost 4°. This observation suggests that the SiC deposition parameters, carbonization step and the elaboration of a low-temperature SiC buffer layer strongly affect the SiC crystal quality. First, the sample SiC-1 and SiC-6 corresponding to a direct SiC growth on the AlN PVD layer at 1300 °C and 1350 °C, respectively, show the better SiC crystal quality. In fact, they display a (111) RC of  $1.09^\circ \pm 0.03^\circ$  and  $1.39^\circ \pm 0.03^\circ$ , respectively. This slight difference in both samples can probably be explained by the better c-axis orientation of the AlN layer on the SiC-1 sample.

Second, the SiC-2 and SiC-3 samples corresponding to a 10 min and 2 min carbonization step at 1150 °C, present higher (111) RC values of  $2.94^\circ \pm 0.03^\circ$  and  $2.83^\circ \pm 0.03^\circ$ , respectively. On one hand, this result shows that the carbonization step degrades the SiC crystal quality of the grown layer compared to a direct growth. On the other hand, as the (111) RC are similar on both samples, it suggests that the duration of the carbonization step is not a parameter affecting the crystal quality of the SiC layer grown on AlN PVD. Moreover, the SiC-4 sample on which a 2 min carbonization step at 1100 °C is performed has a (111) RC of  $3.78^\circ \pm 0.03^\circ$ . Hence, it seems to show that decrease the carbonization step temperature strongly degrades the quality of the SiC layer.

Finally, the SiC-5 sample on which a low-temperature SiC buffer layer is deposited at 1200 °C before a 1350 °C SiC growth also display a degraded (111) RC of  $2.99^\circ \pm 0.03^\circ$ . Hence, the insertion of a SiC buffer layer does not seem suitable to enhance the SiC crystal quality.

To conclude, the best results have been obtained on samples SiC-1 and SiC-6 on which a direct SiC growth is performed on the AlN layer. Hence, these results highlight that the attempts to protect the AlN PVD layer from the H<sub>2</sub> etching with a carbonization step or with a low-temperature SiC buffer layer degrade the crystal quality of the SiC growth. In fact, all these SiC samples (SiC-2 to SiC-5) display a degraded (111) RC compared to SiC-1 and SiC-6. This observation could be explained as follows. On SiC-1 and SiC-6, the SiC growth is performed directly on the AlN PVD layer which could potentially be degraded by the H<sub>2</sub> etching. On the other samples, the SiC layer is assumed to be deposited, either on an aluminum carbide layer (SiC-2 to SiC-4 with a carbonization step) or on a low-temperature SiC buffer layer (SiC-5). Both layers probably display a lower crystal quality than the AlN PVD layer (without mentioning the lattice mismatch). Hence, the resulting SiC growth quality is lower than that performed directly on the 500 nm thick AlN PVD layer.

Another important result is that the synthesized SiC CVD films seem to not display an important bowing or even cracks. In fact, high bowing of 3C-SiC deposited on Si (100) or Si (111) remains an important issue and can lead to cracks films<sup>475–477</sup>. However, the obtained SiC (111) RC remains higher than what can be achieved with a CVD heteroepitaxial growth on silicon substrates. Several studies mentioned SiC layers deposited by CVD displaying a (111) RC below  $1^\circ$ <sup>478–480</sup>. For example Anzalone et al.<sup>481</sup> deposit SiC by Low-Pressure CVD on (110)-



and (111)-Si oriented substrates. They obtain a (111)-oriented 3C-SiC layer with a RC of  $0.16^\circ$  and  $0.10^\circ$  on Si (110) and Si (111) substrates, respectively.

### VI.3.3. Conclusions and perspectives on SiC CVD growth

On one hand, and as expected according to the investigated growth conditions, all the SiC layers are 3C-SiC polytype with a (111) preferential orientation. Moreover, the films are cracks-free but a significant amount of whisker defects remains. On the other hand, all the attempts to protect the AlN PVD layer from the H<sub>2</sub> etching (carbonization step and SiC buffer layer) show a degradation of the resulting SiC crystal compared to a direct SiC growth.

Finally, these SiC CVD growth enable to identify some perspectives. First, the idea to protect the 500 nm thick AlN PVD layer comes from the assumption of etching the AlN under H<sub>2</sub> at  $\approx 1300^\circ\text{C}$  which needs to be confirmed. Hence, SEM and XRD characterizations of an AlN PVD sample before and after a ramp up in temperature under H<sub>2</sub> will clarify this point. In the case of the AlN is etched by H<sub>2</sub>, its protection with an appropriate layer could enhance the SiC crystal quality. Second, and in the case of the AlN PVD layer is not etched, it strongly means that the SiC crystal quality is limited by the AlN PVD layer. Hence, optimized the crystal quality of this layer using a MOCVD instead of PVD technique should enhance the resulting crystal quality of the SiC grown layer.

#### VI.4. Conclusions of chapter 6

Based on the approach developed in this work (2D-MoS<sub>2</sub> modification into MoN<sub>x</sub> through an AlN seed layer), this last chapter opens to the GaN and SiC CVD growth. First, the GaN MOCVD films are cracks-free and show a pronounced c-axis orientation. However, their crystal quality remains lower than what can be reported in the literature on sapphire on SiC substrate. The GaN layers must be optimized, especially in terms of crystal quality and surface coverage/roughness. In addition, and beyond the optimization of GaN deposition parameters (temperature, multi-steps deposition...), different axis of improvement have been identified. An *in situ* AlN MOCVD buffer layer has been rapidly investigated. However, the elaboration of this buffer also needs to be optimized (temperature, thickness...) since its use does not lead to an improvement in GaN crystal quality. Finally, an Al<sub>x</sub>Ga<sub>1-x</sub>N gradient MOCVD buffer layer could also be an interesting approach to enhance the GaN crystal quality. An important development remains to be carried out and could be addressed in another study.

Second, the 3 μm thick SiC films elaborated are cracks-free 3C-SiC polytype and display a (111) preferential orientation. However, an important amount of whiskers defects is still present. In addition, the results show that the direct SiC growth on AlN PVD layer gives the best results with (111) RC close to 1°. In fact, the SiC samples with a carbonization step or with a SiC buffer present a degraded SiC crystal quality. The potential H<sub>2</sub> etching of the AlN layer must also be verified to serenely pursue and optimize the next SiC growth attempts.

To conclude, this chapter enables to open the use of the approach developed in this work thesis into the growth investigation of GaN and SiC materials which are currently driving the power market. However, and as for the study on pure or Sc doped AlN presented in chapter 5, the quality of the grown layer deposited seems strongly clamped by the crystal quality of the AlN seed layer. Hence, improving the crystal quality of the grown layer (AlN, doped AlN, GaN, SiC and eventually others) goes through enhancing the quality of the AlN seed layer. Typically, a low-temperature deposition of a thin AlN MOCVD seed layer could replace the AlN PVD seed layer deposited on 2D-MoS<sub>2</sub>. This perspective which can be implemented at CEA-LETI is presented in the general conclusions of this thesis.



## General conclusions and perspectives

### Reminder of the context and thesis objective

The rapid development of connected objects and wireless communication among the general public lead to a continuous exponential growth of associated data traffic. To address this challenge, the telecommunication industry has been relying on the introduction of additional frequency bands generally wider and positioned in higher frequency through new wireless technologies (6G or Wi-Fi 7). However, the current SAW and BAW filtering technologies face from severe technical limitations to address the wider and higher frequency band envisioned by the next standards. Especially, AlN-based BAW devices, which have been identified as the most promising approach, suffer from an insufficient  $k_{\text{eff}}^2$  to address wider frequency bandwidth. Consequently, and thanks to the collaboration between STMicroelectronics, CEA-LETI and SIMaP laboratory, as the main challenge is the material one, the objective being to propose an innovative solution to improve the AlN material quality.

### Results summary

First, after justifying the use of AlN as a piezoelectric material and highlighting these growth challenges as a thin film, this work thesis enabled to demonstrate the use of an ALD deposited 2D-MoS<sub>2</sub> thin film resulting in an enhanced crystal quality of sputtered AlN films. However, the lamellar VdW structure of MoS<sub>2</sub> combined with the mechanical bi-axial stress deployment in the AlN bulk leads to a delamination at the MoS<sub>2</sub>/SiO<sub>2</sub> interface. This inherent issue is a major hindrance for the integration of these materials in AlN-based devices.

Second, two main solutions based on the thermochemical modification of 2D-MoS<sub>2</sub> have been developed to address the delamination issue, either by plasma or reactive heat treatment. One hand, plasma treatments have a noticeable physical impact on the AlN surfaces, which leads to degradations, and limits any possible regrowth of a well-textured AlN layer. Moreover, the plasma chemical effect is almost insignificant: AlN shows barrier properties against N\* radicals below 450°C. Therefore, in the investigated conditions, we did not find a satisfactory plasma process window to grow an adherent and textured AlN PVD layer. On the other hand, thermal heat treatment under NH<sub>3</sub> demonstrated a suitable way to nitride MoS<sub>2</sub>, remotely through a thin AlN seed layer. The mechanism is based on the diffusion of N through the grain boundaries of the AlN seed, the conversion of MoS<sub>2</sub> into MoN<sub>x</sub> and the

S counter-diffusion. From this approach, the proof of concept of the resolution of the delamination issue while preserving a highly AlN c-axis textured film has been demonstrated.

Third, the developed elaboration process has been applied to deeply study the crystal quality of pure and Sc doped AlN sputtered thin films. The resulting layers deposited on a silicon-based substrate show an enhanced crystalline quality compared to the state of the art. In fact, the pure and Sc doped AlN films show a (002) RC of  $0.7^\circ - 0.8^\circ$  and roughly around  $1^\circ$ , respectively. These results should promote an increase in pure or Sc doped AlN piezoelectric properties, especially  $k_{\text{eff}}^2$ , and lead to better AlN-based devices performances, while ensuring a suitable  $k_{\text{eff}}^2 - Q$  tradeoff for  $\text{Sc}_x\text{Al}_{1-x}\text{N}$  films which is determinant in RF devices. Hence, it opens the way to a new elaboration process of pure and Sc doped AlN thin films. This elaboration process has also been extended to AlN MOCVD enabling to lay the first stone to potential AlN MOCVD films on low-cost substrate addressing power applications.

Finally, this thesis work ended by opening the use of the developed elaboration process into the growth investigation of GaN and SiC materials which are currently driving the power market. The resulting SiC and AlN films are cracks-free but the crystalline quality of both materials remains to be optimized.

### Perspectives

Beyond the classical perspectives such as investigate other AlN (co-)doping elements such as Cr, V or Mg-Hf and optimize the GaN or SiC growth, this thesis work also enabled to identify primordial axis of improvement. These perspectives are detailed hereafter and could be addressed in other studies.

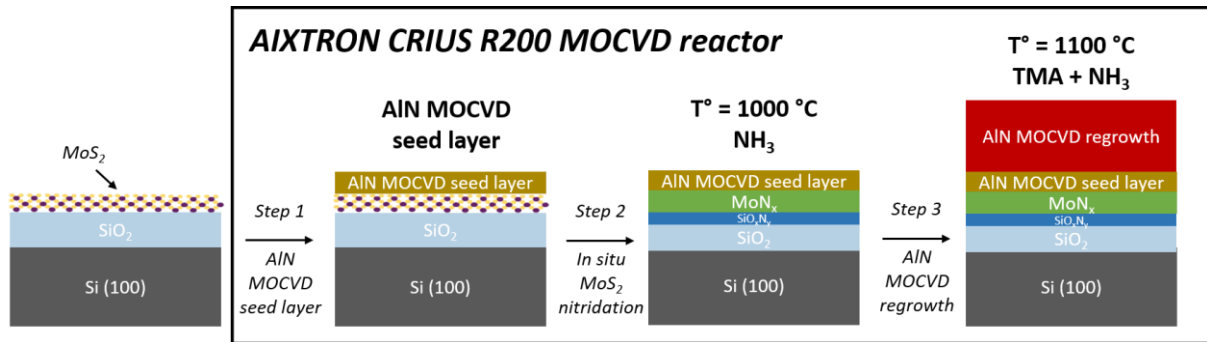
**Optimization of the MoS<sub>2</sub> chemical modification process:** Although this work enables to identify a suitable process window to nitride MoS<sub>2</sub> through an AlN seed layer, it is part of an industrial development perspective. Hence, the resulting process probably should be optimized, especially in terms of duration, NH<sub>3</sub> pressure and annealing temperature. A design of experiments would make possible to limit these suitable ranges enabling to convert MoS<sub>2</sub> through an AlN seed layer. Moreover, the investigation of plasma treatment at temperatures higher than 450 °C while limiting its physical impact should also be a way. Typically, a thermal tool equipped with a remote plasma source could be an interesting perspective to increase

the thermal contribution and favour N\* diffusion through the AlN seed while preserving the AlN surface integrity.

Finally, although a reactional mechanism has been proposed, the mandatory parameters enabling the MoS<sub>2</sub> conversion still need to be clearly clarified. Could a pure nitrogen heat treatment be efficient? Thus, what is the role of the reducing ambient (H<sub>2</sub>) in particular in the adsorption of N and the formation of H<sub>2</sub>S (g) resulting from the assumed counter-diffusion of S? Could a pure N<sub>2</sub> plasma treatment be efficient? What is the contribution of SiO<sub>2</sub> sub-layer in the formation and the kind of de-wetting of Mo(O<sub>x</sub>)N<sub>y</sub> islands? Hence, it may be useful to perform an *in situ* analysis of the gas phase during the MoS<sub>2</sub> conversion to eventually confirm the H<sub>2</sub>S (g) formation. Investigate other nitrogen-based plasma or thermal heat treatment and expand this work to other 2D layers, such as selenides or tellurides 2D films could also be interesting to deeply understand the role of H<sub>2</sub> and SiO<sub>2</sub>.

**Enhancement of piezoelectric properties of pure and Sc doped AlN films:** The elaboration process developed in this work enabled to synthesize pure and Sc doped AlN sputtered layers displaying an enhanced crystal quality on a silicon-based substrate. It should result in an improvement in piezoelectric properties, especially  $k^2_{\text{eff}}$ . However, this increase in piezoelectric response still needs to be proven. In this context, 400 nm thick pure and Sc doped AlN (10 % and 13 %) SAW devices have been processed. Their characterizations should enable to allow to give first elements concerning a possible improvement of the piezoelectric response while comparing the resulting results with the literature. However, they are currently awaiting RF tests.

**Optimization of the AlN seed layer:** A common limit identified about the resulting films is that their crystal quality seems strongly clamped by the crystal quality of the AlN seed layer. Hence, improving the crystal quality of the grown layer (AlN, doped AlN, GaN, SiC and eventually others) goes through enhancing the quality of the AlN seed layer. To remind, this AlN seed layer is sputtered at a low-temperature (350 °C). Hence a thin AlN seed layer deposited by MOCVD in a suitable temperature range (typically 800 °C – 900 °C) could replace the current AlN PVD seed layer deposited on 2D-MoS<sub>2</sub>. On one hand, this perspective can be implemented at CEA-LETI. On the other hand, it enables to *in situ* chain the AlN MOCVD seed layer deposition, NH<sub>3</sub> reactive heat treatment and a second AlN (or eventually Al<sub>x</sub>Ga<sub>1-x</sub>N or GaN) deposition. This perspective is schematically sketched hereafter.



Proposed perspective of the AIN seed layer optimization chain with the NH<sub>3</sub> reactive heat treatment and AIN MOCVD deposition

Finally, the MoS<sub>2</sub> random in-plane orientation (fiber texture) and the perfect VdW epitaxy between AIN and MoS<sub>2</sub> result in a random in-plane orientation of the grown AIN layers (seed and PVD or MOCVD regrowth). These twisted AIN grains are known to affect the mosaicity of the AIN film. Hence, another solution to enhance the AIN mosaicity would be to control this in-plane orientation. On one hand, a potential perspective could be to investigate other experimental conditions of crystallization annealing of the as-deposited ALD MoS<sub>2</sub> layer enabling a controllable grain coalescence and orientations. On the other hand, a CVD-grown MoS<sub>2</sub> layer would also be interesting since it should lead to wider MoS<sub>2</sub> grains and result in a decrease in twisted grains.

**Process application to other substrates:** Finally, this work thesis and the resulting developed elaboration process were only focused a silicon-based substrate, not adapted to elaborate a BAW device. Nevertheless, BAW technology has been identified as the most promising solution to address the new requirements (higher frequency operations and wider bandwidth) envisioned by the next wireless communication standards. Hence, the transfer of the process developed in this work towards a suitable substrate enabling the elaboration of a BAW is still need to be proven. It could also be extended to other substrates targeting power applications.

## References

- (1) Popoff, N.; Malaquin, C. *RF Front-End for Mobile 2023*; YINTR23267; Yole Group, 2023.
- (2) Curie, P.; Curie, J. *Bulletin de Minéralogie*. **1880**, 90.
- (3) Curie, P.; Curie, J. Contractions et Dilatations Produites Par Des Tensions Électriques Dans Les Cristaux Hémihédres à Face Inclonnées. *Compte rendus de l'Académie des Sciences* **1881**, XCIII, 1137.
- (4) Kholkin, A.; Pertsev, N. A.; Goltsev, A. V. Piezoelectricity and Crystal Symmetry. In *Piezoelectric and Acoustic Materials for Transducer Applications*; pp 17–38.
- (5) *IEEE Standard on Piezoelectricity*; IEEE. <https://doi.org/10.1109/IEEESTD.1988.79638>.
- (6) Lefki, K.; Dormans, G. J. M. Measurement of Piezoelectric Coefficients of Ferroelectric Thin Films. *Journal of Applied Physics* **1994**, 76 (3), 1764–1767. <https://doi.org/10.1063/1.357693>.
- (7) Muralt, P.; Kholkin, A.; Kohli, M.; Maeder, T. Piezoelectric Actuation of PZT Thin-Film Diaphragms at Static and Resonant Conditions. *Sensors and Actuators A: Physical* **1996**, 53 (1–3), 398–404. [https://doi.org/10.1016/0924-4247\(96\)01139-9](https://doi.org/10.1016/0924-4247(96)01139-9).
- (8) Defay, E.; Pijolat, M. Formalisme Piézoélectrique. In *Matériaux piézoélectriques intégrés sur silicium*; 2010; p 143.
- (9) Muralt, P.; Antifakos, J.; Cantoni, M.; Lanz, R.; Martin, F. Is There a Better Material for Thin Film BAW Applications than AlN? In *IEEE Ultrasonics Symposium, 2005*; IEEE: Rotterdam, The Netherlands, 2005; Vol. 1, pp 315–320. <https://doi.org/10.1109/ULTSYM.2005.1602858>.
- (10) Chen, Q.; Wang, Q.-M. The Effective Electromechanical Coupling Coefficient of Piezoelectric Thin-Film Resonators. *Appl. Phys. Lett.* **2005**, 86 (2), 022904. <https://doi.org/10.1063/1.1850615>.
- (11) Reinhardt, A.; Billard, C. Résonateurs et Filtres Piézoélectriques. In *Matériaux piézoélectriques intégrés sur silicium*; 2010; p 271.
- (12) Benech, P.; Duchamp, J.-M. Piezoelectric Materials in RF Applications. In *Piezoelectric Materials*; Ogawa, T., Ed.; InTech, 2016. <https://doi.org/10.5772/63125>.
- (13) Tanifuji, S.; Aota, Y.; Kameda, S.; Takagi, T.; Tsubouchi, K. Discussion of Millimeter Wave FBAR with Very Thin AlN Film Fabricated Using MOCVD Method. In *2009 IEEE International Ultrasonics Symposium*; IEEE: Rome, Italy, 2009; pp 2170–2173. <https://doi.org/10.1109/ULTSYM.2009.5441657>.
- (14) Shealy, J. B.; Vetury, R.; Gibb, S. R.; Hodge, M. D.; Patel, P.; McLain, M. A.; Feldman, A. Yu.; Boomgarden, M. D.; Lewis, M. P.; Hosse, B.; Holden, R. Low Loss, 3.7GHz Wideband BAW Filters, Using High Power Single Crystal AlN-on-SiC Resonators. In *2017 IEEE MTT-S International Microwave Symposium (IMS)*; IEEE: Honolulu, HI, USA, 2017; pp 1476–1479. <https://doi.org/10.1109/MWSYM.2017.8058901>.
- (15) Ding, R.; Xuan, W.; Dong, S.; Zhang, B.; Gao, F.; Liu, G.; Zhang, Z.; Jin, H.; Luo, J. The 3.4 GHz BAW RF Filter Based on Single Crystal AlN Resonator for 5G Application. *Nanomaterials* **2022**, 12 (17), 3082. <https://doi.org/10.3390/nano12173082>.
- (16) Moreira, M.; Bjurström, J.; Katardjev, I.; Yantchev, V. Aluminum Scandium Nitride Thin-Film Bulk Acoustic Resonators for Wide Band Applications. *Vacuum* **2011**, 86 (1), 23–26. <https://doi.org/10.1016/j.vacuum.2011.03.026>.
- (17) Yanagitani, T.; Suzuki, M. Electromechanical Coupling and Gigahertz Elastic Properties of ScAlN Films near Phase Boundary. *Appl. Phys. Lett.* **2014**, 105 (12), 122907. <https://doi.org/10.1063/1.4896262>.
- (18) Schneider, M.; DeMiguel-Ramos, M.; Flewitt, A. J.; Iborra, E.; Schmid, U. Scandium Aluminium Nitride-Based Film Bulk Acoustic Resonators. In *Proceedings of Eurosensors 2017, Paris, France, 3–6 September 2017*; MDPI, 2017; p 305. <https://doi.org/10.3390/proceedings1040305>.
- (19) Aigner, R.; Fattinger, G.; Schaefer, M.; Karnati, K.; Rothmund, R.; Dumont, F. BAW Filters for 5G Bands. In *2018 IEEE International Electron Devices Meeting (IEDM)*; IEEE: San Francisco, CA, 2018; p 14.5.1-14.5.4. <https://doi.org/10.1109/IEDM.2018.8614564>.
- (20) Yandrapalli, S.; Plessky, V.; Koskela, J.; Yantchev, V.; Turner, P.; Villanueva, L. G. Analysis of XBAR Resonance and Higher Order Spurious Modes. In *2019 IEEE International Ultrasonics Symposium (IUS)*; IEEE: Glasgow, United Kingdom, 2019; pp 185–188. <https://doi.org/10.1109/ULTSYM.2019.8925993>.
- (21) Bousquet, M.; Enyedi, G.; Dechamp, J.; Zussy, M.; Pokam Kuisseu, P. S.; Mazen, F.; Billard, C.; Reinhardt, A.; Bertucchi, M.; Perreau, P.; Castellan, G.; Maeder-Pachurka, C.; Mercier, D.; Delprato, J.; Borzi, A.; Sejil, S. Single-Mode High Frequency LiNbO<sub>3</sub> Film Bulk Acoustic Resonator. In *2019 IEEE International Ultrasonics Symposium (IUS)*; IEEE: Glasgow, United Kingdom, 2019; pp 84–87. <https://doi.org/10.1109/ULTSYM.2019.8925617>.



- (22) Muralt, P. AlN Thin Film Processing and Basic Properties. In *Piezoelectric MEMS Resonators*; Bhugra, H., Piazza, G., Eds.; Microsystems and Nanosystems; Springer International Publishing: Cham, 2017; pp 3–37. [https://doi.org/10.1007/978-3-319-28688-4\\_1](https://doi.org/10.1007/978-3-319-28688-4_1).
- (23) Liu, Y.; Cai, Y.; Zhang, Y.; Tovstopyat, A.; Liu, S.; Sun, C. Materials, Design, and Characteristics of Bulk Acoustic Wave Resonator: A Review. *Micromachines* **2020**, *11* (7), 630. <https://doi.org/10.3390/mi11070630>.
- (24) Miura, M.; Matsuda, T.; Satoh, Y.; Ueda, M.; Ikata, O.; Ebata, Y.; Takagi, H. Temperature Compensated LiTaO<sub>3</sub>/Sub 3//Sapphire Bonded Saw Substrate with Low Loss and High Coupling Factor Suitable for US-PCS Application. In *IEEE Ultrasonics Symposium, 2004*; IEEE: Montreal, Canada, 2004; Vol. 2, pp 1322–1325. <https://doi.org/10.1109/ULTSYM.2004.1418036>.
- (25) Aigner, R. SAW and BAW Technologies for RF Filter Applications: A Review of the Relative Strengths and Weaknesses. In *2008 IEEE Ultrasonics Symposium*; IEEE: Beijing, China, 2008; pp 582–589. <https://doi.org/10.1109/ULTSYM.2008.0140>.
- (26) Ruppel, C. C. W. Acoustic Wave Filter Technology—A Review. *IEEE Trans. Ultrason., Ferroelect., Freq. Contr.* **2017**, *64* (9), 1390–1400. <https://doi.org/10.1109/TUFFC.2017.2690905>.
- (27) Chen, P.; Li, G.; Zhu, Z. Development and Application of SAW Filter. *Micromachines* **2022**, *13* (5), 656. <https://doi.org/10.3390/mi13050656>.
- (28) Mahon, S. The 5G Effect on RF Filter Technologies. *IEEE Trans. Semicond. Manufact.* **2017**, *30* (4), 494–499. <https://doi.org/10.1109/TSM.2017.2757879>.
- (29) Hashimoto, K. *Surface Acoustic Wave Devices in Telecommunication*, Springer-Verlag.; Berlin, 1998.
- (30) Shirakawa, A. A. Etude, Synthèse et Réalisations de Filtres BAW Pour Applications Mobiles, Université Bordeaux I, 2006.
- (31) Mandal, D.; Banerjee, S. Surface Acoustic Wave (SAW) Sensors: Physics, Materials, and Applications. *Sensors* **2022**, *22* (3), 820. <https://doi.org/10.3390/s22030820>.
- (32) Warder, P.; Link, A. Golden Age for Filter Design: Innovative and Proven Approaches for Acoustic Filter, Duplexer, and Multiplexer Design. *IEEE Microwave* **2015**, *16* (7), 60–72. <https://doi.org/10.1109/MMM.2015.2431236>.
- (33) Yan, Y.; Huang, K.; Zhou, H.; Zhao, X.; Li, W.; Li, Z.; Yi, A.; Huang, H.; Lin, J.; Zhang, S.; Zhou, M.; Xie, J.; Zeng, X.; Liu, R.; Yu, W.; You, T.; Ou, X. Wafer-Scale Fabrication of 42° Rotated Y-Cut LiTaO<sub>3</sub>-on-Insulator (LTOI) Substrate for a SAW Resonator. *ACS Appl. Electron. Mater.* **2019**, *1* (8), 1660–1666. <https://doi.org/10.1021/acsaelm.9b00351>.
- (34) Luo, P.; Zou, Y.; Yang, X.; Li, J.; Huang, X.; Zhou, J.; Han, X.; Liu, Y.; Liu, Y.; Wu, T. Improvement of YX42° Cut LiTaO<sub>3</sub> SAW Filters with Optical Proximity Effect Correction Method. *Micromachines* **2023**, *14* (1), 205. <https://doi.org/10.3390/mi14010205>.
- (35) Sun, J.-H.; Yu, Y.-H. A SAW Filter Using SiO<sub>2</sub>/LiNbO<sub>3</sub> Layered-Structure Phononic Crystals. In *2016 IEEE International Frequency Control Symposium (IFCS)*; IEEE: New Orleans, LA, USA, 2016; pp 1–3. <https://doi.org/10.1109/FCS.2016.7546802>.
- (36) Geng, W.; Zhao, C.; Xue, F.; Qiao, X.; He, J.; Xue, G.; Liu, Y.; Wei, H.; Bi, K.; Mei, L.; Chou, X. Influence of Structural Parameters on Performance of SAW Resonators Based on 128° YX LiNbO<sub>3</sub> Single Crystal. *Nanomaterials* **2022**, *12* (12), 2109. <https://doi.org/10.3390/nano12122109>.
- (37) Nishimura, E.; Okano, K.; Terashima, A.; Hoshikawa, K. Vertical Bridgman Growth of 42°RY-Oriented LiTaO<sub>3</sub> Single Crystal. *Crystal Research and Technology* **2019**, *54* (10), 1900023. <https://doi.org/10.1002/crat.201900023>.
- (38) Kimura, T.; Kadota, M.; Ida, Y. High Q SAW Resonator Using Upper-Electrodes on Grooved-Electrodes in LiTaO<sub>3</sub>. In *2010 IEEE MTT-S International Microwave Symposium*; IEEE: Anaheim, CA, USA, 2010; pp 1740–1743. <https://doi.org/10.1109/MWSYM.2010.5516895>.
- (39) Zhou, C.; Yang, Y.; Cai, H.; Ren, T.-L.; Chan, M.; Yang, C. Y. Temperature-Compensated High-Frequency Surface Acoustic Wave Device. *IEEE Electron Device Lett.* **2013**, *34* (12), 1572–1574. <https://doi.org/10.1109/LED.2013.2283305>.
- (40) Chen, J.; Zhang, Q.; Han, T.; Zhou, L.; Tang, G.; Liu, B.; Ji, X. Theoretical Analysis of Surface Acoustic Wave Propagating Properties of Y-Cut Nano Lithium Niobate Film on Silicon Dioxide. *AIP Advances* **2015**, *5* (8), 087173. <https://doi.org/10.1063/1.4929774>.
- (41) Tomar, M.; Gupta, V.; Sreenivas, K. Temperature Coefficient of Elastic Constants of SiO<sub>2</sub> over-Layer on LiNbO<sub>3</sub> for a Temperature Stable SAW Device. *J. Phys. D: Appl. Phys.* **2003**, *36* (15), 1773–1777. <https://doi.org/10.1088/0022-3727/36/15/304>.
- (42) Abbott, B.; Chen, A.; Daniel, T.; Gamble, K.; Kook, T.; Solal, M.; Steiner, K.; Aigner, R.; Malocha, S.; Hella, C.; Gallagher, M.; Kuypers, J. Temperature Compensated Saw with High Quality Factor. In *2017 IEEE*

- International Ultrasonics Symposium (IUS)*; IEEE: Washington, DC, 2017; pp 1–7. <https://doi.org/10.1109/ULTSYM.2017.8092294>.
- (43) Nishimura, A.; Matsuda, S.; Kabe, Y.; Nakamura, H. Study for Temperature Coefficient of Frequency of Surface Acoustic Wave Devices with SiOxNy Film Using LiTaO<sub>3</sub> Substrate. In *2018 IEEE International Ultrasonics Symposium (IUS)*; IEEE: Kobe, 2018; pp 1–4. <https://doi.org/10.1109/ULTSYM.2018.8580105>.
- (44) Su, R.; Fu, S.; Shen, J.; Lu, Z.; Xu, H.; Yang, M.; Zeng, F.; Song, C.; Wang, W.; Pan, F. Power Durability Enhancement and Failure Analysis of TC-SAW Filter With Ti/Cu/Ti/Cu/Ti Electrodes. *IEEE Trans. Device Mater. Reliab.* **2021**, *21* (3), 365–371. <https://doi.org/10.1109/TDMR.2021.3097151>.
- (45) Kobayashi, H.; Tohyama, K.; Hori, Y.; Iwasaki, Y.; Suzuki, K. A Study on Temperature-Compensated Hybrid Substrates for Surface Acoustic Wave Filters. In *2010 IEEE International Ultrasonics Symposium*; IEEE: San Diego, CA, USA, 2010; pp 637–640. <https://doi.org/10.1109/ULTSYM.2010.5935606>.
- (46) Takai, T.; Iwamoto, H.; Takamine, Y.; Fuyutsume, T.; Nakao, T.; Hiramoto, M.; Toi, T.; Koshino, M. I.H.P. SAW Technology and Its Application to Microacoustic Components (Invited). In *2017 IEEE International Ultrasonics Symposium (IUS)*; IEEE: Washington, DC, USA, 2017; pp 1–8. <https://doi.org/10.1109/ULTSYM.2017.8091876>.
- (47) Butaud, E.; Tavel, B.; Ballandras, S.; Bousquet, M.; Drouin, A.; Huyet, I.; Courjon, E.; Ghorbel, A.; Reinhardt, A.; Clairet, A.; Bernard, F.; Bertrand, I. Smart Cut™ Piezo On Insulator (POI) Substrates for High Performances SAW Components. In *2020 IEEE International Ultrasonics Symposium (IUS)*; IEEE: Las Vegas, NV, USA, 2020; pp 1–4. <https://doi.org/10.1109/IUS46767.2020.9251517>.
- (48) Clairet, A.; Courjon, E.; Laroche, T.; Bernard, F.; Raveski, A.; Michoulier, E.; Aspar, G.; Didier, C.; Huyet, I.; Butaud, E.; Ghorbel, A.; Tavel, B.; Drouin, A.; Ballandras, S. New Generation of Composite Substrates Based on a Layer of LiTaO<sub>3</sub> on Silicon for Surface Acoustic Waves Components. **2020**, 7 pages. <https://doi.org/10.48465/FA.2020.0157>.
- (49) Hao, Z.; Park, M.; Kim, D. G.; Clark, A.; Dargis, R.; Zhu, H.; Ansari, A. Single Crystalline ScAlN Surface Acoustic Wave Resonators with Large Figure of Merit ( $Q \times K_t^2$ ). In *2019 IEEE MTT-S International Microwave Symposium (IMS)*; IEEE: Boston, MA, USA, 2019; pp 786–789. <https://doi.org/10.1109/MWSYM.2019.8700824>.
- (50) Streque, J.; Camus, J.; Laroche, T.; Hage-Ali, S.; M’Jahed, H.; Rammal, M.; Aubert, T.; Djouadi, M. A.; Ballandras, S.; Elmazria, O. Design and Characterization of High-Q SAW Resonators Based on the AlN/Sapphire Structure Intended for High-Temperature Wireless Sensor Applications. *IEEE Sensors J.* **2020**, *20* (13), 6985–6991. <https://doi.org/10.1109/JSEN.2020.2978179>.
- (51) Emanetoglu, N. W.; Gorla, C.; Liu, Y.; Liang, S.; Lu, Y. Epitaxial ZnO Piezoelectric Thin Films for Saw Filters. *Materials Science in Semiconductor Processing* **1999**, *2* (3), 247–252. [https://doi.org/10.1016/S1369-8001\(99\)00022-0](https://doi.org/10.1016/S1369-8001(99)00022-0).
- (52) Fu, S.; Wang, W.; Qian, L.; Li, Q.; Lu, Z.; Shen, J.; Song, C.; Zeng, F.; Pan, F. High-Frequency Surface Acoustic Wave Devices Based on ZnO/SiC Layered Structure. *IEEE Electron Device Lett.* **2019**, *40* (1), 103–106. <https://doi.org/10.1109/LED.2018.2881467>.
- (53) Takai, T.; Iwamoto, H.; Takamine, Y.; Yamazaki, H.; Fuyutsume, T.; Kyoya, H.; Nakao, T.; Kando, H.; Hiramoto, M.; Toi, T.; Koshino, M.; Nakajima, N. High-Performance SAW Resonator on New Multilayered Substrate Using LiTaO<sub>3</sub> Crystal. *IEEE Trans. Ultrason., Ferroelect., Freq. Contr.* **2017**, *64* (9), 1382–1389. <https://doi.org/10.1109/TUFFC.2017.2738119>.
- (54) Takai, T.; Iwamoto, H.; Takamine, Y.; Fuyutsume, T.; Nakao, T.; Hiramoto, M.; Toi, T.; Koshino, M. High-Performance SAW Resonator With Simplified LiTaO<sub>3</sub>/SiO<sub>2</sub> Double Layer Structure on Si Substrate. *IEEE Trans. Ultrason., Ferroelect., Freq. Contr.* **2019**, *66* (5), 1006–1013. <https://doi.org/10.1109/TUFFC.2019.2898046>.
- (55) Kadota, M.; Yunoki, Y.; Shimatsu, T.; Uomoto, M.; Tanaka, S. Near-Zero TCF of HAL SAW Resonator with LiTaO<sub>3</sub>-on-Quartz Structure. In *2018 IEEE International Frequency Control Symposium (IFCS)*; IEEE: Olympic Valley, CA, 2018; pp 1–4. <https://doi.org/10.1109/FCS.2018.8597496>.
- (56) Mudhoni, A.; Gallois, P. *SAW Filter Comparison 2023*; SPR23672; Yole Group, 2023.
- (57) Ruby, R.; Bradley, P.; Larson, J. D.; Oshmyansky, Y. PCS 1900 MHz Duplexer Using Thin Film Bulk Acoustic Resonators (FBARs). *Electron. Lett.* **1999**, *35* (10), 794. <https://doi.org/10.1049/el:19990559>.
- (58) Vetry, R.; Hodge, M. D.; Shealy, J. B. High Power, Wideband Single Crystal XBAW Technology for Sub-6 GHz Micro RF Filter Applications. In *2018 IEEE International Ultrasonics Symposium (IUS)*; IEEE: Kobe, 2018; pp 206–212. <https://doi.org/10.1109/ULTSYM.2018.8580045>.
- (59) Park, M.; Wang, J.; Dargis, R.; Clark, A.; Ansari, A. Super High-Frequency Scandium Aluminum Nitride Crystalline Film Bulk Acoustic Resonators. In *2019 IEEE International Ultrasonics Symposium (IUS)*; IEEE: Glasgow, United Kingdom, 2019; pp 1689–1692. <https://doi.org/10.1109/ULTSYM.2019.8925598>.

- (60) Taniguchi, S.; Yokoyama, T.; Iwaki, M.; Nishihara, T.; Ueda, M.; Satoh, Y. 7E-1 An Air-Gap Type FBAR Filter Fabricated Using a Thin Sacrificed Layer on a Flat Substrate. In *2007 IEEE Ultrasonics Symposium Proceedings*; IEEE: New York, NY, USA, 2007; pp 600–603. <https://doi.org/10.1109/ULTSYM.2007.156>.
- (61) Kok-Wan Tay; Long Wu; Cheng-Liang Huang; Meng-Shan Lin; Long Wu. Growth of AlN Thin Film on Mo Electrode for FBAR Application. In *IEEE Symposium on Ultrasonics, 2003*; IEEE: Honolulu, HI, USA, 2003; Vol. 2, pp 2024–2027. <https://doi.org/10.1109/ULTSYM.2003.1293315>.
- (62) Yang, Q.-W.; Lin, R.-C.; Sun, S.-J. Influence of AlN/ScAlN Piezoelectric Multilayer on the Electromechanical Coupling of FBAR. *Micro and Nanostructures* **2023**, *174*, 207472. <https://doi.org/10.1016/j.micrna.2022.207472>.
- (63) Flewitt, A. J.; Luo, J. K.; Fu, Y. Q.; Garcia-Gancedo, L.; Du, X. Y.; Lu, J. R.; Zhao, X. B.; Iborra, E.; Ramos, M.; Milne, W. I. ZnO Based SAW and FBAR Devices for Bio-Sensing Applications. *Journal of Non-Newtonian Fluid Mechanics* **2015**, *222*, 209–216. <https://doi.org/10.1016/j.jnnfm.2014.12.002>.
- (64) Zhao, X.; Zhao, Z.; Wang, B.; Qian, Z.; Ma, T. The Design of a Frame-Like ZnO FBAR Sensor for Achieving Uniform Mass Sensitivity Distributions. *Sensors* **2020**, *20* (8), 2408. <https://doi.org/10.3390/s20082408>.
- (65) Akiyama, M.; Kamohara, T.; Kano, K.; Teshigahara, A.; Takeuchi, Y.; Kawahara, N. Enhancement of Piezoelectric Response in Scandium Aluminum Nitride Alloy Thin Films Prepared by Dual Reactive Cosputtering. *Adv. Mater.* **2009**, *21* (5), 593–596. <https://doi.org/10.1002/adma.200802611>.
- (66) Manna, S.; Brennecka, G. L.; Stevanović, V.; Ciobanu, C. V. Tuning the Piezoelectric and Mechanical Properties of the AlN System via Alloying with YN and BN. *Journal of Applied Physics* **2017**, *122* (10), 105101. <https://doi.org/10.1063/1.4993254>.
- (67) Suzuki, M.; Kakio, S. Electromechanical Coupling Coefficient  $k_{t}^2$  of Cr Doped AlN Films Grown by Sputtering Deposition. In *2019 IEEE International Ultrasonics Symposium (IUS)*; IEEE: Glasgow, United Kingdom, 2019; pp 716–719. <https://doi.org/10.1109/ULTSYM.2019.8926302>.
- (68) Takano, Y.; Hayakawa, R.; Suzuki, M.; Kakio, S. Increase of Electromechanical Coupling Coefficient  $k_{t}^2$  in (0001)-Oriented AlN Films by Chromium Doping. *Jpn. J. Appl. Phys.* **2021**, *60* (SD), SDDC08. <https://doi.org/10.35848/1347-4065/abef0c>.
- (69) Laidoudi, F.; Amara, S.; Caliendo, C.; Boubenider, F.; Kanouni, F.; Assali, A. High Quality and Low Loss Surface Acoustic Wave SAW Resonator Based on Chromium-Doped AlN on Sapphire. *Appl. Phys. A* **2021**, *127* (4), 255. <https://doi.org/10.1007/s00339-021-04395-y>.
- (70) Liu, H.; Zeng, F.; Tang, G.; Pan, F. Enhancement of Piezoelectric Response of Diluted Ta Doped AlN. *Applied Surface Science* **2013**, *270*, 225–230. <https://doi.org/10.1016/j.apsusc.2013.01.005>.
- (71) Iborra, E.; Olivares, J.; Clement, M.; Capilla, J.; Felmetsger, V.; Mikhov, M. Piezoelectric and Electroacoustic Properties of V-Doped and Ta-Doped AlN Thin Films. In *2013 Joint European Frequency and Time Forum & International Frequency Control Symposium (EFTF/IFC)*; IEEE: Prague, Czech Republic, 2013; pp 262–265. <https://doi.org/10.1109/EFTF-IFC.2013.6702211>.
- (72) Yokoyama, T.; Iwazaki, Y.; Onda, Y.; Nishihara, T.; Sasajima, Y.; Ueda, M. Effect of Mg and Zr Co-Doping on Piezoelectric AlN Thin Films for Bulk Acoustic Wave Resonators. *IEEE Trans. Ultrason., Ferroelect., Freq. Contr.* **2014**, *61* (8), 1322–1328. <https://doi.org/10.1109/TUFFC.2014.3039>.
- (73) Yokoyama, T.; Iwazaki, Y.; Onda, Y.; Nishihara, T.; Sasajima, Y.; Ueda, M. Highly Piezoelectric Co-Doped AlN Thin Films for Wideband FBAR Applications. *IEEE Trans. Ultrason., Ferroelect., Freq. Contr.* **2015**, *62* (6), 1007–1015. <https://doi.org/10.1109/TUFFC.2014.006846>.
- (74) Yokoyama, T.; Iwazaki, Y.; Nishihara, T.; Tsutsumi, J. Dopant Concentration Dependence of Electromechanical Coupling Coefficients of Co-Doped AlN Thin Films for BAW Devices. In *2016 IEEE International Ultrasonics Symposium (IUS)*; IEEE: Tours, France, 2016; pp 1–4. <https://doi.org/10.1109/ULTSYM.2016.7728552>.
- (75) Uehara, M.; Shigemoto, H.; Fujio, Y.; Nagase, T.; Aida, Y.; Umeda, K.; Akiyama, M. Giant Increase in Piezoelectric Coefficient of AlN by Mg-Nb Simultaneous Addition and Multiple Chemical States of Nb. *Appl. Phys. Lett.* **2017**, *111* (11), 112901. <https://doi.org/10.1063/1.4990533>.
- (76) Bousquet, M.; Perreau, P.; Castellan, G.; Bertucchi, M.; Maeder-Pachurka, C.; Delaguillaumie, F.; Joulie, A.; Enyedi, G.; Sailler, B.; Mariolle, D.; Gergaud, P.; Papon, A. M.; Darras, F.-X.; Mazen, F.; Kuisseau, P. S. P.; Lamy, Y.; Billard, C.; Reinhardt, A. Potentialities of LiTaO<sub>3</sub> for Bulk Acoustic Wave Filters. In *2020 IEEE International Ultrasonics Symposium (IUS)*; IEEE: Las Vegas, NV, USA, 2020; pp 1–4. <https://doi.org/10.1109/IUS46767.2020.9251463>.
- (77) Bousquet, M.; Perreau, P.; Joulie, A.; Delaguillaumie, F.; Maeder-Pachurka, C.; Castellan, G.; Enyedi, G.; Delprato, J.; Mazen, F.; Reinhardt, A.; Huyet, I.; Laroche, T.; Clairet, A.; Ballandras, S. 4.2 GHz LiNbO<sub>3</sub> Film Bulk Acoustic Resonator. In *2021 IEEE International Ultrasonics Symposium (IUS)*; IEEE: Xi'an, China, 2021; pp 1–4. <https://doi.org/10.1109/IUS52206.2021.9593774>.

- (78) Bousquet, M.; Borel, E.; Joulie, A.; Perreau, P.; Soulat, E.; Maeder-Pachurka, C.; Delaguillaumie, F.; Castellan, G.; Enyedi, G.; Delprato, J.; Reinhardt, A. LiNbO<sub>3</sub> Film Bulk Acoustic Resonator for N79 Band. In *2022 IEEE International Ultrasonics Symposium (IUS)*; IEEE: Venice, Italy, 2022; pp 1–5. <https://doi.org/10.1109/IUS54386.2022.9957601>.
- (79) Bradley, P.; Kim, J.; Ye, S.; Nikkel, P.; Bader, S.; Feng, C. 12E-0 2X Size and Cost Reduction of Film Bulk Acoustic Resonator (FBAR) Chips with Tungsten Electrodes for PCS/GPS/800 MHz Multiplexers. In *2007 IEEE Ultrasonics Symposium Proceedings*; IEEE: New York, NY, 2007; pp 1144–1147. <https://doi.org/10.1109/ULTSYM.2007.289>.
- (80) Loebel, H. P.; Klee, M.; Metzmacher, C.; Brand, W.; Milsom, R.; Lok, P. Piezoelectric Thin AlN Films for Bulk Acoustic Wave (BAW) Resonators. *Materials Chemistry and Physics* **2003**, *79* (2–3), 143–146. [https://doi.org/10.1016/S0254-0584\(02\)00252-3](https://doi.org/10.1016/S0254-0584(02)00252-3).
- (81) Clement, M.; Olivares, J.; Iborra, E.; González-Castilla, S.; Rimmer, N.; Rastogi, A. AlN Films Sputtered on Iridium Electrodes for Bulk Acoustic Wave Resonators. *Thin Solid Films* **2009**, *517* (16), 4673–4678. <https://doi.org/10.1016/j.tsf.2009.02.139>.
- (82) Akiyama, M.; Nagao, K.; Ueno, N.; Tateyama, H.; Yamada, T. Influence of Metal Electrodes on Crystal Orientation of Aluminum Nitride Thin Films. *Vacuum* **2004**, *74* (3–4), 699–703. <https://doi.org/10.1016/j.vacuum.2004.01.052>.
- (83) Yokoyama, T.; Nishihara, T.; Taniguchi, S.; Iwaki, M.; Satoh, Y.; Ueda, M.; Miyashita, T. New Electrode Material for Low-Loss and High-Q FBAR Filters. In *IEEE Ultrasonics Symposium, 2004*; IEEE: Montreal, Canada, 2004; Vol. 1, pp 429–432. <https://doi.org/10.1109/ULTSYM.2004.1417754>.
- (84) Lakin, K. M.; McCarron, K. T.; Rose, R. E. Solidly Mounted Resonators and Filters. In *1995 IEEE Ultrasonics Symposium. Proceedings. An International Symposium*; IEEE: Seattle, WA, USA, 1995; Vol. 2, pp 905–908. <https://doi.org/10.1109/ULTSYM.1995.495711>.
- (85) Jose, S.; Jansman, A. B. M.; Hueting, R. J. E.; Schmitz, J. Optimized Reflector Stacks for Solidly Mounted Bulk Acoustic Wave Resonators. *IEEE Trans. Ultrason., Ferroelect., Freq. Contr.* **2010**, *57* (12), 2753–2763. <https://doi.org/10.1109/TUFFC.2010.1749>.
- (86) Lv, L.; Shuai, Y.; Huang, S.; Zhu, D.; Wang, Y.; Luo, W.; Wu, C.; Zhang, W. BAW Resonator with an Optimized SiO<sub>2</sub>/Ta<sub>2</sub>O<sub>5</sub> Reflector for 5G Applications. *ACS Omega* **2022**, *7* (24), 20994–20999. <https://doi.org/10.1021/acsomega.2c01749>.
- (87) Garcia-Pastor, D.; Gonzalez-Rodriguez, M.; Hueltes, A.; Collado, C.; Mateu, J.; Gonzalez-Arbesu, J. M.; Kreuzer, S.; Aigner, R. Nonlinear Effects of Electrode and Bragg Reflector Materials in BAW Resonators. In *2017 IEEE International Ultrasonics Symposium (IUS)*; IEEE: Washington, DC, 2017; pp 1–4. <https://doi.org/10.1109/ULTSYM.2017.8091793>.
- (88) Lugo-Hernandez, E.; Mirea, T.; Carmona-Cejas, J. M.; Clement, M.; Olivares, J.; Collado, C.; Mateu, J. High Temperatures BVD Model for AlN-Based Solidly Mounted Resonators. In *2021 IEEE International Ultrasonics Symposium (IUS)*; IEEE: Xi'an, China, 2021; pp 1–3. <https://doi.org/10.1109/IUS52206.2021.9593400>.
- (89) Ansari, A. Single Crystalline Scandium Aluminum Nitride: An Emerging Material for 5G Acoustic Filters. In *2019 IEEE MTT-S International Wireless Symposium (IWS)*; IEEE: Guangzhou, China, 2019; pp 1–3. <https://doi.org/10.1109/IEEE-IWS.2019.8804148>.
- (90) Vetury, R.; Kim, D.; Fallon, K.; Kwon, J.; Winters, M.; Gibb, S. R.; Patel, P.; Hodge, M. D.; Grundman, E.; McLain, M. A.; Shen, Y.; Houlden, R.; Shealy, J. B. Low Loss, Wideband 5.2GHz BAW RF Filters Using Single Crystalline AlN Resonators on Silicon Substrates; 2018.
- (91) Jiao, Z.-Y.; Ma, S.-H.; Yang, J.-F. A Comparison of the Electronic and Optical Properties of Zinc-Blende, Rocksalt and Wurtzite AlN: A DFT Study. *Solid State Sciences* **2011**, *13* (2), 331–336. <https://doi.org/10.1016/j.solidstatesciences.2010.11.030>.
- (92) Boichot, R. Croissance Épitaxiale de Nitrure d'Aluminium Par Procédé CVD : Relation Entre Paramètres Du Procédé et Structure Cristalline. Habilitation à diriger des recherches, Ecole doctorale IMEP2 (Grenoble), 2017. <https://hal.archives-ouvertes.fr/tel-01531049> (accessed 2021-07-01).
- (93) Yeh, C.-Y.; Lu, Z. W.; Froyen, S.; Zunger, A. Zinc-Blende–Wurtzite Polytypism in Semiconductors. *Phys. Rev. B* **1992**, *46* (16), 10086–10097. <https://doi.org/10.1103/PhysRevB.46.10086>.
- (94) Wright, A. F.; Nelson, J. S. Consistent Structural Properties for AlN, GaN, and InN. *Phys. Rev. B* **1995**, *51* (12), 7866–7869. <https://doi.org/10.1103/PhysRevB.51.7866>.
- (95) Goldberg, Y. *Properties of Advanced Semiconductor Materials: GaN, AlN, InN, BN, SiC, SiGe*, John Wiley&Sons.; 2001.
- (96) Saib, S.; Bouarissa, N. Structural Properties of AlN from First Principles Calculations. *Eur. Phys. J. B* **2005**, *47* (3), 379–383. <https://doi.org/10.1140/epjb/e2005-00347-4>.

- (97) Ambacher, O. Growth and Applications of Group III-Nitrides. *J. Phys. D: Appl. Phys.* **1998**, *31* (20), 2653–2710. <https://doi.org/10.1088/0022-3727/31/20/001>.
- (98) Yu, E. T.; Dang, X. Z.; Asbeck, P. M.; Lau, S. S.; Sullivan, G. J. Spontaneous and Piezoelectric Polarization Effects in III–V Nitride Heterostructures. *J. Vac. Sci. Technol. B* **1999**, *17* (4), 1742. <https://doi.org/10.1116/1.590818>.
- (99) Ambacher, O.; Dimitrov, R.; Stutzmann, M.; Foutz, B. E.; Murphy, M. J.; Smart, J. A.; Shealy, J. R.; Weimann, N. G.; Chu, K.; Chumbes, M.; Green, B.; Sierakowski, A. J.; Schaff, W. J.; Eastman, L. F. Role of Spontaneous and Piezoelectric Polarization Induced Effects in Group-III Nitride Based Heterostructures and Devices. *phys. stat. sol. (b)* **1999**, *216* (1), 381–389. [https://doi.org/10.1002/\(SICI\)1521-3951\(199911\)216:1<381::AID-PSSB381>3.0.CO;2-O](https://doi.org/10.1002/(SICI)1521-3951(199911)216:1<381::AID-PSSB381>3.0.CO;2-O).
- (100) Davydov, S. Yu. Estimates of the Spontaneous Polarization and Permittivities of AlN, GaN, InN, and SiC Crystals. *Phys. Solid State* **2009**, *51* (6), 1231–1235. <https://doi.org/10.1134/S1063783409060249>.
- (101) Zoroddu, A.; Bernardini, F.; Ruggerone, P.; Fiorentini, V. First-Principles Prediction of Structure, Energetics, Formation Enthalpy, Elastic Constants, Polarization, and Piezoelectric Constants of AlN, GaN, and InN: Comparison of Local and Gradient-Corrected Density-Functional Theory. *Phys. Rev. B* **2001**, *64* (4), 045208. <https://doi.org/10.1103/PhysRevB.64.045208>.
- (102) Tsubouchi, K.; Mikoshiba, N. Zero-Temperature-Coefficient SAW Devices on AlN Epitaxial Films. *IEEE Trans. Son. Ultrason.* **1985**, *32* (5), 634–644. <https://doi.org/10.1109/T-SU.1985.31647>.
- (103) Sotnikov, A. V.; Schmidt, H.; Wehnacht, M.; Smirnova, E. P.; Chemekova, T. Y.; Makarov, Y. N. Elastic and Piezoelectric Properties of AlN and LiAlO<sub>2</sub> Single Crystals. *IEEE Trans. Ultrason., Ferroelect., Freq. Contr.* **2010**, *57* (4), 808–811. <https://doi.org/10.1109/TUFFC.2010.1485>.
- (104) McNeil, L. E.; Grimsditch, M.; French, R. H. Vibrational Spectroscopy of Aluminum Nitride. *J American Ceramic Society* **1993**, *76* (5), 1132–1136. <https://doi.org/10.1111/j.1151-2916.1993.tb03730.x>.
- (105) Wright, A. F. Elastic Properties of Zinc-Blende and Wurtzite AlN, GaN, and InN. *Journal of Applied Physics* **1997**, *82* (6), 2833–2839. <https://doi.org/10.1063/1.366114>.
- (106) Zagorac, D.; Zagorac, J.; Djukic, M. B.; Jordanov, D.; Matović, B. Theoretical Study of AlN Mechanical Behaviour under High Pressure Regime. *Theoretical and Applied Fracture Mechanics* **2019**, *103*, 102289. <https://doi.org/10.1016/j.tafmec.2019.102289>.
- (107) Yonenaga, I. Hardness of Bulk Single-Crystal GaN and AlN. *MRS Internet j. nitride semicond. res.* **2002**, *7*, e6. <https://doi.org/10.1557/S1092578300000326>.
- (108) Goto, T.; Tsuneyoshi, J.; Kaya, K.; Hirai, T. Preferred Orientation of AlN Plates Prepared by Chemical Vapour Deposition of AlCl<sub>3</sub> + N<sub>2</sub> System. **8**.
- (109) Strite, S. GaN, AlN, and InN: A Review. *J. Vac. Sci. Technol. B* **1992**, *10* (4), 1237. <https://doi.org/10.1116/1.585897>.
- (110) Miao, X. S.; Chan, Y. C.; Pun, E. Y. B. Influence of Reactive Gas Pressure on the Deposition of an AlN Protective Film for Organic Photoconductor. *Thin Solid Films* **1998**, *315* (1–2), 123–126. [https://doi.org/10.1016/S0040-6090\(97\)00269-1](https://doi.org/10.1016/S0040-6090(97)00269-1).
- (111) Ali, F.; Qasim, A. M.; Imran, S.; Mehmood, M.; Jamil, A.; Maqsood, M. Study of the Effect of Coating Thickness, Substrate Temperature and Biasing Voltage on Various Characteristics of AlN Film. *KEM* **2010**, *442*, 211–220. <https://doi.org/10.4028/www.scientific.net/KEM.442.211>.
- (112) Bagcivan, N.; Bobzin, K.; Ludwig, A.; Grochla, D.; Brugnara, R. H. CrN/AlN Nanolaminate Coatings Deposited via High Power Pulsed and Middle Frequency Pulsed Magnetron Sputtering. *Thin Solid Films* **2014**, *572*, 153–160. <https://doi.org/10.1016/j.tsf.2014.06.058>.
- (113) Zhuang, D.; Edgar, J. H.; Liu, L.; Liu, B.; Walker, L. Wet Chemical Etching of AlN Single Crystals. *MRS Internet j. nitride semicond. res.* **2002**, *7*, e4. <https://doi.org/10.1557/S1092578300000302>.
- (114) Slack, G. A.; Tanzilli, R. A.; Pohl, R. O.; Vandersande, J. W. The Intrinsic Thermal Conductivity of AlN. *Journal of Physics and Chemistry of Solids* **1987**, *48* (7), 641–647. [https://doi.org/10.1016/0022-3697\(87\)90153-3](https://doi.org/10.1016/0022-3697(87)90153-3).
- (115) Lei, S.; Mathews, I.; Camus, J.; Bensalem, S.; Djouadi, M. A.; Shen, A.; Duan, G.-H.; Enright, R. ALN Thin-Films as Heat Spreaders in III–V Photonics Devices Part 2: Simulations. In *2016 15th IEEE Intersociety Conference on Thermal and Thermomechanical Phenomena in Electronic Systems (ITHERM)*; IEEE: Las Vegas, NV, USA, 2016; pp 1024–1029. <https://doi.org/10.1109/ITHERM.2016.7517659>.
- (116) Ueda, S. T.; McLeod, A.; Chen, M.; Perez, C.; Pop, E.; Alvarez, D.; Kummel, A. C. Deposition of High Thermal Conductivity AlN Heat Spreader Films. In *2020 International Symposium on VLSI Technology, Systems and Applications (VLSI-TSA)*; IEEE: Hsinchu, Taiwan, 2020; pp 110–111. <https://doi.org/10.1109/VLSI-TSA48913.2020.9203721>.

- (117) Franco Júnior, A.; Shanafield, D. J. Thermal Conductivity of Polycrystalline Aluminum Nitride (AlN) Ceramics. *Cerâmica* **2004**, *50* (315), 247–253. <https://doi.org/10.1590/S0366-69132004000300012>.
- (118) Yim, W. M.; Paff, R. J. Thermal Expansion of AlN, Sapphire, and Silicon. *Journal of Applied Physics* **1974**, *45* (3), 1456–1457. <https://doi.org/10.1063/1.1663432>.
- (119) Alsaad, A. M.; Al-Bataineh, Q. M.; Qattan, I. A.; Ahmad, A. A.; Ababneh, A.; Albataineh, Z.; Aljarrah, I. A.; Telfah, A. Measurement and Ab Initio Investigation of Structural, Electronic, Optical, and Mechanical Properties of Sputtered Aluminum Nitride Thin Films. *Front. Phys.* **2020**, *8*, 115. <https://doi.org/10.3389/fphy.2020.00115>.
- (120) Ababneh, A.; Dagamseh, A. M. K.; Albataineh, Z.; Tantawi, M.; Al-Bataineh, Q. M.; Telfah, M.; Zengerle, T.; Seidel, H. Optical and Structural Properties of Aluminium Nitride Thin-Films Synthesized by DC-Magnetron Sputtering Technique at Different Sputtering Pressures. *Microsyst Technol* **2021**, *27* (8), 3149–3159. <https://doi.org/10.1007/s00542-020-05081-4>.
- (121) Perry, P. B.; Rutz, R. F. The Optical Absorption Edge of Single-crystal AlN Prepared by a Close-spaced Vapor Process. *Appl. Phys. Lett.* **1978**, *33* (4), 319–321. <https://doi.org/10.1063/1.90354>.
- (122) Yamashita, H.; Fukui, K.; Misawa, S.; Yoshida, S. Optical Properties of AlN Epitaxial Thin Films in the Vacuum Ultraviolet Region. *Journal of Applied Physics* **1979**, *50* (2), 896–898. <https://doi.org/10.1063/1.326007>.
- (123) Ballestín-Fuertes, J.; Muñoz-Cruzado-Alba, J.; Sanz-Osorio, J. F.; Laporta-Puyal, E. Role of Wide Bandgap Materials in Power Electronics for Smart Grids Applications. *Electronics* **2021**, *10* (6), 677. <https://doi.org/10.3390/electronics10060677>.
- (124) Shenai, K. High-Density Power Conversion and Wide-Bandgap Semiconductor Power Electronics Switching Devices. *Proc. IEEE* **2019**, *107* (12), 2308–2326. <https://doi.org/10.1109/JPROC.2019.2948554>.
- (125) Kamata, H.; Ishii, Y.; Mabuchi, T.; Naoe, K.; Ajimura, S.; Sanada, K. Single Crystal Growth of Aluminum Nitride. *Fujikura Technical Review* **2009**, 41–45.
- (126) Garrido-Diez, D.; Baraia, I. Review of Wide Bandgap Materials and Their Impact in New Power Devices. In *2017 IEEE International Workshop of Electronics, Control, Measurement, Signals and their Application to Mechatronics (ECMSM)*; IEEE: Donostia, San Sebastian, Spain, 2017; pp 1–6. <https://doi.org/10.1109/ECMSM.2017.7945876>.
- (127) Sumathi, R. R. Review—Status and Challenges in Hetero-Epitaxial Growth Approach for Large Diameter AlN Single Crystalline Substrates. *ECS J. Solid State Sci. Technol.* **2021**, *10* (3), 035001. <https://doi.org/10.1149/2162-8777/abe6f5>.
- (128) Slack, G. A. Growth of AlN Single Crystals. *MRS Proc.* **1998**, *512*, 35. <https://doi.org/10.1557/PROC-512-35>.
- (129) Bickermann, M.; Paskova, T. Vapor Transport Growth of Wide Bandgap Materials. In *Handbook of Crystal Growth*; Elsevier, 2015; pp 621–669. <https://doi.org/10.1016/B978-0-444-63303-3.00016-X>.
- (130) Dalmau, R.; Sitar, Z. AlN Bulk Crystal Growth by Physical Vapor Transport. In *Springer Handbook of Crystal Growth*; Dhanaraj, G., Byrappa, K., Prasad, V., Dudley, M., Eds.; Springer Berlin Heidelberg: Berlin, Heidelberg, 2010; pp 821–843. [https://doi.org/10.1007/978-3-540-74761-1\\_24](https://doi.org/10.1007/978-3-540-74761-1_24).
- (131) Hartmann, C.; Wollweber, J.; Dittmar, A.; Irmscher, K.; Kwasniewski, A.; Langhans, F.; Neugut, T.; Bickermann, M. Preparation of Bulk AlN Seeds by Spontaneous Nucleation of Freestanding Crystals. *Jpn. J. Appl. Phys.* **2013**, *52* (8S), 08JA06. <https://doi.org/10.7567/JJAP.52.08JA06>.
- (132) Boichot, R.; Claudel, A.; Baccar, N.; Milet, A.; Blanquet, E.; Pons, M. Epitaxial and Polycrystalline Growth of AlN by High Temperature CVD: Experimental Results and Simulation. *Surface and Coatings Technology* **2010**, *205* (5), 1294–1301. <https://doi.org/10.1016/j.surfcoat.2010.08.049>.
- (133) Song, Y.; Kawamura, F.; Taniguchi, T.; Shimamura, K.; Ohashi, N. Conditions for Growth of AlN Single Crystals in Al-Sn Flux. *J Am Ceram Soc* **2018**, *101* (11), 4876–4879. <https://doi.org/10.1111/jace.15865>.
- (134) Schlessler, R.; Dalmau, R.; Yakimova, R.; Sitar, Z. Growth of AlN Bulk Crystals from the Vapor Phase. *MRS Proc.* **2001**, *693*, I9.4.1. <https://doi.org/10.1557/PROC-693-I9.4.1>.
- (135) Tsujisawa, K.; Kishino, S.; Liu, Y. H.; Miyake, H.; Hiramatsu, K.; Shibata, T.; Tanaka, M. High Temperature Growth of AlN Film by LP-HVPE. *Phys. Status Solidi (c)* **2007**, *4* (7), 2252–2255. <https://doi.org/10.1002/pssc.200674814>.
- (136) Kumagai, Y.; Kubota, Y.; Nagashima, T.; Kinoshita, T.; Dalmau, R.; Schlessler, R.; Moody, B.; Xie, J.; Murakami, H.; Koukitu, A.; Sitar, Z. Preparation of a Freestanding AlN Substrate from a Thick AlN Layer Grown by Hydride Vapor Phase Epitaxy on a Bulk AlN Substrate Prepared by Physical Vapor Transport. *Appl. Phys. Express* **2012**, *5* (5), 055504. <https://doi.org/10.1143/APEX.5.055504>.

- (137) Koryakin, A. A.; Kukushkin, S. A.; Osipov, A. V.; Sharofidinov, S. Sh.; Shcheglov, M. P. Growth Mechanism of Semipolar AlN Layers by HVPE on Hybrid SiC/Si(110) Substrates. *Materials* **2022**, *15* (18), 6202. <https://doi.org/10.3390/ma15186202>.
- (138) Lai, M.-J.; Chang, L.-B.; Yuan, T.-T.; Lin, R.-M. Improvement of Crystal Quality of AlN Grown on Sapphire Substrate by MOCVD. *Cryst. Res. Technol.* **2010**, *45* (7), 703–706. <https://doi.org/10.1002/crat.201000063>.
- (139) Narang, K.; Pandey, A.; Khan, R.; Singh, V. K.; Bag, R. K.; Padmavati, M. V. G.; Tyagi, R.; Singh, R. High-Quality AlN Nucleation Layer on SiC Substrate Grown by MOVPE: Growth, Structural and Optical Characteristics. *Materials Science and Engineering: B* **2022**, *278*, 115635. <https://doi.org/10.1016/j.mseb.2022.115635>.
- (140) Rong, X.; Wang, X.; Chen, G.; Pan, J.; Wang, P.; Liu, H.; Xu, F.; Tan, P.; Shen, B. Residual Stress in AlN Films Grown on Sapphire Substrates by Molecular Beam Epitaxy. *Superlattices and Microstructures* **2016**, *93*, 27–31. <https://doi.org/10.1016/j.spmi.2016.02.050>.
- (141) Koshelev, O. A.; Nechaev, D. V.; Ivanov, S. V.; Jmerik, V. N. Stress Evolution in AlN Layers Grown on C-Al<sub>2</sub>O<sub>3</sub> by Plasma-Assisted Molecular Beam Epitaxy at Metal-Rich Conditions. *J. Phys.: Conf. Ser.* **2018**, *1124*, 022041. <https://doi.org/10.1088/1742-6596/1124/2/022041>.
- (142) Isobe, H.; Kawamura, F.; Kawahara, M.; Yoshimura, M.; Mori, Y.; Sasaki, T. Synthesis of AlN Grains and Liquid-Phase-Epitaxy (LPE) Growth of AlN Films Using Sn-Ca Mixed Flux. *Jpn. J. Appl. Phys.* **2005**, *44* (4L), L488. <https://doi.org/10.1143/JJAP.44.L488>.
- (143) Adachi, M.; Fukuyama, H. Non-Polar *a*-Plane AlN Growth on Nitrided *r*-Plane Sapphire by Ga-Al Liquid-Phase Epitaxy. *Phys. Status Solidi B* **2018**, *255* (5), 1700478. <https://doi.org/10.1002/pssb.201700478>.
- (144) Ababneh, A.; Schmid, U.; Hernando, J.; Sánchez-Rojas, J. L.; Seidel, H. The Influence of Sputter Deposition Parameters on Piezoelectric and Mechanical Properties of AlN Thin Films. *Materials Science and Engineering: B* **2010**, *172* (3), 253–258. <https://doi.org/10.1016/j.mseb.2010.05.026>.
- (145) Stoeckel, C.; Kaufmann, C.; Hahn, R.; Schulze, R.; Billep, D.; Gessner, T. Pulsed DC Magnetron Sputtered Piezoelectric Thin Film Aluminum Nitride – Technology and Piezoelectric Properties. *Journal of Applied Physics* **2014**, *116* (3), 034102. <https://doi.org/10.1063/1.4887799>.
- (146) Kolaklieva, L.; Chitanov, V.; Szekeres, A.; Antonova, K.; Terziyska, P.; Fogarassy, Z.; Petrik, P.; Mihailescu, I.; Duta, L. Pulsed Laser Deposition of Aluminum Nitride Films: Correlation between Mechanical, Optical, and Structural Properties. *Coatings* **2019**, *9* (3), 195. <https://doi.org/10.3390/coatings9030195>.
- (147) Banerjee, S.; Aarnink, A. A. I.; van de Kruijs, R.; Kovalgin, A. Y.; Schmitz, J. PEALD AlN: Controlling Growth and Film Crystallinity. *Phys. Status Solidi C* **2015**, *12* (7), 1036–1042. <https://doi.org/10.1002/pssc.201510039>.
- (148) Tian, L.; Ponton, S.; Benz, M.; Crisci, A.; Reboud, R.; Giusti, G.; Volpi, F.; Rapenne, L.; Vallée, C.; Pons, M.; Mantoux, A.; Jiménez, C.; Blanquet, E. Aluminum Nitride Thin Films Deposited by Hydrogen Plasma Enhanced and Thermal Atomic Layer Deposition. *Surface and Coatings Technology* **2018**, *347*, 181–190. <https://doi.org/10.1016/j.surfcoat.2018.04.031>.
- (149) Motamedi, P.; Cadien, K. Structural and Optical Characterization of Low-Temperature ALD Crystalline AlN. *Journal of Crystal Growth* **2015**, *421*, 45–52. <https://doi.org/10.1016/j.jcrysgro.2015.04.009>.
- (150) Guinebretière, R. *X-Ray Diffraction by Polycrystalline Materials: Guinebretière/X-Ray*; ISTE: London, UK, 2007. <https://doi.org/10.1002/9780470612408>.
- (151) Fornari, R. Epitaxy for Energy Materials. In *Handbook of Crystal Growth*; Elsevier, 2015; pp 1–49. <https://doi.org/10.1016/B978-0-444-63304-0.00001-9>.
- (152) Goorsky, M. S. X-Ray and Electron Diffraction for Epitaxial Structures. In *Handbook of Crystal Growth*; Elsevier, 2015; pp 1211–1248. <https://doi.org/10.1016/B978-0-444-63304-0.00030-5>.
- (153) Shen, J.; Johnston, S.; Shang, S.; Anderson, T. Calculated Strain Energy of Hexagonal Epitaxial Thin Films. *Journal of Crystal Growth* **2002**, *240* (1–2), 6–13. [https://doi.org/10.1016/S0022-0248\(01\)02209-6](https://doi.org/10.1016/S0022-0248(01)02209-6).
- (154) Bryant, W. A. The Fundamentals of Chemical Vapour Deposition. *J Mater Sci* **1977**, *12* (7), 1285–1306. <https://doi.org/10.1007/BF00540843>.
- (155) Suhir, E. Predicted Thermal- and Lattice-Mismatch Stresses. In *Handbook of Crystal Growth*; Elsevier, 2015; pp 983–1005. <https://doi.org/10.1016/B978-0-444-63304-0.00024-X>.
- (156) Kimoto, T.; Cooper, J. A. Epitaxial Growth of Silicon Carbide. In *Fundamentals of Silicon Carbide Technology: Growth, Characterization, Devices, and Applications*; 2014.
- (157) Pishchik, V.; Lytvynov, L. A.; Dobrovinskaya, E. R. *Sapphire: Material, Manufacturing, Applications*; Springer US: Boston, MA, 2009. <https://doi.org/10.1007/978-0-387-85695-7>.
- (158) Cimalla, V.; Pezoldt, J.; Ambacher, O. Group III Nitride and SiC Based MEMS and NEMS: Materials Properties, Technology and Applications. *J. Phys. D: Appl. Phys.* **2007**, *40* (20), S19. <https://doi.org/10.1088/0022-3727/40/20/S19>.

- (159) Yang, W.; Wang, W.; Liu, Z.; Li, G. Effect of AlN Buffer Layer Thickness on the Properties of GaN Films Grown by Pulsed Laser Deposition. *Materials Science in Semiconductor Processing* **2015**, *39*, 499–505. <https://doi.org/10.1016/j.mssp.2015.05.046>.
- (160) Ramesh, C.; Tyagi, P.; Gupta, G.; Kumar, M. S.; Kushvaha, S. S. Influence of Surface Nitridation and an AlN Buffer Layer on the Growth of GaN Nanostructures on a Flexible Ti Metal Foil Using Laser Molecular Beam Epitaxy. *Jpn. J. Appl. Phys.* **2019**, *58* (SC), SC1032. <https://doi.org/10.7567/1347-4065/ab0f17>.
- (161) Schneider, N.; Donsanti, F. Atomic Layer Deposition (ALD) Principes généraux, matériaux et applications. In *Principes et applications de la technique ALD (Atomic Layer Deposition)*; Techniques de l'Ingénieur, 2016; pp 9–22.
- (162) Abdulagatov, A. I.; Ramazanov, Sh. M.; Dallaev, R. S.; Murliev, E. K.; Palchaev, D. K.; Rabadanov, M. Kh.; Abdulagatov, I. M. Atomic Layer Deposition of Aluminum Nitride Using Tris(Diethylamido)Aluminum and Hydrazine or Ammonia. *Russ Microelectron* **2018**, *47* (2), 118–130. <https://doi.org/10.1134/S1063739718020026>.
- (163) Jung, Y. C.; Hwang, S. M.; Le, D. N.; Kondusamy, A. L. N.; Mohan, J.; Kim, S. W.; Kim, J. H.; Lucero, A. T.; Ravichandran, A.; Kim, H. S.; Kim, S. J.; Choi, R.; Ahn, J.; Alvarez, D.; Spiegelman, J.; Kim, J. Low Temperature Thermal Atomic Layer Deposition of Aluminum Nitride Using Hydrazine as the Nitrogen Source. *Materials* **2020**, *13* (15), 3387. <https://doi.org/10.3390/ma13153387>.
- (164) Dallaev, R.; Sobola, D.; Tofel, P.; Škvarenina, L.; Sedlák, P. Aluminum Nitride Nanofilms by Atomic Layer Deposition Using Alternative Precursors Hydrazinium Chloride and Triisobutylaluminum. *Coatings* **2020**, *10* (10), 954. <https://doi.org/10.3390/coatings10100954>.
- (165) Parkhomenko, R. G.; De Luca, O.; Kołodziejczyk, Ł.; Modin, E.; Rudolf, P.; Martínez Martínez, D.; Cunha, L.; Knez, M. Amorphous AlN Films Grown by ALD from Trimethylaluminum and Monomethylhydrazine. *Dalton Trans.* **2021**, *50* (42), 15062–15070. <https://doi.org/10.1039/D1DT02529E>.
- (166) Kidder, J. N.; Kuo, J. S.; Ludviksson, A.; Pearsall, T. P.; Rogers, J. W.; Grant, J. M.; Allen, L. R.; Hsu, S. T. Deposition of AlN at Lower Temperatures by Atmospheric Metalorganic Chemical Vapor Deposition Using Dimethylethylamine Alane and Ammonia. *Journal of Vacuum Science & Technology A: Vacuum, Surfaces, and Films* **1995**, *13* (3), 711–715. <https://doi.org/10.1116/1.579812>.
- (167) Liu, H.; Rogers, J. W. Molecularly Engineered Low Temperature Atomic Layer Growth of Aluminum Nitride on Si(100). *Journal of Vacuum Science & Technology A: Vacuum, Surfaces, and Films* **1999**, *17* (2), 325–331. <https://doi.org/10.1116/1.581591>.
- (168) Alevli, M.; Ozgit, C.; Donmez, I.; Biyikli, N. Structural Properties of AlN Films Deposited by Plasma-Enhanced Atomic Layer Deposition at Different Growth Temperatures: Structural Properties of Deposited AlN Films. *Phys. Status Solidi A* **2012**, *209* (2), 266–271. <https://doi.org/10.1002/pssa.201127430>.
- (169) Bosund, M.; Sajavaara, T.; Laitinen, M.; Huhtio, T.; Putkonen, M.; Airaksinen, V.-M.; Lipsanen, H. Properties of AlN Grown by Plasma Enhanced Atomic Layer Deposition. *Applied Surface Science* **2011**, *257* (17), 7827–7830. <https://doi.org/10.1016/j.apsusc.2011.04.037>.
- (170) Legallais, M.; Mehdi, H.; David, S.; Bassani, F.; Labau, S.; Pelissier, B.; Baron, T.; Martinez, E.; Ghibaudo, G.; Salem, B. Improvement of AlN Film Quality Using Plasma Enhanced Atomic Layer Deposition with Substrate Biasing. *ACS Appl. Mater. Interfaces* **2020**, *12* (35), 39870–39880. <https://doi.org/10.1021/acsami.0c10515>.
- (171) Shih, H.-Y.; Lee, W.-H.; Kao, W.-C.; Chuang, Y.-C.; Lin, R.-M.; Lin, H.-C.; Shiojiri, M.; Chen, M.-J. Low-Temperature Atomic Layer Epitaxy of AlN Ultrathin Films by Layer-by-Layer, in-Situ Atomic Layer Annealing. *Sci Rep* **2017**, *7* (1), 39717. <https://doi.org/10.1038/srep39717>.
- (172) Kao, W.-C.; Lee, W.-H.; Yi, S.-H.; Shen, T.-H.; Lin, H.-C.; Chen, M.-J. AlN Epitaxy on SiC by Low-Temperature Atomic Layer Deposition via Layer-by-Layer, in Situ Atomic Layer Annealing. *RSC Adv.* **2019**, *9* (22), 12226–12231. <https://doi.org/10.1039/C9RA00008A>.
- (173) Lee, W.-H.; Kao, W.-C.; Yin, Y.-T.; Yi, S.-H.; Huang, K.-W.; Lin, H.-C.; Chen, M.-J. Sub-Nanometer Heating Depth of Atomic Layer Annealing. *Applied Surface Science* **2020**, *525*, 146615. <https://doi.org/10.1016/j.apsusc.2020.146615>.
- (174) Sun, L.; Yuan, G.; Gao, L.; Yang, J.; Chhowalla, M.; Gharahcheshmeh, M. H.; Gleason, K. K.; Choi, Y. S.; Hong, B. H.; Liu, Z. Chemical Vapour Deposition. *Nat Rev Methods Primers* **2021**, *1* (1), 5. <https://doi.org/10.1038/s43586-020-00005-y>.
- (175) A. Claudel. ELABORATION ET CARACTERISATION DE COUCHES DE NITRURE D'ALUMINIUM AlN PAR CVD HAUTE TEMPERATURE EN CHIMIE CHLOREE. **2009**. <https://doi.org/10.13140/2.1.5147.4727>.
- (176) Gaskill, D. K.; Bottka, N.; Lin, M. C. OMVPE of GaN and AlN Films by Metal Alkyls and Hydrazine. *Journal of Crystal Growth* **1986**, *77* (1–3), 418–423. [https://doi.org/10.1016/0022-0248\(86\)90332-5](https://doi.org/10.1016/0022-0248(86)90332-5).



- (177) Interrante, L. V.; Lee, W.; McConnell, M.; Lewis, N.; Hall, E. Preparation and Properties of Aluminum Nitride Films Using an Organometallic Precursor. *J. Electrochem. Soc.* **1989**, *136* (2), 472–478. <https://doi.org/10.1149/1.2096657>.
- (178) Ho, K.-L.; Jensen, K. F.; Hwang, J.-W.; Gladfelter, W. L.; Evans, J. F. MOVPE of AlN and GaN by Using Novel Precursors. *Journal of Crystal Growth* **1991**, *107* (1–4), 376–380. [https://doi.org/10.1016/0022-0248\(91\)90489-R](https://doi.org/10.1016/0022-0248(91)90489-R).
- (179) Jensen, K. F.; Annapragada, A.; Ho, K. L.; Huh, J.-S.; Patnaik, S.; Salim, S. METALORGANIC CHEMICAL VAPOR DEPOSITION : EXAMPLES OF THE INFLUENCE OF PRECURSOR STRUCTURE ON FILM PROPERTIES. *J. Phys. IV France* **1991**, *02* (C2), C2-243-C2-252. <https://doi.org/10.1051/jp4:1991230>.
- (180) Fischer, R. A.; Miehr, A.; Ambacher, O.; Metzger, T.; Born, E. Novel Single Source Precursors for MOCVD of AlN, GaN and InN. *Journal of Crystal Growth* **1997**, *170* (1–4), 139–143. [https://doi.org/10.1016/S0022-0248\(96\)00532-5](https://doi.org/10.1016/S0022-0248(96)00532-5).
- (181) Joo, O.-S.; Jung, K.-D.; Cho, S.-H.; Kyoung, J.-H.; Ahn, C.-K.; Choi, S.-C.; Dong, Y.; Yun, H.; Han, S.-H. MOCVD of Aluminum Nitride Thin Films with a New Type of Single-Source Precursor: AlCl<sub>3</sub>:T<sub>2</sub>BU<sub>2</sub>NH<sub>2</sub>. *Chem. Vap. Deposition* **2002**, *8* (6), 273–276. [https://doi.org/10.1002/1521-3862\(20021203\)8:6<273::AID-CVDE273>3.0.CO;2-O](https://doi.org/10.1002/1521-3862(20021203)8:6<273::AID-CVDE273>3.0.CO;2-O).
- (182) Li, X.-H.; Wang, S.; Xie, H.; Wei, Y. O.; Kao, T.-T.; Satter, Md. M.; Shen, S.-C.; Douglas Yoder, P.; Detchprohm, T.; Dupuis, R. D.; Fischer, A. M.; Ponce, F. A. Growth of High-Quality AlN Layers on Sapphire Substrates at Relatively Low Temperatures by Metalorganic Chemical Vapor Deposition: Growth of High-Quality AlN Layers on Sapphire by MOCVD. *Phys. Status Solidi B* **2015**, *252* (5), 1089–1095. <https://doi.org/10.1002/pssb.201451571>.
- (183) Liu, S.; Yuan, Y.; Sheng, S.; Wang, T.; Zhang, J.; Huang, L.; Zhang, X.; Kang, J.; Luo, W.; Li, Y.; Wang, H.; Wang, W.; Xiao, C.; Liu, Y.; Wang, Q.; Wang, X. Four-Inch High Quality Crack-Free AlN Layer Grown on a High-Temperature Annealed AlN Template by MOCVD. *J. Semicond.* **2021**, *42* (12), 122804. <https://doi.org/10.1088/1674-4926/42/12/122804>.
- (184) Chen, Y.; Song, H.; Li, D.; Sun, X.; Jiang, H.; Li, Z.; Miao, G.; Zhang, Z.; Zhou, Y. Influence of the Growth Temperature of AlN Nucleation Layer on AlN Template Grown by High-Temperature MOCVD. *Materials Letters* **2014**, *114*, 26–28. <https://doi.org/10.1016/j.matlet.2013.09.096>.
- (185) He, C.; Wu, H.; Jia, C.; Zhang, K.; He, L.; Wang, Q.; Li, J.; Liu, N.; Zhang, S.; Zhao, W.; Chen, Z.; Shen, B. Low-Defect-Density Aluminum Nitride (AlN) Thin Films Realized by Zigzag Macrostep-Induced Dislocation Redirection. *Crystal Growth & Design* **2021**, *21* (6), 3394–3400. <https://doi.org/10.1021/acs.cgd.1c00170>.
- (186) Chung, R. B.; Rodak, L. E.; Enck, R. W.; Sampath, A. V.; Wraback, M.; Reed, M. L. Growth and Impurity Characterization of AlN on (0001) Sapphire Grown by Spatially Pulsed MOCVD. *Phys. Status Solidi A* **2016**, *213* (4), 851–855. <https://doi.org/10.1002/pssa.201532571>.
- (187) Chen, X.; Zhang, Y.; Yan, J.; Guo, Y.; Zhang, S.; Wang, J.; Li, J. Effect of AlN Buffer on the Properties of AlN Films Grown on Sapphire Substrate by MOCVD. In *2016 13th China International Forum on Solid State Lighting: International Forum on Wide Bandgap Semiconductors China (SSLChina: IFWS)*; IEEE: Beijing, 2016; pp 123–126. <https://doi.org/10.1109/IFWS.2016.7803774>.
- (188) Guo, Y.; Fang, Y.; Yin, J.; Zhang, Z.; Wang, B.; Li, J.; Lu, W.; Feng, Z. Improved Structural Quality of AlN Grown on Sapphire by 3D/2D Alternation Growth. *Journal of Crystal Growth* **2017**, *464*, 119–122. <https://doi.org/10.1016/j.jcrysgro.2017.01.053>.
- (189) Zhang, X.; Xu, F. J.; Wang, J. M.; He, C. G.; Zhang, L. S.; Huang, J.; Cheng, J. P.; Qin, Z. X.; Yang, X. L.; Tang, N.; Wang, X. Q.; Shen, B. Epitaxial Growth of AlN Films on Sapphire via a Multilayer Structure Adopting a Low- and High-Temperature Alternation Technique. *CrystEngComm* **2015**, *17* (39), 7496–7499. <https://doi.org/10.1039/C5CE01159K>.
- (190) Wang, T. Y.; Liang, J. H.; Fu, G. W.; Wu, D. S. Defect Annihilation Mechanism of AlN Buffer Structures with Alternating High and Low V/III Ratios Grown by MOCVD. *CrystEngComm* **2016**, *18* (47), 9152–9159. <https://doi.org/10.1039/C6CE02130A>.
- (191) Chen, S.; Li, Y.; Ding, Y.; Li, S.; Zhang, M.; Wu, Z.; Fang, Y.; Dai, J.; Chen, C. Defect Reduction in AlN Epilayers Grown by MOCVD via Intermediate-Temperature Interlayers. *Journal of Elec Materi* **2015**, *44* (1), 217–221. <https://doi.org/10.1007/s11664-014-3462-1>.
- (192) Streicher, I.; Leone, S.; Kirste, L.; Ambacher, O. Effect of V/III Ratio and Growth Pressure on Surface and Crystal Quality of AlN Grown on Sapphire by Metal-Organic Chemical Vapor Deposition. *Journal of Vacuum Science & Technology A* **2022**, *40* (3), 032702. <https://doi.org/10.1116/6.0001794>.
- (193) Hirayama, H.; Fujikawa, S.; Norimatsu, J.; Takano, T.; Tsubaki, K.; Kamata, N. Fabrication of a Low Threading Dislocation Density ELO-AlN Template for Application to Deep-UV LEDs. *Phys. Status Solidi (c)* **2009**, *6* (S2). <https://doi.org/10.1002/pssc.200880958>.

- (194) Maeda, N.; Hirayama, H.; Fugikawa, S. Characteristics of AlN Crystal Growth Depending on M- and A-axis Oriented Off-angle of C-sapphire Substrate. *Phys. Status Solidi C* **2012**, *9* (3–4), 810–813. <https://doi.org/10.1002/pssc.201100425>.
- (195) Feng, Y.; Wei, H.; Yang, S.; Chen, Z.; Wang, L.; Kong, S.; Zhao, G.; Liu, X. Competitive Growth Mechanisms of AlN on Si (111) by MOVPE. *Sci Rep* **2014**, *4* (1), 6416. <https://doi.org/10.1038/srep06416>.
- (196) Le Louarn, A.; Vézian, S.; Semond, F.; Massies, J. AlN Buffer Layer Growth for GaN Epitaxy on (111) Si: Al or N First? *Journal of Crystal Growth* **2009**, *311* (12), 3278–3284. <https://doi.org/10.1016/j.jcrysgro.2009.04.001>.
- (197) Ng, T.; Ewoldt, D. A.; Shepherd, D. A.; Loboda, M. J. Reflectance Analysis on the MOCVD Growth of AlN on Si(111) by the Virtual Interface Model. *physica status solidi c* **2015**, *12* (4–5), 385–388. <https://doi.org/10.1002/pssc.201400159>.
- (198) Zhan, X.; Liu, J.; Sun, X.; Huang, Y.; Gao, H.; Zhou, Y.; Li, Q.; Sun, Q.; Yang, H. Crack-Free 2.2 Mm-Thick GaN Grown on Si with a Single-Layer AlN Buffer for RF Device Applications. *J. Phys. D: Appl. Phys.* **2023**, *56* (1), 015104. <https://doi.org/10.1088/1361-6463/ac9fdf>.
- (199) Aota, Y.; Sakyu, Y.; Tanifuji, S.; Oguma, H.; Kameda, S.; Nakase, H.; Takagi, T.; Tsubouchi, K. 4D-4 Fabrication of FBAR for GHz Band Pass Filter with AlN Film Grown Using MOCVD. In *2006 IEEE Ultrasonics Symposium*; IEEE: Vancouver, BC, Canada, 2006; pp 337–340. <https://doi.org/10.1109/ULTSYM.2006.103>.
- (200) Aota, Y.; Tanifuji, S.; Oguma, H.; Kameda, S.; Nakase, H.; Takagi, T.; Tsubouchi, K. P1H-4 FBAR Characteristics with AlN Film Using MOCVD Method and Ru/Ta Electrode. In *2007 IEEE Ultrasonics Symposium Proceedings*; IEEE: New York, NY, USA, 2007; pp 1425–1428. <https://doi.org/10.1109/ULTSYM.2007.358>.
- (201) Yi, X.; Zhao, L.; Ouyang, P.; Liu, H.; Zhang, T.; Li, G. High-Quality Film Bulk Acoustic Resonators Fabricated on AlN Films Grown by a New Two-Step Method. *IEEE Electron Device Lett.* **2022**, *43* (6), 942–945. <https://doi.org/10.1109/LED.2022.3164972>.
- (202) Yin, J.; Chen, D.; Yang, H.; Liu, Y.; Talwar, D. N.; He, T.; Ferguson, I. T.; He, K.; Wan, L.; Feng, Z. C. Comparative Spectroscopic Studies of MOCVD Grown AlN Films on Al<sub>2</sub>O<sub>3</sub> and 6H-SiC. *Journal of Alloys and Compounds* **2021**, *857*, 157487. <https://doi.org/10.1016/j.jallcom.2020.157487>.
- (203) Wu, H.; Zhang, K.; He, C.; He, L.; Wang, Q.; Zhao, W.; Chen, Z. Recent Advances in Fabricating Wurtzite AlN Film on (0001)-Plane Sapphire Substrate. *Crystals* **2021**, *12* (1), 38. <https://doi.org/10.3390/cryst12010038>.
- (204) Levi, B. G. Nobel Prize in Physics Recognizes Research Leading to High-Brightness Blue LEDs. *Physics Today* **2014**, *67* (12), 14–17. <https://doi.org/10.1063/PT.3.2606>.
- (205) Lorenz, K.; Gonsalves, M.; Kim, W.; Narayanan, V.; Mahajan, S. Comparative Study of GaN and AlN Nucleation Layers and Their Role in Growth of GaN on Sapphire by Metalorganic Chemical Vapor Deposition. *Appl. Phys. Lett.* **2000**, *77* (21), 3391–3393. <https://doi.org/10.1063/1.1328091>.
- (206) Demir, I.; Li, H.; Robin, Y.; McClintock, R.; Elagoz, S.; Razeghi, M. Sandwich Method to Grow High Quality AlN by MOCVD. *J. Phys. D: Appl. Phys.* **2018**, *51* (8), 085104. <https://doi.org/10.1088/1361-6463/aaa926>.
- (207) Sun, X.; Li, D.; Chen, Y.; Song, H.; Jiang, H.; Li, Z.; Miao, G.; Zhang, Z. In Situ Observation of Two-Step Growth of AlN on Sapphire Using High-Temperature Metal–Organic Chemical Vapour Deposition. *CrystEngComm* **2013**, *15* (30), 6066. <https://doi.org/10.1039/c3ce40755a>.
- (208) Imura, M.; Nakano, K.; Kitano, T.; Fujimoto, N.; Narita, G.; Okada, N.; Balakrishnan, K.; Iwaya, M.; Kamiyama, S.; Amano, H.; Akasaki, I.; Shimono, K.; Noro, T.; Takagi, T.; Bandoh, A. Microstructure of Epitaxial Lateral Overgrown AlN on Trench-Patterned AlN Template by High-Temperature Metal–Organic Vapor Phase Epitaxy. *Appl. Phys. Lett.* **2006**, *89* (22), 221901. <https://doi.org/10.1063/1.2364460>.
- (209) Imura, M.; Nakano, K.; Narita, G.; Fujimoto, N.; Okada, N.; Balakrishnan, K.; Iwaya, M.; Kamiyama, S.; Amano, H.; Akasaki, I.; Noro, T.; Takagi, T.; Bandoh, A. Epitaxial Lateral Overgrowth of AlN on Trench-Patterned AlN Layers. *Journal of Crystal Growth* **2007**, *298*, 257–260. <https://doi.org/10.1016/j.jcrysgro.2006.10.043>.
- (210) Dong, P.; Yan, J.; Wang, J.; Zhang, Y.; Geng, C.; Wei, T.; Cong, P.; Zhang, Y.; Zeng, J.; Tian, Y.; Sun, L.; Yan, Q.; Li, J.; Fan, S.; Qin, Z. 282-Nm AlGaIn-Based Deep Ultraviolet Light-Emitting Diodes with Improved Performance on Nano-Patterned Sapphire Substrates. *Appl. Phys. Lett.* **2013**, *102* (24), 241113. <https://doi.org/10.1063/1.4812237>.
- (211) Conroy, M.; Zubialevich, V. Z.; Li, H.; Petkov, N.; Holmes, J. D.; Parbrook, P. J. Epitaxial Lateral Overgrowth of AlN on Self-Assembled Patterned Nanorods. *J. Mater. Chem. C* **2015**, *3* (2), 431–437. <https://doi.org/10.1039/C4TC01536C>.

- (212) Zhang, L.; Xu, F.; Wang, J.; He, C.; Guo, W.; Wang, M.; Sheng, B.; Lu, L.; Qin, Z.; Wang, X.; Shen, B. High-Quality AlN Epitaxy on Nano-Patterned Sapphire Substrates Prepared by Nano-Imprint Lithography. *Sci Rep* **2016**, *6* (1), 35934. <https://doi.org/10.1038/srep35934>.
- (213) Ni, R.; Chen, X.; Yan, J.; Zhang, L.; Guo, Y.; Wang, J.; Li, J.; Zhang, Y. Reducing Stimulated Emission Threshold Power Density of AlGaN/AlN Multiple Quantum Wells by Nano-Trench-Patterned AlN Template. *Journal of Alloys and Compounds* **2019**, *777*, 344–349. <https://doi.org/10.1016/j.jallcom.2018.10.402>.
- (214) Miyake, H.; Lin, C.-H.; Tokoro, K.; Hiramatsu, K. Preparation of High-Quality AlN on Sapphire by High-Temperature Face-to-Face Annealing. *Journal of Crystal Growth* **2016**, *456*, 155–159. <https://doi.org/10.1016/j.jcrysgro.2016.08.028>.
- (215) Ben, J.; Sun, X.; Jia, Y.; Jiang, K.; Shi, Z.; Liu, H.; Wang, Y.; Kai, C.; Wu, Y.; Li, D. Defect Evolution in AlN Templates on PVD-AlN/Sapphire Substrates by Thermal Annealing. *CrystEngComm* **2018**, *20* (32), 4623–4629. <https://doi.org/10.1039/C8CE00770E>.
- (216) Miyake, H.; Nishio, G.; Suzuki, S.; Hiramatsu, K.; Fukuyama, H.; Kaur, J.; Kuwano, N. Annealing of an AlN Buffer Layer in N<sub>2</sub>-CO for Growth of a High-Quality AlN Film on Sapphire. *Appl. Phys. Express* **2016**, *9* (2), 025501. <https://doi.org/10.7567/APEX.9.025501>.
- (217) Uesugi, K.; Hayashi, Y.; Shojiki, K.; Miyake, H. Reduction of Threading Dislocation Density and Suppression of Cracking in Sputter-Deposited AlN Templates Annealed at High Temperatures. *Appl. Phys. Express* **2019**, *12* (6), 065501. <https://doi.org/10.7567/1882-0786/ab1ab8>.
- (218) Wang, D.; Uesugi, K.; Xiao, S.; Norimatsu, K.; Miyake, H. Low Dislocation Density AlN on Sapphire Prepared by Double Sputtering and Annealing. *Appl. Phys. Express* **2020**, *13* (9), 095501. <https://doi.org/10.35848/1882-0786/ababec>.
- (219) Tanaka, Y.; Hasebe, Y.; Inushima, T.; Sandhu, A.; Ohoya, S. Comparison of AlN Thin Films Grown on Sapphire and Cubic-SiC Substrates by LP-MOCVD. *Journal of Crystal Growth* **2000**, *209* (2–3), 410–414. [https://doi.org/10.1016/S0022-0248\(99\)00581-3](https://doi.org/10.1016/S0022-0248(99)00581-3).
- (220) Hong, S. Q.; Liaw, H. M.; Linthicum, K.; Davis, R. F.; Fejes, P.; Zollner, S.; Kottke, M.; Wilson, S. R. Epitaxial Growth of AlN on Si Substrates with Intermediate 3C-SiC as Buffer Layers. *MRS Online Proceedings Library* **1999**, No. 572, 407.
- (221) Liaw, H. M.; Doyle, R.; Fejes, P. L.; Zollner, S.; Konkar, A.; Linthicum, K. J.; Gehrke, T.; Davis, R. F. Crystallinity and Microstructures of Aluminum Nitride Films Deposited on Si(111) Substrates. *Solid-State Electronics* **2000**, *44* (4), 747–755. [https://doi.org/10.1016/S0038-1101\(99\)00307-X](https://doi.org/10.1016/S0038-1101(99)00307-X).
- (222) Takeuchi, T.; Amano, H.; Hiramatsu, K.; Sawaki, N.; Akasaki, I. Growth of Single Crystalline GaN Film on Si Substrate Using 3C-SiC as an Intermediate Layer. *Journal of Crystal Growth* **1991**, *115* (1–4), 634–638. [https://doi.org/10.1016/0022-0248\(91\)90817-O](https://doi.org/10.1016/0022-0248(91)90817-O).
- (223) Abe, Y.; Ohmori, N.; Watanabe, A.; Komiyama, J.; Suzuki, S.; Fujimori, H.; Nakanishi, H.; Egawa, T. Role of 3C-SiC Intermediate Layers for III-Nitride Crystal Growth on Si. *Journal of Crystal Growth* **2011**, *318* (1), 460–463. <https://doi.org/10.1016/j.jcrysgro.2010.10.179>.
- (224) Zhang, Q.; Han, T.; Tang, G.; Chen, J.; Hashimoto, K. SAW Characteristics of AlN/SiO<sub>2</sub>/3C-SiC Layered Structure with Embedded Electrodes. In *2015 IEEE International Ultrasonics Symposium (IUS)*; IEEE: Taipei, Taiwan, 2015; pp 1–4. <https://doi.org/10.1109/ULTSYM.2015.0116>.
- (225) Zuo, S.; Wang, J.; Chen, X.; Jin, S.; Jiang, L.; Bao, H.; Guo, L.; Sun, W.; Wang, W. Growth of AlN Single Crystals on 6H-SiC (0001) Substrates with AlN MOCVD Buffer Layer. *Cryst. Res. Technol.* **2012**, *47* (2), 139–144. <https://doi.org/10.1002/crat.201100502>.
- (226) Yoshida, H.; Kimura, S. High-Crystalline-Quality AlN Grown on SiC Substrates by Controlling Growth Mode. *Journal of Crystal Growth* **2020**, *537*, 125605. <https://doi.org/10.1016/j.jcrysgro.2020.125605>.
- (227) Kakanakova-Georgieva, A.; Nilsson, D.; Janzén, E. High-Quality AlN Layers Grown by Hot-Wall MOCVD at Reduced Temperatures. *Journal of Crystal Growth* **2012**, *338* (1), 52–56. <https://doi.org/10.1016/j.jcrysgro.2011.10.052>.
- (228) Zhang, D.; Li, Z.; Peng, D.; Dong, X.; Li, C. Temperature Dependence of the Character of AlN Nucleation Layer Grown on SiC Substrates by MOCVD. *Superlattices and Microstructures* **2016**, *99*, 104–107. <https://doi.org/10.1016/j.spmi.2016.04.029>.
- (229) Imura, M.; Sugimura, H.; Okada, N.; Iwaya, M.; Kamiyama, S.; Amano, H.; Akasaki, I.; Bandoh, A. Impact of High-Temperature Growth by Metal-Organic Vapor Phase Epitaxy on Microstructure of AlN on 6H-SiC Substrates. *Journal of Crystal Growth* **2008**, *310* (7–9), 2308–2313. <https://doi.org/10.1016/j.jcrysgro.2007.11.206>.
- (230) Chen, Z.; Newman, S.; Brown, D.; Chung, R.; Keller, S.; Mishra, U. K.; Denbaars, S. P.; Nakamura, S. High Quality AlN Grown on SiC by Metal Organic Chemical Vapor Deposition. *Appl. Phys. Lett.* **2008**, *93* (19), 191906. <https://doi.org/10.1063/1.2988323>.

- (231) Lu, J.; Chen, J.-T.; Dahlqvist, M.; Kabouche, R.; Medjdoub, F.; Rosen, J.; Kordina, O.; Hultman, L. Transmorphic Epitaxial Growth of AlN Nucleation Layers on SiC Substrates for High-Breakdown Thin GaN Transistors. *Appl. Phys. Lett.* **2019**, *115* (22), 221601. <https://doi.org/10.1063/1.5123374>.
- (232) Uehara, K.; Yang, C.-M.; Furusho, T.; Kim, S.-K.; Kameda, S.; Nakase, H.; Nishino, S.; Tsubouchi, K. AlN Epitaxial Film on 6H-SiC(0001) Using MOCVD for GHz-Band SAW Devices. In *IEEE Symposium on Ultrasonics, 2003*; IEEE: Honolulu, HI, USA, 2003; pp 905–908. <https://doi.org/10.1109/ULTSYM.2003.1293546>.
- (233) Hodge, M. D.; Vetry, R.; Gibb, S. R.; Winters, M.; Patel, P.; McLain, M. A.; Shen, Y.; Kim, D. H.; Jech, J.; Fallon, K.; Houlden, R.; Aichele, D. M.; Shealy, J. B. High Rejection UNII 5.2GHz Wideband Bulk Acoustic Wave Filters Using Undoped Single Crystal AlN-on-SiC Resonators. In *2017 IEEE International Electron Devices Meeting (IEDM)*; IEEE: San Francisco, CA, USA, 2017; p 25.6.1-25.6.4. <https://doi.org/10.1109/IEDM.2017.8268460>.
- (234) Shealy, J. B.; Vetry, R.; Gibb, S. R.; Hodge, M. D.; Patel, P.; McLain, M. A.; Feldman, A. Yu.; Boomgarden, M. D.; Lewis, M. P.; Hosse, B.; Holden, R. Low Loss, 3.7GHz Wideband BAW Filters, Using High Power Single Crystal AlN-on-SiC Resonators. In *2017 IEEE MTT-S International Microwave Symposium (IMS)*; IEEE: Honolulu, HI, USA, 2017; pp 1476–1479. <https://doi.org/10.1109/MWSYM.2017.8058901>.
- (235) Mattox, D. M. *Handbook of Physical Vapor Deposition (PVD) Processing*, 2nd ed.; William Andrew: Oxford, UK, 2010.
- (236) Iqbal, A.; Mohd-Yasin, F. Reactive Sputtering of Aluminum Nitride (002) Thin Films for Piezoelectric Applications: A Review. *Sensors* **2018**, *18* (6), 1797. <https://doi.org/10.3390/s18061797>.
- (237) Cherng, J. S.; Chang, D. S. Effects of Outgassing on the Reactive Sputtering of Piezoelectric AlN Thin Films. *Thin Solid Films* **2008**, *516* (16), 5292–5295. <https://doi.org/10.1016/j.tsf.2007.07.080>.
- (238) Cherng, J. S.; Lin, C. M.; Chen, T. Y. Two-Step Reactive Sputtering of Piezoelectric AlN Thin Films. *Surface and Coatings Technology* **2008**, *202* (22–23), 5684–5687. <https://doi.org/10.1016/j.surfcoat.2008.06.087>.
- (239) Ait Aissa, K.; Achour, A.; Camus, J.; Le Brizoual, L.; Jouan, P.-Y.; Djouadi, M.-A. Comparison of the Structural Properties and Residual Stress of AlN Films Deposited by Dc Magnetron Sputtering and High Power Impulse Magnetron Sputtering at Different Working Pressures. *Thin Solid Films* **2014**, *550*, 264–267. <https://doi.org/10.1016/j.tsf.2013.11.073>.
- (240) Cheng, H.; Sun, Y.; Zhang, J. X.; Zhang, Y. B.; Yuan, S.; Hing, P. AlN Films Deposited under Various Nitrogen Concentrations by RF Reactive Sputtering. *Journal of Crystal Growth* **2003**, *254* (1–2), 46–54. [https://doi.org/10.1016/S0022-0248\(03\)01176-X](https://doi.org/10.1016/S0022-0248(03)01176-X).
- (241) Medjani, F.; Sanjinés, R.; Allidi, G.; Karimi, A. Effect of Substrate Temperature and Bias Voltage on the Crystallite Orientation in RF Magnetron Sputtered AlN Thin Films. *Thin Solid Films* **2006**, *515* (1), 260–265. <https://doi.org/10.1016/j.tsf.2005.12.145>.
- (242) Yang, J.; Jiao, X.; Zhang, R.; Zhong, H.; Shi, Y.; Du, B. Growth of AlN Films as a Function of Temperature on Mo Films Deposited by Different Techniques. *Journal of Elec Materi* **2014**, *43* (2), 369–374. <https://doi.org/10.1007/s11664-013-2867-6>.
- (243) Jin, H.; Feng, B.; Dong, S.; Zhou, C.; Zhou, J.; Yang, Y.; Ren, T.; Luo, J.; Wang, D. Influence of Substrate Temperature on Structural Properties and Deposition Rate of AlN Thin Film Deposited by Reactive Magnetron Sputtering. *Journal of Elec Materi* **2012**, *41* (7), 1948–1954. <https://doi.org/10.1007/s11664-012-1999-4>.
- (244) Iqbal, A.; Walker, G.; Hold, L.; Fernandes, A.; Tanner, P.; Iacopi, A.; Mohd-Yasin, F. The Sputtering of AlN Films on Top of On- and off-Axis 3C-SiC (111)/Si (111) Substrates at Various Substrate Temperatures. *J Mater Sci: Mater Electron* **2018**, *29* (3), 2434–2446. <https://doi.org/10.1007/s10854-017-8163-0>.
- (245) Kar, J. P.; Bose, G.; Tuli, S. Influence of Rapid Thermal Annealing on Morphological and Electrical Properties of RF Sputtered AlN Films. *Materials Science in Semiconductor Processing* **2005**, *8* (6), 646–651. <https://doi.org/10.1016/j.mssp.2006.04.001>.
- (246) Phan, D.-T.; Chung, G.-S. The Effect of Geometry and Post-Annealing on Surface Acoustic Wave Characteristics of AlN Thin Films Prepared by Magnetron Sputtering. *Applied Surface Science* **2011**, *257* (20), 8696–8701. <https://doi.org/10.1016/j.apsusc.2011.05.050>.
- (247) Vergara, L.; Olivares, J.; Iborra, E.; Clement, M.; Sanz-Hervás, A.; Sangrador, J. Effect of Rapid Thermal Annealing on the Crystal Quality and the Piezoelectric Response of Polycrystalline AlN Films. *Thin Solid Films* **2006**, *515* (4), 1814–1818. <https://doi.org/10.1016/j.tsf.2006.07.002>.
- (248) Lin, H. K.; Huang, Y. J.; Shih, W. C.; Chen, Y. C.; Chang, W. T. Crystalline Characteristics of Annealed AlN Films by Pulsed Laser Treatment for Solidly Mounted Resonator Applications. *BMC Chemistry* **2019**, *13* (1), 30. <https://doi.org/10.1186/s13065-019-0550-6>.

- (249) Kusaka, K.; Taniguchi, D.; Hanabusa, T.; Tominaga, K. Effect of Input Power on Crystal Orientation and Residual Stress in AlN Film Deposited by Dc Sputtering. *Vacuum* **2000**, *59* (2–3), 806–813. [https://doi.org/10.1016/S0042-207X\(00\)00351-1](https://doi.org/10.1016/S0042-207X(00)00351-1).
- (250) Singh, A. V.; Chandra, S.; Bose, G. Deposition and Characterization of C-Axis Oriented Aluminum Nitride Films by Radio Frequency Magnetron Sputtering without External Substrate Heating. *Thin Solid Films* **2011**, *519* (18), 5846–5853. <https://doi.org/10.1016/j.tsf.2011.02.074>.
- (251) Vashaei, Z.; Aikawa, T.; Ohtsuka, M.; Kobatake, H.; Fukuyama, H.; Ikeda, S.; Takada, K. Influence of Sputtering Parameters on the Crystallinity and Crystal Orientation of AlN Layers Deposited by RF Sputtering Using the AlN Target. *Journal of Crystal Growth* **2009**, *311* (3), 459–462. <https://doi.org/10.1016/j.jcrysgro.2008.09.046>.
- (252) Kumada, T.; Ohtsuka, M.; Takada, K.; Fukuyama, H. Influence of Sputter Power and N<sub>2</sub> Gas Flow Ratio on Crystalline Quality of AlN Layers Deposited at 823 K by RF Reactive Sputtering. *Phys. Status Solidi C* **2012**, *9* (3–4), 515–518. <https://doi.org/10.1002/pssc.201100489>.
- (253) Lin, C. M.; Lien, W. C.; Yen, T. T.; Felmetzger, V.; Senesky, D. G.; Hopcroft, M. A.; Pisano, A. P. Growth of Highly -Axis Oriented AlN on 3C-SiC / Si Substrate. In *Proceedings of the Solid-State Sensors, Actuators, and Microsystems Workshop* **2010**, 324–327.
- (254) Kar, J. P.; Bose, G.; Tuli, S. Influence of Nitrogen Concentration on Grain Growth, Structural and Electrical Properties of Sputtered Aluminum Nitride Films. *Scripta Materialia* **2006**, *54* (10), 1755–1759. <https://doi.org/10.1016/j.scriptamat.2006.01.038>.
- (255) Zhong, H.; Xiao, Z.; Jiao, X.; Yang, J.; Wang, H.; Zhang, R.; Shi, Y. Residual Stress of AlN Films RF Sputter Deposited on Si(111) Substrate. *J Mater Sci: Mater Electron* **2012**, *23* (12), 2216–2220. <https://doi.org/10.1007/s10854-012-0760-3>.
- (256) Liu, H. Y.; Tang, G. S.; Zeng, F.; Pan, F. Influence of Sputtering Parameters on Structures and Residual Stress of AlN Films Deposited by DC Reactive Magnetron Sputtering at Room Temperature. *Journal of Crystal Growth* **2013**, *363*, 80–85. <https://doi.org/10.1016/j.jcrysgro.2012.10.008>.
- (257) Iqbal, A.; Walker, G.; Hold, L.; Fernandes, A.; Iacopi, A.; Mohd-Yasin, F. DC Sputtering of Highly C-Axis AlN Films on Top of 3C-SiC (111)-on-Si (111) Substrates under Various N<sub>2</sub> Concentrations. *Journal of Vacuum Science & Technology B, Nanotechnology and Microelectronics: Materials, Processing, Measurement, and Phenomena* **2017**, *35* (6), 06GH01. <https://doi.org/10.1116/1.4991748>.
- (258) Abdallah, B.; Chala, A.; Jouan, P.-Y.; Besland, M. P.; Djouadi, M. A. Deposition of AlN Films by Reactive Sputtering: Effect of Radiofrequency Substrate Bias. *Thin Solid Films* **2007**, *515* (18), 7105–7108. <https://doi.org/10.1016/j.tsf.2007.03.006>.
- (259) Chu, A. K.; Chao, C. H.; Lee, F. Z.; Huang, H. L. Influences of Bias Voltage on the Crystallographic Orientation of AlN Thin Films Prepared by Long-Distance Magnetron Sputtering. *Thin Solid Films* **2003**, *429* (1–2), 1–4. [https://doi.org/10.1016/S0040-6090\(02\)01286-5](https://doi.org/10.1016/S0040-6090(02)01286-5).
- (260) Iriarte, G. F.; Rodríguez, J. G.; Calle, F. Synthesis of C-Axis Oriented AlN Thin Films on Different Substrates: A Review. *Materials Research Bulletin* **2010**, *45* (9), 1039–1045. <https://doi.org/10.1016/j.materresbull.2010.05.035>.
- (261) Martin, F.; Murali, P.; Dubois, M.-A.; Pezous, A. Thickness Dependence of the Properties of Highly c - Axis Textured AlN Thin Films. *Journal of Vacuum Science & Technology A: Vacuum, Surfaces, and Films* **2004**, *22* (2), 361–365. <https://doi.org/10.1116/1.1649343>.
- (262) Riadh, A.; Ayad, A.; Camus, J.; Djouadi, M. A.; Rouag, N. Texture Growth of AlN Films Deposited on Si ( 100 ) and ( 111 ) by DC Reactive Magnetron Sputtering ( DcMs ) and by High Power Impulse Magnetron Sputtering ( HiPIMS ). **2016**.
- (263) Zhang, J. X.; Cheng, H.; Chen, Y. Z.; Uddin, A.; Yuan, S.; Geng, S. J.; Zhang, S. Growth of AlN Films on Si (100) and Si (111) Substrates by Reactive Magnetron Sputtering. *Surface and Coatings Technology* **2005**, *198* (1–3), 68–73. <https://doi.org/10.1016/j.surfcoat.2004.10.075>.
- (264) Pandey, A.; Dutta, S.; Prakash, R.; Raman, R.; Kapoor, A. K.; Kaur, D. Growth and Comparison of Residual Stress of AlN Films on Silicon (100), (110) and (111) Substrates. *Journal of Elec Materi* **2018**, *47* (2), 1405–1413. <https://doi.org/10.1007/s11664-017-5924-8>.
- (265) Riah, B.; Camus, J.; Ayad, A.; Rammal, M.; Zernadji, R.; Rouag, N.; Djouadi, M. A. Hetero-Epitaxial Growth of AlN Deposited by DC Magnetron Sputtering on Si(111) Using a AlN Buffer Layer. *Coatings* **2021**, *11* (9), 1063. <https://doi.org/10.3390/coatings11091063>.
- (266) Shin, I.-S.; Kim, J.; Lee, D.; Kim, D.; Park, Y.; Yoon, E. Epitaxial Growth of Single-Crystalline AlN Layer on Si(111) by DC Magnetron Sputtering at Room Temperature. *Jpn. J. Appl. Phys.* **2018**, *57* (6), 060306. <https://doi.org/10.7567/JJAP.57.060306>.

- (267) Dadgar, A.; Hörich, F.; Borgmann, R.; Bläsing, J.; Schmidt, G.; Veit, P.; Christen, J.; Strittmatter, A. Sputter Epitaxy of AlN and GaN on Si(111). *Physica Status Solidi (a)* **2022**, 2200609. <https://doi.org/10.1002/pssa.202200609>.
- (268) Iborra, E.; Clement, M.; Olivares, J.; Gonzalez-Castilla, S.; Sangrador, J.; Rimmer, N.; Rastogi, A.; Ivira, B.; Reinhardt, A. BAW Resonators Based on AlN with Ir Electrodes for Digital Wireless Transmissions. In *2008 IEEE Ultrasonics Symposium*; IEEE: Beijing, China, 2008; pp 2189–2192. <https://doi.org/10.1109/ULTSYM.2008.0542>.
- (269) Yokoyama, T.; Iwazaki, Y.; Nishihara, T.; Ueda, M. Analysis on Electromechanical Coupling Coefficients in AlN-Based Bulk Acoustic Wave Resonators Based on First-Principle Calculations. In *2012 IEEE International Ultrasonics Symposium*; IEEE: Dresden, Germany, 2012; pp 551–554. <https://doi.org/10.1109/ULTSYM.2012.0137>.
- (270) Iborra, E.; Clement, M.; Capilla, J.; Olivares, J.; Felmetzger, V. Optimization of Thin AlN Sputtered Films for X-Band BAW Resonators. In *2010 IEEE International Ultrasonics Symposium*; IEEE: San Diego, CA, USA, 2010; pp 1688–1691. <https://doi.org/10.1109/ULTSYM.2010.5935515>.
- (271) Uchiyama, S.; Ishigami, Y.; Ohta, M.; Niigaki, M.; Kan, H.; Nakanishi, Y.; Yamaguchi, T. Growth of AlN Films by Magnetron Sputtering. *Journal of Crystal Growth* **1998**, 189–190, 448–451. [https://doi.org/10.1016/S0022-0248\(98\)00328-5](https://doi.org/10.1016/S0022-0248(98)00328-5).
- (272) Gu, W.; Liu, Z.; Guo, Y.; Wang, X.; Jia, X.; Liu, X.; Zeng, Y.; Wang, J.; Li, J.; Yan, J. Comprehensive Study of Crystalline AlN/Sapphire Templates after High-Temperature Annealing with Various Sputtering Conditions. *J. Semicond.* **2020**, 41 (12), 122802. <https://doi.org/10.1088/1674-4926/41/12/122802>.
- (273) Sakurai, Y.; Ueno, K.; Kobayashi, A.; Uesugi, K.; Miyake, H.; Fujioka, H. High Electron Mobility AlN on Sapphire (0001) with a Low Dislocation Density Prepared via Sputtering and High-Temperature Annealing. *Phys. Status Solidi A* **2021**, 218 (16), 2100074. <https://doi.org/10.1002/pssa.202100074>.
- (274) Mogami, Y.; Motegi, S.; Osawa, A.; Osaki, K.; Tanioka, Y.; Maeoka, A.; Jo, M.; Maeda, N.; Yaguchi, H.; Hirayama, H. Evolution of Morphology and Crystalline Quality of DC-Sputtered AlN Films with High-Temperature Annealing. *Jpn. J. Appl. Phys.* **2019**, 58 (SC), SC1029. <https://doi.org/10.7567/1347-4065/ab1066>.
- (275) Liu, H.; Guo, W. The Interplay of Process Parameters and Influence on the AlN Films on Sapphire Fabricated by DC Magnetron Sputtering and Annealing. *Semicond. Sci. Technol.* **2023**, 38 (1), 015020. <https://doi.org/10.1088/1361-6641/aca8ca>.
- (276) Takeuchi, H.; Ohtsuka, M.; Fukuyama, H. Effect of Sputtering Power on Surface Characteristics and Crystal Quality of AlN Films Deposited by Pulsed DC Reactive Sputtering: Effect of Sputtering Power on Surface Characteristics of AlN Films. *Phys. Status Solidi B* **2015**, 252 (5), 1163–1171. <https://doi.org/10.1002/pssb.201451599>.
- (277) Kumada, T.; Ohtsuka, M.; Takada, K.; Fukuyama, H. Influence of Sputtering Conditions on Crystalline Quality of AlN Layers Deposited by RF Reactive Sputtering. *Phys. Status Solidi C* **2011**, 8 (5), 1520–1523. <https://doi.org/10.1002/pssc.201000890>.
- (278) Pashchenko, V.; Matloub, R.; Parsapourkolour, F.; Murali, P.; Ballandras, S.; Haffner, K. Hybrid BAW/SAW AlN and AlScN Thin Film Resonator. In *2016 IEEE International Ultrasonics Symposium (IUS)*; IEEE: Tours, 2016; pp 1–4. <https://doi.org/10.1109/ULTSYM.2016.7728649>.
- (279) Lee, T.-W.; Chung, G.-S. Structural Properties of AlN Thin Films Deposited on Si Using 3C-SiC Buffer Layer. In *2007 8th Siberian Russian Workshop and Tutorial on Electron Devices and Materials*; IEEE: Novosibirsk, Russia, 2007; pp 27–29. <https://doi.org/10.1109/SIBEDM.2007.4292897>.
- (280) Chung, G. S.; Chung, J. M.; Lee, T. W. Deposition of AlN Thin Films on Si Substrates Using 3C-SiC as Buffer Layer by Reactive Magnetron Sputtering. *Electron. Lett.* **2008**, 44 (17), 1034. <https://doi.org/10.1049/el:20081366>.
- (281) Chung, G.-S.; Lee, T. W. Reactive Magnetron Sputtering of AlN Films on Si Substrates Using 3C-SiC as a Buffer Layer. *Journal of the Korean Physical Society* **2008**, 53 (4), 21119–22122.
- (282) Hoang, S.-H.; Chung, G.-S. Surface Acoustic Wave Characteristics of AlN Thin Films Grown on a Polycrystalline 3C-SiC Buffer Layer. *Microelectronic Engineering* **2009**, 86 (11), 2149–2152. <https://doi.org/10.1016/j.mee.2009.02.030>.
- (283) Chung, G.-S. Effect of a 3C-SiC Buffer Layer on the SAW Properties of AlN Films Grown on Si Substrate. *J. Korean Phy. Soc.* **2009**, 55 (4), 1446–1450. <https://doi.org/10.3938/jkps.55.1446>.
- (284) Lin, C.-M.; Chen, Y.-Y.; Felmetzger, V. V.; Yen, T.-T.; Lien, W.-C.; Senesky, D. G.; Pisano, A. P. Surface Acoustic Wave Propagation Properties in AlN/3C-SiC/Si Composite Structure. In *2010 IEEE International Ultrasonics Symposium*; IEEE: San Diego, CA, USA, 2010; pp 1696–1699. <https://doi.org/10.1109/ULTSYM.2010.5935478>.

- (285) Lin, C.-M.; Lien, W.-C.; Felmetzger, V. V.; Hopcroft, M. A.; Senesky, D. G.; Pisano, A. P. AlN Thin Films Grown on Epitaxial 3C-SiC (100) for Piezoelectric Resonant Devices. *Appl. Phys. Lett.* **2010**, *97* (14), 141907. <https://doi.org/10.1063/1.3495782>.
- (286) Lin, C.-M.; Chen, Y.-Y.; Felmetzger, V. V.; Lien, W.-C.; Riekkinen, T.; Senesky, D. G.; Pisano, A. P. Surface Acoustic Wave Devices on AlN/3C-SiC/Si Multilayer Structures. *J. Micromech. Microeng.* **2013**, *23* (2), 025019. <https://doi.org/10.1088/0960-1317/23/2/025019>.
- (287) Caliendo, C. Theoretical Analysis of SAW Propagation in 3C-SiC/c-AlN. *Crystals* **2016**, *6* (3), 25. <https://doi.org/10.3390/cryst6030025>.
- (288) Esteves, G.; Habermehl, S. D.; Clews, P. J.; Fritch, C.; Griffin, B. A. AlN/SiC MEMS for High-Temperature Applications. *J. Microelectromech. Syst.* **2019**, *28* (5), 859–864. <https://doi.org/10.1109/JMEMS.2019.2923919>.
- (289) Wang, W. Z.; Ruan, Y.; You, Z. AlN/6H-SiC SAW Resonator for High Temperature Wireless SAW Sensor. In *2017 19th International Conference on Solid-State Sensors, Actuators and Microsystems (TRANSDUCERS)*; IEEE: Kaohsiung, 2017; pp 942–945. <https://doi.org/10.1109/TRANSDUCERS.2017.7994205>.
- (290) Uesugi, K.; Hayashi, Y.; Shojiki, K.; Xiao, S.; Nagamatsu, K.; Yoshida, H.; Miyake, H. Fabrication of AlN Templates on SiC Substrates by Sputtering-Deposition and High-Temperature Annealing. *Journal of Crystal Growth* **2019**, *510*, 13–17. <https://doi.org/10.1016/j.jcrysgro.2019.01.011>.
- (291) Tungasmita, S.; Persson, P. O. Å.; Hultman, L.; Birch, J. Pulsed Low-Energy Ion-Assisted Growth of Epitaxial Aluminum Nitride Layer on 6 H -Silicon Carbide by Reactive Magnetron Sputtering. *Journal of Applied Physics* **2002**, *91* (6), 3551–3555. <https://doi.org/10.1063/1.1448886>.
- (292) Akiyama, M.; Kamohara, T.; Kano, K.; Teshigahara, A.; Takeuchi, Y.; Kawahara, N. Enhancement of Piezoelectric Response in Scandium Aluminum Nitride Alloy Thin Films Prepared by Dual Reactive Cosputtering. *Adv. Mater.* **2009**, *21* (5), 593–596. <https://doi.org/10.1002/adma.200802611>.
- (293) Iborra, E.; Capilla, J.; Olivares, J.; Clement, M.; Felmetzger, V. Piezoelectric and Electroacoustic Properties of Ti-Doped AlN Thin Films as a Function of Ti Content. In *2012 IEEE International Ultrasonics Symposium*; IEEE: Dresden, Germany, 2012; pp 2734–2737. <https://doi.org/10.1109/ULTSYM.2012.0685>.
- (294) Felmetzger, V. V.; Mikhov, M. K. Reactive Sputtering of Highly C-Axis Textured Ti-Doped AlN Thin Films. In *2012 IEEE International Ultrasonics Symposium*; IEEE: Dresden, Germany, 2012; pp 782–785. <https://doi.org/10.1109/ULTSYM.2012.0195>.
- (295) Felmetzger, V. V.; Mikhov, M. K. Reactive Magnetron Sputtering of Piezoelectric Cr-Doped AlN Thin Films. In *2011 IEEE International Ultrasonics Symposium*; IEEE: Orlando, FL, USA, 2011; pp 835–839. <https://doi.org/10.1109/ULTSYM.2011.0204>.
- (296) Luo, J. T.; Fan, B.; Zeng, F.; Pan, F. Influence of Cr-Doping on Microstructure and Piezoelectric Response of AlN Films. *J. Phys. D: Appl. Phys.* **2009**, *42* (23), 235406. <https://doi.org/10.1088/0022-3727/42/23/235406>.
- (297) Mayrhofer, P. M.; Riedl, H.; Euchner, H.; Stöger-Pollach, M.; Mayrhofer, P. H.; Bittner, A.; Schmid, U. Microstructure and Piezoelectric Response of Y Al<sub>1-x</sub>N Thin Films. *Acta Materialia* **2015**, *100*, 81–89. <https://doi.org/10.1016/j.actamat.2015.08.019>.
- (298) Liu, H.; Zeng, F.; Tang, G.; Pan, F. Enhancement of Piezoelectric Response of Diluted Ta Doped AlN. *Applied Surface Science* **2013**, *270*, 225–230. <https://doi.org/10.1016/j.apsusc.2013.01.005>.
- (299) Iborra, E.; Olivares, J.; Clement, M.; Capilla, J.; Felmetzger, V.; Mikhov, M. Piezoelectric and Electroacoustic Properties of V-Doped and Ta-Doped AlN Thin Films. In *2013 Joint European Frequency and Time Forum & International Frequency Control Symposium (EFTF/IFC)*; IEEE: Prague, Czech Republic, 2013; pp 262–265. <https://doi.org/10.1109/EFTF-IFC.2013.6702211>.
- (300) Uehara, M.; Amano, Y.; Anggraini, S. A.; Hirata, K.; Yamada, H.; Akiyama, M. Preparation of YbAlN Piezoelectric Thin Film by Sputtering and Influence of Yb Concentration on Properties and Crystal Structure. *Ceramics International* **2021**, *47* (11), 16029–16036. <https://doi.org/10.1016/j.ceramint.2021.02.177>.
- (301) Hu, X.; Tai, Z.; Yang, C. Preparation and Characterization of Er-Doped AlN Films by RF Magnetron Sputtering. *Materials Letters* **2018**, *217*, 281–283. <https://doi.org/10.1016/j.matlet.2017.12.111>.
- (302) Tagami, K.; Koga, J.; Nohara, Y.; Usami, M. Origin of Enhanced Piezoelectric Constants of MgNbAlN Studied by First-Principles Calculations. *Jpn. J. Appl. Phys.* **2017**, *56* (5), 058004. <https://doi.org/10.7567/JJAP.56.058004>.
- (303) Anggraini, S. A.; Uehara, M.; Yamada, H.; Akiyama, M. Effect of Mg Addition on the Physical Properties of Aluminum Nitride. *Materials Letters* **2018**, *219*, 247–250. <https://doi.org/10.1016/j.matlet.2018.02.091>.
- (304) Yokoyama, T.; Iwazaki, Y.; Onda, Y.; Nishihara, T.; Sasajima, Y.; Ueda, M. Effect of Mg and Zr Co-Doping on Piezoelectric AlN Thin Films for Bulk Acoustic Wave Resonators. *IEEE Trans. Ultrason., Ferroelect., Freq. Contr.* **2014**, *61* (8), 1322–1328. <https://doi.org/10.1109/TUFFC.2014.3039>.

- (305) Yokoyama, T.; Iwazaki, Y.; Onda, Y.; Nishihara, T.; Sasajima, Y.; Ueda, M. Highly Piezoelectric Co-Doped AlN Thin Films for Wideband FBAR Applications. *IEEE Trans. Ultrason., Ferroelect., Freq. Contr.* **2015**, *62* (6), 1007–1015. <https://doi.org/10.1109/TUFFC.2014.006846>.
- (306) Yokoyama, T.; Iwazaki, Y.; Nishihara, T.; Tsutsumi, J. Dopant Concentration Dependence of Electromechanical Coupling Coefficients of Co-Doped AlN Thin Films for BAW Devices. In *2016 IEEE International Ultrasonics Symposium (IUS)*; IEEE: Tours, France, 2016; pp 1–4. <https://doi.org/10.1109/ULTSYM.2016.7728552>.
- (307) Anggraini, S. A.; Uehara, M.; Yamada, H.; Akiyama, M. Mg and Ti Codoping Effect on the Piezoelectric Response of Aluminum Nitride Thin Films. *Scripta Materialia* **2019**, *159*, 9–12. <https://doi.org/10.1016/j.scriptamat.2018.09.001>.
- (308) Uehara, M.; Shigemoto, H.; Fujio, Y.; Nagase, T.; Aida, Y.; Umeda, K.; Akiyama, M. Giant Increase in Piezoelectric Coefficient of AlN by Mg-Nb Simultaneous Addition and Multiple Chemical States of Nb. *Appl. Phys. Lett.* **2017**, *111* (11), 112901. <https://doi.org/10.1063/1.4990533>.
- (309) Manna, S.; Brennecke, G. L.; Stevanović, V.; Ciobanu, C. V. Tuning the Piezoelectric and Mechanical Properties of the AlN System via Alloying with YN and BN. *Journal of Applied Physics* **2017**, *122* (10), 105101. <https://doi.org/10.1063/1.4993254>.
- (310) Hirata, K.; Mori, Y.; Yamada, H.; Uehara, M.; Anggraini, S. A.; Akiyama, M. Significant Enhancement of Piezoelectric Response in AlN by Yb Addition. *Materials* **2021**, *14* (2), 309. <https://doi.org/10.3390/ma14020309>.
- (311) Anggraini, S. A.; Uehara, M.; Yamada, H.; Akiyama, M. Effect of Mg Addition on the Physical Properties of Aluminum Nitride. *Materials Letters* **2018**, *219*, 247–250. <https://doi.org/10.1016/j.matlet.2018.02.091>.
- (312) Bohnen, T.; van Dreumel, G. W. G.; Hageman, P. R.; Algra, R. E.; van Enckevort, W. J. P.; Vlieg, E.; Verheijen, M. A.; Edgar, J. H. Growth of Scandium Aluminum Nitride Nanowires on ScN(111) Films on 6H-SiC Substrates by HVPE: Growth of Scandium Aluminum Nitride Nanowires on ScN(111) Films. *phys. stat. sol. (a)* **2009**, *206* (12), 2809–2815. <https://doi.org/10.1002/pssa.200925060>.
- (313) Hardy, M. T.; Downey, B. P.; Nepal, N.; Storm, D. F.; Katzer, D. S.; Meyer, D. J. (Invited) ScAlN: A Novel Barrier Material for High Power GaN-Based RF Transistors. *ECS Trans.* **2017**, *80* (7), 161–168. <https://doi.org/10.1149/08007.0161ecst>.
- (314) Frei, K.; Trejo-Hernández, R.; Schütt, S.; Kirste, L.; Prescher, M.; Aidam, R.; Müller, S.; Waltereit, P.; Ambacher, O.; Fiederle, M. Investigation of Growth Parameters for ScAlN-Barrier HEMT Structures by Plasma-Assisted MBE. *Jpn. J. Appl. Phys.* **2019**, *58* (SC), SC1045. <https://doi.org/10.7567/1347-4065/ab124f>.
- (315) Leone, S.; Ligl, J.; Manz, C.; Kirste, L.; Fuchs, T.; Menner, H.; Prescher, M.; Wiegert, J.; Žukauskaitė, A.; Quay, R.; Ambacher, O. Metal-Organic Chemical Vapor Deposition of Aluminum Scandium Nitride. *Phys. Status Solidi RRL* **2020**, *14* (1), 1900535. <https://doi.org/10.1002/pssr.201900535>.
- (316) Akiyama, M.; Kano, K.; Teshigahara, A. Influence of Growth Temperature and Scandium Concentration on Piezoelectric Response of Scandium Aluminum Nitride Alloy Thin Films. *Appl. Phys. Lett.* **2009**, *95* (16), 162107. <https://doi.org/10.1063/1.3251072>.
- (317) Tasnádi, F.; Alling, B.; Höglund, C.; Wingqvist, G.; Birch, J.; Hultman, L.; Abrikosov, I. A. Origin of the Anomalous Piezoelectric Response in Wurtzite  $\text{Sc}_x\text{Al}_{1-x}\text{N}$  Alloys. *Phys. Rev. Lett.* **2010**, *104* (13), 137601. <https://doi.org/10.1103/PhysRevLett.104.137601>.
- (318) Ambacher, O.; Christian, B.; Feil, N.; Urban, D. F.; Elsässer, C.; Prescher, M.; Kirste, L. Wurtzite ScAlN, InAlN, and GaAlN Crystals, a Comparison of Structural, Elastic, Dielectric, and Piezoelectric Properties. *Journal of Applied Physics* **2021**, *130* (4), 045102. <https://doi.org/10.1063/5.0048647>.
- (319) Kurz, N.; Ding, A.; Urban, D. F.; Lu, Y.; Kirste, L.; Feil, N. M.; Žukauskaitė, A.; Ambacher, O. Experimental Determination of the Electro-Acoustic Properties of Thin Film AlScN Using Surface Acoustic Wave Resonators. *Journal of Applied Physics* **2019**, *126* (7), 075106. <https://doi.org/10.1063/1.5094611>.
- (320) Arab, F.; Kanouni, F.; Serhane, R.; Pennec, Y.; Özer, Z.; Bouamama, K. Electro-Acoustic Properties of Scandium-Doped Aluminum Nitride ( $\text{Sc}_x\text{Al}_{1-x}\text{N}$ ) Material and Its Application to Phononic Crystal-Coupled SAW Devices. *Crystals* **2022**, *12* (10), 1431. <https://doi.org/10.3390/cryst12101431>.
- (321) Yu, X.; Zhu, L.; Li, X.; Zhao, J.; Wu, T.; Yu, W.; Li, W. Doping Engineering for Optimizing Piezoelectric and Elastic Performance of AlN. *Materials* **2023**, *16* (5), 1778. <https://doi.org/10.3390/ma16051778>.
- (322) Li, M.; Xie, J.; Chen, B.; Wang, N.; Zhu, Y. Microstructural Evolution of the Abnormal Crystallite Grains in Sputtered ScAlN Film for Piezo-MEMS Applications. In *2019 IEEE International Ultrasonics Symposium (IUS)*; IEEE: Glasgow, United Kingdom, 2019; pp 1124–1126. <https://doi.org/10.1109/ULTSYM.2019.8926009>.
- (323) Sandu, C. S.; Parsapour, F.; Mertin, S.; Pashchenko, V.; Matloub, R.; LaGrange, T.; Heinz, B.; Murali, P. Abnormal Grain Growth in AlScN Thin Films Induced by Complexion Formation at Crystallite Interfaces. *Phys. Status Solidi A* **2019**, *216* (2), 1800569. <https://doi.org/10.1002/pssa.201800569>.



- (324) Knisely, K. E. LDRD 191204: OPTimization of Sputtered Aluminum Nitride for the Seeding of Metal Organic Chemical Vapor Deposition Gallium Nitride Films. **2018**, 32.
- (325) Moreira, M.; Bjurström, J.; Katardjev, I.; Yantchev, V. Aluminum Scandium Nitride Thin-Film Bulk Acoustic Resonators for Wide Band Applications. *Vacuum* **2011**, 86 (1), 23–26. <https://doi.org/10.1016/j.vacuum.2011.03.026>.
- (326) Kim, D.; Moreno, G.; Bi, F.; Winters, M.; Houlden, R.; Aichele, D.; Shealy, J. B. Wideband 6 GHz RF Filters for Wi-Fi 6E Using a Unique BAW Process and Highly Sc-Doped AlN Thin Film. In *2021 IEEE MTT-S International Microwave Symposium (IMS)*; IEEE: Atlanta, GA, USA, 2021; pp 207–209. <https://doi.org/10.1109/IMS19712.2021.9574981>.
- (327) Fichtner, S.; Wolff, N.; Krishnamurthy, G.; Petraru, A.; Bohse, S.; Lofink, F.; Chemnitz, S.; Kohlstedt, H.; Kienle, L.; Wagner, B. Identifying and Overcoming the Interface Originating C-Axis Instability in Highly Sc Enhanced AlN for Piezoelectric Micro-Electromechanical Systems. *Journal of Applied Physics* **2017**, 122 (3), 035301. <https://doi.org/10.1063/1.4993908>.
- (328) Aigner, R.; Fattinger, G.; Schaefer, M.; Karnati, K.; Rothemund, R.; Dumont, F. BAW Filters for 5G Bands. In *2018 IEEE International Electron Devices Meeting (IEDM)*; IEEE: San Francisco, CA, 2018; p 14.5.1-14.5.4. <https://doi.org/10.1109/IEDM.2018.8614564>.
- (329) Hashimoto, K.; Sato, S.; Teshigahara, A.; Nakamura, T.; Kano, K. High Performance Surface Acoustic Resonators in 1–3 GHz Range Using ScAlN/6H-SiC Structure. In *2012 IEEE/MTT-S International Microwave Symposium Digest*; IEEE: Montreal, QC, Canada, 2012; pp 1–3. <https://doi.org/10.1109/MWSYM.2012.6257776>.
- (330) Aigner, R.; Ella, J.; Timme, H.-J.; Elbrecht, L.; Nessler, W.; Marksteiner, S. Advancement of MEMS into RF-Filter Applications. In *Digest. International Electron Devices Meeting*; 2002; pp 897–900. <https://doi.org/10.1109/IEDM.2002.1175981>.
- (331) Kumar, A.; Prasad, M.; Janyani, V.; Yadav, R. P. Optical Characterization of RF Sputtered AlN Thin Film for Acoustic and Optoelectronics Devices. In *2019 9th Annual Information Technology, Electromechanical Engineering and Microelectronics Conference (IEMECON)*; 2019; pp 60–63. <https://doi.org/10.1109/IEMECONX.2019.8877067>.
- (332) Hsu, W.-F.; Lu, L.-S.; Kuo, P.-C.; Chen, J.-H.; Chueh, W.-C.; Yeh, H.; Kao, H.-L.; Chen, J.-S.; Chang, W.-H. Monolayer MoS<sub>2</sub> Enabled Single-Crystalline Growth of AlN on Si(100) Using Low-Temperature Helicon Sputtering. *ACS Appl. Nano Mater.* **2019**, 2 (4), 1964–1969. <https://doi.org/10.1021/acsanm.8b02358>.
- (333) Chien, H.-Y.; Kuo, P.-C.; Kao, H.-L.; Chen, J.-S.; Chen, M.-R.; Lu, L.-S.; Chueh, W.-C.; Chang, W.-H. Low Temperature Deposition of High Quality Single Crystalline AlN Thin Films on Sapphire Using Highly Oriented Monolayer MoS<sub>2</sub> as a Buffer Layer. *Journal of Crystal Growth* **2020**, 544, 125726. <https://doi.org/10.1016/j.jcrysgro.2020.125726>.
- (334) Samy, O.; Zeng, S.; Birowosuto, M. D.; El Moutaouakil, A. A Review on MoS<sub>2</sub> Properties, Synthesis, Sensing Applications and Challenges. *Crystals* **2021**, 11 (4), 355. <https://doi.org/10.3390/cryst11040355>.
- (335) Li, X.; Zhu, H. Two-Dimensional MoS<sub>2</sub>: Properties, Preparation, and Applications. *Journal of Materials* **2015**, 1 (1), 33–44. <https://doi.org/10.1016/j.jmat.2015.03.003>.
- (336) Cadot, S.; Renault, O.; Frégnaux, M.; Rouchon, D.; Nolot, E.; Szeto, K.; Thieuleux, C.; Veyre, L.; Okuno, H.; Martin, F.; Quadrelli, E. A. A Novel 2-Step ALD Route to Ultra-Thin MoS<sub>2</sub> Films on SiO<sub>2</sub> through a Surface Organometallic Intermediate. *Nanoscale* **2017**, 9 (2), 538–546. <https://doi.org/10.1039/C6NR06021H>.
- (337) Jariwala, D.; Sangwan, V. K.; Lauhon, L. J.; Marks, T. J.; Hersam, M. C. Emerging Device Applications for Semiconducting Two-Dimensional Transition Metal Dichalcogenides. *ACS Nano* **2014**, 8 (2), 1102–1120. <https://doi.org/10.1021/nn500064s>.
- (338) Song, I.; Park, C.; Choi, H. C. Synthesis and Properties of Molybdenum Disulphide: From Bulk to Atomic Layers. *RSC Adv.* **2015**, 5 (10), 7495–7514. <https://doi.org/10.1039/C4RA11852A>.
- (339) Wyckoff, R. W. G. *Crystal Structures*; 1963; Vol. 1.
- (340) Wang, Q. H.; Kalantar-Zadeh, K.; Kis, A.; Coleman, J. N.; Strano, M. S. Electronics and Optoelectronics of Two-Dimensional Transition Metal Dichalcogenides. *Nature Nanotech* **2012**, 7 (11), 699–712. <https://doi.org/10.1038/nnano.2012.193>.
- (341) Eda, G.; Yamaguchi, H.; Voiry, D.; Fujita, T.; Chen, M.; Chhowalla, M. Photoluminescence from Chemically Exfoliated MoS<sub>2</sub>. *Nano Lett.* **2011**, 11 (12), 5111–5116. <https://doi.org/10.1021/nl201874w>.
- (342) Yim, C.; O'Brien, M.; McEvoy, N.; Winters, S.; Mirza, I.; Lunney, J. G.; Duesberg, G. S. Investigation of the Optical Properties of MoS<sub>2</sub> Thin Films Using Spectroscopic Ellipsometry. *Appl. Phys. Lett.* **2014**, 104 (10), 103114. <https://doi.org/10.1063/1.4868108>.

- (343) Hsu, C.; Frisenda, R.; Schmidt, R.; Arora, A.; Vasconcellos, S. M.; Bratschitsch, R.; Zant, H. S. J.; Castellanos-Gomez, A. Thickness-Dependent Refractive Index of 1L, 2L, and 3L MoS<sub>2</sub>, MoSe<sub>2</sub>, WS<sub>2</sub>, and WSe<sub>2</sub>. *Adv. Optical Mater.* **2019**, *7* (13), 1900239. <https://doi.org/10.1002/adom.201900239>.
- (344) Tsai, M.-L.; Su, S.-H.; Chang, J.-K.; Tsai, D.-S.; Chen, C.-H.; Wu, C.-I.; Li, L.-J.; Chen, L.-J.; He, J.-H. Monolayer MoS<sub>2</sub> Heterojunction Solar Cells. *ACS Nano* **2014**, *8* (8), 8317–8322. <https://doi.org/10.1021/nn502776h>.
- (345) Yin, Z.; Li, H.; Li, H.; Jiang, L.; Shi, Y.; Sun, Y.; Lu, G.; Zhang, Q.; Chen, X.; Zhang, H. Single-Layer MoS<sub>2</sub> Phototransistors. *ACS Nano* **2012**, *6* (1), 74–80. <https://doi.org/10.1021/nn2024557>.
- (346) Krasnozhon, D.; Lembke, D.; Nyffeler, C.; Leblebici, Y.; Kis, A. MoS<sub>2</sub> Transistors Operating at Gigahertz Frequencies. *Nano Lett.* **2014**, *14* (10), 5905–5911. <https://doi.org/10.1021/nl5028638>.
- (347) Bertolazzi, S.; Krasnozhon, D.; Kis, A. Nonvolatile Memory Cells Based on MoS<sub>2</sub>/Graphene Heterostructures. *ACS Nano* **2013**, *7* (4), 3246–3252. <https://doi.org/10.1021/nn3059136>.
- (348) Li, H.; Wu, J.; Yin, Z.; Zhang, H. Preparation and Applications of Mechanically Exfoliated Single-Layer and Multilayer MoS<sub>2</sub> and WSe<sub>2</sub> Nanosheets. *Acc. Chem. Res.* **2014**, *47* (4), 1067–1075. <https://doi.org/10.1021/ar4002312>.
- (349) Li, Y.; Kuang, G.; Jiao, Z.; Yao, L.; Duan, R. Recent Progress on the Mechanical Exfoliation of 2D Transition Metal Dichalcogenides. *Mater. Res. Express* **2022**, *9* (12), 122001. <https://doi.org/10.1088/2053-1591/aca6c6>.
- (350) Dumcenco, D.; Ovchinnikov, D.; Marinov, K.; Lazić, P.; Gibertini, M.; Marzari, N.; Sanchez, O. L.; Kung, Y.-C.; Krasnozhon, D.; Chen, M.-W.; Bertolazzi, S.; Gillet, P.; Fontcuberta i Morral, A.; Radenovic, A.; Kis, A. Large-Area Epitaxial Monolayer MoS<sub>2</sub>. *ACS Nano* **2015**, *9* (4), 4611–4620. <https://doi.org/10.1021/acs.nano.5b01281>.
- (351) Shi, Y.; Zhou, W.; Lu, A.-Y.; Fang, W.; Lee, Y.-H.; Hsu, A. L.; Kim, S. M.; Kim, K. K.; Yang, H. Y.; Li, L.-J.; Idrobo, J.-C.; Kong, J. Van Der Waals Epitaxy of MoS<sub>2</sub> Layers Using Graphene As Growth Templates. *Nano Lett.* **2012**, *12* (6), 2784–2791. <https://doi.org/10.1021/nl204562j>.
- (352) Ruzmetov, D.; Zhang, K.; Stan, G.; Kalanyan, B.; Bhimanapati, G. R.; Eichfeld, S. M.; Burke, R. A.; Shah, P. B.; O'Regan, T. P.; Crowne, F. J.; Birdwell, A. G.; Robinson, J. A.; Davydov, A. V.; Ivanov, T. G. Vertical 2D/3D Semiconductor Heterostructures Based on Epitaxial Molybdenum Disulfide and Gallium Nitride. *ACS Nano* **2016**, *10* (3), 3580–3588. <https://doi.org/10.1021/acs.nano.5b08008>.
- (353) Jurca, T.; Moody, M. J.; Henning, A.; Emery, J. D.; Wang, B.; Tan, J. M.; Lohr, T. L.; Lauhon, L. J.; Marks, T. J. Low-Temperature Atomic Layer Deposition of MoS<sub>2</sub> Films. *Angew. Chem. Int. Ed.* **2017**, *56* (18), 4991–4995. <https://doi.org/10.1002/anie.201611838>.
- (354) Zeng, L.; Richey, N. E.; Palm, D. W.; Oh, I.-K.; Shi, J.; Maclsaac, C.; Jaramillo, T.; Bent, S. F. Modified Atomic Layer Deposition of MoS<sub>2</sub> Thin Films. *Journal of Vacuum Science & Technology A* **2020**, *38* (6), 060403. <https://doi.org/10.1116/6.0000641>.
- (355) Li, L.; Qin, Z.; Ries, L.; Hong, S.; Michel, T.; Yang, J.; Salameh, C.; Bechelany, M.; Miele, P.; Kaplan, D.; Chhowalla, M.; Voiry, D. Role of Sulfur Vacancies and Undercoordinated Mo Regions in MoS<sub>2</sub> Nanosheets toward the Evolution of Hydrogen. *ACS Nano* **2019**, *13* (6), 6824–6834. <https://doi.org/10.1021/acs.nano.9b01583>.
- (356) Yanase, T.; Uehara, F.; Naito, I.; Nagahama, T.; Shimada, T. Healing Sulfur Vacancies in Monolayer MoS<sub>2</sub> by High-Pressure Sulfur and Selenium Annealing: Implication for High-Performance Transistors. *ACS Appl. Nano Mater.* **2020**, *3* (10), 10462–10469. <https://doi.org/10.1021/acsanm.0c02385>.
- (357) Cadot, S. Élaboration de monocouches de dichalcogénures de métaux de transition du groupe (VI) par chimie organométallique de surface. 211.
- (358) Verble, J. L.; Wieting, T. J. Lattice Mode Degeneracy in MoS<sub>2</sub> and Other Layer Compounds. *Phys. Rev. Lett.* **1970**, *25* (6), 362–365. <https://doi.org/10.1103/PhysRevLett.25.362>.
- (359) Wieting, T. J.; Verble, J. L. Infrared and Raman Studies of Long-Wavelength Optical Phonons in Hexagonal MoS<sub>2</sub>. *Phys. Rev. B* **1971**, *3* (12), 4286–4292. <https://doi.org/10.1103/PhysRevB.3.4286>.
- (360) Li, X.; Li, J.; Wang, K.; Wang, X.; Wang, S.; Chu, X.; Xu, M.; Fang, X.; Wei, Z.; Zhai, Y.; Zou, B. Pressure and Temperature-Dependent Raman Spectra of MoS<sub>2</sub> Film. *Appl. Phys. Lett.* **2016**, *109* (24), 242101. <https://doi.org/10.1063/1.4968534>.
- (361) Liang, F.; Xu, H.; Wu, X.; Wang, C.; Luo, C.; Zhang, J. Raman Spectroscopy Characterization of Two-Dimensional Materials. *Chinese Phys. B* **2018**, *27* (3), 037802. <https://doi.org/10.1088/1674-1056/27/3/037802>.
- (362) Pollard, A. J. Metrology for Graphene and 2D Materials. *Meas. Sci. Technol.* **2016**, *27* (9), 092001. <https://doi.org/10.1088/0957-0233/27/9/092001>.

- (363) Lee, C.; Yan, H.; Brus, L. E.; Heinz, T. F.; Hone, J.; Ryu, S. Anomalous Lattice Vibrations of Single- and Few-Layer MoS<sub>2</sub>. *ACS Nano* **2010**, *4* (5), 2695–2700. <https://doi.org/10.1021/nn1003937>.
- (364) Li, H.; Zhang, Q.; Yap, C. C. R.; Tay, B. K.; Edwin, T. H. T.; Olivier, A.; Baillargeat, D. From Bulk to Monolayer MoS<sub>2</sub>: Evolution of Raman Scattering. *Adv. Funct. Mater.* **2012**, *22* (7), 1385–1390. <https://doi.org/10.1002/adfm.201102111>.
- (365) Zhang, X.; Qiao, X.-F.; Shi, W.; Wu, J.-B.; Jiang, D.-S.; Tan, P.-H. Phonon and Raman Scattering of Two-Dimensional Transition Metal Dichalcogenides from Monolayer, Multilayer to Bulk Material. *Chem. Soc. Rev.* **2015**, *44* (9), 2757–2785. <https://doi.org/10.1039/C4CS00282B>.
- (366) Liang, L.; Meunier, V. First-Principles Raman Spectra of MoS<sub>2</sub>, WS<sub>2</sub> and Their Heterostructures. *Nanoscale* **2014**, *6* (10), 5394. <https://doi.org/10.1039/c3nr06906k>.
- (367) Yan, Y.; Li, F.; Gong, Y.; Yao, M.; Huang, X.; Fu, X.; Han, B.; Zhou, Q.; Cui, T. Interlayer Coupling Affected Structural Stability in Ultrathin MoS<sub>2</sub>: An Investigation by High Pressure Raman Spectroscopy. *J. Phys. Chem. C* **2016**, *120* (43), 24992–24998. <https://doi.org/10.1021/acs.jpcc.6b06562>.
- (368) Yang, L.; Cui, X.; Zhang, J.; Wang, K.; Shen, M.; Zeng, S.; Dayeh, S. A.; Feng, L.; Xiang, B. Lattice Strain Effects on the Optical Properties of MoS<sub>2</sub> Nanosheets. *Sci Rep* **2015**, *4* (1), 5649. <https://doi.org/10.1038/srep05649>.
- (369) McCreary, A.; Berkdemir, A.; Wang, J.; Nguyen, M. A.; Elías, A. L.; Perea-López, N.; Fujisawa, K.; Kabius, B.; Carozo, V.; Cullen, D. A.; Mallouk, T. E.; Zhu, J.; Terrones, M. Distinct Photoluminescence and Raman Spectroscopy Signatures for Identifying Highly Crystalline WS<sub>2</sub> Monolayers Produced by Different Growth Methods. *J. Mater. Res.* **2016**, *31* (7), 931–944. <https://doi.org/10.1557/jmr.2016.47>.
- (370) Wang, Y.; Cong, C.; Qiu, C.; Yu, T. Raman Spectroscopy Study of Lattice Vibration and Crystallographic Orientation of Monolayer MoS<sub>2</sub> under Uniaxial Strain. *Small* **2013**, *9* (17), 2857–2861. <https://doi.org/10.1002/sml.201202876>.
- (371) Li, H.; Contryman, A. W.; Qian, X.; Ardakani, S. M.; Gong, Y.; Wang, X.; Weisse, J. M.; Lee, C. H.; Zhao, J.; Ajayan, P. M.; Li, J.; Manoharan, H. C.; Zheng, X. Optoelectronic Crystal of Artificial Atoms in Strain-Textured Molybdenum Disulphide. *Nat Commun* **2015**, *6* (1), 7381. <https://doi.org/10.1038/ncomms8381>.
- (372) Parkin, W. M.; Balan, A.; Liang, L.; Das, P. M.; Lamparski, M.; Naylor, C. H.; Rodríguez-Manzo, J. A.; Johnson, A. T. C.; Meunier, V.; Drndić, M. Raman Shifts in Electron-Irradiated Monolayer MoS<sub>2</sub>. *ACS Nano* **2016**, *10* (4), 4134–4142. <https://doi.org/10.1021/acsnano.5b07388>.
- (373) Tuschel. Effect of Layer Number and Crystal Stacking Orientation on the Raman Spectra of Two-Dimensional MoS<sub>2</sub>. 2020.
- (374) Mattila, S.; Leiro, J. A.; Heinonen, M.; Laiho, T. Core Level Spectroscopy of MoS<sub>2</sub>. *Surface Science* **2006**, *600* (24), 5168–5175. <https://doi.org/10.1016/j.susc.2006.08.038>.
- (375) Zeng, Z.; Yin, Z.; Huang, X.; Li, H.; He, Q.; Lu, G.; Boey, F.; Zhang, H. Single-Layer Semiconducting Nanosheets: High-Yield Preparation and Device Fabrication. *Angew. Chem. Int. Ed.* **2011**, *50* (47), 11093–11097. <https://doi.org/10.1002/anie.201106004>.
- (376) Li, B.; Jiang, L.; Li, X.; Ran, P.; Zuo, P.; Wang, A.; Qu, L.; Zhao, Y.; Cheng, Z.; Lu, Y. Preparation of Monolayer MoS<sub>2</sub> Quantum Dots Using Temporally Shaped Femtosecond Laser Ablation of Bulk MoS<sub>2</sub> Targets in Water. *Sci Rep* **2017**, *7* (1), 11182. <https://doi.org/10.1038/s41598-017-10632-3>.
- (377) Griffin, J.; Watters, D. C.; Yi, H.; Iraqi, A.; Lidzey, D.; Buckley, A. R. The Influence of MoO<sub>x</sub> Anode Stoichiometry on the Performance of Bulk Heterojunction Polymer Solar Cells. *Adv. Energy Mater.* **2013**, *3* (7), 903–908. <https://doi.org/10.1002/aenm.201200886>.
- (378) Syari'ati, A.; Kumar, S.; Zahid, A.; Ali El Yumin, A.; Ye, J.; Rudolf, P. Photoemission Spectroscopy Study of Structural Defects in Molybdenum Disulfide (MoS<sub>2</sub>) Grown by Chemical Vapor Deposition (CVD). *Chem. Commun.* **2019**, *55* (70), 10384–10387. <https://doi.org/10.1039/C9CC01577A>.
- (379) Baker, M. A.; Gilmore, R.; Lenardi, C.; Gissler, W. XPS Investigation of Preferential Sputtering of S from MoS<sub>2</sub> and Determination of MoS<sub>x</sub> Stoichiometry from Mo and S Peak Positions. *Applied Surface Science* **1999**, *150* (1), 255–262. [https://doi.org/10.1016/S0169-4332\(99\)00253-6](https://doi.org/10.1016/S0169-4332(99)00253-6).
- (380) Rajamani, A.; Beresford, R.; Sheldon, B. W. Intrinsic Stress Evolution in Aluminum Nitride Thin Films and the Influence of Multistep Processing. *Appl. Phys. Lett.* **2001**, *79* (23), 3776–3778. <https://doi.org/10.1063/1.1420774>.
- (381) Raghavan, S.; Acord, J.; Redwing, J. M. *In Situ* Observation of Coalescence-Related Tensile Stresses during Metalorganic Chemical Vapor Deposition of GaN on Sapphire. *Appl. Phys. Lett.* **2005**, *86* (26), 261907. <https://doi.org/10.1063/1.1968436>.
- (382) Yin, Y.; Ren, F.; Wang, Y.; Liu, Z.; Ao, J.; Liang, M.; Wei, T.; Yuan, G.; Ou, H.; Yan, J.; Yi, X.; Wang, J.; Li, J. Direct van Der Waals Epitaxy of Crack-Free AlN Thin Film on Epitaxial WS<sub>2</sub>. *Materials* **2018**, *11* (12), 2464. <https://doi.org/10.3390/ma11122464>.

- (383) Chang, S.-J.; Wang, S.-Y.; Huang, Y.-C.; Chih, J. H.; Lai, Y.-T.; Tsai, Y.-W.; Lin, J.-M.; Chien, C.-H.; Tang, Y.-T.; Hu, C. Van Der Waals Epitaxy of 2D  $h$ -AlN on TMDs by Atomic Layer Deposition at 250 °C. *Appl. Phys. Lett.* **2022**, *120* (16), 162102. <https://doi.org/10.1063/5.0083809>.
- (384) Benetti, M.; Cannatà, D.; Di Pietrantonio, F.; Verona, E.; Generosi, A.; Paci, B.; Rossi Albertini, V. Growth and Characterization of Piezoelectric AlN Thin Films for Diamond-Based Surface Acoustic Wave Devices. *Thin Solid Films* **2006**, *497* (1–2), 304–308. <https://doi.org/10.1016/j.tsf.2005.10.073>.
- (385) Chiu, K.-H.; Chen, J.-H.; Chen, H.-R.; Huang, R.-S. Deposition and Characterization of Reactive Magnetron Sputtered Aluminum Nitride Thin Films for Film Bulk Acoustic Wave Resonator. *Thin Solid Films* **2007**, *515* (11), 4819–4825. <https://doi.org/10.1016/j.tsf.2006.12.181>.
- (386) Jia, H.; Zheng, X.-Q.; Faizan, M.; Larsen, T.; Villanueva, L. G.; Feng, P. X.-L. Molybdenum Disulfide (MoS<sub>2</sub>) Nanoelectromechanical Resonators with on-Chip Aluminum Nitride (AlN) Piezoelectric Excitation. In *2018 IEEE Micro Electro Mechanical Systems (MEMS)*; IEEE: Belfast, 2018; pp 527–530. <https://doi.org/10.1109/MEMSYS.2018.8346606>.
- (387) Chung, J.-W.; Ohuchi, F. S. Deposition of AlN on WS<sub>2</sub> (0001) Substrate by Atomic Layer Growth Process. *MRS Proc.* **1996**, *449*, 379. <https://doi.org/10.1557/PROC-449-379>.
- (388) Ohuchi, F. S. Fabrication of AlN Thin Film Substrates by Van Der Waals Lift-Off Technique. Report of Air Force Office of Scientific Research. 1998.
- (389) *Sigma® Deposition Systems | SPTS*. <https://www.spts.com/product/sigma-metal-deposition-systems> (accessed 2023-01-23).
- (390) Yoo, W. S.; Harima, H.; Yoshimoto, M. Polarized Raman Signals from Si Wafers: Dependence of In-Plane Incident Orientation of Probing Light. *ECS J. Solid State Sci. Technol.* **2015**, *4* (9), P356–P363. <https://doi.org/10.1149/2.0061509jss>.
- (391) Van der Drift, A. *Evolutionary Selection, a Principle Governing Growth Orientation in Vapour-Deposited Layers*; Philips Research; Technical report 22; 1967; pp 267–288.
- (392) Knisely, K. E.; Hunt, B.; Troelsen, B.; Douglas, E.; Griffin, B. A.; Stevens, J. E. Method for Controlling Stress Gradients in PVD Aluminum Nitride. *J. Micromech. Microeng.* **2018**, *28* (11), 115009. <https://doi.org/10.1088/1361-6439/aad91a>.
- (393) Lu, T.-Y.; Yang, Y.-P.; Lo, H.-H.; Wang, P. J.; Lai, W.; Fuh, Y.-K.; Li, T. T. Minimizing Film Residual Stress with in Situ OES Big Data Using Principal Component Analysis of Deposited AlN Films by Pulsed DC Reactive Sputtering. *Int J Adv Manuf Technol* **2021**, *114* (7–8), 1975–1990. <https://doi.org/10.1007/s00170-021-07003-8>.
- (394) Deng, S.; Gao, E.; Xu, Z.; Berry, V. Adhesion Energy of MoS<sub>2</sub> Thin Films on Silicon-Based Substrates Determined via the Attributes of a Single MoS<sub>2</sub> Wrinkle. *ACS Appl. Mater. Interfaces* **2017**, *9* (8), 7812–7818. <https://doi.org/10.1021/acsami.6b16175>.
- (395) Rokni, H.; Lu, W. Direct Measurements of Interfacial Adhesion in 2D Materials and van Der Waals Heterostructures in Ambient Air. *Nat Commun* **2020**, *11* (1), 5607. <https://doi.org/10.1038/s41467-020-19411-7>.
- (396) Torres, J.; Zhu, Y.; Liu, P.; Lim, S. C.; Yun, M. Adhesion Energies of 2D Graphene and MoS<sub>2</sub> to Silicon and Metal Substrates. *Phys. Status Solidi A* **2018**, *215* (1), 1700512. <https://doi.org/10.1002/pssa.201700512>.
- (397) Chiu, Y.-J.; Yen, C.-Y.; Chiang, M.-S.; Chen, G.-J.; Jian, S.-R.; Wang, C.; Kao, H.-L. Mechanical Properties and Fracture Toughness of AlN Thin Films Deposited Using Helicon Sputtering. *nanosci nanotechnol lett* **2017**, *9* (4), 562–566. <https://doi.org/10.1166/nnl.2017.2357>.
- (398) Wei, S.; Xie, Z.; Xue, W.; Yi, Z.; Chen, J.; Cheng, L. Fracture Toughness of Aluminum Nitride Ceramics at Cryogenic Temperatures. *Ceramics International* **2014**, *40* (8), 13715–13718. <https://doi.org/10.1016/j.ceramint.2014.05.012>.
- (399) Shimizu, H.; Kondo, N.; Shimamura, A.; Hotta, M.; Harada, S.; Ujihara, T.; Ohnishi, Y. High Fracture Toughness AlN Achieved by Addition of AlN Whiskers and Tape-Casting. *J. Ceram. Soc. Japan* **2022**, *130* (1), 195–198. <https://doi.org/10.2109/jcersj2.21143>.
- (400) Lee, D.; Ahn, G.; Ryu, S. Two-Dimensional Water Diffusion at a Graphene–Silica Interface. *J. Am. Chem. Soc.* **2014**, *136* (18), 6634–6642. <https://doi.org/10.1021/ja4121988>.
- (401) David-Viffantzeff, J. Etude du spalling comme procédé de transfert du Graphène et d'autres matériaux 2D, Grenoble Alpes, 2016.
- (402) Shivayogimath, A.; Eriksson, L.; Whelan, P. R.; Mackenzie, D. M. A.; Luo, B.; Bøggild, P.; Booth, T. J. Atomic Layer Deposition Alumina-Mediated Graphene Transfer for Reduced Process Contamination. *Phys. Status Solidi RRL* **2019**, *13* (11), 1900424. <https://doi.org/10.1002/pssr.201900424>.
- (403) Marchand, R.; Gouin, X.; Tessier, F.; Laurent, Y. Preparation and Characterization of New Molybdenum Nitride or Oxynitride Phases. *MRS Proceedings* **1994**, *368*. <https://doi.org/10.1557/PROC-368-15>.

- (404) Marchand, R.; Gouin, X.; Tessier, F.; Laurent, Y. New Routes to Molybdenum Nitrides Andoxynitrides: Preparation and Characterization of New Phases. In *The Chemistry of Transition Metal Carbides and Nitrides*; Oyama, S. T., Ed.; Springer Netherlands: Dordrecht, 1996; pp 252–273. [https://doi.org/10.1007/978-94-009-1565-7\\_13](https://doi.org/10.1007/978-94-009-1565-7_13).
- (405) Tessier, F.; Marchand, R.; Laurent, Y. Preparation of Transition Metal Nitrides Using Unusual Routes. *Journal of the European Ceramic Society* **1997**, *17* (15–16), 1825–1829. [https://doi.org/10.1016/S0955-2219\(97\)00062-9](https://doi.org/10.1016/S0955-2219(97)00062-9).
- (406) Marchand, R.; Tessier, F.; DiSalvo, F. J. New Routes to Transition Metal Nitrides: And Characterization of New Phases. *J. Mater. Chem.* **1999**, *9* (1), 297–304. <https://doi.org/10.1039/A805315D>.
- (407) Ganin, A. Yu.; Kienle, L.; Vajenine, G. V. Synthesis and Characterisation of Hexagonal Molybdenum Nitrides. *Journal of Solid State Chemistry* **2006**, *179* (8), 2339–2348. <https://doi.org/10.1016/j.jssc.2006.05.025>.
- (408) Sun, G.-D.; Zhang, G.-H.; Chou, K.-C. Synthesis of Molybdenum Nitrides Nanosheets by Nitriding 2H-MoS<sub>2</sub> with Ammonia. *J Am Ceram Soc* **2018**, *101* (7), 2796–2808. <https://doi.org/10.1111/jace.15467>.
- (409) Cao, J.; Li, T.; Gao, H.; Lin, Y.; Wang, X.; Wang, H.; Palacios, T.; Ling, X. Realization of 2D Crystalline Metal Nitrides via Selective Atomic Substitution. *Sci. Adv.* **2020**, *6* (2), eaax8784. <https://doi.org/10.1126/sciadv.aax8784>.
- (410) Azcatl, A.; Qin, X.; Prakash, A.; Zhang, C.; Cheng, L.; Wang, Q.; Lu, N.; Kim, M. J.; Kim, J.; Cho, K.; Addou, R.; Hinkle, C. L.; Appenzeller, J.; Wallace, R. M. Covalent Nitrogen Doping and Compressive Strain in MoS<sub>2</sub> by Remote N<sub>2</sub> Plasma Exposure. *Nano Lett.* **2016**, *16* (9), 5437–5443. <https://doi.org/10.1021/acs.nanolett.6b01853>.
- (411) Effects of Nitrogen Plasma Treatment on the Electrical Property and Band Structure of Few-Layer MoS<sub>2</sub>. *Appl. Phys. Lett.* **2016**, *108* (3), 033103. <https://doi.org/10.1063/1.4939978>.
- (412) Qian, Q.; Zhang, Z.; Hua, M.; Tang, G.; Lei, J.; Lan, F.; Xu, Y.; Yan, R.; Chen, K. J. Enhanced Dielectric Deposition on Single-Layer MoS<sub>2</sub> with Low Damage Using Remote N<sub>2</sub> Plasma Treatment. *Nanotechnology* **2017**, *28* (17), 175202. <https://doi.org/10.1088/1361-6528/aa6756>.
- (413) Zeng, Y.; Zeng, X.; Wang, S.; Hu, Y.; Wang, W.; Yin, S.; Ren, T.; Zeng, Y.; Lu, J.; Guo, Z.; Xiao, Y.; Jin, W. Low-Damaged p-Type Doping of MoS<sub>2</sub> Using Direct Nitrogen Plasma Modulated by Toroidal-Magnetic-Field. *Nanotechnology* **2020**, *31* (1), 015702. <https://doi.org/10.1088/1361-6528/ab4402>.
- (414) Costa, R. G.; Barbosa, A. do N.; Maia da Costa, M. E. H.; Freire, F. L. Resonance Raman Spectroscopy of MoS<sub>2</sub> Monolayers Treated with Nitrogen Plasma. *Vibrational Spectroscopy* **2022**, *123*, 103454. <https://doi.org/10.1016/j.vibspec.2022.103454>.
- (415) Tuschel, D. Resonance Raman and Photoluminescence Spectroscopy and Imaging of Few-Layer MoS<sub>2</sub>. *Spectroscopy* **2015**, *30* (3), 14–19.
- (416) Lei, Y.; Butler, D.; Lucking, M. C.; Zhang, F.; Xia, T.; Fujisawa, K.; Granzier-Nakajima, T.; Cruz-Silva, R.; Endo, M.; Terrones, H.; Terrones, M.; Ebrahimi, A. Single-Atom Doping of MoS<sub>2</sub> with Manganese Enables Ultrasensitive Detection of Dopamine: Experimental and Computational Approach. *Sci. Adv.* **2020**, *6* (32), eabc4250. <https://doi.org/10.1126/sciadv.abc4250>.
- (417) Gao, J.; Kim, Y. D.; Liang, L.; Idrobo, J. C.; Chow, P.; Tan, J.; Li, B.; Li, L.; Sumpter, B. G.; Lu, T.; Meunier, V.; Hone, J.; Koratkar, N. Transition-Metal Substitution Doping in Synthetic Atomically Thin Semiconductors. *Adv. Mater.* **2016**, *28* (44), 9735–9743. <https://doi.org/10.1002/adma.201601104>.
- (418) Bhowmik, G.; Gruenewald, K.; Malladi, G.; Mowll, T.; Ventrice, C.; Huang, M. Tunable Photoluminescence of Atomically Thin MoS<sub>2</sub> via Nb Doping. *MRS Advances* **2019**, *4* (10), 609–614. <https://doi.org/10.1557/adv.2019.24>.
- (419) Vandalon, V.; Verheijen, M. A.; Kessels, W. M. M.; Bol, A. A. Atomic Layer Deposition of Al-Doped MoS<sub>2</sub>: Synthesizing a p-Type 2D Semiconductor with Tunable Carrier Density. *ACS Appl. Nano Mater.* **2020**, *3* (10), 10200–10208. <https://doi.org/10.1021/acsnm.0c02167>.
- (420) Qian, J.; Li, S.; Pu, J.; Cai, Z.; Wang, H.; Cai, Q.; Ju, P. Effect of Heat Treatment on Structure and Properties of Molybdenum Nitride and Molybdenum Carbonitride Films Prepared by Magnetron Sputtering. *Surface and Coatings Technology* **2019**, *374*, 725–735. <https://doi.org/10.1016/j.surfcoat.2019.06.062>.
- (421) Bécue, T.; Manoli, J.-M.; Potvin, C.; Djéga-Mariadassou, G.; Delamar, M. Preparation and Characterization of a Novel Class of Catalysts: Ultradispersed Molybdenum Oxynitrides Supported on NaEMT and HEMT Zeolite. *J. Phys. Chem. B* **1997**, *101* (33), 6429–6435. <https://doi.org/10.1021/jp9622492>.
- (422) Choi, J.-G.; Choi, D.; Thompson, L. T. Surface Properties of High-Surface-Area Powder and Thin Film Molybdenum Nitrides Treated in H<sub>2</sub> and H<sub>2</sub>S. *Applied Surface Science* **1997**, *108* (1), 103–111. [https://doi.org/10.1016/S0169-4332\(96\)00561-2](https://doi.org/10.1016/S0169-4332(96)00561-2).

- (423) Kim, G.-T.; Park, T.-K.; Chung, H.; Kim, Y.-T.; Kwon, M.-H.; Choi, J.-G. Growth and Characterization of Chloronitroaniline Crystals for Optical Parametric Oscillators. *Applied Surface Science* **1999**, *152* (1–2), 35–43. [https://doi.org/10.1016/S0169-4332\(99\)00293-7](https://doi.org/10.1016/S0169-4332(99)00293-7).
- (424) Shi, C.; Zhu, A. M.; Yang, X. F.; Au, C. T. Catalytic Activities and Surface Properties of Zeolite-Supported Molybdenum Nitrides for NO Reduction with H<sub>2</sub>. *Applied Catalysis A: General* **2005**, *293*, 83–90. <https://doi.org/10.1016/j.apcata.2005.07.028>.
- (425) McKay, D.; Hargreaves, J. S. J.; Howe, R. F. XPS Evidence for Molybdenum Nitride Formation in ZSM-5. *Catal Lett* **2006**, *112* (1–2), 109–113. <https://doi.org/10.1007/s10562-006-0172-1>.
- (426) Wu, H.; Lian, K. The Development of Pseudocapacitive Molybdenum Oxynitride Electrodes for Supercapacitors. *ECS Transactions* **2014**, *58* (25), 67–75. <https://doi.org/10.1149/05825.0067ecst>.
- (427) Jehn, H. Molybdenum and Nitrogen. In *Mo Molybdenum*; Katscher, H., Kurtz, W., Schröder, F., Eds.; Springer Berlin Heidelberg: Berlin, Heidelberg, 1989; pp 1–66. [https://doi.org/10.1007/978-3-662-06327-9\\_1](https://doi.org/10.1007/978-3-662-06327-9_1).
- (428) Marchand, R. J.; Gouin, X.; Tessier, F.; Laurent, Y. Preparation and Characterization of New Molybdenum Nitride or Oxynitride Phases. *MRS Proceedings* **1994**, *368*. <https://doi.org/10.1557/PROC-368-15>.
- (429) Tessier, F.; Marchand, R.; Laurent, Y. Preparation of Transition Metal Nitrides Using Unusual Routes. *Journal of the European Ceramic Society* **1997**, *17* (15–16), 1825–1829. [https://doi.org/10.1016/S0955-2219\(97\)00062-9](https://doi.org/10.1016/S0955-2219(97)00062-9).
- (430) Sun, G.-D.; Zhang, G.-H.; Chou, K.-C. Synthesis of Molybdenum Nitrides Nanosheets by Nitriding 2H-MoS<sub>2</sub> with Ammonia. *J Am Ceram Soc* **2018**, *101* (7), 2796–2808. <https://doi.org/10.1111/jace.15467>.
- (431) Tsakonas, C.; Manikas, A. C.; Andersen, M.; Dimitropoulos, M.; Reuter, K.; Galiotis, C. In Situ Kinetic Studies of CVD Graphene Growth by Reflection Spectroscopy. *Chemical Engineering Journal* **2021**, *421*, 129434. <https://doi.org/10.1016/j.cej.2021.129434>.
- (432) Xiao, X.; Wang, H.; Urbankowski, P.; Gogotsi, Y. Topochemical Synthesis of 2D Materials. *Chem. Soc. Rev.* **2018**, *47* (23), 8744–8765. <https://doi.org/10.1039/C8CS00649K>.
- (433) Wagner, C. Theoretical Analysis of the Diffusion Processes Determining the Oxidation Rate of Alloys. *J. Electrochem. Soc.* **1952**, *99* (10), 369. <https://doi.org/10.1149/1.2779605>.
- (434) Sarrazin, P.; Galerie, A.; Fouletier, J. *Les Mécanismes de La Corrosion Sèche: Une Approche Cinétique*; EDP Sciences, 2000. <https://doi.org/10.1051/978-2-7598-0243-2>.
- (435) Abautret, F.; Eveno, P. Diffusion of Nitrogen Implanted in Titanium Nitride (TiN<sub>1-x</sub>). *Rev. Phys. Appl. (Paris)* **1990**, *25* (11), 1113–1119. <https://doi.org/10.1051/rphysap:0199000250110111300>.
- (436) Poon, M. C.; Kok, C. W.; Wong, H.; Chan, P. J. Bonding Structures of Silicon Oxynitride Prepared by Oxidation of Si-Rich Silicon Nitride. *Thin Solid Films* **2004**, *462–463*, 42–45. <https://doi.org/10.1016/j.tsf.2004.05.043>.
- (437) Perevalov, T. V.; Volodin, V. A.; Kamaev, G. N.; Gismatulin, A. A.; Cherkova, S. G.; Prosvirin, I. P.; Astankova, K. N.; Gritsenko, V. A. Electronic Structure of Silicon Oxynitride Films Grown by Plasma-Enhanced Chemical Vapor Deposition for Memristor Application. *Journal of Non-Crystalline Solids* **2022**, *598*, 121925. <https://doi.org/10.1016/j.jnoncrysol.2022.121925>.
- (438) Rauch, E. F.; Véron, M. Automated Crystal Orientation and Phase Mapping in TEM. *Materials Characterization* **2014**, *98*, 1–9. <https://doi.org/10.1016/j.matchar.2014.08.010>.
- (439) Dadgar, A.; Hörich, F.; Borgmann, R.; Bläsing, J.; Schmidt, G.; Veit, P.; Christen, J.; Strittmatter, A. Sputter Epitaxy of AlN and GaN on Si(111). *Physica Status Solidi (a)* **2022**, *2200609*. <https://doi.org/10.1002/pssa.202200609>.
- (440) Bairagi, S.; Järrendahl, K.; Eriksson, F.; Hultman, L.; Birch, J.; Hsiao, C.-L. Glancing Angle Deposition and Growth Mechanism of Inclined AlN Nanostructures Using Reactive Magnetron Sputtering. *Coatings* **2020**, *10* (8), 768. <https://doi.org/10.3390/coatings10080768>.
- (441) Liu, L.; Liu, B.; Edgar, J. H.; Rajasingam, S.; Kuball, M. Raman Characterization and Stress Analysis of AlN Grown on SiC by Sublimation. *Journal of Applied Physics* **2002**, *92* (9), 5183–5188. <https://doi.org/10.1063/1.1506195>.
- (442) Lughì, V.; Clarke, D. R. Defect and Stress Characterization of AlN Films by Raman Spectroscopy. *Appl. Phys. Lett.* **2006**, *89* (24), 241911. <https://doi.org/10.1063/1.2404938>.
- (443) Chen, D.; Xu, D.; Wang, J.; Zhao, B.; Zhang, Y. Influence of the Texture on Raman and X-Ray Diffraction Characteristics of Polycrystalline AlN Films. *Thin Solid Films* **2008**, *517* (2), 986–989. <https://doi.org/10.1016/j.tsf.2008.07.029>.
- (444) Yang, S.; Miyagawa, R.; Miyake, H.; Hiramatsu, K.; Harima, H. Raman Scattering Spectroscopy of Residual Stresses in Epitaxial AlN Films. *Appl. Phys. Express* **2011**, *4* (3), 031001. <https://doi.org/10.1143/APEX.4.031001>.

- (445) Wang, J.; Chen, D.; Xu, Y.; Liu, Q.; Zhang, L. Influence of the Crystal Texture on Raman Spectroscopy of the AlN Films Prepared by Pulse Laser Deposition. *Journal of Spectroscopy* **2013**, *2013*, 1–6. <https://doi.org/10.1155/2013/103602>.
- (446) Auger, M. A.; Vázquez, L.; Jergel, M.; Sánchez, O.; Albella, J. M. Structure and Morphology Evolution of ALN Films Grown by DC Sputtering. *Surface and Coatings Technology* **2004**, *180–181*, 140–144. <https://doi.org/10.1016/j.surfcoat.2003.10.054>.
- (447) Brien, V.; Miska, P.; Bolle, B.; Pigeat, P. Columnar Growth of ALN by r.f. Magnetron Sputtering: Role of the  $\{101\bar{3}\}$  Planes. *Journal of Crystal Growth* **2007**, *307* (1), 245–252. <https://doi.org/10.1016/j.jcrysgro.2007.06.013>.
- (448) Zhu, W.; Pezzotti, G. Raman Spectroscopic Assessments of Structural Orientation and Residual Stress in Wurtzitic AlN Film Deposited on (001) Si. *Microelectronics Reliability* **2015**, *55* (1), 66–73. <https://doi.org/10.1016/j.microrel.2014.10.001>.
- (449) Lay, S.; Mercier, F.; Boichot, R.; Giusti, G.; Pons, M.; Blanquet, E. Prediction of Dislocation Density in AlN or GaN Films Deposited on (0001) Sapphire. *J Mater Sci* **2020**, *55* (22), 9152–9162. <https://doi.org/10.1007/s10853-019-04240-x>.
- (450) Lu, Y.; Reusch, M.; Kurz, N.; Ding, A.; Christoph, T.; Prescher, M.; Kirste, L.; Ambacher, O.; Žukauskaitė, A. Elastic Modulus and Coefficient of Thermal Expansion of Piezoelectric  $\text{Al}_{1-x}\text{Sc}_x\text{N}$  (up to  $x = 0.41$ ) Thin Films. *APL Materials* **2018**, *6* (7), 076105. <https://doi.org/10.1063/1.5040190>.
- (451) Beaucejour, R.; Roebisch, V.; Kochhar, A.; Moe, C. G.; Hodge, M. D.; Olsson, R. H. Controlling Residual Stress and Suppression of Anomalous Grains in Aluminum Scandium Nitride Films Grown Directly on Silicon. *J. Microelectromech. Syst.* **2022**, *31* (4), 604–611. <https://doi.org/10.1109/JMEMS.2022.3167430>.
- (452) Mertin, S.; Heinz, B.; Rattunde, O.; Christmann, G.; Dubois, M.-A.; Nicolay, S.; Muralt, P. Piezoelectric and Structural Properties of C-Axis Textured Aluminium Scandium Nitride Thin Films up to High Scandium Content. *Surface and Coatings Technology* **2018**, *343*, 2–6. <https://doi.org/10.1016/j.surfcoat.2018.01.046>.
- (453) Fichtner, S.; Reimer, T.; Chemnitz, S.; Lofink, F.; Wagner, B. Stress Controlled Pulsed Direct Current Co-Sputtered  $\text{Al}_{1-x}\text{Sc}_x\text{N}$  as Piezoelectric Phase for Micromechanical Sensor Applications. *APL Materials* **2015**, *3* (11), 116102. <https://doi.org/10.1063/1.4934756>.
- (454) Beaucejour, R.; D'Agati, M.; Kalyan, K.; Olsson, R. H. Compensation of the Stress Gradient in Physical Vapor Deposited  $\text{Al}_{1-x}\text{Sc}_x\text{N}$  Films for Microelectromechanical Systems with Low Out-of-Plane Bending. *Micromachines* **2022**, *13* (8), 1169. <https://doi.org/10.3390/mi13081169>.
- (455) Mishin, S.; Oshmyansky, Y. Magnetron Deposition of AlN and ScAlN for Mass-Production for BAW Devices and MEMS. In *2019 IEEE International Ultrasonics Symposium (IUS)*; IEEE: Glasgow, United Kingdom, 2019; pp 891–893. <https://doi.org/10.1109/ULTSYM.2019.8925969>.
- (456) Pirro, M.; Zhao, X.; Herrera, B.; Simeoni, P.; Rinaldi, M. Effect of Substrate-RF on Sub-200 Nm  $\text{Al}_0.7\text{Sc}_0.3\text{N}$  Thin Films. *Micromachines* **2022**, *13* (6), 877. <https://doi.org/10.3390/mi13060877>.
- (457) Aota, Y.; Tanifuji, S.; Oguma, H.; Kameda, S.; Takagi, T.; Tsubouchi, K. AlN Film Using Low Temperature MOCVD Process for FBAR. In *2008 IEEE Ultrasonics Symposium*; IEEE: Beijing, China, 2008; pp 2197–2200. <https://doi.org/10.1109/ULTSYM.2008.0544>.
- (458) Hodge, M. D.; Vetry, R.; Gibb, S. R.; Winters, M.; Patel, P.; McLain, M. A.; Shen, Y.; Kim, D. H.; Jech, J.; Fallon, K.; Houlden, R.; Aichele, D. M.; Shealy, J. B. High Rejection UNII 5.2GHz Wideband Bulk Acoustic Wave Filters Using Undoped Single Crystal AlN-on-SiC Resonators. In *2017 IEEE International Electron Devices Meeting (IEDM)*; IEEE: San Francisco, CA, USA, 2017; p 25.6.1-25.6.4. <https://doi.org/10.1109/IEDM.2017.8268460>.
- (459) Pizzagalli, L.; Belabbas, I.; Kioseoglou, J.; Chen, J. First-Principles Calculations of Threading Screw Dislocations in AlN and InN. *Phys. Rev. Materials* **2018**, *2* (6), 064607. <https://doi.org/10.1103/PhysRevMaterials.2.064607>.
- (460) Byung Hak Lee; Dong Kyun Sohn; Ji-Soo Park; Chang Hee Han; Yun-Jun Huh; Jeong Soo Byun; Jae Jeong Kim. In-Situ Barrier Formation for High Reliable W/Barrier/Poly-Si Gate Using Denudation of WN/Sub x/ on Polycrystalline Si. In *International Electron Devices Meeting 1998. Technical Digest (Cat. No.98CH36217)*; IEEE: San Francisco, CA, USA, 1998; pp 385–388. <https://doi.org/10.1109/IEDM.1998.746380>.
- (461) Cho, I. H.; Park, J.-S.; Sohn, D. K.; Ha, J. H. Increased Thermal Stability of  $\text{W}/\text{Ta}_2\text{O}_5$  Gate Structure Using Effective Diffusion Barrier of Denuded Tungsten Nitride. *Jpn. J. Appl. Phys.* **2001**, *40* (8R), 4854. <https://doi.org/10.1143/JJAP.40.4854>.
- (462) Yao Zhi Hu; Sing-Pin Tay. Applications of Rapid Thermal Process to Nitridation of Tungsten and Denudation of WN/Sub x/ for Poly-Si/Metal Gates. In *10th IEEE International Conference of Advanced Thermal Processing of Semiconductors*; IEEE: Vancouver, BC, Canada, 2002; pp 125–130. <https://doi.org/10.1109/RTP.2002.1039450>.

- (463) Roccaforte, F.; Fiorenza, P.; Greco, G.; Lo Nigro, R.; Giannazzo, F.; Iucolano, F.; Saggio, M. Emerging Trends in Wide Band Gap Semiconductors (SiC and GaN) Technology for Power Devices. *Microelectronic Engineering* **2018**, *187–188*, 66–77. <https://doi.org/10.1016/j.mee.2017.11.021>.
- (464) Zhang, Y. Comparison Between Competing Requirements of GaN and SiC Family of Power Switching Devices. *IOP Conf. Ser.: Mater. Sci. Eng.* **2020**, *738* (1), 012004. <https://doi.org/10.1088/1757-899X/738/1/012004>.
- (465) Zhong, Y.; Zhang, J.; Wu, S.; Jia, L.; Yang, X.; Liu, Y.; Zhang, Y.; Sun, Q. A Review on the GaN-on-Si Power Electronic Devices. *Fundamental Research* **2022**, *2* (3), 462–475. <https://doi.org/10.1016/j.fmre.2021.11.028>.
- (466) Liu, B. L.; Lachab, M.; Jia, A.; Yoshikawaa, A.; Takahashi, K. MOCVD Growth of Device-Quality GaN on Sapphire Using a Three-Step Approach. *Journal of Crystal Growth* **2002**, *234* (4), 637–645. [https://doi.org/10.1016/S0022-0248\(01\)01755-9](https://doi.org/10.1016/S0022-0248(01)01755-9).
- (467) Zhang, X. G.; Soderman, B.; Armour, E.; Paranjpe, A. Investigation of MOCVD Growth Parameters on the Quality of GaN Epitaxial Layers. *Journal of Crystal Growth* **2011**, *318* (1), 436–440. <https://doi.org/10.1016/j.jcrysgro.2010.10.047>.
- (468) Lin, Y.; Yang, M.; Wang, W.; Lin, Z.; Gao, J.; Li, G. High-Quality Crack-Free GaN Epitaxial Films Grown on Si Substrates by a Two-Step Growth of AlN Buffer Layer. *CrystEngComm* **2016**, *18* (14), 2446–2454. <https://doi.org/10.1039/C5CE02525G>.
- (469) Wang, H.; Lin, Z.; Wang, W.; Li, G.; Luo, J. Growth Mechanisms of GaN Epitaxial Films Grown on Ex Situ Low-Temperature AlN Templates on Si Substrates by the Combination Methods of PLD and MOCVD. *Journal of Alloys and Compounds* **2017**, *718*, 28–35. <https://doi.org/10.1016/j.jallcom.2017.05.009>.
- (470) Chen, D.-Y.; Wen, K.-H.; Thorsell, M.; Lorenzini, M.; Hjelmgren, H.; Chen, J.-T.; Rorsman, N. Impact of the Channel Thickness on Electron Confinement in MOCVD-Grown High Breakdown Buffer-Free AlGaIn/GaN Heterostructures. *Physica Status Solidi (a)* **2022**, 2200496. <https://doi.org/10.1002/pssa.202200496>.
- (471) Li, Y.; Hu, X.; Song, Y.; Su, Z.; Jia, H.; Wang, W.; Jiang, Y.; Chen, H. The Influence of Temperature of Nitridation and AlN Buffer Layer on N-Polar GaN. *Materials Science in Semiconductor Processing* **2022**, *141*, 106423. <https://doi.org/10.1016/j.mssp.2021.106423>.
- (472) Luo, W.; Wang, X.; Guo, L.; Xiao, H.; Wang, C.; Ran, J.; Li, J.; Li, J. Influence of AlN Buffer Layer Thickness on the Properties of GaN Epilayer on Si(111) by MOCVD. *Microelectronics Journal* **2008**, *39* (12), 1710–1713. <https://doi.org/10.1016/j.mejo.2008.01.042>.
- (473) Kumagai, Y.; Akiyama, K.; Togashi, R.; Murakami, H.; Takeuchi, M.; Kinoshita, T.; Takada, K.; Aoyagi, Y.; Koukitsu, A. Polarity Dependence of AlN {0 0 0 1} Decomposition in Flowing H<sub>2</sub>. *Journal of Crystal Growth* **2007**, *305* (2), 366–371. <https://doi.org/10.1016/j.jcrysgro.2007.04.005>.
- (474) Kimoto, T.; Cooper, J. A. *Fundamentals of Silicon Carbide Technology: Growth, Characterization, Devices, and Applications*, 1st ed.; Wiley, 2014. <https://doi.org/10.1002/9781118313534>.
- (475) Ferro, G.; Chassagne, T.; Leycuras, A.; Cauwet, F.; Monteil, Y. Strain Tailoring in 3C-SiC Heteroepitaxial Layers Grown on Si(100). *Chem. Vap. Deposition* **2006**, *12* (8–9), 483–488. <https://doi.org/10.1002/cvde.200506461>.
- (476) Bosi, M.; Attolini, G.; Watts, B. E.; Rossi, F.; Ferrari, C.; Riesz, F.; Jiang, L. Wafer Curvature Analysis in 3C-SiC Layers Grown on (001) and (111) Si Substrates. *Journal of Crystal Growth* **2011**, *318* (1), 401–405. <https://doi.org/10.1016/j.jcrysgro.2010.10.042>.
- (477) Ferro, G.; Yeghoyan, T.; Cauwet, F.; Coindeau, S.; Encinas, T.; Soulière, V. 3C-SiC Heteroepitaxial Layers Grown on Silicon Substrates with Various Orientations. *MSF* **2022**, *1062*, 23–27. <https://doi.org/10.4028/p-aaf11g>.
- (478) Chaudhuri, J.; Thokala, R.; Edgar, J. H.; Sywe, B. S. X-Ray Double Crystal and X-Ray Topographic Characterization of Silicon Carbide Thin Films on Silicon, Titanium Carbide, 6H-Silicon Carbide, and Aluminum Nitride/Sapphire Substrates. *Thin Solid Films* **1996**, *274* (1–2), 23–30. [https://doi.org/10.1016/0040-6090\(95\)07087-7](https://doi.org/10.1016/0040-6090(95)07087-7).
- (479) Wang, L.; Walker, G.; Chai, J.; Iacopi, A.; Fernandes, A.; Dimitrijević, S. Kinetic Surface Roughening and Wafer Bow Control in Heteroepitaxial Growth of 3C-SiC on Si(111) Substrates. *Sci Rep* **2015**, *5* (1), 15423. <https://doi.org/10.1038/srep15423>.
- (480) Severino, A.; Frewin, C. L.; Anzalone, R.; Bongiorno, C.; Fiorenza, P.; D'Arrigo, G.; Giannazzo, F.; Foti, G.; La Via, F.; Saddow, S. E. Growth of 3C-SiC on Si: Influence of Process Pressure. *MSF* **2008**, *600–603*, 211–214. <https://doi.org/10.4028/www.scientific.net/MSF.600-603.211>.
- (481) Anzalone, R.; Bongiorno, C.; Severino, A.; D'Arrigo, G.; Abbondanza, G.; Foti, G.; La Via, F. Heteroepitaxial Growth of (111) 3C-SiC on (110) Si Substrate by Second Order Twins. *Appl. Phys. Lett.* **2008**, *92* (22), 224102. <https://doi.org/10.1063/1.2920164>.



- (482) Yang, C.-M.; Kim, S.-K. AlN Epitaxial Film Growth Using MOCVD For a GHz-Band FBAR. *J. Korean Phy. Soc.* **2009**, *55* (3(1)), 1132–1135. <https://doi.org/10.3938/jkps.55.1132>.
- (483) Yang, C.-M.; Uehara, K.; Kim, S.-K.; Kameda, S.; Nakase, H.; Tsubouchi, K. Highly C-Axis-Oriented AlN Film Using MOCVD for 5GHz-Band FBAR Filter. In *IEEE Symposium on Ultrasonics, 2003*; IEEE: Honolulu, HI, USA, 2003; pp 170–173. <https://doi.org/10.1109/ULTSYM.2003.1293381>.
- (484) Sun, H.; Wu, F.; Park, Y. J.; Al tahtamouni, T. M.; Li, K.-H.; Alfaraj, N.; Detchprohm, T.; Dupuis, R. D.; Li, X. Influence of TMAI Preflow on AlN Epitaxy on Sapphire. *Appl. Phys. Lett.* **2017**, *110* (19), 192106. <https://doi.org/10.1063/1.4983388>.
- (485) Wang, J.; Xu, F.; He, C.; Zhang, L.; Lu, L.; Wang, X.; Qin, Z.; Shen, B. High Quality AlN Epilayers Grown on Nitrided Sapphire by Metal Organic Chemical Vapor Deposition. *Sci Rep* **2017**, *7* (1), 42747. <https://doi.org/10.1038/srep42747>.
- (486) Nakano, K.; Imura, M.; Narita, G.; Kitano, T.; Hirose, Y.; Fujimoto, N.; Okada, N.; Kawashima, T.; Iida, K.; Balakrishnan, K.; Tsuda, M.; Iwaya, M.; Kamiyama, S.; Amano, H.; Akasaki, I. Epitaxial Lateral Overgrowth of AlN Layers on Patterned Sapphire Substrates. *phys. stat. sol. (a)* **2006**, *203* (7), 1632–1635. <https://doi.org/10.1002/pssa.200565389>.
- (487) Chen, X.; Yan, J.; Zhang, Y.; Tian, Y.; Guo, Y.; Zhang, S.; Wei, T.; Wang, J.; Li, J. Improved Crystalline Quality of AlN by Epitaxial Lateral Overgrowth Using Two-Phase Growth Method for Deep-Ultraviolet Stimulated Emission. *IEEE Photonics J.* **2016**, *8* (5), 1–11. <https://doi.org/10.1109/JPHOT.2016.2614102>.
- (488) Long, H.; Dai, J.; Zhang, Y.; Wang, S.; Tan, B.; Zhang, S.; Xu, L.; Shan, M.; Feng, Z. C.; Kuo, H.; Chen, C. High Quality 10.6  $\mu$  m AlN Grown on Pyramidal Patterned Sapphire Substrate by MOCVD. *Appl. Phys. Lett.* **2019**, *114* (4), 042101. <https://doi.org/10.1063/1.5074177>.
- (489) Wei, W.; Peng, Y.; Yang, Y.; Xiao, K.; Maraj, M.; Yang, J.; Wang, Y.; Sun, W. Study of Defects and Nano-Patterned Substrate Regulation Mechanism in AlN Epilayers. *Nanomaterials* **2022**, *12* (22), 3937. <https://doi.org/10.3390/nano12223937>.
- (490) Khan, R.; Narang, K.; Padmavati, M. V. G.; Tyagi, R.; Bag, R. K.; Riaz, U. Investigation and Optimization of AlN Nucleation Layers Grown on 4H-SiC by MOCVD. *Materials Today: Proceedings* **2021**, *36*, 637–641. <https://doi.org/10.1016/j.matpr.2020.04.154>.
- (491) Krishnaswamy, S. V.; Adam, J. D.; Aumer, M. P1J-4 High-Q FBARs Using Epitaxial AlN Films. In *2006 IEEE Ultrasonics Symposium*; IEEE: Vancouver, BC, Canada, 2006; pp 1467–1470. <https://doi.org/10.1109/ULTSYM.2006.369>.
- (492) Umeda, K.; Takeuchi, M.; Yamada, H.; Kubo, R.; Yoshino, Y. Improvement of Thickness Uniformity and Crystallinity of AlN Films Prepared by Off-Axis Sputtering. *Vacuum* **2006**, *80* (7), 658–661. <https://doi.org/10.1016/j.vacuum.2005.11.024>.
- (493) Kano, K.; Arakawa, K.; Takeuchi, Y.; Akiyama, M.; Ueno, N.; Kawahara, N. Temperature Dependence of Piezoelectric Properties of Sputtered AlN on Silicon Substrate. *Sensors and Actuators A: Physical* **2006**, *130–131*, 397–402. <https://doi.org/10.1016/j.sna.2005.12.047>.
- (494) Abdallah, B.; Duquenne, C.; Besland, M. P.; Gautron, E.; Jouan, P. Y.; Tessier, P. Y.; Brault, J.; Cordier, Y.; Djouadi, M. A. Thickness and Substrate Effects on AlN Thin Film Growth at Room Temperature. *Eur. Phys. J. Appl. Phys.* **2008**, *43* (3), 309–313. <https://doi.org/10.1051/epjap:2008082>.
- (495) Iriarte, G. F.; Reyes, D. F.; González, D.; Rodríguez, J. G.; García, R.; Calle, F. Influence of Substrate Crystallography on the Room Temperature Synthesis of AlN Thin Films by Reactive Sputtering. *Applied Surface Science* **2011**, *257* (22), 9306–9313. <https://doi.org/10.1016/j.apsusc.2011.05.025>.
- (496) García-Gancedo, L.; Zhu, Z.; Iborra, E.; Clement, M.; Olivares, J.; Flewitt, A. J.; Milne, W. I.; Ashley, G. M.; Luo, J. K.; Zhao, X. B.; Lu, J. R. AlN-Based BAW Resonators with CNT Electrodes for Gravimetric Biosensing. *Sensors and Actuators B: Chemical* **2011**, *160* (1), 1386–1393. <https://doi.org/10.1016/j.snb.2011.09.083>.
- (497) Lim, W. T.; Son, B. K.; Kang, D. H.; Lee, C. H. Structural Properties of AlN Films Grown on Si, Ru/Si and ZnO/Si Substrates. *Thin Solid Films* **2001**, *382* (1–2), 56–60. [https://doi.org/10.1016/S0040-6090\(00\)01780-6](https://doi.org/10.1016/S0040-6090(00)01780-6).
- (498) Bi, X.; Wu, Y.; Wu, J.; Li, H.; Zhou, L. A Model for Longitudinal Piezoelectric Coefficient Measurement of the Aluminum Nitride Thin Films. *J Mater Sci: Mater Electron* **2014**, *25* (6), 2435–2442. <https://doi.org/10.1007/s10854-014-1885-3>.
- (499) Stan, G. E.; Botea, M.; Boni, G. A.; Pintilie, I.; Pintilie, L. Electric and Pyroelectric Properties of AlN Thin Films Deposited by Reactive Magnetron Sputtering on Si Substrate. *Applied Surface Science* **2015**, *353*, 1195–1202. <https://doi.org/10.1016/j.apsusc.2015.07.059>.
- (500) Lanz, R.; Lambert, C.; Senn, L.; Gabathuler, L.; Reynolds, G. J. P1J-9 Aluminum-Nitride Manufacturing Solution for BAW and Other MEMS Applications Using a Novel, High-Uniformity PVD Source. In *2006 IEEE*

- Ultrasonics Symposium*; IEEE: Vancouver, BC, Canada, 2006; pp 1481–1485. <https://doi.org/10.1109/ULTSYM.2006.372>.
- (501) Lanz, R.; Senn, L.; Gabathuler, L.; Huiskamp, W.; Strijbos, R. C.; Vanhelmont, F. P1H-5 Uniformity Optimization of the Electromechanical Coupling Coefficient in AlN Based Bulk Acoustic Wave Resonators. In *2007 IEEE Ultrasonics Symposium Proceedings*; IEEE: New York, NY, USA, 2007; pp 1429–1432. <https://doi.org/10.1109/ULTSYM.2007.359>.
- (502) Qamar, A.; Rais-Zadeh, M. Coupled BAW/SAW Resonators Using AlN/Mo/Si and AlN/Mo/GaN Layered Structures. *IEEE Electron Device Lett.* **2019**, *40* (2), 321–324. <https://doi.org/10.1109/LED.2018.2890755>.
- (503) Yang, J.; Jiao, X.; Zhang, R.; Zhong, H.; Shi, Y. Fabrication of Bulk Acoustic Wave Resonator Based on AlN Thin Film. In *2012 Symposium on Piezoelectricity, Acoustic Waves, and Device Applications (SPAWDA)*; IEEE: Shanghai, China, 2012; pp 191–194. <https://doi.org/10.1109/SPAWDA.2012.6464068>.
- (504) Lanz, R.; Dubois, M.-A.; Mural, P. Solidly Mounted BAW Filters for the 6 to 8 GHz Range Based on AlN Thin Films. In *2001 IEEE Ultrasonics Symposium. Proceedings. An International Symposium (Cat. No. 01CH37263)*; IEEE: Atlanta, GA, USA, 2001; Vol. 1, pp 843–846. <https://doi.org/10.1109/ULTSYM.2001.991851>.
- (505) Clement, M.; Vergara, L.; Olivares, J.; Iborra, E.; Sangrador, J.; Sanz-Hervas, A.; Zinck, C. SAW and BAW Response of C-Axis AlN Thin Films Sputtered on Platinum. In *IEEE Ultrasonics Symposium, 2004*; IEEE: Montreal, Canada, 2004; Vol. 2, pp 1367–1370. <https://doi.org/10.1109/ULTSYM.2004.1418049>.
- (506) Guo, Q. X.; Tanaka, T.; Nishio, M.; Ogawa, H. Growth Properties of AlN Films on Sapphire Substrates by Reactive Sputtering. *Vacuum* **2006**, *80* (7), 716–718. <https://doi.org/10.1016/j.vacuum.2005.11.037>.
- (507) Kim, J. Low-Temperature Epitaxial Growth of AlN Thin Films on a Mo Electrode/Sapphire Substrate Using Reactive Sputtering. *Coatings* **2021**, *11* (4), 443. <https://doi.org/10.3390/coatings11040443>.
- (508) Seo, H.-C.; Petrov, I.; Kim, K. Structural Properties of AlN Grown on Sapphire at Plasma Self-Heating Conditions Using Reactive Magnetron Sputter Deposition. *Journal of Elec Materi* **2010**, *39* (8), 1146–1151. <https://doi.org/10.1007/s11664-010-1275-4>.
- (509) Ohtsuka, M.; Takeuchi, H.; Fukuyama, H. Effect of Sputtering Pressure on Crystalline Quality and Residual Stress of AlN Films Deposited at 823 K on Nitrided Sapphire Substrates by Pulsed DC Reactive Sputtering. *Jpn. J. Appl. Phys.* **2016**, *55* (5S), 05FD08. <https://doi.org/10.7567/JJAP.55.05FD08>.
- (510) Lin, C.-M.; Chen, Y.-Y.; Felmetzger, V. V.; Senesky, D. G.; Pisano, A. P. Acoustic Characteristics of the Third-Order Quasi-Symmetric Lamb Wave Mode in an AlN/3C-SiC Plate. In *2013 IEEE International Ultrasonics Symposium (IUS)*; IEEE: Prague, Czech Republic, 2013; pp 1093–1096. <https://doi.org/10.1109/ULTSYM.2013.0280>.
- (511) Kuang, X.-P.; Zhang, H.-Y.; Wang, G.-G.; Cui, L.; Zhu, C.; Jin, L.; Sun, R.; Han, J.-C. AlN Films Prepared on 6H-SiC Substrates under Various Sputtering Pressures by RF Reactive Magnetron Sputtering. *Applied Surface Science* **2012**, *263*, 62–68. <https://doi.org/10.1016/j.apsusc.2012.08.121>.
- (512) Wolborski, M.; Rosén, D.; Hallén, A.; Bakowski, M. Aluminium Nitride Deposition on 4H-SiC by Means of Physical Vapour Deposition. *Thin Solid Films* **2006**, *515* (2), 456–459. <https://doi.org/10.1016/j.tsf.2005.12.261>.
- (513) Kim, K.-H.; Kim, Y.-S.; Jeong, S.-H.; Jung, S.-W. Fabrication and Properties of an Epitaxial AlN Film on a SiC Substrate Using Reactive RF Magnetron Sputtering. *Journal of the Korean Physical Society* **2005**, *48* (2), 275–278.
- (514) Fujii, S.; Shimizu, S.; Sumisaka, M.; Suzuki, Y.; Otomo, S.; Omori, T.; Hashimoto, K. Deposition of Highly C-Axis-Oriented ScAlN Thin Films by RF Magnetron Sputtering Using a Sc-Al Alloy Target. In *2014 IEEE International Frequency Control Symposium (FCS)*; IEEE: Taipei, Taiwan, 2014; pp 1–4. <https://doi.org/10.1109/FCS.2014.6859938>.
- (515) Kusano, Y.; Luo, G.-L.; Horsley, D.; Ishii, I. taru; Teshigahara, A. 36% Scandium-Doped Aluminum Nitride Piezoelectric Micromachined Ultrasonic Transducers. In *2018 IEEE International Ultrasonics Symposium (IUS)*; IEEE: Kobe, 2018; pp 1–4. <https://doi.org/10.1109/ULTSYM.2018.8579694>.
- (516) Fujii, S.; Sumisaka, M.; Tang, G.; Suzuki, Y.; Otomo, S.; Omori, T.; Hashimoto, K. Highly C-Axis-Oriented ScAlN Thin Films Deposited Using Sc-Al Alloy Target. In *2015 IEEE MTT-S International Microwave Symposium*; IEEE: Phoenix, AZ, USA, 2015; pp 1–4. <https://doi.org/10.1109/MWSYM.2015.7166841>.
- (517) Matloub, R.; Artieda, A.; Sandu, C.; Milyutin, E.; Mural, P. Electromechanical Properties of Al<sub>0.9</sub>Sc<sub>0.1</sub>N Thin Films Evaluated at 2.5 GHz Film Bulk Acoustic Resonators. *Appl. Phys. Lett.* **2011**, *99* (9), 092903. <https://doi.org/10.1063/1.3629773>.
- (518) Tokuda, S.; Takayanagi, S.; Matsukawa, M.; Yanagitani, T. Film Growth of C-Axis Tilted ScAlN on the Sapphire Substrate for SAW Devices. In *2017 IEEE International Ultrasonics Symposium (IUS)*; IEEE: Washington, DC, USA, 2017; pp 1–4. <https://doi.org/10.1109/ULTSYM.2017.8092072>.

- (519) Umeda, K.; Kawai, H.; Honda, A.; Akiyama, M.; Kato, T.; Fukura, T. Piezoelectric Properties of ScAlN Thin Films for Piezo-MEMS Devices. In *2013 IEEE 26th International Conference on Micro Electro Mechanical Systems (MEMS)*; IEEE: Taipei, Taiwan, 2013; pp 733–736. <https://doi.org/10.1109/MEMSYS.2013.6474347>.
- (520) Wang, Q.; Lu, Y.; Mishin, S.; Oshmyansky, Y.; Horsley, D. A. Design, Fabrication, and Characterization of Scandium Aluminum Nitride-Based Piezoelectric Micromachined Ultrasonic Transducers. *J. Microelectromech. Syst.* **2017**, *26* (5), 1132–1139. <https://doi.org/10.1109/JMEMS.2017.2712101>.
- (521) Yanagitani, T.; Arakawa, K.; Kano, K.; Teshigahara, A.; Akiyama, M. Giant Shear Mode Electromechanical Coupling Coefficient K15 in C-Axis Tilted ScAlN Films. In *2010 IEEE International Ultrasonics Symposium*; IEEE: San Diego, CA, USA, 2010; pp 2095–2098. <https://doi.org/10.1109/ULTSYM.2010.5935791>.
- (522) Sandu, C. S.; Parsapour, F.; Mertin, S.; Pashchenko, V.; Matloub, R.; LaGrange, T.; Heinz, B.; Mural, P. Abnormal Grain Growth in AlScN Thin Films Induced by Complexion Formation at Crystallite Interfaces. *Phys. Status Solidi A* **2019**, *216* (2), 1800569. <https://doi.org/10.1002/pssa.201800569>.
- (523) Sano, K.; Karasawa, R.; Yanagitani, T. High Electromechanical Coefficient  $k_{t2} = 19\%$  Thick ScAlN Piezoelectric Films for Ultrasonic Transducer in Low Frequency of 80 MHz. In *2017 IEEE International Ultrasonics Symposium (IUS)*; IEEE: Washington, DC, 2017; pp 1–1. <https://doi.org/10.1109/ULTSYM.2017.8092425>.
- (524) Sano, K.-H.; Karasawa, R.; Yanagitani, T. Thick ScAlN Film for High Efficient Ultrasonic Transducer in Low Frequency of 81 MHz. In *2017 19th International Conference on Solid-State Sensors, Actuators and Microsystems (TRANSDUCERS)*; IEEE: Kaohsiung, 2017; pp 862–865. <https://doi.org/10.1109/TRANSDUCERS.2017.7994185>.
- (525) Tominaga, T.; Takayanagi, S.; Yanagitani, T. Deterioration in the Piezoelectric Property of ScAlN Thin Films by Negative Ion Bombardment Increased in Low-Pressure Sputtering Deposition. In *2020 IEEE International Ultrasonics Symposium (IUS)*; IEEE: Las Vegas, NV, USA, 2020; pp 1–4. <https://doi.org/10.1109/IUS46767.2020.9251438>.
- (526) Arakawa, K.; Yanagitani, T.; Kano, K.; Teshigahara, A.; Akiyama, M. Deposition Techniques of C-Axis-Tilted ScAlN Films by Conventional RF Magnetron Sputtering. In *2010 IEEE International Ultrasonics Symposium*; IEEE: San Diego, CA, USA, 2010; pp 1050–1053. <https://doi.org/10.1109/ULTSYM.2010.5935747>.
- (527) Felmetsger, V.; Mikhov, M.; Ramezani, M.; Tabrizian, R. Sputter Process Optimization for Al<sub>0.7</sub>Sc<sub>0.3</sub>N Piezoelectric Films. In *2019 IEEE International Ultrasonics Symposium (IUS)*; IEEE: Glasgow, United Kingdom, 2019; pp 2600–2603. <https://doi.org/10.1109/ULTSYM.2019.8925576>.
- (528) Zhang, Q.; Chen, M.; Liu, H.; Zhao, X.; Qin, X.; Wang, F.; Tang, Y.; Yeoh, K. H.; Chew, K.-H.; Sun, X. Deposition, Characterization, and Modeling of Scandium-Doped Aluminum Nitride Thin Film for Piezoelectric Devices. *Materials* **2021**, *14* (21), 6437. <https://doi.org/10.3390/ma14216437>.
- (529) Sinusía Lozano, M.; Pérez-Campos, A.; Reusch, M.; Kirste, L.; Fuchs, T.; Žukauskaitė, A.; Chen, Z.; Iriarte, G. F. Piezoelectric Characterization of Sc<sub>0.26</sub>Al<sub>0.74</sub>N Layers on Si (001) Substrates. *Mater. Res. Express* **2018**, *5* (3), 036407. <https://doi.org/10.1088/2053-1591/aab232>.
- (530) Delbergue, D.; Texier, D.; Lévesque, M.; Bocher, P. Comparison of Two X-Ray Residual Stress Measurement Methods: Sin<sup>2</sup>  $\psi$  and Cos  $\alpha$ , Through the Determination of a Martensitic Steel X-Ray Elastic Constant; 2017; pp 55–60. <https://doi.org/10.21741/9781945291173-10>.
- (531) Luo, Q. A Modified X-Ray Diffraction Method to Measure Residual Normal and Shear Stresses of Machined Surfaces. *Int J Adv Manuf Technol* **2022**, *119* (5–6), 3595–3606. <https://doi.org/10.1007/s00170-021-08645-4>.
- (532) Deleuze, C. Méthodologie d’analyse des contraintes résiduelles par diffraction des rayons X sur des pièces d’alliage de titane de nuance Ti-10V-2Fe-3Al, Arts et Métiers ParisTech, 2010.
- (533) Kusaka, K.; Hanabusa, T.; Tominaga, K. Effect of Nitrogen Gas Pressure on Residual Stress in AlN Films Deposited by the Planar Magnetron Sputtering System. *Thin Solid Films* **1996**, *281–282*, 340–343. [https://doi.org/10.1016/0040-6090\(96\)08633-6](https://doi.org/10.1016/0040-6090(96)08633-6).
- (534) Kusaka, K.; Taniguchi, D.; Hanabusa, T.; Tominaga, K. Effect of Sputtering Gas Pressure and Nitrogen Concentration on Crystal Orientation and Residual Stress in Sputtered AlN Films. *Vacuum* **2002**, *66* (3–4), 441–446. [https://doi.org/10.1016/S0042-207X\(02\)00168-9](https://doi.org/10.1016/S0042-207X(02)00168-9).
- (535) de Jong, M.; Chen, W.; Angsten, T.; Jain, A.; Notestine, R.; Gamst, A.; Sluiter, M.; Krishna Ande, C.; van der Zwaag, S.; Plata, J. J.; Toher, C.; Curtarolo, S.; Ceder, G.; Persson, K. A.; Asta, M. Charting the Complete Elastic Properties of Inorganic Crystalline Compounds. *Sci Data* **2015**, *2* (1), 150009. <https://doi.org/10.1038/sdata.2015.9>.

- (536) Rountree, C. L.; Kalia, R. K.; Lidorikis, E.; Nakano, A.; Van Brutzel, L.; Vashishta, P. Atomistic Aspects of Crack Propagation in Brittle Materials: Multimillion Atom Molecular Dynamics Simulations. *Annu. Rev. Mater. Res.* **2002**, *32* (1), 377–400. <https://doi.org/10.1146/annurev.matsci.32.111201.142017>.
- (537) Beuth, J. L. Cracking of Thin Bonded Films in Residual Tension. *International Journal of Solids and Structures* **1992**, *29* (13), 1657–1675. [https://doi.org/10.1016/0020-7683\(92\)90015-L](https://doi.org/10.1016/0020-7683(92)90015-L).
- (538) Dundurs, J. Discussion: “Edge-Bonded Dissimilar Orthogonal Elastic Wedges Under Normal and Shear Loading” (Bogy, D. B., 1968, ASME J. Appl. Mech., 35, Pp. 460–466). *Journal of Applied Mechanics* **1969**, *36* (3), 650–652. <https://doi.org/10.1115/1.3564739>.
- (539) Suga, T.; Elssner, G.; Schmauder, S. Composite Parameters and Mechanical Compatibility of Material Joints. *Journal of Composite Materials* **1988**, *22* (10), 917–934. <https://doi.org/10.1177/002199838802201002>.
- (540) Marrier, E. Modélisation de l'évolution de La Composition Du Substrat Au Cours de l'oxydation Sélective Des Alliages à Haute Température, Ecole Nationale Supérieure des Mines de Saint-Etienne, 2015.
- (541) Paul, A.; Laurila, T.; Vuorinen, V.; Divinski, S. V. *Thermodynamics, Diffusion and the Kirkendall Effect in Solids*; Springer International Publishing: Cham, 2014. <https://doi.org/10.1007/978-3-319-07461-0>.
- (542) Zhu, L. Q.; Barrett, N.; Jégou, P.; Martin, F.; Leroux, C.; Martinez, E.; Grampeix, H.; Renault, O.; Chabli, A. X-Ray Photoelectron Spectroscopy and Ultraviolet Photoelectron Spectroscopy Investigation of Al-Related Dipole at the HfO<sub>2</sub>/Si Interface. *Journal of Applied Physics* **2009**, *105* (2), 024102. <https://doi.org/10.1063/1.3066906>.
- (543) Jacquemin, M.; Genet, M. J.; Gaigneaux, E. M.; Debecker, D. P. Calibration of the X-Ray Photoelectron Spectroscopy Binding Energy Scale for the Characterization of Heterogeneous Catalysts: Is Everything Really under Control? *ChemPhysChem* **2013**, *14* (15), 3618–3626. <https://doi.org/10.1002/cphc.201300411>.
- (544) Knausgard Hommedal, Y. Spectroscopic Investigation of Band Alignment in Novel 2DEG Devices Based on K-(MxGa1-x)2O3-Alloys, University of Oslo, Oslo, 2021.
- (545) David-Viffantzeff, J. Etude Du Spalling Comme Procédé de Transfert Du Graphène et d'autres Matériaux 2D, Université Grenoble Alpes, Grenoble, 2022.
- (546) Li, X.; Zhu, H. Two-Dimensional MoS<sub>2</sub>: Properties, Preparation, and Applications. *Journal of Materiomics* **2015**, *1* (1), 33–44. <https://doi.org/10.1016/j.jmat.2015.03.003>.



## Annex part 1: Literature review of AlN and doped AlN thin films deposition

In chapter 2, a non-exhaustive literature review of AlN thin films deposition by MOCVD and reactive sputtering on sapphire, silicon carbide (cubic and hexagonal) and silicon-based substrates is presented. The multi-steps deposition and ELOG approaches are also discussed for AlN MOCVD on sapphire substrate. A similar review was also realized for (co-)doped AlN thin films elaborated by reactive sputtering with a strong focus on scandium (Sc) doping. When available, the electromechanical coupling coefficient  $k_{eff}^2$  and quality factor  $Q$ , which are the characteristics parameters of an acoustic device, are mentioned. These reviews are hereafter presented in eleven different tables as follows:

*Table I: Literature review of AlN MOCVD deposition on silicon-based substrates*

*Table II: Literature review of AlN MOCVD deposition on sapphire substrate using multi-step approach*

*Table III: Literature review of AlN MOCVD deposition on sapphire substrate using ELOG approach*

*Table IV: Literature review of AlN MOCVD deposition on cubic silicon carbide*

*Table V: Literature review of AlN MOCVD deposition on hexagonal silicon carbide*

*Table VI: Literature review of AlN deposition by reactive sputtering on silicon-based substrate*

*Table VII: Literature review of AlN deposition by reactive sputtering on sapphire*

*Table VIII: Literature review of AlN deposition by reactive sputtering on 3C-SiC*

*Table IX: Literature review of AlN deposition by reactive sputtering on hexagonal silicon carbide*

*Table X: Literature review of (co-)doped of AlN deposition by reactive sputtering (except Sc)*

*Table XI: Review of Sc doped of AlN deposition by reactive sputtering*

**Annex part 1: Literature review of AlN and doped AlN thin films deposition**

Substrate	Electrode	AlN thickness (μm)	AlN (002) RC	$k^2_{\text{eff}}$	Q (operating frequency)	FOM ( $k^2_{\text{eff}} \cdot Q$ )	Remarks	References
Si (111)	/	0.38	0.68°	/	/	/	Influence of V/III ratio	195
Si (100)/SiO <sub>2</sub>	Mo	0.95	2.4°	1.1 %	1557 (3.7GHz)	17	Improvement of Mo electrode resistance	199
Si (100)/SiO <sub>2</sub>	Ru/Ta	0.35	1.2°	7.0 %	329 (5.3 GHz)	23	Seems indicate better results with Ru/Ta electrode	200
Si (100)/SiO <sub>2</sub>	Ru/Ta	0.03 to 0.75	1.0° to 1.5°	/	/	/	Influence of thermal annealing on Ru/Ta electrodes	457
Si (100)/SiO <sub>2</sub> and Si (111)/SiO <sub>2</sub>	Mo	1.1	4.0° (Si (100)) and 3.8° (Si (111))	2.65 %	24.7 (3.2 GHz)	0.65	Better (002) RC with Si (111) substrate	482
Si (100)/SiO <sub>2</sub>	Mo	1.0	2.98°	6.4 %	/	/	Influence of deposition temperature (optimum at 1050 °C)	483
Si (111)	Mo	0.9	1.48° (full PVD growth)	5.3 %	1208 (2.6 GHz)	64	Comparison of a standard PVD growth with a two-step growth using an AlN MOCVD buffer layer	201
Si (111)	Mo	0.9	0.33° (MOCVD buffer layer) 0.68° (MOCVD buffer layer + PVD growth)	6.4 %	1904 (2.6 GHz)	122		
Si	/	0.7	0.028°	6.07 %	1497 (5.2 GHz)	100	Electrode material not mentioned and MOCVD process not described	90
Si	/	0.5	≈0.03°	6.03 %	3685 (1.8 GHz)	222	Electrode material not mentioned and MOCVD process not described	58
Si	/	0.5	0.03°	6.30 %	2589 (3.8 GHz)	163		
Si	/	0.5	0.03°	6.26 %	2136 (5.2 GHz)	134		

Table I: Literature review of AlN MOCVD deposition on silicon-based substrates

**Annex part 1: Literature review of AlN and doped AlN thin films deposition**

Low-temperature AlN (LT AlN)		High-temperature AlN (HT AlN)		AlN RC		Remarks	Reference
Thickness (μm)	Deposition temperature (°C)	Thickness (μm)	Deposition temperature (°C)	(002)	(102)		
0.036	880 to 1020	1.05	1300	/	/	Influence of LT AlN deposition temperature. Crystal quality characterized by Raman spectroscopy.	184
0.040	880	0.27 to 0.45	1130	0.12° to 0.23°	0.30° to 0.48°	Influence of V/III ratio. Optimized growth for high V/III ratios.	192
0.050	950	1.0	1300	0.02° to 0.19°	0.15° to 0.20°	Influence of sample preparation surface.	207
/	550	1.0	1200	0.01° to 0.17°	0.15° to 0.18°	Influence of LT AlN thickness (deposition time of 4, 6, 8 and 10 minutes)	187
0.015	940	3.0	1100	/	/	Influence of TMA precursor preflow.	484
0.015	930	3.4	1100	0.08°	0.13°	Three-steps AlN MOCVD deposition (intermediate AlN layer of 0.05 μm at 1130 °C). Off-cut sapphire substrate.	182
0.5	/	0.2	1200	0.05°	0.78°	LT AlN layer deposited by PVD and annealed at 1700 °C	183
/	920	0.3 to 0.8	1050 to 1130	0.03° to 0.22°	0.61° to 1.08°	Spatially pulsed MOCVD. Influence of growth pressure of AlN on surface morphology	186
0.02	850	0.5 to 2.0	1050 and 1070	0.01° to 0.15°	0.04° to 0.15°*	Better results obtained via an AlN sandwiched method growth. *(105) Rocking Curves	206
/	/	4.0	≈ 1270	0.05° to 0.06°	0.09° to 0.13°	Investigation of different sapphire orientation (m- and a-axis off-angle)	194
0.02	540	0.3	1200	0.01° to 0.05°	0.16° to 0.21°	Multi-steps AlN deposition via MOCVD and Pulse-atomic Layer Epitaxy (PALE)	191
0.01	960	0.3 to 2.6	1220	0.09° to 0.2°	0.80° to 0.18°	Multi-steps AlN deposition with alternation of LT AlN and HT AlN layers (intermediate LT layers deposited at 1080 °C)	189
0.027	1000	1.0	1100	≈0.06°	1.18° to 0.56°	Multi-steps AlN deposition with alternation of high and low V/III ratios.	190
0.02	950	1.0	1240	0.02° to 0.11°	0.20° to 0.28°	Influence of V/III ratios during LT AlN deposition. Sapphire nitridation (high V/III ratio) promote c-axis orientation.	485
0 to 1.5	105	0 to 1.5	1150	/	/	Multi-steps AlN deposition with alternation of LT AlN and HT AlN layers between 0 and 0.5 μm. The period is repeated 3 times to reach 1.5 μm	188
0.02	650	1.0	1250	/	/	Influence of off-cut angles of sapphire substrates	185

Table II: Literature review of AlN MOCVD deposition on sapphire substrate using multi-step approach



**Annex part 1: Literature review of AlN and doped AlN thin films deposition**

AlN nucleation layer		AlN thick layer		Process	AlN RC		Remarks	Reference
Thickness (μm)	Temperature deposition (°C)	Thickness (μm)	Temperature deposition (°C)		(002)	(102)		
/ (20 min)	1400	/ (120 min)	1400	Standard photolithography (trenches)	/	/	Better coalescence along $[1\bar{1}\bar{2}0]$ sapphire direction Decrease in dislocation density from $10^9 \text{ cm}^{-2}$ to less than $10^7 \text{ cm}^{-2}$	208
/ (20 min)	1400	/ (120 min)	1400	Standard photolithography (trenches)	0.08°	0.11°	Better coalescence along $[10\bar{1}0]$ sapphire direction Dislocation density of $4 \times 10^7 \text{ cm}^{-2}$	209
/	/	≈ 5 μm and 7-8 μm (TEM cross-section)	1100 and 1300	Standard photolithography (trenches)	≈0.09°	/	Growth directly on patterned sapphire substrate Better coalescence at 1300 °C and crystal quality along $[1\bar{1}\bar{2}0]$	486
0.9	550	7.3	1250	Standard photolithography (trenches)	0.05°	0.12°	Influence of V/III ratio during AlN growth Dislocation density around $10^8 \text{ cm}^{-2}$	487
3.4	1200 to 1300	15.0	1270 to 1350	Standard photolithography (trenches)	/	0.09°	Influence of V/III ratio and temperature deposition during AlN growth Decrease in threading dislocation density from $2 \times 10^9 \text{ cm}^{-2}$ to $3 \times 10^8 \text{ cm}^{-2}$	193
0.02	650	10	1045	Standard photolithography (pyramids)	0.05°	0.05°	Three-step growth with an AlN intermediate layer (0.6 μm at 1060 °C) Screw and edge dislocation density of $5.9 \times 10^7 \text{ cm}^{-2}$ and $2.3 \times 10^8 \text{ cm}^{-2}$ , respectively	488
2	800 to 1250	≈ 4	1100	Nanosphere lithography	/	/	Three-step growth for AlN nucleation layer Dislocation density of $3.5 \times 10^8 \text{ cm}^{-2}$	211
0.025	950	6	1250	Nano-imprint lithography (hole array)	0.05° to 0.07°	0.06° to 0.11°	Variation in hole diameter (optimum for 650 nm) Screw and edge dislocation density estimated to $6.3 \times 10^7 \text{ cm}^{-2}$ and $3.2 \times 10^8 \text{ cm}^{-2}$ , respectively	212
/	550	1	1200	Nano-imprint lithography (hole array or trenches)	0.02° to 0.03°	0.09° to 0.10°	Trench patterns along $[1\bar{1}00]$ sapphire direction Better results with nano-hole array Decrease only in edge density dislocation after ELOG from $4.5 \cdot 10^9 \text{ cm}^{-2}$ to $1.1 \times 10^9 \text{ cm}^{-2}$ (hole array)	213
0.015	/	3.02 and 5.12	1250	Nano-imprint lithography (cone)	0.06° to 0.08°	0.11° to 0.13°	Comparison of a nano-patterned and conventional sapphire substrate AlN nucleation layer deposited by PVD Better results on nano-patterned substrate	489

Table III: Literature review of AlN MOCVD deposition on sapphire substrate using ELOG approach

**Annex part 1: Literature review of AlN and doped AlN thin films deposition**

Substrate	Electrode	AlN layer		AlN RC		$k_{\text{eff}}^2$	Q (operating frequency)	FOM ( $k_{\text{eff}}^2 \cdot Q$ )	Remarks	Reference
		Thickness ( $\mu\text{m}$ )	Deposition temperature ( $^{\circ}\text{C}$ )	(002)	(102)					
Si (100)/3C-SiC (100)	/	0.3	600 and 1050	/	/	/	/	/	Comparison with sapphire substrate influence of deposition temperature	219
3° off axis Si (111)/3C-SiC (111)	/	0.1	1100	/	/	/	/	/	Comparison with Si (111)	220
Si (111)/3C-SiC (111)	/	$\approx 0.1$	1100	1.8°	/	/	/	/	Comparison with Si (111)	221

Table IV: Literature review of AlN MOCVD deposition on cubic silicon carbide

**Annex part 1: Literature review of AlN and doped AlN thin films deposition**

Substrate	Electrode	AlN layer		AlN RC		$k^2_{eff}$	Q (operating frequency)	FOM ( $k^2_{eff} \cdot Q$ )	Remarks	Reference
		Thickness ( $\mu\text{m}$ )	Deposition temperature ( $^{\circ}\text{C}$ )	(002)	(102)					
6H-SiC	Al	1.0	1100 and 1200	/	/	/	/	/	Influence of V/III ratio	232
6H-SiC	/	1.5	1070 and 1170	0.02 $^{\circ}$	0.10 $^{\circ}$	/	/	/	Multilayer structure alternating between 2D and 3D AlN growth modes Decrease in dislocation density with this modulating method	230
4H-SiC	/	0.7	1100 and 1200	0.05 $^{\circ}$	0.05 $^{\circ}$ *	/	/	/	Simple AlN growth with NH <sub>3</sub> pulsed Nanopipes defects and oxygen contamination for 1100 $^{\circ}\text{C}$ AlN growth *(103) reflection	227
6H-SiC	/	0.3	1100	0.12 $^{\circ}$ *	/	/	/	/	3D AlN growth followed by AlN single crystal growth by PVT *PVT regrowth	225
6H-SiC	/	0.68 (6H-SiC) 0.25 (sapphire)	Above 1000	1.86.10 <sup>-5</sup> $^{\circ}$ (6H-SiC) 3.61.10 <sup>-5</sup> $^{\circ}$ (sapphire)	/	/	/	/	Comparison with sapphire substrate. Better crystal quality on 6H-SiC than sapphire	202
4H-SiC	/	0.01 to 0.3	1140	0.09 $^{\circ}$ to 0.21 $^{\circ}$ *	0.14 $^{\circ}$ to 0.26 $^{\circ}$ *	/	/	/	Very high V/III ratio ( $\approx$ 5000) and optimized thickness of 100 nm *(004) and (204) reflections	490
4H-SiC	/	0.1	1180 to 1220	0.12 $^{\circ}$ 0.20 $^{\circ}$ *	0.17 $^{\circ}$ to .18*	/	/	/	High V/III ratio and optimized deposition temperature at 1220 $^{\circ}\text{C}$ *(004) and (105) reflections	228
4H-SiC	/	0.5	/	0.027 $^{\circ}$	/	6.32 %	1532 (5.2 GHz)	97	Electrode and AlN MOCVD deposition parameters not mentioned	233
4H-SiC	/	0.6	/	0.025 $^{\circ}$	/	5.87 % and 7.63 %	858 and 1572 (3.8 GHz)	66 and 92	Electrode and AlN MOCVD deposition parameters not mentioned	234
6H-SiC	Al	0.35	1200 – 1300	0.06 $^{\circ}$	/	4.2 % and 5.6 %	250 and 80 (12 GHz)	10.5 and 4.5	Q factor degrade by the mechanical and resistive damping of the electrodes	491
6H-SiC	/	0.5 and 0.6	1200	0.05 $^{\circ}$ to 0.11 $^{\circ}$	0.14 $^{\circ}$ to 0.25 $^{\circ}$	/	/	/	Investigation of V/III ratio (optimum at high ratio)	226
6H-SiC	/	1.0 to 2.0	1100 to 1600	0.02 $^{\circ}$	0.10 $^{\circ}$	/	/	/	Investigation of V/III ratio and growth temperature	229

Table V: Literature review of AlN MOCVD deposition on hexagonal silicon carbide

**Annex part 1: Literature review of AlN and doped AlN thin films deposition**

Substrate	Electrodes	AlN thickness ( $\mu\text{m}$ )	AlN (002) RC	$k^2_{\text{eff}}$	Q (operating frequency)	FOM ( $k^2_{\text{eff}} \cdot Q$ )	Remarks	Reference
Si (100), (110) and (111)	/	$\approx 0.9$	$4.2^\circ$ to $16.0^\circ$	/	/	/	Better c-axis orientation on Si (111)	264
Si (100) and (111)	/	$\approx 0.6$	$2.3^\circ$ to $3.2^\circ$	/	/	/	Better c-axis orientation on Si (111) Decrease in AlN (002) RC using 1 nm AlN MBE buffer layer ( $1.2^\circ$ )	265
Si (111)	/	0.1	/	/	/	/	Pre-deposition of a 5 nm Al layer increase AlN (002) peak intensity	266
Si (111)	/	0.1	$0.63^\circ$	/	/	/	Influence of gas ( $\text{N}_2$ and $\text{NH}_3$ ) and investigation of AlGaIn/GaN regrowth Al pre-deposition and optimum AlN thickness at $0.2 \mu\text{m}$	267
Si (100)	Mo	$\approx 1.2$	$2.40^\circ$ and $4.09^\circ$	3.7 % and 5.9 %	/	/	Influence of deposition temperature. Optimum at $400^\circ\text{C}$ Comparison of DC and RF power (better results with RF)	242
Si (100)	/	$\approx 0.4$	$3.1^\circ$ to $7.4^\circ$	/	/	/	Decrease in (002) RC with the increase in $\text{N}_2$ concentration	256
Si (100)	/	1.9	$\approx 2.0^\circ$	/	/	/	Influence of sputter power and Ar/ $\text{N}_2$ ratio	238
Si (100) and Si (100)/Pt/Ti	/	/	$1.4^\circ$ to $6.0^\circ$ (Si (100)) $2n1^\circ$ on (Si (100)/Pt/Ti)	/	/	/	Influence on off-axis sputtering. sputter power and gas pressure	492
Si (100)/SiO <sub>2</sub>	Al	1.2	$4.9^\circ$	/	/	/	Measurement of $d_{33}$ ( $1.38 \text{ pC} \cdot \text{N}^{-1}$ )	493
Si (100)	/	0.3 and 1.5	$10^\circ$ ( $1.5 \mu\text{m}$ )	/	/	/	Improvement of sputtered AlN layer using AlN MBE buffer layer	494
Oxidized Si (100)	Ir	1.0	$\approx 2.0^\circ$	$\approx 7.5 \%$	$\approx 4$ to $10$	/	Influence of soft-etching and comparison with Mo bottom electrode Use of Ti/Mo seed layer to improve Ir electrode adhesion Better quality factor with Ir electrode and $k^2_{\text{eff}}$ with soft-etched Ir	81
Si (100) and Si (111)	Au	1.5	$1.3^\circ$ (on Si (111)) $3.14^\circ$ (on Si (111)/Au)	/	/	/	AlN degradation on Au electrode	495
Si (100)/ Bragg reflector	Ir and Carbon Nano Tube (CNT)	1.55	$1.8^\circ$	/	$> 2000$ (1.8 GHz)	/	Use of Ti/Mo seed layer to improve Ir electrode adhesion Comparison with Cr/Au top electrode Better results with CNT electrodes	496
Si (100)	Pt/Ti and Cr/Au	1.0	$2.26^\circ$	5.1 %	(2.4GHz)	/	Influence of substrate temperature	243

**Annex part 1: Literature review of AlN and doped AlN thin films deposition**

Si (100), Si (100)/Ru and Si (100)/ZnO	/	0.5 to 0.6	5.96° (Si (100) 4.05° (Si (100)/Ru 1.19° (Si (100)/ZnO	/	/	/	Better AlN crystal quality on Si (100)/ZnO but more important stress	497
Si (100)	Ti and Al	1.8	1.63°	/	/	/	Calculated values of $d_{33}$	498
Si (100)	/	≈ 0.6 and 1.3	7.1° (1.3 μm) 11° (0.6 μm)	/	/	/	Study on electric and pyroelectric AlN properties	499
Si/Bragg reflector	Mo	2.0	1.23° to 1.38°	≈ 6 %	1167 (1.9 GHz)	≈ 70	Optimization of AlN sputtering process to obtain constant parameters (stress, thickness...) at the wafer scale	500
Si (100)	Ru	/	≈ 1.0°	6.5 %	/	/	Increase $k_{eff}^2$ with decrease in c-axis lattice constant and increase in stress (tensile to compressive)	269
Si/Bragg reflector	Mo	0.5	< 2°	≈ 6.0 % to 6.8 %	/	/	Strong correlation between XRD and $k_{eff}^2$ measurements	501
Si (111) and Si (111)/GaN	Mo	1.0	1.30° (Si (111) 1.50° (Si (111)/GaN)	2.4 % (Si (111) 3.2 % (Si (111)/GaN)	/	/	Enhancement of $k_{eff}^2$ using thick AlN buffer layer	502
Si/Bragg reflector polished and rough	Ir	0.16 to 0.2	1.6° to 3.0° (polished) 9.0 to 11.0° (rough)	5.8 %	160 ( $Q_r$ ) and 930 ( $Q_a$ ) (8.0 GHz)	7.5 at $f_a$ 54 at $f_r$	Influence of substrate roughness on (002) RC and acoustic device performances	270
Si/Bragg reflector	Ir	≈ 0.9 – 1.0 μm	0.89°	6.5 %	360 ( $Q_r$ ) and 450 ( $Q_a$ ) (2.0 GHz)	23 at $f_a$ 29 at $f_r$	Use of Ti/Mo seed layer to improve Ir electrode adhesion	268
Si/SiO <sub>2</sub>	Mo	2.5	2.29°	2.9 %	(1.5 GHz)	/	Classic approach to elaborate a BAW device	503
Si (100)/Bragg reflector	Pt/Ta and Al/Ti	0.31 and 0.49	/	5.5 %	585 (7.4 GHz)	32	High operating frequency	504
Si (100)/SiO <sub>2</sub> /SiN/Ti/Pt	Pt and Al	≈ 1.2	/	4.77 %	/	/	Investigation of $k_{31}^2$ coefficient	505

Table VI: Literature review of AlN deposition by reactive sputtering on silicon-based substrate

**Annex part 1: Literature review of AlN and doped AlN thin films deposition**

Substrate	Temperature deposition (°C)	AlN thickness (μm)	AlN (002) RC after deposition	Annealing temperature (°C)	AlN (002) RC after annealing	Remarks	Reference
Sapphire	300 to 1000	/	0.02° to 0.06°	/	/	Influence of growth temperature (300 °C to 1000 °C) and Ar/N <sub>2</sub> ratio Suitable temperature between 800 °C and 1000 °C	271
Sapphire or nitrided sapphire	600 (nitrided at 1530 °C – 1580 °C)	/(2.2 μm.h <sup>-1</sup> )	0.41° (0.01° - 0.02° on nitrided sapphire)	/	/	Influence of sputtering power and N <sub>2</sub> gas flow ratio Better results by increasing sputtering power	252
Sapphire	100	≈ 0.48 to 1.92	/	/	/	Increase and decrease in growth rate and roughness with the increase in RF power	506
Sapphire	350	0.2	4.15° (13.0° on Si/SiO <sub>2</sub> )	/	/	Comparison with a Si/SiO <sub>2</sub> substrate Better results on sapphire substrate	507
Sapphire	550 to 700	0.2	0.07°	1700	0.03°	Influence of thermal annealing. RF power. deposition temperature and N <sub>2</sub> flux on AlN crystal quality (102) RC also measured (0.81° and 0.07° before and after annealing, respectively)	272
Sapphire	600	0.43 and 1.0	/	1725	0.01°	Sputtered AlN layer annealed targeting HEMTs applications (102) RC of 0.05° after annealing	273
Nitrided sapphire	550 (nitrided at 1530°C)	1.15 to 1.55	0.04°	/	/	Influence of sputtering power (optimum at 400 W) (101) RC of 0.17°	276
Sapphire	200 to 500	0.2	0.04° to 0.1°	1650 to 1700	0.02° (after annealing) 0.1° (after annealing + MOCVD growth)	Influence of substrate temperature. sputter power and pressure Enhancement of AlN crystal quality after annealing and investigation of AlN MOCVD regrowth (102) RC also measured	275
Sapphire	650	0.17 and 0.34	0.15°	1600 to 1700	0.01°	Influence of annealing temperature Enhancement of AlN crystal quality after annealing (102) RC also measured	214
Sapphire	300	0.2	0.27°	1500 to 1700	0.01° 0.06° (after annealing + MOCVD)	Influence of annealing temperature Enhancement of AlN crystal quality after annealing (102) RC also measured	274
Nitrided sapphire	300 to 500 (nitrided at 1500 °C)	1.0	0.02° to 1.1°	/	/	Influence substrate temperature. sputter power and N <sub>2</sub> flux Better results at 400 W with 50 % N <sub>2</sub> (volume) and 300°C. (101) RC also measured	277
Sapphire	900	0.25	≈ 1.8° to 2.5°	/	/	Decrease in (002) RC by increasing sputtering pressure	508
Sapphire	550	1.5	3.3°	/	/	Influence of sputtering pressure	509

Table VII: Literature review of AlN deposition by reactive sputtering on sapphire

**Annex part 1: Literature review of AlN and doped AlN thin films deposition**

Substrate	Electrodes	AlN thickness ( $\mu\text{m}$ )	AlN (002) RC	$k_{\text{eff}}^2$	Q (operating frequency)	FOM ( $k_{\text{eff}}^2 \cdot Q$ )	Remarks	Reference
3C-SiC (111) on and off-axis ( $4^\circ$ )	/	$\approx 0.65$	2.58° to 3.84° (on-axis) 1.91° to 2.78° (off-axis)	/	/	/	Influence of AlN temperature deposition. Optimum at 400 °C and 450 °C for on-axis and off-axis, respectively Better results on off-axis 3C-SiC (111)	244
Si (100) / 3C-SiC (100)	Mo	1.0 to 3.0 (with a 0.05 AlN seed layer)	1.31° to 2.61°	/	/	/	Influence of sputtering power, AlN thickness, plasma etching, deposition temperature...	253
Si (100) / 3C-SiC (100)	Al	2.5 and 5.1	/	0.05 % to 0.23 %	1840 (2.5 GHz) 5510 (2.9 GHz) 526 (3.3 GHz)	0.79 to 12.7	AlN (002) orientation no characterized. Better results with 2.5 $\mu\text{m}$ thick AlN layer (and 2.6 $\mu\text{m}$ thick 3C-SiC)	510
Si (100) / SiO <sub>2</sub> / 3C-SiC (111)	Al	2.0	1.3°	/	/	/	(10-12) and (103) AlN orientations observed resulting in low performance of SAW device (acoustic velocity of 153.6 m/s <sup>-1</sup> )	282
Si (100) / 3C-SiC (100)	Al or Mo	1.0 to 2.5 (with a 0.05 AlN seed layer)	1.36° to 1.73°	0.42 %	/	/	SAW device elaborated with a 2.5 $\mu\text{m}$ thick AlN layer (and 2.6 $\mu\text{m}$ thick 3C-SiC) displaying an AlN (002) RC of 1.36°	286
Si (100) / SiO <sub>2</sub> / 3C-SiC (111)	Al	2.0	0.2° (on Si (100)) 1.3° (on 3C-SiC)	1.95 % (on Si (100)) 0.79% (on 3C-SiC)	/	/	Extremely low AlN (002) RC reported on Si (100): 0.2° without the scan (surprising) Better SAW performances without the 3C-SiC (111) seed layer	283
Si (100) / 3C-SiC (111)	/	$\approx 1.0$ (TEM cross-section)	1.3°	/	/	/	(102) and (103) AlN orientations observed	279

Table VII: Literature review of AlN deposition by reactive sputtering on 3C-SiC

Substrate	Electrodes	AlN thickness ( $\mu\text{m}$ )	AlN (002) RC	$k_{\text{eff}}^2$	Q (operating frequency)	FOM ( $k_{\text{eff}}^2 \cdot Q$ )	Remarks	Reference
6H-SiC	/	/	/	/	/	/		511
SiC	Ti and TiN	0.75	1.8° (1.7° after annealing)	$\approx 0.3$ %	$\approx 900$ to 1500 (0.285 GHz)		Device test in temperature Variation of Q with the test temperature Polytype not mentioned	288
6H-SiC	Mo	1.5	0.62°	/	/	/	Device test in temperature Variation of center frequency with the temperature	289
6H-SiC	/	0.02 to 0.6	$\approx 0.05^\circ$ to $0.42^\circ$	/	/	/	Influence of AlN thickness (optimum c-axis orientation at 0.1 $\mu\text{m}$ ) Decrease in (002) RC after 1700°C thermal annealing Investigation AlN MOCVD regrowth	290
6H-SiC	/	2.2 and 4.5	0.33° and 0.41°	/	/	/	Comparison between a pulsed ion-assisted growth and dc bias ion-assisted growth. Better results with pulsed ion-assisted growth	291
4H-SiC	/	0.19	/	/	/	/	AlN no-stoichiometric. (100) and (101) AlN contributions observed	512
6H-SiC	/	0.05 to 0.1	0.12° (after annealing)	/	/	/	/	513

Table IX: Literature review of AlN deposition by reactive sputtering on hexagonal silicon carbide

**Annex part 1: Literature review of AlN and doped AlN thin films deposition**

Doping		Substrate	Electrode	Doped AlN		$k^2_{eff}$	Q (operating frequency)	FOM ( $k^2_{eff} \cdot Q$ )	Remarks	Reference
Element	Range (% at.)			Thickness ( $\mu\text{m}$ )	(002) RC					
Ti	0 to 5.8	Si(100)/Bragg reflector	Mo	1.0	1.75° to 2.5°	≈ 1 % to 6 %	/	/	Decrease in $k^2_{eff}$ with increase in Ti content	293
		Si (100)/SiO <sub>2</sub> /Mo	Mo	1.0						294
Cr	0 to 16	Silica glass	Ti	3.0 to 5.0	2.2° to > 5°	0 % to 5.5 %	/	/	RC > 5° and decrease in $k^2_{eff}$ for Cr > 4 % at.	67
	0 to 21	Silica glass	Ti	3.0 to 5.0	1.8° to 5.5°	0 % to 5.9 %	/	/	RC < 3° for Cr ≤ 4 % at. Decrease in $k^2_{eff}$ for Cr > 4 % at.	68
	4.72	Si (100)/Mo	Mo	0.1 to 3.0	1.5° (1 $\mu\text{m}$ )	5.6 % (0.18 $\mu\text{m}$ )	/	/	Drastic increase in surface roughness from film > 0.6 $\mu\text{m}$	295
	0 to 9.1	Si (111)	/	0.6	1.3° to 3.4°	/	/	/	Decrease in RC and increase $d_{33}$ coefficient with increase in Cr content up to 6.3 % (optimum)	296
Y	1.0 to 11.6	Si (100)		0.42 to 1.45	/	/	/	/	Lower (002) orientation of Y <sub>x</sub> Al <sub>1-x</sub> N for Y = 11.6 % Increase in $d_{33}$ coefficient with increase in Y content up to 6 – 8 %	297
Ta	0 to 7.9	Si (100)		≈ 0.6	2.5° to 4.4°	/	/	/	Decrease in RC and increase $d_{33}$ coefficient with increase in Ta content up to 5.1 % (optimum)	298
	3 to 6	Si (100)/Bragg reflector/Mo		1.1	/	0 % to 6 %	/	/	Decrease in $k^2_{eff}$ with increase in Ta content Probable two crystal environments for Ta = 2.5 – 3.0 %	299
V	3 to > 7	Si (100)/Bragg reflector/Mo		1.1	/	2.5 % ( for V = 4.8 %)	/	/	Destroyed crystallinity and piezoelectricity for V > 7 % Formation of VN inclusion phase for V = 6.4 %	299
Yb	0 to 58	Si (100)		0.50 to 0.84	2.06° to 9.99°	/	/	/	Increase in RC and decrease in $d_{33}$ for Yb content ≥ 33 %	300
Er	6.23	Sapphire		≈ 1.15	/	/	/	/	Influence of substrate temperature (optimum at 200 °C)	301



**Annex part 1: Literature review of AlN and doped AlN thin films deposition**

									Increase in $d_{33}$ coefficient with increase in intensity of (002) planes	
Mg	0 to 30	Si (100)		< 1.0	1.9° to 2.5°	/	/	/	Slight enhance in $d_{33}$ between Mg a Mg content of 2.5 % to 7 % (decrease above) Relatively constant (002) RC with Mg content	303
Mg-Zr	4.0 to 34.8 (Mg + Zr)	Si (100) with Ru/Cr and Cr/Ru electrodes		0.15 and 1.1	6.0 to 6.9° (for 0.15 $\mu\text{m}$ thick)	8.5 % (for Mg + Zr = 13 % and 1.1 $\mu\text{m}$ thick)	821 (1.8 GHz)		Increase in (002) RC by with increase Mg + Zr content Increase in $d_{33}$ and $k_{\text{eff}}^2$ for Mg + Zr = 13 %	304
	0 to 35 (Mg + Zr)	Si (100) with Ru/Cr and Cr/Ru electrodes		1.1	/	8.5 % (for Mg + Zr = 13 %)	808 ( $\approx$ 1.82 GHz)	68.9	Increase in $d_{33}$ with the increase in Mg + Zr content Better with Mg + Zr (8.5 %) than pure AlN (7.1 %)	305
Mg-Hf	13 (Mg + Hf)	Si (100) with Ru/Cr and Cr/Ru electrodes		1.1	/	10.0 %	781 ( $\approx$ 1.85 GHz)	78.1	Better FOM (78.1) with Mg + Hf than Mg + Zr (68.9)	305
	0 to 13 (Mg + Hf)	Si (100) with Ru/Cr and Cr/Ru electrodes		1.1	$\approx$ 1.0° (pure AlN) $\approx$ 1.35° (MgHfAlN)	$\approx$ 7.1 % (pure AlN) to 10.0 % (MgHfAlN)	/	/	Constant (002) RC with increase in Mg + Hf content Increase in $d_{33}$ , $e_{33}$ and $k_{\text{eff}}^2$ with increase in Mg + Hf content	306
Mg-Ti	0 to 60 (Mg + Ti)	Si (100)		0.7	/	/	/	/	Decrease in $d_{33}$ when Mg or Ti used as single dopant Increase in $d_{33}$ with Mg + Ti co-doping up tp Mg + Ti $\approx$ 19 % Better results with Mg/Ti = 1.3 than Mg/Ti = 1.0	307
Mg-Nb	0.2 to 0.72 (Mg + Nb)	Si (100)		$\approx$ 0.6 – 0.7 - TEM)	/	/	/	/	Decrease in $d_{33}$ when Mg or Nb used as single dopant Increase in $d_{33}$ with Mg + Nb co-doping up tp Mg + Ti $\approx$ 60 % Better results with Mg/Nb = 1.6	308

Table X: Literature review of (co-)doped of AlN deposition by reactive sputtering (except Sc)

**Annex part 1: Literature review of AlN and doped AlN thin films deposition**

Doping range (% at.)	Substrate	Electrode	Sc doped AlN thickness ( $\mu\text{m}$ )	ScAlN (002) RC	$k^2_{\text{eff}}$	Q (operating frequency)	FOM ( $k^2_{\text{eff}} \cdot Q$ )	Remarks	Reference
0 to 72	Si (100)	Cu	0.5 to 1.1	$\approx 2^\circ$ to $8^\circ$	/	/	/	Increase in $d_{33}$ and decrease $c/a$ axial ratio with the Sc content	292
43	Si (100)	Cu	1.6	$3.25^\circ$	1.8 %	384 ( $Q_a$ ) and 170 ( $Q_r$ ) (2 GHz)	7 ( $Q_a$ ) 3 ( $Q_r$ )	Targeted Sc content of 43 % but measured at 32 %	514
36	Si and B-doped Si	Al	1.0	$1.49^\circ$ (center) $2.23^\circ$ (edge)	/	/	/	Increase in $d_{33}$ with Sc content	515
32 and 43	Si (100)	Cu	1.6	$\approx 3^\circ$	1.3 % (Sc = 32 %) 2.7 % (Sc = 43 %)	910 (Sc = 32 %) 305 (Sc = 43 %)	12 (Sc = 32 %) 8 (Sc = 43 %) (2 GHz)	Targeted Sc content of 32 % and 43 % but measured at 22 % and 32 %, respectively. Increase and decrease in $k^2_{\text{eff}}$ in Q with increase in Sc content, respectively.	516
10	Si (100)	Pt/Ti	1.0	/	7.3 %	650 (2.5 GHz)	47	$k^2_{\text{eff}}$ of 7.9 % calculated from material constants	517
15	Si	Mo	0.2 to 1.0	$< 1.6^\circ$ (1 $\mu\text{m}$ thick)	/	/	/	Increase in AOG with the ScAlN thickness	322
0 to 15	Si (100)	Mo	1.2	$1.7^\circ$ to $2.0^\circ$	5.50 % (Sc = 0 % to 12.07 % (Sc = 15 %)	348 to 739	40 to 65 (best for Sc content = 9 %)	Decrease in (002) RC and Q with increase in Sc content Increase in $k^2_{\text{eff}}$ with Sc content	16
0 to 70	Silica glass	Ti	4 - 5	$\approx 2^\circ$ to $12^\circ$	0 % to 12 % (optimum at Sc = 40 %)	/ (0.5 – 0.6 GHz)	/	Important degradation of (0002) RC and $k^2_{\text{eff}}$ above Sc content of 40 %	17
40	sapphire	/	/	/	3.7 % and 3.9 %	/	/		518
0 and 35	Si (100)	Pt/Au/Pt	0.9	/	5.8 % and 15.5 %	/ (1.9 and 2.4 GHz)	/	Decrease in $c/a$ ration and increase in $d_{33}$ and $k^2_{\text{eff}}$ with the increase in Sc content	519
20	Si	Mo and Al	1.0	$1.7^\circ$	1.8 %	/ ( $\approx 0.02$ GHz)	/	Better $k^2_{\text{eff}}$ with Sc doped AlN than pure AlN	520
/	Silica glass	Al	1.5 to 16	/	15 %	/ ( $\approx 0.25$ GHz)	/	Investigation of shear mode ( $k_{15}$ ) and temperature test. PMUT application	521
0 to 43	/	/	0.5 and 1.0	/	/	/	/	Study focus on AOG	522
43	Silica glass	Ti	43 and 90	/	18.5 % (43 $\mu\text{m}$ ) 11 %.9 % (90 $\mu\text{m}$ )	/ (0.08 GHz and 0.04 GHz)	/	PMUT application	523
43	Silica glass	Ti	43	$4.4^\circ$	5.8 % at 0.56 GHz 18.5 % at 0.08 GHz	/ (0.56 GHz)	/	PMUT application	524
0 to /	Si/Bragg reflector	Cr/Ir and Mo	1.25	/	3.14 % to 11.37 %	101.1 to 559.6 (2 – 2.5 GHz)	8.1 to 21.8	Increase and decrease in $k^2_{\text{eff}}$ and Q with increase in Sc content, respectively.	18
/	Silica glass	Al and Cu	$\approx 2.0$	/	0.9 % to 13 %	/	/	Influence of sputtering pressure	525
/	Silica glass	Al and Cu	1.8 to 6.1	/	$\approx 10$ %	/	/	Comparison between co-sputtering and single sputtering	526
/	Si (100)	/	/	$1.8^\circ$	13.2 %	992 ( $Q_a$ ) and 1126 ( $Q_r$ ) (5.7 GHz)	131 ( $Q_a$ ) 149 ( $Q_r$ )	Sc content, ScAlN thickness and electrode materials are not mentioned	326
30	Si (100)	Mo	0.5 to 2.0	$1.44^\circ$ (on Si (100)) $1.58^\circ$ (on Si (100)/Mo)	/	/	/	AlN pre-deposition before ScAlN deposition	527

**Annex part 1: Literature review of AlN and doped AlN thin films deposition**

30	SOI/AlN/SiO <sub>2</sub>	Mo	0.78	4.13°	/8	/	/	Increase in d <sub>33</sub> with ScAlN compare to pure AlN	528
15	Si (100) or sapphire	Pt	2.5 and 3.0	/	0.02 % to 3.8 %	(0.6 GHz)	/	Better results on sapphire substrate	278
/	6H-SiC	Cu	2.0	2.1°	4.5 % and 4.8 %	660 (1.6 GHz) 340 (3.75 GHz)	29 and 15	Difference in k <sup>2</sup> <sub>eff</sub> between calculation and experimental	329
26	Si (100) and B-doped Si (100)	Ti	2.0	≈ 2.2° to 5.0°	5.7 %	/	/	Influence of target power and pressure deposition	529
12	Si (100) and Si (111)	/	≈ 0.02 to 1.15	≈ 1.3° to 5.9°	/	/	/	Influence of substrate RF bias power and thickness on RC (002)	324

Table XI: Review of Sc doped of AlN deposition by reactive sputtering

## Annex part 2: Experimental conditions and theoretical models

### II.1. Characterizations methods

#### II.1.1. Raman spectroscopy

Raman spectra were collected in the backscattering geometry using a Renishaw In-Via spectrometer equipped with a Peltier cooled charge coupled device detector. The light was focused onto the sample surface using a x100 (0.85 numerical aperture) short working objective lens (0.27 mm). The resulting spot diameter was around 0.7  $\mu\text{m}$ . A 532 nm wavelength laser diode was used as light source with a typical laser power of 1 mW. Raman spectra experimental line shapes were fitted with Gaussian–Lorentzian components on WiRE software.

#### II.1.2. X-Ray Photoelectron Spectroscopy (XPS)

The XPS spectra were recorded with a PHI 5000 VersaProbe II spectrometer (Physical Electronics) using monochromatic Al  $K_{\alpha}$  radiation (1486.6 eV) and with an overall energy resolution of 0.6 eV (with silver as reference). The analysis angle was set at 45°. The experimental line shapes were fitted with Gaussian–Lorentzian (G-L (70-30)) components on CasaXPS software.

#### II.1.3. Atomic Force Microscopy (AFM)

The 1  $\mu\text{m}^2$  scan showing the evolution of the surface morphology were recorded by TappingMode Atomic Force Microscopy (AFM) with a Bruker Dimension FastScan equipment using Bruker FASTCAN-A tip. After acquisition, AFM data were treated using a line-by-line flattening using Bruker Nanoscope Analysis software. When necessary, the particles contributions was annihilated by an image processing using Gwyddion v2.59 software.

#### II.1.4. X-Ray Diffraction (XRD) and X-Ray Reflectometry (XRR)

The structural properties have been characterized using X-Ray Diffraction (XRD) and X-Ray Reflectometry (XRR) giving each complementary information. The angles definition for the diffraction geometry (symmetric scan) and the out-of-plane and in-plane measurements are presented in Figure I (Annex part 2) a) and b), respectively.

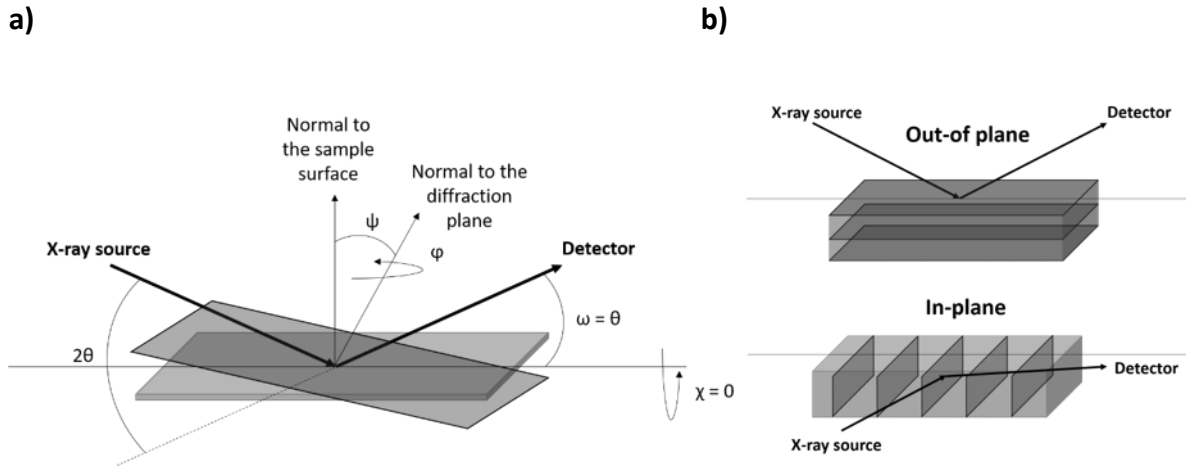


Figure I (Annex part 2): a) Diffraction geometry and angles definition ; b) Out-of-plane and in-plane geometry measurement

#### II.1.4.1. In-plane and out-of-plane measurements

Out-of-plane measurements (Rocking curve,  $2\theta/\theta$  scans and XRR) have been performed using Panalytical® Xpert 4 circles goniometer equipped with a Cu anode ( $\lambda = 1.5406 \text{ \AA}$ ) as source. The beam is monochromatized and collimated with a multilayer curved mirror and a parallel plate collimator is mounted in the diffracted beam path.

In-plane measurements and pole figure were performed on a Rigaku, SmartLab diffractometer equipped with Cu  $K_{\alpha}$  radiation ( $\lambda = 1.5418 \text{ \AA}$ ). The copper anode was operated at 30 kV and 15 mA.

#### II.1.4.2. Stress/strain analysis: Crystallite Group Method (CGM)

Stress/strain analysis by X-Ray Diffraction (XRD) is based on the measurement of the variation of interreticular distances  $\Delta d_{hkl}$  of a family of crystal planes<sup>530,531</sup>. When a material is exposed to stress, the interreticular distances vary which leads to a shift  $\Delta 2\theta_{hkl}$  in the diffraction peak (Bragg's law). This strain in interreticular distances varies with  $\psi$  angle (angle between the normal of the sample surface and the normal of considered  $d_{hkl}$  crystal planes). The measurement geometry is presented in Figure II (Annex part 2). Based on continuum mechanics equations of isotropic and homogeneous media, strain and stress are related by an equation defined by the law of  $\sin^2 \psi$ :

$$\varepsilon_{\varphi\psi} = \frac{1}{2} S_2^{hkl} \sigma_{\varphi} \sin^2 \psi + S_1^{hkl} (\sigma_{11} + \sigma_{22}) \quad \text{Equation 1}$$

Where  $\varepsilon_{\varphi\psi}$  is the strain,  $S_i^{hkl}$  are elastic compliances and  $\sigma_{ij}$  is the stress tensor components.

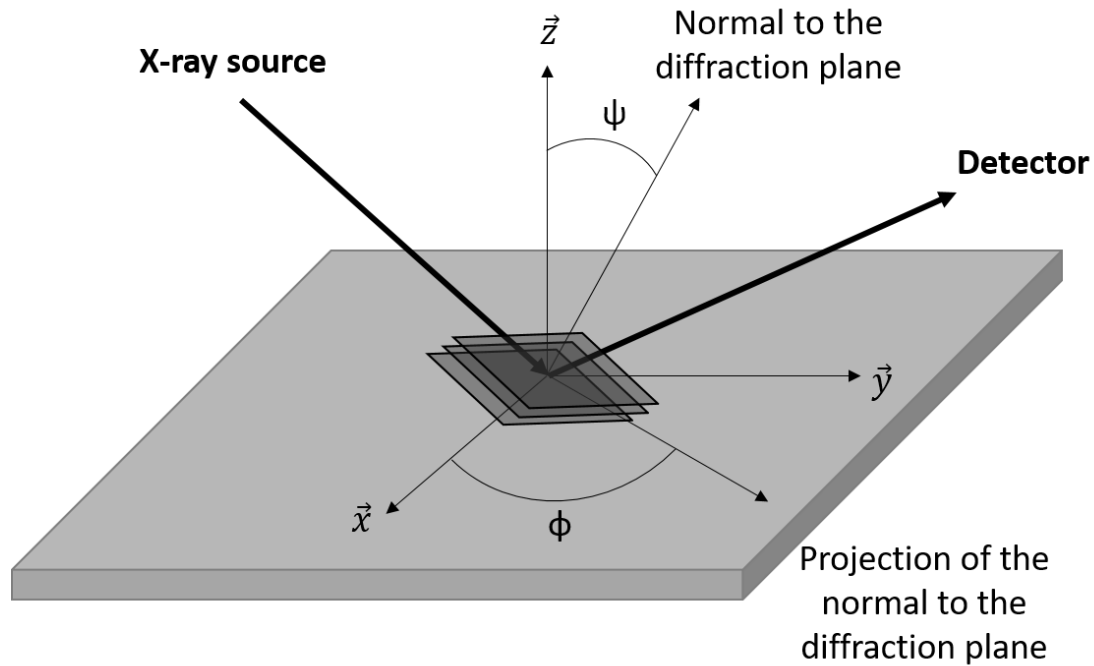


Figure II (Annex part 2): Geometry of  $\sin^2 \psi$  method and angles definition

This  $\sin^2 \psi$  method is focalised on a unique family of crystal planes and its equation relates linearly strain and  $\sin^2 \psi$ . The slope determination enables to calculate the stress  $\sigma_\phi$ . However, this method is valid only with the following assumptions<sup>532</sup>:

- The stress state is assumed to be biaxial ( $\sigma_{33} = 0$ )
- The polycrystalline material is homogeneous (no composition gradient) and isotropic (no pronounced preferential orientation)
- The macroscopic state of stresses and strains is homogeneous in the irradiated volume (no gradient)
- The strains and stresses are elastics in nature (plastic nature does not lead to a displacement  $\Delta 2\vartheta_{hkl}$  of the diffraction peak but to a broadening)

As shown previously, AlN PVD deposited on 2D-MoS<sub>2</sub> seed layer exhibits a c-axis preferential orientation. Thus,  $\sin^2 \psi$  method is not adapted since the linear relation between  $\epsilon_{\phi\psi}$  and  $\sin^2 \psi$  is not respected anymore<sup>533,534</sup>. In fact, a textured film leads to a so-called “snake” curve.

In 2004, Murali et al.<sup>261</sup> propose another stress measurement method to explain the discrepancy between the theoretical lattice values and their measurements. In particular, they assumed that the observed deviations from theoretical constants result mainly from the

residual stress within the AlN layer excluding for instance impurities effects or stoichiometry variation. Hence, the strain perpendicular to the film surface could be determined by the shift  $\Delta 2\theta_{hkl}$  of the AlN (002) peak from its theoretical position ( $d_{002} = 2,49 \text{ \AA}$ ). However, with this method, the assumptions considered seem strong and assume that

AlN is strictly stoichiometric as well as, for an unstressed thin film, the  $d_{002}$  inter-planar distance is identical to that of the bulk ( $d_{002} = 2,49 \text{ \AA}$ ).

In this work, the AlN biaxial stress was determined with another analysis method called “Crystallit Group Method” (CGM). It is based on the following two assumptions: the stress state of the film is equi-biaxial, the crystal is very small where each crystal has a random orientation around the c-axis with  $2\pi$  rotational freedom. With these assumptions, the perpendicular lattice strain  $\varepsilon_{33}$  can be written as:

$$\varepsilon_{33} = ((S_{11} + S_{12} - 2S_{13})\sin^2\psi + 2S_{13})\sigma \quad \text{Equation 2}$$

where  $S_{ij}$  are the AlN elastic compliances ( $S_{11} = 3.1 \times 10^{-12} \text{ Pa}^{-1}$ ;  $S_{12} = -0.9 \times 10^{-12} \text{ Pa}^{-1}$  and  $S_{13} = -0.6 \times 10^{-12} \text{ Pa}^{-1}$  from materialsprojects.org website where calculations are based on Jong et al. study<sup>535</sup>,  $\psi$  is the angle between the normal of the diffracting plane and the surface normal and  $\sigma$  is the equi-biaxial stress. The studied planes are (002), (004), (101), (102), (112) and (203).

Contrary to Murali study<sup>261</sup>, we did not assume that an unstressed AlN film as an identical  $d_{002}$  interreticular distances. This assumption logically leads to slight variation in lattice constants compared its bulk counterpart. Thus, the a-axis lattice constant for an unstressed AlN film has been corrected as follows: from the  $2\theta$  position of each (hkl) planes measured, inter-plane  $d_{hkl}$  distance has been extracted and a-axis lattice has been calculated using the following equation:

$$d_{hkl} = \frac{a}{\left\{ (h^2 + k^2 + hk) \frac{4}{3} + l^2 \frac{a^2}{c^2} \right\}^{1/2}} \quad \text{Equation 3}$$

Then, the calculated a-axis as a function of  $\sin^2 \psi$  is plotted in Figure 3 (Annex part 2) a).

According to Equation 2, the stress (and therefore the strain) is null when:

$$\begin{aligned} \varepsilon_{33} &= ((S_{11} + S_{12} - 2S_{13})\sin^2\psi_0 + 2S_{13})\sigma = 0 \\ \Leftrightarrow (S_{11} + S_{12} - 2S_{13})\sin^2\psi_0 + 2S_{13} &= 0 \end{aligned}$$

$$\Leftrightarrow \sin^2 \psi_0 = \frac{-2S_{13}}{(S_{11}+S_{12}-2S_{13})} \approx 0,3529 \quad \text{Equation 4}$$

Thus, according to the linear regression of Figure 3 (Annex part 2) a), a-axis is free of strain when its value is  $a_0 = 0.00792 \sin^2 \psi_0 + 3.11269 \approx 3.115 \text{ \AA}$ . Therefore, the strain is not calculated anymore from the a-axis theoretical value (3.110 Å) but from the corrected value (3.115 Å) and is illustrated as a function of  $\sin^2 \psi$  in Figure 3 (Annex part 2) b). Moreover, Equation 4 enables to add a supplementary point on this figure corresponding to a free of strain/stress state in AlN PVD film.

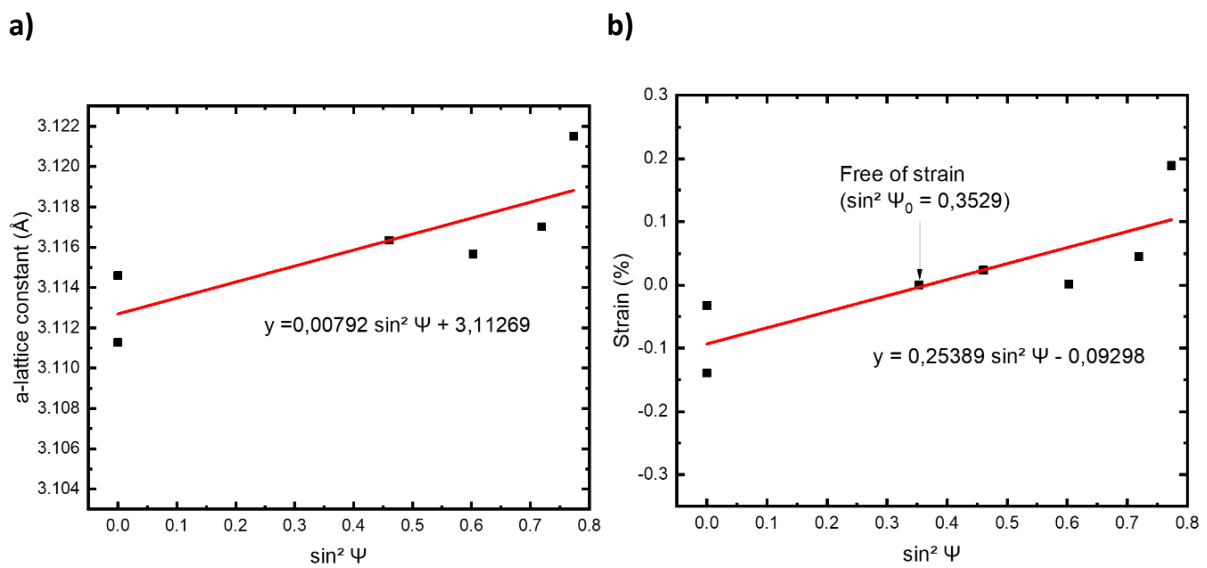


Figure III (Annex part 2): a) a-lattice parameter ; b) strain as a function of  $\sin^2 \psi$  for a 100 nm AlN PVD deposition grown on Si (100)/SiO<sub>2</sub> (500 nm)/ MoS<sub>2</sub> (3 monolayers).

In addition, the CGM method also enable to determine the AlN in-plane and out-of-plane strain. In fact, according to Figure II (Annex part 2), when  $\psi = 0^\circ$  (and therefore  $\sin^2 \psi = 0^\circ$ ), the X-Ray beam is normal to the sample surface. Hence, we only focus on the out-of plane strain. Similarly, when  $\psi = 90^\circ$  (and therefore  $\sin^2 \psi = 1$ ), the X-Ray beam is parallel to the sample surface. Hence, we focus on the in-plane strain. Therefore, from the linear regression presented in Figure 3 (Annex part 2) and by fixing  $\sin^2 \psi = 0$  or 1, we can estimate the out-of plane and in-plane strain denoted as  $\epsilon_{out}$  and  $\epsilon_{in}$ , respectively.

#### II.1.4.3. Pole figure

Pole figure measurement is a classical measurement to determine the texture of a film. Figure IV (Annex part 2) presents the measurement geometry of this XRD measurement. It is a based on two rotations ( $\varphi$  and  $\chi$ ) on a  $d_{hkl}$  family of crystal planes whose the stereographic projection gives a distribution of the intensity in every direction of the sample. For each



position  $(\varphi, \chi)$ , the measured intensity is proportional to the volume of crystallites presenting their normal hkl in this direction.

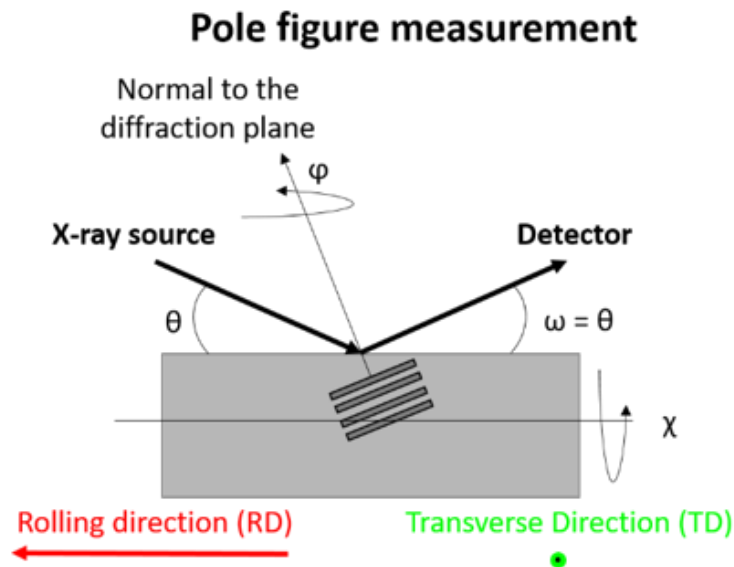


Figure IV (Annex part 2): Geometry of a pole figure measurement

#### II.1.5. Transmission Electron Microscopy and Energy Dispersive X-Ray (TEM/EDX)

The sample was prepared by  $\text{Ga}^+$  Focused Ion Beam (FIB) milling. The thin foil was observed in STEM mode at 200 kV using a convergence semi-angle of  $\approx 18$  mrad for the incident electron probe in a probe-corrected ThermoFisher Titan Themis microscope equipped with the Super-X detector system for Energy Dispersive X-ray (EDX) spectrometry. EDX hypermaps were acquired with a pixel size of 50 pm, a pixel dwell time of 18  $\mu\text{s}$  and a total acquisition time of  $\approx 4$  min. Hypermaps were processed in the Bruker Esprit v2.2 software using standard TEM recipes for background subtraction and Gaussian peak deconvolution. STEM HAADF images were acquired with a camera length of 86 mm corresponds to inner and outer collection angles of the HAADF detector (Fischione Model M3000) of  $\approx 78$  and 230 mrad. Gun lens and spot size values were selected to provide a probe current of approximately 20 pA. We paid attention to verify that there was no electron beam induced damage by comparing STEM images before and after each STEM/EDX acquisition.

#### II.1.6. Scanning Electron Microscopy (SEM)

Scanning Electron Microscopy (SEM) images were recorded on HITACHI S5500 microscope with a voltage of 3 kV.

### II.1.7. Automatic Crystal and Orientation Mapping (ACOM)

ACOM is an automatic crystallographic indexing and orientation phase mapping tool developed at SIMaP laboratory and which can be adapted to any Transmission Electronic Microscope. We can refer to Rauch et al.<sup>438</sup> study to obtain a detailed explanation of the technique. The principle is the mapping of phases and orientations of a zone of interest by an electron beam (in precession mode or not). The spot is around 1 to 2 nm in diameter and it is then moved along the area of interest with a fixed pitch (minimum pitch 2 nm). At each point, a diffraction pattern is recorded enables to identify the phases on crystalline orientations. Then, theoretical diffraction patterns, called templates, are compared to these acquired patterns to perform a phase and orientation identification. The matching index between these patterns enable to reduce this identification to an image, called index mapping, similar to a human fingerprint indexing. This strategy always ends with a solution but its validity can be questionable, especially for overlapping grains. Therefore, a new parameter is introduced to address this problem: reliability. It is a ratio of the matching indexes of the two best solutions and it indicates how safe the indexing is. It is a value ranges between 0 (unsafe) and 100 (a unique solution). Typically, a value above 15 is sufficient to valid the matching. Hence, it is primordial to consider these two parameters (index and reliability) to obtain consistent results. The thickness of the observed zone must therefore be compatible with the size of the grains.

### II.2. Theory of Beuth model

A crack can propagate according to three modes of propagation: opening mode (I), sliding mode (II) and tearing mode (III) as illustrated in Figure V (Annex part 2). Opening mode (I) occurs due a tensile stress normal to the plane of the crack which is a common rupture mechanism. Sliding mode (II) corresponds to shearing of the crack due to in-plane shear stresses which influences the crack growth direction. Tearing mode (III) is infrequent and is a shear stresses parallel to the plane of the crack.

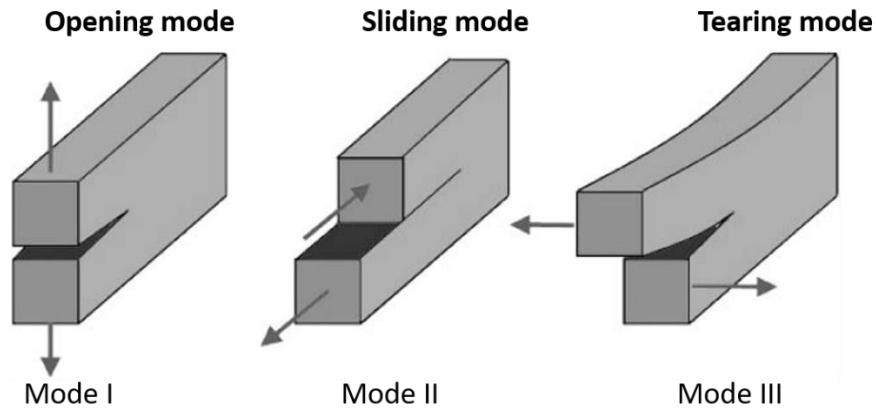


Figure V (Annex part 2): Three modes of fracture in a cracked body<sup>536</sup>

The fracture energy of the AlN PVD film failure can be determined from the spontaneous cracking of AlN film due to its internal stresses. This calculation is based on Beuth model<sup>537</sup>. This model describes the formation of a crack perpendicularly to the film surface (i.e. at the normal direction of the substrate) considering elastic mismatches between layers as depicted in Figure VI (Annex part 2). It is assumed that the crack propagates in opening mode (I) which naturally receives the most attention in research since it is the most critical. This model also uses the following assumptions: first, the ruin of the film is due to its cracking which leads to a spalling of the film and second, the film is fully cracked in its thickness (crack tip touching the film/substrate interface). It implies that the release energy from the interface debonding (delamination) is negligible compared to the elastic energy released during its transverse cracking.

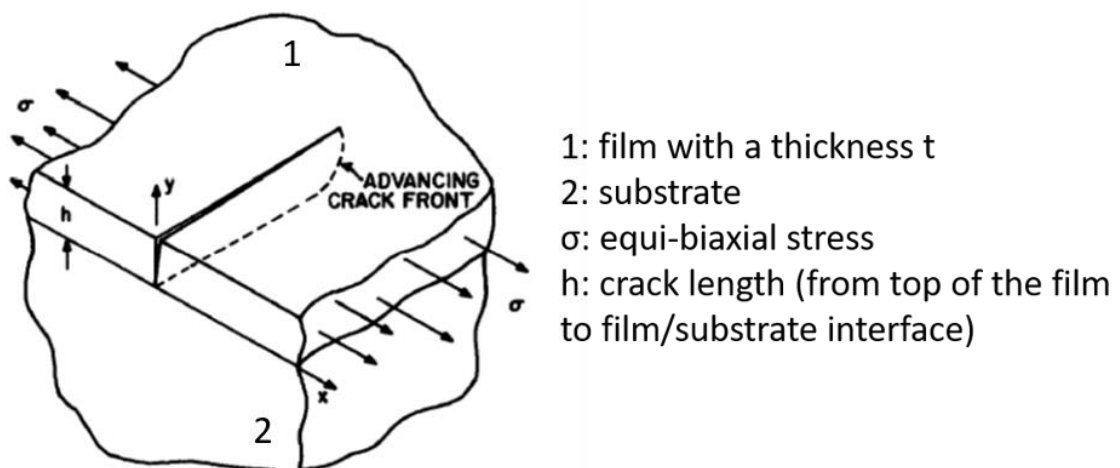


Figure VI (Annex part 2): Illustration of Beuth model for a fully cracked film

Beuth model has been substantially simplified thanks to the research work of Dundurs<sup>538</sup>. In the case of a composite body made of two isotropic and elastic materials (1 and 2) with

prescribed tractions (the interface between material 1 and material 2 is abrupt, smooth and adherent), the mismatch dependence of the elastic constants can be described with two parameters  $\alpha$  and  $\beta$  which depend of Young's moduli  $E_i$ , Poisson ratios  $\nu_i$  and shear modulus  $\mu_i$ , as follows:

$$\alpha = \frac{E_1^* - E_2^*}{E_1^* + E_2^*} \text{ and } \beta = \frac{\mu_1(1-2\nu_2) - \mu_2(1-2\nu_1)}{2\mu_1(1-2\nu_2) + 2\mu_2(1-\nu_1)} \quad \text{Equation 5}$$

$$\text{With } E_i^* = \frac{E_i}{(1-\nu_i^2)} \quad \text{Equation 6}$$

$$\text{and for isotropic materials, } \mu_i = \frac{E_i}{2(1+\nu_i)} \quad \text{Equation 7}$$

Where,  $E_i^* = E_i$  for plane stress is Young's modulus (Pa),  $\mu_i$  is the shear modulus (Pa) and  $\nu_i$  the Poisson's ratio.

In this work, the assumption to have an adherent interface between material 1 and 2 is questionable. In fact, as previously demonstrated, if we assume that material 1 is assimilated to AlN + 2D-MoS<sub>2</sub> and material 2 is SiO<sub>2</sub> substrate, the adherence between both materials is weak. Therefore, the determined elastic energy released from AlN failure should be overestimated. We also have to keep in mind that Beuth model determines the elastic energy release from the failure of the film and not the energy due to the interface debonding (delamination), which is negligible and a consequence of the failure.

Suga et al.<sup>539</sup> shows that for most practical material combinations,  $\beta$  typically lies between 0 and  $\alpha/4$  and is, in most cases, typically insignificant compared to  $\alpha$  value. Thus, Beuth model leads to the following equation to express the steady-state energy release rate for a through-thickness channelling crack induced by equi-biaxial stress:

$$G = \frac{\pi}{2} g(\alpha, \beta) \frac{\sigma_f^2 t_f}{E_f^*} \quad \text{Equation 8}$$

Where,  $G$  is the energy release rate (J.m<sup>-2</sup>),  $\sigma_f$  the equi-biaxial stress in the film (Pa),  $t_f$  the film thickness (m),  $E_f^*$  the plane strain tensile modulus of the film (Pa) and  $\alpha$  and  $\beta$  are the Dundurs coefficients where  $g(\alpha, \beta)$  are tabulated values.

For a crack propagation in opening mode (I), this energy release rate  $G$  is related to the toughness  $K_I$  which is a most common parameter used in the literature. The equation related  $G$  and  $K_I$  is:

$$G = \frac{K_I^2}{E_i^*} \quad \text{Equation 9}$$

Where,  $G$  is the energy release rate ( $J.m^{-2}$ ),  $E_i^*$  is calculated from Equation 6 and  $K_I$  is the toughness ( $Pa.m^{-1/2}$ )

Therefore, it is possible to consider that when the film failure occurs at a critical thickness, the energy release rate  $G$  is equal to the critical energy for its failure, which induces the delamination.

### II.3. Wagner's theory

In chapter 4 section IV.2.4.2.1, we demonstrate that the conversion of  $MoS_2$  into  $MoN_x$  through the AlN seed layer is limited by the diffusion of N species in AlN. The resulting parabolic kinetic law is based on Wagner's theory <sup>433</sup>.

Wagner's theory applies to the growth of compact and adherent oxides ( $> 1 \mu m$ ) and demonstrates a parabolic growth kinetic. This model assumes that the limiting process of oxidation mechanisms is the diffusion through the oxide layer. Hence, the flux of particles is proportional to the partial pressure gradient in oxygen (assuming that we are in a quasi-stationary regime). As this model is applied to thick oxide layer, it seems difficult to apply this model to thin oxide. However, Wagner's theory has been applied to many materials enabling to understand and predict the kinetic oxidation of wide range of metal (change in oxidation temperature, different composition of the oxide...) <sup>540</sup>.

### II.4. Fick's laws

In chapter 4 section IV.2.4.2.1, we use a model based on Fick's laws to determine the diffusion coefficient of N in AlN. Here, we propose to briefly address these laws leading to the equation ... presented in 4 section IV.2.4.2.1. Fick's laws have been developed by Adolf Fick and propose to describe diffusion phenomena <sup>541</sup>. To simplify this section, we consider a one dimensional system. He considers that, the flux of particles (atoms, molecules, ions...) caused by a concentration gradient can be expressed as:

$$J = -D \frac{\partial C}{\partial x} \quad \text{Equation 10}$$

Where  $J$  is the flux ( $mol.m^{-2}.s$ ),  $D$  is the diffusion coefficient ( $m^2.s^{-1}$ ) and  $C$  is the concentration of the particles ( $mol.m^{-3}$ ).

## ***Annex part 2: Experimental conditions and theoretical models***

This first equation is denoted as first Fick' laws. It shows that the flux of particles in space is proportional to the concentration gradient. However, in most cases, the concentration at a particular position changes with time. Hence, Fick has developed a second law based on the first one and the consideration of mass conversation. This law is written as:

$$\frac{\partial C(x,t)}{\partial t} = D \frac{\partial^2 C(x,t)}{\partial x^2} \quad \text{Equation 11}$$

Solving this partial differential equation denoted as second Fick's law and assuming that a material B is deposited on a surface of a material A and diffuses in only one direction, we can write:

$$C_B(x, t) = \frac{M_B}{\sqrt{\pi D_B t}} e^{-\frac{x^2}{4D_B t}} \quad \text{Equation 12}$$

*Where  $M_B$  is the total amount of material B,  $D_B$  is the diffusion coefficient,  $t$  is the time and  $C_B$  is the concentration of B material at the position  $x$ .*

This equation enables to describe the concentration profile  $C_B$  of the material along the direction  $x$  at any time  $t$  (and at a particular temperature). It is the equation used to determine the diffusion coefficient of N in AlN in chapter 4 section IV.2.4.2.1.



## Annex part 3: Complementary results

## III.1. X-Ray Reflectometry (XRR)

III.1.1. Comparison of MoS<sub>2</sub> XRR pattern fitting with two software

In chapter 3 section III.1.3.1.2, a MoS<sub>2</sub> XRR pattern is presented and fitted in J VXRR software with a model detailing each MoS<sub>2</sub> atomic and VdW planes. To valid this model, it has also been used and fitted with another software: X'Pert Reflectivity. The resulting densities, thicknesses and roughness determined with these two softwares are compared in Table I below.

Formula	Fitt with J VXRR software			Fitt with X'pert Reflectivity software		
	Density (g.cm <sup>-3</sup> )	Thickness (nm)	Roughness (nm)	Density (g.cm <sup>-3</sup> )	Thickness (nm)	Roughness (nm)
<b>MoS<sub>2</sub> monolayer</b>	7.21	0.61	0.38	6.30	0.69	0.53
<b>VdW plan</b>	0.09	0.19	0.19	0.21	0.18	0.17
<b>MoS<sub>2</sub> monolayer</b>	6.00	0.31	0.17	6.30	0.29	0.19
<b>VdW plan</b>	0.09	0.12	0.14	0.19	0.13	0.13
<b>MoS<sub>2</sub> monolayer</b>	6.99	0.56	0.35	6.30	0.48	0.34
<b>VdW plan</b>	0.09	0.27	0.24	0.22	0.16	0.20
<b>SiO<sub>2</sub></b>	2.29	/	0.08	2.30	/	0.23

Table I (Annex part 3): Comparison of the extracted values from the MoS<sub>2</sub> XRR pattern fitting with J VXRR and X'Pert Reflectivity software

In both software, the determined thicknesses, densities and roughness of each layer are relatively similar. Hence, it strongly suggests that the model developed in this work enable to properly describe the structural properties of the 2D-MoS<sub>2</sub> layer.

## III.1.2. Correspondence between AlN deposition time and thickness

In this work thesis, MoS<sub>2</sub> + AlN *x*s samples with *x* being the AlN deposition time in second (s) are elaborated and used to describe the thickness of the AlN seed layer. The correspondence between the AlN deposition time (s) and the thickness (nm) has been addressed by XRR. The results are depicted in Figure 1 (Annex part 3). A linear regression enables to determine an AlN deposition rate of 0.57 nm.s<sup>-1</sup> which is coherent with what we could expect in the investigated AlN PVD deposition.



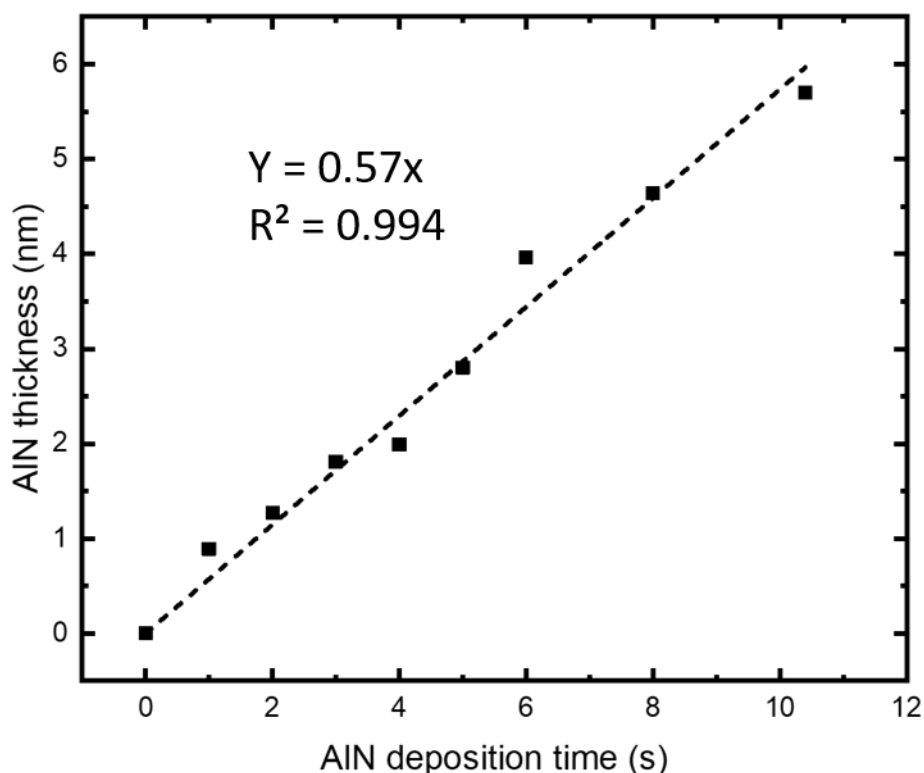


Figure 1 (Annex part 3): Correspondence between AlN deposition time (s) and AlN thickness (nm) determined by XRR

## III.2. X-Ray Photoelectron Spectroscopy (XPS)

### III.2.1. SiO<sub>2</sub>/MoS<sub>2</sub> stack and delaminated area

In chapter 3 section III.1.3.2, XPS is used to determine the surface chemical composition of the 2D-MoS<sub>2</sub> layer. In the same chapter section III.3.1.2, XPS have confirmed that the delamination occurs at the MoS<sub>2</sub>/SiO<sub>2</sub> interface. The overall atomic concentrations, binding energy position and their attribution of the 2D-MoS<sub>2</sub> and the delaminated area obtained by XPS are presented in Table II below.

Name	MoS <sub>2</sub> reference		Delaminated area		
	Binding Energy (eV)	% Conc.	Binding Energy (eV)	% Conc.	Attribution
C 1s	284.8	17.0	284.8	3.5	C-C / C-H
C 1s	286.2	5.6	286.4	2.3	C-O / C-N
C 1s	/	/	288.2	0.4	O=C=O
		<b>22.6</b>		<b>6.3</b>	
S 2p 3/2	162.5	15.7	/	/	MoS <sub>2</sub>
S 2p 1/2	163.7	7.9	/	/	MoS <sub>2</sub>
		<b>23.6</b>			
O 1s	531.2	6.8	531.2	3.9	MoO <sub>x</sub> /MoO <sub>3</sub>
O 1s	533.2	20.2	532.6	61.1	C-O/SiO <sub>x</sub> /SiO <sub>2</sub>
		<b>27.0</b>		<b>65.0</b>	
Si 2p 3/2	103.7	7.1	103.1	18.0	SiO <sub>x</sub> /SiO <sub>2</sub>
Si 2p 1/2	104.4	3.5	103.7	9.0	SiO <sub>x</sub> /SiO <sub>2</sub>
		<b>10.6</b>		<b>27.0</b>	
Mo 3d 5/2	229.8	8.1	/	/	MoS <sub>2</sub>
Mo 3d 3/2	232.8	5.4	/	/	MoS <sub>2</sub>
Mo 3d 5/2	233.4	1.6	232.3	0.6	MoO <sub>x</sub> /MoO <sub>3</sub>
Mo 3d 3/2	236.5	1.1	235.4	0.4	MoO <sub>x</sub> /MoO <sub>3</sub>
		<b>16.2</b>		<b>1.0</b>	
Total		<b>100.0</b>		<b>100.0</b>	
[S]/[Mo]		1.7		/	
[O]/[Mo]		2.6		3.9	
[O]/[Si]		1.9		2.3	
Mo 3d 5/2 - S 2p 3/2	67.2		/		

Table II (Annex part 3): Binding energies positions and atomic concentrations (at.%) of the different chemical environments identified by XPS at the surface of of Si (100)/SiO<sub>2</sub>(500 nm)/MoS<sub>2</sub>(3 monolayers) stack and of the delaminated area

### III.2.2. MoS<sub>2</sub> Reference and MoS<sub>2</sub> + AlN xs BP (Before Plasma) and AP (After Plasma)

In chapter 4 section IV.1.3.2.2, MoS<sub>2</sub> Reference and MoS<sub>2</sub> + AlN xs sample have been characterized by XPS before (BP) and after (AP) a N<sub>2</sub> plasma. The overall atomic concentrations and binding energies of each sample are presented in Table III and Table IV below.

Before N <sub>2</sub> plasma treatment (BP)															
	MoS <sub>2</sub> + Reference BP		MoS <sub>2</sub> + AlN 1s BP		MoS <sub>2</sub> + AlN 3s BP		MoS <sub>2</sub> + AlN 3s BP		MoS <sub>2</sub> + AlN 4s BP		MoS <sub>2</sub> + AlN 6s BP		MoS <sub>2</sub> + AlN 8s BP		
Name	B.E (eV)	% Conc.	B.E (eV)	% Conc.	B.E (eV)	% Conc.	B.E (eV)	% Conc.	B.E (eV)	% Conc.	B.E (eV)	% Conc.	B.E (eV)	% Conc.	Attribution
C 1s	284.8	17.0	284.8	23.1	284.8	15.1	284.8	18.2	284.8	12.0	284.8	13.3	284.8	13.4	C-C / C-H
C 1s	286.2	5.6	286.4	3.6	286.4	3.5	286.7	2.3	286.5	2.6	286.2	2.7	286.5	2.4	C-O / C-N
C 1s	/	/	288.9	3.5	288.8	3.1	289.0	3.4	289.2	2.8	288.9	2.0	289.1	2.2	O-C=O
		<b>22.6</b>		<b>30.2</b>		<b>21.7</b>		<b>23.9</b>		<b>17.3</b>		<b>18.0</b>		<b>18.0</b>	
N 1s	/	/	396.4	3.3	396.0	6.3	396.1	8.4	396.4	20.3	396.8	21.4	396.8	20.6	MoN <sub>x</sub> /AlN
				<b>3.3</b>				<b>8.4</b>		<b>20.3</b>		<b>21.4</b>		<b>20.6</b>	
S 2p 3/2	162.5	15.7	160.9	5.4	160.9	4.2	160.9	2.5	161.0	2.8	161.3	1.5	161.0	0.9	MoS <sub>2</sub>
S 2p 1/2	163.7	7.9	162.1	2.7	162.0	2.1	162.1	1.2	162.2	1.6	162.5	0.8	162.2	0.4	MoS <sub>2</sub>
		<b>23.6</b>		<b>8.1</b>		<b>6.3</b>		<b>3.7</b>		<b>4.4</b>		<b>2.3</b>		<b>1.3</b>	
O 1s	531.2	6.8	530.7	14.3	530.7	17.6	530.6	11.1	530.7	8.5	530.8	5.7	530.8	5.9	MoO <sub>3</sub> /Al <sub>2</sub> O <sub>3</sub>
O 1s	533.2	20.2	832.0	23.1	532.1	23.0	532.1	29.0	532.1	16.5	532.1	20.9	532.1	22.6	AlO <sub>x</sub> /SiO <sub>x</sub>
		<b>27.0</b>		<b>37.5</b>		<b>40.6</b>		<b>40.0</b>		<b>25.0</b>		<b>26.6</b>		<b>28.5</b>	
Si 2p 3/2	103.7	7.1	102.3	3.2	102.3	2.7	102.4	2.5	102.5	1.6	102.7	1.2	101.9	0.7	SiO <sub>x</sub>
Si 2p 1/2	104.4	3.5	102.9	1.6	102.9	1.3	103.0	1.2	103.1	0.8	103.3	0.6	102.5	0.3	SiO <sub>x</sub>
		<b>10.6</b>		<b>4.8</b>		<b>4.0</b>		<b>3.7</b>		<b>2.5</b>		<b>1.8</b>		<b>1.0</b>	
Al 2p 3/2	/	/	73.4	2.8	73.0	3.6	72.9	5.7	73.1	12.5	74.0	14.5	73.6	17.3	AlN
Al 2p 1/2	/	/	73.8	1.4	73.3	1.8	73.3	2.9	73.5	6.2	74.4	7.2	74.0	8.6	AlN
Al 2p 3/2	/	/	74.5	3.8	74.1	7.2	74.1	5.6	74.0	5.8	74.8	4.5	74.6	2.6	Al <sub>2</sub> O <sub>3</sub> /AlO <sub>x</sub>
Al 2p 1/2	/	/	74.8	1.9	74.5	3.6	74.5	2.8	74.4	2.9	75.2	2.2	75.0	1.3	Al <sub>2</sub> O <sub>3</sub> /AlO <sub>x</sub>
		<b>/</b>		<b>9.9</b>		<b>16.2</b>		<b>17.0</b>		<b>27.4</b>		<b>28.4</b>		<b>29.8</b>	
Mo 3d 5/2	229.8	8.1	228.2	3.2	228.1	2.5	228.1	1.5	228.2	1.7	228.5	0.8	228.2	0.4	MoS <sub>2</sub>
Mo 3d 3/2	232.8	5.4	231.3	2.2	231.2	1.7	231.1	1.0	231.2	1.1	231.6	0.5	231.3	0.3	MoS <sub>2</sub>
Mo 3d 5/2	233.4	1.6	232.2	0.5	232.1	0.4	232.0	0.1	232.2	0.2	232.6	0.1	232.4	0.1	MoO <sub>3</sub>
Mo 3d 3/2	236.5	1.1	235.3	0.3	235.1	0.2	235.0	0.1	235.1	0.1	235.7	0.1	235.5	0.0	MoO <sub>3</sub>
		<b>16.2</b>		<b>6.2</b>		<b>4.8</b>		<b>2.7</b>		<b>3.2</b>		<b>1.5</b>		<b>0.8</b>	
<b>Total</b>		<b>100.0</b>		<b>100.0</b>		<b>100.0</b>		<b>100.0</b>		<b>100.0</b>		<b>100.0</b>		<b>100.0</b>	
[S]/[Mo]		1.7		1.5		1.5		1.5		1.7		1.6		1.9	
[N]/[Al]		/		0.8		1.2		1.0		1.1		1.0		0.8	
[AlO <sub>x</sub> ]/[Al]		/		0.6		0.7		0.5		0.3		0.2		0.1	
Mo 3d 5/2 - S 2p 3/2		67.2		67.2		67.2		67.1		67.2		67.3		67.2	

Table III (Annex part 3): Binding energies positions and atomic concentrations (at.%) of the different chemical environments identified by XPS at the surface of MoS<sub>2</sub> Reference and MoS<sub>2</sub> + AlN xs samples before N<sub>2</sub> plasma treatment

After N <sub>2</sub> plasma treatment															
	MoS <sub>2</sub> + Reference AP		MoS <sub>2</sub> + AlN 1s AP		MoS <sub>2</sub> + AlN 3s AP		MoS <sub>2</sub> + AlN 3s AP		MoS <sub>2</sub> + AlN 4s AP		MoS <sub>2</sub> + AlN 6s AP		MoS <sub>2</sub> + AlN 8s AP		
Name	B.E (eV)	% Conc.	B.E (eV)	% Conc.	B.E (eV)	% Conc.	B.E (eV)	% Conc.	B.E (eV)	% Conc.	B.E (eV)	% Conc.	B.E (eV)	% Conc.	Attribution
<b>C 1s</b>	284.8	16.4	284.8	16.6	284.8	15.8	284.8	13.5	284.8	12.3	284.8	14.8	284.8	12.7	C-C / C-H
<b>C 1s</b>	286.5	3.8	286.4	3.2	286.5	2.8	286.6	2.2	286.4	2.8	286.5	2.4	286.7	1.8	C-O / C-N
<b>C 1s</b>	288.7	2.8	288.9	2.5	288.9	2.6	289.0	1.8	289.0	1.5	289.0	2.4	289.1	1.7	O-C=O
		<b>22.9</b>		<b>22.3</b>		<b>21.2</b>		<b>17.6</b>		<b>16.6</b>		<b>19.6</b>		<b>16.3</b>	
<b>F 1s</b>	/	/	685.6	3.5	685.5	5.2	/	/	/	/	/	/	/	/	Conta F
				<b>3.5</b>		<b>5.2</b>		<b>/</b>		<b>/</b>		<b>/</b>		<b>/</b>	
<b>N 1s</b>	397.7	3.1	397.0	13.2	396.7	13.5	397.4	0.5	396.8	4.5	396.4	16.7	396.8	4.9	MoN <sub>x</sub> /AlN
<b>N 1s</b>	/	/	/	/	402.5	0.8	/	/	401.8	/	402.7	0.6	/	/	NO <sub>x</sub>
		<b>3.1</b>				<b>14.3</b>		<b>0.5</b>		<b>4.5</b>		<b>17.2</b>		<b>4.9</b>	
<b>S 2p 3/2</b>	/	/	161.5	1.2	161.3	1.9	162.1	0.5	161.8	1.3	161.1	1.6	161.8	0.4	MoN <sub>x</sub> /MoS <sub>2</sub>
<b>S 2p 1/2</b>	/	/	162.7	0.6	162.5	0.9	163.3	0.3	163.0	0.7	162.3	0.8	163.0	0.2	MoN <sub>x</sub> /MoS <sub>2</sub>
<b>S 2p 3/2</b>	168.8	0.2	/	/	/	/	169.1	3.7	169.1	3.0	169.7	0.1	169.2	3.8	MoSO <sub>x</sub>
<b>S 2p 1/2</b>	169.9	0.1	/	/	/	/	170.3	1.8	170.3	1.5	170.9	0.1	170.4	1.9	MoSO <sub>x</sub>
		<b>0.3</b>		<b>1.8</b>		<b>2.8</b>		<b>6.3</b>		<b>6.5</b>		<b>2.6</b>		<b>6.2</b>	
<b>O 1s</b>	531.2	24.1	530.9	11.7	530.8	11.4	531.1	12.5	531.1	9.7	530.9	10.5	531.4	9.6	MoO <sub>3</sub> /Al <sub>2</sub> O <sub>3</sub>
<b>O 1s</b>	532.7	26.7	532.2	22.8	532.2	20.8	532.5	47.8	532.4	41.7	532.2	19.9	532.5	43.9	AlO <sub>x</sub> /SiO <sub>x</sub>
		<b>50.8</b>		<b>34.4</b>		<b>32.2</b>		<b>60.3</b>		<b>51.4</b>		<b>30.4</b>		<b>53.5</b>	
<b>Si 2p 3/2</b>	103.3	7.8	102.2	7.4	102.1	4.9	102.9	1.1	102.8	1.1	102.4	1.1	102.7	0.3	SiO <sub>x</sub>
<b>Si 2p 1/2</b>	103.9	3.9	102.9	3.7	102.8	2.4	103.6	0.5	103.4	0.5	103.0	0.5	103.3	0.2	SiO <sub>x</sub>
		<b>11.7</b>		<b>11.0</b>		<b>7.3</b>		<b>1.6</b>		<b>1.6</b>		<b>1.6</b>		<b>0.5</b>	
<b>Al 2p 3/2</b>	/	/	73.6	1.0	73.4	3.1	73.6	0.4	73.5	3.7	73.0	9.073	73.4	4.2	AlN
<b>Al 2p 1/2</b>	/	/	74.0	0.5	73.8	1.5	74.0	0.2	73.9	1.8	73.5	4.537	73.8	2.1	AlN
<b>Al 2p 3/2</b>	/	/	74.7	3.0	74.5	4.8	74.9	5.8	74.8	6.4	74.2	8.612	74.8	6.9	Al <sub>2</sub> O <sub>3</sub> /AlO <sub>x</sub>
<b>Al 2p 1/2</b>	/	/	75.1	1.5	74.9	2.4	75.3	2.9	75.2	3.2	74.6	4.307	75.2	3.5	Al <sub>2</sub> O <sub>3</sub> /AlO <sub>x</sub>
				<b>6.1</b>		<b>11.9</b>		<b>9.3</b>		<b>15.2</b>		<b>26.5</b>		<b>16.6</b>	
<b>Mo 3d 5/2</b>	229.9	1.5	229.0	3.0	228.7	2.1	229.4	0.6	229.0	1.0	228.3	1.0	229.0	0.3	MoN <sub>x</sub> /MoS <sub>2</sub>
<b>Mo 3d 3/2</b>	233.0	1.0	232.1	2.0	231.8	1.4	232.5	0.4	232.0	0.7	231.4	0.7	232.0	0.2	MoN <sub>x</sub> /MoS <sub>2</sub>
<b>Mo 3d 5/2</b>	231.3	1.0	230.1	0.8	229.8	0.7	231.2	0.3	230.9	0.3	230.5	0.1	231.5	0.4	MoO <sub>x</sub>
<b>Mo 3d 3/2</b>	234.4	0.7	233.2	0.6	232.9	0.4	234.3	0.2	233.9	0.2	233.5	0.0	234.6	0.3	MoO <sub>x</sub>
<b>Mo 3d 5/2</b>	233.3	4.2	232.8	0.7	232.6	0.3	232.8	1.7	232.8	1.2	232.4	0.1	233.0	0.4	MoO <sub>3</sub>
<b>Mo 3d 3/2</b>	236.4	2.8	235.9	0.5	235.7	0.2	235.9	1.2	235.9	0.8	235.5	0.1	236.1	0.3	MoO <sub>3</sub>
		<b>11.2</b>		<b>7.6</b>		<b>5.2</b>		<b>4.4</b>		<b>4.2</b>		<b>2.0</b>		<b>2.0</b>	
<b>Total</b>		<b>100.0</b>				<b>100.0</b>		<b>100.0</b>		<b>100.0</b>		<b>100.0</b>		<b>100.0</b>	

**Annex part 3: Complementary results**

[S]/[Mo]	/	/	1.3	2.5	0.8	1.5	1.4	0.8
[N]/[Al]	/	/	9.4	2.9	0.7	0.8	1.3	0.8
[AlO <sub>x</sub> ]/[Al]	/	/	2.4	2.8	0.9	0.6	0.5	0.6
Mo 3d 5/2 - S 2p 3/2		/	67.5	67.4	67.3	67.2	67.2	67.2

Table IV (Annex part 3): Binding energies positions and atomic concentrations (at.%) of the different chemical environments identified by XPS at the surface of MoS<sub>2</sub> Reference and MoS<sub>2</sub> + AlN xs samples after N<sub>2</sub> plasma treatment

As listed in Table 3 (Annex part 3), the down-shifting in binding energies is commonly observed on all MoS<sub>2</sub> with the AlN seed layer, whatever the AlN seed thickness, and is visible on Mo 3d, S2p, Si 2p and O 2s spectra. It seems to indicate an interaction between the 2D-MoS<sub>2</sub> and AlN PVD seed layers. Several phenomena can explain this observation. Firstly, this peaks shift could be attributed to a doping of the 2D-MoS<sub>2</sub> seed layer. Indeed, several studies report a shifting of binding energies due to the introduction of a doping element such as niobium (Nb)<sup>417,418</sup>, manganese (Mn)<sup>416</sup> or Aluminum (Al)<sup>419</sup> in MoS<sub>2</sub> or WS<sub>2</sub> materials. Moreover, as it is a down-shifting, it suggests a down-shift of the MoS<sub>2</sub> Fermi Level due to a p-type doping which is consistent with Raman results presented earlier. Secondly, this observation can also be induced by a screening effect of the AlN seed layer. In fact, the electronegativity difference between two bonded atoms create local charges  $\delta^-$  and  $\delta^+$  (in our case, Al and Mo are  $\delta^+$  and N and S are  $\delta^-$ ). These local charges can interact with each others and generate a modification in the valence charge distribution. These changes in electronic interactions can modify binding energies up to few eV<sup>542</sup>. Stated differently, the band bending increases as a function of AlN thickness. Finally, this phenomenon also contributes to a shift in binding energies positions of the calibration. In XPS, C-C / C-H components of C 1s peak (from residual carbon) are used as it is an internal standard for the calibration of the binding energy scale at the surface<sup>543</sup>. The valence band edge is expected to be sharp and the valence band maximum (VBM) is found by fitting the middle of the curve<sup>544</sup>. In our case, focusing on O 2s spectrum (not discussed here), the C 1s calibration lead to a variation in VBM and therefore in Fermi level positions up to 1.9 eV on some samples while others seem pretty well calibrated (Fermi Level positioned at 0.1 eV). This variation in Fermi level position suggests that the contribution of the C 1s calibration has a nonnegligible impact on the binding energies positions. However, it is difficult to know if this calibration effect is predominant compared to doping or screening effect. Therefore, it seems that the down-shifting of the binding energies positions for MoS<sub>2</sub> + AlN<sub>x</sub> samples is due to a combination of these three described phenomena.

III.2.3. *MoS<sub>2</sub> Reference and after 700 °C and 1000 °C vacuum heat treatment*

In chapter 4 section IV.2.2.3, the thermal budget impact on MoS<sub>2</sub> Reference sample has been assessed with a 700 °C and 1000 °C vacuum heat treatments. The overall atomic concentrations, binding energy and their attribution of each sample are presented in Table V below.

Name	MoS <sub>2</sub> Reference		MoS <sub>2</sub> after 700 °C heat treatment		MoS <sub>2</sub> after 1000 °C heat treatment		Attribution
	Binding Energy (eV)	% Conc.	Binding Energy (eV)	% Conc.	Binding Energy (eV)	% Conc.	
C 1s	284.8	17.0	284.8	22.8	284.8	18.0	C-C / C-H
C 1s	286.2	5.6	286.2	6.5	286.4	4.0	C-O / C-N
C 1s	/	/	288.8	2.6	288.9	1.8	O-C=O
		<b>22.6</b>		<b>31.9</b>		<b>23.8</b>	
S 2p 3/2	162.5	15.7	162.5	8.7	/	/	MoS <sub>2</sub>
S 2p 1/2	163.7	7.9	163.7	4.4	/	/	MoS <sub>2</sub>
		<b>23.6</b>		<b>13.1</b>			
O 1s	531.2	6.8	530.9	5.7	530.8	0.9	MoO <sub>x</sub> /MoO <sub>3</sub>
O 1s	533.2	20.2	532.8	26.4	533.0	51.9	C-O/SiO <sub>x</sub> /SiO <sub>2</sub>
		<b>27.0</b>		<b>32.1</b>		<b>52.9</b>	
Si 2p 3/2	103.7	7.1	103.3	8.7	103.5	15.1	SiO <sub>x</sub> /SiO <sub>2</sub>
Si 2p 1/2	104.4	3.5	104.0	4.4	104.1	7.5	SiO <sub>x</sub> /SiO <sub>2</sub>
		<b>10.6</b>		<b>13.1</b>		<b>22.6</b>	
Mo 3d 5/2	/	/	/	/	228.5	0.3	Mo°
Mo 3d 3/2	/	/	/	/	231.6	0.2	Mo°
Mo 3d 5/2	229.8	8.1	229.7	4.7	/	/	MoS <sub>2</sub>
Mo 3d 3/2	232.8	5.4	232.8	3.2	/	/	MoS <sub>2</sub>
Mo 3d 5/2	233.4	1.6	233.0	1.2	232.7	0.2	MoO <sub>x</sub> /MoO <sub>3</sub>
Mo 3d 3/2	236.5	1.1	236.1	0.8	235.8	0.1	MoO <sub>x</sub> /MoO <sub>3</sub>
		<b>16.2</b>		<b>9.9</b>		<b>0.8</b>	
<b>Total</b>		<b>100.0</b>		<b>100.0</b>		<b>100.0</b>	
[S]/[Mo]		1.7		1.7		/	
[O]/[Mo]		2.6		2.9		2.8	
[O]/[Si]		1.9		2.0		2.3	
Mo 3d 5/2 - S 2p 3/2	67.2		67.2		/		

Table V (Annex part 3): Binding energies positions and atomic concentrations (at.%) of the different chemical environments identified by XPS at the surface of MoS<sub>2</sub> Reference, after 700 °C and 1000 °C vacuum heat treatment

III.2.4. *MoS<sub>2</sub> + AlN* xs before and after 1000 °C NH<sub>3</sub> heat treatment

In chapter 4 section IV.2.3.3, *MoS<sub>2</sub> + AlN* xs samples have been characterized by XPS before and after 1000 °C NH<sub>3</sub> heat treatment. The overall atomic concentrations and binding energies of each sample are presented in Table VI below.

	Before 1000 °C NH <sub>3</sub> heat treatment								After 1000 °C NH <sub>3</sub> heat treatment								Attribution
	MoS <sub>2</sub> + AlN 4s		MoS <sub>2</sub> + AlN 6s		MoS <sub>2</sub> + AlN 8s		MoS <sub>2</sub> + AlN 10.4s		MoS <sub>2</sub> + AlN 4s		MoS <sub>2</sub> + AlN 6s		MoS <sub>2</sub> + AlN 8s		MoS <sub>2</sub> + AlN 10.4s		
Name	B.E (eV)	% Conc.	B.E (eV)	% Conc.	B.E (eV)	% Conc.	B.E (eV)	% Conc.	B.E (eV)	% Conc.	B.E (eV)	% Conc.	B.E (eV)	% Conc.	B.E (eV)	% Conc.	
<b>C 1s</b>	284.8	12.0	284.8	13.3	284.8	13.4	284.8	8.3	284.8	13.7	284.8	10.4	284.8	11.4	284.8	13.4	C-C / C-H
<b>C 1s</b>	286.5	2.6	286.2	2.7	286.5	2.4	286.2	1.2	286.2	2.2	286.0	2.1	285.9	3.6	286.1	2.8	C-O / C-N
<b>C 1s</b>	289.2	2.8	288.9	2.0	289.1	2.2	289.4	1.6	288.9	2.1	289.2	1.6	288.8	1.7	288.9	2.0	O-C=O
		<b>17.3</b>		<b>18.0</b>		<b>18.0</b>		<b>11.1</b>		<b>18.0</b>		<b>14.0</b>		<b>16.7</b>		<b>18.2</b>	
<b>N 1s</b>	396.4	20.3	396.8	21.4	396.8	20.6	396.8	24.7	396.4	17.9	396.5	20.0	396.7	19.7	396.6	19.4	MoN <sub>x</sub> /AlN
<b>N 1s</b>			/	/	/	/	398.6	3.6	397.6	3.3	398.0	2.8	398.0	2.9	397.7	2.8	NO
		<b>20.3</b>		<b>21.4</b>		<b>20.6</b>		<b>28.3</b>		<b>21.2</b>		<b>22.9</b>		<b>22.6</b>		<b>22.2</b>	
<b>S 2p 3/2</b>	161.0	2.8	161.3	1.5	161.0	0.9	160.8	0.5	/	/	/	/	/	/	/	/	MoS <sub>x</sub>
<b>S 2p 1/2</b>	162.2	1.6	162.5	0.8	162.2	0.4	162.0	0.2	/	/	/	/	/	/	/	/	MoS <sub>x</sub>
		<b>4.4</b>		<b>2.3</b>		<b>1.3</b>		<b>0.7</b>									
<b>O 1s</b>	530.7	8.5	530.8	5.7	530.8	5.9	530.2	5.0	530.3	8.2	530.2	7.9	530.0	5.3	530.2	6.0	MoO <sub>3</sub> /Al <sub>2</sub> O <sub>3</sub>
<b>O 1s</b>	532.1	16.5	532.1	20.9	532.1	22.6	531.4	12.4	531.6	20.2	531.5	18.4	531.3	16.7	531.5	16.9	AlO <sub>x</sub> /SiO <sub>x</sub>
<b>O 1s</b>	/	/	/	/	/	/	532.5	9.0	532.7	3.5	532.7	5.8	532.6	10.9	532.6	8.2	Al(OH) <sub>x</sub>
		<b>25.0</b>		<b>26.6</b>		<b>28.5</b>		<b>26.4</b>		<b>31.9</b>		<b>32.0</b>		<b>32.9</b>		<b>31.2</b>	
<b>Si 2p 3/2</b>	102.5	1.6	102.7	1.2	101.9	0.7	102.2	0.5	102.3	1.8	102.6	1.3	103.0	0.6	102.6	0.4	SiO <sub>x</sub>
<b>Si 2p 1/2</b>	103.1	0.8	103.3	0.6	102.5	0.3	102.8	0.3	102.9	0.9	103.2	0.6	103.6	0.3	103.3	0.2	SiO <sub>x</sub>
<b>Si 2p 3/2</b>	/	/	/	/	/	/	/	/	101.0	1.0	101.0	0.3	101.5	0.3	101.5	0.2	SiO <sub>x</sub> N <sub>y</sub>
<b>Si 2p 1/2</b>	/	/	/	/	/	/	/	/	101.6	0.5	101.7	0.2	102.3	0.1	102.1	0.1	SiO <sub>x</sub> N <sub>y</sub>
		<b>2.5</b>		<b>1.8</b>		<b>1.0</b>		<b>0.8</b>		<b>4.2</b>		<b>2.4</b>		<b>1.3</b>		<b>0.9</b>	



**Annex part 3: Complementary results**

Name	Before NH <sub>3</sub> heat treatment								After NH <sub>3</sub> heat treatment								Attribution
	MoS <sub>2</sub> + AlN 4s		MoS <sub>2</sub> + AlN 6s		MoS <sub>2</sub> + AlN 8s		MoS <sub>2</sub> + AlN 10.4s		MoS <sub>2</sub> + AlN 4s		MoS <sub>2</sub> + AlN 6s		MoS <sub>2</sub> + AlN 8s		MoS <sub>2</sub> + AlN 10.4s		
	B.E (eV)	% Conc.	B.E (eV)	% Conc.	B.E (eV)	% Conc.	B.E (eV)	% Conc.	B.E (eV)	% Conc.	B. (eV)	% Conc.	B.E (eV)	% Conc.	B.E (eV)	% Conc.	
Mo 3d 5/2	228.2	1.7	228.5	0.8	228.2	0.5	228.0	0.3	/	/	/	/	/	/			MoS <sub>x</sub>
Mo 3d 3/2	231.2	1.1	231.6	0.5	231.3	0.3	331.0	0.2	/	/	/	/	/	/			MoS <sub>x</sub>
Mo 3d 5/2	/	/	/	/	/	/	/	/	228.0	0.7	228.1	0.5	228.1	0.1	228.2	0.1	MoN <sub>x</sub>
Mo 3d 3/2	/	/	/	/	/	/	/	/	231.0	0.4	231.2	0.3	231.2	0.1	231.3	0.1	MoN <sub>x</sub>
Mo 3d 5/2	/	/	/	/	/	/	/	/	228.6	0.8	229.0	0.2	228.9	0.3	228.9	0.1	MoO <sub>x</sub> N <sub>y</sub>
Mo 3d 3/2	/	/	/	/	/	/	/	/	231.7	0.5	232.1	0.2	232.0	0.2	232.0	0.1	MoO <sub>x</sub> N <sub>y</sub>
Mo 3d 5/2	232.2	0.2	232.6	0.1	/	/	/	/	232.2	0.3	232.2	0.1	232.4	0.1	232.5	0.1	MoO <sub>x</sub>
Mo 3d 3/2	235.0	0.1	235.7	0.1	/	/	/	/	235.3	0.2	235.3	0.1	235.5	0.1	235.6	0.0	MoO <sub>x</sub>
				<b>1.5</b>		<b>0.8</b>		<b>0.5</b>		<b>3.0</b>		<b>1.5</b>		<b>0.9</b>		<b>0.5</b>	
Al 2p 3/2	73.1	12.5	74.0	14.5	73.6	17.3	73.4	18.4	73.1	11.9	73.2	15.1	73.2	11.9	73.2	12.7	AlN
Al 2p 1/2	73.5	6.2	74.4	7.2	74.0	8.6	73.8	9.2	73.5	5.9	73.6	7.5	73.7	6.0	73.6	6.3	AlN
Al 2p 3/2	74.0	5.8	74.8	4.5	74.6	2.6	74.4	3.1	74.2	2.5	74.3	3.1	74.2	5.1	74.2	5.3	Al <sub>2</sub> O <sub>3</sub> /AlO <sub>x</sub>
Al 2p 1/2	74.4	2.9	75.2	2.2	75.0	1.3	74.8	1.5	74.6	1.3	74.7	1.5	74.6	2.6	74.6	2.7	Al <sub>2</sub> O <sub>3</sub> /AlO <sub>x</sub>
		27.4		<b>28.4</b>		<b>29.8</b>		<b>32.2</b>		<b>21.6</b>		<b>27.2</b>		<b>25.6</b>		<b>27.0</b>	
<b>Total</b>		<b>100.0</b>		<b>100.0</b>		<b>100.0</b>		<b>100.0</b>		<b>100.0</b>		<b>100.0</b>		<b>100.0</b>		<b>100.0</b>	
[S]/[Mo]		1.6		1.7		1.9			/		/		/		/		
[N]/[Al]		1.1		1.0		0.8		0.9		1.0		0.9		1.1		1.0	
[AlO <sub>x</sub> ]/[Al]		0.3		0.2		0.1		0.1		0.2		0.2		0.3		0.3	
Mo 3d 5/2 - S 2p 3/2		67.2		67.3		67.2		67.1		/		/		/		/	

Table VI (Annex part 3): Binding energies positions and atomic concentrations (at.%) of the different chemical environments identified by XPS at the surface of MoS<sub>2</sub> + AlN xs samples before after 1000 °C NH<sub>3</sub> heat treatment

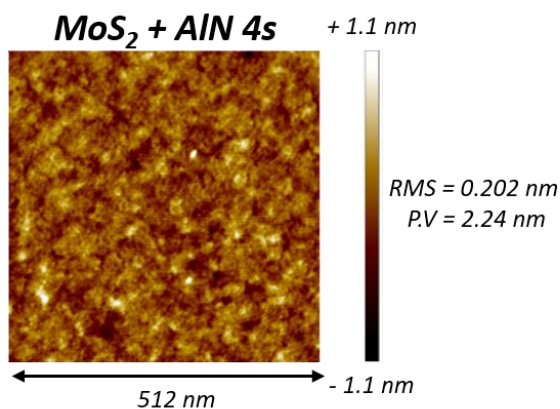
### III.3. Atomic Force Microscopy (AFM)

In chapter 4 section IV.2.4.3, we have demonstrated that, after the 1000 °C NH<sub>3</sub> heat treatment, the second AlN growth displays a higher crystal quality when the growth is performed on the thicker AlN seed layer (10.4s). This result has been attributed to better preservation of the thicker AlN seed surface.

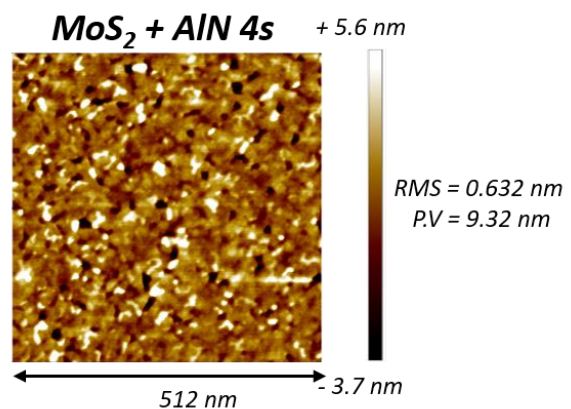
In fact, the surface state in terms of oxidation but also in smoothness is an essential point to perform a quality second thick AlN growth. Thus, the morphological modification has been evaluated by AFM analysis in PeakForce Tapping in order to have a more resolving tip compare to a classical analysis. AFM images before and after 1000 °C NH<sub>3</sub> heat treatment are presented in Figure II (Annex part 3).

a)

**Before heat treatment**

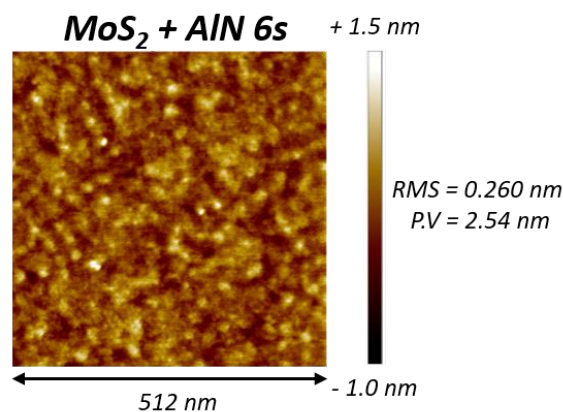


**After heat treatment**

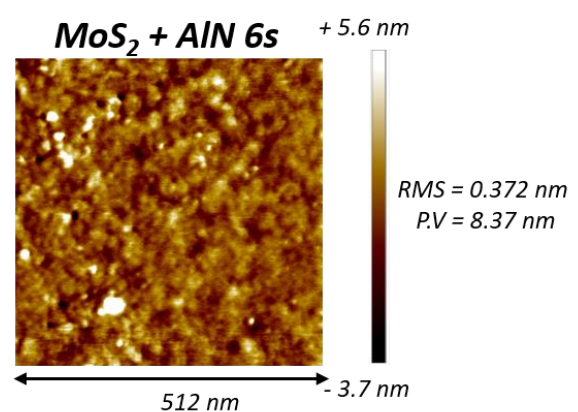


b)

**Before heat treatment**

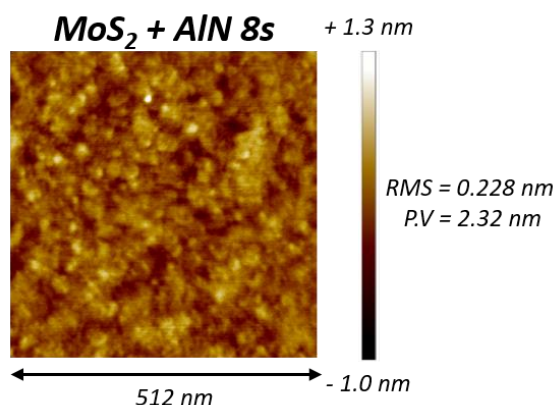


**After heat treatment**

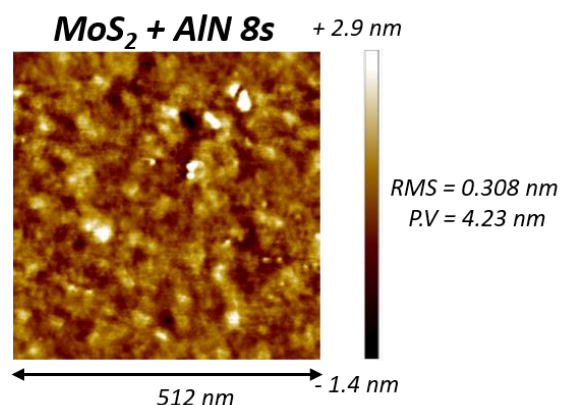


c)

Before heat treatment

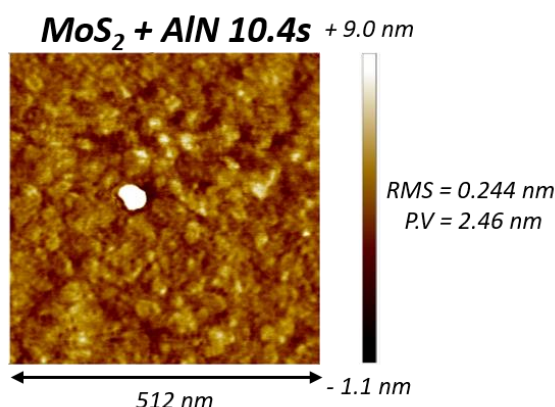


After heat treatment



d)

Before heat treatment



After heat treatment

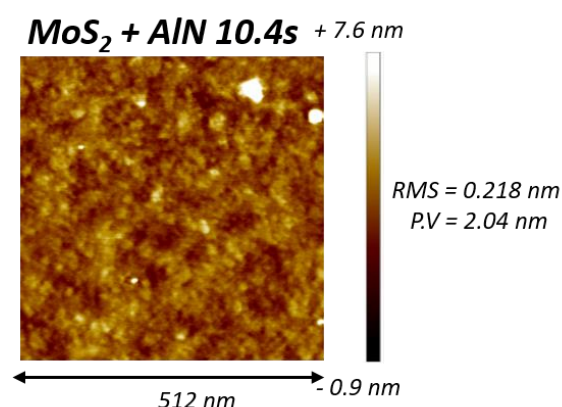


Figure II (Annex part 3): AFM images of a) MoS<sub>2</sub> + AlN 4s ; b) MoS<sub>2</sub> + AlN 6s ; c) MoS<sub>2</sub> + AlN 8s ; MoS<sub>2</sub> + AlN 10.4s before and after 1000 °C NH<sub>3</sub> heat treatment

Before NH<sub>3</sub> heat treatment, the surface is extremely smooth and RMS and P.V are independent of the AlN thickness: RMS ≈ 0.20 – 0.25 nm and P.V ≈ 2.5 nm. Surface morphology and roughness are similar and AlN film seem to be dense and homogeneous.

After NH<sub>3</sub> heat treatment, different surface morphologies and interesting tendencies are observed. In fact, if we focus on MoS<sub>2</sub> + AlN 4s, RMS is 3 times higher and P.V almost 4 times higher than before NH<sub>3</sub> heat treatment. An AlN deposition time of 4s corresponding to ≈ 2 nm thick layer, P.V value strongly suggests that the AlN film is not covering anymore and the sample surface seems pitted. This result is faded with the increase in AlN seed layer thickness: RMS and P.V decrease progressively until reaching a RMS and P.V value very close to the references for the MoS<sub>2</sub> + AlN 10.4s sample.

Therefore, to preserve a suitable AlN surface after  $\text{NH}_3$  heat treatments, these AFM analyses strongly suggest to perform the heat treatments on the samples with the thicker AlN PVD seed layer (deposition time of 10.4s).

#### III.4. AlN/MoS<sub>2</sub> local etching and Epitaxial Lateral Over Growth (ELOG)

As depicted in Figure III (Annex part 3), the idea of this approach is to deposit a thin AlN layer on 2D-MoS<sub>2</sub> and etch locally the stack AlN/MoS<sub>2</sub> to expose the bottom SiO<sub>2</sub> substrate in etched areas. Once this step is achieved, a thick AlN growth is performed on the remaining AlN/MoS<sub>2</sub> and etched areas. It is expected that this thick AlN growth is anchor onto the substrate since it is deposited on SiO<sub>2</sub> (etched areas) and c-axis textured since the deposition is also performed on AlN/MoS<sub>2</sub>.

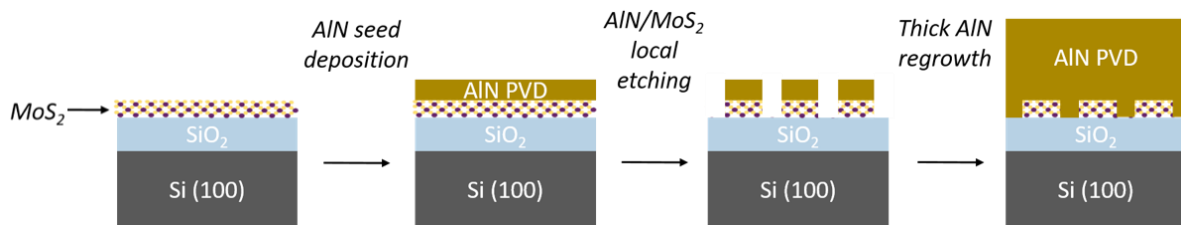


Figure III (Annex part 3): Illustration of the ELOG process on AlN/MoS<sub>2</sub>

This section is divided in four parts. The first part is a brief presentation on the experimental conditions with a strong focus on the stripping of etching polymers since it has been identified as the most critical step. The second part describes the physical optimizations performed in terms of lateral (etched areas) and vertical (AlN thickness) dimensions. The third part details the experimental approach implemented and the results of the stripping step. Finally, the last part concludes on the difficulties encountered by investigating this solution.

##### III.4.1. Experimental conditions

The AlN/MoS<sub>2</sub> local etching and ELOG approach was carried out on 200 mm wafers. A specific mask geometry was designed for this approach. The mask shows four different circular pattern diameters in order to optimize the size of the etching areas. Each pattern is designed by quarter of a Si-wafer. The thickness of the AlN layer deposited on MoS<sub>2</sub> before the etching step was also optimized and set below 100 nm. These optimizations in the dimension will be discussed in the next sub-section.

UV sensitive resist and an anti-reflective coating (recommended on nitride films to avoid poisoning effects) were used, following by a time exposure in an ASM300 lithography tool.

The resin was revealed in a base solution, and the opened regions were plasma etched in a LAM9400A tool. After etching, to remove the resist, a first dry plasma stripping (aching step) process step with different chemistries was performed in a MATTSON 1 equipment. Then, the dry etch polymers were removed by wet stripping and carried out using various chemistries in a wet bench. Experimental details of the stripping steps are presented in Table VII.

	Dry plasma stripping process			Wet stripping process			
	H <sub>2</sub> (in N <sub>2</sub> H <sub>2</sub> flow)	O <sub>2</sub>		Hydrofluoric acid (HF) 0.1%	SSEC3302 DMSO + IPA	EKC265	Acetone
<b>Gas/chemistry</b>							
<b>Temperature (°C)</b>	250	100	250	25	80	65	25
<b>Time (s)</b>	120	20	20	60	180	30 ; 180 and 600	25

*Table VII (Annex part 3): Experimental conditions of the wet and dry stripping processes investigated*

#### III.4.2. Dimensional optimization (pattern and AlN thickness)

Firstly, the ratio of opened areas in the first MoS<sub>2</sub>/AlN seed layer was optimized. It seems intuitive that the smaller the etched area, the better would be the quality (in term of RC) of the regrown AlN, but at the same time, small etched area reduces anchoring of the regrown AlN. Thus, a tradeoff must be found between the size of the opened areas, the quality of regrown AlN and the anchoring of the layer. For this purpose, circular patterns (i.e. holes where AlN seed is etched off) with various diameters and pitches have been designed in a physical chromium-based mask to obtain quadrant regions on a 200mm wafer. Design rules for local etching are presented in Table VIII and schematically sketched in Figure IV (Annex part 3) a). Figure IV (Annex part 3) b) displays the four different pattern dimensions in each quarter of a 200 mm wafer.

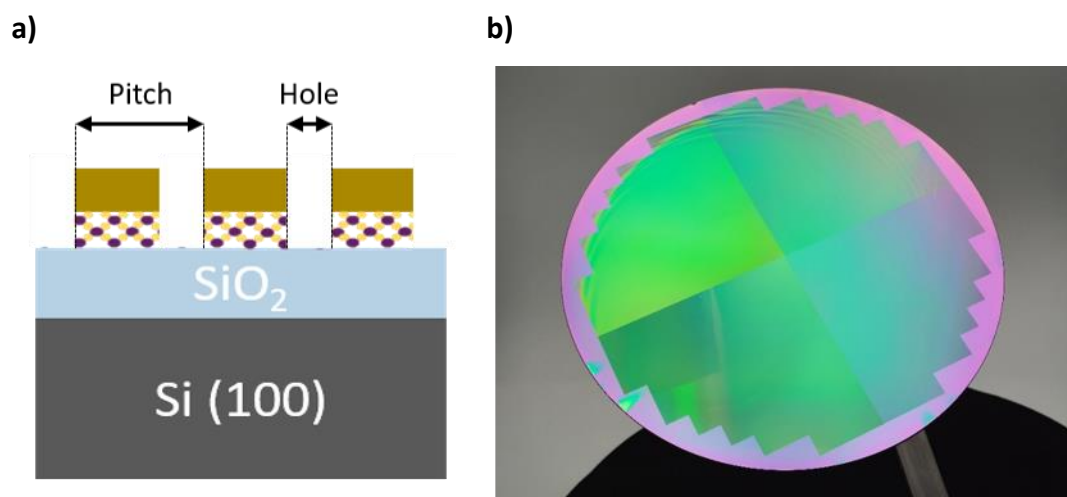


Figure IV (Annex part 3): a) Illustration of the local etching ; b) Four different pattern dimensions in each quarter of a 200 mm wafer

Hole diameter ( $\mu\text{m}$ )	Etched area (%)	Pitch ( $\mu\text{m}$ )
2.0	69	2.4
1.0	51	1.4
0.6	36	1.0
0.4	25	0.8

Table VIII (Annex part 3): Design rules for local etching

Secondly, the thickness of the AlN seed layer deposited on MoS<sub>2</sub> was also optimized. First trials using 100 nm thick AlN as seed led to the delamination of the stack either during photolithography developing step in WET chemistry or during polymers stripping post-etching. As already seen in the previous chapter, we know that a 100 nm thick AlN PVD layer is stressed ( $\sigma = 0.70$  GPa). Thus, it is expected that the delamination is due to the couple contributions of the AlN bi-axial stress and the chemistries used for the developing or stripping of the masking resin. To avoid the delamination of the stack, we first decided to reduce the AlN thickness below 100 nm in order to limit the mechanical stress.

#### III.4.3. Chemical optimization (stripping step)

The delamination encounter during the developer exposure (based on tetramethylammonium hydroxide (TMAH) chemistry) was rapidly solved and we speculated that the water was the main cause, in particular during the rinsing steps post-stripping. We explain here the process that help us to draw this conclusion. First, we optimized the plasma stripping steps. The idea was to etch away the resist in an oxidizing free ambient, to limit alumina formation on top of the seed layer. Hydrogen plasma was preferred to O<sub>2</sub> plasma in

order to prevent the AlN seed top surface from re-oxidation, this to ensure a good regrowth of the second AlN. Hence, after etching, wafers were exposed to a first dry hydrogen plasma to remove the residual resist. After a deep analysis, H<sub>2</sub> dry plasma was identified to be efficient to remove the photo-resist but not enough to remove the dry etch polymers. The SEM images given in Figure V (Annex part 3) a) and b) show these polymers, in particular on the flanks of the etched structures. In fact, these etching polymers are composed of a mixture of aluminium and carbon. The aluminium element is etched away from the AlN seed, and some atoms are embedded into a matrix composed of carbons from the resin, leading to an inorganic/organic polymer laying on the borders of structures. Hydrofluoric (HF)-based chemistry is known to remove Al-based layers. A common solution to this problem (used as standard in the AlN BAW technology), is to expose the structure to a HF acid 0.1 % diluted in deionized (DI) water. Unfortunately, we observed the complete delamination of the AlN/MoS<sub>2</sub> stack after this HF treatment. We speculated that the infiltration of water within 2D-MoS<sub>2</sub> plans is the cause to the separation of the AlN from its deposited surface. Indeed, water is used to separate 2D layers from the growth substrate in film transfer methodologies<sup>545</sup>. Therefore, we decided to find a solution that avoids any exposure of the 2D/AlN stack to water, and tested other H<sub>2</sub>O-free chemistries.

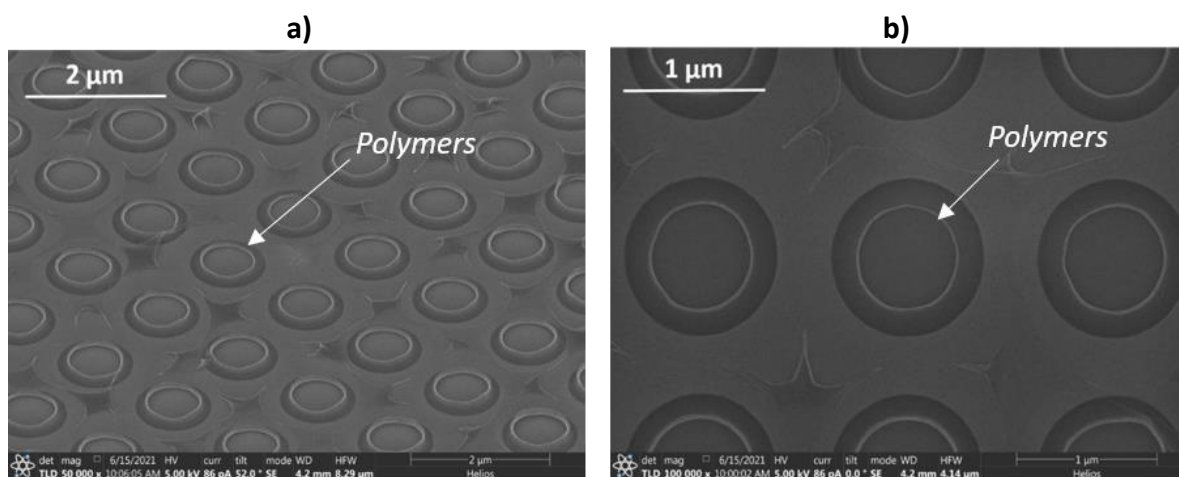


Figure V (Annex part 3): SEM images of the residues observed after dry stripping on AlN/MoS<sub>2</sub> a) Tilted view (52°) ; b) Top view

Alternative chemistries were tested to remove polymers residues such as DMSO (dimethyl sulfonate) + IPA (isopropyl alcohol), EKC265 (a post-etch residues remover based on an organic solvent widely used in the semiconductor industry) or acetone. However, whatever the investigated solution, delamination was observed during the wet stripping step. We observed that part of the problem was due to the way the chemistry was delivered (using jet

nozzles to add a mechanical effect) on the wafer. But in any case, we concluded that water must be at least avoided, and that the polymers stripping step was critical in term on reproducibility in this ELOG solution.

#### III.4.4. Conclusions on AlN/MoS<sub>2</sub> local etching

To conclude, the stripping process is identified as a limiting and challenging step of this ELOG route. We faced to two main issues: dry stripping is not sufficient to remove polymers residues and wet stripping leads to the delamination of the AlN/MoS<sub>2</sub> stack. Therefore, it seems difficult to find a suitable and reliable way to form well defined structures on Si substrates. Most probably, the reason is that AlN is a rigid ceramic that does not easily accommodate any geometry modifications, meaning no reduction of the internal stress due to geometry compensation, and that MoS<sub>2</sub> interlayers are too fragile and prompt to separate the rigid ceramic in particular if water is used.





## Résumé de la thèse en français

### I. Contexte et introduction

Depuis ces dernières années, les communications sans fils se sont développées de manière intensive menant à une croissance exponentielle du trafic de données associé. Afin d'adresser cette augmentation de trafic de données, l'industrie des télécommunications s'est appuyée sur l'introduction de bandes de fréquences supplémentaires généralement plus larges et positionnées dans des fréquences plus élevées. La 5<sup>ème</sup> génération de communication sans fils (5G) est un bon exemple illustrant ce développement avec l'introduction de nouvelles fréquences dans la bande C (autour de 3,5 GHz) et dans le spectre des ondes millimétriques (autour de 28 GHz).

Ce développement fait de la connectivité un élément essentiel de notre quotidien. L'exemple le plus parlant est certainement le smartphone avec près de 7 milliards d'utilisateurs dans le monde. Au sein de ces objets connectés, la transmission et réception des données est réalisée via une chaîne de radiofréquence (RF). Celle-ci est constituée d'éléments classiques (amplificateurs, filtres, décaleurs de fréquence...) permettant de moduler le signal transmis ou émis et communément appelée technologies RF Front-End.

#### I.1. Filtres acoustiques

Les filtres et plus précisément les filtres acoustiques représentent les éléments les plus importants, en termes de parts de marché, de la technologie RF Front-End. En outre, leur développement va continuer à croître de manière significative suite à l'essor des communications sans fils <sup>1</sup>. Ce type de filtres se divise en deux technologies : Surface Acoustic Wave (SAW) et Bulk Acoustic Wave (BAW). Elles sont notamment dédiées aux communications mobiles 2G, 3G et 4G utilisées quotidiennement par des milliards d'utilisateurs. La brique élémentaire d'un filtre acoustique est un résonateur acoustique <sup>30</sup>. Le filtrage en fréquence est assuré par un matériau piézoélectrique générant une onde acoustique qui se propage latéralement pour les technologies SAW et verticalement pour les technologies BAW. La structure de ces résonateurs est schématiquement représentée sur la Figure 1 a) et b) pour les technologies SAW et BAW, respectivement.

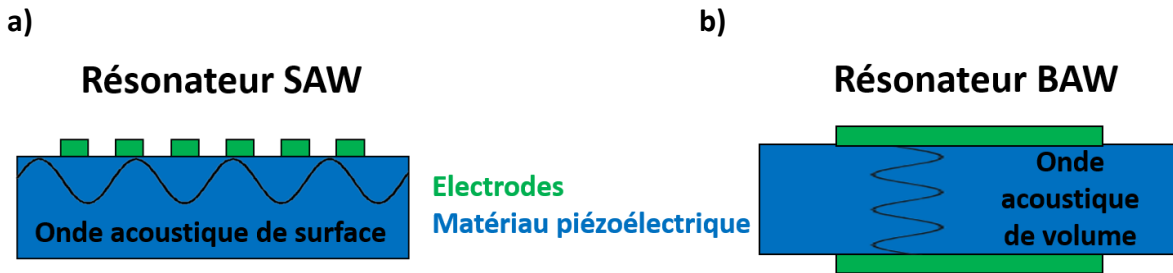


Figure 1: Structure élémentaire d'un résonateur de type a) SAW ; b) BAW

Ces dispositifs acoustiques sont caractérisés par deux paramètres. D'une part, le coefficient de couplage électromécanique ( $k_{\text{eff}}^2$ ) détermine la largeur de la bande passante du filtre. Plus cette valeur est élevée, plus la largeur de la bande passante du filtre est importante. D'autre part, le facteur de qualité (Q) caractérise la perte d'insertion (atténuation du signal) et la sélectivité du filtre. Maximiser cette valeur permet de diminuer la perte d'insertion et d'augmenter la sélectivité du filtre. Ainsi, la figure de mérite (FDM) des technologies SAW et BAW naturellement définie par :  $\text{FDM} = k_{\text{eff}}^2 \cdot Q$ , doit elle aussi être maximisée.

### 1.2. Challenges et objectifs de la thèse

Les défis actuels de la communication mobile sans fils sont relativement simples : les dispositifs SAW et BAW ne sont pas adaptés pour répondre aux besoins envisagés par les prochains standards (par exemple Wi-Fi et 6G) nécessitant des fréquences de fonctionnement plus élevées et une bande de fréquences plus large. D'une part, la technologie SAW présente des limitations dans les fréquences de fonctionnement supérieures à 2 GHz. D'autre part, les technologies BAW permettent de fonctionner à des fréquences plus élevées (jusqu'à 3,5 GHz) mais la qualité cristalline actuelle du matériau piézoélectrique (nitrure d'aluminium : AlN) utilisé dans les résonateurs BAW n'est pas optimale. Ainsi, le coefficient de couplage électromécanique  $k_{\text{eff}}^2$  et le facteur de qualité Q sont insuffisants pour répondre aux futures exigences des normes de communications sans fils. Typiquement, le  $k_{\text{eff}}^2$  de l'AlN est actuellement limité autour de 7 %, alors qu'une bande passante plus large nécessitant un  $k_{\text{eff}}^2$  d'environ 10 % avec un impact limité sur le facteur Q est requis par les nouvelles normes de communications sans fils.

L'objectif principal de cette thèse est de développer une solution innovante et compatible économiquement avec une production en masse afin de répondre aux nouveaux défis auxquels sont confrontées les technologies de filtres RF. D'après une étude menée au cours de cette thèse, il a été déterminé que la technologie BAW semble la plus prometteuse. Par

conséquent, l'enjeu principal concerne la qualité du matériau piézoélectrique (AlN), l'objectif étant de proposer une solution innovante pour améliorer la qualité du matériau piézoélectrique permettant le filtrage en fréquence.

Dans un premier temps, les travaux portent sur l'amélioration de la qualité cristalline de films de nitrure d'aluminium (AlN) ciblant les applications des dispositifs acoustiques. L'AlN est élaboré via une technique de dépôt physique en phase vapeur (PVD) à basse température sur un substrat à base de silicium à faible coût. L'innovation vient de l'utilisation d'un matériau bidimensionnel (2D) : le disulfure de molybdène ( $\text{MoS}_2$ ). Ce matériau sert de couche d'accommodation et affiche une différence de paramètre de maille raisonnable (1,6 %) avec AlN. Son utilisation devrait augmenter de manière significative la qualité cristalline du film d'AlN, permettant d'améliorer ses propriétés piézoélectriques, dont le  $k^2_{\text{eff}}$ .

Dans un second temps, le dépôt PVD de films d'AlN dopés au scandium (Sc) est étudié. En effet, l'utilisation du Sc est connue pour améliorer la réponse piézoélectrique de l'AlN, et notamment le  $k^2_{\text{eff}}$ , mais au détriment du facteur de qualité Q. Si l'utilisation du matériau 2D innovant comme couche d'accommodation texturante pour l'AlN PVD est prouvée, l'AlN dopé Sc pourrait être une solution intéressante pour répondre aux besoins des dispositifs acoustiques et en particulier au compromis  $k^2_{\text{eff}} - Q$ . En effet, il pourrait être possible d'atteindre un  $k^2_{\text{eff}}$  relativement élevé (proche de 10 %) avec un faible dopage Sc permettant de conserver un facteur de qualité Q raisonnable. Ainsi, la FDM du résonateur acoustique ( $k^2_{\text{eff}} \cdot Q$ ) devrait être augmentée.

## II. Les matériaux AlN et $\text{MoS}_2$

Dans des conditions normales de température et de pression, le matériau AlN cristallise dans une structure hexagonale de type wurtzite avec un paramètre de maille  $a = 3,11 \text{ \AA}$ <sup>175</sup>. La projection de cette structure dans le plan  $(\vec{a}, \vec{b})$  est représentée sur la Figure 2. Cette structure cristalline est non centro-symétrique ce qui permet de justifier ses propriétés piézoélectriques. Par ailleurs, la réponse piézoélectrique de l'AlN est maximale suivant l'axe  $\vec{c}$  et il convient donc de maximiser l'orientation cristalline de l'AlN suivant cet axe pour optimiser la réponse piézoélectrique.

$\text{MoS}_2$  est un matériau possédant une structure lamellaire. Cela signifie qu'il présente une structure bidimensionnelle dans laquelle les atomes au sein des couches S-Mo-S (également

appelées feuillets) sont liés par de fortes liaisons covalentes tandis que les couches sont regroupées avec des liaisons faibles de type Van der Waals (VdW)<sup>546</sup>. Ces liaisons de VdW se retrouvent également à l'interface entre le MoS<sub>2</sub> et le substrat sur lequel il est déposé : Si (100)/SiO<sub>2</sub> (500 nm). Le MoS<sub>2</sub> possède également une structure hexagonale avec une différence de paramètre de maille dans le plan ( $\vec{a}, \vec{b}$ ) raisonnable avec l'AlN ( $a_{\text{AlN}} = b_{\text{AlN}} = 3,11 \text{ \AA}$  et  $a_{\text{MoS}_2} = b_{\text{MoS}_2} = 3,16 \text{ \AA}$  comme illustré sur la Figure 2.

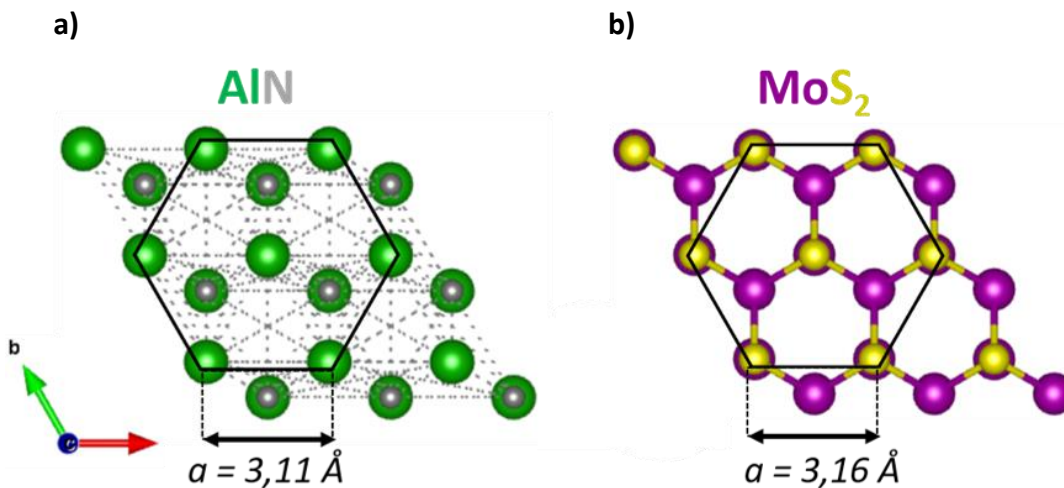


Figure 2: Représentation de la projection dans le plan ( $\vec{a}, \vec{b}$ ) des mailles cristallines hexagonales de a) AlN et b) MoS<sub>2</sub>

L'intérêt du matériau MoS<sub>2</sub> est d'exploiter la différence de paramètres de maille  $a$  modérée avec l'AlN (1,6 %) pour améliorer l'orientation cristalline de AlN déposé sur MoS<sub>2</sub> suivant l'axe  $\vec{c}$  (texturation). Ainsi, l'utilisation de MoS<sub>2</sub> en tant que couche d'accommodation texturante pour la croissance d'AlN devrait améliorer les propriétés piézoélectriques des films d'AlN élaborés, et augmenter la valeur de  $k^2_{\text{eff}}$ .

### III. Texturation de l'AlN sur MoS<sub>2</sub>

La preuve de concept concernant l'utilisation du matériau MoS<sub>2</sub> en vue d'améliorer la texturation de l'AlN suivant l'axe  $\vec{c}$  a été démontrée sur un wafer 200 mm standard : Si (100)/SiO<sub>2</sub> (500 nm). La texturation de l'AlN est caractérisée par une mesure de diffraction des rayons X (DRX) appelé « Rocking Curve (RC) » ou  $\omega$ -scan. Cette mesure est réalisée en considérant la famille de plans cristallins (002) de l'AlN menant à l'obtention d'un pic de diffraction. De manière générale, plus la largeur à mi-hauteur (appelée abusivement RC) de ce pic est faible, plus l'AlN est orienté préférentiellement suivant l'axe  $\vec{c}$ . Les RC d'une couche d'AlN 100 nm déposée par PVD sur le substrat standard Si (100)/SiO<sub>2</sub> (500 nm) avec et sans la couche de MoS<sub>2</sub> sont représentées sur la Figure 3.

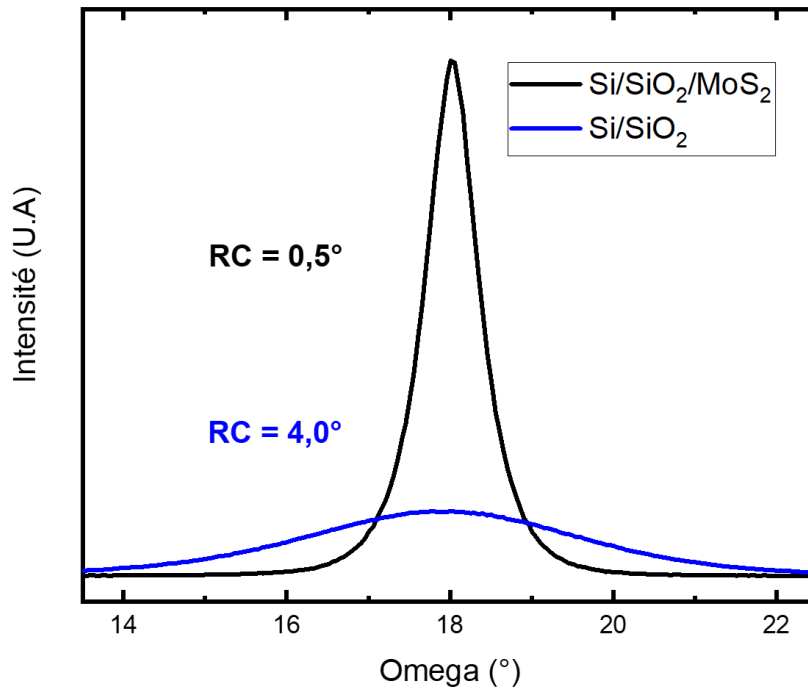


Figure 3: Mesures de Rocking Curve et de largeur à mi-hauteur (RC) en considérant le pic (002) d'une couche mince d'AlN (épaisseur 100 nm) élaborée par PVD sur substrat de Si/SiO<sub>2</sub> et Si/SiO<sub>2</sub>/MoS<sub>2</sub> (3 feuillets)

Nous observons clairement que la RC (002) de l'AlN déposé sur le substrat avec la couche de MoS<sub>2</sub> est significativement plus étroite que la RC de l'AlN déposé sans cette couche d'accommodation (RC  $\approx$  0,5° vs. RC  $\approx$  4,0°). En d'autres termes, l'orientation suivant l'axe  $\vec{c}$  de l'AlN déposé est favorisée par l'utilisation du MoS<sub>2</sub>.

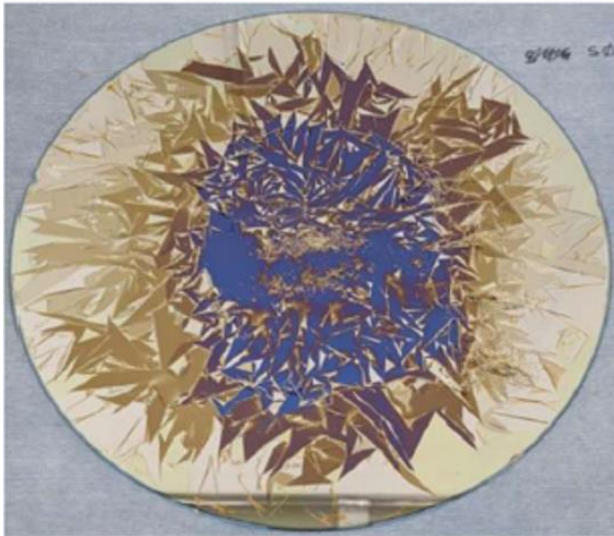
#### IV. Problématique de délamination et solution

Il est bien connu dans la littérature <sup>261</sup> que l'orientation cristalline suivant l'axe  $\vec{c}$  d'une couche mince d'AlN augmente avec l'épaisseur de la couche mince. Par conséquent, nous avons étudié l'effet de l'augmentation de l'épaisseur de la couche mince d'AlN obtenue par PVD sur substrat de Si/SiO<sub>2</sub> (500 nm)/MoS<sub>2</sub> (3 feuillets) sur l'amélioration de son orientation cristalline suivant l'axe  $\vec{c}$ . Des problématiques de contraintes mécaniques de la couche mince d'AlN sur le substrat de Si/SiO<sub>2</sub> (500 nm)/MoS<sub>2</sub> (3 feuillets) sont présentes. En effet, l'adhérence de la couche mince d'AlN sur le substrat Si/SiO<sub>2</sub> (500 nm)/MoS<sub>2</sub> (3 feuillets) peut devenir critique avec l'augmentation de l'épaisseur de la couche mince d'AlN.

Pour répondre à cette question d'adhésion, nous avons déposé un film d'AlN plus épais de 200 nm par PVD. Cependant et comme illustré sur la Figure 4, une délamination de l'empilement AlN/MoS<sub>2</sub> se produit. L'interface sujette à la délamination a été déterminée par deux caractérisations : la spectroscopie Raman et la spectroscopie photoélectronique X (XPS)

et celle-ci est l'interface  $\text{MoS}_2/\text{SiO}_2$ . La délamination est induite par deux phénomènes conjoints. Tout d'abord les liaisons VdW entre les monocouches de  $\text{MoS}_2$  et à l'interface  $\text{MoS}_2/\text{SiO}_2$  ne sont pas assez fortes pour éviter une délamination de l'empilement  $\text{AlN}/\text{MoS}_2$ . Ensuite, la déformation/contrainte de la couche mince d' $\text{AlN}$  ne peut pas être supportée par le  $\text{MoS}_2$ .

a)



b)

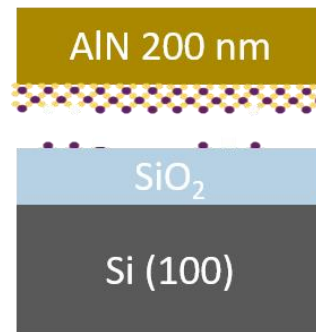


Figure 4: a) Délamination de l'empilement  $\text{AlN PVD}$  (200 nm)/ $\text{MoS}_2$  (3 feuillets) sur le substrat de  $\text{Si (100)}/\text{SiO}_2$  (500 nm) (wafer de 200 mm); b) Schématisation de l'interface de la délamination

Plusieurs tentatives de croissance d' $\text{AlN PVD}$  sur l'empilement  $\text{Si}/\text{SiO}_2$  (500 nm)/ $\text{MoS}_2$  (3 feuillets) ont permis de déterminer l'épaisseur critique de délamination autour de 200 nm d' $\text{AlN}$ . Cette épaisseur est insuffisante pour les dispositifs acoustiques visés puisque des épaisseurs jusqu'à 1  $\mu\text{m}$  sont requises. Ainsi, ce problème inhérent à la croissance d' $\text{AlN PVD}$  sur  $\text{MoS}_2$  est un verrou technologique et scientifique pour l'intégration de dispositifs à base d' $\text{AlN}$  et a besoin d'être solutionné.

Plusieurs solutions potentielles ont été testées afin de résoudre le problème de délamination. La solution la plus performante est schématisée sur la Figure 5. Elle repose sur un traitement thermique sous atmosphère nitrurante d'un empilement  $\text{Si (100)}/\text{SiO}_2$  (500 nm)/ $\text{MoS}_2/\text{AlN PVD}$  (< 5 nm)). Le but de ce recuit sous  $\text{NH}_3$  est de transformer les liaisons VdW au sein du  $\text{MoS}_2$  et à l'interface  $\text{MoS}_2/\text{SiO}_2$  en de fortes liaisons covalentes. Cette conversion est assurée par la nitruration du  $\text{MoS}_2$  de l'interface  $\text{MoS}_2/\text{SiO}_2$  en  $\text{MoN}_x/\text{SiO}_x\text{Ny}$ . La fine couche mince d' $\text{AlN}$  (< 5 nm) sert de couche de pré-texturation et permet d'assurer

une reprise de croissance d'AlN PVD en maintenant une forte orientation préférentielle suivant l'axe  $\vec{c}$ .

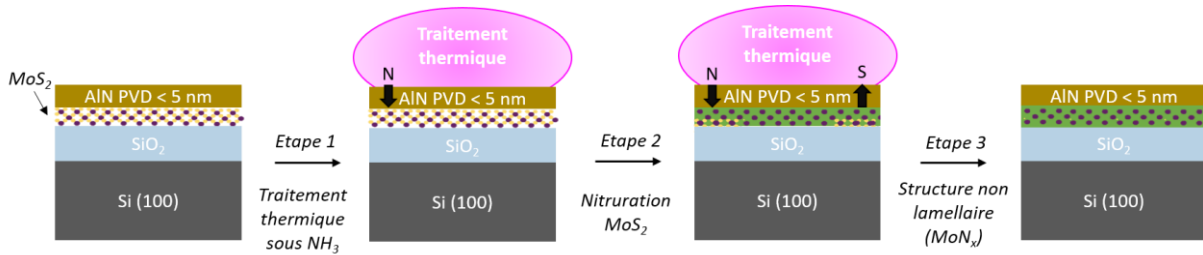


Figure 5: Schématisation de la nitruration du MoS<sub>2</sub> à travers une couche mince d'AlN PVD (< 5 nm) et proposition de mécanisme

## V. Résultats

La mise en place de ce procédé suivi d'une reprise de croissance d'un film d'AlN PVD de 1  $\mu\text{m}$  a permis de démontrer la preuve de concept de la résolution de la problématique de délamination tout en conservant une forte orientation préférentielle de l'AlN suivant l'axe  $\vec{c}$ . Ainsi, cette approche a été poussée et approfondie à travers des dépôts d'AlN par PVD avec des épaisseurs allant de 100 nm à 1  $\mu\text{m}$ . Par la suite, des films d'AlN dopés au Scandium (Sc) ont également été étudiés.

### V.1. Dépôts d'AlN par PVD

La RC (002) des films d'AlN PVD de 100 nm à 1  $\mu\text{m}$  élaborés via l'approche décrite ci-dessus est représentée sur la Figure 6 (triangles bleus). Elle est comparée à la RC (002) de l'AlN élaboré par PVD au sein du CEA-LETI directement déposé sur des substrats de Si (100) (points gris). La tendance est représentée par une courbe en pointillé gris. Ces valeurs de RC de l'AlN sont également comparées à différentes études de la littérature discutées dans le chapitre 2 sur des substrats à base de silicium (carrés noirs).



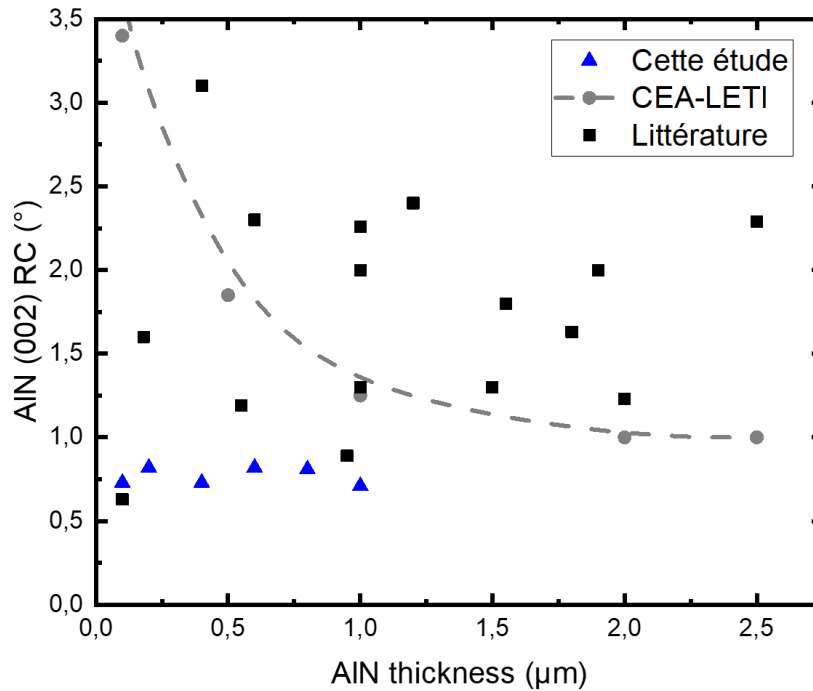


Figure 6: Comparaison des valeurs de RC (002) de l'AlN obtenues dans cette étude avec les capacités du CEA-LETI et la littérature sur des substrats à base de silicium

Dans un premier temps, les résultats obtenus dans cette étude montrent clairement que la RC (002) de l'AlN se situe autour de  $0,7^\circ - 0,8^\circ$  et est indépendante de l'épaisseur dans la gamme investiguée. Ceci suggère fortement que la qualité et l'orientation du film d'AlN est dépendante de la qualité de la couche mince d'AlN pré-texturante ( $< 5$  nm) déposé sur le  $\text{MoS}_2$  avant sa modification chimique. Dans un second temps, ces valeurs de RC (002) de l'AlN sont plus faibles que la plupart des valeurs répertoriées dans la littérature. Elles sont comparables à la plus faible valeur de RC ( $0,63^\circ$ ) obtenue pour un film d'AlN élaboré par PVD qui repose sur le pré-dépôt d'une fine couche d'aluminium avant la croissance d'AlN <sup>267</sup>. Cette amélioration de la texturation de l'AlN suivant l'axe  $\vec{c}$  devrait promouvoir une meilleure réponse piézoélectrique et spécifiquement le  $k_{\text{eff}}^2$ . Ainsi, il semble intéressant d'intégrer cet empilement dans des dispositifs RF à base d'AlN.

## V.2. Dépôts d'AlN dopés au Scandium (Sc) par PVD

Dans la continuité des dépôts d'AlN, des films d'AlN dopés au Sc ont également été élaborés par PVD en utilisant le procédé de nitruration de  $\text{MoS}_2$  décrit sur la Figure 5. La gamme d'alliage de Sc étudiée est de 4 % à 13 % atomique. Similairement aux dépôts d'AlN, leurs RC (002) (triangles bleus) sont comparées sur la

Figure 7 à d'autres films de ScAlN élaborés par PVD au CEA-LETI déposés directement sur des substrats de Si (100) (points gris) et à des valeurs issues de différentes études de la littérature discutées dans le chapitre 2 sur des substrats à base de silicium (carrés noirs).

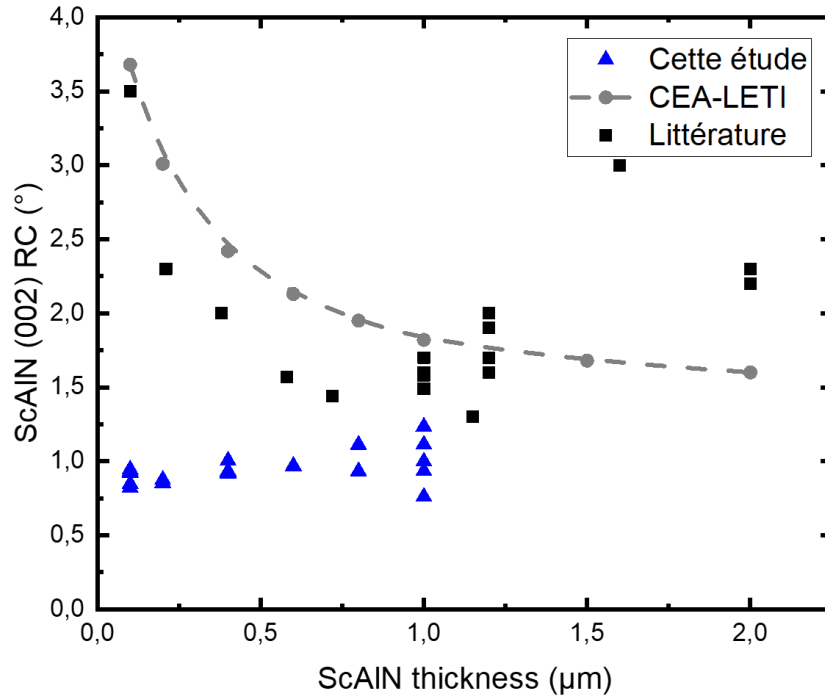


Figure 7: Comparaison des valeurs de RC (002) du ScAlN obtenues dans cette étude avec les capacités du CEA-LETI et la littérature sur des substrats à base de silicium

Indépendamment des épaisseurs (100 nm à 1 µm) et des gammes de dopages investiguées, les films de  $Sc_xAl_{1-x}N$  présentent une RC (002) autour de  $1^\circ$  (entre  $0,75^\circ$  et  $1,25^\circ$ ). De façon similaire aux dépôts d'AlN, ceci suggère fortement que la qualité et l'orientation des films de ScAlN élaborés est dépendante de la qualité de couche mince d'AlN pré-texturante (< 5 nm) déposée sur  $MoS_2$  avant sa nitruration. De plus, ces valeurs sont les plus faibles répertoriées à ce jour pour des films de ScAlN élaborés par PVD sur un substrat à base de silicium. De la même manière que pour les dépôts d'AlN, ces résultats indiquent que l'approche décrite sur la Figure 5 permet d'améliorer la texturation suivant l'axe  $\vec{c}$  des films de ScAlN. Ainsi, l'intégration de cet empilement dans des dispositifs RF est intéressante puisqu'elle pourrait permettre d'améliorer significativement le  $k_{eff}^2$  sans dégrader drastiquement le facteur de qualité Q.

### V.3. Ouverture vers des dépôts CVD haute température

Pour terminer, et sans détailler cette partie, il est intéressant de noter que l'approche présentée sur la Figure 5 ne se limite pas à une croissance de films d'AlN ou d'AlN dopés par PVD ou même à croissance de type homoépitaxiale. En effet, des dépôts à plus haute température de type CVD ont été mis en œuvre et permettent l'élaboration de films d'AlN, de nitrure de gallium (GaN) et de carbure de silicium (SiC). Des résultats prometteurs ont été obtenus même si un travail important d'optimisation reste à mettre en place pour améliorer la qualité des films élaborés.

## VI. Conclusions et perspectives

Ces travaux de thèse ont permis de démontrer que l'utilisation du matériau MoS<sub>2</sub> comme couche d'accommodation permet d'améliorer de manière significative la texturation de l'AlN déposé par PVD. Cependant, au-delà d'une épaisseur critique d'environ 200 nm, la croissance directe d'AlN PVD sur MoS<sub>2</sub> engendre une délamination inhérente à cet empilement. Ainsi, un procédé reposant sur la nitruration du MoS<sub>2</sub> à travers une fine couche d'AlN PVD (< 5 nm) a été développé. Il permet de résoudre la problématique de délamination tout en conservant une forte orientation préférentielle des films d'AlN et AlN dopés au Sc élaborés par PVD. Cette approche peut également adresser des dépôts de type CVD ainsi que la croissance d'autres matériaux comme SiC ou GaN.

Un axe d'amélioration essentiel de cette thèse semble être l'optimisation de la couche mince d'AlN (< 5 nm) servant de couche de pré-texturation déposée sur MoS<sub>2</sub> avant la nitruration. En effet, la qualité cristalline des films d'AlN et d'AlN dopés Sc élaborés semble être limitée par la qualité de cette couche de pré-texturation. Une approche intéressante serait de réaliser cette couche mince d'AlN par CVD dans une gamme de température permettant de conserver l'intégrité cristalline du MoS<sub>2</sub>. Ainsi, le procédé de nitruration sous NH<sub>3</sub> pourrait être réalisé *in situ* et suivi d'une reprise de croissance d'AlN, GaN ou AlGaIn par CVD.

